European
Southern
Observatory

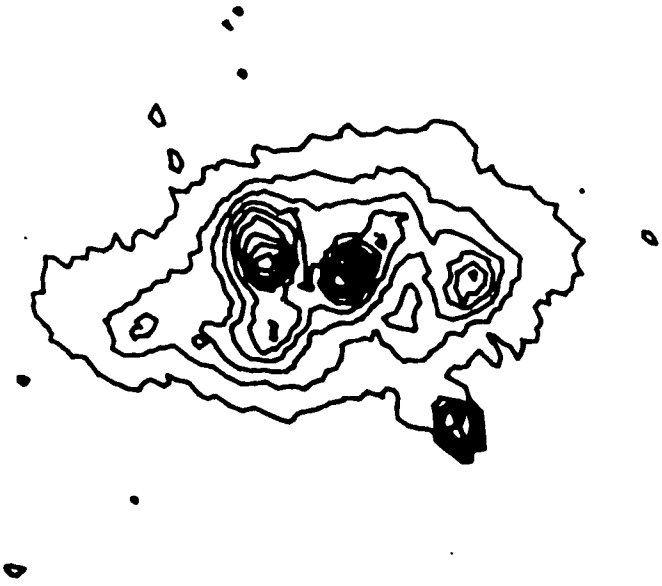

ESO WORKSHOP ON

TWO DIMENSIONAL PHOTOMETRY

Arranged in Cooperation
with the Leiden Observatory

Noordwijkerhout,
21–23 November 1979

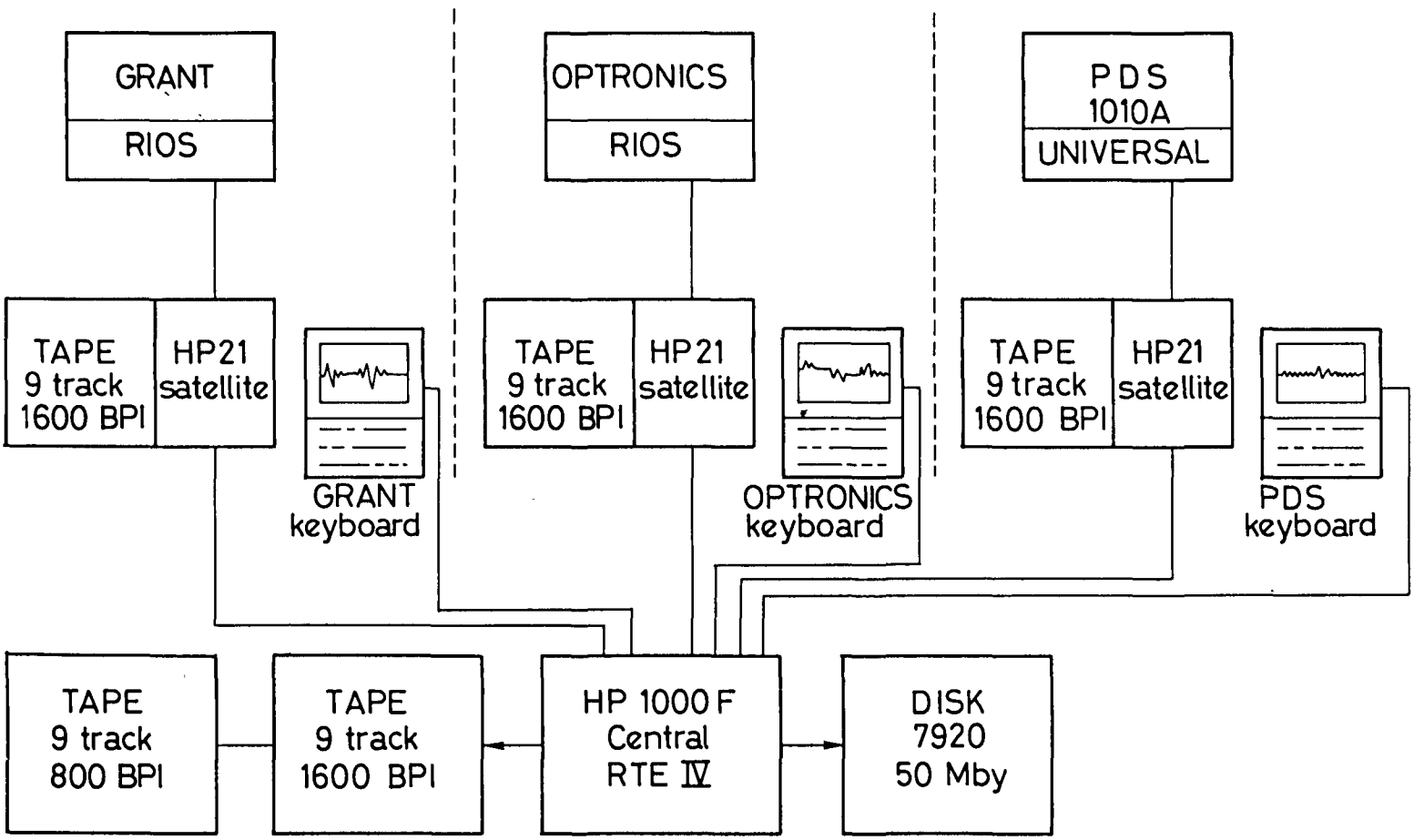

PROCEEDINGS

Edited by P. Crane and K. Kjär
March 1980

ESO WORKSHOP ON

TWO DIMENSIONAL PHOTOMETRY

Arranged in Cooperation with the Leiden Observatory

Noordwijkerhout, 21–23 November 1979

PROCEEDINGS

Edited by P. Crane and K. Kjär

March 1980

ACKNOWLEDGEMENT

This workshop grew out of the realisation that two dimensional photometry is a rapidly expanding area of astrophysical interest. This is clearly evident from the number of papers presented and from the number of participants. We would like to thank the authors and participants for their contributions to this workshop. We would also like to thank the sponsoring institutions, European Southern Observatory and Leiden Observatory, for their full and generous support.

The Organizing Committee

P. Crane
P.O. Lindblad
R. le Poole
H. van der Laan

EDITORS' NOTE

These proceedings are the result of a three day workshop sponsored by the European Southern Observatory (ESO) in collaboration with the Leiden Observatory. This workshop was similar to others sponsored by ESO being a combination of invited and contributed papers. The proceedings have been reproduced from camera ready manuscripts provided by the authors themselves in final form. The discussion portion of the actual workshop has not been included in these proceedings.

Many people helped to make this a successful workshop and to produce these proceedings. We would like to thank in particular Renate van Doesburg and Petra Steehouwer.

P. Crane K. Kjär

LIST OF PARTICIPANTS

van Albada, T.	Kapteyn Astronomical Institute Postbus 800, NL-9700 AV Groningen
Albrecht, R.	Institut für Astronomie Türkenschanzstrasse 17, A-1180 Wien
Ardeberg, A.	ESO - Chile
Athanassoula, E.	Observatoire de Besançon, 41, av de l'Observatoire, F-25000 Besançon
Becker, H.J.	Max Planck Institut für Radioastronomie Auf dem Hügel 69, D-5300 Bonn
Bijaoui, A.	Observatoire de Nice B.P.252,F-06007 Nice
Blaauw, A.	Sterrewacht Leiden Postbus 9513, NL-2300 RA Leiden
Bloemen, H.	Sterrewacht Leiden Postbus 9513, NL-2300 RA Leiden
van Breugel, W.	Sterrewacht Leiden Postbus 9513, NL-2300 RA Leiden
Brinks, E.	Sterrewacht Leiden Postbus 9513, NL-2300 RA Leiden
de Bruyn, A.G.	Radiosterrewacht Dwingeloo Postbus 2, NL-7990 AA Dwingeloo
Crane, P.	ESO - Geneva
Davenhall, A.C.	University Observatory Buchanon Garden, GB-St. Andrews
Davoust, E.	Observatoire de Besançon 41, av de l'Observatoire, F-25000 Besançon
Degewij, J.	Jet Propulsion Laboratory Mail-Stop 183-501, 4800 Oak Grove Drive, Pasadena, CA 91103, USA
Disergo, S.	Osservatorio Astronomico I-35100 Padova
Dodd, R.J.	Royal Observatory Blackford Hill, GB-Edinburgh EH9 3HJ
Eichendorf, W.	Astronomisches Institut Postfach 102148, D-4630 Bochum 1
Ekers, R.D.	Kapteyn Astronomical Institute Postbus 800, NL-9700 AV Groningen

Ekman, A.	Astronominska Observatoriet Box 515, S-751 20 Uppsala
Ellis, R.S.	University of Durham Dept of Physics, Science Labs., South Road, GB-Durham DH1 3LE
Feitzinger, J.	Astronomisches Institut Postfach 102148, D-4630 Bochum 1
Frandsen, S.	Institute of Astronomy University of Aarhus, DK-8000 Aarhus C
Fraser, C.W.	University Observatory Buchanon Gardens, GB - St. Andrews
Frisk, U.	Stockholm Observatory S-133 00 Saltsjöbaden
Gaida, G.	Landessternwarte Königstuhl, D-6900 Heidelberg 1
Gilmore, G.	Royal Observatory Blackford Hill, GB-Edinburgh EH9 3HJ
Greenberg, J.M.	Sterrewacht Leiden Postbus 9513, NL-2300 RA Leiden
van Groningen, E.	Sterrewacht Leiden Postbus 9513, NL-2300 RA Leiden
Grosbøl, P.	ESO - Geneva
Hagerbo, O.	Lund Observatory Svanegatan 9, S-222 24 Lund
Harten, R.	Sterrewacht Leiden Postbus 9513, NL-2300 RA Leiden
Illingworth, G.D.	Kitt Peak National Observatory P.O. Box 26732, Tucson, AZ 85726, USA
Jørgensen, H.	Copenhagen Observatory Ostervoldgade 3, DK-1350 Copenhagen
Katgert, J.K.	Sterrewacht Leiden Postbus 9513, NL-2300 RA Leiden
Kormendy, J.	Kitt Peak National Observatory P.O.Box 26732, Tucson, AZ 85726, USA
Kron, R.	Yerkes Observatory Williams Bay, WI 53191, USA
van der Kruit, P.C.	Kapteyn Astronomical Institute Postbus 800, NL-9700 AV Groningen

van der Laan, H.	Sterrewacht Leiden Postbus 9513, NL-2300 RA Leiden
Lachièze-Rey, M.	Centre d'Etudes Nucléaires de Saclay Service d'électronique physique, B.P. 2, F-91190 Gif-sur-Yvette
Lindblad, P.O.	ESO - Geneva
Linde, P.	Lund Observatory Svanegatan 9, S-222 24 Lund
Lindgren, H.	Lund Observatory Svanegatan 9, S-222 24 Lund
Lortet, M.C.	Observatoire de Paris D.A.F., F-92190 Meudon
Lundgren, K.	Astronomical Observatory Box 515, S-751 20 Uppsala
Lynga, G.	Lund Observatory Svanegatan 9, S-222 24 Lund
Macchetto, F.	European Space Agency - ESTEC Domeinweg, NL - Noordwijk
Malagnini, M.L.	Osservatorio Astronomico via Tiepolo 10, I-34131 Trieste
Marcelin, M.	Observatoire de Marseille 2 place le Verrier, F-13009 Marseille
Materne, J.	Astronomisches Institut Ernst-Reuter-Platz 7, D-1000 Berlin
McMullan, D.	Royal Greenwich Observatory Herstmonceux Castle, GB-Hailsham, Sussex
Melnick, J.	ESO - Geneva
Nanni, D.	Osservatorio Astronomico di Roma Viale del Parco Mellini, I - Roma
Nielsen, F.	Copenhagen Observatory Ostervoldgade 3, DK-1350 Copenhagen
Nieto, J.L.	Observatoire du Pic-du-Midi F-65200 Bagnères-de-Bigorre
Nieuwenhuizen, H.	Sterrewacht "Zonnenborgh" Zonnenborgh 2, NL - Utrecht
Norman, C.	Sterrewacht Leiden Postbus 9513, NL-2300 RA Leiden

Norris, P.	European Space Agency - ESTEC Domeinweg, NL-Noordwijk
Oostrijk, L.	ESO - Geneva
van Paradijs, J.	Astronomical Institute Roeterstraat 15, NL-1018 WB Amsterdam
Pel, W.	Kapteyn Astronomical Institute Mensinghweg 20, NL-Roden
Pittella, G.	Osservatorio Astronomico di Roma Via del Parco Mellini, I - Roma
le Poole, R.	Sterrewacht Leiden Postbus 9513, NL-2300 RA Leiden
Poncet, P.F.	IRAM, 53 av de Martyrs, F-38026 Grenoble
Radeke, H.W.	Observatorium Hoher List D-5568 Daun
de Ruiter, H.	ESO - Geneva
Scharnweber, P.	Firma C. Zeiss Postfach 1369, D-7082 Oberkochen
Schnur, G.	ESO - Chile
Schoenmaker, A.A.	Sterrewacht Leiden Postbus 9513, NL-2300 RA Leiden
von Sengbusch, K.	Max Planck Institut für Physik u.Astrophysik Föhringer Ring 6, D-8000 München 40
Shane, W.	Sterrenkundig Instituut Toernooiveld, NL-6225 Nijmegen
Shostak, S.	University of Groningen Postbus 800, NL-9700 AV Groningen
Spaenhauer, A.	Astronomisches Institut Venusstrasse 7, CH-4102 Binningen
Staller, R.A.	Sterrewacht Leiden Postbus 9513, NL-2300 RA Leiden
Swaans, L.	Sterrewacht Leiden Postbus 9513, NL-2300 RA Leiden
Thomsen, B.	Institute of Astronomy University of Aarhus, DK-8000 Aarhus C

Tremmel, R.	Max Planck Institut für Astronomie Königstuhl, D-6900 Heidelberg 1
Trevese, D.	Osservatorio Astronomico di Roma Via del Parco Mellini, I - Roma
Ulrich, M.H.	ESO - Geneva
Valentijn, E.	ESO - Geneva
Vignato, A.	Osservatorio Astronomico di Roma Via del Parco Mellini, I - Roma
Wamsteker, W.	ESO - Chile
Wehinger, P.	Max Planck Institut für Astronomie Königstuhl, D-6900 Heidelberg 1
Weliachew, L.	IRAM 53, av de Martyrs, F-38026 Grenoble
Westphal, J.A.	California Institute of Technology Pasadena, CA 91125, USA
Wielebinski, R.	Max Planck Institut für Radioastronomie Auf dem Hügel 69, D-5300 Bonn
Windhorst, R.	Sterrewacht Leiden Postbus 9513, NL-2300 RA Leiden
Wlérick, G.	Observatoire de Paris F-92190 Meudon
Woltjer, L.	ESO - Geneva
Worswick, S.	Royal Greenwich Observatory Herstmonceux Castle, GB-Hailsham, Sussex
de Zeeuw, P.	Sterrewacht Leiden Postbus 9513, NL-2300 RA Leiden

CONTENTS

SECTION IV

SECTION V

SECTION I

Photographic and Electronographic Recording and Data Extraction

PHOTOGRAPHIC RECORDING AND DATA EXTRACTION

R.S. Le Poole
Sterrewacht Leiden

Although the drawbacks of photographic emulsions with respect to photoelectric detectors (notably their non-linear and relatively low response) has been obvious for more than 3 decades, there is actually only one area of application, where they have effectively been replaced by photoelectric devices. This is in photometry of rather bright stars, brighter than the integrated sky contribution in the enclosing diaphragm.

The uneasy feeling that one is doing something wrong in "wasting" so many expensive photons when using a photographic plate has at the same time contributed significantly to the optimisation of its application, and also to the development of new and better emulsions, notably IIIaJ and IIIaF. It has stimulated the identification and use of those parameters in terms of which the photometric and detective performance of a photographic plate can be best evaluated. This in turn has greatly contributed to the development of almost "standard" recipes for pre- or post-exposure treatment, dependent on the type of application (see e.g. Millikan, A.G. (1978) and Millikan, A.G. and Sim, M.E. (1978)).

The result of the use of a photographic plate is a record of the (mean) intensity distribution across the emulsion during the exposure in terms of a varying surface density of silver. This silver is deposited in the form of very small clumps, deriving from those grains of silver-halide which were stimulated to development by the photons of the exposure. These clumps ($\lesssim$ 1 μm) cause something like "shot noise" in the relevant recorded parameter, which is the density (D) of the plate, defined as D = -log (fractional transmission (T)). Simple considerations make it clear, that surface density of silver and density D are equivalent, although e.g. the size distribution of the developed grains causes deviations from perfect proportionality.

The noise in a photographic record, σ_D, is caused by the Poisson-distributed grains, which act both as absorbers and as scatterers. It is determined by the size-distribution of the developed grains, which reflects the size-dependent sensitivity distribution of the original silverhalide crystals, while it also depends on the scattering properties of the silverdeposit. As one may expect one finds indeed that σ_D varies as $(\text{area})^{-1/2}$ with the scanning aperture used for the read out. Also one may expect σ_D to be an emulsion characteristic. Indeed Furenlid et al.(1977) have shown for IIIaJ plates, that σ_D is essentially independent of

the sort and amount of hypersensitising treatment given. This indicates that hypersensitisation apparently affects the grain sensitivity distribution independent of grain size.

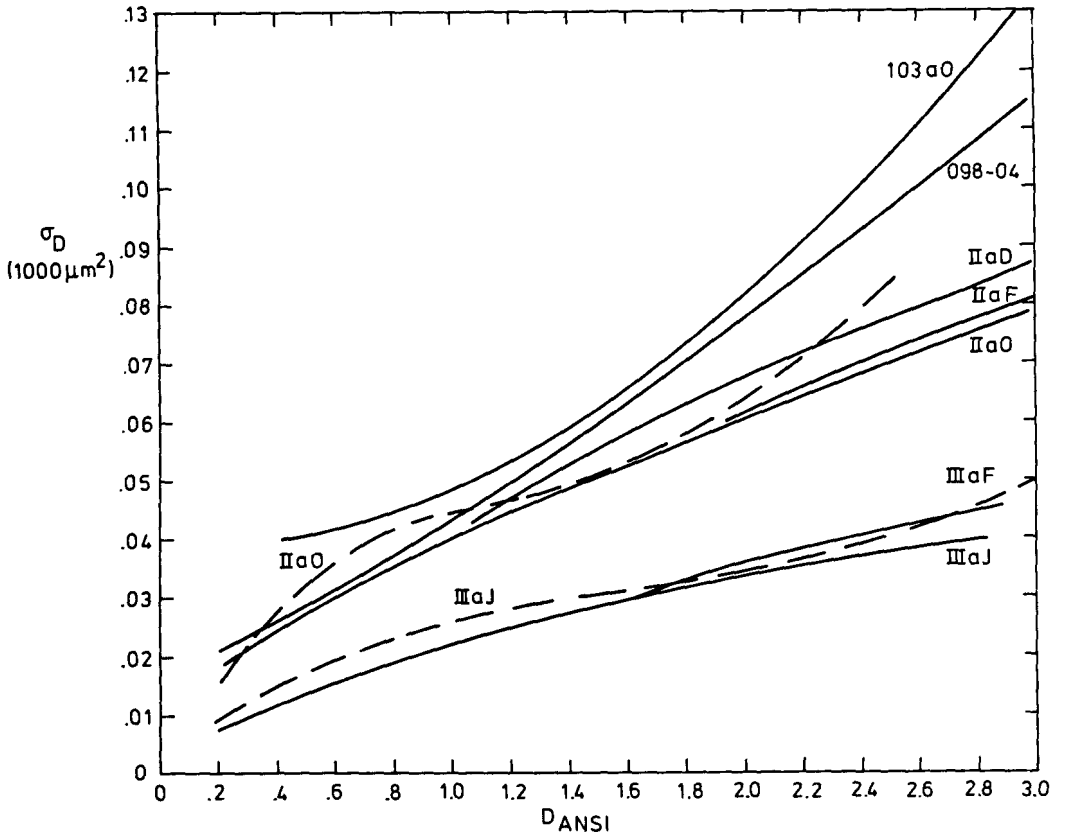

Fig. 1. Noise of some photographic plates commonly used in astronomy. Data by Furenlid (1978) are indicated by full lines, those by Latham (1978) by dotted lines.

Figure 1 shows the σ_D relations for some commonly used astronomical emulsions. The data are taken from Furenlid (1978) and Latham (1978). Although the general agreement between the two authors is quite good, especially in the useful density range, the difference is considerably larger than can be explained by their measuring errors. In view of the results of Furenlid et al. (1977) it is not likely that the differences are caused by real differences between the respective emulsion samples. The data however are converted from instrumental densities, which are semispecular and measured with aperture sizes different from the "standard" 1000 μm^2 (see figure 2). Latham converted from semispecular density to diffuse density (D_{ANSI}) assuming a linear relation between the two, and Furenlid probably did the same. Furthermore conversion to 1000 μm^2 was achieved through the $(area)^{-1/2}$ dependence of σ_D. However, due to the scattering properties of the silver grains both relationships require modification. At low densities the transition from mainly single to mainly multiple scattering will affect the repartition of the

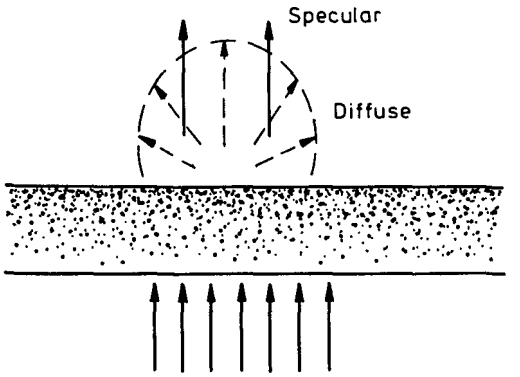

Fig. 2. Specular density is measured using only the light, that leaves the emulsion in the direction of the collimated input beam (negligible solid angle). Diffuse density is defined by all the light leaving the emulsion (solid angle = 2π steradian). In reality semispecular densities are measured using optics with reception solid angles of the order of 10^{-1} to 10^{-2} steradian.

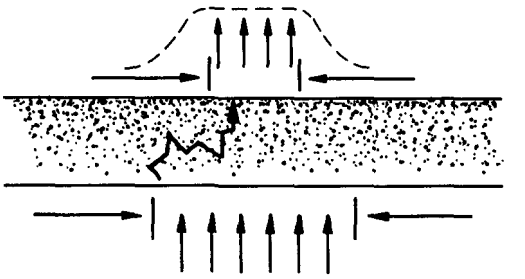

Fig. 3. The influence of multiple scattering on the definition of the bounderies of the measuring aperture. The dotted line indicates the weight with which a given position enters the transmission reading. (Note that very small illuminating apertures, matched to the read out aperture for stray light suppression, will change this picture again by modifying the density dependence of the effective measuring aperture in a more complex way.)

light over the exit solid angle. This changes the ratio between instrumental density and D_{ANSI} in a way, which depends on density and on the semispecularness of the microdensitometer. Moreover, at high densities the dominant contribution from multiple scattering causes lateral displacement of the photons between entry and exit from the emulsion with a characteristic distance comparable to the thickness of the silver grain deposit. Thus one should reckon with a read out Point Spread Function which has a density dependent characteristic width, thus causing the effective measuring aperture to exceed the nominal aperture by a density dependent amount (figure 3).

Note also, that e.g. for IIIaJ the density noise $\sigma_D \approx 0.04$ at a density $D_{ANSI} \approx 3$. This imposes severe requirements on microdensitometers, if they are to read out the full information content of such a dark area on the plate. The required dynamic range for full read out of a plate to these densities amounts to better than 10^4. At these levels stability, detector noise and stray light all become very serious aspects.

Although we are of course not astronomically interested in the noise itself of a photographic plate, and therefore the aforegoing has only a limited relevance for most practical applications, it shows that it would actually be almost surprising, if two investigators would actually agree quantitatively on the detailed densitometry of one and the same plate. And this not even considers

yet the conversion of density into surface-brightness during the exposure!

The parameter which is of interest of course is the signal to noise ratio rather than the noise itself. It describes the information-recording capacity of the photographic material, and together with the signal to noise ratio in the exposure, given by photon statistic, it allows an evaluation of the Detective Quantum Efficiency (DQE), which is simply the square of the ratio of the respective signal to noise ratios. Let E denote Exposure and σ_E the one standard deviation uncertainty in E. The quantity

$$(S/N)_{out} = (\frac{E}{\sigma_E})_{out}$$

is now to be expressed in terms of parameters of the plate. Note that

$$\sigma_E = \sigma_D \frac{dE}{dD}$$

and

$$dE = Ed(\ln E) = \frac{E}{\log e} d(\log E),$$

thus

$$(S/N)_{out} = \frac{0.4343}{\sigma_D} \frac{dD}{d(\log E)} = 0.4343 \frac{\gamma(D)}{\sigma_D} ,$$

a relation which has been given by many authors (see e.g. Furenlid (1978)).

These parameters are displayed in fig. 4 (data from Hoag et al.(1979)), together with the respective characteristic curves for Hydrogen-hypersensitised IIIaJ and IIaO. The exposure scale is calibrated absolutely in photons/1000 μm^2 and the results are given for a 1 hour exposure. This allows the construction of figure 5 by the relations

$$(\frac{E}{\sigma_E})_{in} = \frac{E}{\sqrt{E}} = \sqrt{E} \quad \text{(in photons per unit area)}$$

and

$$DQE = \{\frac{(S/N)_{out}}{(S/N)_{in}}\}^2$$

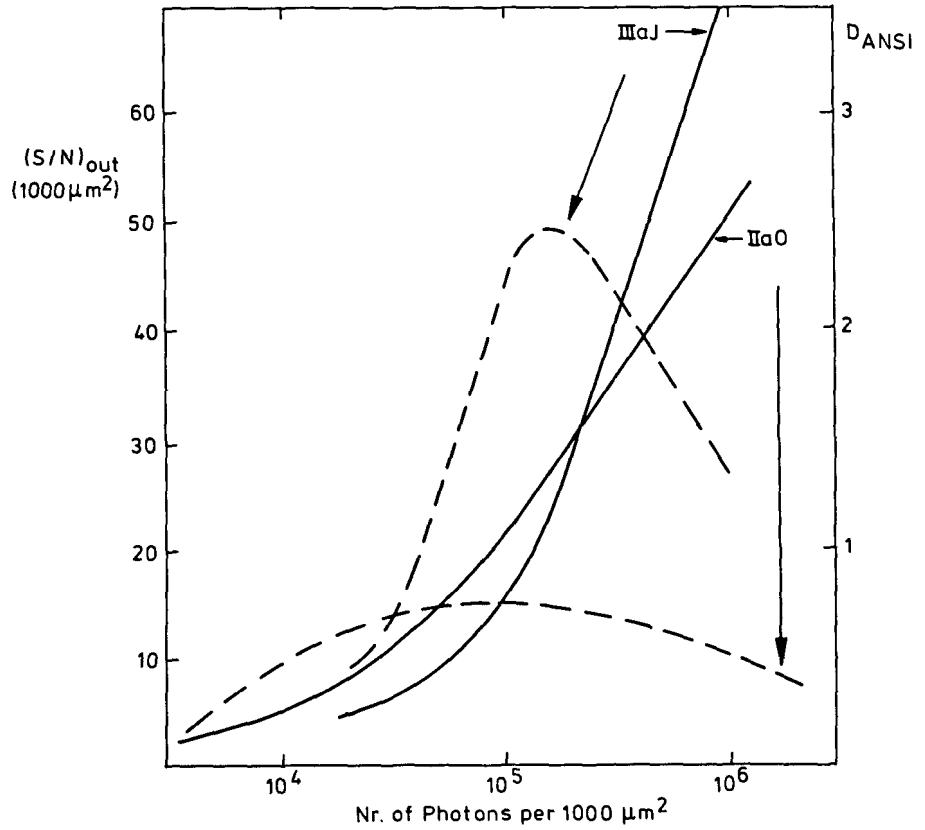

Fig. 4. Characteristic curves and signal to noise ratios per 1000 μm^2 for IIIaJ and IIaO, both hypersensitised in Hydrogen, and for an exposure duration of 1 hour. The exposure scale is calibrated absolutely, which allows the construtions of fig. 5 (data by Hoag et al.(1979)).

Many performance characteristics of photographic material can be read from these two figures

- The dynamic range in terms of exposure near optimal performance is very narrow indeed (of order factor 2). The extremely narrow peak in DQE with exposure is caused by the fact that at least a few photons ($\sim$ 4-5) are needed to render a silverhalide grain developable. The fact that it is wider for IIaO than for IIIaJ and also at a lower density means that among the most sensitive grains in IIaO there is a relatively larger fraction for which 2-4 photons suffice (c.f. Bird (1973)).
- It is clear that maximum DQE occurs at lower exposure than maximum $(S/N)_{out}$, which corresponds to maximum recorded information content. Although indeed the data gathering power of the telescope is best exploited at maximum DQE this will usually be offset by the logistics of changing plates and adding them after processing, so usually one wants to expose to about (just short of) maximum $(S/N)_{out}$.

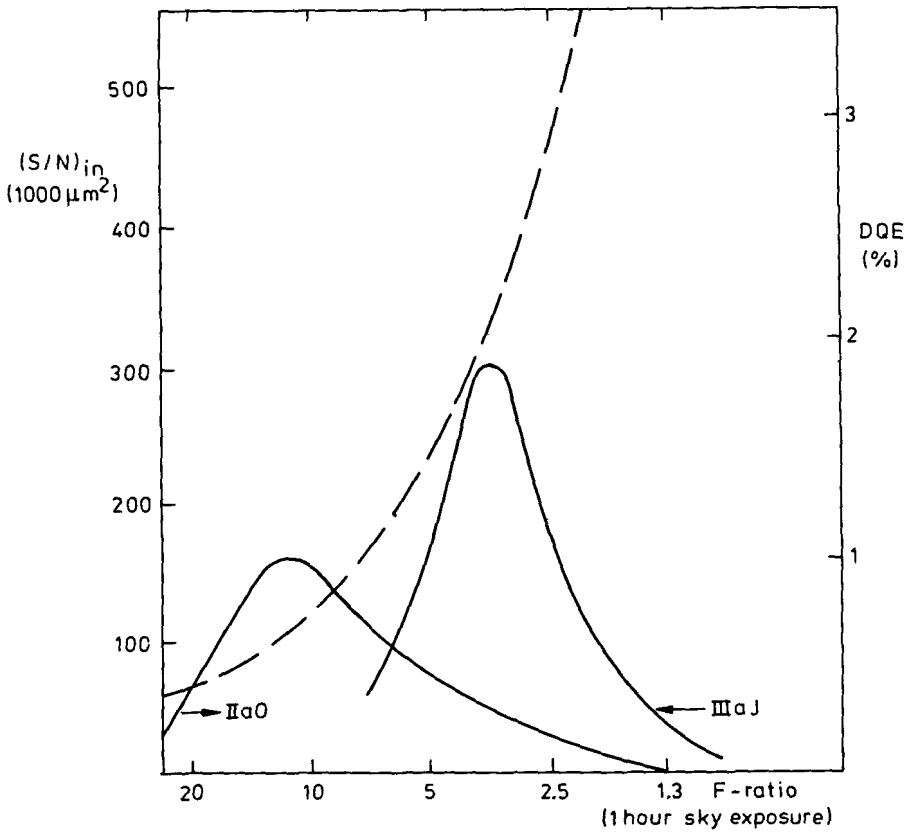

Fig. 5. $(S/N)_{in}$ per 1000 μm^2 and DQE of IIIaJ and IIaO, both hypersensitised in Hydrogen, and for an exposure duration of 1 hour. The exposure scale is the same as in fig. 4, but here expressed in terms of focal ratio of the telescope at a sky brightness of $22^m.5$ per $(arcsec)^2$.

- The fact that IIaO is superior to IIIaJ at a lower range of exposure is mainly important for the choice of emulsion with the focal ratio of the telescope. As long as one can put the optimum exposure onto IIIaJ in a realistic time, without giving away too much to reciprocity failure IIIaJ remains of course superior due to its larger DQE.

The fact that the dynamic range for optimum performance is so low makes it clear that photographic plates are best used in applications, where the dynamic range of the input signal is low, as is the case in detection of objects or features which are in intensity comparable to or dominated by the sky background. As calibration is relatively simple in this case, since it requires essentially only γ at the sky exposure, and as one may exploit the $(area)^{-1/2}$ dependence of the noise, rather impressive results in terms of accuracy are obtainable. The dominant problem here is non-uniformity of the developed plate which is usually caused by the development. The uniformity achieved depends on the agitation technique used (c.f. Miller (1971) and Millikan and Tinney (1977)). Even with special efforts aimed at achieving the best possible uniformity it appears that at a

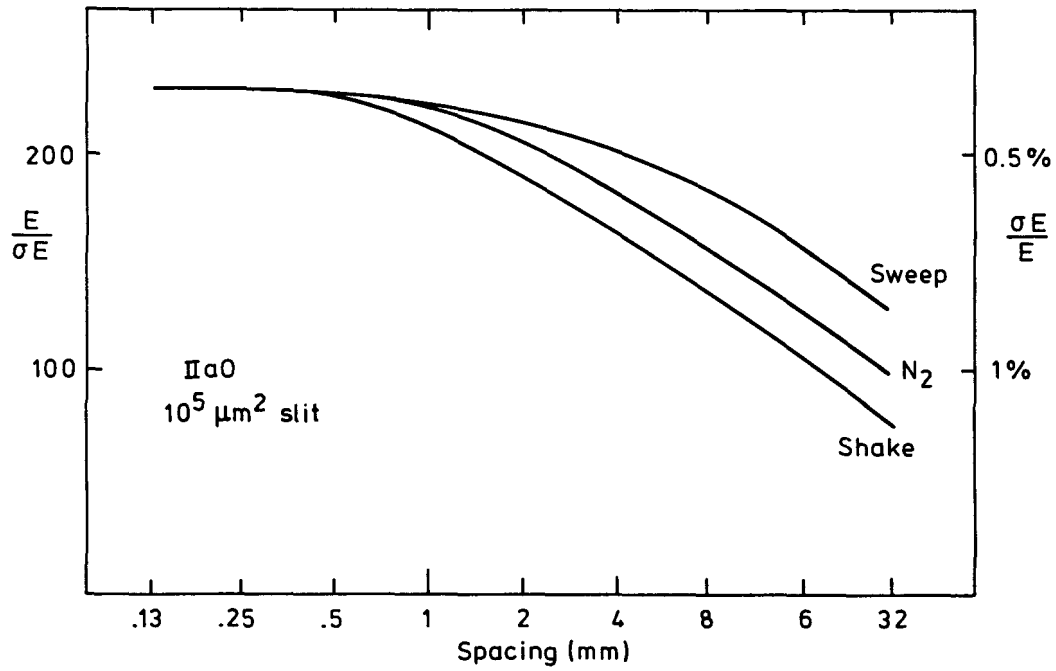

Fig. 6. $(S/N)_{out}$ and percentage accuracy as a function of spacing on the plate for IIaO, developed by means of different agitation techniques (due to Latham (1978)).

level of about 1% of sky background non-uniformity becomes the dominant impediment for surface photometry of larger areas (see figure 6, due to Latham (1978)). Latham (1978) has used "grid-photography", where he partially prevents exposure by means of a grid, and subsequently exposes this blank area to a "flat field" to separately calibrate the non-uniformities present after development. This way it appears possible to gain about 1 order of magnitude, reaching about 10^{-3} of sky, or 30^m per $(arcsec)^2$! For ultimate faintness, for example in the surface photometry of outer regions of nearby galaxies, a technique of this type seems imperative to get significantly fainter than 1% of sky.

The very narrow dynamic range as given by the DQE curves however is only part of the story. The $(S/N)_{out}$ shows a considerably larger dynamic range. In the case of IIIaJ this amounts to slightly more than a decade in exposure (actually limited by the very large density) at half maximum $(S/N)_{out}$, which is still 3% accuracy per 1000 μm^2, or for a coarser emulsion like IIaO almost two decades, amounting still to 10% accuracy per 1000 μm^2. This implies, that although one operates the photographic detector in these darkly exposed areas (very) inefficiently, one may still expect good performance as a pictorial photometer to about 5 magnitudes brighter than the sky. The lack of efficiency in fact often is of no concern, as one obtains these heavily exposed areas on the plate as a "bonus"

while exposing for sky-limited performance. As one in such applications has "managed" the calibration of the full response and therefore the sky background has lost its significance as a reference level, the limitation of 5 magnitudes brighter than sky in fact is not relevant. Thus one may also expect good performance at arbitrarily brighter levels like e.g. in stellar photometry with slow focal-ratio telescopes.

The "snag" however was already mentioned in passing: the calibration of the full response. Until now it is a major achievement to attain 5% accuracy over any appreciable fraction of the characteristic curve, although considerable effort has been and is being spent on this problem (e.g. Kormendy, later this session; see also Burstein (1979) or the recent circular no. 4 of the Working Group on Astronomical Image Processing). The approach has always been a rather empirical one, taking as a starting point the approximate linearity between density and log Exposure over a sizable range of the total response, and trying to describe the deviations from this relation in an empirically parametrised way.

There is however only one physical mechanism producing a genuine log Exposure dependence of density. This is the exponential intensity distribution with depth in the emulsion while exposing. Even that is not fully operative as the commonly used emulsions have an optical depth in the wavelength range of interest of only about 3. This optical depth is wavelength dependent (among other reasons because of sensitising dyes) and therefore γ is too. Hence the spectral sensitivity of the plate is significantly dependent on intensity (γ may vary as much as 20% in only 50 nm). The wavelength dependence of the opacity per unit length of the emulsion also causes the mean intensity averaged over depth to depend on wavelength, thereby causing shifts of the reciprocity characteristic along the log Exposure axis with wavelength. The approximate log-normality of the grain size distribution and the grain sensitivity distribution also cause an approximately linear dependence of D on log Exposure, but the deviations of these distribution functions from log normality are reflected in the characteristic curves. Furthermore the width of the grain sensitivity distribution is wavelength dependent, causing again γ-variation with wavelength.

In addition to the causes for systematic photometric errors mentioned above there are many more well-understood mechanisms affecting photometry, that do not appear in the calibration of photographic plates in common practice. I think the present knowledge and understanding of the photographic process warrants a hope for improvement if one were to express the response as completely as possible in terms of parameters describing the known physical mechanisms that determine the photographic response properties. Such a description should also contain adjacency effects (which cause response-dependent modifications of the effective

point spread function), and fog correction (c.f. Domini (1978); Miller (1977)). Both these problems again are mainly relevant in the large dynamic range applications.

In any case Astronomy need not despair, as most of these large dynamic range objects have sufficiently small angular sizes to fit well within the fields of the photoelectric pictorial techniques. Although disturbingly few quantitative data, collected with photoelectric pictorial detectors have sofar entered the literature one may expect their output to match their inherent performance capabilities in the near future. It seems that calibration of these devices has given many more problems than anticipated, something which is common to newly developed techniques. In particular stability and uniformity from pixel to pixel may not have been as good as for photographic material. However I feel confident, that in the near future both photographic material and photoelectric pictorial detectors will take their appropriate respective places. That should imply that photographic emulsions are exploited for their favorable aspects as there are: enormous number of pixels, a uniformity, reasonable at large - but very good at small scales, and very good dimensional stability, this all properly calibratable if used for small dynamic range applications. The by-product of obtaining a quantitative record of enormous amounts of information not aimed at in the particular observing program is thereby a very distinct bonus. The use of photographic plates will greatly benefit from the availability of photoelectric pictorial detectors, as these allow setting up photoelectric sequences, which will finally bring the calibration of plates up to standards.

Finally a few remarks on plate scanning equipment seem in place. We have seen that technical requirements for microdensitometers increase very steeply with the maximum density to be properly measurable. However large densities only cause dynamic range problems in the read out of a photographic record with a large dynamic range in the input signal, an application for which the photographic plate is not particularly suited. In fact most of the information available in the very dense areas of a photographic plate can be obtained more easily (and often better) by making an additional short exposure at the telescope on another plate or doing away with photography altogether, using photoelectric techniques.

So the need to be able to read "all" information from the plate actually applies only to plates, which cannot be retaken, because the sky looks different now than at the time when the plates were taken. This mainly refers to variable stellar magnitudes and to astrometry. If however in these applications one were to limit the dynamic range of a microdensitometer to about 2.5 in density above plate background the result would only be a slight loss in weight of the para-

meters derived for the few very bright stars on the plate with respect to exploitation of all information in the plate, while one need not worry about introducing biasses worse than those already introduced by the inherent non-linearity of the photographic detection. So it appears that a reasonable dynamic range of say $\Delta D \gtrsim 2.5$ of a microdensitometer suffices for $(100 - \varepsilon)\%$ of all applications, particularly if the observing program at the telescope is geared to it. The savings on plate scanning equipment made by relaxing the requirements this far may well buy you a nice CCD camera!

References

Bird, G.R.: 1973, A.A.S. Photobulletin No. 7, p. 4.

Burstein, D.: 1979, A.A.S. Photobulletin No. 20, p. 6.

Domini, J.F.: 1978, A.A.S. Photobulletin No. 18, p. 8.

Furenlid, I.: 1978, in "Modern Techniques in Astronomical Photograph", Proceedings ed. by West, R.M. and Heudier, J.L. (ESO), p. 153.

Furenlid, I., Schoening, W.E. and Carder, Jr., B.E.: 1977, A.A.S. Photobulletin No. 16, p. 17.

Hoag, A.A., Furenlid, I. and Schoening, W.E.: 1979, A.A.S. Photobulletin No. 14, p. 3.

Kormendy, J.: 1980, this volume.

Latham, D.W.: 1978, A.A.S. Photobulletin No. 18, p. 3.

Latham, D.W.: 1978, in "Modern Techniques in Astronomical Photography", Proceedings ed. by West, R.M. and Heudier, J.L. (ESO), p. 141.

Miller, W.C.: 1971, A.A.S. Photobulletin No. 4, p. 3.

Miller, W.C.: 1977, A.A.S. Photobulletin No. 16, p. 3.

Millikan, A.G.: 1978, in "Modern Techniques in Astronomical Photography", Proceedings ed. by West, R.M. and Heudier, J.L. (ESO), p. 287.

Millikan, A.G. and Sim, M.E.: 1978, in "Modern Techniques in Astronomical Photography", Proceedings ed. by West, R.M. and Heudier, J.L. (ESO), p. 294.

Millikan, A.G. and Tinney, J.R.: 1977, A.A.S. Photobulletin No. 15, p. 8.

General References

a) "Modern Techniques in Astronomical Photography", 1978, Proceedings of a workshop held in Geneva May 16-18, 1978, edited by West, R.M. and Heudier, J.L. (ESO).

b) "The Theory of the Photographic Process", third edition, 1966, Ed. Mees, C.E.K. and James, T.H., The MacMillan Company, New York.

c) "Kodak Plates and Films for Scientific Photography", first edition, 1973, Eastman Kodak Company, Publication Nr. P-315.

REVIEW OF ELECTRONOGRAPHIC SYSTEMS

D. McMullan
Royal Greenwich Observatory, Herstmonceux, Sussex, England.

1. INTRODUCTION

In the 45 years that have elapsed since the late André Lallemand invented the electronographic camera, an immense amount of work has been done in laboratories in Europe and in the United States, with the aim of making electronography a common astronomical technique.

Most of the effort has been directed towards improving the cameras, making them more efficient and easier to operate. Unfortunately much less attention has been paid to the other components of the electronographic system: the recording emulsion, the microdensitometer, and image processing.

The emulsions used have been mainly those produced for nuclear physics applications in which a high recording efficiency for chargedparticles and good resolution are of prime importance but uniformity of the coating and freedom from blemishes are of lesser concern. On the other hand, for astronomy the latter factors are of equal importance with the first two; unfortunately since the market for astronomical emulsions is comparatively small, manufacturers have been reluctant to invest the rather large amount of money that seems to be required if nuclear track emulsions are to have the high quality that is expected from photographic emulsions.

The microdensitometers that are commonly used are those which have been developed for the measurement of photographic plates and although on the whole they are satisfactory for electronographic applications difficulty is often experienced because of the much larger range of densities that are encountered. Also, because of the linear relationship between exposure and density with some nuclear track emulsions, microdensitometer non-linearities assume a much greater importance than in the photographic case.

Image processing techniques of varying sophistication have been used for a number of years, particularly for flat-fielding and density integration in stellar photometry, but not to the extent that is usual in the case of electronic detectors with digital output. A microdensitometer can be regarded as such a detector and most of the processing that is possible on the output from a digital detector can be done on electronographic images; one of the obstacles has possibly been that on many microdensitometer systems the setting up is very time-consuming.

Each of these components is discussed later in the paper but first it is of interest to answer the question "how efficient could an electronographic

TABLE I

"Benchmark" Camera

DQE λ(nm)	Photocathode type	Camera DQE
300-450	bialkali	30%
300-600	trialkali	20%
500-800	GaAs	17%
900	GaAs	1%

Resolution	∿200 lp mm^{-1} (5% MTF)
Storage capacity	15 x 15 μm^2 pixels: ∿10^4 electrons per pixel
Background	∿1 electron per hour per pixel (with cooled trialkali photocathode, 15 x 15μm^2 pixels)
Number of pixels	15 x 15 μm^2 pixels: 85 mm Ø field: 2.5 x 10^7 200 mm Ø field: 1.4 x 10^8

system be?" This will provide a benchmark for the assessment of the performance of actual systems and the possibilities of improvement, and may be useful when comparing electronographic detectors with the new solid-state detectors, such as CCD's. Eventually the latter will no doubt supersede all other types of detector but at the moment they also have their limitations.

Let us consider a very basic electronographic camera: transparent photocathode, photoelectron accelerating and focussing system, and electronographic emulsion. Forgetting about all the technological difficulties that follow because of the incompatibility of the photocathode and the emulsion, let us assume that we have a good example of a modern photocathode matched to the spectral range being used, photoelectron acceleration to 30 keV and focussing by parallel electric and magnetic fields, and a really uniform very fine grain nuclear track emulsion. The microdensitometer is assumed to be linear to D = 5 and to scan at such a rate that photon noise is negligible.

The detective quantum efficiency (DQE) will approach the responsive quantum efficiency (RQE) of the photocathode because virtually every photoelectron that enters the emulsion leaves a track of several developable grains. Although approximately 5% of the electrons will be reflected at the surface of the emulsion these could still contribute to the image if a sufficiently strong magnetic focussing field were used to ensure that the electrons returned to from where they were reflected. The electronographic emulsion is not a completely noise-free detector of electrons because of the variance in the sizes and number of grains per track but an overall DQE of about 85% of the photocathode RQE appears to be realisable.[1] Table I shows the DQE's that could be obtained over the indicated spectral ranges with good examples of existing types of photocathode.

The spatial resolution of the "benchmark" tube would be limited by electron scattering in the emulsion to about 200 lp mm^{-1} (5% MTF).[2] The storage capacity with a very fine grain emulsion is $\sim$50 electrons μm^{-2} for a density D = 5, i.e. $\sim 10^4$ electrons per pixel for 15 x 15 μm^2 pixels. These figures are also shown in Table I together with those for background (thermal emission from the photocathode) and the number of pixels for cameras the size of the 85-mm RGO camera[3] and the proposed camera for the Space Schmidt telescope.[4]

This performance is not of course reached by actual systems and each of the system components will now be discussed and their failings identified.

2. ELECTRONOGRAPHIC CAMERAS

There are now at least 6 types of electronographic camera in astronomical use and it would take too long to describe them all. However, they fall into two general classes: a) the classical Lallemand type[5] where the emulsion is

TABLE II

Electronographic Cameras

	Classical	Lenard Window
Examples	(a) Lallemand[5] (b) Kron [6]	(a) Spectracon[7] (b) RGO[9] (c) Griboval (UT)[8]
Photocathodes	(a) S.1, S.9, S.11, S.20	(a),(b) any (III-V ?) (c) S.9, S.11 (S.20 ?) RGO λ(nm) 445 545 645 793 trialkali Thick 17% 16% 7% 0.6% Thin 24% 13% 5% 0.2%
*DQE (with efficient emulsion)	∿ 80% of RQE	55 - 65% of RQE
Resolution (5% MTF)	depends on electron optics up to emulsion limit	(a),(c) up to 100 lp mm^{-1} (b) ∿50 lp mm^{-1}
Plate/film size	(a) 15 to 81 mm Ø (b) 20 mm Ø	(a) 10 x 25 mm^2 (b) 40, 85 mm Ø (c) 50 mm Ø
Ease of operation and calibration	(a) More difficult (b) Medium difficulty	Easy
Availability	?	(a),(b) Commercial (c) ?

* neglecting signal induced background

cooled by liquid nitrogen to prevent gas desorption, and there may or may not be a valve[6] to facilitate plate changing, and b) the Lenard window type,[7-9] first successfully employed by McGee,[7] where the emulsion is separated from the photocathode by a gas-tight membrane (Lenard window) which is thin enough to transmit high energy electrons.

Table II shows the salient characteristics of the two classes of camera. There are some limitations on the types of photocathode that can be used in particular cameras. In general the photocathodes in Lenard window tubes will be more efficient than those in the "classical" tubes because of the higher vacuum in the former. An exception would seem to be the Griboval (University of Texas) camera which employs a polyimide (Kapton) window that is not completely vacuum-tight.[8] Quantum efficiencies realised in the RGO cameras with trialkali photocathodes are also shown.[9]

The DQE of the classical type of camera generally fall short of the figures given for the "Benchmark" camera because the electrons reflected from the emulsion do not return to their point of reflection and so produce a signal-induced background. Neglecting the signal-induced background from this and other causes the DQE is thus $\sim$ 80% of the photocathode RQE. With the Lenard window tubes there is reflection and absorption of the electrons in the window material and only some 75% of the electrons are transmitted (40 keV electrons, 4μm thick mica). The electrons that are transmitted are no longer monoenergetic because of inelastic scattering in the window and this increases the variance in the number of grains per track and hence the emulsion noise. The DQE is thus only about 55% of the photocathode RQE although it can be increased to over 60% by raising the accelerating voltage to say 60 kV to obtain higher electron transmission.[9]

The resolution of the "classical" cameras seems to depend mainly on the electron optical system rather than electron scattering in the emulsion but the reflected electrons may also be a factor. Electron scattering in the Lenard window is the main limiting factor with this type of tube and in addition to the window thickness the closeness of the contact between the emulsion and the window surface is of cardinal importance. The Griboval camera is particularly good in this respect because electrostatic force is used.[8] Back scattered electrons have little effect in Lenard window tubes because they have lost energy and are unable to penetrate the window. Other characteristics of the cameras are given in Table II.

All of the cameras can produce good electron images within their particular physical limitations, but it must be admitted that actual cameras in the field often do not function as well as advertised in published

TABLE III

Factors limiting Camera Performance

Calibratable (in principle)		
Non-uniformities	Photocathode	sensitivity f(R,θ), f(λ) dead spots
	Barrier membrane	electron absorption f(R,θ) particles (fixed)
Signal-induced background	Faceplate	multiple reflections
	Photocathode	transmitted and backscattered light
	Barrier membrane or emulsion	backscattered electrons (effect small in barrier membrane tubes.)
Background	Photocathode	thermal emission (if const)
	Faceplate	radioactivity
Non-calibratable		
Non-uniformities	Faceplate) Photocathode) Barrier membrane)	particles (not fixed)
Background	Photocathode	dark current f(t)
	Tube structure	dark current f(t)
	Faceplate	cosmic rays
Other f(t)	Drift, photocathode stability, etc.	

papers written by their inventors; however it would be invidious to discuss these matters in terms of particular cameras. Instead, some of the deficiencies that afflict all cameras to some degree are listed in Table III. They may be divided into those that can be calibrated or described in terms of an instrumental profile and those that vary randomly in time and cannot be removed by processing the image. It is necessary to study each type of camera in detail if the relative importance of these factors is to be assessed.

In spite of their deficiencies, present day electronographic cameras are reasonably efficient if the requisite care is taken in their preparation. Unfortunately the position regarding electronographic emulsions is not so satisfactory.

3. ELECTRONOGRAPHIC EMULSIONS

Almost any photographic emulsion can be used for exposure to electrons. In fact, in electron microscopy photographic plates or film are commonly employed in preference to nuclear track emulsions because high quantum efficiency and linearity are of lesser importance compared with uniformity. A nuclear emulsion differs from a photographic one mainly by having a much higher proportion of silver halide: 50% as compared with about 15% in the photographic case. This is to give a high stopping cross-section but it also results in a very high saturation density - at least 30 with L4 - with the consequence that the initial part of the exposure characteristic is linear within a few percent up to quite a high density ($\sim$ 5 with L4). Incidentally it should be mentioned that linearity is not only desirable for simplifying data reduction but is also essential since any serious departure indicates a fall-off in DQE. The main difference between nuclear track emulsions is in the saturation density and in the size of the developed grains which determines the sensitivity of the emulsion and also of course the storage capacity.

There are two manufacturers of nuclear track emulsions - Ilford Ltd and Eastman Kodak. The characteristics of the raw emulsion made by Ilford are very good but difficulties arise when the emulsion is coated onto the base which may be polyester (Melinex) or glass. The principal faults are non-uniformity in thickness, pinholes, and foreign particles embedded in the emulsion and on the surface. Non-uniformity is not a problem as long as the minimum thickness is greater than the range of the electrons ($\sim$ 10μm for 40 keV electrons). The accelerating voltage in the RGO cameras

is 40 kV and an emulsion thickness of 15μm is now specified to ensure that the electrons cannot reach the film base. The difficulties Ilford experience appear to be partly due to the fact that the emulsion is coated on to individual plates in small batches. Over the past year they have made considerable efforts to improve the quality of this product and it is pleasant to report that the quality control tests now carried out at RGO on samples of all incoming film indicate considerable improvement during the past year. These tests include visual inspection and sensitometry.

Eastman Kodak emulsions on polyester (Estar) film base are coated in continuous lengths by machine and appear to be freer from defects although not entirely so. They have not yet marketed an emulsion with the desirable characteristics of L4 although an experimental film seems very promising: it has about one half the speed of L4 but grain counts indicate that the DQE is as high.

Some cameras, and in particular the RGO type, need film on thin polyester base ($\leq$ 70μm thick). Until recently this has prevented the use of Eastman Kodak film but it now appears that this firm is ready to supply nuclear emulsions on 2.5 mil (64μm) base.

Photographic emulsions such as Agfa Gevalith (on 50μm polyester) which has the same speed as L4 but is linear to only about D = 1, and Kodak Definix X-ray film have been used for electronography. Since they are mass produced they are cleaner and more uniform, and also much cheaper. The DQE has not been measured but they have been used for astronomical observations.[10, 11]

4. MICRODENSITOMETERS

Desirable characteristics of a microdensitometer system for measuring electronographic emulsions may be summarised as follows:

1. Accurate density measurement (linear) over the range 0-5D (specular) in increments of $\pm$ 0.001D.

2. High speed (thousands of samples per second). Even at 10^4 sec^{-1} it would take 6 hours to measure an 85 mm Ø area with a 5 x 5 μm^2 aperture.

3. Small sampling aperture (say 5 x 5 μm^2), to reduce inaccuracy due

to transmission averaging.[12]

4. High positional accuracy (at least 0.5 μm), to enable accurate convolution with photocathode maps, etc.

Unfortunately with present technology it does not appear to be possible to satisfy all these requirements simultaneously. For example at high densities photon noise becomes the limiting factor and necessitates a much slower speed than that indicated above. These problems are discussed in the literature[12, 13] and in the accompanying paper by B Thomsen on the PDS microdensitometer, which is one of the most often used by astronomers.

The digitised output images from the microdensitometer may be processed in the same way as images produced by other types of detectors; these techniques are reviewed in other papers in this volume.

5. THE FUTURE

Of the three parts of an electronographic system - camera, emulsion and microdensitometer - the Achilles' heel is undoubtedly the emulsion. And unfortunately it is the least under the control of the astronomer although some have attempted to coat their own plates using Ilford gel emulsion. Even if high quality emulsions were available, the random incidence of the inevitable plate defects would put the electronographic camera at some disadvantage compared to other types of electron detector (photoemissive or solid-state) that can be fully calibrated before or after use, although the degree of handicap from this cause may well be small compared with other advantages.

Existing microdensitometers also fall short of what is technologically possible but their limitations are more of an inconvenience than an insurmountable barrier to high accuracy.

Acting on the assumption that solid-state detectors having several million pixels, high quantum efficiency from the ultraviolet to the near infrared, and freedom from some of the more serious defects of some existing CCD's will still be some time in arriving, we must ask what steps should be taken to improve the performance of existing electronographic systems. Pressure on the manufacturers of cameras, emulsions. and microdensitometers to improve their products may bear fruit particularly in the case of the cameras and the microdensitometers, but is less likely to be as

effective in the case of the nuclear emulsions because these form an infinitesimal proportion of their products, and given these circumstances both Ilford and Eastman Kodak have been, and are being, very cooperative.

Consideration should perhaps be given to possible changes in the way electronography is employed. Firstly is it really worthwhile exposing and measuring to D = 4 rather than to a maximum D = 2 ? The difference is only 0.75 magnitudes but the bulk of the microdensitometry problems occur at high densities (photon noise, transmission averaging across the aperture which is about twice as serious at D = 4 as at D = 2, emulsion pinholes, emulsion non-linearity, microdensitometer non-linearity). However, 0.75 mag is 0.75 mag and will be needed. I suggest that more use should be made of multiple exposures: apart from the relaxation in the microdensitometry requirement because of the smaller density range, emulsion defects can be discriminated against. Even a double exposure would be of considerable benefit. There are also of course disadvantages: film changes at the telescope, and increased measurement time. The first would be of little importance if an automatic film or plate changer is provided on the camera; such a device is being considered for the 85-mm electronographic camera at the prime focus of the ESO 3.6-m telescope. The increase in the measurement time may be more serious but if the density range is limited the microdensitometer can work faster. It would be essential that clear fiducial marks be impressed on the emulsion in the camera, and rapid means for superimposing scans with the microdensitometer. An automated alignment system would be needed - probably a motor driven turntable and encoder on the platen so that electronographs could be placed on the machine and automatically aligned. Alternatively the alignment could be done by rotating the images in the computer. The areas corresponding to those measured on the first plate of a set would be automatically scanned and the data combined using an image processing program that would reject obvious plate blemishes.

It could well be more productive to use available effort to add such a facility to a microdensitometer rather than trying to increase the dynamic range which may in any case be limited by other parts of the system.

To sum up, I suggest that even with emulsions of present available quality, a system comprising an automatic film changing camera used to produce multiple electronographs with a maximum density of $D \approx 2$ programmed for the rapid superposition of images and with suitable image processing, would enable photometry to be done as a routine to at least

the best accuracies that have been obtained with considerable labour by earlier workers. These appear to be about 0.02 integrated magnitude[14-16] although higher accuracies are being achieved in specialised applications, eg 0.5% in polarimetry by Scarrott et al.[17-18]

REFERENCES

1. C. I. Coleman, Adv. E. E. P. 40B, 661 (1976).
2. K. F. Hartley and D. McMullan, Adv. E. E. P. 40A, 493 (1976).
3. D. McMullan, J. R. Powell and N. A. Curtis, Adv. E. E. P. 40B, 627 (1976).
4. "A Fast, Wide-Angle Telescope for Spacelab" ESA Assessment Study SCI(79)5, (1979).
5. A. Lallemand, B. Servan and L. Renard, In Proceedings IAU Colloquium No. 40, p. 1-1, Paris-Meudon Observatory (1976).
6. G. E. Kron, H. D. Ables and A. V Hewitt, Adv. E. E. P. 28A, 1 (1969).
7. J. D. McGee, A. Khogali, A. Ganson and W. A. Baum, Adv. E. E. P. 22A 11 (1966).
8. P. J. Griboval, Adv. E. E. P. 52, 305 (1979).
9. D. McMullan and J. R. Powell, Adv. E. E. P. 52, 315 (1979).
10. R. Florentin Nielsen, Copenhagen University Observatory. Private Communication.
11. G. Wlérick et al., Adv. E. E. P. 52, 295 (1979).
12. J. Ring and S. P. Worswick, Adv. E. E. P. 40B, 679, (1976).
13. J. D. H. Pilkington, In Proceedings IAU Colloquium No. 40, p 10-1, Paris-Meudon Observatory (1976).
14. M. F. Walker, Adv. E. E. P. 33B, 679 (1972).
15. G. Wlérick, D. Michet and C. Labeyrie, In "Electrography and Astronomical Applications" p. 177 McDonald Observatory, University of Texas, Austin (1974).
16. M. A. R. Hardwick, A. B. Harrison and B. L. Morgan, Adv. E. E. P. 52, 329 (1979).
17. S. M. Scarrott et al., M.N.R.A.S. 178, 93P (1977).
18. R. F. Warren-Smith, Thesis, University of Durham (1979).

Applications of a Lithographic Emulsion in Electronography

R. Florentin Nielsen
Copenhagen University Observatory.

For more than one year Danish and British observers have used 44 mm and 93 mm McMullan type electronographic cameras on the Danish 1.5 m telescope at La Silla. [1)]

We have been painfully aware of the fact that our supplies of G5 and L4 emulsions have been of somewhat unconstant quality. In a search for alternative emulsions we have found the Agfa Gevaert 080 p lithographic emulsion on a 50 μm thick polyester base useful for many of our observations. The film being mass produced is very clean (freedom from foreign particles embedded in the emulsion) and has a uniform emulsion layer. These are the main problems with G5 and L4.

The grain size is similar to that of L4.

The speed of 080 p when exposed to electrons in the McMullan cameras is 1.7 times that of the L4, corresponding to 3 electrons/μm^2 to produce density = 1.0.

The saturation density is stated by Agfa to be "very high". So far linearity tests made in the laboratory have only covered the range

$$0 \leq D \leq 1.3.$$

Within this range and within the measurement errors (0.005 D) the response is perfectly linear.

The emulsion has a protective super-coating and is insensitive to pressure marks.

At the telescope the 080 p emulsions have been used for photometric sequences with limited dynamic range, flat field calibration and photometry on galaxies with low surface brightness, where the uniformity of the emulsion is of paramount importance.

1) K. Gyldenkerne, R. Florentin Nielsen and D. McMullan, ESO Messenger, No. 17, p.36, 1979.

Linearity tests to higher densities - at least to D = 3.0 - should be carried out before attempting to use the 080 p emulsion in applications where large dynamic ranges in magnitude are required.

DIX ANNEES DE PHOTOMETRIE BIDIMENSIONNELLE AVEC LA CAMERA ELECTRONIQUE. *

G. WLERICK, M. DUCHESNE, G. LELIEVRE, F. GEX, A. SELLIER, D. MICHET,
Observatoire de Paris, Département Optique et Photométrie.

M.C. LORTET, C. VANDERRIEST, M. HEYDARI- MALAYERI, G. TESTOR,
Observatoire de Paris, Département d'Astrophysique Fondamentale.

P. LAQUES, R. DESPIAU, J.L. VIDAL,
Observatoire du Pic du Midi et de Toulouse.

R. DUBOUT,
Observatoire de Lyon.

RESUME :nous rappelons les propriétés particulières grâce auxquelles la Caméra électronique est un excellent récepteur bidimensionnel. Nous décrivons les méthodes originales développées pour la photométrie et leur application dans de nombreux domaines de l'Astronomie.

SUMMARY : we recall the specific properties of the electronic camera that make it very suitable for bidimensionnal photometry. We describe the photometric methods developped for this receptor and the applications to very numerous fields of Astronomy.

A. LALLEMAND (1936) fut le pionnier de l'Electronographie en indiquant les gains importants que permettrait d'obtenir la méthode électronographique dans la détection et la mesure des flux faibles que l'on observe en Astronomie. Grâce aux progrès réalisés à l'Observatoire de Paris, il a été possible d'équiper plusieurs Observatoires avec des Caméras électroniques : Observatoire de Haute-Provence, Observatoire du Pic du Midi, Observatoire de La Silla (ESO) et Observatoire de Lick. Ces matériels sont couramment utilisés par les astronomes français et étrangers pour des observations de spectroscopie et de photométrie bidimensionnelle. Les observations mentionnées par la suite ont été obtenues à l'aide des caméras électrostatiques de 20 mm et des caméras magnétiques de 90 mm de photocathodes.

* Les observations ont été effectuées aux Observatoires de Haute-Provence et du Pic du Midi.

I - RAPPEL DES PRINCIPALES QUALITES DE LA CAMERA ELECTRONIQUE LALLEMAND.

Nous nous sommes attachés à obtenir avec ces récepteurs la meilleure qualité possible en vue d'effectuer des mesures précises de photométrie bidimensionnelle.

a) Lumière parasite :

L'étude menée par Wlérick et Grosse (1966) a permis de réduire considérablement les lumières parasites dans le récepteur, puisqu'il a été possible d'abaisser le taux de lumière parasite à moins de 1% pour les photocathodes de type S 11 dans le domaine 350 - 650 nm.

b) Bruit de fond :

Lorsque les tubes électronographiques sont bien préparés, suivant le protocole établi, le bruit de fond des tubes est extrêmement faible. Par exemple, au cours d'expériences d'interférométrie en lumière faible, M. Duchesne a réalisé des poses de 12 heures avec photocathodes S11 et plaques Ilford G5 qui donnent une densité optique de l'émission parasite inférieure à 0,02. Actuellement, ces phénomènes peuvent être contrôlés, détectés et, éventuellement mesurés sur les clichés astronomiques grâce à des pastilles d'argenture sur le ménisque de la photocathode qui couvre une petite partie de l'image optique focale.

c) Propriétés géométriques :

Le grandissement électronique dans la caméra peut être éventuellement adapté aux programmes de recherche. Les aberrations géométriques, notamment la distorsion, sont connues stables et contrôlées par des expériences de laboratoire.

d) Photocathodes:

Grâce à la méthode de transfert originale proposée par Lallemand et Duchesne (1955), les astronomes ont la possibilité de choisir leur propre photocathode en fonction des buts astronomiques recherchés (état de surface, sensibilité spectrale, homogénéité spatiale, etc...). Les caméras électrostatiques actuelles permettent d'employer des cathodes de type S11, S20 et S1.

Dans le but d'amélioter l'homogénéité de la couche photoémissive, nous avons étudié les divers défauts de structure de la photocathode,visibles à l'examen des clichés électronographiques. Nous nous sommes efforcés de déterminer leur origine ainsi que l'étape de la fabrication à laquelle ils apparaissent. Cette étude nous a conduits à modifier les procédés de contrôle, de nettoyage et de montage. Les inhomogénéités observées peuvent se classer en deux catégories :

1) Les défauts d'aspect quasi ponctuels qui sont :

- soit des défauts de polissage du support : rayures, filandres, trous.
- soit des poussières.
- soit des cristaux d'antimoine dans le cas très accidentel d'un mauvais fonctionnement de l'évaporateur.
- soit des poussières de verre venues se coller sur le ménisque au moment de la casse de son enveloppe dans la caméra.

2) Les défauts étendus qui peuvent être :

- soit des auréoles laissées par les solvants utilisés pour dégraisser les ménisques.
- soit des marbrures dues à la sous-couche conductrice d'oxyde d'étain.
- soit un aspect diffusant de toute la surface, provoqué par des condensations sur le support. Ces condensations se forment pendant le scellement du ballon et pendant l'étuvage de la cellule sur le bâti d'évaporation.

Une salle à flux d'air filtré, équipée d'enceintes à flux laminaire, a été spécialement conçue et réalisée pour assurer le dépoussiérage, l'assemblage et le scellement des cellules photoélectriques. Le dépoussiérage se fait sous éclairage rasant à l'aide d'un microscope à vision binoculaire. Les mêmes conditions d'observations sont respectées pour tous les contrôles à chaque étape de la fabrication. Ces précautions ont permis d'éliminer la majorité des défauts quasi ponctuels. Pour éviter tout dépôt de solvants, les ménisques sont dégraissés mécaniquement avec une pâte à polir, rincés abondamment à l'eau distillée courante, puis séchés à l'étuve. Nous avons diminué l'épaisseur de la sous-couche conductrice d'oxyde d'étain afin de la rendre plus transparente. Sur des plaques de 80 mm de diamètre nous avons réalisé des sous-couches conductrices ayant une transmission $T = 87 \pm 4\ \%$ dans le domaine visible.

Enfin, un étuvage préalable, sous vide, à 550° de tous les éléments intervenant dans le montage de la cellule, ainsi qu'un nettoyage méticuleux des ballons de verre, a permis de diminuer notablement les condensations sur le support de la couche. Au cours de difficiles expériences conduites avec la Caméra électronique, M. Duchesne a montré que l'effet photoélectrique reste linéaire aux faibles flux, en lumière incohérente aussi bien qu'en lumière cohérente (Bozec et al. 1970 ; Duchesne, 1970 ; Duchesne et Vigier, 1971).

e) Emulsions électronographiques :

Linéarité et sensibilité.

Sur ces deux points,on constate une large hétérogénéité dans la production des émulsions Ilford de type G5, K5 ou L4. La linéarité $D \propto Ext$ (densité optique proportionnelle au produit de l'éclairement par le temps de pose) peut ne pas se trouver vérifiée pour certains lots de plaques comme l'ont noté Duchesne et Bijaoui (1970). Pour des tensions d'accélération supérieures à 22 KV, certains lots G5 ou L4 sont parfaitement linéaires jusqu'à des densités supérieures à 4. Par contre, dans d'autres cas, apparaît une densité de saturation D_S et la courbe caractéristique de l'émulsion est de la forme $D = D_S(1 - e^{-A \times E \times t})$ et dépend de deux paramètres D_S et A que l'on peut obtenir par des expériences de laboratoire. La figure I .e. $\propto$ montre des exemples de telles courbes et l'on voit que l'on se rapproche d'autant plus de la linéarité, que l'on augmente les tensions d'accélération. En règle générale, sensibilité et linéarité paraissent liées car, plus les émulsions sont sensibles et plus elles sont linéaires. Les émulsions Industrex (Kodak Definix) courbent rapidement avec des D_S de l'ordre de 3 à 4. Nous avons essayé des émulsions expérimentales Kodak X322 - 82. Elles sont sensibles et bien linéaires, cependant la finesse du support ne permet pas de les fixer correctement dans les porte-plaques de la caméra pour des utilisations astronomiques.

Homogénéité :

Les émulsions Ilford conduisent parfois à des variations importantes de sensibilité sur un cliché, qui peuvent atteindre 20 %. Par contre, l'émulsion Kodak Definix ne dépasse pas 3 % pour les variations locales de sensibilité.

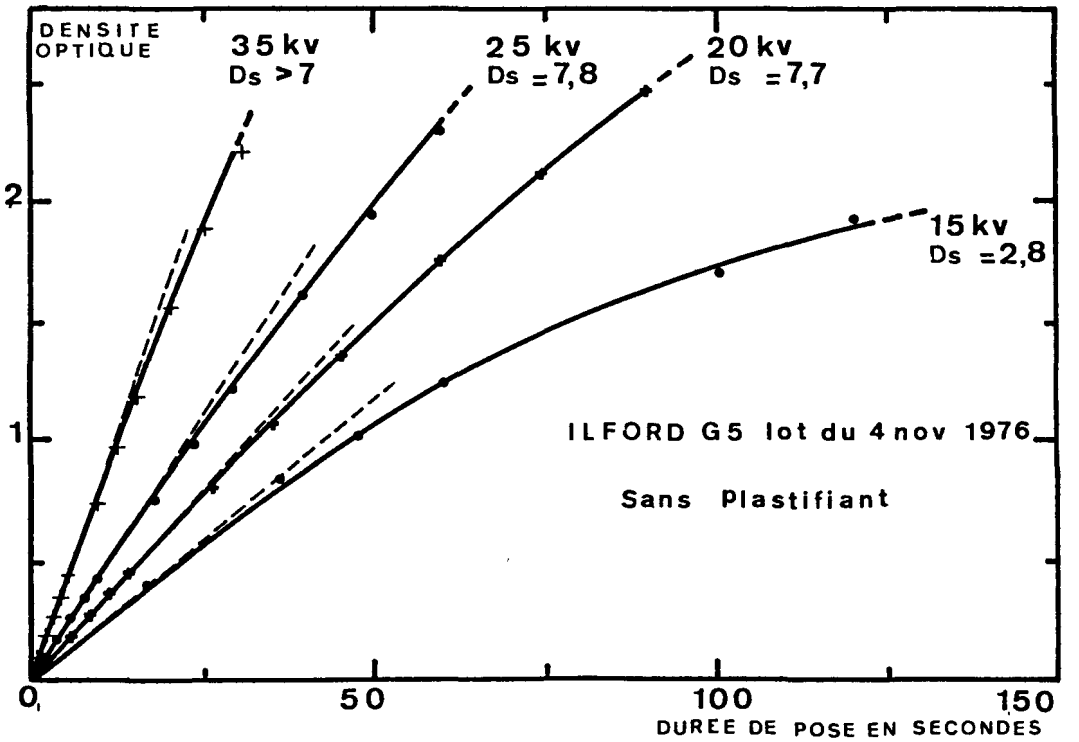
DENSITE OPTIQUE
35 kv
Ds >7
25 kv
Ds =7,8
20 kv
Ds =7,7
15 kv
Ds =2,8
ILFORD G5 lot du 4 nov 1976
Sans Plastifiant
0
50
100
150
DUREE DE POSE EN SECONDES

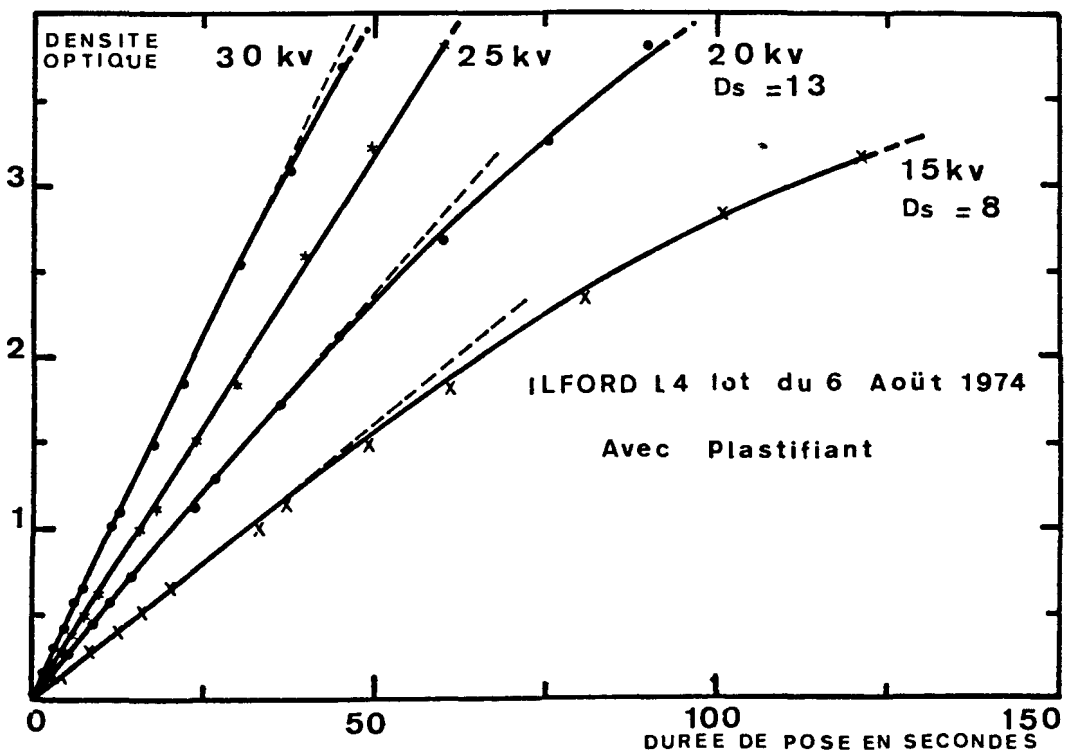
DENSITE OPTIQUE
30 kv
25 kv
20 kv
Ds =13
15 kv
Ds = 8
ILFORD L4 lot du 6 Aoüt 1974
Avec Plastifiant
0
50
100
150
DUREE DE POSE EN SECONDES

fig I.e.α

II - ANALYSE MICROPHOTOMETRIQUE DES CLICHES:

La caméra électronique possède d'excellentes qualités photométriques. Elle a été utilisée avec succès pendant les 10 dernières années. Les méthodes de dépouillement ont été adaptées en fonction des informations à extraire et elles diffèrent suivant le type d'objet.

II-A- CHAMPS STELLAIRES PEU DENSES ET GALAXIES DE FAIBLE DIAMETRE APPARENT ($< 1'$):

Dès 1966, Lallemand et al. (1966) montrent que la linéarité de l'électronographie permet une photométrie précise, par la méthode de Schilt, des étoiles faibles dans une gamme de 2,5 magnitudes. Kron et Walker (1967), sur plaques L 4, par la méthode dite des "aires totales", élargissent cet intervalle à 5 magnitudes; Wlérick et al. (1974) analysent les différentes méthodes de photométrie stellaire ainsi que les corrections nécessaires pour tenir compte des aberrations géométriques.

La méthode microphotométrique par comptage de traces (Lallemand et al. 1959) n'est pas applicable pour la photométrie bidimensionnelle à cause de la présence gênante du fond de ciel mais, avec les moyens modernes de dépouillement, elle pourrait être avantageusement exploitée en spectroscopie d'objets très faibles.

Pour avoir une bonne précision photométrique, Wlérick et al. (1971) ont montré que la densité du fond de ciel mesurée sur le cliché est un excellent critère de sensibilité "in situ". Celui-ci permet, en effet, de tenir compte des facteurs principaux : photocathode, émulsion, télescope, optique électronique, etc... Naturellement, la méthode ne s'applique que si le bruit de fond du récepteur est négligeable.

II-A-1- Etude des objets extragalactiques à noyaux actifs:

De nombreux objets extragalactiques actifs (galaxies N, objets de type BL Lacertae,...) présentent deux composantes :

- Un noyau central bleu, d'apparence stellaire et dont les propriétés sont voisines d'un quasar.
- Une composante étendue assimilable à une galaxie.

Les clichés obtenus avec la caméra électronique ont permis de séparer les deux composantes et d'étudier leurs propriétés : éclat et couleurs du noyau ; éclat, couleurs et dimension de la galaxie.

Le premier objet sur lequel la décomposition a été effectuée fut BL Lacertae (Wlérick et al. 1974 ; Wlérick 1974), voir figure II-A-1.α . G. Lelièvre (1976 a) a étudié systématiquement les galaxies N du Catalogue 3C R et, particulièrement, 3C 120 (Lelièvre 1976 b). Dans le cas de Ton 1542, Vanderriest et Lelièvre (1977) ont mis en évidence une galaxie spirale. Vanderriest & Schneider (197) ont étudié également de nombreux objets dont certains difficiles ($z \sim 0,2$), voir figure II.A.1.β . Au total, des résultats ont été obtenus sur une vingtaine d'objets actifs et leurs caractéristiques ont été rassemblées par G. Lelièvre (1979). Les grandeurs absolues trouvées sont compatibles avec l'hypothèse cosmologique.

La caméra électronique "grand champ" a commencé à être utilisée, en Haute-Provence, en 1978, pour ces études (Wlérick et al. 1978) et son emploi se révèle très prometteur : voir figure II.A.1.γ . Associée au télescope C.F.H. de 3,6 m, elle constituera un récepteur bidimensionnel très puissant.

II-A-2- Astrométrie et photométrie des étoiles doubles visuelles:

La caméra électronique a été utilisée pour l'enregistrement d'étoiles doubles visuelles serrées (Laques 1964 ; Laques 1972 a et b ; Laques et Morel 1971 ; Laques, Bücher et Despiau 1971 ; Despiau et Laques 1972 ; Laques et Despiau 1976). La photographie classique, employée jusqu'alors, permettait une mesure précise, essentiellement en astrométrie. Toutefois, compte tenu des temps de pose importants imposés par les émulsions photographiques, cette méthode était limitée, à cause des perturbations introduites par l'atmosphère terrestre, à des couples stellaires dont l'écartement était supérieur à 2" à 3" d'arc. Cette limitation avait pour effet de diminuer beaucoup l'intérêt de ces mesures pour l'Astrophysique, puisque les binaires permettant la détermination directe des masses stellaires, sont celles qui ont des périodes relativement courtes donc, des écartements statistiquement réduits.

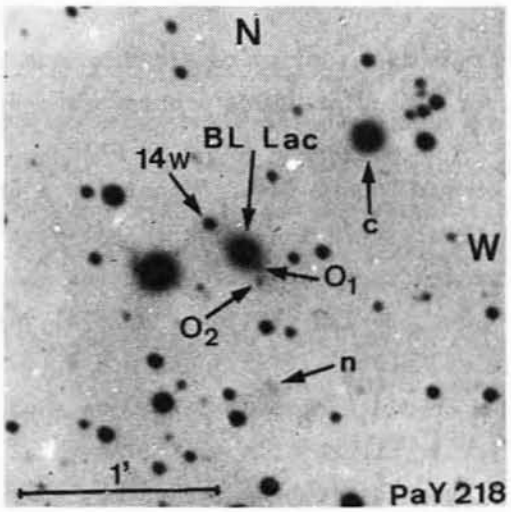

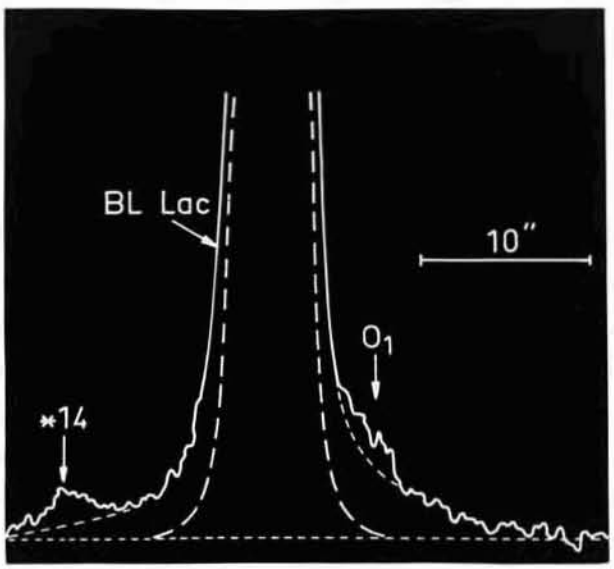

Fig. II. A. 1. α

IMAGE ELECTRONOGRAPHIQUE ET COUPE PHOTOMETRIQUE DE BL LACERTAE - La courbe en pointillé représente la coupe d'une étoile de même éclat que le noyau supposé ponctuel de BL Lac.

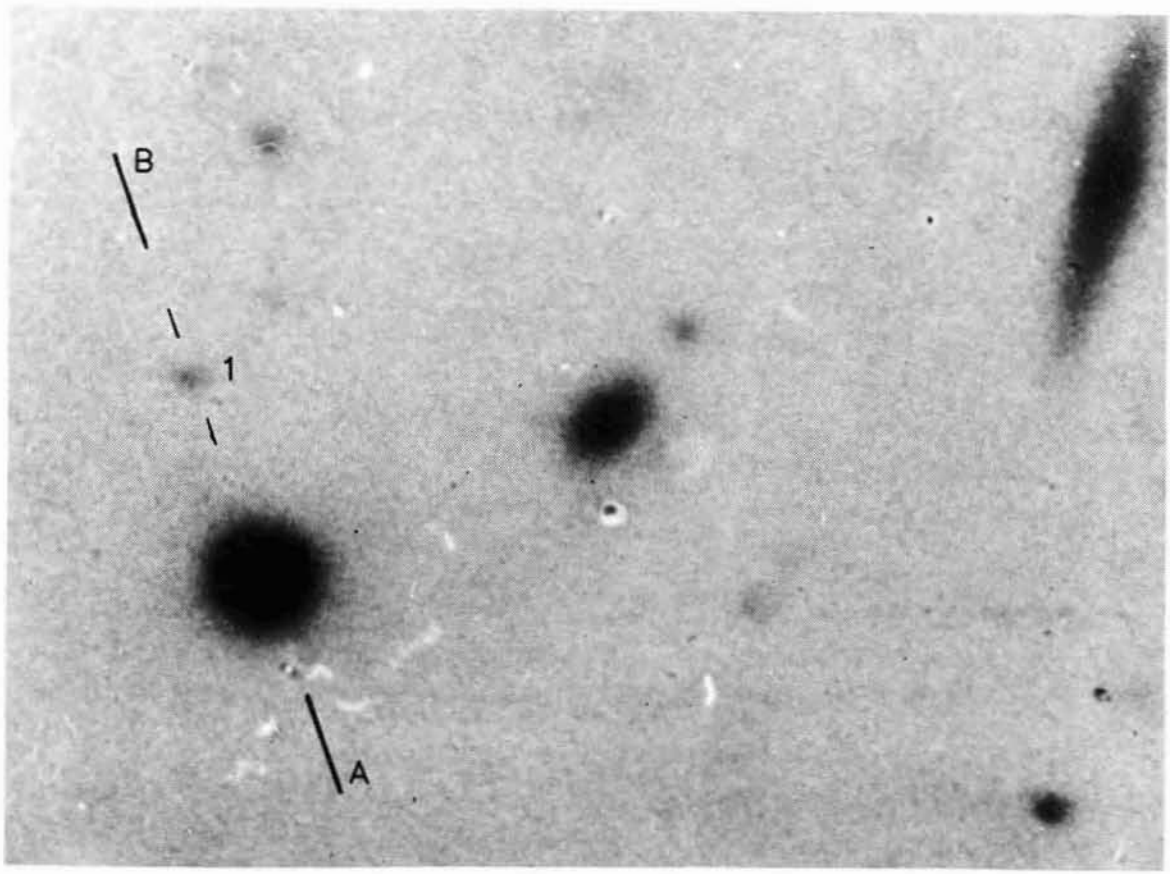

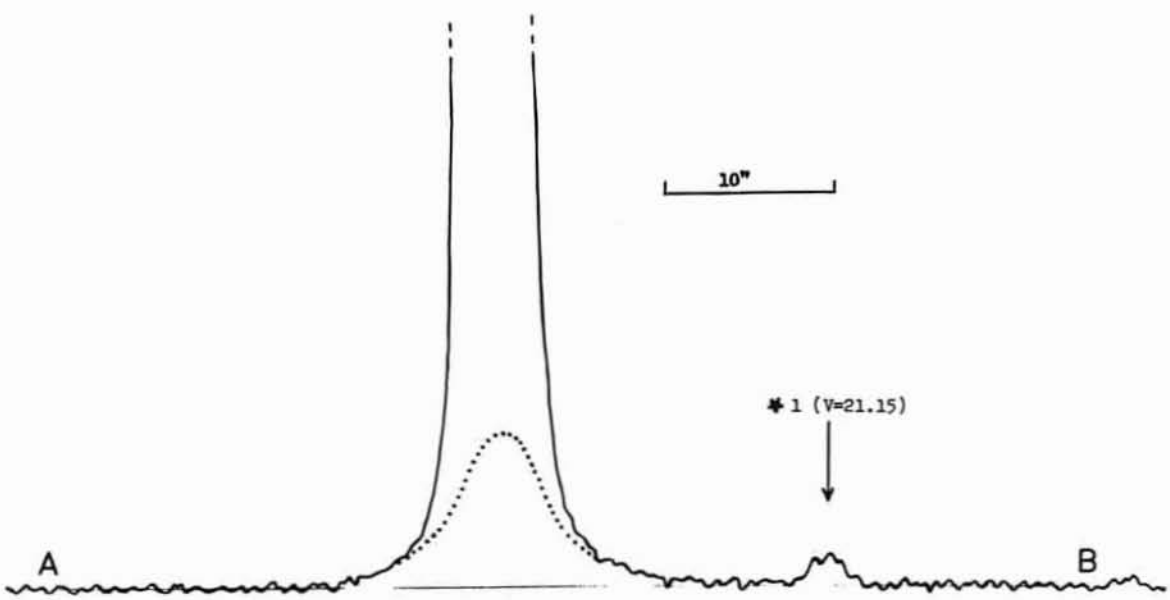

Fig. II.A.1.β : image électronographique et coupe photométrique du quasar PG 1351 + 64 - couleur V - pose 90 min. émulsion Ilford L 4.

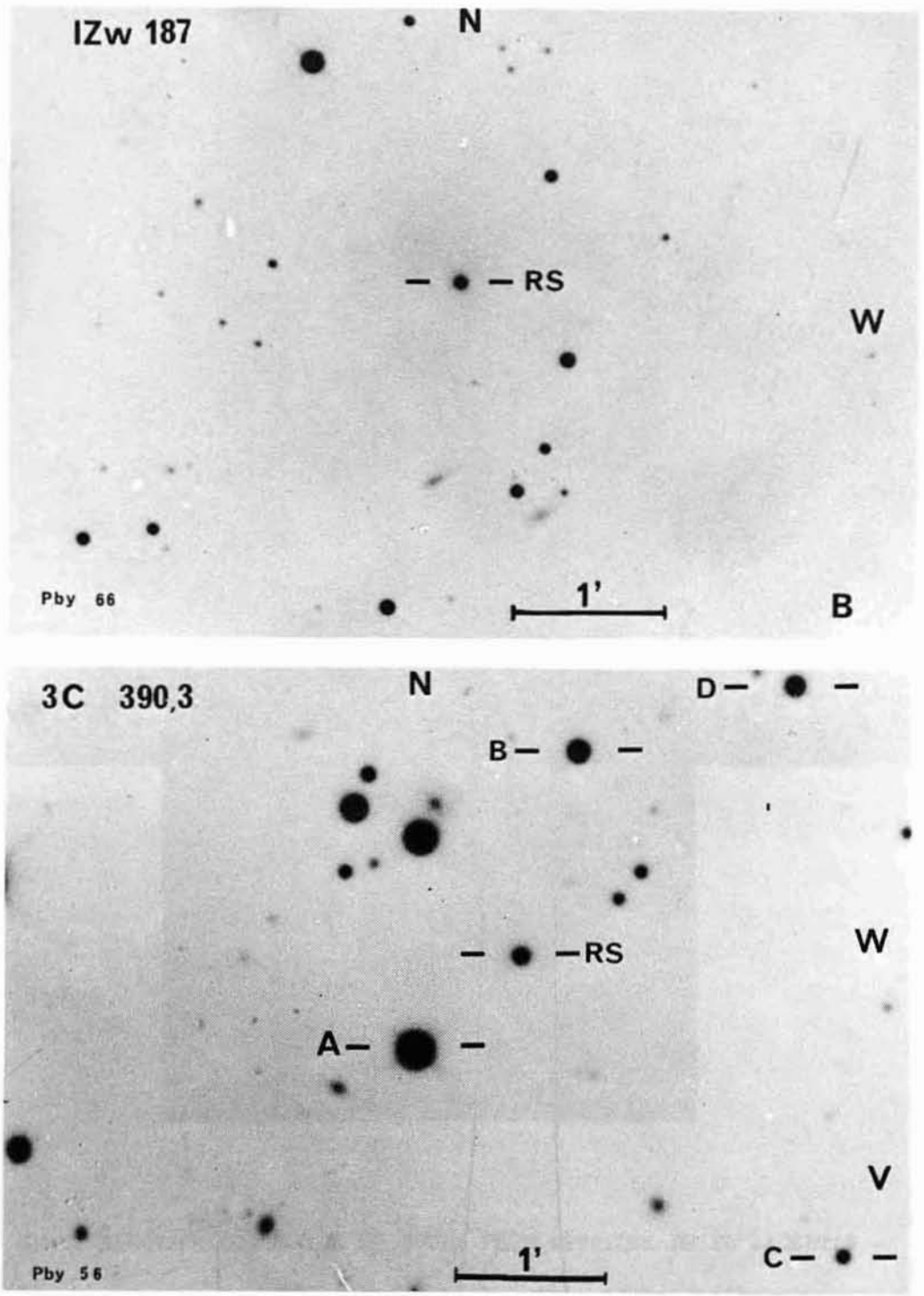

(a)

(b)

Radiosources de type galaxie N :
(a) IZw 187 filtre B, pose 102 min, émulsion Industrex A ; 11 juillet 1978.
(b) 3C 390,3, filtre V, pose 80 min, émulsion Industrex A. L'éclat des galaxies associées à ces sources est faible par rapport à celui d'une galaxie elliptique géante.

Clichés obtenus au foyer Cassegrain du Télescope de 1,93 mètre de l'Observatoire de Haute Provence à l'aide de la Caméra Electronique à Grand Champ.

Fig. II.A.1.γ.

Grâce au gain de sensibilité apporté par la caméra électronique, il est devenu possible de diminuer le temps de pose. Certes, la détérioration due à l'atmosphère est inchangée mais on peut enregistrer les figures de diffraction des images des composantes avec des temps d'intégration courts. La mesure peut alors s'effectuer en utilisant la similitude de ces figures, lorsque les composantes de la binaire ont une séparation inférieure à 2" d'arc environ. Ainsi, on a obtenu des résultats jusqu'à des séparations de 0"36 (ADS 8804 ; 1970,4) ; pour ADS 10229, considérée comme très difficile par les observateurs visuels, on a obtenu $\rho = 0{,}43$" pour une différence de magnitude égale à 1,7. L'étoile ADS 9347 a pu être mesurée malgré une différence de magnitude de 5,2.

Par ailleurs, les propriétés photométriques de la caméra permettent d'accéder à la différence de magnitude. Dans le système UBV, nous avons pu ainsi obtenir une information photométrique différentielle originale.

Les mesures astrométriques ont permis d'améliorer quelques orbites d'étoiles. Les mesures photométriques sont effectuées avec une précision de l'ordre de 0,1 magnitude, cette précision serait insuffisante pour des étoiles isolées mais elle constitue un gain appréciable pour des étoiles doubles ou triples.

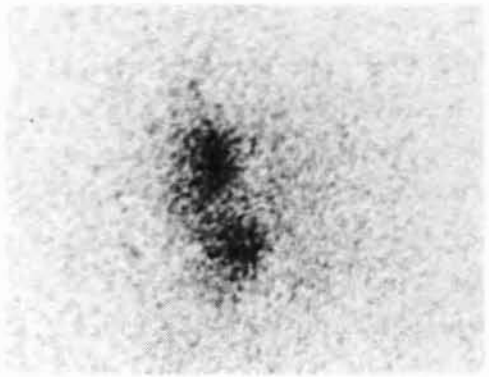

Fig. 1. Image de ADS 8804 : 1969,27; ρ = 0.43". Filtre V du système de Jonhson et Morgan.
Pose : 2.10^{-2} sec.

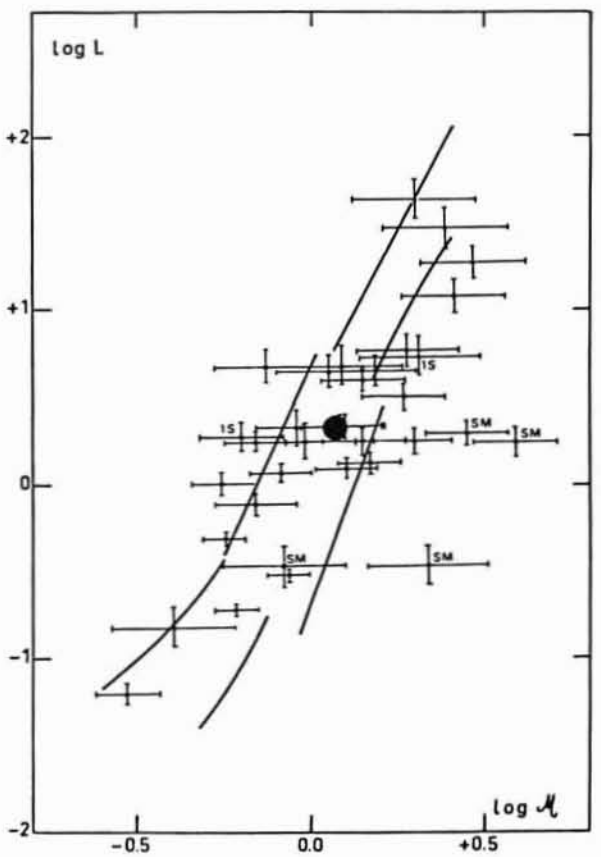

Fig. 2. L'information astrométrique et photométrique tirée de tels clichés apporte une contribution d'un très haut poids à la détermination des paramètres physiques des composantes de la binaire. Celle-ci est représentée par un cercle plein sur un diagramme masse-luminosité. (Astron. and Astrophys., 1976 48,101).

II-B- REGIONS ETENDUES A RAIES D'EMISSION:

Dans l'étude des nébuleuses gazeuses, on s'intéresse, en général, au rapport d'intensité de certaines raies, par exemple OIII/Hβ . Si les études sont effectuées avec la même photocathode et la même position de l'objet sur celle-ci, on est dans de bonnes conditions photométriques, en particulier quand les longueurs d'onde des raies à comparer sont voisines. Dans les autres cas, il faut disposer de cartes de sensibilité monochromatiques de la cathode obtenues avec des clichés auxiliaires.

II-B - 1- Etude de petites régions HII galactiques:

M. Heydari-Malayeri, M.C. Lortet, G. Testor, de l'Observatoire de Meudon, en collaboration avec L. Deharveng et J. Caplan, de l'Observatoire de Marseille, ont développé l'étude bidimensionnelle des clichés obtenus à la caméra Lallemand derrière le télescope 193 cm de l'Observatoire de Haute-Provence (Testor, Lortet 1977), en liaison étroite avec d'autres données d'observations (spectres, interférogrammes) pour comprendre la structure physique détaillée de petites régions HII galactiques : distribution des densités et des mouvements de divers ions et des poussières, étude des zones périphériques (bornées par un nuage moléculaire ou au contraire par la densité).

Les sources étudiées (de 1' à 5' de diamètre) sont observées le plus souvent à travers des filtres interférentiels (bande passante de l'ordre de 10 Å). Les auteurs se sont attachés à la comparaison quantitative de 2 clichés (voir par exemple les Fig. II.3.1 α et β ainsi que l'étude de Sh2-156, Heydari-Malayeri et al. 1980). Ils ont également réalisé des coupes des clichés monochromatiques selon la direction des spectres.

Les principaux résultats obtenus sont les suivants :

On a obtenu une description très précise de la géométrie du gaz ionisé et de la localisation des fronts d'ionisation (voir par exemple l'étude de Sh2-156 par Heydari-Malayéri 1979 et Heydari-Malayeri et al. 1980). En particulier, les différences considérables entre les variations sur la nébuleuse des rapports Hα/Hβ et radio continuum/Hα en certains bords, indiquent que le gaz ionisé y est partiellement caché par le nuage moléculaire aux longueurs d'onde optiques.

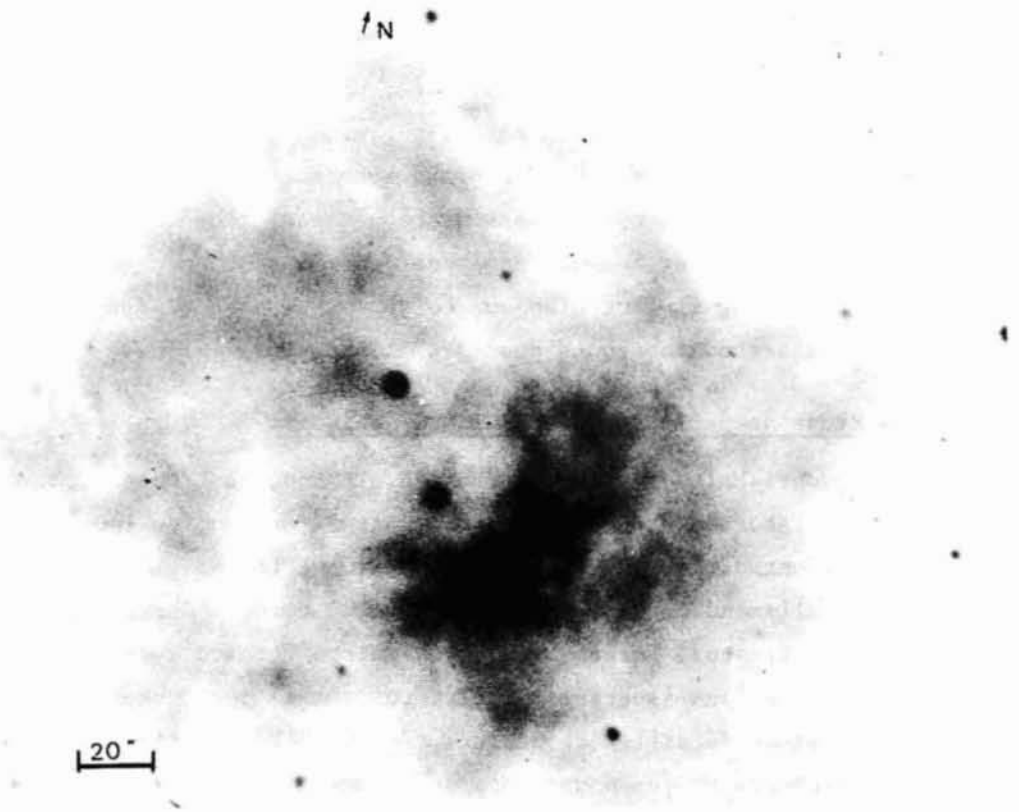

Fig. II.B.1. α : La nébuleuse galactique Sharpless 2-158 (NGC 7538) dans la raie [O III] λ 5007 Å (d'après Deharveng et al. 1979). Cliché obtenu avec la caméra électronique au foyer Newton du télescope de 193 cm de l'Observatoire de Haute-Provence. Remarquer l'aspect pommelé et l'indication d'un anneau incomplet autour de l'étoile IRS 6.

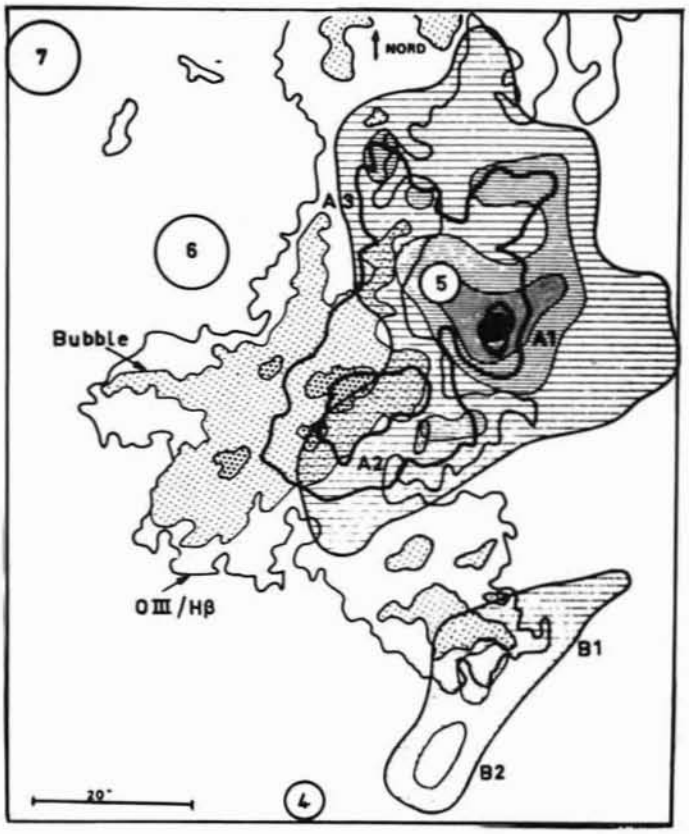

Fig. II.B.1.β : traitement quantitatif de plusieurs clichés du centre de la fig. II.B.1. en [O III], [N II] , Hβ . Les étoiles excitatrices sont IR 6 et IRS 5 (type spectral O7). Deux isophotes Hβ (trait épais) sont indiquées. La structure d'ionisation est clairement visible : rapport [O III] /Hβ plus élevé près de IRS 6 (surfaces couvertes de points) tandis que l'intensité [N II] est renforcée vers les bords (surfaces hachurées). Les courbes d'isorapport pour [O III]/Hβ correspondent aux valeurs 4.74, 5.76, 7.08, 7.56. On voit nettement une bulle de haute excitation ([O III] /Hβ $>$ 5.76) et une région encore plus excitée près de la composante A2 qui est aussi la région présentant les plus hautes densités.

D'autre part on a mis en évidence des variations des rapports d'intensité de raies plus grandes qu'on ne le soupçonnait par l'étude spectrale, simplement parce que les rapports sont ici obtenus sur toute la surface de la nébuleuse et non le long de quelques fentes. Par exemple, dans Sh2-158 (Fig. II.B.1 α et β), le rapport OIII /Hβ atteint des valeurs élevées (environ 7) le long d'un arc de cercle. Cet arc est interprété comme une bulle de haute excitation, résultat de l'interaction d'un vent stellaire (issu de l'étoile IRS 6) et de la matière interstellaire, en présence d'un gradient de densité de cette matière. La bulle est mieux visible sur les courbes isorapports (Fig. II.B.1 β) que sur les photos monochromatiques (Fig. II.B.1 α)

A l'avenir, nous voudrions effectuer des comparaisons de champs de vitesse obtenues au Perot-Fabry (raies optiques) ou en radio, ainsi que des champs de densité ou de cartes en diverses longueurs d'onde. Nous espérons réaliser ces comparaisons de façon plus efficace et beaucoup plus rapide grâce aux progrès des techniques de traitement en photométrie bidimensionnelle, notamment, par la visualisation en couleurs et la cinématographie.

II-B-2- Photométrie bidimensionnelle de nébuleuses gazeuses diffuses de type "globule":

Ce programme a été entrepris à l'Observatoire du Pic du Midi, en 1975. Les observations ont porté principalement sur la nébuleuse d'Orion, en vue d'une détermination des conditions physiques (température et densité) avec une meilleure résolution spatiale.

Ainsi, des informations sur la structure d'ionisation, grâce au rapport O III /Hβ ont été obtenues dans la partie centrale (Despiau, Laques, Vidal 1976). De même, la carte des températures (ibid. et Laques, Vidal 1980) du milieu à haute excitation, a été dressée grâce au rapport des deux raies à 4363 Å et 5007 Å de O III (rapport de l'ordre de 300, pratiquement impossible à mesurer en photographie classique).

D'autre part, l'utilisation de cellules S 20, fabriquées au Département "Optique et Photométrie" de l'Observatoire de Paris, a permis à Laques et Vidal (1979), grâce à des clichés dans les raies Hα, [N II] 6584 Å, [S II] 6717 Å, [S II] 6731 Å et le continu à λ 6440 Å et à des informations recueillies précédemment dans les raies Hβ et [O III] λ 5007 Å grâce à des cellules S 11, de détecter des condensations nébulaires d'un type nouveau au centre de cette nébuleuse.

Les figures 6, 7, 8 et 9, correspondant à des agrandissements des clichés en Hα, [N II] et [O III] de la région du trapèze et à une carte explicative, permettent de bien distinguer les condensations d'apparence stellaire des étoiles du champ.

Le diamètre mesuré de ces globules sur nos meilleures plaques est de 1,4" à mi-hauteur. La proximité des étoiles brillantes du trapèze (6" en moyenne) rendait cette détection quasiment impossible en photographie classique.

Pour ces condensations, nous avons présenté un modèle de globules partiellement ionisé (Laques et Vidal 1979, op. cit.) qui correspond bien aux observations. Il n'est pas déraisonnable d'imaginer que les étoiles d la Nébuleuse d'Orion se sont formées à partir de globules semblables mais de masse supérieure pour que l'effondrement gravitationnel puisse se déclencher.

II-C- ETUDE DES OBJETS ETENDUS A SPECTRE CONTINU:

Dans ce cas la méthode photométrique décrite au paragraphe II.A ne s'applique plus. La méthode qui donne les meilleures résultats consiste à prendre le cliché de l'objet étendu entre deux clichés de champs stellaires, de mesurer la densité du fond de ciel sur ces clichés et d'utiliser cette donnée comme critère de sensibilité (voir II-C-1).

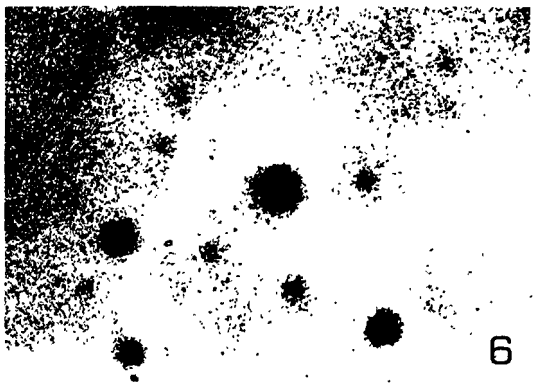

Figure 6.Trapèze d'Orion et son environnement.Filtres interférentiels de $\Delta\lambda \simeq$ 10 A.
$H\alpha$; photo-cathode S20 ; pose : 3 minutes .

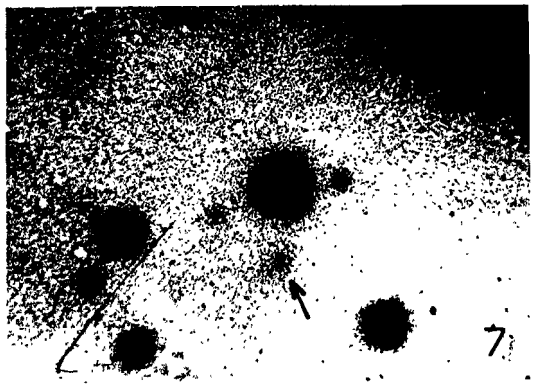

Figure 7.Filtre[NII] 6584 Å; photo-cathode S20;pose :4 mn.

Figure 8.Filtre [O III]5007 Å;photo-cathode S11; pose : 1 mn.

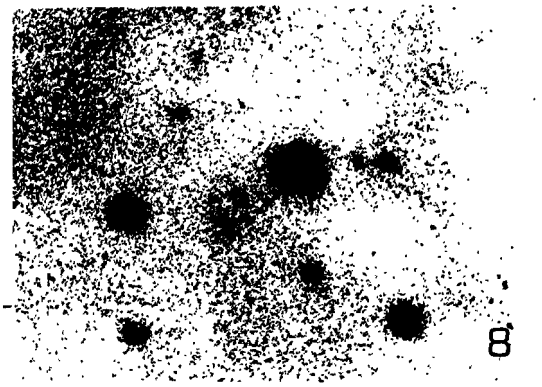

Figure 9. Carte de l'environnement du Trapèze d'Orion.Les étoiles principales sont notées A, B, C, D,E et F, selon la notation d'Aitken. Les cercles évidés,notés de 1 à 6, sont des condensations de matière gazeuse de dimension stellaire,bien visibles sur les clichés 6 et 8.Celles-ci disparaissent sur lecliché 7,tandis que l'on voit bien l'etoile F,invisible sur 6 etvisible sur 8.La tâche désignée parune flèche surl'image 7 est un reflet.

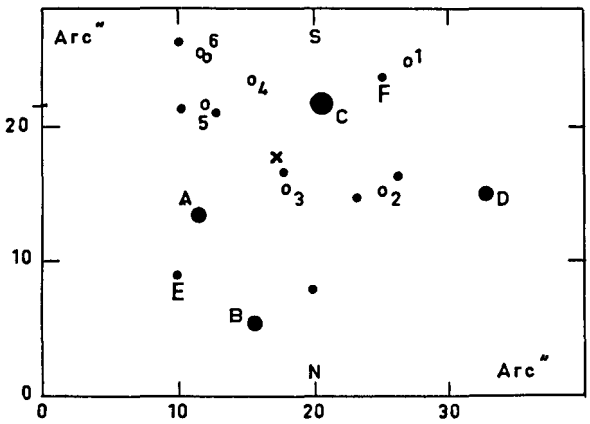

Nota : ces 4 figures se rapportent au paragraphe II-B-2.

II-C-1- Etude de la population stellaire du bras Sud de Messier 33:

La galaxie M33 est située à 720 Kpc. R. DUBOUT a observé individuellement les plus brillants des objets qui la composent : des supergéantes plus ou moins évoluées, des étoiles très massives et des amas, globulaires ou ouverts, d'apparence quasistellaire.

Préciser la nature des composantes de cette population en grande majorité massive et jeune, afin de mettre en évidence l'évolution au sein d'un bras de galaxie à partir du front du bras et afin d'avoir une détermination de la proportion des amas dans une population déterminée, sont les buts de l'étude photométrique entreprise avec la caméra électronique.

Ce sont des astres faibles dont les magnitudes relatives sont comprises entre 16 et 20 et qui se superposent au fond galactique, de magnitude 22 par seconde carrée. Ce fond relativement brillant est, en outre, très variable d'un point à un autre du bras, rendant les mesures d'intensité très délicates par les méthodes classiques, d'autant plus que la plupart des étoiles font partie de groupes serrés.

Cinq bons clichés pour chacune des couleurs U et B et quatre pour la couleur V ont été dépouillés à l'aide d'un Microphotomètre JOYCE par la méthode de l'aire centrale. Les profils des objets mesurés permettent de déterminer s'il s'agit d'étoiles, d'amas, si les profils sont bien élargis ou d'objets multiples quand ils sont déformés. La photométrie correcte des amas et des objets multiples demande une exploration complète de la tache image.

Nous avons effectué la photométrie des objets dont les profils peuvent être considérés comme des profils stellaires. La précision est $\pm$ 0,05 magnitude en U et B et $\pm$ 0,06 magnitude en V pour chaque cliché. Les mesures ont été raccordées à la séquence photoélectrique établie par Johnson et Sandage 1974,(Ap.J. 191, 63) dans des zônes plus extérieures de M33, en établissant en photométrie photographique classique une séquence de raccordement dans la région étudiée. Les corrections de sensibilité de photocathodes ne pouvant être faites "in situ", des clichés pris dans la même couleur avec la même photocathode, ont permis de les connaître, par la mesure, en chaque point de leur densité due au fond de ciel (mais les inhomogénéités possibles dans la sensibilité des plaques ne sont pas connues).

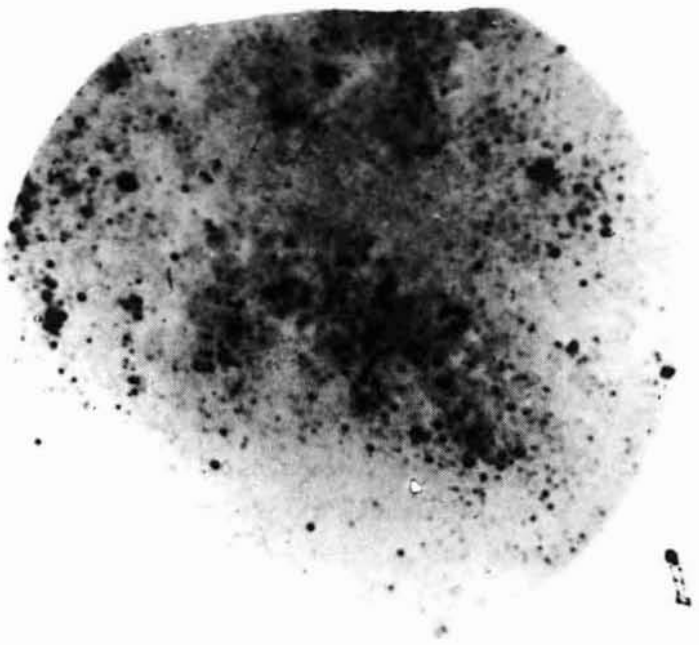

M 33 : bras sud à
7' du noyau

filtre V pose 50 mn
plaque L_4
Tél. 193 cm OHP

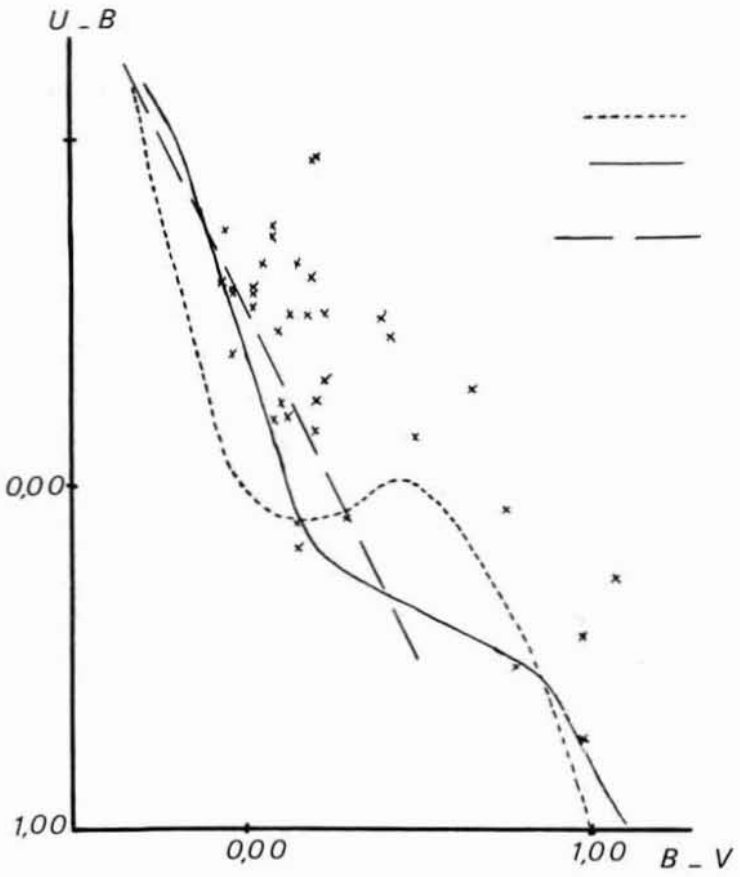

Fig. 2C.1

Le diagramme U - B, B - V obtenu, permet de différencier les étoiles galactiques des étoiles appartenant à M33 et d'avoir, pour la première fois, une idée des types spectraux des étoiles massives de cette région, ainsi que de l'absorption intrinsèque à M33 dans leur direction (la précision sur les couleurs est essentiellement déterminée par la précision de la séquence de raccordement).(Fig. II.C.1).

II-C-2- Etude des amas globulaires :

A partir de 1975, la caméra électronique a été utilisée pour l'étude du centre de l'amas globulaire M15 (Leroy, Aurière, Laques 1976). D'une part, comme pour les étoiles doubles, on a bénéficié du gain de sensibilité pour résoudre la partie centrale de l'amas, grâce à des poses courtes permettant d'obtenir des dimensions d'images stellaires (largeur du profil photométrique à mi-hauteur) de 0,7". La connaissance de la position des étoiles dans cette région, mal établie jusqu'alors, a permis l'amélioration de mesures photométriques obtenues, par ailleurs, en photographie classique. Aurière (1980, en préparation) a pu ainsi obtenir le tracé du diagramme HR des étoiles centrales de cet amas, connu aussi comme source X.

D'autre part, l'utilisation de filtres interférentiels étroits a permis de rechercher des émissions de type nébulaire à l'intérieur de cet amas (Aurière, Leroy, Laques 1978). Le résultat s'est avéré négatif : comme on le voit sur la figure 5, la "différence" de deux clichés numérisés centrés sur [O III] λ 5007 Å, l'un à bande large, l'autre à bande étroite, ne fait apparaître aucune source, à part la nébuleuse planétaire bien connue K 648 (Fig. 3 et 4).

II-C-3- Etude des noyaux de galaxies:

La caméra électronique a été utilisée pour l'étude photométrique et morphologique de quelques noyaux de galaxie. Ce sont les noyaux à "hot spots" de NGC 3351 (Fig. 11) et NGC 5248. On remarque la structure en forme de couronne des condensations de NGC 3351 dont la rotation a été mise en évidence par ailleurs. Une condensation centrale quasi-ponctuelle apparait de façon très distincte sur le cliché. D'autre part l'étude photométrique en [O III] et Hβ de ce noyau,est actuellement en cours.

Nous avons étudié le noyau de la galaxie de Seyfert, NGC 1068, en Hα à l'aide d'une photocathode S 20 (Pellat, Alloin, Despiau, Laques 1980). Ce travail a permis de confirmer la structure nuageuse en expansion du centre de la galaxie, déjà étudiée en spectro par Walker en 1968.

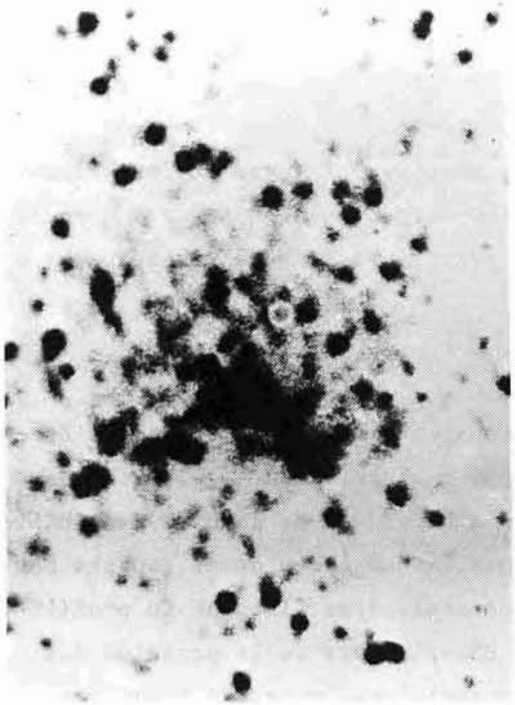

Fig. 3

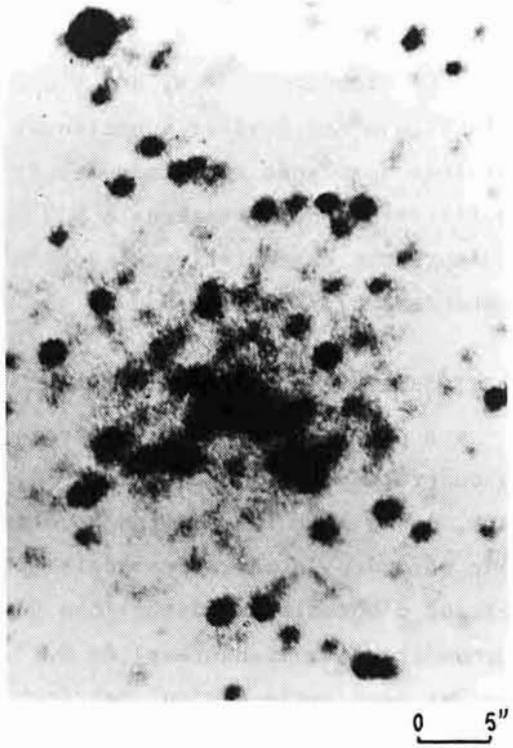

Fig. 4

Fig. 3. Partie centrale de l'amas M 15. Image obtenue au moyen d'une photocathode S11 sans filtre et une pose de 15 sec.

Fig. 4. Photocathode S 11; filtre interférentiel de $\Delta\lambda \simeq 8$ A, centré sur la raie nébulaire [O III] 5007 A. Pose de 20mn On remarque l'importance prise par la nébuleuse planétaire K 648.

Fig. 5. Résultats sous forme de cartes d'isodensité (CDCA de Nice) de la fonction différence entre le cliché à bande étroite et le cliché à bande large. Seule l'émission de la nébuleuse planétaire persiste, mettant en évidence lanature stellaire du centre de l'amas.

NB : ces figures se rapportent au paragraphe II.C.2.

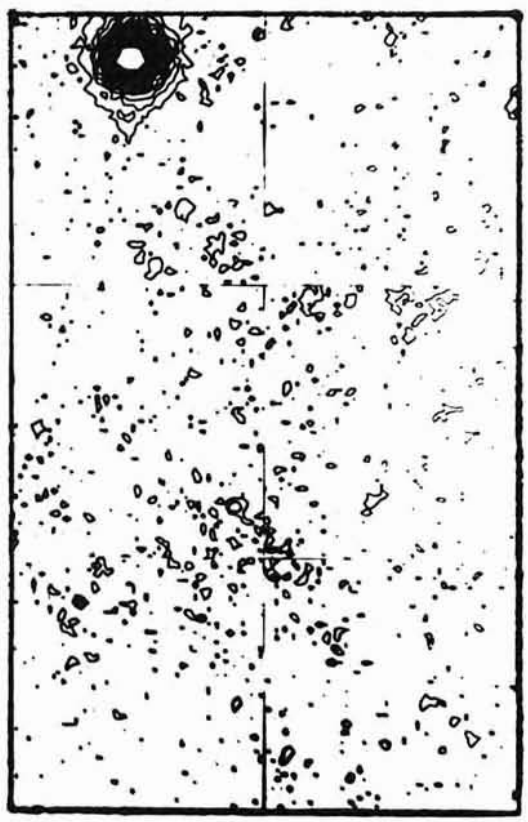

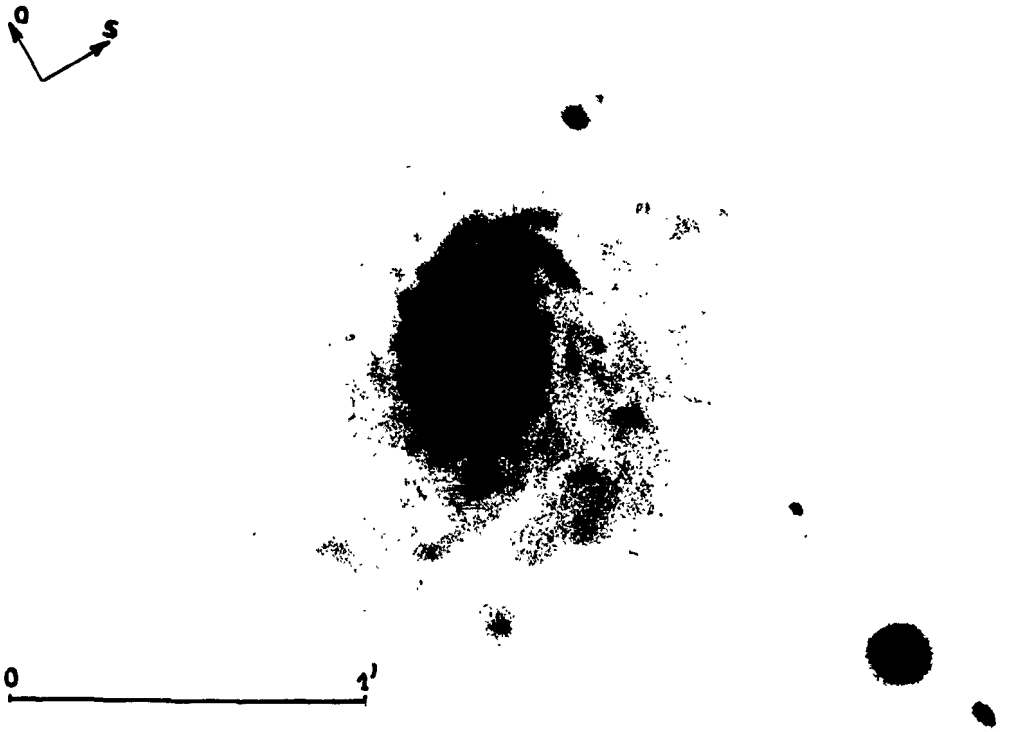

Figure 10. Photographie de lagalaxie de Seyfert NGC 1068,obtenue le 13 Octobre 1977,à l'aide d'une cellule S 20,sans filtre.Le temps de pose était de 5 minutes.L'étude faite en Hα correspond à une structure de quelques secondes d'arc seulement,dans la partie centrale de la galaxie.

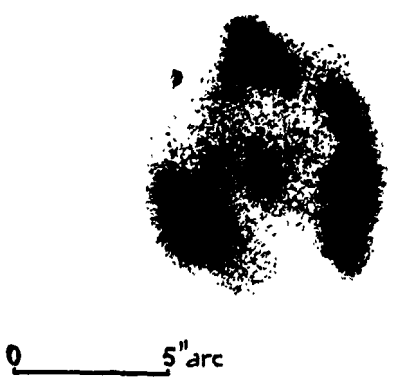

Figure 11. Noyau hautement résolu de la galaxie NGC 3351.Cette photographie est obtenue au moyen d'une cellule S 11,sans filtre, avec un temps de pose de 8 minutes.

NB : ces figures se rapportent au paragraphe II.C.3.

Très récemment, des observations ont été effectuées sur des galaxies de Markarian et les galaxies doubles NGC 7603 et NGC 1199 (collaboration avec J.L. Niéto).

III - CONCLUSION :

Nous avons présenté un ensemble d'observations effectuées avec la caméra électronique et décrit les résultats astronomiques correspondants. Cet ensemble ne représente qu'une petite partie des travaux qui utilisent ce récepteur. D'une part, nous n'avons pas abordé les observations spectroscopiques pour lesquelles la caméra s'est révélée être très bien adaptée et très sensible ; d'autre part, en imagerie directe, nous n'avons pas mentionné les travaux réalisés dans divers domaines tels que la Couronne solaire, les grosses Planètes,...

En fait, la caméra électronique est utilisable avec fruit, pour toutes les observations astronomiques qui, d'une part, n'exigent pas un champ linéaire supérieur à 80 mm, d'autre part, n'exigent pas un nombre de clichés trop grand au cours d'une même nuit. Son domaine de prédilection est donc l'étude directe ou spectroscopique des astres faibles dans l'intervalle spectral 300 - 1100 nm. Dans ce domaine, sa détectivité et la précision photométrique obtenue n'ont pas été surpassées par d'autres détecteurs.

BIBLIOGRAPHIE

Aurière,M., Leroy, J.L., Laques, P. 1978, Astron. Astrophys. 63, 341.

Bozec, P., Cagnet, M., Duchesne, M., Le Conte, J.M., Vigier, J.P. 1970, C.R. Acad. Sci. Paris 270, 324.

Deharveng, L., Lortet, M.C., Testor, G. 1979, Astroh. Astrophys. 71, 151.

Despiau, R., Laques, P. 1972, Astron. Astrophys. 18, 16.

Despiau, R., Laques, P., Vidal, J.L. 1976, in "Applications astronomiques des récepteurs d'image à réponse linéaire", Colloque U.A.I. N° 40, éd. M. Duchesne et G. Lelièvre, Paris.

Duchesne, M. 1970, C.R. Acad. Sci. Paris 271, 142.

Duchesne, M. et Vigier, J.P. 1971, C.R. Acad. Sci. Paris 273, 911.

Duchesne, M. et Bijaoui, A. 1970, Nouv. Rev. Opt. Appl. 1, 287.

Heydari-Malayeri, M. 1979, Thèse de 3ème cycle, Université Paris VII.

Heydari-Malayeri, M., Testor, G., Lortet, M.C. 1980, Astron. Astrophys. (sous presse).

Lallemand, A. 1936, C.R. Acad. Sci. Paris 203, 243.

Lallemand, A. 1936, Acad. Sci. Paris 203, 990.

Lallemand, A. et Duchesne, M. 1955, C.R. Acad. Sci. Paris 240, 1329.

Lallemand, A., Canavaggia, R., Amiot, F. 1966, C.R. Acad. Sci. Paris 262,838.

Lallemand, A., Duchesne, M., Goldzahl, L., Duflo, J., Banaig, J. 1959, C.R. Acad. Sci. Paris 248, 2191.

Laques, P. 1964, in "Photo Electronic Image Devices", Third Symposium, Academic Press.

Laques, P. 1971 (a), Astrophys. Space Sci. 11, 59.

Laques, P. 1971 (b), Astrophys. Space Sci. 11, 181.

Laques, P., Bücher, A., Despiau, R. 1971, Astron. Astrophys. 15, 179.

Laques, P., Despiau, R. 1976, Astron. Astrophys. 48, 101.

Laques, P., Morel, J.P. 1971, Astron. Astrophys. 10, 476.

Laques, P., Vidal, J.L. 1979, Astron. Astrophys. 73, 97.

Laques, P., Vidal, J.L. 1980 (en préparation).

Lelièvre, G. 1976 (a), Thèse, Paris.

Lelièvre, G. 1976 (b), Astron. Astrophys. 51, 347.

Leroy, J.L., Aurière, M., Laques, P. 1976, Astron. Astrophys. 53, 227.

BIBLIOGRAPHIE (Suite)

Pellat, D., Alloin, D., Despiau, R., Laques, P. 1980 (en préparation).

Testor, G., Lortet, M.C. 1977, Journées d'Etude du C.D.C.A., Lanslebourd pp. F3-1 à F3-21.

Vanderriest, Ch. et Lelièvre, G. 1977, Astron. Astrophys. **56**, 71.

Vanderriest, Ch. et Schneider, J. 1978, Astron. Astrophys.

Walker, M.F., Kron, G. 1967, P.A.S.P. 79, 551.

Wlérick, G. et Grosse, A. 1966, Adv. Electronics Electron Physics 22, 465.

Wlérick, G. Michet, D., Labeyrie, C. 1974, "Electrography and Astronomical Applications (éd. G. Chincarini, P. Griboval, H. Smith), p. 177.

Wlérick, G., Lelièvre, G., Véron, P. 1971, Astron. Astrophys. 11, 142.

Wlérick, G., Michet, D. et Lelièvre, G. 1974, C.R. Acad. Sci. Paris 278, 245B.

Wlérick, G. 1974, "Electrography and Astronomical Applications", éd. G. Chincarini, P. Griboval, H. Smith, p. 307.

Wlérick, G., Lelièvre, G., Servan, B., Renard, L., Lefèvre, B. 1978, Adv. Electronics Electron Physics (sous presse).

ESO PLATE MEASURING FACILITIES

Jorge Melnick
European Southern Observatory, Geneva

I. Introduction

Modern digital image processing techniques enable astronomers to extract accurate photometric information from photographic or electronographic plates. The combination of large format and good photometric accuracy make photographic emulsions an unmachted detector for a wide range of astronomical applications.

In this talk, I will briefly describe the work done at ESO over the past two years to provide European astronomers with a first class facility for the digitalization and analysis of photographic and electrographic material.

The ESO plate measuring center I shall describe is open to visiting astronomers from all countries. Priority is given to visitors from ESO member institutions working with plates obtained at La Silla.

II. Hardware

Figure 1 presents a layout of the hardware organization. Three computer controlled microdensitometers linked to a powerfull central processor constitute the basis hardware of our plate measuring facility.

Each microdensitometer has a dedicated control computer which assures all low level control functions (read encoders, display coordinates, move motors, etc) plus the transferring of photometric data to magnetic tape.

The central computer handles the communications between the user and the control computers. In addition, the flexible operating system of this machine (RTE IV) enables the user to create and manipulate files on a 50 Mby disc, to list data on a high speed line printer or to create and run application programmes.

In section III the computer organization will be described in detail. In what follows, I will outline the main characteristics of the microdensitometers.

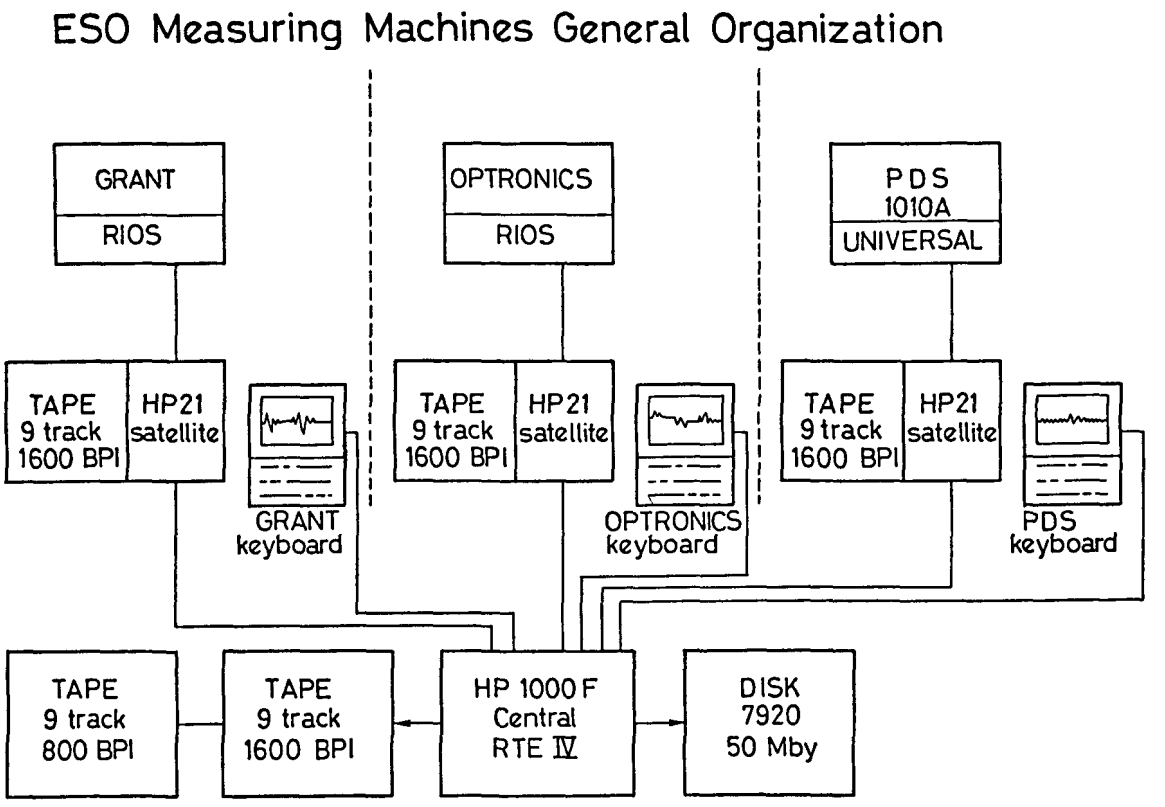

2.1 Grant comparator/densitometer

This is a standard 800 series Grant Measuring Comparator with a scanning option. This machine was originally installed in the ESO headquarters in Santiago and was taken to Geneva when ESO moved to La Silla in 1977. The driving system of the machine was seriously damaged during the transfer from Chile to Switzerland and, because it was excessively complicated (consisting of 4 motors and 5 clutches) we decided to replace it by essentially the standard driving system used at ESO for telescope control. This basically consists of DC servos and a computer controlled position feedback loop from Heidenhein encoders.

In the case of the Grant machine, the positional accuracy is limited by periodical errors in the driving screw. Figure 2 shows the results of testing this accuracy with a laser interferometer mounted on the moving stage and accurate to ±0.01μ. Plotted on this figure is the difference abs (ΔX) = |LASER-ENCODER| as a function of table displacement in centimeters. After correcting for scale errors

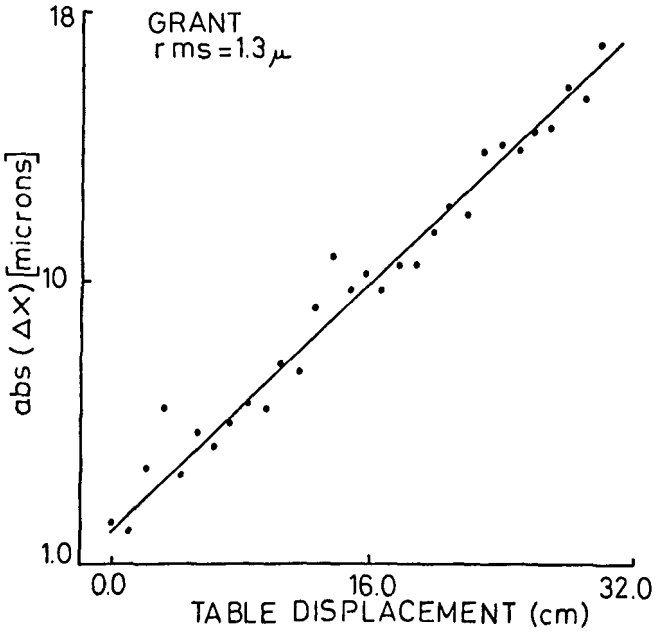

in the encoder (straight line) the residual rms scatter is 1.3μ over a displacement of 32cm. In practice, the use of higher order plate helps equations to better account for these periodic errors; the actual accuracy of radial velocity measurements is normally significantly less than one micron. Experience on 12 Å/mm Coudé plates from the 1.5m telescope at La Silla shows typical rms deviations from the plate solution of order 0.7μ and plate-to-plate accuracies of better than 1 km/sec for late-type stars.

The Grant can also be used as a one axis microdensitometer and is particularly useful for scanning Coudé plates where the spectral curvature is low and can be neglected over the in-focus portion of the spectrogramme. Due to the design of the pre-slit assembly and the large slits usually used at the Grant scanning is limited to densities below D 3. Beyond this value, the readings start to be substantially affected by scattered light.

2.2 OPTRONICS Specscan S-3000

This is a flat-bed scanning microdensitometer built for ESO as a prototype by Optronics Inc. It features a granite base with air-bearing stages where plates of up to 35x35 cm can be mounted on plate-holders.

The machine was installed in Geneva in early 1974 and after a long series of

malfunctions it was decided in 1975 to modify it rather drastically. I will mention the modifications necessary to bring this machine into operation as a warning to anybody considering purchasing a flat-bed densitometer from Optronics Inc. From the original electronics we only kept the Heidenhein linear encoder; everything-else motors, power supplies, DC amplifiers, light detector system, etc. was replaced. A similar control system to that used on the Grant and largely based on research done at ESO for telescope control applications was installed on the S-3000. The installation of a sophisticated driving system revealed a series of mechanic weaknesses which had to be repaired. In addition the turn-table used for mounting plates was re-designed and a new one built. Aside from these major modifications a great number of minor changes were introduced to improve the performance of the machine.

The final result is quite rewarding. The positional accuracy of the machine is excellent. Figure 3 shows the result of the laser interferometer calibration for the S-3000. Here the rms scatter about the scale-line is less than 0.3μ! This coupled with the outstanding thermal stability provided by the granite support makes the S-3000 a powerful instrument for astrometric work.

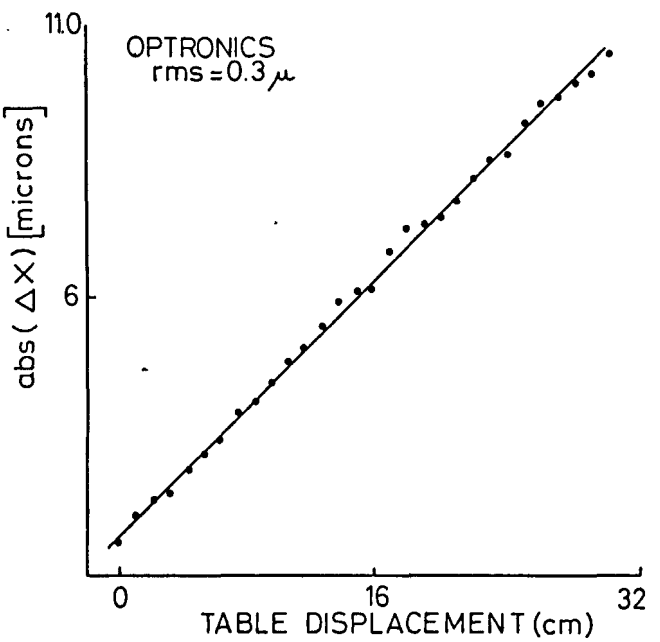

The size of the stage limits the maximum area which can be scanned to 35 x 35 cm. Much larger plates can be mounted on the stage; individual objects on a large number of 50x50 cm plates from the 2.5m Dupont telescope at Las Campanas have been successfully digitized with this machine.

The photometric system of the S-3000 is linear for densities up to D$\sim$3.0 and saturates rapidly at higher values. Again scattered light is responsible for most of this non-linearity. The photometric stability of the machine is remarkable; over a period of 48 hours the S-3000 is stable to ±0.01D and this figure also includes mechanical shifts.

2.3 PDS 1010A

Partly due to the high cost involved in upgrading the S-3000 to measure densities up to D=5 and mostly due to plans of installing a multi-element diode array in this machine to convert it into a fast scanner for Schmidt plates, it was decided to incorporate a PDS 1010A (5D) microdensitometer to the measuring facilities already in existence.

Aside from the 5D option this is the standard 25 x 25 cm PDS microdensitometer. This machine was installed in Geneva in August 1979 and since October it has been regularly used for astronomical research.

We have interfaced it to an HP21MX computer using the standard PDS universal interface which we modified to allow DMA transfer of data to the control computer. In addition to simplifying the control software, this modification has increased the speed of the machine. At present we can scan seven 40x40-pixel "stars" per minute. For larger areas, and high density gradients, however, the scanning speed is entirely limited by the time constant of the logarithmic amplifier. We are at present surveying the market for a faster component.

The photometric system of the PDS is well known and in our machine has been tested to be linear to at least D = 4.0.

3. The Control System

A schematic diagram of the organization of the control system is shown in Figure 4. Each microdensitometer is controlled by a dedicated HP21MX computer (satellite). An assembler program in the satellites handles all low level functions as described in section 2. Commands from the users are relaid to the satellites from a central HP 1000 F machine operating under RTE-IV by a high-speed parallel link program developed at ESO for telescope control applications.

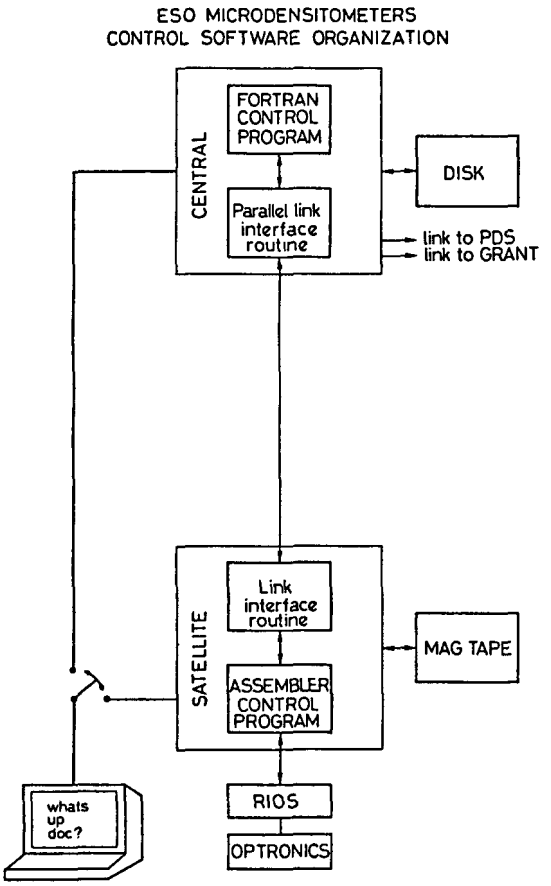

Under normal operation, therefore, the user runs a FORTRAN control program at the central computer. This program in turn initializes the link program, communicates instructions to the satellites, receives data from the satellites and displays it back in the user console or stores it on disk. The RTE-IV operating system of the central system also allows the user to create and manipulate files on the 50 MBy disk, to run application programs, to reduce or display one or two dimensional data etc.. All this without leaving the microdensitometer. Each of the

satellites has 24K of memory out of which 8K are data buffers and another 2K are used to store different types of files as I will describe later. The central system has 128K of memory out of which three 14K partitions are used by the control programs. An effort has been made to implement a large number of rather sophisticated features into the standard control programs in order to increase its flexibility. This has been done hierarchially so the user can operate a machine in its simplest mode without knowing about this sophistication. In addition, users having special requirements can write their own control programs using Fortran-callable routines to control the microdensitometers i.e. (MOVE, SET, READ, SCAN, etc.). This is illustrated in the appendix which is a simple control program written to scan pupil plates.

Exceptionally, during breakdown of the central computer or other unforeseen reasons, a stand-alone program can be loaded into the satellites which then assume the complete operation of any given microdensitometer. A switch on the console connects it either to the central or the satellite computers. To the user both modes of operation are identical except that in the stand-alone mode no access to the operating system is possible and all input/output of data must be done using magnetic tapes.

Typical commands from the operators are:

command	instruction
SET, X,Y	set coordinate display to (X,Y)
MOVE, X,Y	move stage to position (X,Y)
FROM, X,Y	define starting position for a scan at (X,Y)
TO, X,Y	define ending position to (X,Y)
SCAN	start scanning
ETC	

After a MOVE or a SCAN command the FORTRAN control program is turned off by the

SATELLITE and is re-scheduled after the instruction has been completed. Thus load on the central system due to the control programs is actually minimal since, as I have already mentioned, all time consuming control functions and output of data to mag tapes are handled by the satellites.

In order to automatize as much as possible the operation of the microdensitometers we have introduced several types of disc files. These are:

DATAFILES files where the user stores manual measurements of coordinates and A/D converter readings. Simple commands (CREATE, OPEN, CLOSE, PURGE, LIST) enable the user to manipulate these files.

REFFILES the reference files are used to store catalogues of objects (stars, comparison lines, scratches, etc) for later access. The command REFFILE, name stores the content of the file name in memory for fast access. To move to an entry identified as id on the file the user types GO,id. The command NEXT (N) instructs the machine to move to the next entry in the file. The Grant machine is equipped with a Pedal which can be programmed with any of these instructions. Thus, by storing the positions of the comparison lines on a REFFILE, it is possible by simply pushing the pedal to automatically center these lines. A Coudé plate can be measured and reduced in less than 10 minutes using REFFILES! In addition there are commands like SCAN, ALL which instructs a machine to scan a rectangle of pre-specified dimensions around each entry of the reference file (up to 500).

BATCH FILES These files allow the user to store series of instructions to be executed sequentially. This is useful for long scans around areas centered on several objects on a plate.

In additions to these files there are HELP files used to store new information for the user and SOFT files used to program the console software keys.

4. Application Programs

The user CRTS are HP2148A graphics consoles where the operator can display his data immediately after completion of a scan. Alternatively, since the control programs on the CENTRAL machine are not active driving a scan, the user can display and manipulate data from a previous scan while the machine is scanning a new one. The standard ESO image handling package (IHAP) is available to the user for these operations and can be directly run from any console.

In addition to IHAP there are standard programs for astrometry, radial velocities, stellar photometry etc. developped by users of the system.

Conclusion

ESO has developped extensive facilities where astronomers can digitize and/or reduce their two dimensional images. In order to refine and expand these facilities we need imput from users with a variety of interests. The ESO facilities are open to all of you. Use them!

```
0002          PROGRAM PUPIL
0003    C
0004    C
0005    C  PROGRAM TO MEASURE PUPIL PLATES USED TO
0006    C  TO DETEMINE COMATIC ABERRATIONS OF A TELESCOPE
0007    C
0008    C  RUN AS: RU,PUPIL AND ANSWER QUERRIES
0009    C  LOAD WITH ROUTINES: %MEAS1,%MEAS2,%MEAS3
0010    C
0011          INTEGER LINE(5),PNAME(3),SFILE(3),IPLAT(8)
0012          COMMON ICOM(50)
0013          DATA PNAME/2HPU,2HPI,2HL /
0014          DATA PI/3.14159/
0015          DATA X,Y/0.,0./
0016    C
0017    C GET TERMINAL LU
0018    C
0019          CALL RMPAR(LINE)
0020          LU=LINE(1)
0021    C
0022    C INITIALIZE MICRODENSITOMETER (1=OPTRO, 3=PDS)
0023    C
```

```
0024        CALL INIT(1,0,PNAME)
0025  C
0026  C SET DISPLAY COORDINATES TO X=0, Y=0
0027  C
0028        CALL SET(IER,X,Y)
0029        IF(IER.NE.0) GOTO 900
0030  C
0031  C GET PLATE IDENTIFICATION FOR OUTPUT
0032  C
0033        WRITE(LU,1001)
0034   1001 FORMAT(" GIVE PLATE IDENTIFICATION (8A2) _")
0035        READ(LU,1002) IPLAT
0036   1002 FORMAT(8A2)
0037  C
0038  C GET RADIUS OF PUPIL
0039  C
0040     100 WRITE(LU,1003)
0041   1003 FORMAT(" ENTER RADIUS IN MICRONS _")
0042        READ(LU,*) IRAD
0043  C
0044  C TERMINATE IF RADIUS = 0
0045  C
0046        IF(IRAD.EQ.0) CALL BYE
0047        R=FLOAT(IRAD)
0048  C
0049  C MOVE ON A CIRCLE OF RADIUS R CENTERED AT (0,0)
0050  C
0051        DO 200 N=1,32
0052        RN=FLOAT(N)*PI/16.
0053        ALFA=N*360./32.
0054        X=COS(RN)*R
0055        Y=SIN(RN)*R
0056  C
0057  C MOVE TO (X,Y) AT SPEED 40
0058  C
0059        CALL MOVE(IER,X,Y,40)
0060        IF(IER.NE.0) GOTO 900
0061  C
0062  C READ COORDINATES AND A/D CONVERTER
0063  C
0064        CALL READ(IER,X,Y,IAD,1)
0065        IF(IER.NE.0) GOTO 900
0066  C
0067  C OUTPUT TO LINE PRINTER
0068  C
0069        WRITE(6,2001) N,ALFA,X,Y,IAD
0070    2001 FORMAT(1X,I4,3F10.1,I10)
0071     200 CONTINUE
0072  C
0073  C SCAN END, MOVE TO CENTER
0074  C
0075        CALL MOVE(IER,0.,0.,40)
0076        IF(IER.NE.0) GOTO 900
0077  C
0078  C REPEAT AT WITH A DIFFERENT RADIUS
0079  C
0080        GO TO 100
0081  C
0082  C TURN OFF MACHINE AND CLOSE ALL FILES
0083  C
0084     300 CALL BYE
0085        STOP
0086  C
0087  C PRINT ERROR MESSAGES
0088  C
0089     900 WRITE(LUPRT,9001) IER
0090    9001 FORMAT(" COMMUNICATION ERROR # " I3)
0091        CALL BYE
0092        END
0093  END$
```

THE CALIBRATION OF A MULTI-ELEMENT MICRODENSITOMETER.

L. Swaans
Sterrewacht, Huygenslaboratorium
Wassenaarseweg 78, 2300 RA Leiden, The Netherlands

Although I will discuss in this paper the calibration procedure as it is developed for the ASTROSCAN, a 128 elements microdensitometer in use in Leiden and equipped with a Reticon photodiode-array type RL 128 EC, the general idea and the remarks I will make apply also to other densitometers.
The main task of a microdensitometer is to produce a map of densities in digital form from a specified area on a photographic plate. The for measuring and digitizing essential part of the ASTROSCAN is schematicly represented in fig. 1. The optical system of the ASTROSCAN is fixed except for focussing, so the pixelsize is fixed also (10 x 10 μm^2). The response of the Reticon-array to the light transmitted through the plate is digitized into an array of ten bits numbers. The aim of the calibration is to find parameters which will make it possible to convert these numbers into densities.
In case of a multi-element microdensitometer these parameters should not only describe the individual characteristics of the diodes, but also, if necessary, their sensitivity to scattered light (the illuminated area on the plate is of course much bigger than just one pixel) and to crosstalk (the response of one diode due to the illumination of an other).
But let us start with the most simple case in which the response of a photodiode is linear to light intensity. Then the next equation will hold:

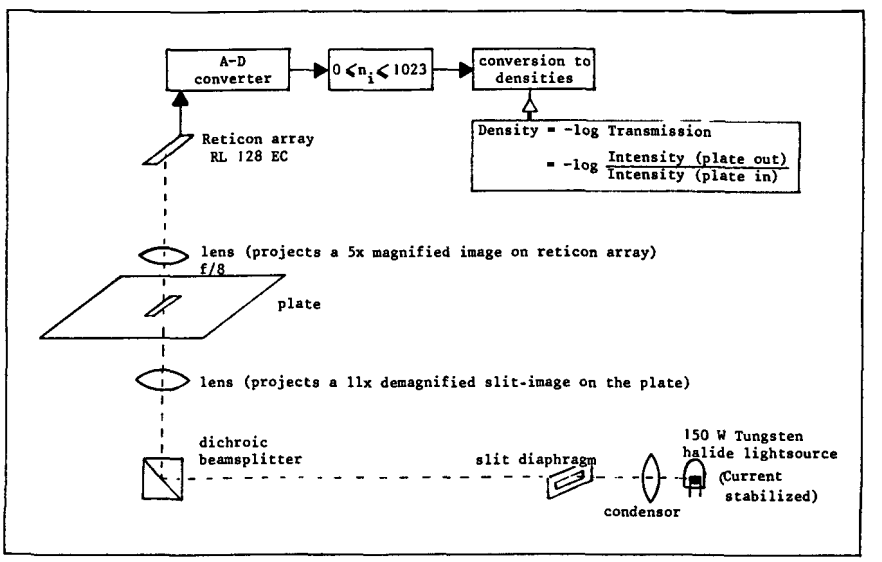

fig. 1 *Schematic representation of the measuring and digitizing process in the ASTROSCAN.*

$$\frac{I}{I_o} \cdot T = c \cdot (r - dc) \qquad (1)$$

where
- I is the intensity of the light source,
- I_o the chosen intensity unit,
- T the transmission of the plate,
- c a constant dependent of I_o,
- r the digitized readout of a photodiode,
- dc the digitized darkcurrent of that diode.

The choice of the intensity unit defines also the constant. Say $I=I_o$ if $T=1$ yields $(r-dc)=1024$ then $c=1/1024$. So the right hand side of the expression is determined. Taking the negative $^{10}\log$ of each term transforms equation (1) into the following:

$$M + D = x \qquad (2)$$

where
- $M = - {}^{10}\log \frac{I}{I_o}$ the magnitude of the light source,
- $D = - {}^{10}\log T$ the density of the plate,
- $x = {}^{10}\log 1024 - {}^{10}\log(r-dc)$

so the readout is converted to a scale analogous to density.
If one measures a set of uniform neutral density filters, of which one does not need to know the density, at different, also not necessarily known magnitudes of the light source, one can make the following scheme:

	filter densities								
	D_1	D_2	D_3	D_4					D_n
magnitudes									
M_1	x_{11}	x_{12}	x_{13}	x_{14}	-	-	-	-	x_{1n}
M_2	x_{21}	x_{22}	x_{23}	x_{24}	-	-	-	-	x_{2n}
M_3	x_{31}	x_{32}	x_{33}	x_{34}	-	-	-	-	x_{3n}
M_4	x_{41}	x_{42}	x_{43}	x_{44}	-	-	-	-	x_{4n}
⋮	⋮	⋮	⋮	⋮					⋮
⋮	⋮	⋮	⋮	⋮					⋮
⋮	⋮	⋮	⋮	⋮					⋮
M_m	x_{m1}	x_{m2}	x_{m3}	x_{m4}	-	-	-	-	x_{mn}

If the response is indeed linear then the difference between each two columns or rows is constant, because this difference is determined only by the difference between either two filter densities or two lamp magnitudes. Deviations indicate non-linearity of the diode responses. For the Astroscan the latter is the case. But then one can write equation (2) for each matrix point x_{ij} in the following form:

$$M_i + D_j = (1 + \Delta)(x_{ij}) \qquad (3)$$

where Δ is the function describing the deviation from linearity.
Because M_i and D_j are independent of the diodes used, and in first order approximation Δ will not differ much for different diodes, one can set up a set of equations (3) where x_{ij} is calculated from averaged readout minus darkcurrent values over all diodes. Take for Δ a linear broken function with fixed abscisses for the breaking points and one has a set of condition equations which can be solved by a least squares method.
The least squares method will give non trivial solutions if one difference between either two filter densities or two lamp magnitudes is defined a priori. If one uses in one case no filter at all, say for D_1, then $D_1 = 0$, and if one assigns a certain density to another filter, then the densities resulting from the least squares fit will be equal to real densities except for a factor which is equal to the ratio of the real and assigned density of that particular reference filter. This factor can be kept close to one if the assigned density results from measurements by other means.
Errors in the resulting values for M_i, D_j and Δ are very small (mainly below 0.001), only for the higher ($3 \rightarrow 4$) densities and x-values for $\Delta(x)$ the errors reach up to 0.01. Fig. 2 displays the results for Δ for a well chosen set of breaking points. Note that the dynamic range of the readouts can be, and for the ASTROSCAN in fact is, increased by taking the average of many readings, as the readout noise is comparable to 1 unit of the A-D converter.

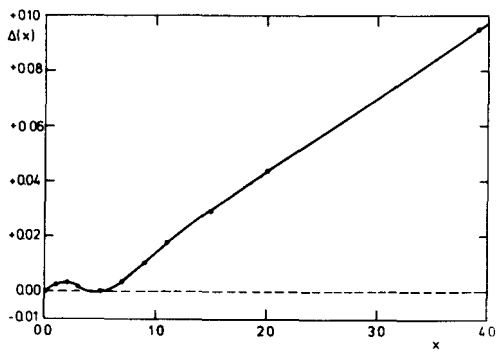

Fig. 2 Mean deviation from linear response of Reticon array RL 128 EC. x is the readout converted to a scale analogous to density. Δ(x) is the deviation in density.

The deviations from linearity of the diode response result from three effects:

i) A sinusoidal component caused by electronics.

ii) A possible slope component caused by assigning a slightly incorrect value to the reference filter.

iii) Another slope component caused by the characteristics of the diodes.

Applying these results to individual diode-readouts I found a systematic difference in the residuals of the even and odd numbered diodes, caused by the fact that the readout is accomplished by two independent channels.
From these residuals one can derive a second order correction for each group, and split this correction in two parts, one being constant, the other one dependent of x, so that the latter one is as small as possible.
Doing the same procedure again for individual diode residuals, one gets a set of third order corrections for the alinearity and the final equation becomes:

$$M_i + M_b + M_l + D_j = (1 + \Delta + \Delta_b + \Delta_l)(x_{ijl}) \qquad (4)$$

where
- l is a diode index,
- b an index for the even or odd group to which l belongs,
- Δ_b the dependent component of the second order correction,
- Δ_l the dependent component of the third order correction,
- M_b the constant component of the second order correction,
- M_l the constant component of the third order correction.

Note that variations in the M_l are also caused by a possibly non uniform illumination of areas seen by different diodes.

Δ_b and Δ_l came out to be negligible. As the Δ's mainly describe the properties of the diode responses one may hope and somewhat expect that they will be stable over longer times. Indeed experience over more than one year has not revealed any change of the Δ's, so that in fact this kind of calibration must be done only once between component changes.
Thus in case of an actual measurement the only parameters left to be determined are the darkcurrents and the individual magnitudes M^l (= $M + M_b + M_l$, where M is the magnitude of the light source during the measurement).
This is done by reading the darkcurrents and the same set of filters (of which the densities are known now) with the appropriate lamp magnitude.
Once these measurements are done scan readouts are transformed to density in real time by using equation (4) but now with density as the unknown. This on-line conversion can be done very fast by using tables for the darkcurrents, the individual magnitudes and for Δ, and using a special algorithm for a base 2 logarithm for the conversion from readout to its x-value.
One of the advantages of on-line conversion to densities by software is the possibility to average over larger samples in the proper quantity. For instance if the signal to noise ratio of a readout is too low, one can first average in readouts coming from one pixel, or if a 10x10 μm^2 pixelsize is too small (which can be the case if one does not need such a high resolution) one can average over a sample of pixels after transformation to density, but before storage of the data on tape or disk.

What about the quality of the resulting densities?
Except for calibration errors, which can be kept very small (mainly below 0.001 in density) there are other error introducing factors:

i) Readout noise
ii) Instability of darkcurrents and light source intensity
iii) Pixelsize
iv) Scattered light and crosstalk

For some of these it is immediately clear that they introduce systematic errors, but for others which have for instance Gaussian error distributions one has to realize that this is mainly true in transmission but not in density.
So let us give them a closer look and see if something can be done about it.

The readout noise.
Fig. 3 gives the readout noise $\sigma(r)$ as function of the readout r for moving and not moving table. The higher values of $\sigma(r)$ for moving table are caused by inhomogeneities in and dust particles on the condensor, which is close to a focal plane and which is slightly vibrating because of the step movements of the table holding the plate. But this affects only the effective lamp intensity so this noise contribution will be proportional to the readout. The increase of $\sigma(r)$ is so low however that in terms of density this does not exceed 0.001 . What is left is an almost constant noise of about 0.65 expressed in A-D converter units.

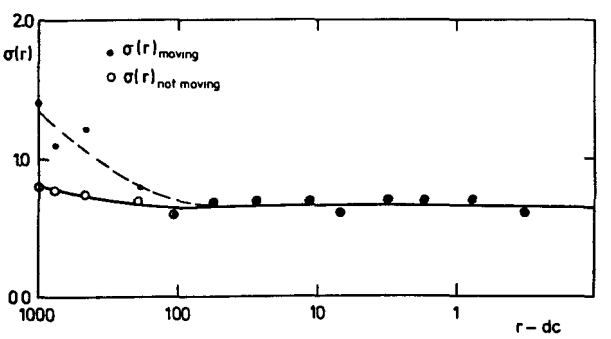

Fig. 3 Standard deviation of readout ($\sigma(r)$) as function of readout minus dark-current (r-dc) .

This noise is caused by the electronics and may be constant in readout scale, due to the logarithmic operation it will increase very rapidly in density scale for the higher x-values, and thus for the higher densities.
Measured densities are becoming unreliable as soon as the noise induced by the measuring machine becomes comparable to the plate noise. Except for that the noise distribution in density is no longer gaussian but skew and thus generates a bias in the mean density obtained. One can diminish these effects by decreasing $\sigma(r)$ by taking a larger sample of readouts and/or by modifying the very low or even negative (r-dc) values so that after conversion into density they will yield in the mean approximately the proper density. The modification is done by a kind of error function which fits smoothly to the unmodified part of the readout scale. (For more details see Schoenmaker et al. (1978))

The instability of darkcurrents and light source intensity.
These instabilities can be seen as drift in time and thus cause also systematic errors. Calibrations executed with time intervals of five minutes up to more than two days showed that variations in intensity are negligible or less than 0.002 in density for the longer periods. Darkcurrent drift is normally less than 0.1 readout units per hour, but not negligible small for time consuming measurements, including also areas with considerable density. This problem is solved by refreshing the darkcurrents at much shorter time scales.

The pixelsize.
Densities are calculated from the mean transmission over a pixel although one wants to know the mean density. In doing this again a systematic error is introduced, which increases as the density gradient over the pixel increases. One can make an estimate of this error by neglecting the plate noise and assuming that the density gradient over the pixel is constant.
This is the case if the pixelsize is much smaller than the point spread function of the emulsion and much bigger than the grain size.
Fig. 5 shows the systematic error as a function of pixelsize for several density gradients.
In case of the ASTROSCAN, which has a fixed pixelsize of 10x10 μm^2, larger pixelsizes are realized on line by software, but because of the here mentioned reason, this is done after transformation to density of elementary pixel readouts.

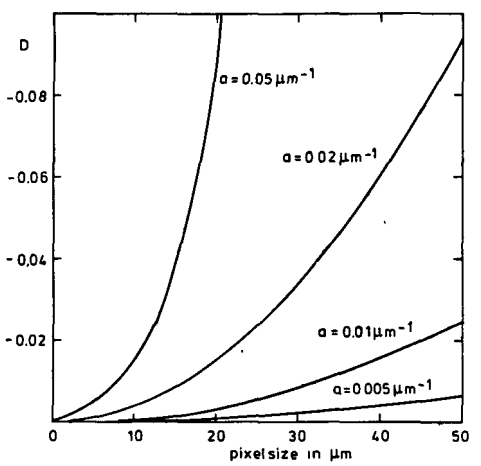

Fig. 4 Systematic error (D) expressed in density due to averaging in transmission in stead of density as a function of pixelsize (in µm) for several gradients (a) expressed in density per µm.

Scattered light and Crosstalk.
Scattered light and crosstalk are typical phenomena for multi-element machines (see Swaans(1979)). Scattered light because one has to illuminate a larger area of the plate than needed for the detection area of one element, and crosstalk because it causes a modified element response due to the illumination of other

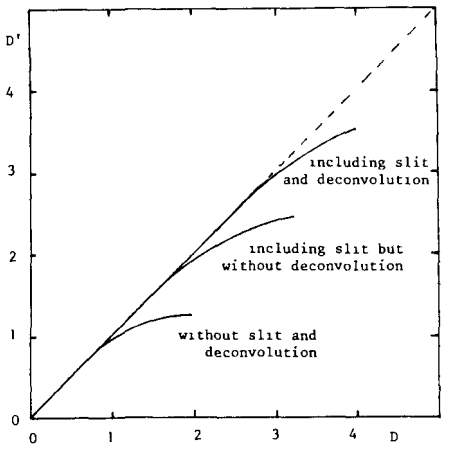

Fig. 5 Relation between calculated (D') and true (D) densities in various stages of improvement.

elements in the detection system. The influence of scattered light can be minimized by minimizing the illuminated area (for the ASTROSCAN this is done by placing a slit-diaphragm) but can never be eliminiated. It can be further reduced by deconvolution if one knows the sensitivity distribution of the elements over the illuminated area and to the illumination of the other elements for the crosstalk effect. These distributions have been determined experimentally and an off-line program takes care of the deconvolution. Fig. 5 shows the improvement which is achieved for the ASTROSCAN by each of these steps.

References:

Schoenmaker and Swaans: ASTROSCAN, Description of the on-line software (1978) (To be obtained from Leiden Observatory)

Swaans: Scattered Light and Crosstalk in a Multi-element Microdensitometer. Proceedings of the International Workshop on Image Processing in Astronomy. Triëste, June 1979. (in press)

AVERAGING PHOTOGRAPHIC CHARACTERISTIC CURVES

John Kormendy
Kitt Peak National Observatory[1]

We review the advantages of combining the calibration spots of similarly treated photographic plates into an average characteristic curve. This process increases the accuracy and dynamic range of the H & D curve, especially when the spots are too few in number or too far apart in intensity. Systematic errors in spot intensities can be identified and corrected.

The theme of this paper is that there are many advantages to combining the photographic characteristic curves of different plates which have received similar treatment (Kormendy 1977; Burstein 1979). Generally, Kodak spectroscopic plates can be averaged if (1) they come from the same emulsion batch and box, (2) they receive identical (but not necessarily simultaneous) hypersensitizing, (3) they are exposed similarly, with the usual latitude of a factor of $\leqslant 2$, and (4) they receive the same development. This development need not be simultaneous for all the plates, but it must be reproducable and uniform, as with the standard Mt. Wilson plate rocker (Miller 1971). Under the above conditions, it is usually possible to combine 5-20 or more sets of spots taken on different nights of the same observing run.

Different spot exposures define a series of H & D curves which are parallel but mutually separated by arbitrary shifts in log (It), produced by differing lamp intensities I or exposure times t. To combine these curves, we demand that the same functional form fit all sets of spots. For example (Kormendy 1977; cf. de Vaucouleurs 1968), we ask that the intensity of the ith spot in the jth spot set be given by

$$\log I_{ij} = a_{0j} + \sum_{k=1}^{n} a_k (\log \omega_{ij})^{k/2} \quad . \tag{1}$$

where opacitance $\omega = 1/T - 1$, T the transmission, and $n \approx 6$. The coefficients

---

[1]Operated by the Association of Universities for Research in Astronomy, Inc., under contract with the National Science Foundation.

a_k are the same for all spot sets. The a_{0j} values are the shifts in log I which are required to bring the various spot sets into coincidence. The above functional form is arbitrary; other polynomial relations between suitable functions of I and T would work equally well. The procedure is to make a single least-squares solution for equation (1) which simultaneously calculates the coefficients a_k and the shifts a_{0j}. This is an easy generalization of least-squares algorithms in which the zero-order term is calculated separately from the other coefficients (e.g., Bevington 1969).

We can illustrate the advantages of this technique with a series of examples. Figure 1 shows a characteristic curve obtained by using the Palomar Schmidt sensitometer. This has only 12 spots spaced by $\sqrt{2}$ in intensity; several of these are usually overexposed or underexposed in any spot set. However, ten sets of 89 spots altogether define the curve very well. This is especially true in the critical region of the toe, which is essential for those applications

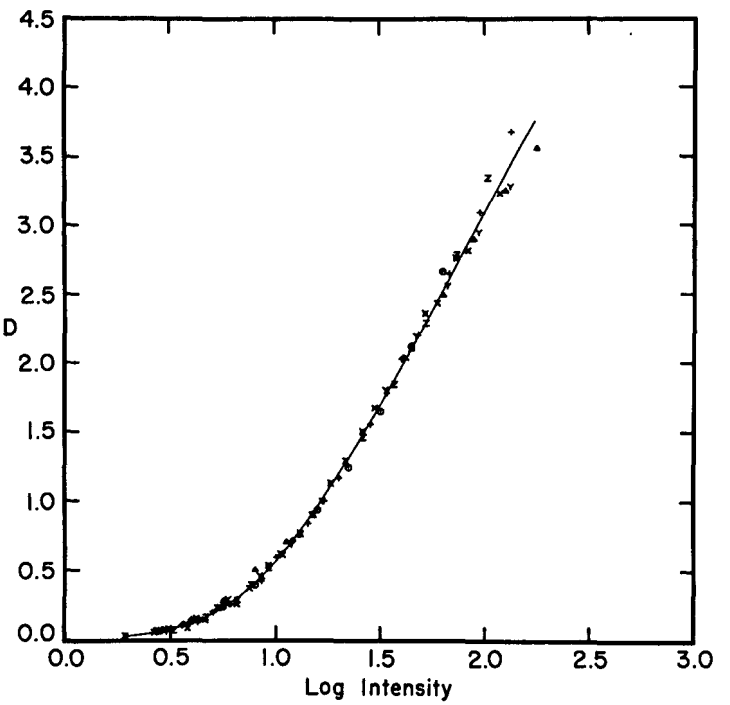

FIG. 1.—Characteristic curve for a series of ten sets of calibration spots exposed 3 min onto 103a-D plates behind a Wr 4 filter. The plates were developed 4 min in D-19. Each set of spots is represented by a different symbol. The line is equation (1) displayed as a standard H & D curve; D = -log T. The characteristic curves in this and the next two figures refer to the mask calibration plates discussed in the Appendix of Kormendy (1977).

where light exposures are unavoidable (e.g., at very large f/ ratios). Thus averaging characteristic curves largely solves problems of having too few spots, or spots which cover an insufficient intensity range, or spots which are too far apart in intensity. Occasionally discrepant spots (e.g., due to dust in the sensitometer) can be discarded without compromising the accuracy of the calibration. Similarly, a large error in the exposure of one spot set is no longer a problem, but is actually useful to increase the dynamic range of the H & D curve.

Figure 2 illustrates another use of average characteristic curves, namely the correction of systematic errors in the spot intensity scale. The initial solution shows that the seventh spot from the low-intensity end of the Palomar sensitometer is consistently a factor of 1.185 more intense than the nominal $\sqrt{2}$ spacing would predict. Correcting this error yields Figure 3, in which the rms deviation of the points from the line is only $\sigma = 0.026$ mag arcsec^{-2}. Only one kind of error cannot be detected and recalibrated by this technique.

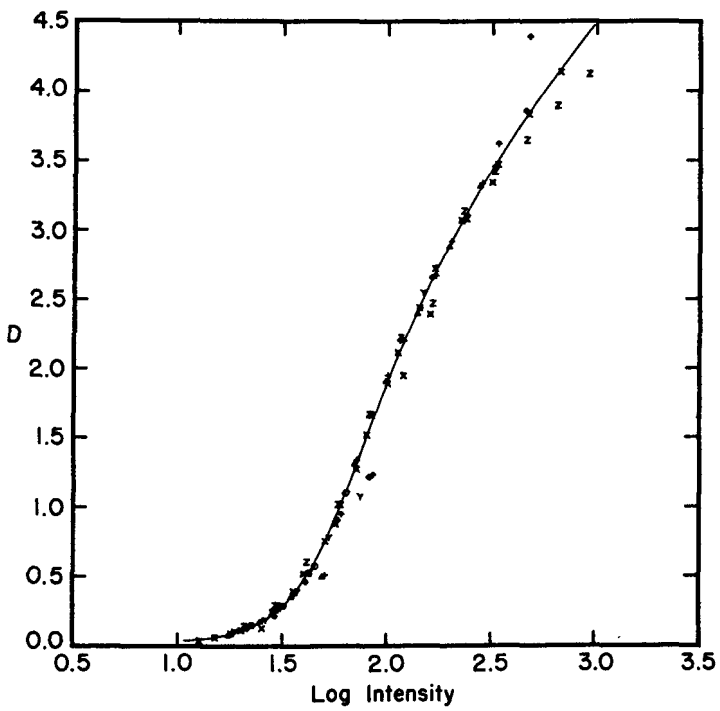

FIG. 2.—Initial calibration curve for a series of 103a-D + Wr 4 plates similar to those in Fig. 1, except that the plates were developed for 7 min in MWP-2. The same spot is consistently too high in intensity in all the spot sets.

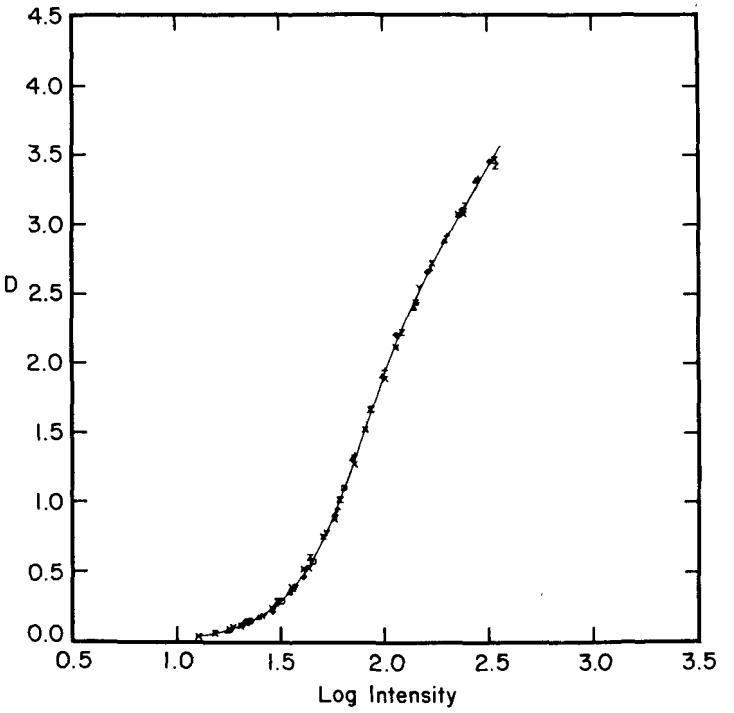

FIG. 3.—Final version of the characteristic curve in Fig. 2. The intensity of spot seven has been corrected, and the high-D end of the curve appropriately truncated. Similar corrections have been applied in Figs. 1 and 4.

If the whole log I scale is incorrect by the same constant factor, then the only effect is to change the slope of the H & D curve to an incorrect value. However, it would be difficult to manufacture this kind of error in the spot intensity scale.

Figures 1 and 3 are slightly unrealistic as practical illustrations because the exposures were all taken and developed in rapid succession during a single afternoon. Figure 4 shows an H & D curve based on seven IIIa-J + Wr 4 plates taken with the 1.2 m Palomar Schmidt telescope over the course of three nights. The different plates agree very well, despite the fact that the 2B4 emulsion batch used was very nonuniform, and despite the fact that the plates were developed in MWP-2 (which increases nonuniformities in IIIa-J plates). The only correction for varying sensitivity which has been applied was to subtract the local fog density from each spot. Figure 5 shows the deviations of individual

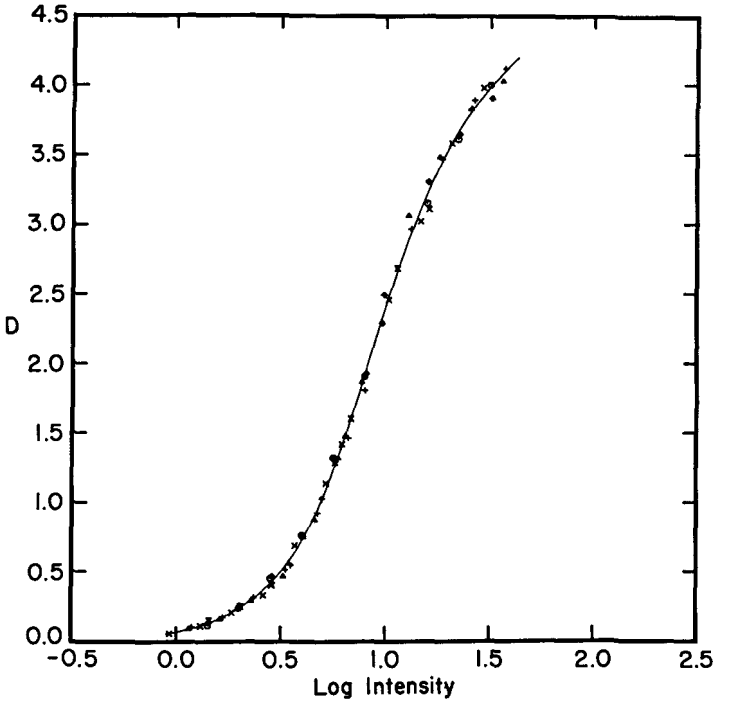

FIG. 4.—Final calibration curve for seven 1^h15^m - 2^h15^m IIIa-J + Wr 4 plates taken over a three-night observing run.

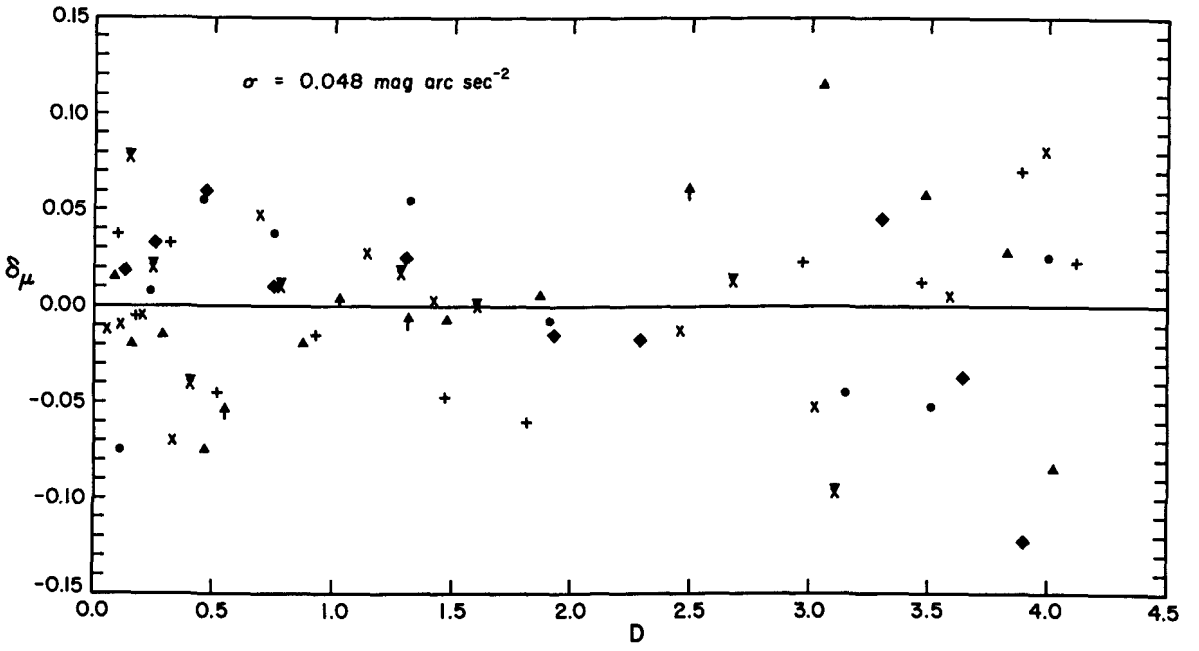

FIG. 5.—Deviations in mag arcsec^{-2} of the spots in Fig. 4 from the adopted curve. The symbols are the same as in Fig. 4. The dispersion σ is small, and there is little sign of any systematic difference in the shapes of characteristic curves for the different plates.

spots from the adopted curve, in mag arcsec^{-2}. The dispersion is only σ = 0.048 mag arcsec^{-2}, which means that the mean curve is determined to much better than 5%. Entirely similar results were found by Burstein (1979); for his (more uniform) 103a plates, σ ranged from 0.020 to 0.045 mag arcsec^{-2} in 12 calibration runs. For comparison, $\sigma \approx 0.015$ mag arcsec^{-2} for the same spot set measured repeatedly; this illustrates typical measuring errors due to the microphotometer.

Very occasionally a set of "similar" plates has clearly different characteristic curves. This is usually symptomatic of serious problems with the handling of the plates. For example, we have found that very old plates do not average well; they are of sufficiently low quality that they should be replaced in any case.

In summary, we confirm results of Burstein (1979) that it is very helpful to average characteristic curves of plates that have received similar treatment.

1. This allows discovery and recalibration of systematic errors in spot intensities.

2. It increases the accuracy of the calibration, compensating for spots which are too few in number, too far apart in intensity, or too restricted in intensity range.

3. Random measuring errors are essentially eliminated.

The resulting calibration is generally accurate to a few percent; i.e., the dispersion of individual spots from the adopted curve is $\sigma \approx 0.02$ to 0.05 mag arcsec^{-2}.

REFERENCES

Bevington, P. R. 1969, Data Reduction and Error Analysis for the Physical Sciences (New York: McGraw-Hill), p. 165.

Burstein, D. 1979, A.A.S. Photo-Bulletin, No. 20, p. 6.

de Vaucouleurs, G. 1968, Appl. Optics, 7, 1513.

Kormendy, J. 1977, Ap. J., 214, 359.

Miller, W. C. 1971, A.A.S. Photo-Bulletin, No. 4, p. 3.

SECTION II

Direct Electronic Data Acquisition. Panoramic Detector Arrays

A SHORT REVIEW OF THE PRESENT STATUS OF ELECTRONIC PANORAMIC DETECTORS

J.A. Westphal
Hale Observatories, Pasadena, California USA

Abstract

A short review of the present status of direct electronic panoramic detectors including SIT camera tubes, bare and UV enhanced CCDs, ICCDs, and CIDs is presented. Systems with image tubes and electronic detector outputs ("Boksecons") are also discussed. Examples of recent CCD results are shown.

I. INTRODUCTION

This review paper will rather selectively describe the present state of two-dimensional electronic readout detectors. An excellent and much more complete review has just appeared in Annual Reviews of Astronomy and Astrophysics (Ford, 1979) and the reader is referred to this paper for a complete bibliography and broad overview. Here I will primarily discuss the most modern, and I believe most promising, of these devices - the CCD (Charge Coupled Device) showing some recent results and summarizing the status and immediate plans of the three major manufacturers. Over the next few years I believe the CCD will displace most other electronic detectors due to its near-ideal properties for astronomical use.

First, however, I will review some of the older, more mature detectors, followed by the CCD, the intensified CCD (ICCD) and another silicon chip sensor, the CID. Some recent results from 500x500 pixel TI CCDs will complete the review.

II. "BOKSECONS"

Combinations of image intensifiers and TV camera tubes can be used to produce two-dimensional "pulse counting" systems which are to a great extent noiseless for low light levels and are therefore essentially "ideal" detectors limited only by the quantum efficiency of the input photosurface. These systems were popularized by Alex Boksenburg (1973), and a modern version using a SIT camera tube to be flown on Space Telescope as the Faint Object Camera, will be described in the next paper by Ducchio Macchetto.

III. SIT CAMERA TUBES

SIT (Silicon Intensified Target) camera tubes were first applied to astronomical observations by Westphal and his colleagues (1973) and have since been used by a number of people for both two-dimensional photometry and especially spectroscopy. The discussion by Ford (1979) fairly represents the present state-of-the-art. In general SITs are most useful for faint object spectroscopy in the blue, although, as we will see below, even this part of the spectrum may likely be usurped by the most modern versions of the CCD which have blue light quantum efficiencies near 60% in contrast to SIT values near 10%.

IV. CCDs

Charge coupled devices are small silicon chips with two-dimensional arrays of essentially isolated photosites which can be electronically interrogated to generate low noise electrical signals proportional to the number of captured incoming photons during an exposure. The most modern devices are capable of

collecting up to 80% of the incident photons near 7000Å and have quantum efficiencies of more than 10% from shortward of 4000Å to longward of 10000Å. The "readout" noise levels are in the range from 12-30 electron equivalent, and by cooling to below -100°C the thermal dark current can be made negligible even for multi-hour exposures. Since the total number of charge carriers that can be stored is greater than 10^5/pixel, the CCD usually has wide dynamic range (approaching 10^4) while having essentially a linear response. CCD arrays have been built with up to 800x800 elements and during the next few years it is likely that 1200x1200 or larger arrays will be made.

A major difficulty for most astronomers who would like to use CCDs has been the limited availability of these almost ideal detectors. In the following paragraphs the present (November 1979) status and plans of the three major manufacturers will be described. This data was gleaned primarily from an informal meeting at Goddard Space Flight Center convened by NASA in November 1979.

The first commercially available CCDs were manufactured by Fairchild. Presently the largest arrays available are 488x380 pixels, each 12x18 microns. These chips are "front" illuminated. That is, the light enters the silicon chip on the same side as the CCD circuitry. This techinque allows the chip to be quite thick (~250μ) and therefore rugged. Noise levels obtained while reading the array run near 30 e^-. By a special processing step now available from Fairchild the useful area of the array has been substantially increased and quantum efficiencies are expected to range from about 50% near 7000Å to perhaps 10% at 4000Å. An undesirable side effect of the thick silicon substrate has been identified and described by Marcus et al. (1979). When high energy cosmic radiation enters the chip long trails of charge carriers are formed which then diffuse into the electrically active area forming "comets" in the image. Several of these events are normally observed each hour over the chip causing serious degradation during long exposures. It is expected that special processing techniques during manufacture can relieve or eliminate this problem with some possible loss of infrared sensitivity.

For several years Texas Instruments has been developing CCD sensors for eventual use on NASA flight projects under contract to the Jet Propulsion Laboratory. To maximize the quantum efficiency and the spatial resolution (MTF) of these sensors TI has used "backside" illumination of thinned silicon chips. During the processing of the CCD, silicon is removed from the optically active area on the side opposite the electrical circuitry until the substrate is about 10μ thick. In this way all the incoming photons have an opportunity to interact with the CCD generally yielding much higher net quantum efficiencies, particularly in the blue part of the spectrum.

The very much thinner CCD also does not suffer so severely from cosmic ray "comets", since each event is almost always confined to a single pixel where it deposits ~2500 charge carriers, well within the storage capacity of the pixel. The thinned chip is more fragile but in fact adequately durable, even for astronomers, as long as it's protected from physical contact.

The TI chips which have until now been used for astronomy are evolutionary test devices of 100x160, 400x400 and 500x500 pixels. Most of the experience has been related to the development of the Wide Field/Planetary Camera to be flown on Space Telescope. The WF/PC will use eight 800x800 TI chips, four in the Wide Field Camera and four in the Planetary Camera, to produce 1600x1600 pixel formats by optical multiplexing. The 500x500 units now being used on ground-based telescopes have 15μ square pixels, quantum efficiencies near 70% at 7000Å, readout noise levels of 12-15 e^- and "full well" storage capacities of about 5×10^4 e^-/pixel. Since surface property difficulties will prevent

CCDs from being sensitive in the UV below about 3500Å, the ST sensors will be vacuum coated with about 1500Å of an organic phosphor (probably Coronene) to "down convert" the UV photons to 5200Å where the CCD is sensitive. Tests indicate net quantum efficiencies from 1200Å-3500Å of more than 20%.

Unfortunately it is likely to be some time before the 800x800 TI chips, developed by NASA for Galileo and ST, are generally available for ground-based users. It is likely that a newer technology recently developed at TI will produce commercially available chips fairly soon. TI expects much the same properties from these "Uniphase" chips with much better blue quantum efficiency along with much better manufacturing "yield".

Very recently astronomers have become aware of the potential of a commercially available TV format CCD manufactured by RCA. These chips have a 512x320 format of 25μ pixels. They are thinned, back illuminated and can be obtained bonded onto a transparent substrate for protection and antireflection coating. These chips are only now being tested to determine noise, dark current levels and linearity. However, there is a strong expectation that these properties will be well behaved and that a CCD with 50% quantum efficiency at 4000Å can be obtained for ground-based use immediately! The potential of bonding to special optical elements (field flatteners, etc.) and maybe to sapphire, which is a much better index match to silicon, will soon be explored with RCA.

V. ICCDs

Following the same idea as the SIT camera tube, a number of groups have attempted to use a CCD sensor in a vacuum bottle with a conventional photocathode to produce an intensified CCD. Various techniques are being tried: a proximity focus system using a Varo photosurface with a Texas Instrument CCD is being developed by the Goddard Space Flight Center (Williams, 1976), and an electrostatic tube is being developed with an Electron Vision Corporation photosurface and a Fairchild CCD by Doug Currie (1976) at the University of Maryland. Until recently no consistent results have been obtained, although the promise of a compact, simple, pulse counting system is attractive for very low light level applications.

VI. CIDs

The Charge Injection Device is manufactured by General Electric (Aikens et al., 1976) in fairly small array sizes (100x100 pixels of 60x80μ size and 244x248 of 30x40μ pixels). Although the single frame readout noise is high ($\sim$250 e^-) the CID can be non-destructively read out a large number of times ($\sim 3 \times 10^5$), without significant degradiation, and the signals averaged digitally to reduce the effective noise level to values approaching 1 e^-. Unfortunately, at reasonable readout rates this requires some days, limiting the technique to only extremely important observations. Also, since the CID has a thick substrate the cosmic ray problem limits usable readout times to a few hours and, therefore, effective readout noise levels to about 10 e^-. An added advantage of CIDs is the capability of randomly addressing the pixels in any order, allowing great flexibility in format and speed. General Electric has recently indicated that they have an active development program to build bigger and better CID devices.

VII. RECENT CCD RESULTS

Several TI developmental CCDs have been sporadically available to the author and his colleagues in connection with the development of the Wide Field/Planetary Camera for Space Telescope. These CCDs, with various electrical problems and highly variable optical quality, were made to aid in the ultimate

development of 800x800x15μ pixel flight sensors. In spite of the less than ideal properties, we have used these chips on telescopes at Palomar, Las Campanas, Kitt Peak, Lowell and Mt. Lemon to begin to understand how to handle such data and to aid in the testing and development of the CCDs. In this section, a few recent results will be shown to illustrate some of the properties of these chips.

Figure 1 is a two-hour exposure of the field surrounding QSO Q1315+346 which has a redshift of 1.050. The picture covers 200x200 arcseconds and was taken with a 500x500 15μ pixel TI device in Gunn r light (6100-7000Å) by Jerome Kristian and Peter Young with the 200-inch Hale telescope using a special focal reducer (Gunn et al., 1980). The faintest images are about m_r = 26.0.

The same focal reducer (PHUEI) has a spectrographic mode and Figures 2 and 3 show spectra of faint galaxies taken at the 200-inch and at the Palomar 60-inch by James Gunn and John Hoessel. The details are given in the captions.

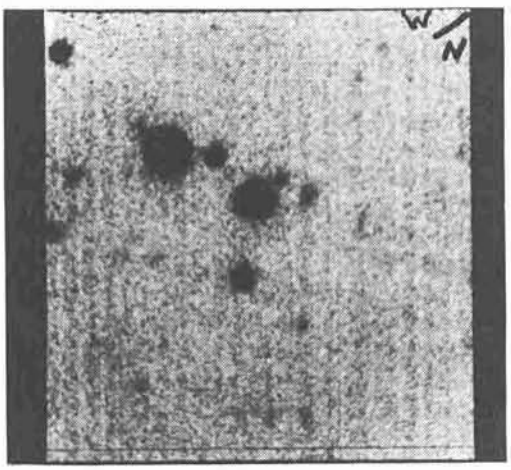

Figure 1. Two-hour 200-inch PHUEI exposure of the field of QSO 1315+346. The QSO of z = 1.050 is the bright circular image just above the center. Most of the other images are galaxies. The limiting images are fainter than 26.0 in Gunn r.

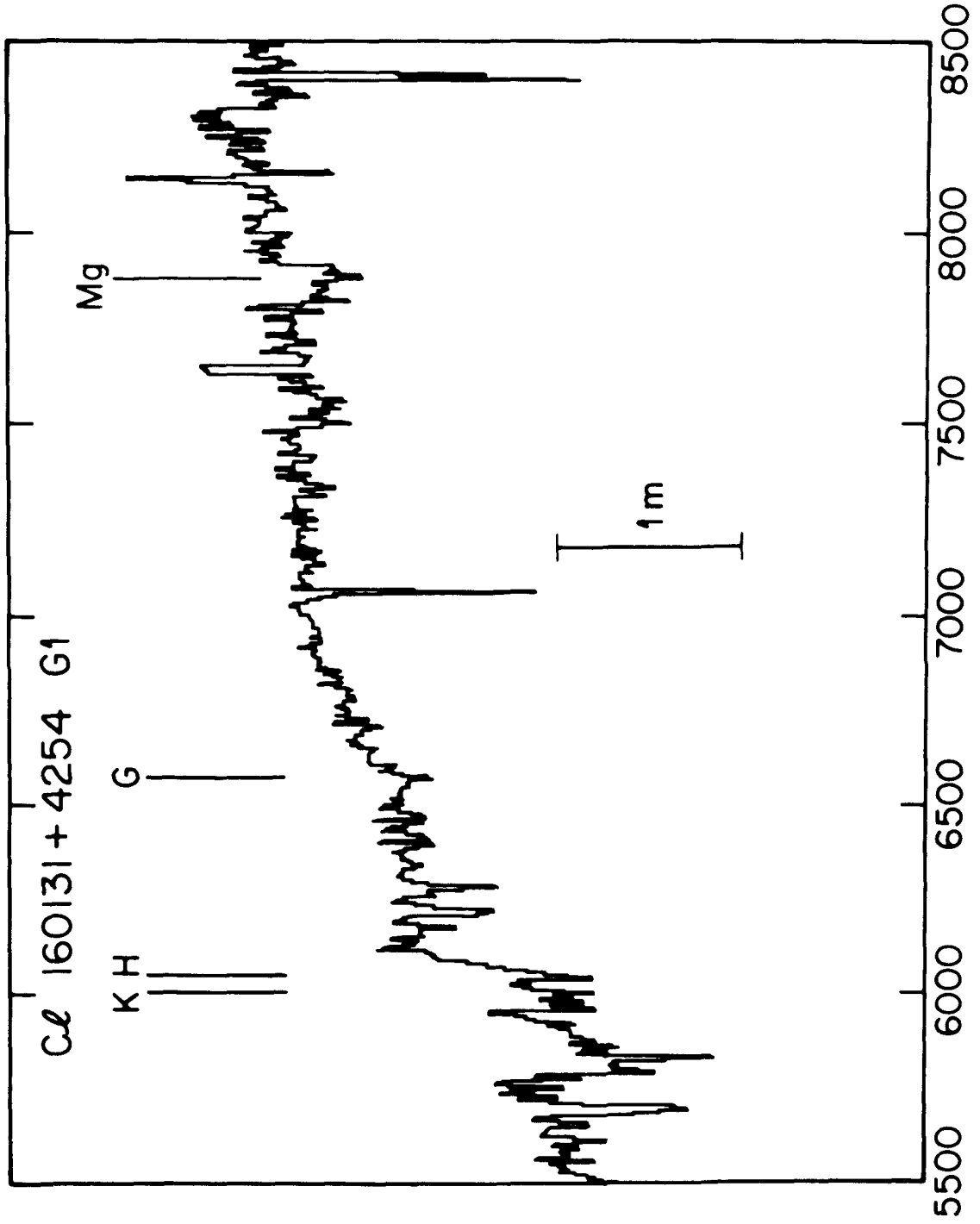

Figure 2. CCD spectrum of 150131+4254 G1 a cluster galaxy of z = 0.53. Obtained with PHUEI at the 200-inch prime focus in 50 minutes.

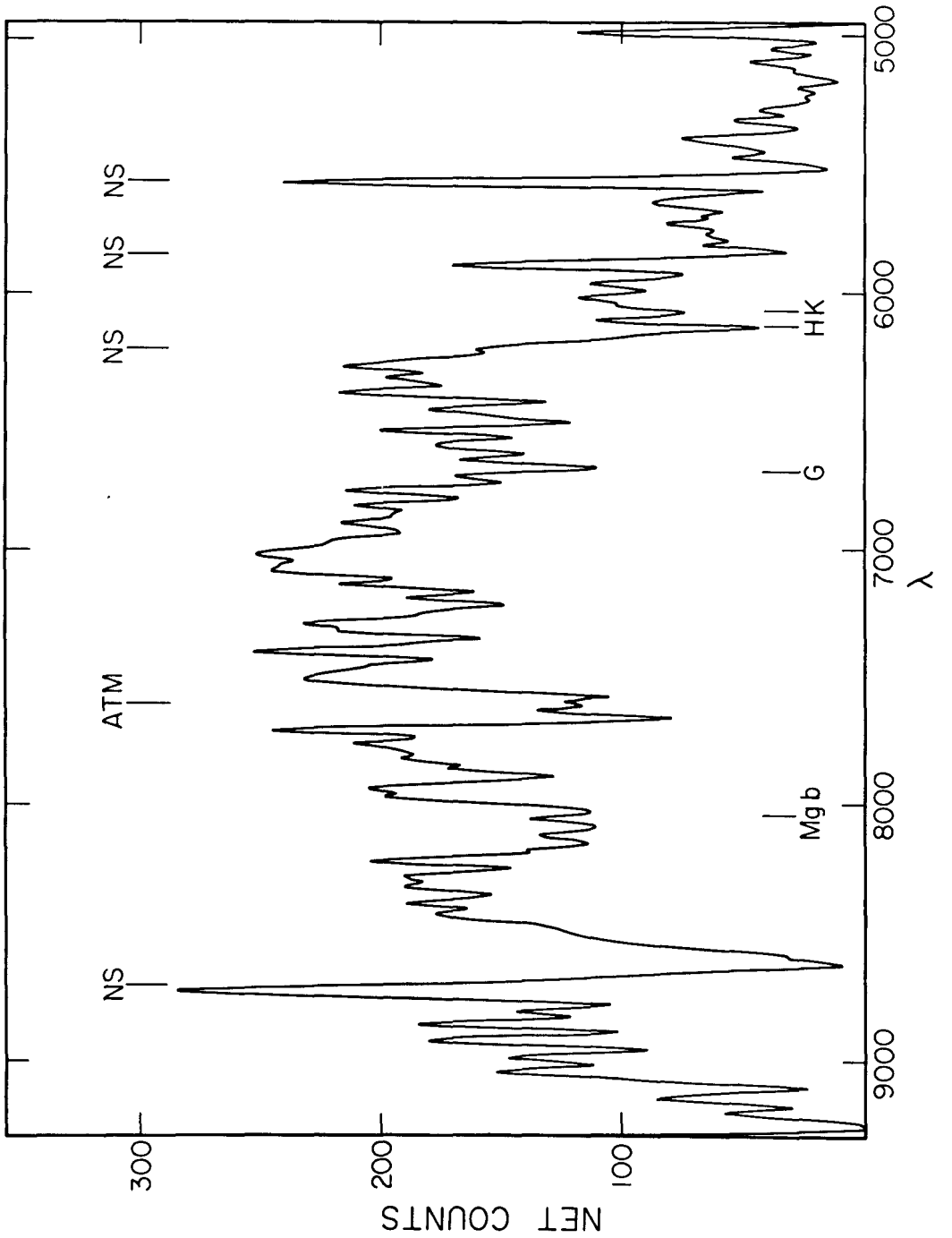

Figure 3. Raw exposure of a cluster galaxy of m_V = 22.2, redshift = 0.55, Palomar 60-inch telescope, 3 hour exposure.

REFERENCES

Aikens, R.S., Harvey, J.W., and Lynds, C.R., Proceeding of IAU Colloquium 40, Meudon, 1976.

Boksenburg, A. and Burgess, D.E., Proceedings of Symposium on T.V. Sensors, University of British Columbia, May 1973.

Ford, W. Kent, Annual Reviews of Astronomy and Astrophysics, pp. 189-212, 1979.

Gunn, J.E., Hoessel, J., and Westphal, J.A., In preparation, 1980.

Marcus, S., Nelson, R., and Lynds, C.R., Proc. Soc. Photo-Optical Instrum. Eng. 172, 207, 1979.

Williams, J.T., Proc. Soc. Photo-Optical Instrum. Eng. 78, 78, 1976.

THE FAINT OBJECT CAMERA

F. Macchetto
Astronomy Division, Space Science Department of ESA, ESTEC,
Domeinweg, 2200 AG Noordwijk, The Netherlands

ABSTRACT.

The Faint Object Camera is the ESA instrument to be flown in the Space Telescope. This paper describes the main characteristics of the instrument, its scientific capabilities, and the software required to analyze the data that it produces.

I. INTRODUCTION.

The NASA Space Telescope (ST) is one of the most ambitious projects in space astronomy presently planned, and will undoubtedly provide great impetus to astronomical research for the rest of this century. This 2.4 metre telescope is expected to be placed in orbit by the Space Shuttle in December 1983 and will carry a complement of highly sophisticated scientific instruments. A general description of the Space Telescope and its astronomical applications can be found in Reference 1.

The European Space Agency (ESA) participates in the ST programme with three basic elements:

- a contribution to the spacecraft hardware; these are the solar arrays and associated deployment mechanisms
- the contribution of one of the focal plane instruments namely the Faint Object Camera
- the provision of personnel support to the activities of the Science Institute.

In return for this participation, European astronomers from the ESA member states will be guaranteed a minimum of 15% of the ST observing time, and this can be utilized on every instrument on-board the ST. The 15% minimum does not seem a large figure at first sight, but even this would be invaluable to Europe: in terms of hours per year, this share would exceed the entire clear dark time on a ground-based telescope and it will give European astronomers the chance to share in the order-of-magnitude improvement offered by ST.

II. THE FAINT OBJECT CAMERA DESIGN.

The most interesting aspect of ESA's contribution to the ST programme is undoubtedly the Faint Object Camera (FOC). The aim of the FOC is to fully exploit the spatial resolution capability of the Space Telescope over a broad wavelength range on the very faintest objects detectable.

With the FOC it will be possible to obtain imagery and accurate photometry of stellar objects as faint as $m_v = 28$, for which a cumulative exposure of 10 hours will yield a signal-to-noise ratio of not less than 4. In the U-band a similar exposure will yield s/n $\simeq$ 3 on a 29th magnitude star with an A0 V flux distribution. For observations of extended objects such as galaxies, at full resolution of the telescope, an exposure of 10 hours will yield a s/n $\simeq$ 3 at the 24th

magnitude per arc sec^2 (U-band) brightness level. With these performance capabilities the scientific applications are essentially unlimited. They include, for example, observations of RR Lyrae stars, Cepheids, bright supergiants, globular clusters and giant HII regions as distance indicators out to expansion velocities greater than 10^4 km $\cdot$ s^{-1}; resolution of spectroscopic and astrometric binaries to establish fundamental stellar masses, detailed studies of shock fronts, condensing gas clouds and the relationship of young stars to the gas around them in regions of star formation; optical identification of X-ray sources; velocity dispersion and mass densities studies in the central regions of normal and compact elliptical galaxies; spectrography of active nuclei of galaxies and objective prism surveys of high latitude X-ray sources. An expanded list of scientific uses of the FOC can be found in Reference 1. The FOC is one of the four axial scientific instruments located at the focal plane of the Space Telescope and has overall dimensions of about 0.9 x 0.9 x 2.2 meters. The FOC configuration is modular and interchangeable with other axial scientific instruments; this design ensures that removal and installation can be achieved in-orbit by a suited astronaut. The basic performance characteristics of the FOC are shown in Table 1 and a photograph of the full-size mock-up is shown in Fig. 1. The FOC consists of two main elements; the Camera Module which includes the optics, mechanisms and electronics and the Photon Detector Assembly which consists of two detectors and the associated electronics.

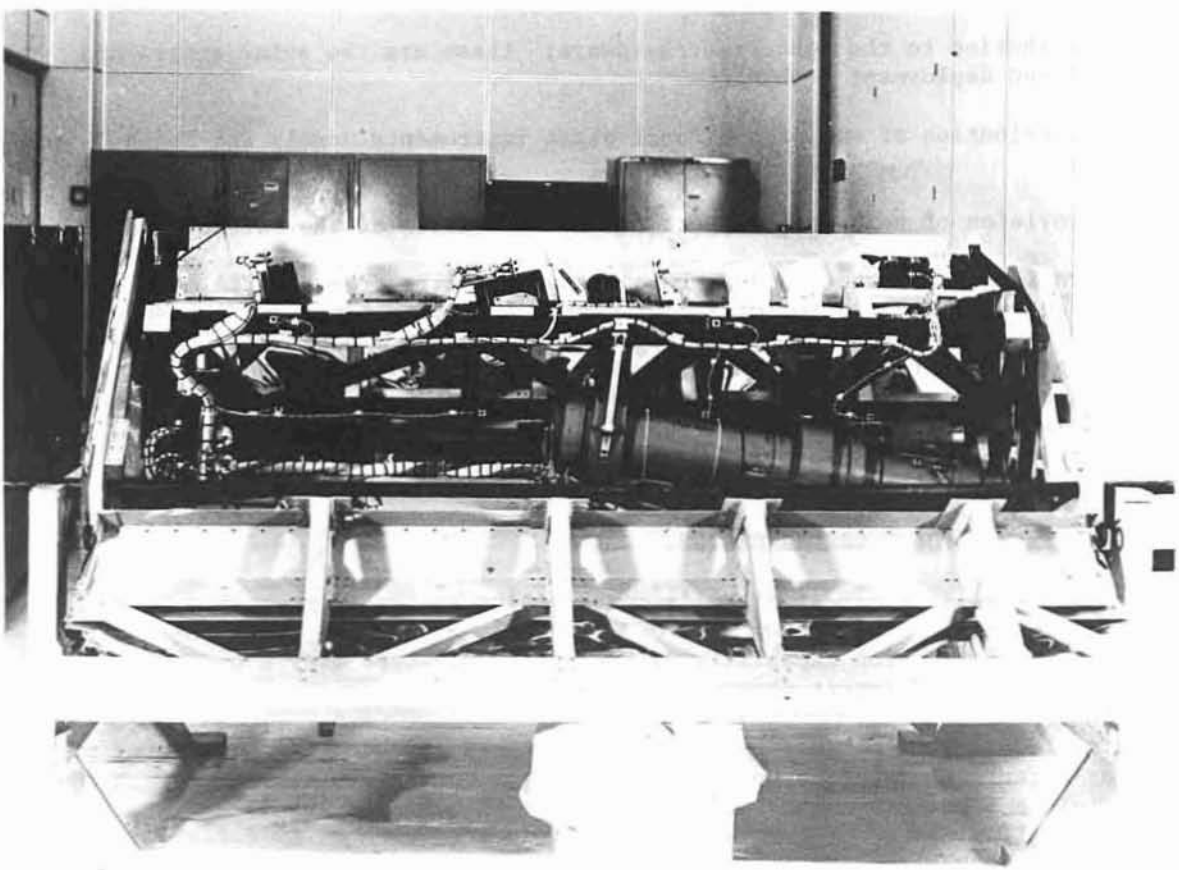

Figure 1: Full size model of the Faint Object Camera

Optics design.

The Camera Module provides two optical relays which image a dedicated part of the field of view of the Space Telescope onto one of the two detectors. The baseline mode of the FOC involves imaging at f/96. A three-element optical relay corrects for the astigmatism of the ST off-axis image and focusses it on the photocathode of a detector dedicated to f/96. At this focal ratio, the 25μm pixels of the FOC detector subtend 0.022 arc sec thus oversampling the ST point spread function. This is shown in Fig. 2 where the encircled energy fraction as given by the ST optics is plotted as a function of image radius in arc seconds. Although the formal specification is for 70% of the light to fall within a circle of 0.1 arc sec radius it can be seen that considerable spatial information is available at smaller radii. This of course will be even more true at shorter wavelengths. The f/96 pixel size of the FOC is thus ideally matched to the ST performance.

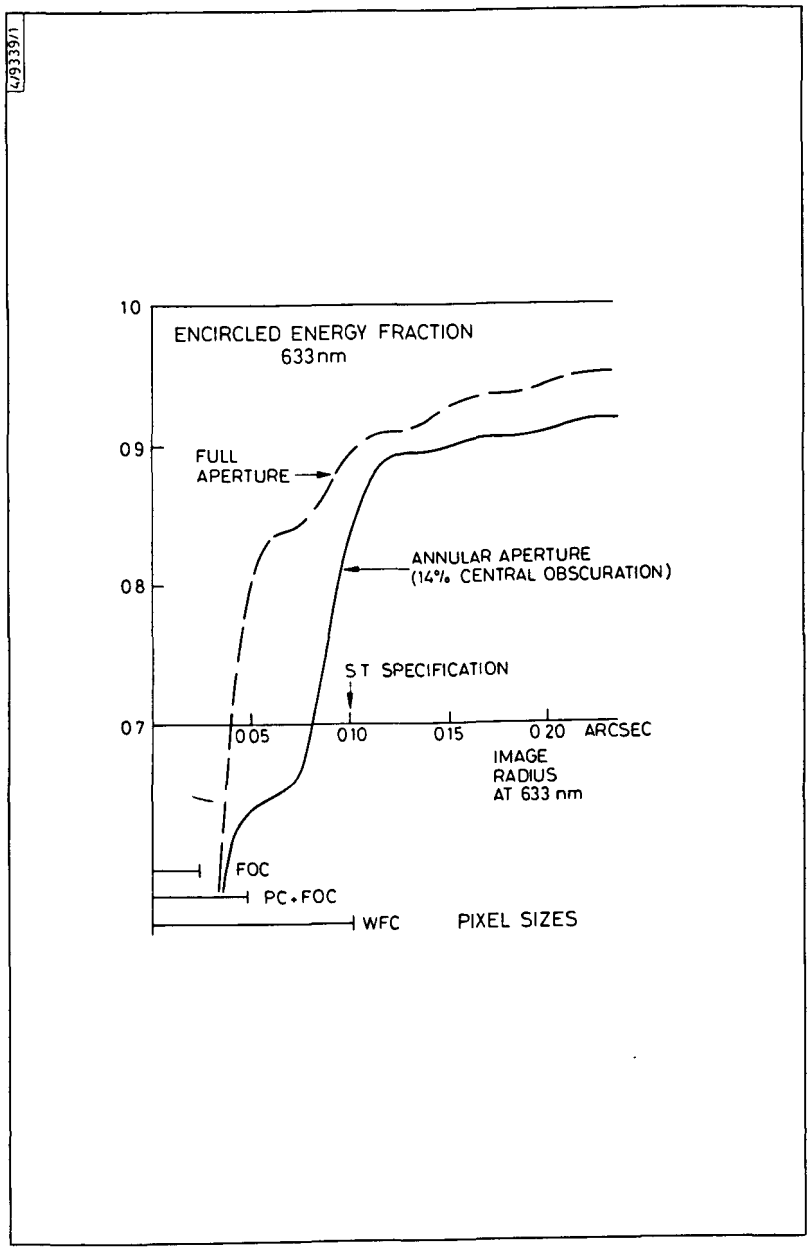

Figure 2: Optical performance characteristics of the Space Telescope.

There will be four filter wheels in the f/96 optical path, located near the pupil, each with 12 positions, Fig. 3. They will carry a wide range of colour and neutral filters, polarizers and two objective prisms optimized for response at 150 nm and 250 nm respectively. By suitably combining the neutral density filters a maximum attenuation of $\Delta m = 12$ can be achieved thus allowing the overall linear dynamic range of the FOC to extend from about $m_v = 5$ to $m_v = 29$. In addition the f/96 camera includes a coronographic facility consisting of a small (0.6 arc sec diameter) spot in the ST focal plane and an apodizer mask located at the pupil. This combination ensures the removal of the light from the bright source and the scattered light from the telescope mirror and spider and will allow the imaging of a faint object near a bright one with a difference in magnitudes of $\Delta m_v \simeq 14$ to 16.

The second optical relay, is an f/48 system which provides images at a reduced resolution but over a field of view four times as large. Also in this case a three element system images the aperture onto its dedicated detector. In this optical relay two filter wheels are included carrying coloured filters and two objective prisms. In addition the f/48 can be converted into a long slit spectrograph, Fig. 4. This is achieved by inserting a toroidal mirror into the beam to relay it to a fixed concave grating which disperses and focusses the light onto the f/48 detector. The entrance slit of the spectrograph is a fixed 0.1 x 10.0 arc sec aperture. Thus with a Space Telescope spatial resolution of 0.2 arc sec, up to 50 separate spectra can be taken in a single observation. The spectrograph covers the following wavelength ranges in three orders: 1st order: 360-540 nm; 2nd order: 180-270 nm; 3rd order: 120-180 nm. The dispersion is such that in the first order each 25μ pixel covers 0.18 nm of spectra. This corresponds to a dispersion of $\lambda/\Delta\lambda \simeq 1300$. The spectrograph is then ideally suited to perform dynamical studies of galaxies and other extended objects.

Detector design.

The two detectors included in the FOC are of identical design. They consist of a three stage, magnetically focussed image intensifier tube which is lens coupled onto the faceplate of a television type camera tube. A schematic representation is shwon in Fig. 5 and a layout of the Detector in Fig. 6. The intensifier utilizes a "hot-bialkali" photocathode deposited on a MgF_2 window. This combination allows the useful response of the detector to extend from $115 \text{ nm} < \lambda < 700 \text{ nm}$, with an extremely low dark current characteristic. The detector operates in a photon counting mode where every photon detected by the photocathode is recognized as a single photon event whose positions of arrival is stored as an x-y coordinate in a dedicated memory. The advantages of this system are that the spatial resolution is maintained, the dark noise contribution minimized and the linearity of the system extends over many decades being limited only by the rate of arrival of photons, when it becomes too great for each of them to be identified individually. The main limitation of this detector system stems from the requirement of storing, at a high speed of 10 MHz, the x, y coordinates of the photon events. This can be achieved by utilizing a dedicated memory, which in the FOC case is limited because of power and mass reasons to a maximum of 4 Megabits. With a 16 bit word this translates to a total number of pixels capability of 512 x 512 or equivalent combinations. A new mode has been recently implemented which utilizes an 8 bit address allowing a total number of 1024 x 512 pixels to be scanned. Thus the limitation on the number of pixels arise from the data store size rather than from the detector as this would be capable in principle to deliver 1024 x 1024 pixels. Another useful characteristic of the detector is that the size of the pixel can be changed, by command, from 25μm to 50μm thus allowing a larger field of view to be scanned, albeit at a lower resolution. The basic characteristics of the photon counting detector are shown in Table 1c.

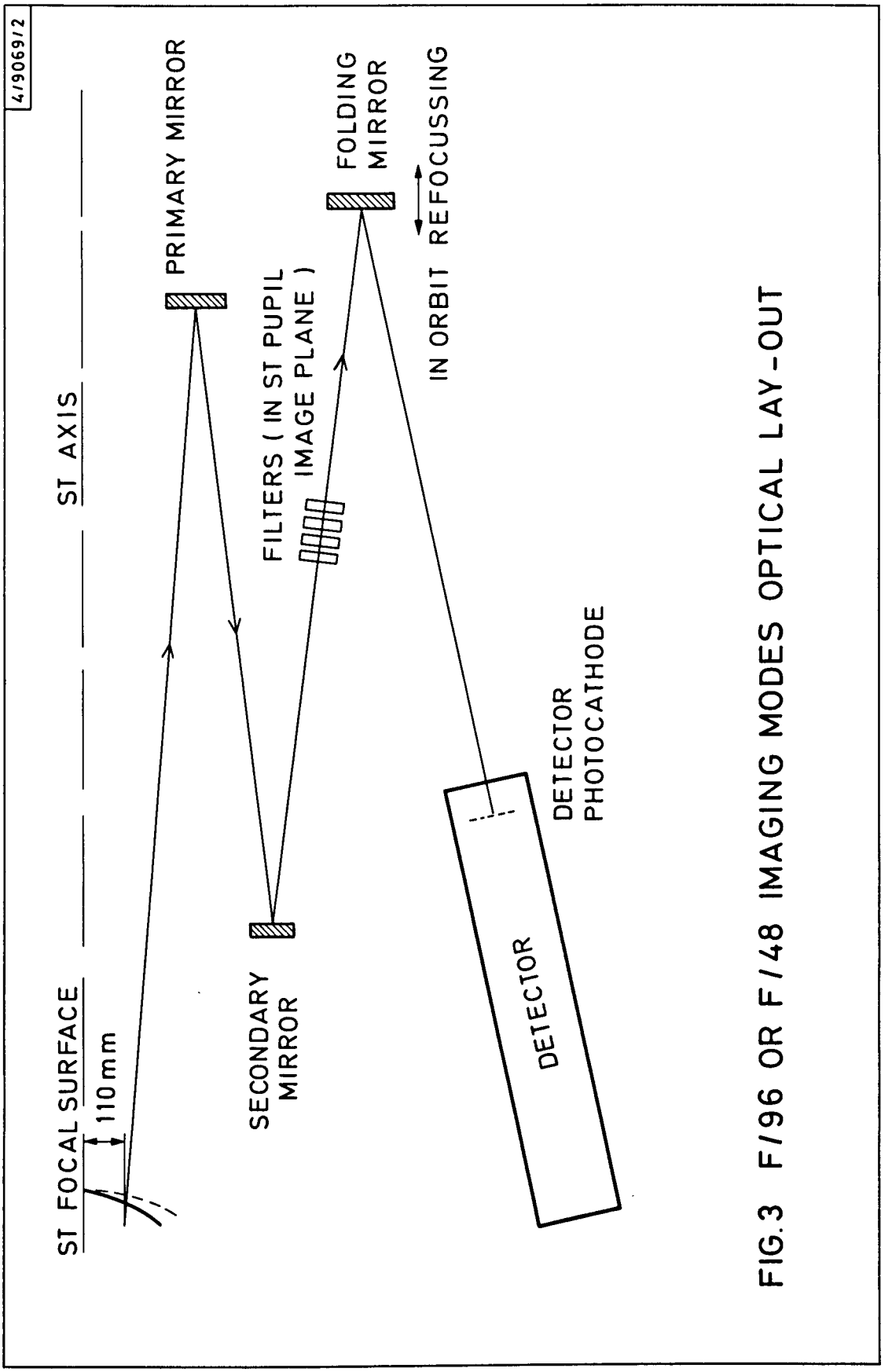

FIG.3 F/96 OR F/48 IMAGING MODES OPTICAL LAY-OUT

There will be four filter wheels in the f/96 optical path, located near the pupil, each with 12 positions, Fig. 3. They will carry a wide range of colour and neutral filters, polarizers and two objective prisms optimized for response at 150 nm and 250 nm respectively. By suitably combining the neutral density filters a maximum attenuation of $\Delta m = 12$ can be achieved thus allowing the overall linear dynamic range of the FOC to extend from about $m_v = 5$ to $m_v = 29$. In addition the f/96 camera includes a coronographic facility consisting of a small (0.6 arc sec diameter) spot in the ST focal plane and an apodizer mask located at the pupil. This combination ensures the removal of the light from the bright source and the scattered light from the telescope mirror and spider and will allow the imaging of a faint object near a bright one with a difference in magnitudes of $\Delta m_v \simeq 14$ to 16.

The second optical relay, is an f/48 system which provides images at a reduced resolution but over a field of view four times as large. Also in this case a three element system images the aperture onto its dedicated detector. In this optical relay two filter wheels are included carrying coloured filters and two objective prisms. In addition the f/48 can be converted into a long slit spectrograph, Fig. 4. This is achieved by inserting a toroidal mirror into the beam to relay it to a fixed concave grating which disperses and focusses the light onto the f/48 detector. The entrance slit of the spectrograph is a fixed 0.1 x 10.0 arc sec aperture. Thus with a Space Telescope spatial resolution of 0.2 arc sec, up to 50 separate spectra can be taken in a single observation. The spectrograph covers the following wavelength ranges in three orders: 1st order: 360-540 nm; 2nd order: 180-270 nm; 3rd order: 120-180 nm. The dispersion is such that in the first order each 25μ pixel covers 0.18 nm of spectra. This corresponds to a dispersion of $\lambda/\Delta\lambda \simeq 1300$. The spectrograph is then ideally suited to perform dynamical studies of galaxies and other extended objects.

Detector design.

The two detectors included in the FOC are of identical design. They consist of a three stage, magnetically focussed image intensifier tube which is lens coupled onto the faceplate of a television type camera tube. A schematic representation is shwon in Fig. 5 and a layout of the Detector in Fig. 6. The intensifier utilizes a "hot-bialkali" photocathode deposited on a MgF_2 window. This combination allows the useful response of the detector to extend from $115 \text{ nm} < \lambda < 700 \text{ nm}$, with an extremely low dark current characteristic. The detector operates in a photon counting mode where every photon detected by the photocathode is recognized as a single photon event whose positions of arrival is stored as an x-y coordinate in a dedicated memory. The advantages of this system are that the spatial resolution is maintained, the dark noise contribution minimized and the linearity of the system extends over many decades being limited only by the rate of arrival of photons, when it becomes too great for each of them to be identified individually. The main limitation of this detector system stems from the requirement of storing, at a high speed of 10 MHz, the x, y coordinates of the photon events. This can be achieved by utilizing a dedicated memory, which in the FOC case is limited because of power and mass reasons to a maximum of 4 Megabits. With a 16 bit word this translates to a total number of pixels capability of 512 x 512 or equivalent combinations. A new mode has been recently implemented which utilizes an 8 bit address allowing a total number of 1024 x 512 pixels to be scanned. Thus the limitation on the number of pixels arise from the data store size rather than from the detector as this would be capable in principle to deliver 1024 x 1024 pixels. Another useful characteristic of the detector is that the size of the pixel can be changed, by command, from 25μm to 50μm thus allowing a larger field of view to be scanned, albeit at a lower resolution. The basic characteristics of the photon counting detector are shown in Table 1c.

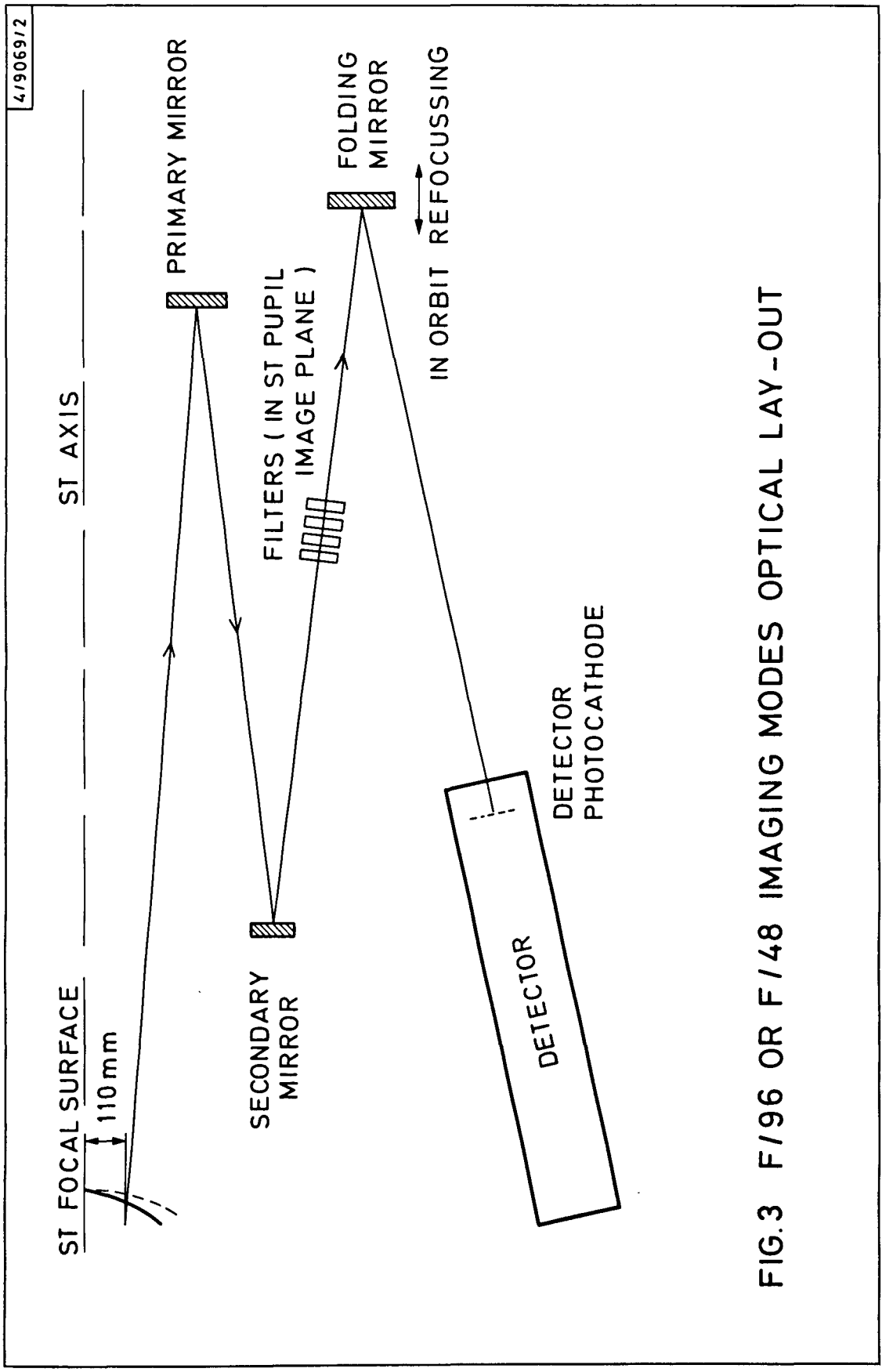

FIG.3 F/96 OR F/48 IMAGING MODES OPTICAL LAY-OUT

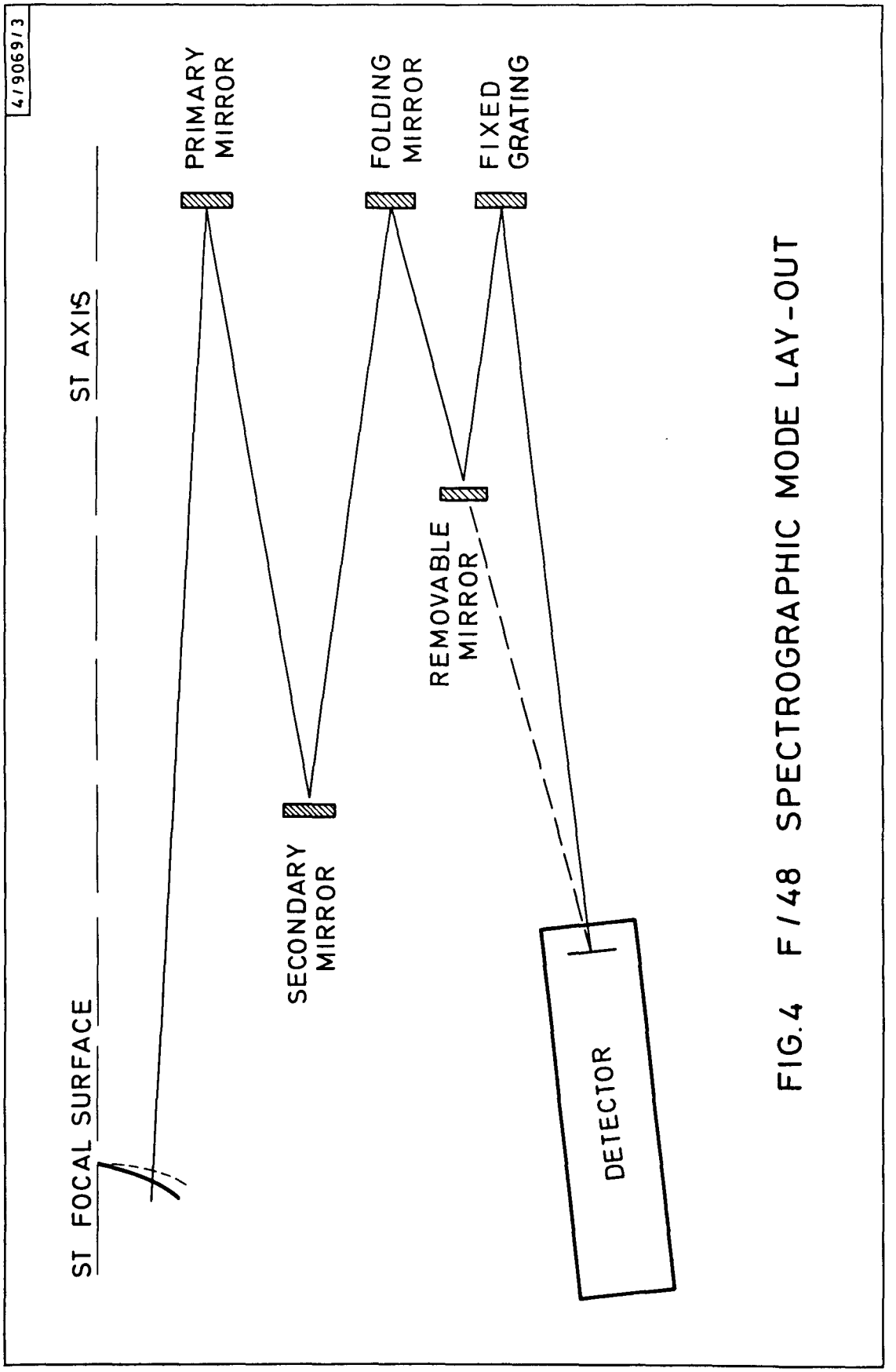

FIG.4 F/48 SPECTROGRAPHIC MODE LAY-OUT

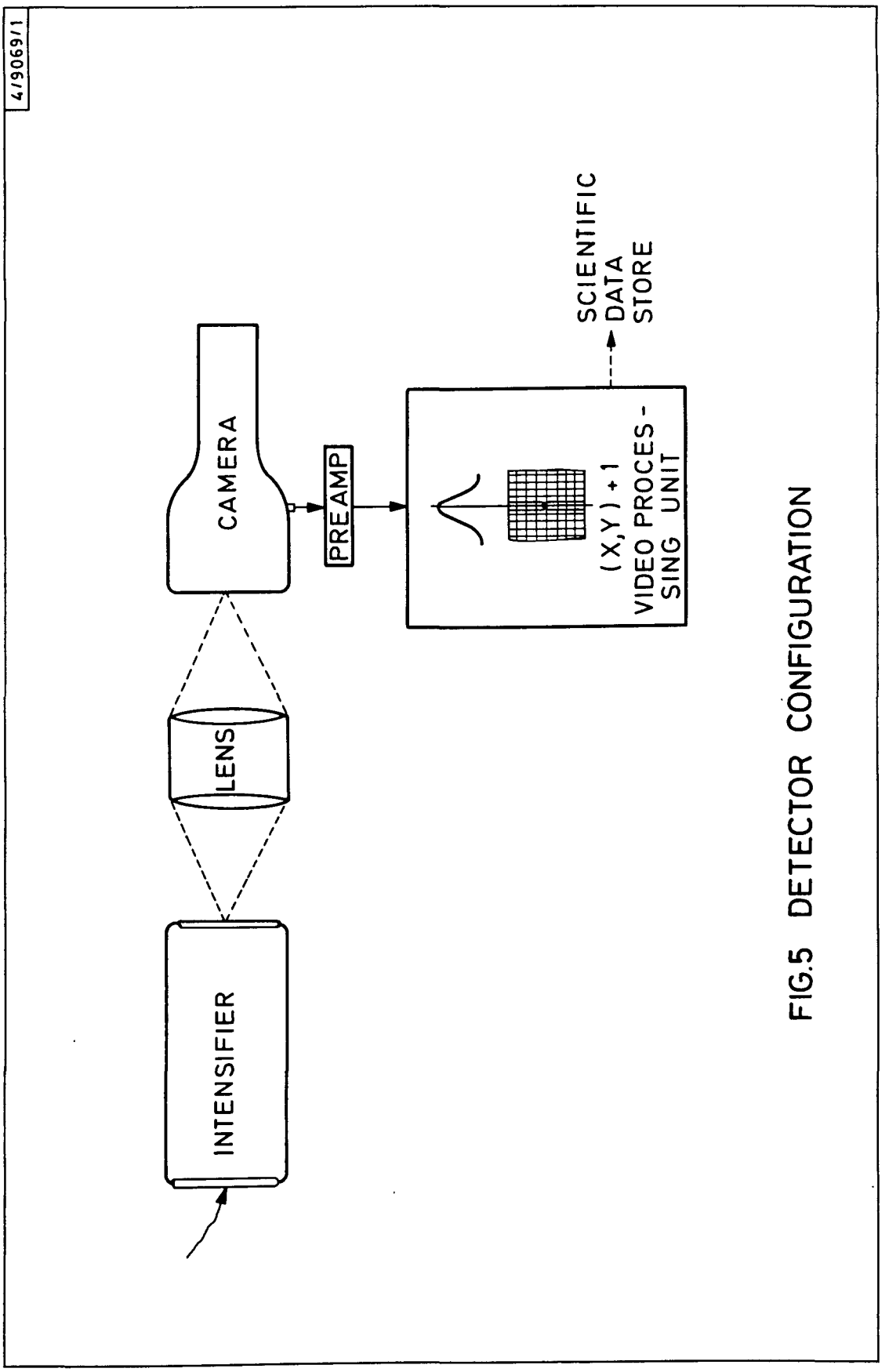

FIG.5 DETECTOR CONFIGURATION

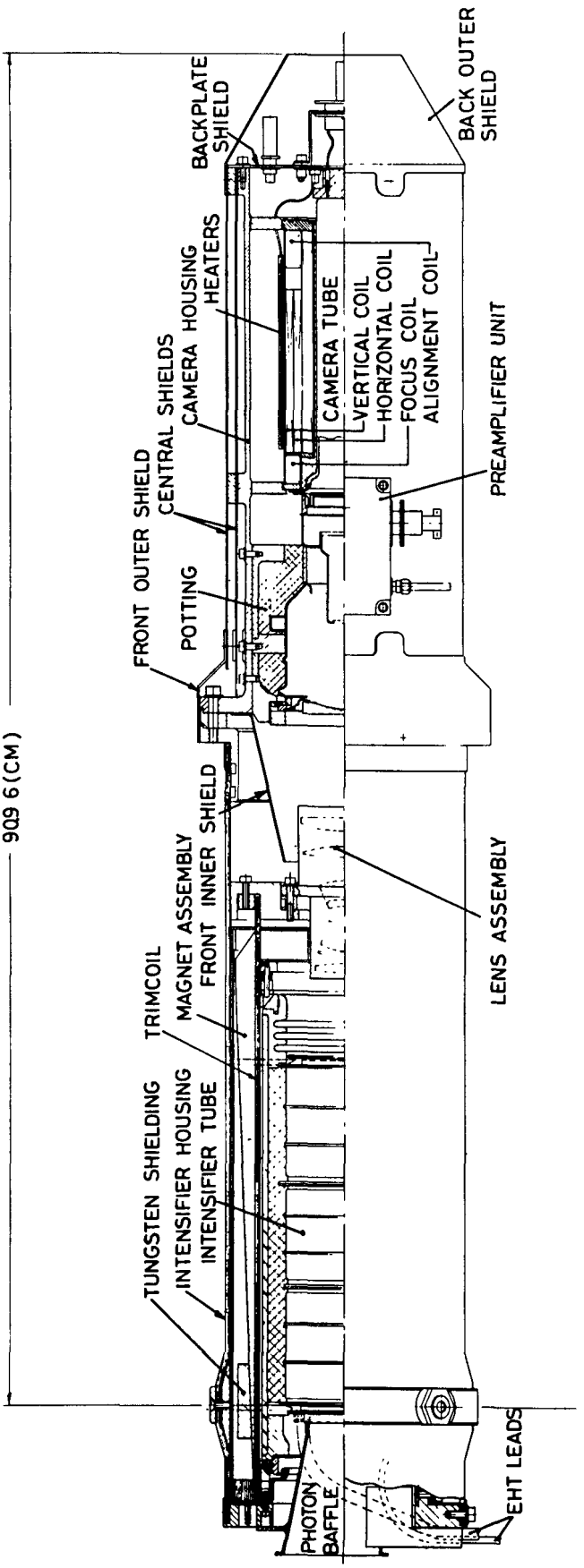

DETECTOR HEAD UNIT

FIG.6

TABLE 1A

Performance Characteristics of the Faint Object Camera

Optical Paths	f/96 and f/48
Angular Resolution	Performance essentially limited by telescope
Field of View (nominal)	11 x 11 arc sec, 22 x 22 arc sec
Pixel Format (nominal)	500 x 500
Pixel Sizes	25μm and 50μm
Angular Pixel Sizes (arc sec)	f/96 : 0.022 : 0.044; f/48 : 0.044 , 0.088.
Wavelength Range	120 nm to 700 nm
Photometric Accuracy	∿ 1% when not photon-noise limited
Linear Dynamic Range (single observation)	m_v = 21 to 28 point sources m_v = 15 to 22 (arc sec)^2 extended objects
Linear Dynamic Range (including neutral densities)	m_v = 5 to 28 point sources
Maximum S/N per exposure	∿ 400

TABLE 1B

Selectable Pixel Formats and Resulting Field of Views in units of arc seconds

FORMAT	f/96	f/48
1000 x 500 (8 bit only)	22 x 11	44 x 22
1000 x 250	22 x 5.5	44 x 11
500 x 500	11 x 11	22 x 22
250 x 250	5.5 x 5.5	11 x 11
120 x 120	2.6 x 2.6	5.5 x 5.5
60 x 60	1.3 x 1.3	2.6 x 2.6

TABLE 1C

Photon Detector Assembly
Photon Counting System Characteristics

Detector Configuration	I + Lens + EBS
Photocathode Material	Sb. Na. K. (Hot bialkali)
Useful Area of Photocathode	∅ = 40 mm circle, 28.2 x 28.2 mm square
Pixel Sizes	25μ and 50μ (selectable)
Number of Pixels	1024 and 512
Pixel Formats	1024 x 512; 1024 x 256; 512 x 512; 256 x 256; 128 x 128; 64 x 64 (selectable)
Positioning of Formats	Anywhere within useful area in increments of 32 pixels
Positioning Accuracy of Pixels	∿ 1/3 pixel
Pixel Rate	10^7 pixels/sec
Quantum Efficiency	∿ 20% UV; 10% Visible; 1% Hα
Uniformity	Better than 15%
Dark Current	3 x 10^{-5} photons/pixel • sec (at room temp.)
Count Rate in 512 x 512 Format	0.8 photons/pixel • sec (to 1% accuracy) 4.0 photons/pixel • sec (to 10% accuracy)
Maximum s/n	∿ 300 (single exposure, per pixel)
Photometric Accuracy	∿ 1%
Dynamic Range	∿ 20000 (single exposure)
Exposure Times	Minimum = 1 frame time; Maximum = ∿10 hours

FOC Performance Characteristics.

The combination of the detector and optics result in a total system performance for the FOC including the Space Telescope, as shown in the Tables 2, 3, 4, 5 ,6,7. These performance characteristics have been computed in magnitudes for a point object, or magnitudes per arc sec^2 for extended objects. In each case the spectrum of the source has been taken to be equivalent to an A0 V star and the integration has been carried out over a bandpass of 100 nm centered around the U-band for the imaging mode and around the V band for the spectroscopic mode. These performance characteristics together with the versatility of the instrument make of the FOC one of the most exciting instruments ever to be flown.

TABLE 2

F/96 Nominal Performance for Point Sources

Mu	TIME FOR S/N = 10	S/N IN 1000 S	S/N IN 10 HRS
21	25	63.58	381.45
22	63	39.97	239.84
23	160	25.00	150.01
24	419	15.44	92.67
25	1163	9.27	55.64
26	3615	5.26	31.56
27	13456	2.73	16.36
28	61411	1.28	7.66
29	328468	0.55	3.31
30	1924277	0.23	1.37

TABLE 3

F/96 Nominal Performance for Extended Objects
(in magnitudes per arc sec^2)

Mu	TIME FOR S/N = 10	S/N IN 1000 S	S/N IN 10 HRS
15	35	58.19	319.12
16	89	33.55	201.29
17	224	21.15	126.91
18	564	13.32	79.93
19	1429	8.37	50.19
20	3673	5.22	31.31
21	9758	3.20	19.21
22	17863	1.89	11.37
23	91131	1.05	6.29
24	362313	0.53	3.15
25	1751807	0.24	1.43

TABLE 4

F/48 Nominal Performance for Point Sources

Mu	TIME FOR S/N = 10	S/N IN 1000 S	S/N IN 10 HRS
21	25	63.61	381.68
22	62	40.03	250.20
23	159	25.10	150.58
24	412	15.59	93.52
25	1115	9.47	56.82
26	3312	5.50	32.97
27	11543	2.94	17.66
28	49340	1.42	8.54
29	252301	0.63	3.78
30	1443688	0.26	1.58

TABLE 5

F/48 Nominal Performance for Extended Objects
(in magnitudes per arc sec^2)

Mu	TIME FOR S/N = 10	S/N IN 1000 S	S/N IN 10 HRS
17	14	83.62	501.71
18	36	52.69	316.11
19	91	33.13	198.75
20	233	20.72	124.31
21	611	12.80	76.78
22	1694	7.68	46.09
23	5270	4.36	26.14
24	19634	2.26	13.54
25	89679	1.06	6.34
26	479913	0.46	2.74
27	2812231	0.19	1.13

TABLE 6

Spectroscopic Mode Performance AO Point Star, 480 nm Band

Mu	TIME FOR S/N = 10	S/N IN 1000 S	S/N IN 10 HRS
12	5	138.48	830.87
13	13	87.37	524.23
14	33	55.12	330.73
15	83	34.77	208.63
16	208	21.93	131.56
17	524	13.82	82.89
18	1325	8.69	52.12
19	3388	5.43	32.60
20	8879	3.36	20.14
21	24638	2.01	12.09
22	76617	1.14	6.85
23	285393	0.59	3.55

TABLE 7

Spectroscopic Mode Performance AO Extended Object, 480 nm Band
(mangitudes per arc sec^2)

Mu	TIME FOR S/N = 10	S/N IN 1000 S	S/N IN 10 HRS
8	8	115.38	692.27
9	19	72.80	436.77
10	47	45.92	275.55
11	119	28.97	173.80
12	300	18.26	109.57
13	756	11.50	69.00
14	1919	7.22	43.31
15	4941	4.50	26.99
16	13180	2.75	16.53
17	37951	1.62	9.74
18	125892	0.89	5.35

III. ANALSYIS OF THE FOC DATA.

Routine Image Correction

FOC image data are typically in the form of 512 x 512 x 16 bit images or 1024 x 512 x 8 bit images, and these in turn are of three different types:-

- sky pictures
- objective prism pictures
- slit spectrometer pictures.

In all three, geometric distortions introduced by the Space Telescope and the FOC will be present. Typically, pincushion distortion will be of the order of 1% and S-distortion will be around 5%. So, at the edges of the field of view, the pictures will be distorted by a few tens of picture elements (pixels).

Each pixel contains a number, called a count, which is related to the number of photons incident on the corresponding part of the detector faceplate. This count, however, is non-linear, especially at high incident photon rates (i.e. at high count rates). Predictions are that the counts will be reasonably linear up to a count-rate of about one detected photon (called an "event") per pixel every 50 frame scans - this represents about 0.8 events per pixel per second in the 500 x 500 format.

Ground and in-orbit calibration of the instrument will permit the count values to be corrected to within about 1%. Pixel to pixel accuracy will be achieved using ground based results, but accurate absolute calibration will have to await in-orbit observations of reference celestial objects.

The routine, geometric and photometric correction of FOC images will be carried out with software produced as part of the FOC development. This softwar e package will correct for the known imperfections of the FOC and will produce images calibrated to a linear amplitude on a rectangular grid.

Non-routine corections

In addition to the standard processing described above the astronomer may want to carry out a number of other corrections to the data which however depend on the precise nature of the scientific information being sought. These include for

example pixel overflow correction, particle events correction, removal of internal reflection "ghosts" and removal of known blemishes and fiducial marks. Special software will also be required for the various non-imaging modes of the FOC. In the spectroscopic mode there will be a requirement for transformation to wavelength scale, correction of the curvature of the spectrum and precise determinaton of the position of the slit in the sky. In the objective prism mode a wavelength scale transformation and location of the sources in the sky will be required.

Scientific data analysis

After completing the tasks described in the preceding two sections the astronomer is only at the beginning of the process of scientifically analysing his data. Some of the operations that the astronomer may wish to perform with his data are the following.

- Obtain relative angular distances between the peaks or centroids of two objects.
- Determine geometrical parameters of an object, e.g. eccentricity and inclination of a disk galaxy.
- Compute radial profiles of surface brightness for an object of known geometry.
- Fit model curves to surface brightness profiles in order to determine standard parameters such as "stellar" nucleus size, disk scale length, etc.
- Distinguish between stars and non-stars and then perhaps remove all of one or the other (i.e. smooth over them).
- Compute stellar magnitudes using multiple pictures, and curve fitting techniques. The grainy nature of the FOC pictures may disqualify some of the curve fitting methods used with photographically recorded ground based images.
- The coronographic facility in the FOC will produce sky pictures requiring special processing software and algorithms. The astronomer will try to detect objects of interest in the presence of that part of the bright central body's light not eliminated by the coronograph and its apodizing mask. One ingenious scheme for doing this has been described by Bonneau, et al. (2).
- To achieve the maximum possible resolution with the FOC, the technique of speckle interferometery may be used - a useful review of this subject has been given by Worden (3), and its particular application to the FOC has been proposed by Lohmann and Weigelt (4).
- With slit spectrometer pictures, it will be required to analyse profiles at any given position in terms of such characteristics as continuum levels, absorption and emission line intensity, wavelength and width.

While the software required to carry out the routine corrections is formaly part of the present development effort, the rest of the software, namely that needed for non-routine corrections or for scientific analysis is not yet included. However, ESA has just completed a study of the requirements and costs associated with providing these additional items and will soon take a decision regarding their implementation. A more detailed description of this software can be found in Ref. 5. We are convinced that a Faint Object Camera which includes both the hardware and data analysis software as described in this paper will be an extremely powerful tool for the astronomy of the 1980's.

REFERENCES.

1. F. Macchetto, F. Pacini, M. Tarenghi (eds.), "Proceedings of the ESA/ESO Workshop on astronomical uses of the Space Telescope", Geneva, 12-14 February 1979.

2. D. Bonneau, M. Josse, A. Labeyrie, "Locking image subtraction: detectability of circumstellar planets with the Large Space Telescope", in de Jager, Nieuwenhuijzen (eds.), "Image Processing Techniques in Astronomy", D. Reidel, Dordrecht, 1975, p. 403.

3. S.P. Worden, "Astronomical image reconstruction", Vistas in Astronomy 20, 301 (1977).

4. A.W. Lohmann, G.P. Weigelt, "Image restoration of ST photographs", in F. Macchetto, et al. (eds.),op cit. p. 353.

5. F. Macchetto, P. Norris, "Scientific Data Analysis for the Faint Object Camera", in "Proceedings of the International Workshop on Image Processing in Astronomy", Trieste, June 1979, in press.

THE DETECTOR PROGRAM AT KITT PEAK

Garth Illingworth and Harvey Butcher
Kitt Peak National Observatory[1]

I. INTRODUCTION

During the past few years Kitt Peak has made a strong commitment to two-dimensional detector systems. While the primary impetus for a commitment such as this has always been the ability to tackle new observing problems, these detector systems can also result in more efficient and effective use of scarce telescope time, as well as satisfying a need for the general purpose instruments required by an observatory such as Kitt Peak that serves a wide range of user needs.

Individual efforts during the evolution and implementation of these systems have been considerable. Most of the detector systems are the result of research and development efforts initiated by scientific staff, in particular Roger Lynds, and supported by the excellent engineering and technical support available at Kitt Peak, notably Steve Marcus, Bill Robinson, Warren Ball, and Dick Aikens.

Most of our recent instrumental development for imaging (and to some extent spectroscopy) has been guided by a reappraisal of, first, the type of image intensifier systems that we should use and, second, by the choice of analog (i.e., integrating systems) as opposed to photon event detection systems (with or without event centroiding). The impetus for these moves was only partly due to instrument cost considerations. Versatility and ease of use have also been prime considerations.

In particular, we have made a conscious effort to move away from the use of high-gain image-tube systems of the magnetic focus type. While these devices (e.g., the RCA C33063 two-stage "Carnegie" systems) have generally had some good features, notably efficient, uniform photocathodes with good ultraviolet response, they do suffer from several disadvantages: bulk — these are large, heavy systems, especially if solenoids are used instead of a permanent magnet system; cost — the presently available multistage systems are becoming extremely expensive; and, depending on application, magnetic susceptibility, internal scattered light, and poor MTF.

If intensification is required, we have now begun to use proximity focus tube/microchannel plate tube combinations. But these tubes do have disadvantages; scattered light in the proximity tubes, poor pulse height distribution, limited lifetime, and dead time problems in the channel plate

---

[1]Operated by the Association of Universities for Research in Astronomy, Inc., under contract with the National Science Foundation.

devices (although the systems are improving in the latter two areas) mean that care is required in their application. However, we have used such devices in our new Intensified Reticon Scanner (IRS) — an intensified dual-channel 936-element reticon spectroscopic system — with considerable success. A less successful application so far has been the use of an ITT F8-1297-1A high-gain, ultraviolet/blue sensitive proximity focus tube coupled to a SIT vidicon. The aim here is to give our Video Camera system a detector with response through the ultraviolet at wavelengths less than the ~4000 Å cutoff imposed by the fiber-optic input of the current ISIT system. The problem with the proximity tube appears to be illumination-level-sensitive events that have the appearance of ion events even though they may well not be. This behavior is currently under investigation.

The second decision, that of the use of analog detection for these intensified systems, may seem unusual for those accustomed to the current enthusiasm for photon counting systems such as the IPCS system (Boksenberg and Burgess 1973) used at the AAT 4-m telescope and its offshoot, the Space Telescope Faint Object Camera (FOC). However, for ground-based imaging, there are very good reasons for utilizing analog techniques (for moderate-to-high resolution spectroscopy, the case is reversed and the advantages of event detection and centroiding are considerable).

The advantage of analog detection occurs mainly through the much wider, useful dynamic range that is available. This allows one, first, to measure much brighter objects than can be accommodated within the count-rate limitation of an event detector and, second, the ease and speed at which calibration can be done. This latter point is important. Obtaining the necessary signal-to-noise ratio in one's calibration frames can be very tedious and time consuming. Operationally, one wants to minimize the time spent on calibrations.

Given this approach to imaging instrumentation, we have, therefore, concentrated on building up a strong technical capability in low-level analog technology. In particular, we now feel that we have under control most of those problems (especially drifts) that have in the past given analog detectors a bad name.

II. VIDEO CAMERA

The current instrument whose design philosophy is based on these precepts is the Video Camera. This system has been our mainstay two-dimensional detector system for the past two years. It is a direct imaging system for the 4-m and

2.1-m Cassegrain foci that is based on an RCA 4849 ISIT vidicon tube.[2] The input photocathode is an S-25 and has response to beyond 8000 Å, albeit with poor response at such wavelengths. However, the sensitivity drops rapidly to zero below ~4000 Å because the input photocathode is fed by a fiber-optic bundle.

The system is formatted to have 256 x 256 pixels, each ~40 μ square over an ~10-mm^2 area (a nominal 16-mm target-diameter tube). At the 4-m Cassegrain focus, each pixel corresponds to 0".27 in the sky, giving a spatial coverage of just over ~1' — these figures are approximately doubled at the 2.1-m.

The mode of operation of our system differs substantially from that utilized by others. The usual mode of operation is to integrate the data on the target for the full duration of the exposure, then read the target completely, digitize the data, and store the resulting array on tape, disk, etc. (again, see Westphal's discussion in this volume). Our system differs in that we read the ISIT target down every 1.6 seconds and co-add the data into a separate, fast, 256 x 256 x 20 bits deep memory. System gain is high enough that single photon events (at ~5000 electrons upon readout) are unambiguously detected above the system-noise level of ~800 electrons rms. The advantages of this mode of operation — the so-called "equilibrium" mode — appear to be fourfold:

1) The need for target bias is eliminated. For applications where the input event rate is low (e.g., narrow-band imaging), thermal write-up of the target provides the necessary bias — we run our system at the moderately high temperature of -12°C.

2) The linearity is noticeably better than target integration systems.

3) The dynamic range is very large — approaching 4000:1.

4) Real-time evaluation of the data is possible since the updated co-added data are transferred to the system display memory after every 1.6-second readout. This display memory is 256 x 256 x 20 bits deep and drives a TV monitor at standard frame rates, a linear window function being used to set the data range to be displayed.

The layout of the Video Camera system is shown in Figure 1. The operating setup in the Cassegrain cage of the 4-m is shown in Figure 2. Two large racks that contain the accumulation memory and the display memory and monitor are kept in the telescope control room, near the observer. A more detailed discussion of the layout and system hardware can be found in Robinson et al. (1979).

A considerable fraction of our engineering effort on this system was

---

[2]An ISIT is a SIT vidicon like that used by Jim Westphal (see the discussion in this volume) with an additional electrostatic-intensifier stage fiber-optically coupled to the SIT; hence, Intensified Silicon Intensified Target, i.e., two stages of gain before the target.

directed toward achieving the stability required for low-level photometry, particularly for narrow-band filter imaging (and in the spectroscopic mode, see below). We found that extremely accurate control of the temperature of the ISIT and the preamplifier electronics was required to keep bias drift to a satisfactory level. Figure 3 shows the construction of the camera head. Dry-ice cooled methanol is circulated by a pump driven by a closed-loop control system that maintains short- and long-term temperature stability at better than $\pm 0.05^{\circ}C$. This level of stability has, unfortunately, been found in practice to be necessary. Bias drifts and geometrical changes can be detected if the temperature control falls significantly outside these limits.

Similar high levels of stability were found to be required for the preamplifier and integrator electronics that precede the 12-bit analog-to-digital (A-D) converter. By careful attention to detail, we have, however, managed to keep bias drift to less than 0.2% of the bias level for periods of hours.

At the telescope, we typically integrate for 512 reads or ~13 minutes. In principle, a signal that is at saturation in a single read, i.e., 12 bits or 2^{12} will saturate our 20-bit deep memory in $2^{20}/2^{12} = 2^{8}$ or 256 reads. In practice, one does not image stars that exceed one-half device saturation (and preferably less), allowing typical integrations to be 2^{9} or 512 reads. Longer integrations (>13 min) are made by taking successive 512 read integrations and adding the data subsequently in the computer.

The Video Camera has proved itself to be a powerful photometric instrument. In practice, stellar photometry, to a few percent accuracy, can be

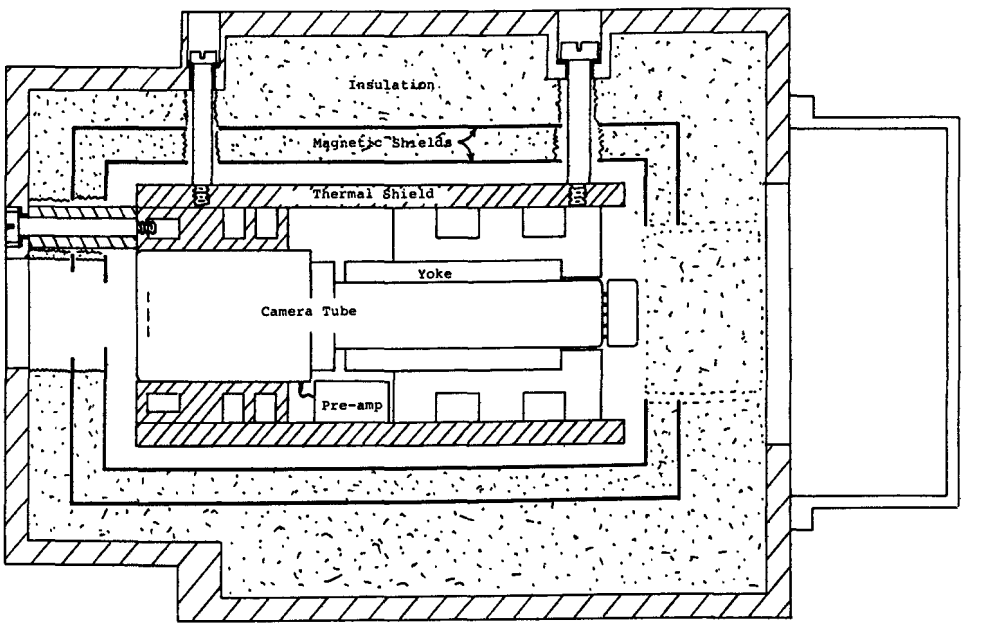

FIG. 3.—The camera head. The interior is cooled to $-12^{\circ}C$ during operation.

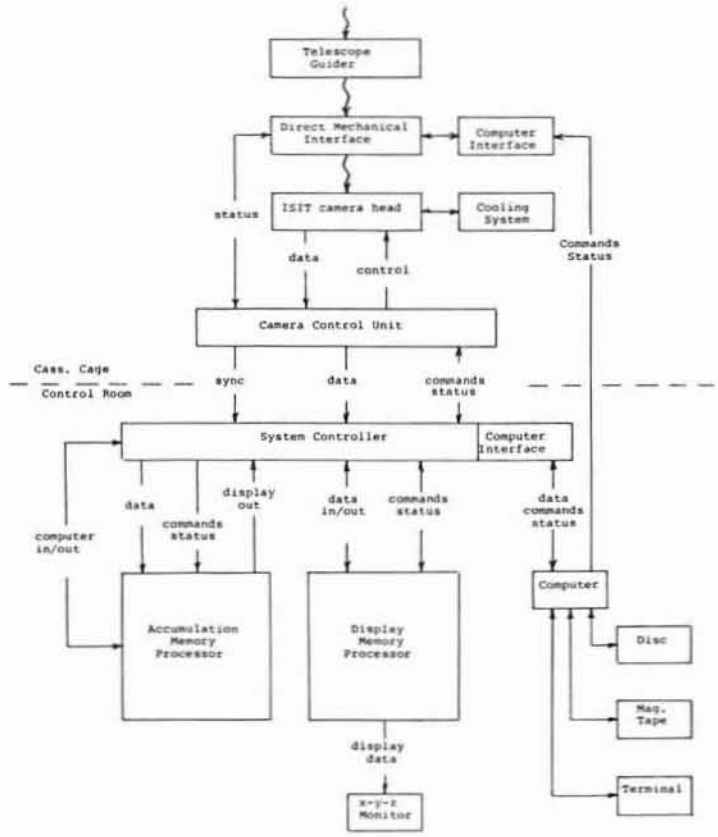

FIG. 1.—Block diagram of the Video Camera direct system. Figures 1-3 are from Robinson et al. (1979).

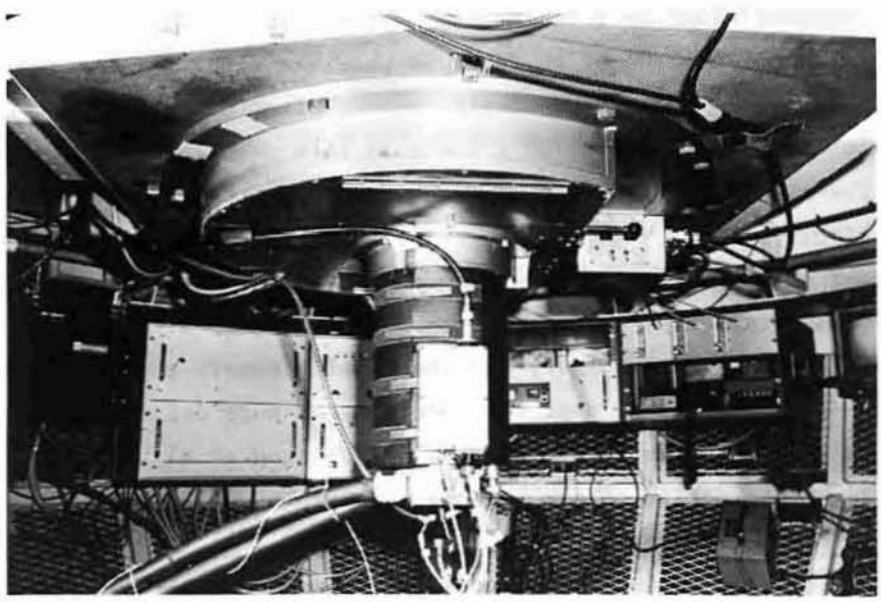

FIG. 2.—The 4-m telescope Cassegrain cage setup for the direct Video Camera system. The camera head is shown (center) mounted to the instrument interface. The methanol cooling cables run to the left from the head. Analog and digital control crates and power supplies are mounted in racks behind the camera.

readily obtained. The system seems to be quantum-noise limited even after 2 hours of integration with broad-band filters. Magnitude limits of V = 25 mag have been achieved and limits of V ~ 24 mag in less than 0.5 hour are routine under superior seeing conditions. While the original conception of this system was as a faint-object, broad-band detector, in practice the majority of the imaging that has been done with it has been through on- and off-line narrow-band filters, e.g., Hα, [O III] λ5007, etc.

Figures 15-18, later in the discussion, show how favorably this system compares to one of our current CCD cameras.

The Video Camera system is also used at the 4- and 2.1-m telescopes for moderate resolution (R ~ 1000-5000) spectroscopy, the system being known in this mode as the High Gain Video Spectrometer (HGVS). The HGVS has proved to be an excellent low-level spectroscopic system for certain problems (see, e.g., Kormendy and Illingworth 1980), but suffers from two major problems that limit its usefulness as a general-purpose, two-dimensional spectroscopic detector system. First, we have found that beam bending, i.e., local target charge-level-dependent deflection of the electron read beam, severely limits the useful dynamic range of the system if accurate radial velocities are required. Second, the available number of resolution elements (~150) is too small for most problems. For these spectroscopic applications, the photon-counting, event-centroiding systems, such as the IPCS developed by Boksenberg and his engineering group (Boksenberg and Burgess 1973) and used by him and large numbers of collaborators, have considerable advantages over analog detectors such as the HGVS. This HGVS system is also discussed by Robinson et al. (1979).

III. CID

The other two-dimensional imaging system that is routinely supported at Kitt Peak is a GE 244 x 248 Charge Injection Device (CID) with 35 x 45 μ pixels. This is used primarily in solar applications in a barefoot mode (i.e., no preceding intensification), since, first, it is characterized (like CCDs) by high quantum efficiency (QE) over a wide wavelength range and, second, this mode best utilizes the very large dynamic range of which the system is capable.

The CID chips are now becoming available with two different substrate structures: "bulk" and "epitaxial." While the bulk device can collect carriers from its several hundred micron thick substrate and hence have good response out to beyond 1 μ, the epitaxial device utilizes a thin (~25 μ) layer epitaxially grown upon its substrate as the carrier collection zone. The red response is significantly reduced but so is the epitaxial chip's sensitivity to cosmic rays. This, combined with the until now somewhat limited availability of the bulk devices, has led us to use the epitaxial chip.

Both devices have similar QE at 4000 Å (~20%) with the epitaxial device rising to ~40% at 6000 Å and decreasing to low QEs beyond 7000 Å, while the bulk chip reaches ~60% at 7500 Å and still has a QE of ~10% at 1 μ (GE QE data).

The dynamic range of these devices is excellent, being >5000 even though system noise is high at ~250 electrons rms. This is possible because full well capacity is very large at ~2 x 10^6 electrons (CCD well capacities are typically a factor 5 to 40 smaller). In fact, even greater dynamic range is possible when we utilize a nondestructive read technique. By this we mean that, following the integration, the data on the chip are read out many times and co-added into a separate memory or onto the computer disk. In this way system noise can be decreased by the square root of the number of reads. While tests have indicated that thousands of reads do not significantly degrade the data (i.e., the loss of carriers per read is extremely low), we typically limit ourselves to ~25 reads, thereby reducing system noise from ~250 to ~50 electrons rms. Since each read takes ~2 sec, only 1 min is needed for this very significant decrease in system noise. A dynamic range as high as 4 x 10^4 is then in principle possible.

Currently, no significant new effort is being carried out on CID systems, since we felt that CCD offered more long-term advantages for our typical applications of low light-level imaging and spectroscopy while still being satisfactory high-S/N detectors. We hope this was the right decision! This decision notwithstanding, we are routinely using our CID system for high-S/N applications at the solar telescopes on Kitt Peak. A more detailed technical discussion can be found in a paper by Aikens (1980).

IV. CCD

While vidicons were the two-dimensional detectors of the 1970s, the detector of the 1980s is clearly the Charge Coupled Device (CCD). These devices hold great promise for imaging and certain classes of spectroscopy. The reason why there is so much enthusiasm for these chips amongst observers, even though the currently available devices suffer from a significant number of shortcomings, is that they are expected to be a panacea for the problems that afflict vidicons and photographic plates. While this may be true for the major problems of these detectors, CCDs, as we shall see below, have their very own problems that will be the cause of much frustration among instrumentalists and observers, at least during the development phase.

The advantages that we all expect to see with CCDs are many, ranging from their high QE, large dynamic range, simplicity of operation, linearity, through their stable and orthogonal geometry. Their excellent stability and more uniform photometric response are also important features. These advantages, however, are certainly not all achievable within any given chip of those currently

available. In fact, there are chips that have characteristics that render them completely unsuited for our low light level, low noise situation. Prime examples are the surface-channel devices of many of the current Japanese manufacturers and the early RCA chips. These have much higher noise levels than are generally acceptable in astronomy. Most manufacturers are interested in the TV market — be it military, consumer, or industrial, where operational requirements differ from ours — and so they design their chips with that market in mind, not ours. Since very large sums are required for the development of a high-yield chip (at least millions of dollars and possibly even tens of millions), it is clear that at the moment astronomers will have to find those chips from the production line that work for us and not expect to have major architectural changes made to suit our applications.

This is not to say that chip manufacturers are not interested in our problems. It has certainly been the case, particularly with Fairchild and RCA (if significantly less so with TI), that they are very interested in our findings and are often prepared to make minor changes in their chips if this would be of value to astronomers. Their constraints are clearly (1) the time involved, (2) the cost, and (3) disruption of production lines. If the required changes have minimal to zero impact in the above areas, then the manufacturers have been responsive and probably will be in the future. However, without very large sums of money, we simply cannot expect major changes.

One further result of the different applications which we, compared to the chip manufacturers, foresee for their devices is that the operating conditions recommended by the manufacturers are quite likely to be unsuitable for our mode of operation. This arises primarly because of our low-noise, high-transfer efficiency, low-light-level linearity requirements (implying cold operation and slow readout) compared with the manufacturer's usual high level, fast readout (TV frame rate) mode of operation. Considerable experimentation may well be required to find the correct clock timing and levels to achieve our desired operating conditions. This has implications for the philosophy of one's chip controller/readout system discussed below. It is also apparent to us that even chips from the same manufacturer can differ in operating conditions and structure, requiring the optimization of the driver parameters for each individual chip. The extent of these changes will vary from manufacturer to manufacturer, but it is clear that minor architectural changes can sometimes have profound effects on our operational mode.

The uncertain state of the chip market led us (specifically Steve Marcus) to design a controller system for CCDs that is very versatile in its operation, allowing fairly easy change of the operating conditions in the front end analog electronics. The modular format that we have used allows us to implement new

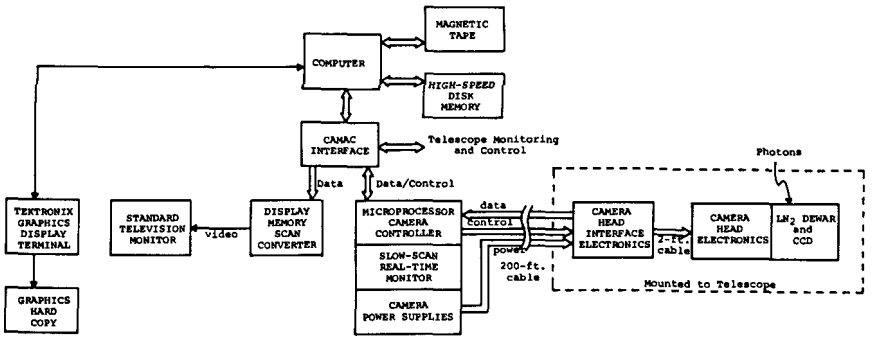

FIG. 4.—Overall block diagram of our prototype CCD imaging system. Current systems differ primarily in that the Camac interface, the display scan converter, and the TV monitor are replaced by a DEC LSI 11/23 computer plus CDC 80 Mbyte disk, Grinnell GMR-270 display system, and a DMA link to our telescope system computer. Figures 4-6 are from Marcus, Nelson, and Lynds (1979).

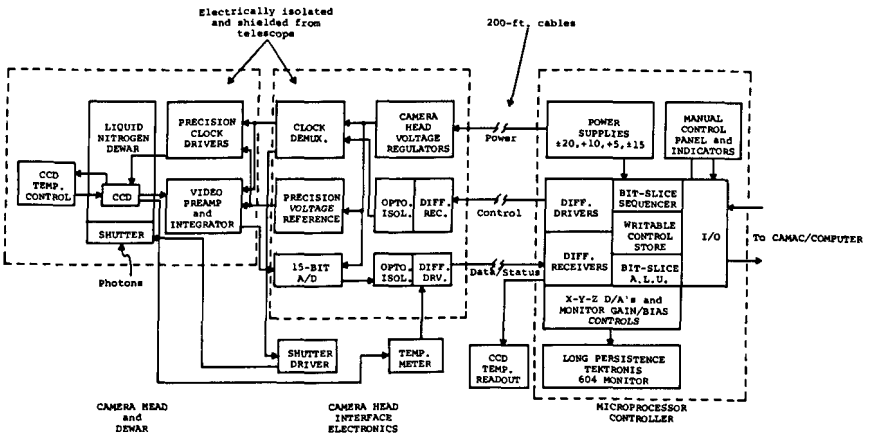

FIG. 5.—The CCD system electronics block diagram. Again (as in Fig. 4), the microprocessor controller now links directly to the LSI 11/23 microcomputer.

devices with only a minimum of hardware changes. Detailed discussion of this can be found in Marcus, Nelson, and Lynds (1979). In addition, Xerox copies of our electronic circuit diagrams can be obtained directly from either of the authors here at Kitt Peak.

The basic layout of our CCD camera system can be seen in Figures 4 and 5. The chip is mounted in a liquid nitrogen cooled dewar (Fig. 6) operated at $-112^{\circ}C$, the temperature being kept stable to better than $\pm 0.1^{\circ}C$ by a heater placed in the chip mounting plate so as to minimize bias drifts. Closely associated with the dewar is a small box containing four cards of analog electronics (clock drivers, preamps, the dual-slope integrator, and the temperature controller; the clock levels are controlled here by potentiometer adjustments). Changing chips may require the rebuilding of one or two cards in some cases, none in others. Nearby, another box contains power supplies and the A-D converter. These two units are closely associated with the dewar at the

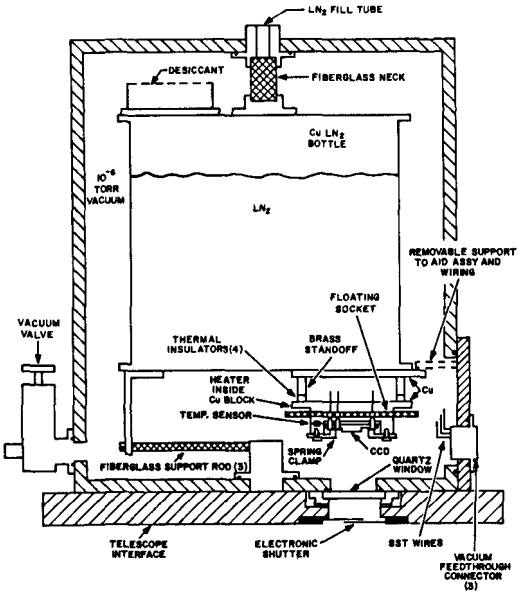

FIG. 6.—Our prototype liquid nitrogen dewar configured for illumination from below. For applications in which the illumination is from above, the CCD is mounted on the upper, flat surface of the nitrogen bottle and the outer case is inverted. Current dewars differ and are less versatile for no good reason.

telescope. Long cables (up to 400 feet) then connect these units to the controller that resides in the observing room. This is a microprocessor-controlled system that generates timing signals for the chip and controls the overall operation of the system (data transfer, integration initiation, etc.). This structure allows us considerable flexibility as new chips become available since different chips can, first, be of different format and size, and, second, require different clock timing patterns; these changes can be accommodated by software changes in this system. The microcode changes can be down-loaded from the system computer as required.

One change which we have recently made to the system that is not shown in Figure 4 is to place a DEC LSI 11/23 microcomputer between the controller and the telescope computer system. This computer has an 80 Mbyte, Winchester technology disk attached as a temporary data store. We expect this to be a particularly valuable addition as CCDs grow to sizes of the order of 1000 pixels square. A Grinnell GMR-270 display system having two 512 square, 8-bit deep memories will also be driven by the LSI 11/23 and will be used as the primary display for the incoming CCD data at the telescope, thereby replacing the scan converter shown in Figure 4.

The CCD chip that we have used several times at the telescope (for 4-m prime focus imaging) with the above system is a Fairchild device, CCD-211, that was optimized by us for low light level operation. This chip has 244 x 190 pixels, a low system noise near 20 electrons rms, superb linearity, and a dynamic range in excess of 10^4. The peak of its sensitivity occurs near 7000 Å, where it has a QE of 12%. The chip's response extends from less than 5000 Å to beyond 1 μ, the QE being about 3% at each of these wavelengths. This low QE is a major limitation of the CCD-211 chip (its small size also renders it unsuitable for many problems).

The low QE arises partly because the chip is 60% blind, i.e., the vertical shift registers which alternate with and parallel the sensing sites in this design are covered by opaque aluminum strips. The reason for this particular architecture was to allow unshuttered readout (TV versus astronomy again!) of the device. The structure of the chip is shown in Figure 7. The opaque aluminum strips clearly make for poor sampling in the horizontal direction, as well as markedly degrading the sensitivity. However, not all the QE loss can be attributed to these strips. It appears that the polysilicon electrode structure is also rather thick (it is a front-illuminated device), and this in itself would degrade the QE from the ~50% maximum expected for these devices (as indicated by experience with TI and claims by RCA).

While the QE is a problem that can and is being rectified in more recent Fairchild chips, there is another problem with these devices that is of considerable concern. This is the sensitivity of thick substrate devices like the Fairchild to cosmic rays. Figures 8 and 9 show examples of these events. Figure 9, in particular, scares those of us who plan long integrations with this device. This 75-minute exposure by Roger Lynds can be used to estimate an event rate for this 5.7 mm x 4.4 mm chip of ~1 event min^{-1}, or a basic event rate of ~0.08 events cm^{-2} s^{-1}. The distribution over event charge for a 40-minute integration with this chip is given in Figure 10.

While we intend to perform a simple lead-brick shielding experiment in the near future, it is unlikely that this will be a successful means of eliminating the problem. The best solution is clearly to work wherever possible with thinned

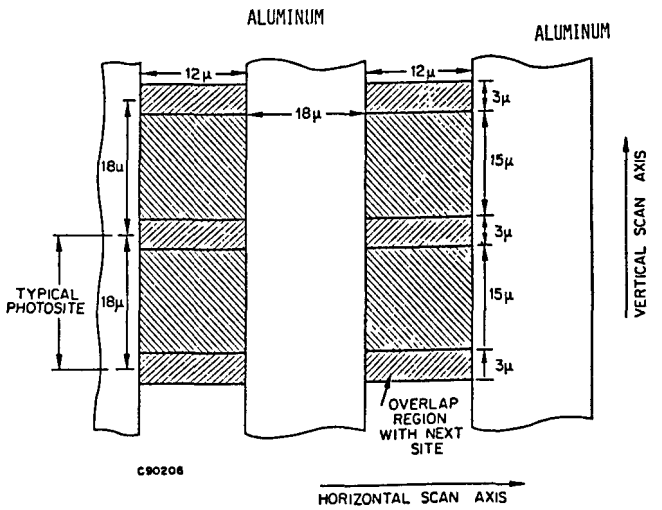

PHOTOSITE DIMENSIONS

FIG. 7.—The photosite dimensions and layout of the Fairchild CCD-211 and CCD-221 chips from the Fairchild data manual for the CCD-221 chip. The aluminum strips cover the ~18 μ x 36 μ vertical shift registers. These are the strips to be removed in the special order CCD-221s.

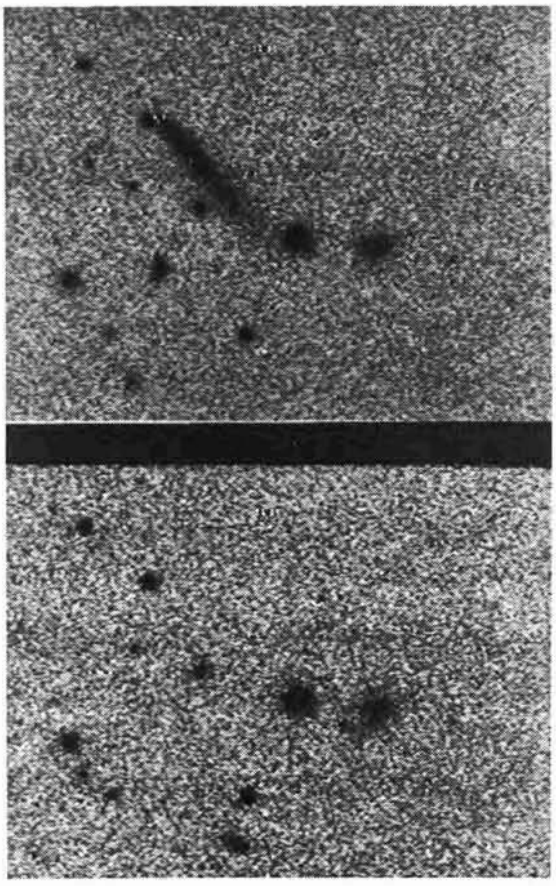

FIG. 8.—A Westerbork Background Survey source region taken with the Fairchild CCD-211 chip. These are sequential five-minute exposures of the same region. The striking cosmic ray event is due to a particle(s) traversing the chip at a very low angle of incidence. Other more direct events can also be seen.

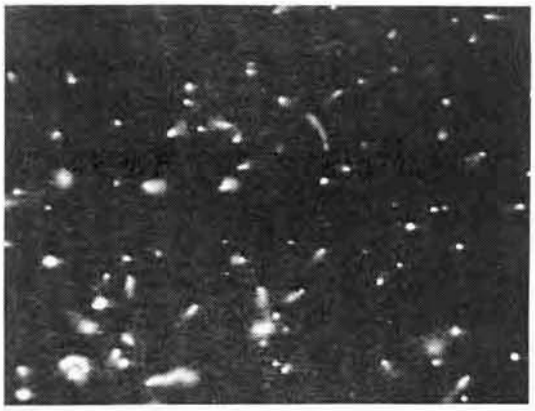

FIG. 9.—A 75-minute accumulation of cosmic ray events on the CCD-211 chip. Both this and Fig. 10 are from Marcus, Nelson, and Lynds (1979).

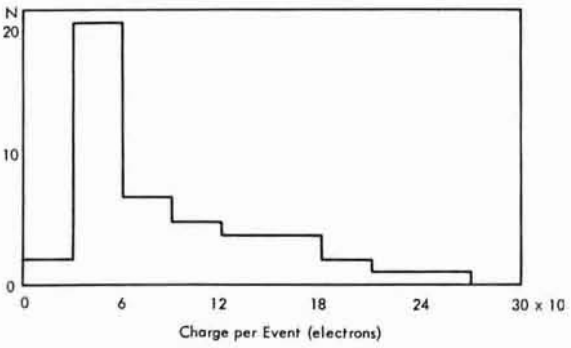

FIG. 10.—A histogram of the cosmic ray event magnitude (in electrons) for a 40-minute exposure like that in Fig. 9. The scarcity of small charge events is real.

devices. The current Fairchild chips and some RCA chips are front-illuminated, thick devices (~250 μ substrate). The TI chips currently used by Westphal and co-workers, and to be used in Galileo and the Space Telescope Wide Field Camera, are thinned to ~10 μ by chemical etching. These devices show no evidence of significant cosmic ray events, consistent with the order of magnitude improvement expected by thinning the chip substrate from ~250 μ to ~10-20 μ. While this gain in itself is valuable, thinning can (but does not necessarily do so) also result in much improved blue sensitivity (see below). RCA has recently announced a thinned device that should also have minimal cosmic ray problems.

Sensitivity to cosmic ray events may also be lessened by reducing the mean free path of carriers in the substrate material. However, this also reduces red sensitivity, so for many uses it will not be an acceptable procedure (this situation may also be intrinsic to some devices, depending upon the materials and manufacturing processes used).

Meanwhile we are developing the means to remove the cosmic ray events by taking several (preferably >4) frames of each field and statistically removing pixels that are affected by cosmic ray events. This looks to be a successful approach to the problem, although it requires a nearly dedicated minicomputer to enable the cleaning operation to be done in almost real time.

While the cosmic ray sensitivity, the low QE, and the small format of the chip are limitations, the CCD-211 is still a superb detector; particularly at 6000 Å and redward. For example, the linearity exhibited by this chip is remarkable, even at very low levels. In fact, it is probably the best of those with which we have had experience or seen in operation. Marcus, Nelson, and Lynds discuss this in some detail and note that there is no evidence for nonlinearity in the lowest 30% of the total range of the chip.

In dynamic range this chip exceeds by a significant factor every other detector that we have ever used, except the CID. Full well capacity of the CCD-211 is ~2.5×10^5 electrons, yet system noise is ≤20 electrons rms, giving a dynamic range $>10^4$. Figure 11 is a demonstration of this, being an 80-second R band integration of the inner region of M81 (field ~1' x 1!5). The central surface brightness of M81 in R is ~13.8 mag arcsec^{-2}, while the star to the right of the nucleus is ~20 mag and is a >10 σ detection (in the background noise). The dynamic range here is an impressive 4000. Another example can be seen in Figures 12 and 13.

While we have noted that this chip has poor QE compared with that expected for CCDs, it is still excellent compared with other detectors, particularly in the red ($\lambda \geq 6000$ Å). One example of the capability of the system can be seen in Figure 14, where we compare a 5-min, R band CCD-211 frame of the 3C265 field (lower) with the sum of three 45-min, IIIa-J, 4-m prime focus plates from

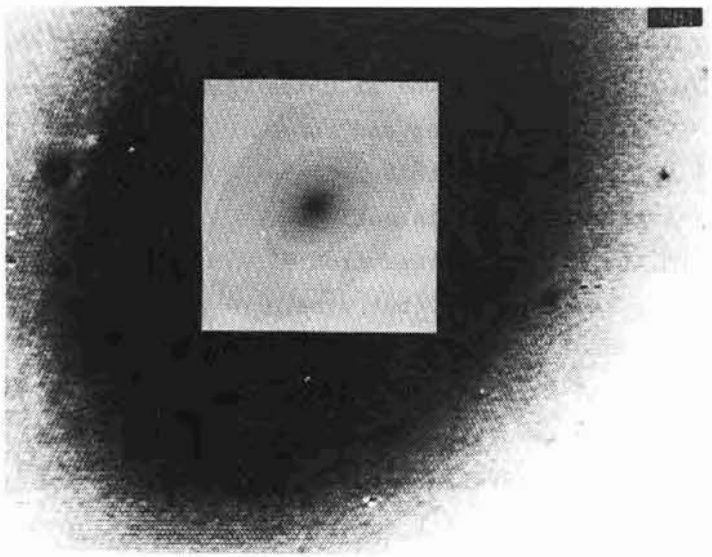

FIG. 11.—An R band CCD frame of M81 from the 4-m prime focus, using the CCD-211 chip. The exposure is 80 seconds. The field of the chip is ~80" x 100". This is a composite of two displays of the same data on the KPNO IPPS. Different contrast settings were used. The small, inner square region is at the same scale and is overlaid to show just the nucleus of M81. The dynamic range available in this frame is >4000.

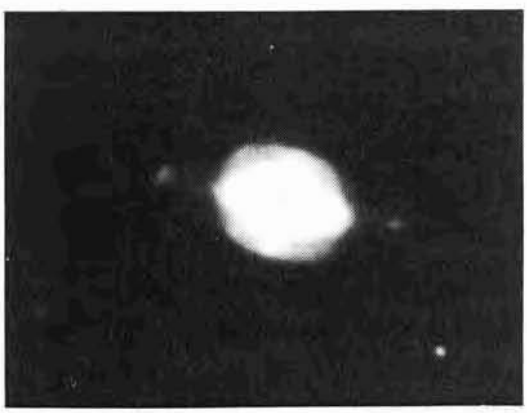

FIG. 12.—NGC 7009, the Saturn Nebula, a planetary. The exposure was 50 seconds with the CCD-211 in the R band (λ_{eff} ~ 6500 Å) at the 4-m prime focus. This and Fig. 13 are from Marcus, Nelson, and Lynds (1979).

Saslaw, Tyson, and Crane (1978). Clearly, the S/N is higher in the photographic data. Also some of the objects are rather red. However, even if the true gain was not 135/5 but really only ~10, this is still a remarkable gain. The power of these devices becomes even more incredible when we consider that the high QE chips like the TI and the new RCA SID 52501 would reach the same S/N as the lower CCD frame in Figure 14 in ~1 minute!

Comparison of this CCD-211 chip with the Video Camera ISIT is made in Figures 15-18. These frames were taken by Roger Lynds. The object (Arp 147) is

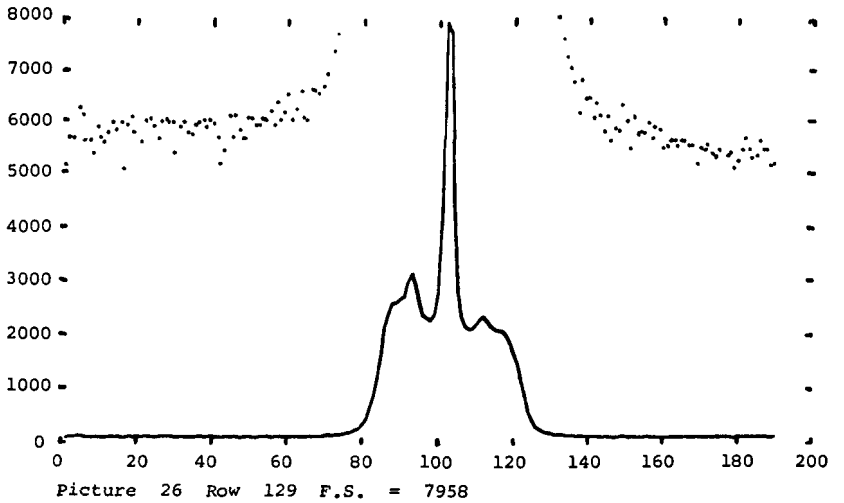

FIG. 13.—X axis profiles through the central star of the planetary in Fig. 12. The level in ADU (for electrons multiply by 8.5) on the ordinate is appropriate for the solid curve. The dots are the same data multiplied by a factor of 100 to show the sky background level and noise. At the level of the star, the S/N is 250 against signal shot noise, 1870 against sky background shot noise, and 4000 against system noise. Because the signal level of the star is only about $\frac{1}{4}$ of device saturation, the potential dynamic range of the CCD-211 is an incredible 16,000.

an interacting pair of galaxies, one of which is a good example of a "ring" galaxy (Lynds and Toomre 1976). The Video Camera data are shown in Figures 16 and 18, while the CCD data are displayed in Figures 15 and 17. Both are I band exposures. Although the limiting magnitude is similar in both cases, the CCD data frame was obtained in only ~1/8 the exposure time of the Video Camera frame, reflecting the large QE difference between the detectors around 8000 Å where the frames were taken.

As good as this CCD-211 chip is, devices that improve on its limitations are becoming available. Keeping the CCD-211s dynamic range and linearity while improving the QE, blue ($\leq$4500 Å) sensitivity, format size, and reducing the cosmic ray sensitivity are the major items on the astronomer's ideal CCD shopping list.

The current TI devices look to be rather satisfactory, although there are questions concerning their high defect densities, their linearity (particularly transfer efficiency and threshold effects) at low light levels, and their rather poor blue response, especially for thinned, back-illuminated devices. This probably arises from damage to the surface structure of the bulk silicon substrate that occurs during the chemical etching process, whereupon surface states are formed that trap the carriers generated by the blue photons (the mean free path of blue photons in silicon is extremely small, being of the order of 0.4 μ or less). Different etching procedures can improve this situation.

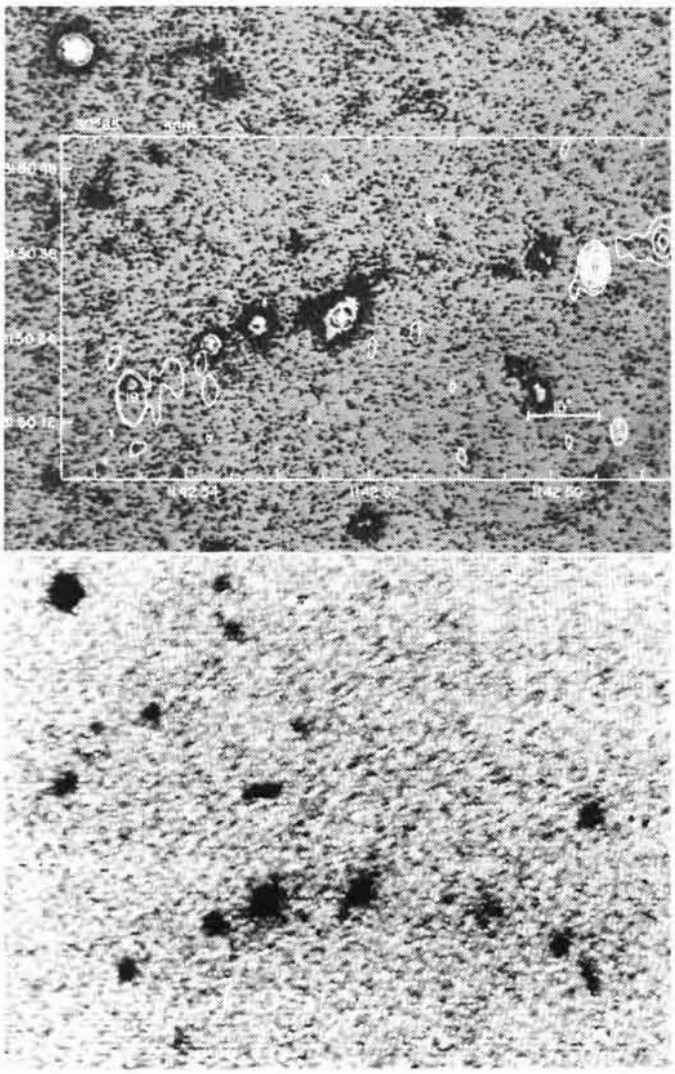

FIG. 14.—Comparison between photographic and CCD data of a field around the radio source 3C265. The upper frame is the average of three 45' IIIa-J plates from the 4-m prime focus at Kitt Peak. This 135' of integration is to be compared with the 5' of integration in the lower frame from the Fairchild CCD-211 with an R band filter. The S/N is better in the upper frame and the objects are red, favoring the CCD exposure. Even so, the gain of the CCD is impressive, being probably an order of magnitude improvement over the plates.

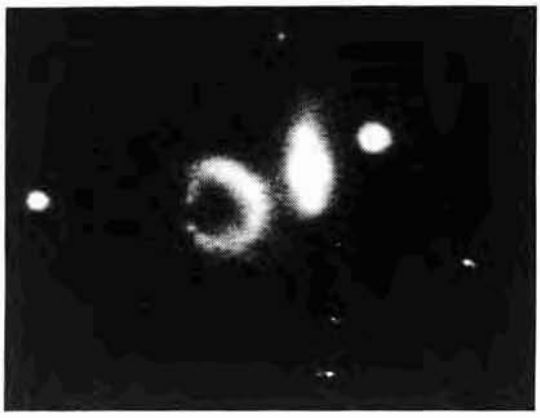

FIG. 15.—A CCD-211 I band (λ_{eff} ~ 8200 Å) exposure of Arp 147, an interacting pair of galaxies, one of which is a "ring" galaxy. This is a 200-second, 4-m prime focus exposure. Figures 15-18 are from Marcus, Nelson, and Lynds (1979).

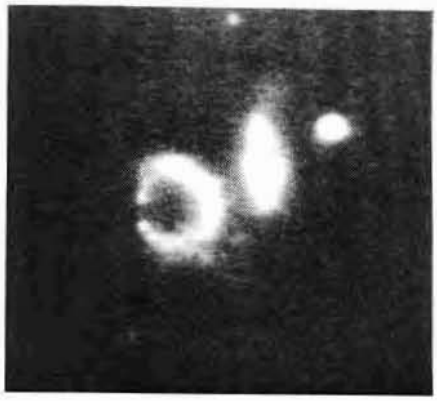

FIG. 16.—An ISIT (Video Camera) exposure of the same object as in Fig. 15 made also with the 4-m telescope in the I band ($\lambda_{eff} \sim 7600$ Å). The exposure here was 1638 seconds, the difference reflecting the poor response of S-20 photocathodes in the red compared with silicon devices.

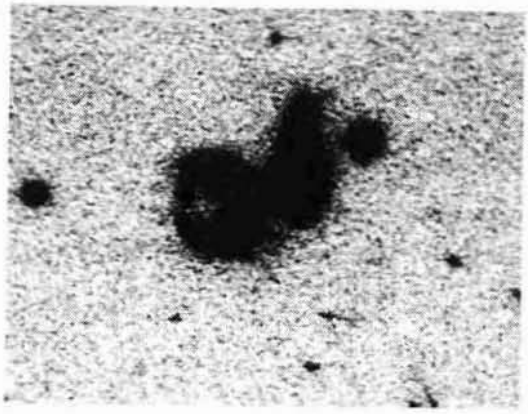

FIG. 17.—Limiting detectability display of the same CCD data as in Fig. 15.

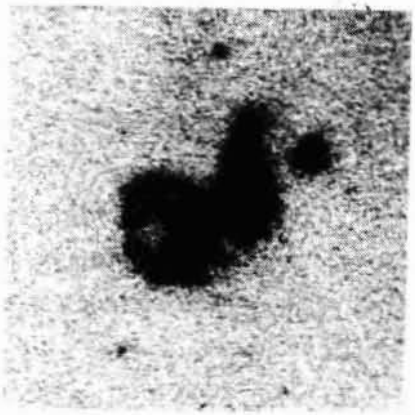

FIG. 18.—The same ISIT data as in Fig. 16. The Video Camera compares very favorably with the CCD in the lack of low level fixed pattern noise.

Early, thinned TI devices (the 400 square JPL-11) displayed serious internal interference problems in the red ($\lambda \geq 7000$ Å) (presumably from multiple internal reflections between the front and back surfaces of the chip) that resulted in a ring-like modulation pattern in the data, even with broad-band red filters.

These patterns were time-variable (from night sky line spectral variations most likely) and could not be fully removed by normal calibration procedures. Fortunately, later TI thinned devices do not show this effect as strongly, if at all (less than specular internal reflections?). This will always be a latent problem with thinned devices; whether or not the thinned RCA 52501-20 chip has this problem is still not known.

We are currently evaluating a large Fairchild chip (CCD-221) with 380 x 488 pixels that has the same pixel size and structure (Fig. 7) as the smaller CCD-211 device. The cosmic ray problem will still exist with this chip since it is an unthinned device. This evaluation is preliminary to our acquiring Fairchild chips of this format and architecture with one important change: in these the aluminum above the vertical shift registers would be removed. The shift registers would then become additional sensing sites, though being ~15 μ x 36 μ instead of the ~15 μ x 18 μ of the adjacent original sensing sites. The overall QE of the chip will then improve by a factor ≥ 2, possibly to 40% or more, since this CCD-221 chip has somewhat thinner polysilicon electrode structures than our current CCD-211 chip.

Our preliminary evaluation indicated some problems with the charge transfer efficiency at low light levels apparently due to minor design or manufacturing changes between the CCD-211 and CCD-221 devices. However, we are receiving valuable assistance from Fairchild, and we hope to understand (and correct?) the problem in the near future.

The other device with which we will be gaining experience is the RCA SID 52501-12 (or -20 if thinned) buried channel chip. This is formatted to have 512 x 320 pixels, each being 30 μ square. The enthusiasm centered on this device results primarily from the incredible QE claimed for the glass-mounted, thinned device recently announced by RCA. The thinning technique used does not destroy the blue response of the device and, as a result, RCA claims a blue (4000 Å) QE that exceeds 50% with a maximum QE beyond 70% at ~6500 Å and still having a QE ~8% at 1 μ. If these chips have sufficiently low noise on-chip electronics, good charge transfer efficiency at low levels, and the overall linearity required by astronomers (and as yet there is no guarantee of any of these requirements being satisfied), they should be superb devices.

Those interested in our up-to-date experience with either the Fairchild or RCA devices should contact the authors at Kitt Peak.

While these detectors will surely find widespread use in most applications in optical astronomy, our current high-priority applications are for an imaging system at the 4-m prime focus and a low resolution spectroscopic system at the 4-m Cassegrain (the Cryogenic Camera). Later developments will include a system for high S/N spectroscopy at the coudé spectrograph on the coudé feed, an imager

at the 1-m telescope, and a spectroscopic system for our large telescope spectrographs (both unintensified and intensified, echelle and lower resolution).

The 4-m prime focus imaging system will utilize either the RCA SID 52501 or the Fairchild CCD-221 no-aluminum special as the detector and will have a wide range of broad and narrow-band filters (including Polaroids) as well as a low dispersion grating/prism system for slitless spectroscopy. Completely remote operation is foreseen with an automatic guider based on the acquisition ISIT TV system. We expect that this will eventually become the primary dark-time imaging system at the 4-m.

Our second high-priority instrument using a CCD as a detector is an f/1 Schmidt Camera system which also functions as a vacuum dewar, the CCD being mounted at its prime focus. This system mounts to the R.C. spectrograph at the 4-m telescope Cassegrain. While this system can be mounted on one of the normal camera ports and thus utilize the available R.C. spectrograph gratings (giving high S/N data and excellent red response), its most popular mode of operation will surely be the low-resolution transmission-optics mode. In this mode we precede the camera by a transmission grating replicated onto a prism and use a lens collimator. This whole assembly then replaces the standard collimator mirror on the spectrograph, yielding a high-throughput, low-resolution system. Dispersions of ~250 Å mm^{-1} (resolution ~15 Å FWHM) and ~570 Å mm^{-1} (resolution ~35 Å FWHM) will be available with coverage from ~4000 Å to $\geq$1 μ (depending on the chip and grating/prism used). While this system can be used in the normal slit mode, we are planning to use interchangeable aperture plates with holes/slits at object positions over an ~5' diameter field. This will allow simultaneous observations of tens of objects, thereby enhancing the telescope throughput by a large factor. We envisage that this system will be especially valuable for redshifts and spectrophotometric observations of very faint and distant objects.

This system will also function as an imager by removing the grating/prism assembly, giving us an f/1 CCD camera with ~1".5 pixel; this is by no means optimum for general imaging (where 0".3-0".5 pixels are best) but may be adequate for some problems.

Of critical importance to the successful use of these new detectors is the availability of adequate data handling facilities. The data volume from a broad-band imaging system is horrendous. Including calibration frames, of the order of 100-150 frames could be generated in a typical night, each frame being 400-800 pixels square (available chips! what of future chips?). A single 2400-foot, 9-track, 1600 bpi magnetic tape holds only ~25 of the larger 800 square frames. This volume of data is unprecedented in optical astronomy, and, unfortunately, very little is being done in the U.S. toward planning for the problems this data

flood will cause. Kitt Peak is planning to implement the first stages of a facility for data processing, but the major problem is clearly a lack of the required funds, and Kitt Peak alone cannot accommodate all the data analysis that will be desired. In this respect the situation in England (Starlink) and on the Continent (particularly at ESO) looks much better.

Still these new detectors will revolutionize much of optical astronomy and will mean that, at least, we will be utilizing a very large fraction of the available photons that reach the telescope. Future major advances in the optical will clearly have to come through more light gathering power, i.e., bigger telescopes!

More extensive discussion of the structure, operation, and capabilities of CCDs can be obtained from papers by Lynds (1980a,b) in addition to that of Marcus, Nelson, and Lynds (1979) previously mentioned.

We thank the engineering staff for the excellent support they have given the astronomers at Kitt Peak in the design, construction, and implementation of new instrumentation.

Copies of papers referenced here can be obtained by contacting the authors at Kitt Peak.

REFERENCES

Aikens, R. 1980, IEEE/OSA Symposium on Laser and Electro-Optical Systems, San Diego, 1980 February 28.

Boksenberg, A., and Burgess, D. E. 1973, in Proc. Symposium on Astronomical Observations with Television-Type Sensors, ed. J. W. Glaspey and G. A. H. Walker (Vancouver: University of British Columbia), p. 21.

Kormendy, J., and Illingworth, G. 1980, in preparation.

Lynds, R. 1980a, in Proc. Symposium on Recent Advances in Observational Astronomy; Instrumentation and Results, Ensenada, Baja California, 1979 September 18-19.

----------. 1980b, in Proc. Conference on Optical and Infrared Telescopes for the 1990s, KPNO, 1980 January.

Lynds, R., and Toomre, A. 1976, Ap. J., 209, 382.

Marcus, S., Nelson, R., and Lynds, R. 1979, in Proc. of SPIE Symposium on Instrumentation in Astronomy III, 172, 207.

Robinson, W., Ball, W., Vokac, P., Piegorsch, W., and Reed, R. 1979, in Proc. of SPIE Symposium on Instrumentation in Astronomy III, 172, 98.

Saslaw, W. C., Tyson, J. A., and Crane, P. 1978, Ap. J., 222, 435.

MARSEILLE OBSERVATORY I.P.C.S. (IMAGE PHOTON COUNTING SYSTEM)

J. BOULESTEIX and M. MARCELIN

Observatoire de Marseille
2, Place Le Verrier
13004 Marseille, France

Introduction

The I.P.C.S. of Marseille Observatory has been presented at the 7th Symposium on Electronic Image Devices (Boulesteix, London 1978). Since then the receptor has been associated with a new special electronic equipment for data acquisition and treatment. The I.P.C.S. has been tested in its new configuration in November 1979 with the 1.93 m telescope of the "Observatoire de Haute Provence" and the results are under analysis. The main change in data acquisition is that every event detected is counted and stored with its arrival time ; this temporal acquisition will permit a noticeable improvement of the detection capabilities of the system.

1. The receptor - Comparison with other detectors

The receptor

The receptor is constituted by the coupling (through optic fibres) of a microchannel plate intensifier (Thomson CSF - TH 9034) and a SIT camera (Thomson CSF - TH 9655).

Since its presentation in London (1978) it did not suffer much modification. The main improvement is the smaller size of the pixel, which is now 45 µm long instead of 55 µm, the limitation depending on electronics itself.

Comparison with other detectors

A good basis of comparison is to compute the signal to noise ratio, S/N, for different detectors. Let us define S/N as the ratio of the useful signal to the square root of the total signal counted by the receptor :

$$S/N = \frac{S.q.\Delta\lambda.t}{\sqrt{S.q.\Delta\lambda.t + S_s.q.\Delta\lambda.t + S_t.n.t + N_R.n.R}}$$

where :

- S = signal coming from the object (in number of events pixel^{-1} Å^{-1} s^{-1})
- q = detective quantum efficiency
- $\Delta\lambda$ = band width
- t = exposure time
- S_s = signal from sky background (events pixel^{-1} Å^{-1} s^{-1})
- S_t = signal from thermal background (events pixel^{-1} s^{-1}, or density of the plate)

n = number of pixels in the image of the object

N_R = number of readouts of the image

R = readout noise of the image (or density of the chemical background of the plate).

Let us now consider a numerical application for a 4^h exposure time of a star like object (considered here as a 1" square object) in Hα light with the 3.60 m ESO telescope, using different detectors, such as photographic plates, the Electronic Camera, C.C.D, or I.P.C.S. Table I shows the typical values of the above parameters for those different detectors. The value of S_t (10^{-4}) for the I.P.C.S. is the value obtained recently, owing to the acquisition with temporal information. Up to now it was strongly increased by parasitic flashes due to electric discharges on the entrance window of the receptor, near the photocathode, giving rise to a noise S_t approximately equal to $2\ 10^{-3}$ events per pixel per second. In the same table we took a 30 µm size for the pixels. Although it is, by now, limited to 45 µm we hope to attain 30 µm soon, and even less with a 512 x 512 image instead of 256 x 256. Concerning the C.C.D. we considered two cases, whether the readout noise is 10 or 50 e^-rms.

TABLE I

Receptor	I.P.C.S.	C.C.D.	Electronic Camera	IIaO plate	IIaJ plate
q	0.15	0.6	0.15	0.01	0.035
S_t events $px^{-1}\ s^{-1}$ or density	10^{-4}	0.1	$3\ 10^{-5}$	d = 0.05	d = 0.05
N_R	1 every 1/50s	1 every 1/2h	1 per exposure	1 per exposure	1 per exposure
R	0	10 to 50 e^- rms	d = 0.02 (150 e^- rms)	d = 0.1	d = 0.05
pixel size n	30 µm 3	25 µm 4	15 µm 12	25 µm 4	15 µm 12

The results are shown on Figure 1 where S/N is plotted as a function of the magnitude of the object for different bandwidths. It appears that the I.P.C.S. gives the best results for faint objects and for very narrow bandwidths. This is merely due to the fact that the influence of S_t and N_R is greater as the bandwidth decreases ; those terms appearing in the formula giving S/N it explains that the I.P.C.S. is advantaged with its readout noise, N_R ,

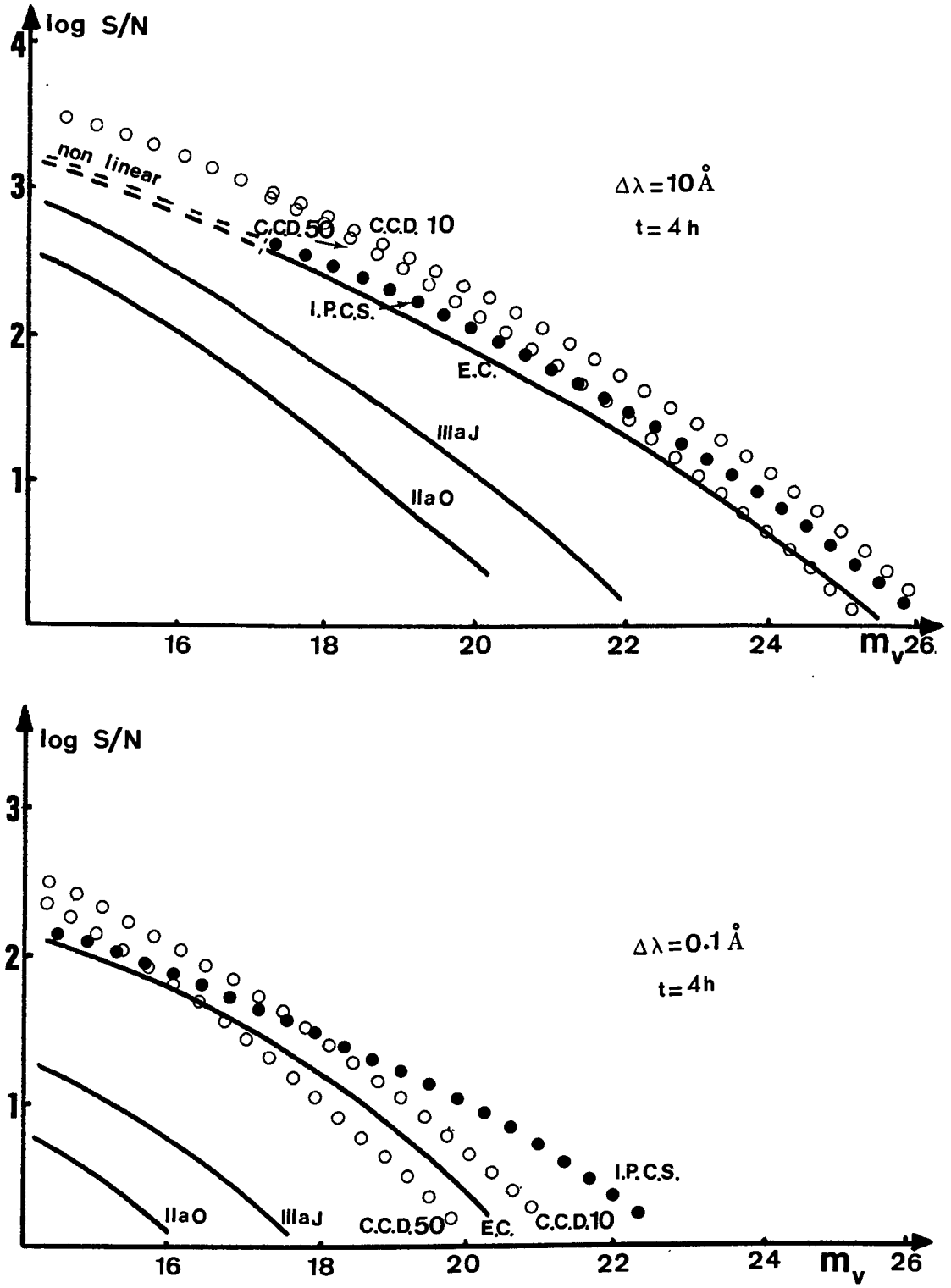

Fig. 1 Comparison between different types of detectors.
log S/N is computed for the observation of a starlike object in Hα light with a 3.6 m telescope.

equal to zero. All of this shows that I.P.C.S. is very well designed for uses such as interferometry where both advantaging conditions of narrow bandwidth and very faint flux are found together. An example of such an observation is shown on Figure 2.

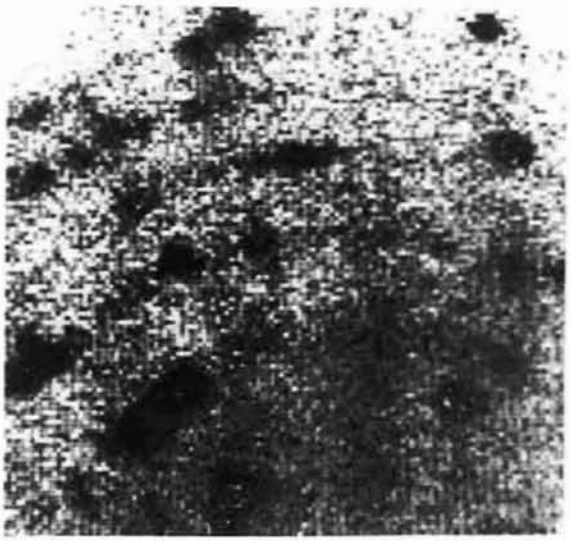

Fig. 2 : Enlargement (128 x 128) of an interferogram of M 33 taken in OIII line. Interference order of the Perot Fabry : 1051.
Exposure time : 3^h at f/3 (telescope 1.93 m).
Parts of rings due to individual HII regions can be seen here also with faint rings due to the diffuse emission of the disk.

In our comparison between different detectors we took into account the detective quantum efficiency and the different sources of noise. It is to be noted that I.P.C.S. attributes the same weight to each detected event ; such a thing improves the signal to noise ratio too, compared with detectors where the dispersion of the weight attributed to each event can diminish by some tens of percent the equivalent d.q.e. (this problem has been pointed out by Coleman (1974)).

2. The I.P.C.S. as a photometric detector

Although it is not the purpose for which it was conceived such a system offers some interest for photometry. The main advantage is due to the very good linearity of the instrumental response, which is true for each of the pixels. This linearity is quite perfect providing that the received flux is not too high, the upper limit (insuring a linearity better than 90%) being about 900 events pixel^{-1} h^{-1} for the whole image (256x256) and about 18 000 events pixel^{-1} h^{-1} for an individual pixel.

The main problem for a photometric use of the I.P.C.S. is due to the inhomogeneity of the response to a uniform light, which necessitates to obtain a precise "response-map" of the detector, this can be obtained by recording the image of a uniform lightning. Now, let us define the accuracy of this map, for each of the pixels, on a statistical basis as being the ratio $\sqrt{N}/N$ where N is the number of events counted for a given pixel. One can see that a one hour exposure time to a uniform light, the level of which insures a very good linearity (500 events px^{-1} h^{-1} for example) will provide an accuracy of about 4-5% for the "response-map". A good map will be obtained through a 10^h exposure time, the accuracy becoming then 1.4%.

Now, what is the photometric accuracy one can hope when recording the image of an object ? Considering the ratio $\sqrt{N}/N$ mentioned above we can estimate the photometric accuracy for different types of objects. For a one hour exposure time with a narrow bandwidth (10 Å) centered on the Hα emission line :

- Object giving a minimum rate of counts (almost lost in the noise)
  Typical count rate : 4 ev. px^{-1} h^{-1}. Accuracy : $\sqrt{N}/N \sim 50\,\%$
- HII region in the arm of a galaxy
  Typical count rate : 100 ev. px^{-1} h^{-1}. Accuracy : $\sqrt{N}/N \sim 10\,\%$
- HII region in our Galaxy
  Typical count rate : 1000 ev. px^{-1} h^{-1}. Accuracy : $\sqrt{N}/N \sim 3\,\%$

For the one hour exposure time considered here the accuracy remains limited to some percents, because with higher fluxes non linearity will appear.

An interesting fact with our system is that it permits direct superimposition of images of the same object obtained through different narrow bandwidths. This permits to compute rapidly the ratio of different emission lines for each pixel. Such a thing allows to define for example the conditions of excitation (temperature and density) for each point of a nebula.

3. Astrophysical results

Previous tests and observations have been performed concerning the detector itself (which was first tried two years ago), showing its capabilities and its limitations. Some of the results obtained were presented in London (Boulesteix, 1978).

Since then the tests went on at the "Observatoire de Haute Provence". The observations, led with the 1.93 m telescope, concerned imagery as well as spectroscopy. An interesting result concerning the determination of the redshift of a Q.S.O. is to be noted. It concerns the Q.S.O. 1356 + 581,

whose visual magnitude is 16. Up to now the redshift was given as being equal to 0.321 or 1.377. We took two spectra between 6450 Å and 6750 Å of this object with our I.P.C.S. behind a nebular spectrograph at the Cassegrain focus of the 1.93 m telescope ; the exposure times were 2800 s and 6600 s. The dispersion was 30 Å mm^{-1} and we observed a broad (compared with the nearby night sky emission lines) emission feature at about 6653 Å which is certainly a MgII line (rest wavelength : 2798 Å) which had been looked for, but not detected, with other receptors, thus confirming the greater value $z = 1.377$ for the redshift of the Q.S.O.

The last observation round, in November 1979, permitted to test our I.P.C.S. with all of its data treatment elements at the "Observatoire de Haute Provence". For the first time we could record the arrival of each event in time (and not only in space as was done up to now by integration in time of the data). Although the results are still under analysis we expect good improvements from such an acquisition of the data.

4. Improvements awaited from "temporal acquisition"

This acquisition of data, with both spatial and temporal information will permit :

1) To improve our signal to noise ratio by suppressing the parasitic flashes mentioned above. Eliminating such parasitic events is quite easy because the silicium target is swept every 1/50 s and the parasitic flashes appear all of a sudden, giving rise to the arrival of some hundreds photons on the frame instead of some one to ten photons per frame. This parasitic noise amounts to about 6 ev. $px^{-1}\,h^{-1}$, while the thermal noise due to the photocathode itself is less than 0.5 ev. $px^{-1}\,h^{-1}$, so that the S/N ratio will be increased by a factor of 3 to 4 for the faintest detectable objects.

2) To suppress the remanence coming from the SIT camera. This can be done through a simple comparison of the successive frames, one by one.

3) To improve the resolution of the receptor by following, and then correcting, the evolution of the turbulent displacement of the images with time. Each frame is 1/50 s long and it seems possible to build up a new integrated image, grouping for instance the frames five by five and determining a new center for each of them (assuming that the turbulent image is moving as a whole) so as to obtain the maximum of correlation with the previous recentered integrated image.

4) The use of a scanning "Perot-Fabry" interferometer for observing faint extended sources. This will permit to obtain directly the complete two dimensional velocity map of an object.

Acknowledgements

We want to thank Dr. Deharveng for fruitfull discussions concerning the comparison between different detectors.

References

A. Boksenberg, P.J. Bowen, C.I. Coleman and A.D. Petford : 1975, Report : "Study and evolution of I.P.C.S. for a spaceborne astronomical instrument"

J. Boulesteix : 1978, 7th Symposium on photoelectronic image devices. London (Mac Mullan)

J. Boulesteix : 1979, Thesis, Université de Provence, Marseille

V. Cenalmor : 1978, Thesis, Université de Provence, Marseille

C.I. Coleman : 1974, Ph. D. Thesis, University of London

D. Wills and Beverley J. Wills : 1974, Astrophys. J. 190, 271-277

THEORETICAL SURFACE PHOTOMETRY OF SPIRALS.

C. Yuan
The City College of the City University of New York, New York
and
P. J. Grosbøl
European Southern Observatory, c/o CERN, Geneva

Abstract

A method is developed to construct the color variation and surface brightness across a spiral arm using the ideas and results of the density-wave theory. An application of this method to the Milky Way shows that the surface brightness across a spiral arm is smooth and symmetric with little dependence on the galacto-centric distance. The color variation measured by the index Q varies with the ratio of the number of young stars to that of the old stars, the initial mass function and the pattern speed. In general, the color profiles are smooth and symmetric in the inner parts of the galaxy and become more asymmetric towards the corotational region. The results are in good agreement with recent optical observations (Schweizer, F. 1976, Ap.J. Suppl., 31, 313; Talbot, R.J., Jensen, E.B. and Dufour, R.J. 1979, Ap.J. 229, 91). Two effects responsible for the relative smooth and symmetric variation of the brightness and the color across a spiral arm instead of a sharp one as the galactic shock picture might imply are discussed in lenght.

The paper has been submitted for publication elsewhere.

SECTION III

Processing and Manipulation of Digitized Calibrated Images

COMMENTS ON FACILITIES FOR INTERACTIVE PROCESSING OF ASTRONOMICAL MAPS

R.D. Ekers
Kapteyn Laboratory
University of Groningen
The Netherlands

I. Motivation for using Interactive Graphics

1) Data display

In this workshop many ways of obtaining high quality two dimensional digital data have been discussed. However, if we want to "see" what we are doing as we interpret this data we have the problem of converting it into a suitable visual form. Since an excellent review of various methods of displaying data is given by Allen (1979) I will not repeat this here but I do wish to stress the point that it is important to have available many different display methods to emphasize different features of the data.

2) Why do it interactively?

Interactive processing facilities make greater demands on both the hardware (eg. quick response) and the user (eg. constant attendance) so why is it so important?

i) by looking at the result of each step of the analysis errors can be immediately detected and corrected. This can substantially reduce the total processing time required.

ii) it is possible to modify the reduction strategy depending on the results of previous steps. In this way the astronomer is expected to think and to make decisions using the computer as a tool.

iii) since the astronomer is involved at every step in the reduction there is less discrimination against the unexpected result.

These points are illustrated in the discussion of an earlier interactive map processing system developed in Groningen (Ekers, Allen and Luyten, 1973).

II. Hardware Implementation

Because of the rapid evolution of the hardware available I will not even attempt to make a market survey. Instead I will give a "check list" of features which might be incorporated in a processing facility. The associated comments reflect my own views but they are based on experience and discussions with users of a number of systems.

1) User Interaction

Keyboards	- an excellent way to enter alphanumeric information into a computer if that is what is desired. For other purposes it is a poor interface device. Lengthy command strings are not a good substitute for a simple switch.
Light pens	- not much use. Too much parallax for accurate work.
Displayed cursors	- when combined with a joystick or a trackball this is preferable to the light pen.
Joystick or trackball	- best method for genuinely two-dimensional analogue inputs eg. to position the cursor. If two or more

independant analogue inputs are needed independent potentiometers are much easier to use.

Scratch pads - an alternative to the joystick - no obvious advantages except for use with preprinted information (eg. menus).

Menus - displayed menus are commonly used in interactive systems where they are liked by novice users but are usually inconvenient for serious work.

Control panels - although less flexible, this is surely the best final solution. A set of potentiometers, buttons and switches with specific functions and settings provide an excellent method of interactive control.

Bells - some audio feedback is very useful, eg. to indicate the end of an operation.

2) Vector or line scanned graphics?

Vector based systems do good line graphics but line scanned devices are needed for photographic type display. If you need to do both well you will need both types of device.

3) Colour display

This is a relatively inexpensive addition but the real advantages are yet to be proved.

4) Hard-copy device

This is an essential but sometimes difficult piece of hardware to integrate into a system. If you want a hard copy of what you see on the screen, and you often do, a direct link to a hard copy device is simplest. Beware of the software approach in which it is argued that the program which generated the display can also give the same information to the hard-copy device. Although this may be true, the resultant software overhead and user inconvenience are disadvantages.

5) Storage capacity for displayed images

8-bit memories are standard but it should be noted that although 8-bits is more than enough dynamic range for a given display, it is often quite inadequate to take advantage of the dynamically adjustable look-up tables to exploit the full dynamic range of the data.

6) Processing capacity in the display system

Look up tables - needed for dynamic adjustment of contrast or pseudo coloring.

Cursor generation - needed for user inputs referring to positions in the displayed image.

Graphics overlay - optional.

Zoom - to look at details in any part of the image, preferably at a speed comparable to the video frame rate.

Pan - useful to look at images larger than the maximum instantaneous display size.

Video rate arithmetic - can make very high speed image processing possible, eg. Allen (1980), but the software development may be time consuming and debugging is much more difficult in this hardware-critical environment.

Division of responsibility - the separation between host computer and display system tasks should be given very careful consideration.

7) Host computer

Excess capacity can reduce software development costs and implementation timescales. Good Input/Output capacity is an obvious requirement for image processing.

8) Video Disc

A convenient high capacity analogue storage device for images. Makes cinematography possible.

9) Video Input

Eg. a TV camera or video tape recorder may have useful applications.

III. Software Implementation

The standard mistake is to expend all the resources on the hardware, thinking that the software is a minor in-house affair which comes essentially for free. In fact it is more likely that the software will totally dominate the real cost, the timescale to get a system going, and the capabilities of the final system.

1) Languages - only use high level languages, preferably those with good structure. A number of structured Fortran precompilers are now available if you want to combine a good structure with a well known and well supported language.

2) Structure - the modular approach is well suited to interactive graphics software. It eases maintenance and debugging and it makes it possible to develop extensive software systems with multiple contributors.

3) User participation - this is required at application program level to obtain software which is convenient to use.

4) Interactive v Batch - the choice often depends on the personal preferences of the user, and this should not be ignored. Both possibilities may be needed.

5) Compatibility - complete compatibility between different systems is so rarely achieved that it may not be worth the effort. However some agreements on general structures to be used can make software exchange less arduous. A recent attempt at compatible tape formats for exchange of 2-D images is the FITS system (Wells and Greisen, 1980, Wells et al, 1980). It seems very likely to succeed and I strongly advocate its use.

6) Book keeping - documentation is essential. Also an organised method to maintain software libraries, to protect the operational system and to prevent divergence is required.

7) Prototyping - be prepared to discard your first system as soon as it is finished!

8) Maintenance - often underestimated. Good structure, documentation and machine independance can decrease the load but

a significant drain on your manpower resources will always remain.

References

Ekers, R.D., Allen, R.J. and Luyten, J.R. 1973, Astron. and Astrophys. 27, 77-83

Allen, R.J. 1979, p. 143 in "Image Formation from Coherence Functions in Astronomy", ed. C. van Schoonveld (Reidel)

Allen, R.J. 1980, to be published in the proceedings of the "International Workshop on Image Processing in Astronomy", Trieste, June 1979

Wells, D.C. and Greisen, E.W. 1980, ibid

Wells, D.C., Greisen, E.W. and Harten, R.H. 1980, Astron. and Astrophys. (submitted).

TITLE : GENERAL DIGITAL IMAGE PROCESSING IN ASTRONOMY

Author : BIJAOUI Albert
Nice Observatory
Le Mont-Gros - 06300 NICE

I.- DIGITAL IMAGES

1) Acquisition

Since about ten years, many astronomers have introduced digital image processing (D.I.P.) to enhance, analyse and measure their images. These can provide from classical photography, electronography and image tube, leading to use fast computer driven microdensitometers. The digital images can be also obtained with TV receivers (slow scan SIT, CCD, Reticon Array, Image disector, Image picture counting systems,...)or Radio, X, IR imaging systems.

A D.I.P. system contains displaying and interaction, image enhancements, photometric and geometric corrections, general operations and specialised software adapted to astronomical images. Many of them have been achieved (1,2,3).

2) Scanning parameters

In case of microdensitometers, we have define the values of the scanning parameters : spot size, sampling step, density levels.

The spot size and the sampling step are, in principle, determined by the classical Shannon's theorem (4) : If a function f(x) has a cut-off frequency ν_c, all the values are known if we have a sampling step $\Delta x = 1/2\ \nu_c$. So :

$$f(x) = \sum_{-\infty}^{+\infty} f(k/2\nu_c)\ \frac{\sin 2\pi\ \nu_c\ (x - k/2\ \nu_c)}{2\pi\ \nu_c\ (x - k/2\ \nu_c)}$$

Generally, we use linear or spline interpolation, so use of Shannon's step is not so rigourous. In fact, the spot size is just smaller than the star size and the step is the half of it.

A decreasing of the step by a factor 2 leads to increase the number of points by a factor 4 and the process by a factor often greater than 10.

The discretised levels are generally fixed by hardware. We do not loss any information if the interval between two levels is order of the density r.m.s. (5).

II.- IMAGE ENHANCEMENTS

One of the major interest of D.I.P. consists on the great capability to improve the image quality.

1) Noise smoothing

A very great number of methods have been achieved to diminish the noise. They can be classified as :

a) Two dimensional filtering

This operation can be achieved by two differents ways : localised convolution with well defined masks ($f \otimes p$) or FFT ($\hat{f}.\hat{p}$). The operator p can be derived from many considerations

- weighted sliding mean. The Sheppard smoothing (6) can be considered as one of the best method. It consists to a local fitting of the data with a k degree polynomial.

- Wiener-kind filtering (7). If we admit that the 2nd order signal ($S(\nu)$) and noise ($n(\nu)$) characteristics are the same on all the field , the best linear filter in the L.M.S. estimator sense is given by

$$\hat{p}(\nu) = \frac{s(\nu)}{s(\nu) + n(\nu)}$$

FFT algorithms allow us to use this filter.

- Recursive filter (8). This filter consists on an iterative process with an linear convolution using the preceeding computed data. In some cases (electo-radiograms for example) theses filters conduct to very nice results.

- Filter adapted to a given profile s(x) (9). This filter consists to a cross correlation ($p(x) = s(-x)$). It is very nice for faint star detection.

Many other filtering have been studied to specific applications as apodisation (10)

b) Spline approximation

Since some few years, some people (11,12) have achieved smoothing using interpolation. The signal is approximed by interval $f(x) = P_n(x)$ for $x \in (x_n , x_{n+1})$ where $P_n(x)$ is a k degree polynomial.

The set x_n is generally given (regular under sampling).

The polynomial is an interpolation (linear or spline (13)) or a B - spline

approximation (14). The value of the function at the point x_n are fitted with the L.M.S. estimator.

This process leads to easy computations, nice results and a numerical information compression.

c) "Noise cheating enhancement" and related smoothing

For many objects like galaxies, the dynamic range is too high for a linear filtering. So some people have achieved smoothing taking this fact into account (15, 16).

For example, in noise cheating enhancement, a simple mean is done in a field around a pixel with a size leading to give a sufficient S/N ratio. This leads to detect the outer part of galaxies.

d) Clean procedure (17).

In case of radio astronomical maps, rings corresponding to bright sources can be deleted using a procedure in which the image is decomposed in discrete sources.

2) Deconvolution

It consists to solve the equation :

Image I = Unknown object O convolved by Point Spread function P + Noise

A great number of numerical techniques exists

a) Iterative Van Citter's method (18). It is the oldest technique. It consists to a recursive filter defined as

$$O_n = I + O_{n-1} - O_{n-1} \otimes P$$

$$O_1 = I$$

This technique permits a gain of about two in resolution but it is very sensitive to the noise.

b) Convolution with a mask

Some people have introduced digital filters allowing an improvment in the resolution. For example these filters can provide from the Fourier transform of an optimal filter.

c) The use of FFT permits to have a wide possibility. Deconvolution with Wiener filter (19) is an excellent technique. Use of the singular decomposition of the PSF (20) is also a beautiful one.

d) Use of peculiar conditions : following the well-known Biraud's technique (21), it can be possible to improve the resolution by quite a factor 4 using methods based on log O decomposition, using maximum entropy (22). These digital methods lead to very complex computations but can be considered as the one to be

used in important cases.

e) Parametric techniques : in case of gaussian or Voigt functions it is very easy to do the deconvolution.

3) Constrast enhancement

To improve the feature of the picture on a display, we can change the contrast. It is easy to show that we have only to modify the picture histogram. Many equations (23) have been purposed. The experience shows that the best one is given empiricallry by a user in front of the display.

4) Edge enhancement

A first méthod to improve the contrast consists in the edge enhancement. That operation permits also the object detection. Many methods are allowed

a) High frequency filtering (24). It is the oldest one and it can be achieved with analog technique. The results are not very good.

b) The Laplacian $\nabla D = \frac{\partial^2 D}{\partial x^2} + \frac{\partial^2 D}{\partial y^2}$ (25). This method is very easy to introduce, but the edges do not strictly correspond to the visual edges.

c) The gradient $\left(\left(\frac{\partial D}{\partial x}\right)^2+\left(\frac{\partial D}{\partial y}\right)^2\right)^{1/2}$ is max along an edge. This is only available on a displaying system.

d) Many other edge definitions have been introduced (26) : Huckel, Sobel, Roberts,... They consist to perform local mask operations.

e) With M. Froeschlé we have introduced the quantity (27)

$$B = \frac{\partial^2 D}{\partial x^2}\left(\frac{\partial D}{\partial y}\right)^2 + \frac{\partial^2 D}{\partial y^2}\left(\frac{\partial D}{\partial x}\right)^2 + 2\frac{\partial^2 D}{\partial x \partial y}\frac{\partial D}{\partial x}\frac{\partial D}{\partial y}$$

This edge correponds to the maximum gradient line.

5) Photometric corrections

a) Characteristic curves

Many characteristic have been purposed for photometric emulsions (28,29,30). The simplest one consists to use Baker's density ($B = - \log \frac{T}{1-T}$)

All the problems are not solved with that operation : Saturation in the central part of the stars or of the galaxies, variations of the corrections with the color index,...

b) Background

It is generally included in the skybackground. For TV systems or IPCS, the mapping and the substraction are achieved in real time.

c) Defects

All modern receivers present some pixels with defects : holes, white spot,... Some digital techniques permit to diminish the effects : local interpolation or

median filter (using a local histogram) (31).

6) Geometric corrections

That corrections are necessary when we have to compare different plates when the area is small, a linear transform is sufficient and all the image may be in memory. When the area is great, non linear transform is used leading to complex computations.

The linear interpolation is generally used.

III.- GENERAL OPERATIONS

A system contains always a list of operations necessary to process images : copying, image fusion, interpolation, arithmetical operations between two images, mean and r.m.s., line by line, point by point, histogram, transposition,rotation, relation between the value of two images, autocorrelation functions, software for image coding and decoding,...

IV.- STELLAR ASTROMETRY

In an astronomical D.I.P. system, stellar astronomy plays generally an important part. Many reliated operations do not belong to image processing - as the reduction of the x , y in equatorial coordinates - but are needed.

1) Stellar photometry (separated stars)

Many methods have been tried. Generally the limitations do not provide from the digital technique, but from the quality picture.

a) Integration : the flux is integrated as we have a photoelectric photometer . Square aperture is easier to program than circular one. The aperture can be also defined by isophot or by edge. Interactive mode can be used line by line or using a mean radial profile

b) Cross-correlation : if P(x,y) is the star profile

$C(x,y) = I(x,y) \otimes p(-x,-y)$ We measure cross-correlation function for all desired stars. It is the optimal way to detect faint stars (32). Many digital ways exist : FFT, local convolution for all known stars or for all the fields, global convolution. If we search to eliminate the unknown background, we are lead to a cross-corrèlation with a modified profile (zero mean).

c Fitting : that is the apparent best way, but it is sensitive to effect of the saturation, the neighbouring stars,... The circular gaussian is the general function used (33,34). In some case more realistic profiles are used (35).

d) Histogram : this method (36) seems to be very nice. Using the fact that the intensity is about :

$$I = I_c \, e^{-\frac{(x^2 + y^2)}{2\sigma^2}} + I_s$$

We can see that $x^2 + y^2$ is the area corresponding to I level, that is also the number of pixel S corresponding to an intensity greater or equal to I. So

$$\log (I - I_s) = \log I_c - S/2\ \sigma^2$$

In fact the relation is not strickly linear a 3rd degree polynomial can be fitted.

This method is well adapted to satured star and to few levels microdensitometer. The effects of the neighbourhood stars are also fainter than in case of fitting.

For all these methods, one of the major difficulties lies in the skybackground determination. We discuss this point later.

2) Photometry in crowded fields

This problem is reliated to many interest observations : central part of globular clusters, clusters in Magellanic clouds, stars in M 31 , M 33,..

The general technique (35) lies in the formulation

$$I(x,y) = \Sigma\ A_i\ p(x - x_i\ ,\ y - y_i) + S(x,y)$$

p is a known star profile, independant of the magnitude, S(x,y) is the unknown skybackground, for which we suppose that the variations are slow.

Use of the least mean squares estimator is general. There are different versions taking into account a prior star map or a known skybackground.

When the number of stars is important (>100), iterative techniques are more interesting than the rough resolution of the linear system.

3) Star positions

A great numerous techniques are available to compute star positions :

a) Barycenter : the density barycenter can be estimated using a defined aperture or in a surface defined by isophot or edge line.

b) Cross-correlation : the stars positions are given by the maximum of the cross-correlation function with a star profile.

c) Fitting : many people (33 ,34) have programmed such techniques using gaussian profiles, with or without corrections of the saturated central part of the stars.

e) Symetry center : this technique (37) consists to determine the value (x,y) as

$$\sum_{i,j} \left\| (I(x-i, y-j) - I(x+i, y+j) \right\| \quad \text{minimum}$$

All these methods have their own advantages and their own defects. The choice is governed by the desired computing time, the accuracy and the necessity of a parallel flux measurement.

4) Star reductions

After the parameters estimation, we have always to do some operations to publish the results :

a) Measurement into magnitude transform : even if we use characteristic curve and sophisticated fitting, it may exist non-linearity which can be suppressed by simple tranform.

b) Astrometric reduction : to transform the x,y into α ,δ

c) Identification in a catalogue or in another plate : that problem is not easy if the number of objects is great. Fast algorithms (38) exist.

d) Magnitude-color or color-color diagrams : after that point we can consider that the processing doest not belong to image processing.

V.- TWO DIMENSIONAL ASTRONOMICAL PHOTOMETRY

Many operationsare needed for that work.

1) Skybackground : a great deal of work has been done on that important problem.

a) Numerical mapping with polynomial (39, 40) : It is the first efficient technique. The background is computed with an iterative scheme in which we suppress at each step the pixels for which data are too far from the approximation.

b) Methods using density histogram : in k•σ clipping technique (41), the pixels too far from the mean are suppressed. A model of the density histogram permits also to have a nice approximation (42).

c) Star substraction : from the star determination we can compute the background in each point.

d) Some techniques like low frequence filtering, or interactive determination can be also used.

2) Intensity into magnitude above the sky transform : suitable calibration curve does not suppress all the difficulties. In external parts of galaxies, we can have pixels with an intensity smaller than the sky, so we cannot compute the magnitude using log tranform. A solution to that problem lies in bayesian estimation (42).

3) Object detection : the best method is reliated to image segmentation (43). This operation consists in dividing the image on some connex fields. A pixel belongs to a field if a property is true.

Many properties can be used : density greater than a threshold, maxima, négative laplacian, given color,...

4) Pattern recognition : two different ways exist, if we possess or not a parametric model. In positive case, we can use L.M.S. estimator and χ^2 test. In the other case, the best technique is associated to image segmentation. A field classification is made, using for examplefactor analysis (44) and cluster analysis (45). For complex objects like spiral galaxies, comets,... we need to do a recognition using syntatic methods (46).

5) Textural properties : some statiscal parameters reliated to a field around a pixel can be very interesting in object description (47) : local intensity r.m.s., correlation length, histogram, mean of the parameters connected to image segmentation,...

6) Isophot approximation : in many cases we have to do that operation. The classical technique is interactive, the computed ellipsis is plotted after the fitting.

7) Component study : the image segmentation is a very nice technique to study the component reliated to a physical object. Adjustment with gaussian or other profiles permits to increase the accuracy.

8) Multispectral analysis : the analysis of many images obtained with differents filters allows to detect interesting astrophysical features. We can do the ratio of two pictures, but we can use all the informations using the well known technique of multispectral analysis (48) : in a first time the correlation matrix of the data is determined. A factor analysis (44) is made,leading to principal componants. In the space of the first principal componants, à cluster analysis (45) is performed leading to a separation of all the pixels corresponding to a given group. An image segmentation corresponding to a specified group permits to indicate to the astronomers where they are on the plate. Using color displays that technique is very nice (49).

V.- ASTRONOMICAL DIGITAL IMAGE PROCESSING SYSTEMS

1) Hadware for DIP

The systems depends evidently of the configuration.

a) Central unit : with 32 bits CPU all the image can be stored in memory allowing a high speed and simple algorithm. With 16 bits CPU often access to disks are necessary.

b) Disk storage : absolutly need, with direct access.

c) Arrays processors : very useful for automatic processing

d) Display : interactive, high resolution, color and using auxiliary memory).

e) Plot and playback

2) Running systems

A system is defined by :

- a minimum hardware : number of bits/words,minimum of words, kind of display, array processor.
- kind and structure of the data files
- Computer language used (FORTRAN, PASCAL, BASIC,...)

A system must possess a kernel of about 60 operations. Some image processors are now saled with this kernel.

The major effort in own community must be the development of specialised software reliated to own specific problems.

REFERENCES

(1) ARP H. and LORRE J. 1976, Astrophys. J. 210 p. 58

(2) BIJAOUI A., MARCHAL J. and OUNNAS C. 1978, Astron. and Atrophys. 65 p. 71

(3) MIDDLEBURG F. 1977, The Messager n° 10, p. 16

(4) SHANNON C.E. 1948, Bell Sys. Tech. J. 27 p. 379 et 623

(5) BILLINGSLEY F.C. 1975, in "Picture Processing and Digital Filtering" Huang T.S. Ed. p. 259 Springer New-York

(6) MINEUR H. 1966, Technique du Calcul Numérique, p. 447, Dunod Paris

(7) PAPOULIS A., 1965, Probability, Random Variables and Stochastic Process p. 405, Mac Graw Hill, New-York

(8) R.R. READ, J.L. SHAWKS and S. TREITEL, 1975, in "Picture Processing and Digital Filtering" Huang T.S. ed. p. 131 Springer New-York

(9) MIDDLETON D. 1960, An Introduction to Statistical Communication Theory, p. 714, Mac Graw Hill, New-York

(10) LANDAU H.J. and POLLAK H.O. 1961, Bell Sys. Tech. J. p. 63

(11) RENES J.J. and BEINTEMA D.A. 1979, in "International Workshop on Image Processing in Astronomy" ed. G. Sedmak, Trieste Observatory

(12) HOUH. S., ANDREWS H.C. 1978, I.E.E.E. Trans Acoust. Speech Sign. Proc. 26 p 508

(13) ALHBERG S.H., NILSON E.N., WALSH J.L. 1967, The Theory of Splines and their Applications p. 10, Academic Press New-York

(14) RIESENFELD R. 1973, University of Utah UTEC C.S.C. 73 p. 126

(15) H.J. ZWEIG, E.B. BARRETT et HU P.C. 1975, J. Opt. Soc. Am. 65 p. 1347

(16) PITTELLA G. 1979, Personal Communication

(17) HÖGBOM J.A. 1974, Astron. Astrophys. Suppl. 15 417

(18) BURGER H.C. and VANCITTERT P.H. 1932 Z. Physik 79 p. 722

(19) HELSTROM C.W. 1967, J. Opt. Soc. Am. 57 p. 297

(20) HUANG T.S. and NARENDRA P.M. 1975, Appl. Opt. 14 2213

(21) BIRAUD Y. 1969 Astron. Astrophys. 1 p 124

(22) FRIEDEN B.R. 1972, J. Opt. Soc. Am. 62 p. 511

(23) HUMMEL R. 1977, Comp. Graph. and Im. Proces 6 p. 184

(24) HUANG T.S. , TRETIAK O.J. 1965 in"Optical and Electro-Optical Information Processing" J.T. Tippet, D.A. Berkowitcz,L.C. Clapp, C.S. Koestet and A. Vandeburgh Jnr. eds., The M.I.T. Press Cambridge, Massachusetts.

(25) ROSENFELD A. and KAK A.C. 1976, in "Digital Image Processing" p. 281 Academic Press New-York

(26) SHAW G.B. 1979, Comp. Graph. and Image Proces. 9 p. 135

(27 BIJAOUI A. and FROESCHLE M. 1980, to be published in Astron. and Astrophys.

(28) SCHNEIDER M. 1967, Ann. Astrophys. 30 p. 207

(29) HONEYCUTT R. K. and CHALDU R.S. 1970 AAS. Photo bul. n° 2 p. 14

(30) TSUBAKI T. and ENGWOLD O. 1975, A.A.S. Photo bul n° 2, p. 17

(31) PRATT W.K. 1978, in "Digital Image Processing" p. 330 ed. Wiley and Sons New-York

(32) BIJAOUI A., DANTEL M. 1970, Astron. Astrophys. 6 p. 51

(33) VAN ALTENA W.F. and AUER L.H. 1975, in Image Processing Techniques in Astronomy" p. 411, C. de Jager and H. Nieuwenhuijzen ed. Reidel Dordrecht

(34) CHIU L.T.G. 1977 Astron. J. 62 p. 842

(35) LEROY J.L., AURIERE M. and LAQUES P. 1976, Astron. Astrophys. 53 p. 227

(36) P.L. BRAND, W.S. ZEALEY 1978, Astron. Astrophys. 63 p. 345

(37) R. ALBRECHT, H. JENKWER, W.W. WEISS and H.J. WOOD 1977, Astron. Astrophys. 58 p. 93

(38) BIJAOUI A. 1979, In Proc. of International Workshop on Image Processing in Astronomy, ed. G. Sedmak Trieste Obs.

(39) JONES W. B., OBBITS D.L., GALLET R.M.,DE VAUCOULEURS G.1967, Publ. Dpt. Astronom. University of Texas Austin Ser. II 1 n° 8

(40) BARBON R., BENACCHIO L., CAPACCIOLI M. 1975 Mem. della Soc. Astron. Ital. 47 p 263

(41) NEWELL B. 1979, in Proc. of International Workshop on Image Processing in Astronomy ed. G. Sedmak Trieste Obs.

(42) BIJAOUI A. 1980, Astron. Astrophys. in press

(43) ROSENFELD A. 1969, Picture Processing by Computer p. 127, Academic Press New-York

(44) BENZECRI J.P. et al. 1973 Analyse des données t. 2 p. 64

(45) BENZECRI J.P. et al. 1973 Analyse des données t. 1

(46) FU K.S. 1974, Syntatic Methods in Pattern Recognition Academic Press New-York

(47) ZUCKER S.W. 1976, Comp. Graph. and Im. Proces. 5 p. 190

(48) PRATT W.K. 1978, in Digital Image Processing p. 338 ed. Wiley and Sons New-York

(49) LORRE J.J. 1978, Astrophys. J. 222 p. 99

TWO DIMENSIONAL PHOTOMETRY IN BAADE'S WINDOW

Rudolf ALBRECHT (1)
Bruce ATWOOD (2)
Betty BLANCO (2)

(1) Institute for Astronomy, University of Vienna
Türkenschanzstr. 17, A-1180 Vienna, Austria

(2) Cerro Tololo Interamerican Observatory (*)
Casilla 63-D, La Serena, Chile

ABSTRACT

The faint end of a sequence in Baade's Window (near the galactic center) has been measured from a series of two-dimensional images acquired in B and V with an integrating SIT vidicon. The general purpose interactive software required to sky-subtract stellar images, to deconvolve overlapping images, and to obtain magnitudes is described. Some preliminary results are presented.

INTRODUCTION

The so-called Baade Window is a low absorption region around NGC 6522, through which a relatively unobscured view of the center of the galaxy is possible.

Photoelectric photometry in this region has always suffered from the fact that the apparent star density in the field is very high: it is almost impossible to place a diaphragm of reasonable size (5 to 8 arcsec) around any of the stars without including other objects. And it is quite impossible to find uncontaminated areas of sky for sky subtraction.

The obvious answer is the use of a panoramic detector together with image processing techniques to numerically eliminate the contamination from the measurements.

THE OBSERVATIONS

The observations were carried out during three half-nights in August 1978, using the Tololo 4-m Telescope in the Cassegrain focus.

(*) Cerro Tololo Inter-American Observatory is supported by the National Science Foundation under contract No. AST 78-27879.

A total of about 120 frames were taken in Johnson B and V, using the Tololo Integrating SIT Vidicon as described by Atwood et. al. (1979). The frames are 280 by 280 pixels and the scale was chosen such that the half- width of the stellar profiles was covered by at least 6 to 8 pixels. A range of exposure times was chosen to avoid problems with saturated profiles. The typical exposure time was some tens of seconds.

DATA REDUCTION

Data reduction was carried out with the Tololo Interactive Image Processing System (Albrecht, 1979). Following the ideas of Harvey Butcher (1979), we developed the methods described here.

First, the center of the object of interest is determined from the uncontaminated parts, using first moments. Selection of the uncontaminated parts is done interactively. A plot of signal levels versus distance from the center is generated. For an uncontaminated star, this plot looks like Fig. 1. This plot amounts to a radial cut through the image. An (instrumental) profile could now be fitted and numerically integrated, resulting into a stellar magnitude. In order to become somewhat independent of the instrumental profile, the distribution can also be divided up into one-pixel wide bins, amounting to annuli around the center of the star. The average value in each annulus is calculated and used for the integration. The outermost annulus is considered sky and a plateau of this level is subtracted.

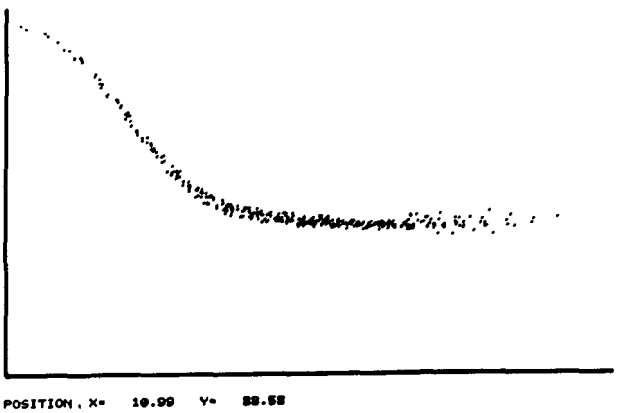

Fig. 1:
Signal level vs. distance from the center for an uncontaminated star.

Fig. 2 shows the plot of a contaminated star. The sky level at the position indicated is determined with the following method: the histogram of the distribution of data points in a one pixel wide annulus around the stellar center with the indicated radius is constructed and the mode of the histogram is determined. As long as contamination does not dominate, this mode will be where most (=uncontaminated) data points are.

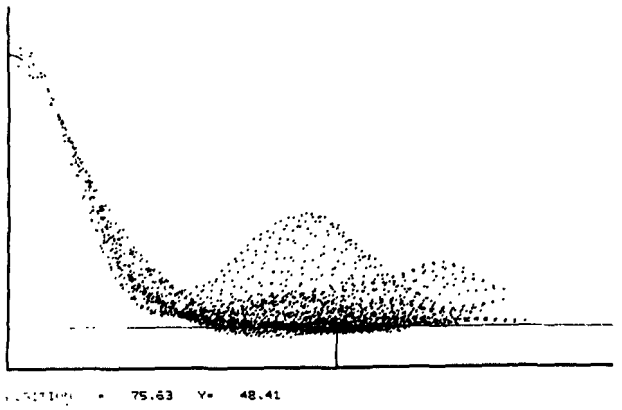

Fig. 2.:
Signal level vs. distance from the center for a contaminated star. The sky level and the peak of the profile are indicated.

This method can be used to determine the uncontaminated signal level in all the annuli around the stellar center. A practical limitation is the small number of data points in the annuli near the center, which prohibits the construction of a histogram with sufficient resolution. The mode is therefore found in the following way: the average of all the points in the annulus is taken and the point with the highest residual is eliminated. This process is repeated until there are only ten points left. These are considered to be the most representative points of the annulus and their average is taken as the level in this annulus.

To test the method the uncontaminated star of Fig. 1 was contaminated by itself in the following way: a subset, containing the star, was copied out of the digital frame, shifted, and added to the original frame. The photometry operator applied to the uncontaminated and the contaminated frame gave magnitudes that differed by the insignificant amount of 0.013 mag.

The application of the technique to crowded test frames is shown in Fig. 3. "Hand integration" is essentially photoelectric photometry: it is the result of careful interactive cleaning up of slices of the stellar profile with subsequent integration, which was performed in a numer of test frames. It was then reduced to actual

magnitudes on the sky using photoelectric standards. "Annulus integration" is the result of the photometric operator as described above in instrumental magnitudes. A 45 degree least squares straight line is fitted to the data.

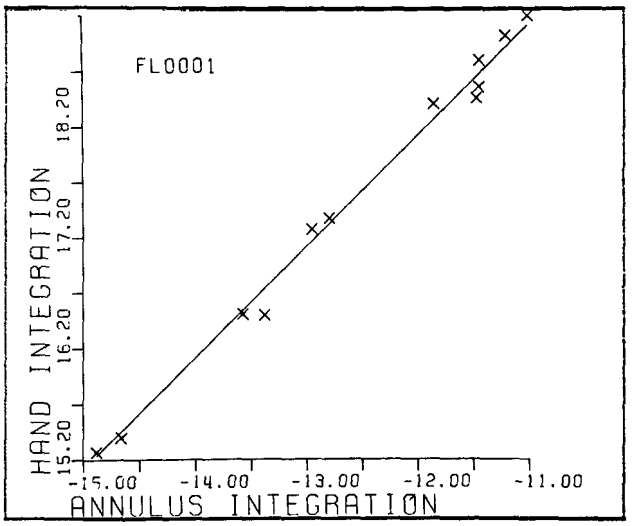

Fig. 3.:
Comparison between annulus integration and photoelectric photometry.

Using the fact that there has to be a linear correlation between the height of the central peak of the stellar image, and assuming a well-behaved instrumental profile, it is also possible to derive an instrumental magnitude by determining the amplitude of the profile. As indicated in Fig. 2, the central peak is calculated by fitting a parabola to the innermost nine points in the signal versus distance plot (corresponding to the innermost 3 x 3 pixels). The sky level is determined via the histogram method.

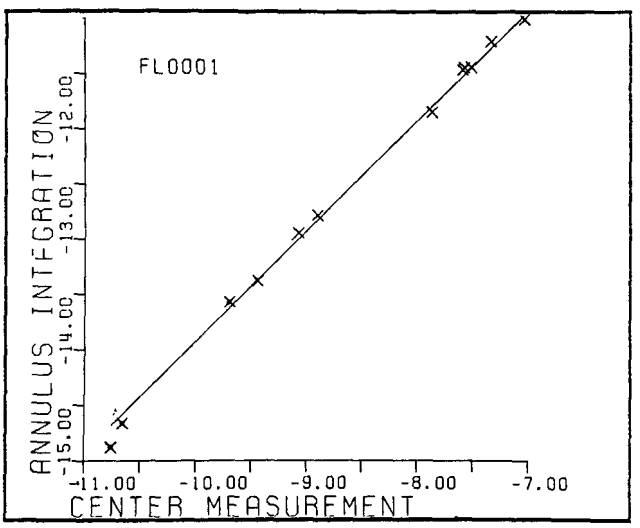

Fig. 4.:
Comparison between the annulus integration and amplitude measurement photometry techniques.

Comparing the "annulus integration" with the "center measurement" method, we get Fig. 4. We note that there is extremely good agreement, even for a star that deviates in Fig. 3, indicating that the photoelectric results are

uncertain. Examination a posteriori showed contamination blended into the wings of the profile of the very brightest star, which was not taken into account by both photoelectric and annulus photometry.

RESULTS

The photoelectric values used for the standard stars are based on observations of V. M. Blanco (obtained in 1978 on the Tololo 4-m and 1.5 m telescopes), as we have more confidence in them than in the other two available data sets (Van den Bergh, 1971; Arp, 1965). The reason for this is evident in Figs. 5 and 6, showing the systematic errors in the photoelectric sequences comparing Van den Bergh to Arp and Blanco. Arp's data showed no systematic effect, but as they were taken from the northern hemisphere they do have some random scatter.

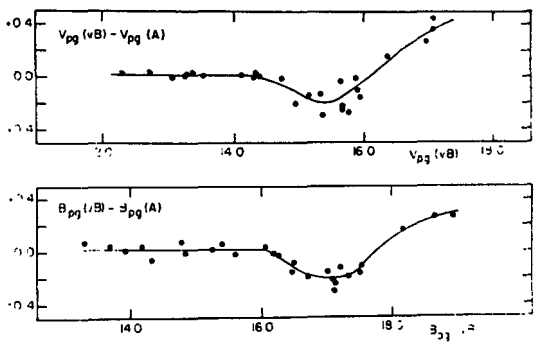

Fi. 5.:
Fig. 12 of Van den Bergh's 1971 paper, comparing his observations with Arp's data.

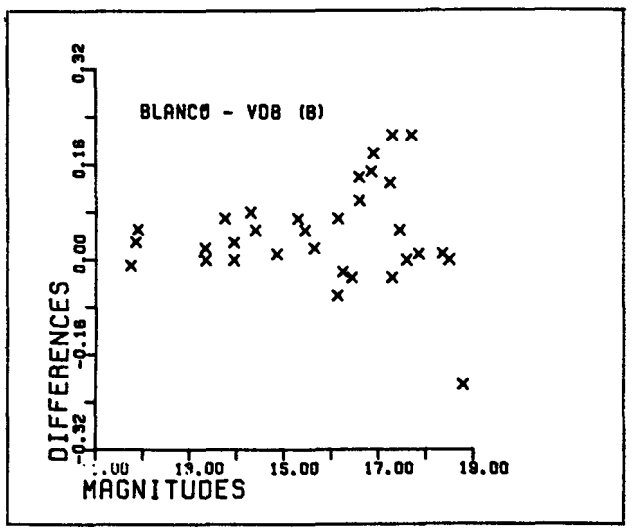

Fig. 6.:
Comparison between Blanco's and Van den Bergh's data.

The method of reduction was in every frame to fit a 45-degree least squares straight line through the standards that appear on the frame. Mean errors are derived from the residuals from the line: they average +/- 0.01 to 0.20 in the worst case.

In trying to compare the two-dimensional results with classical photoelectric photometry, we had difficulties to find stars with good photoelectric measurements that we did not have to use as standards.

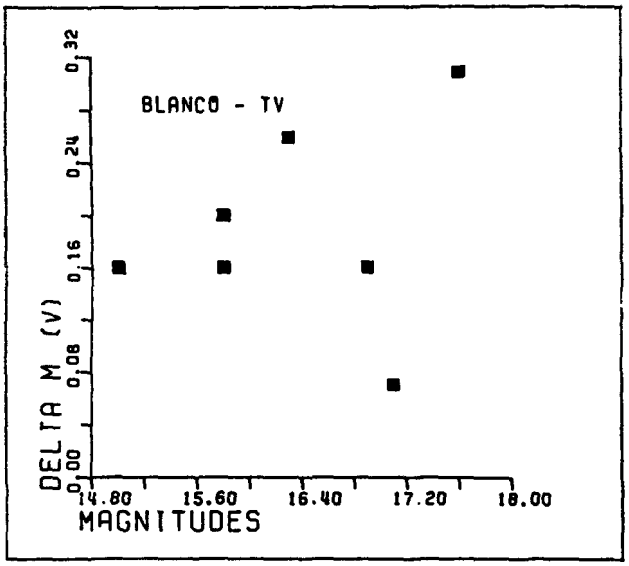

Fig. 7.:
Comparison between Blanco's photoelectric photometry and two-dimensional photometry.

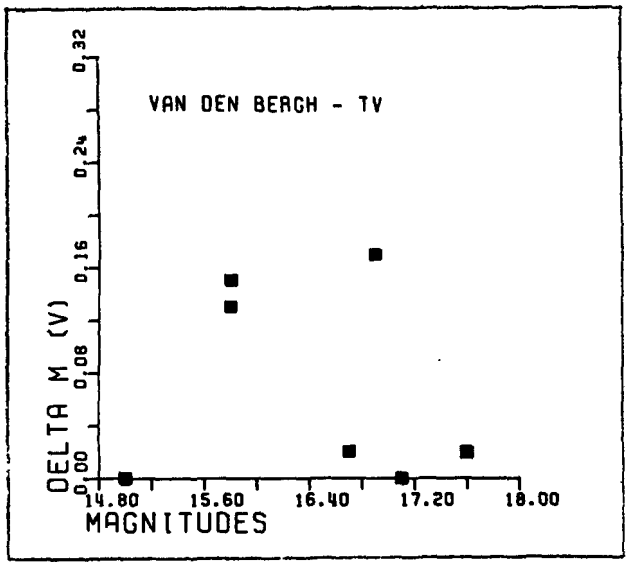

Fig. 8.:
Comparison between Van den Bergh's photographic photometry and two- dimensional photometry.

Figs. 7 and 8 show the comparison (in V) between Blanco and Van den Bergh on the one hand and two- dimensional (TV) photometry on the other hand. There appears to be a systematic difference in the sense that the TV data gives brighter results- which is not surprising, since this method resolves the contaminated background much better.

The above clearly shows this to be a viable method of doing two- dimensional photometry in crowded fields. The errors are well within the uncertainties of the photoelectric standard sequences and in fact strongly reflect these uncertainties.

REFERENCES

Albrecht, R., 1979, Intern. Workshop on Image Processing in Astronomy, G. Sedmak (Ed.), Trieste, Italy.

Arp, H. C., 1965, Astroph. J. 141, 43

Atwood, B. et. al., 1979, PASP 91, 539, 120.

Butcher, H., 1979, private communication.

Van den Bergh, S., 1971, Astron. J. 76, 1082.

ELECTRONOGRAPHY AND THE LUMINOSITY FUNCTIONS OF THE MAGELLANIC CLOUDS

I. Technique and preliminary results

H. Lindgren, A. Ardeberg, P. Linde
and G. Lyngå

Lund Observatory, Sweden

ABSTRACT

We have used Spectracons on ESO telescopes to obtain deep electronographic exposures for UBV photometry of field stars in the Magellanic Clouds. Our aim is to study colour magnitude diagrams and luminosity functions in these extragalactic systems. In the present report we give some preliminary results for an area in the halo of the Large Magellanic Cloud. For the measurements we have used the PDS machine at Lund and the technique developed for evaluation of the measurements deals with two major problems: image crowding and background noise.

INTRODUCTION

The luminosity function is a key parameter for our understanding of stellar evolution as well as of the large-scale evolution of galaxies. Through extensive work on the main-sequence luminosity function for the solar neighbourhood summarized by McCuskey (1966) it has been possible to trace the history of star formation in our part of the Galaxy. For obvious reasons our knowledge of the luminosity functions of other galaxies is much more restricted. This constitutes a major limitation to the proper understanding of extra-galactic systems and their evolution.

The practical derivation of a main-sequence luminosity function for an external galaxy is an undertaking fraught with considerable difficulties. In order to give adequate information, photometry must reach faint magnitudes. As a result, the observational data are affected not only by effects of detector noise and background brightness but also by image crowding. Provided proper choice is made of observing parameters and positioning of programme fields, the effects of detector noise and background brightness can often be largely diminished. On the other hand, image crowding is a problem hard to avoid, and it is often emphasized by effects of poor seeing. A successful photometry aimed at derivation of the main-sequence luminosity function for an external galaxy must therefore be able to cope with overlapping stellar images without significant loss of information content.

1. THE LUMINOSITY FUNCTION IN THE MAGELLANIC CLOUDS

For investigations of main-sequence luminosity functions outside the Galaxy, the Magellanic Clouds are attractive targets. They are close enough to allow photometry down to absolute visual magnitudes close to that of the

sun. They show to a very limited degree the effect of internal absorption. Moreover, the Magellanic Clouds are situated at galactic latitudes high enough for the influence of galactic foreground extinction to be small, as is the number of foreground stars in the field.

At the same time as the Magellanic Clouds are characterized by features favourable for observational approaches, they are also of considerable intrinsic interest for investigations of luminosity functions as well as colour-magnitude diagrams. Orbital calculations by Fujimoto and Sofue (1977) indicate that the LMC and the SMC have a common origin, different from that of our Galaxy. The Magellanic Clouds constitute examples of a type of galaxy otherwise observationally inaccessible. Further, they display large-scale star-formation structures and histories clearly different from that of the Galaxy. Whereas this has been demonstrated for the Large Magellanic Cloud (Westerlund, 1974; Ardeberg, 1976), it seems even more characterstic of the Small Magellanic Cloud (Azzopardi and Vigneau, 1977; Ardeberg and Maurice, 1979). An additional attractive feature is the fact that one can with reasonable certainty distinguish the different populations forming the overall systems (Westerlund, 1974).

In the present project we will compare the luminosity function for the Solar neighbourhood with those derived for different areas in the Magellanic Clouds. We aim to derive adequate data for a sample of fields ranging from the old halo populations of both galaxies to the young population forming the Wing of the Small Magellanic Cloud. Coordinates of the fields are listed in Table 1a and the electronographic exposures discussed in the present paper are in Table 1b. Additional observations are in course of being taken mainly with the ESO 3.6 m telescope.

Table 1a. Fields for luminosity function investigations

Name	R.A. (1950.0)	Dec. (1950.0)
SMC Halo	1^h00^m	-73°30'
SMC Wing	2 00	-74 30
LMC Halo	5 20	-71 00

Table 1b. The LMC Halo electronographic exposures

Colour	Exposure times in minutes
V	120, 15, 10, 5
B	120, 25

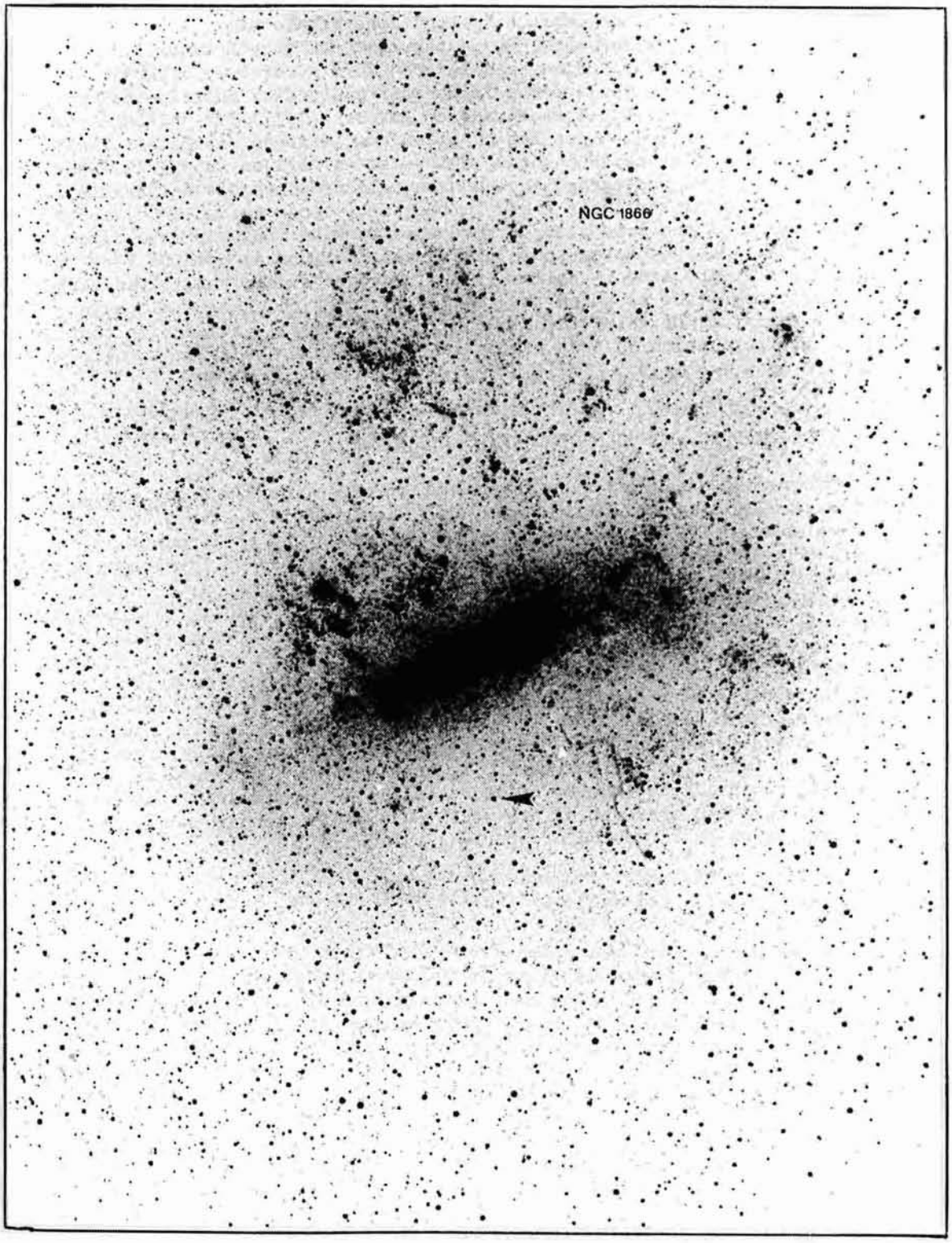

Figure 1. The Large Magellanic Cloud from a 15 min exposure with the 8-inch f/1 Schmidt at Mount Stromlo Observatory. Our sample field of the halo is marked with an arrow.

So far, most work on the luminosity functions of the Magellanic Clouds concern stars brighter than $M_V = -2$; in that interval the luminosity function of a nearby, external galaxy can be even more accurately determined than the one of our own galaxy. The faint star luminosity function has been studied by Brück (1978) for the SMC and by Butcher (1977) for the LMC. For the SMC Wing, Brück finds a population older than extreme population I but younger than the solar neighbourhood. This work as well as Butcher's study of the LMC halo uses photographic plates and electronographic calibrations. The study by Butcher samples a field in the halo, close to NGC 1866, about 4 degrees north of the bar, i.e. on the opposite side from our investigation (see Fig. 1). The photographic plates were calibrated down to $V = 22^m.5$ with electronography made by Walker (1974). Butcher's main result was that the absolute magnitude at which the luminosity function changes slope is about one magnitude brighter than in our galaxy, strongly suggesting that the LMC halo population in that region is younger than the galactic halo population by a factor 3.

2. ELECTRONOGRAPHIC VERSUS PHOTOGRAPHIC TECHNIQUE

For programmes concerned with determination of luminosity functions and colour-magnitude diagrams in the Magellanic Clouds it is feasible to cover star samples adequate for statistical purposes either by electronographic techniques or by photographic photometry. In spite of recent developments in photographic techniques we feel that there is little reason to choose that method if adequate electronographic equipment is at hand. The linearity of the latter method minimizes problems of calibration, normally quite cumbersome and error-prone for photographic photometry. Further, the dynamic range and the resolution are larger for the electronographic emulsion than for photographic plates normally used. For our programme, characterized by frequent image overlapping, the linearity is a feature of special value. The main intrinsic advantage of the photographic technique, its larger field, is of limited value for our purposes. The area that we do cover gives a statistically significant number of stars in the luminosity range of interest to us. Further, transfer of previously available standard-sequence data always implies an extra source of spurious influence.

3. OBSERVATIONS

All observations have been made with a Spectracon electronographic camera (McGee, 1976; Walker, 1976) attached to ESO telescopes. The test exposures were made with the 1 m telescope and the programme exposures described in this paper were obtained with the 1.5 m telescope. The field for which preliminary results are now presented is situated 1.2 degrees south of the bar of the LMC (see Fig. 1) and should sample the halo population of that galaxy. Using a distance modulus of $18^m.7$ (Crampton, 1978) this would be 1200 parsecs from the bar and 1900 parsecs from the centre of the cluster system (Lyngå and Westerlund, 1963). The useful field of the Spectracon camera is 8 x 27 mm^2 corresponding to 1.2 x 4 arc min^2 at the Cassegrain focus of the 1.5 m telescope, i.e. 19 x 64 $parsecs^2$ at the distance of the LMC. We have also obtained a number of exposures from the prime focus of the 3.6 m telescope. For them the useful field is 2.8 x 9.3 arc min^2.

We have consistently used the nuclear track emulsion Ilford L4 which compared to G5 has a very high signal to noise ratio if adequate measuring procedures are carried out. As developer we used D19.

To determine the sensitivity of the Spectracon we observed the sky at different angular distances from the moon. Simultaneously, B. Reipurth observed photoelectrically the same areas with the Danish 50 cm telescope on La Silla. The result was that one incoming photon per μm^2 of cathode gives a density of 0.011 units. The large-scale uniformity of the sensitivity over the field was good to within a few percent, a result that also emerged from flat field exposures. This all concerns ESO Spectracon No. 83, which was used for the observations now presented.

All the measurements have been made in the UBV system. We have chosen this in preference to more discriminating intermediate band systems for the following reasons:

- Luminosity functions and colour-magnitude diagrams which we want to compare with are usually based on the UBV system.
- It is of highest importance to reach very faint magnitudes.
- The equipment available at the beginning of the project was adapted for UBV electronography.

4. MEASUREMENTS

For the measurements of the electrographs we have used the Lund PDS machine (Elvius et al., 1978; Lindgren et al., 1979) and carried through a programme of detailed information retrieval using an effective slit size of 25 x 25 μm^2 and a pixel size of 15 x 15 μm^2 corresponding to 0.13 x 0.13 arc sec^2. These values can be decreased to 12 x 12 μm^2 and 8 x 8 μm^2 respectively for the 3.6 m exposures which have a considerably higher image resolution. Since we felt it desirable to use a speed not higher than 2 mm/s on the measuring machine, it took 3 hours to measure one exposure. The drift obtained is less than one hundredth of a density unit during the run of such a measurement.

5. TECHNIQUES FOR THE ANALYSIS OF STELLAR FIELDS

With the advent of fast, two-dimensional measuring machines there has recently been much interest in the analysis of stellar fields by automatic methods. Our own methods are to a large extent determined by our astronomical aims, by our observational material and by our limited image processing hardware. There are three major problems in the evaluation of the observations:

- Calibration of the photometry
- Analysis of crowded images
- Determination of accurate parameters for faint images

To transform our data to UBV quantities we need to measure some stars photoelectrically. The situation with a diaphragm of 15.5 arc sec diameter is that there will as an average be two stars brighter than V = 20.0 in the diaphragm if one works in any of the Magellanic Cloud halo fields. For an inaccuracy of less than $0^m.06$ it is a requirement that any extraneous star in the diaphragm be at least three magnitudes fainter than the star to be measured. Thus, to go as faint as $V = 20^m$ in such fields requires very meticulous planning, to go to $V = 23^m$ photoelectrically is not possible if

any sensible accuracy is desired. We conclude that it is necessary to use a linear, panoramic detector to preserve the photometric system from the brighter calibration stars to the fainter ones, which are of largest interest in the present project.

For our LMC field we have used four stars to calibrate the photometry. These stars were measured photoelectrically in the UBV system and the resulting magnitudes and colours are given in Table 2. The relation between the electronographic and the photoelectric V and B magnitudes was assumed to be a straight line with a slope of 45 degrees. No colour term could be determined due to the limited range in B-V of the calibration stars.

Table 2. Calibration stars used to determine the photometric zeropoint

RA (1950.0)	Dec (1950.0)	V	B-V	U-B
$5^h20^m.5$	$-71^\circ01'.9$	13.59	0.70	0.19
5 20.6	-71 02.2	14.83	0.63	0.05
5 20.6	-71 03.0	15.25	0.80	0.12
5 20.5	-71 03.5	15.21	0.57	-0.10

In order to study the luminosity functions for A and early F type stars in the Magellanic Clouds it is necessary to determine photometric quantities for 23rd magnitude stars. Exposures down to these brightnesses are characterized by a large amount of overlapping. It is thus essential for us to separate overlapped images and this requires a two-dimensional

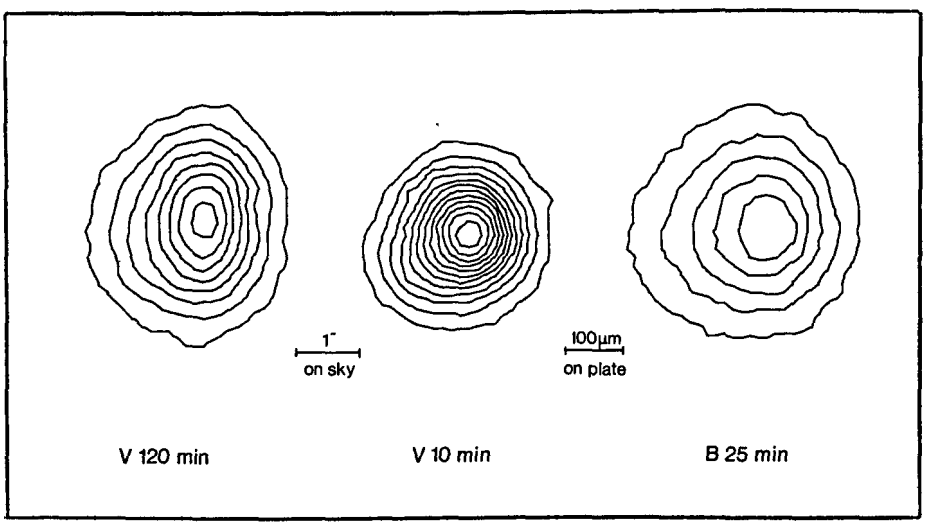

Figure 2a-c. Standard profiles for three different exposures.

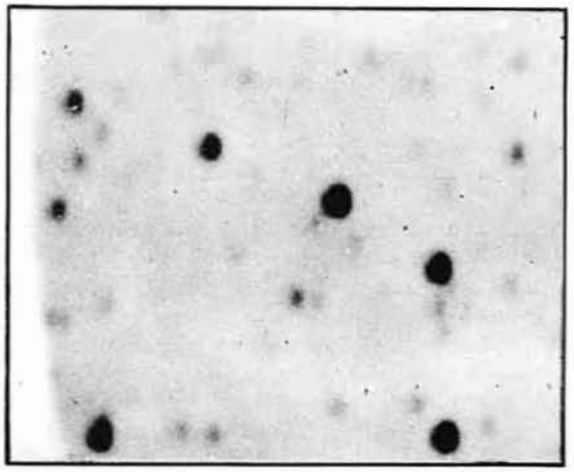

Figure 3a. A part of the LMC Halo field from a 120 min electrograph with the 1.5 m telescope. Images somewhat distorted by differential refraction.

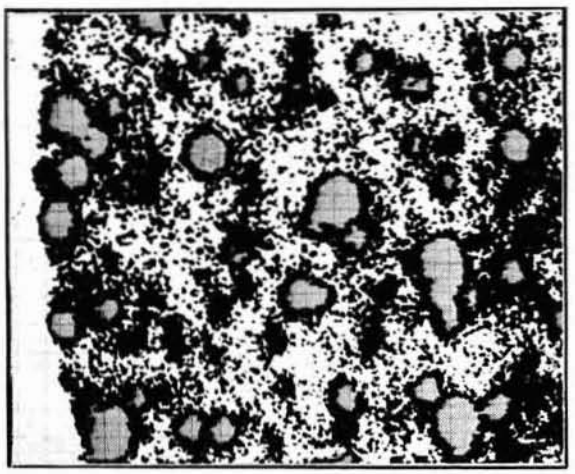

Figure 3b. Density levels near background densities. Such plots are used to study the background behaviour and image overlaps. Same field as in Fig. 3a.

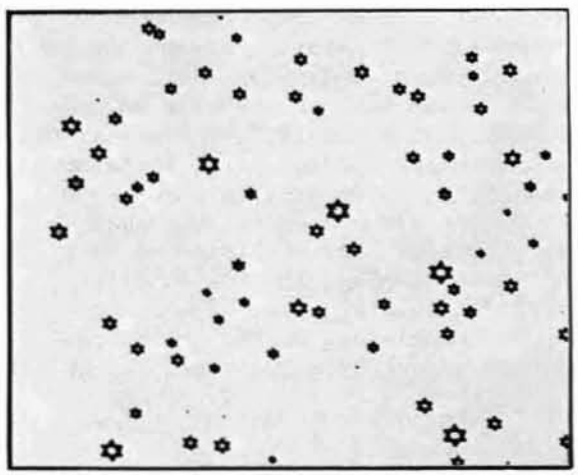

Figure 3c. Display of result of analysis. Sizes of symbols correspond to magnitudes of stars. Same field as in Fig. 3a.

profile for a stellar image. Particularly from 1.5 m exposures, the actual stellar image does not have a symmetric, two-dimensional Gaussian structure. We have tried to fit higher order moments, particularly skewness coefficients, but such profiles have turned out to be very sensitive to noise in the outer part of the image. In fact, the most unambiguous fits were achieved by the use of a numerical profile and we have for each plate determined a particular profile using at least four and sometimes up to twenty undisturbed images. Fig. 2a shows a display of such a profile. Figs. 2b and 2c show profiles from other plates demonstrating the different image structure caused by different observing conditions. The full half-intensity width is typically around 1 arc sec. In all calculations we have limited the data to measurements with $D < 3.0$ as the microphotometer shows non-linear effects for higher densities. This is usually not a severe limitation; only the very brightest stars in the field have such high densities and for undisturbed images it is a simple procedure to exclude the undesirable part of the image.

Using the numerical profile we may reduce the measurements of an undisturbed image to three parameters: two coordinates and one factor from which a magnitude can be derived. It would have been possible to calculate the magnitude by a simple integration. However, we have even for single images referred to the standard profiles to make the results compatible with those from disturbed images.

The greatest use of these profiles is when a complex of images is to be resolved. The problem is to find that sum of profiles which in a least square sense best fits the original data. This is done by varying the assumed coordinates of each contributing star and doing a least square solution for the multiplicative terms which describe the individual intensities. This method works well but is time-consuming when several stars overlap. The property of linearity is very important during this procedure. The initial assumptions about the number of stars in each complex and about their approximate coordinates are based on visual examination of the electrograph and the corresponding plot of low density levels. (Fig. 3a and Fig. 3b, respectively).

Finally, the problem of accuracy of faint measurements is largely a problem of studying the background carefully. The dark current of the Spectracon tube used is very low. The laboratory tests showed a dark current effect of less than 0.08 d.u. per hour for the tube used in the ESO 1.5 m run. However, since the fields are crowded it is very important to study the sky background in some detail. The sky background has been evaluated by first correcting for the linear term of the background variation over the field. The difference in background density between two edges of the field is usually a few hundredths of a density unit. Comparisons between different exposures make it likely that this should be ascribed to dark current variations rather than to sensitivity variations. In addition to the linear interpolation we have selected local background areas to be used in the vicinity of each star. These areas are 165 x 165 μm^2 on the exposures, i.e. 2.2 arc sec^2 on the sky. In order to select background areas and to inspect the structure of star complexes we have made plots of all measurements. Fig. 3b thus displays the low density levels of the section of an electrograph shown in Fig. 3a. Fig. 3c shows which stars have been found to make up the complexes. During the inspection of background areas it was found that adjacency effects are negligible.

6. ACCURACY ACHIEVED

Fig. 4 shows the imprecision (= internal standard error) as determined from intercomparisons between the different exposures. This graph was derived with the abscissa calibrated in image intensity for the shorter of

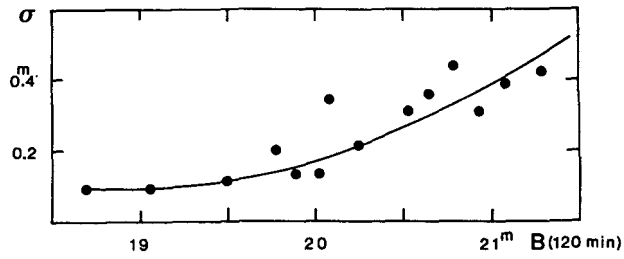

Figure 4. Standard error as a function of magnitude for one of the exposures.

two compared exposures. However, for each specified exposure the abscissa can be expressed in magnitudes; as an example Fig. 4 shows the relation applied to the 120 min B exposure.

7. RESULTS

a. The colour-magnitude diagram

Although these first measurements mainly were aimed at the study of techniques, some astronomical results are already available. Fig. 5 shows the colour-magnitude diagram for the LMC halo field. The accuracy as well as the completeness will fail for faint stars. The dashed lines correspond to standard errors in B-V. The zero-age main sequence is the one given by Johnson (1963) and the fit is made assuming a distance modulus of $18\overset{m}{.}7$ (Crampton, 1978) and a foreground extinction of $0\overset{m}{.}22$ (Brunet, 1975) in V. This diagram is entirely different from the one obtained by Butcher (1977) in the LMC halo region near NGC 1866. We find an unexpectedly large number of red stars, particularly among the brightest stars, for which the errors are small - of the order of $0\overset{m}{.}1$ or smaller. Another surprising feature, which will need confirming from the deeper 3.6 m exposures concerns the stars with B-V between 1.3 and 2.0. While there are some 20 of these stars between $M_V = -1$ and $M_V = -3$ and a great number fainter than $M_V = 0$, there is a dearth of such red stars between $M_V = -1$ and $M_V = 0$. We note that the spread in B-V is much larger than the amount of interstellar colour excess in the LMC ($< 0\overset{m}{.}2$ according to Brunet, 1975).

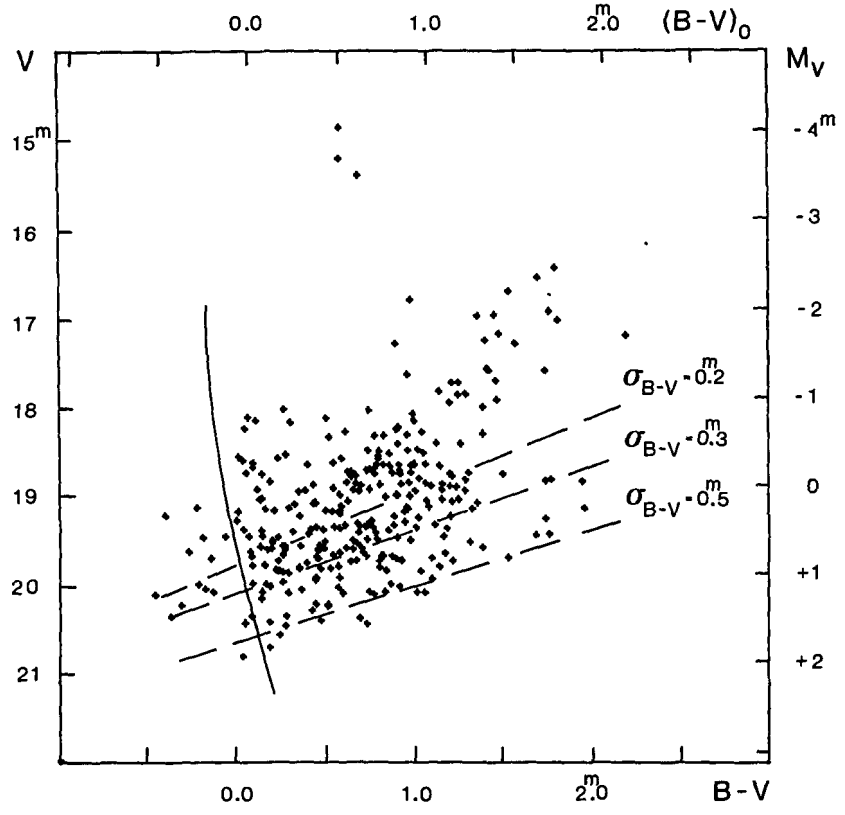

Figure 5. Colour-magnitude diagram for the LMC Halo field. Observed data use left and lower scales; ZAMS uses right and upper scales.

b. The luminosity function

The luminosity function in V comes out as a marginal distribution from the colour-magnitude diagram and it is seen from Fig. 5 that the limit for completeness is about $M_V = +1$ from the present data. Comparing with the results by Butcher, we find about 5 times as many stars per square parsec of the LMC. This excess mainly consists of a high number of stars away from the main sequence (Butcher studies only the main sequence luminosity function). It is partly caused by a larger path length through the LMC halo for our field.

One of the aims of this study is to reach the knee of the luminosity function near $M_V = +4$. For this purpose the present material is not sufficient but it should be well within the reach of our exposures from the ESO 3.6 m telescope.

ACKNOWLEDGEMENTS

The plate material was obtained at the European Southern Observatory. The measurements and evaluation were made with the ASTOL measuring system, which has been funded by the K. & A. Wallenberg Foundation and by the Swedish Natural Sciences Research Council.

REFERENCES

Ardeberg, A. 1976: In Stars and Galaxies from Observational Points of View, ed. E.K. Kharadze. Proc. 3rd European Astron. Meeting, p. 193
Ardeberg, A., Maurice, E. 1979: Astron.Astrophys. 77, 277
Azzopardi, M., Vigneau, J. 1977: Astron.Astrophys. 56, 151
Brück, M.T. 1978: Astron.Astrophys. 68, 181
Brunet, J.P. 1975: Astron.Astrophys. 43, 345
Butcher, H. 1977: Astrophys.J. 216, 372
Crampton, D. 1978: In IAU Symposium No. 80, p. 259
Elvius, T., Lindgren, H., Lyngå, G., Wihlborg, N. 1978: Reports from the Observatory of Lund No. 14
Fujimoto, M., Sofue, Y. 1977: Astron.Astrophys. 61, 199
Johnson, H.L. 1963: In Basic Astronomical Data (ed. K. Aa. Strand) p. 204
Lindgren, H., Lyngå, G., Linde, P., Hagerbo, H.O. 1979: Proc. International Workshop on Image Processing in Astronomy, Trieste, in press
Lyngå, G., Westerlund, B.E. 1963: Monthly Notices Royal Astron. Soc. 127, 31
McCuskey, S.W, 1966: In Vistas in Astronomy (ed. A. Beer) 7, 141
McGee, J.D. 1976: In IAU Colloquium No. 40, p. 4-1
Walker, M.F. 1974: Monthly Notices Royal Astron. Soc. 169, 199
Walker, M.F. 1976: In IAU Colloquium No. 40, p. 37-1
Westerlund, B.E. 1974: In Galaxies and Relativistic Astrophysics, eds. B. Barbanis and J.D. Hadjidemetriou. Proc. 1st European Astron. Meeting, Vol. 3, 39

A VIDEO FACILITY TO DETECT EARTH APPROACHING ASTEROIDS (Late abstract)

by
J. Degewij, J. Frecker, T. Gehrels, and E. Shoemaker

The use of state of the art Vidicon/CID type detectors, behind an average size telescope and in conjunction with a computer, makes it possible to detect an Earth approaching object within minutes after the image pair is obtained.
Such a short discovery time allows the detection of asteroids with diameters on the order of 10 - 100 meters. Because of their fast motion these objects are often lost with photographic detection techniques, where the discovery is usually made on the afternoon after the observing night.

THE GRONINGEN IMAGE PROCESSING SYSTEM

G.Seth Shostak and Ronald J. Allen
Kapteyn Astronomical Institute
Postbus 800
9700 AV GRONINGEN, The Netherlands

INTRODUCTION

The Groningen Image Processing System "GIPSY" is an interactive picture display and processing system designed to handle large sets of radio maps obtained with the Westerbork Synthesis Telescope. In particular, this system is being developed to efficiently reduce multichannel maps produced by the new digital line backend. A typical twelve-hour observation will produce 32 or 64 maps, sequential in velocity, having array sizes of 256- or 512-square. The observation may be thought of as producing a "data cube" (axes α, δ and v) of 10^{6-7} pixels. An ideal processing system enables the astronomer to efficiently search this cube for signal, and to extract relevant source parameters. An interactive system is preferable in that real-time decisions may be made regarding the next step in the processing. Further, such a system allows rapid confirmation that the reduction is proceeding as intended.

The Groningen Image Processing system is being developed primarily in response to the needs of radio astronomers. However, it is obvious that a wide range of astronomical data can be handled with GIPSY including data obtained with optical telescopes, provided they are supplied in compatible input format.

HARDWARE DESCRIPTION

The hardware consists of a Model 70E image computer and display unit manufactured by International Imaging Systems, connected to a PDP 11/70 host computer. The latter is fitted with standard peripherals, including a tape drive, RP05 disk packs and a Gould plotter. Data are first read from magnetic tape onto an astronomer's private disk pack, where they are available for rapid access. Communication between the user and the system is done with a keyboard and video display unit, and a trackball-cursor/function key input box. Pictorial output is displayed on a standard studio colour television monitor. An Information Processing Systems video disk is attached to the colour monitor, permitting the recording of up to one hundred colour frames (512 x 512). Recorded images can then be played back at virtually anny rate up to standard video (25 frames/sec) and in any order. The ability to make a "film loop" of the data has proven to be quite useful in recognizing faint features which are correlated from map to map (e.g., features extended in velocity and faint continuum sources).

A blsck-and-white video camera and associated digitizing electronics are available, and these are frequently used to superimpose optical photographs on the radio maps.

The image computer itself contains five random access refresh memories, each capable of storing a 512^2 map, 8 bits deep. These memories feed their data into a high-speed pipeline processing system for operating on images at video rates.

A series of look-up tables, initially loaded from the host computer, allow modification of the data stream into and out of the memories for operations such as contrast enhancement and colouring. Hardware zoom and panning permit examining a subsection of any map in detail. A histogram generator is available for analysing the output data stream within an arbitrarily-shaped region of interest.

The processing chain described above is given additional capability by means of a feedback loop, including a 16-bit arithmetic logic unit (ALU). This feature makes possible iterative processing of entire maps within the image terminal at video rates. The nature of this processing may be altered within the region of interest.

In summary, GIPSY comprises a sophisticated, high-resolution colour display

and cinematographic recording system, attached to a modern computer. Additionally the i) five refresh memories and the ii) feedback loop allow it to perform data analysis on multiple-byte precision images (e.g. 16 bits) without the necessity of frequently transferring maps into and out of the host computer. For some operations this results in a considerable improvement in processing speed.

AVAILABLE SOFTWARE

Approximately fifty user-oriented programs are presently available, and new tasks are being added to the system at a rate of several per week. This figure does not include a similarly large body of support programs and subroutines designed to provide standardized input, read disk files, enhance images, etc. The latter are largely provided by a small professional programming staff or were purchased with the image terminal. The intention is to allow astronomers to write their own programs without requiring them to be conversant with the details of file structures, look-up table initializations, etc. These are handled by the support routines. Experience has borne out the obvious supposition that users know best which programs and which options are necessary in a data reduction system. By buffering astronomers from the more esoteric details of programming, the support software has allowed relatively novice users to quickly write useful program tasks.

When operating GIPSY, all programs are run under a master control program, which initiates the relevant processing tasks and keeps a log of all operations. The master control program allows several tasks to run concurrently, and additionally provides many user-friendly options such as storage of repeated input parameters, looping through a series of tasks, and passing parameters between tasks.

GIPSY user software can be sorted roughly into three main categories. While not exhaustive, the following listing gives some idea of the types of programs available:

1. DISPLAY PROGRAMS: These include the standard image display options such as viewing a series of maps, contrast enhancement, zooming, pseudocolouring, histogramming, roaming through a mosaic of all image memories, scrolling, cursor positioning, producing graphics and character annotation, and digitizing television images. The bulk of these programs rely on simple calls to support subroutines provided with the image terminal.

2. PROCESSING PROGRAMS: These are number-crunching tasks generally done in the host computer by reading or writing maps line by line from disk. They include adding/subtracting maps, finding the minima and maxima in maps, determining noise statistics, smoothing, integration, beam corrections, and contours, ruled surface, and grey scale plots. The display programs are interfaced with these tasks so that users may define areas, positions, etc. by using a trackball-controlled cursor on a map image. The speed of these programs is generally limited by disk access times; as an example, the addition of two 512^2 maps requires $\sim$ 30 seconds.

3. ANALYSIS PROGRAMS: These comprise the most specific and frequently the most complicated of user tasks. They include source finding and subtraction, convolution and deconvolution (the so-called CLEAN procedure), profile analysis and fourier transformation.

These programs, in particular, can make use of the two extraordinary GIPSY hardware features: the five refresh memories and the feedback loop. As examples, we mention here two specific tasks: CLEAN and a profile-parameter program, WINDOW.

CLEAN is an iterative numerical procedure for modifying the instrumental response in a map. The first step is to decompose the "dirty" map into a set of delta functions which, when convolved with the "dirty" response and added to the residual map, yield the original map. The second step is to do a reconstitution by convolving the set of delta functions with a "clean" response (e.g. free of grating responses and sidelobes) and adding them into the residual map to produce

a final "clean" map. It is a good example of a processing job in which the image and the instrument response function can be read into the image computer memories once, and thereafter iteratively processed entirely within that machine. In order to use the feedback facility, and to have a "scratchpad" work area, 8-bit image memories are ganged together in pairs, and the map and antenna pattern are stored in 16-bit integer format. Since the operations occur at video rates the procedure is significantly faster than if carried out within the PDP 11/70 host computer operating from disk-based data. For instance the decomposition step on a 512^2 map can be carried out in the image computer at the rate of one component about every two seconds. For a map of similar area, the same procedure in the PDP 11/70 requires an order of magnitude more time. A further advantage of processing within the image terminal is that the user can observe his map during the processing, and can make immediate judgement as to when the task may be stopped.

WINDOW is a program designed to determine line profile parameters, such as velocity, area and width, as a function of sky coordinates. It proceeds by generating a set of position-velocity maps (line intensity as a function of right ascension and radial velocity), and the astronomer visually determines where in such a map the signal is located. This region is outlined by the user using the trackball, and the signal "window" so defined is used to restrict the region within which the line parameters are computed. Crudely speaking, this is a scheme for dynamically matching a data acceptance fitter to the signal. It both improves signal-to-noise and minimizes biases caused by the finite number of velocity channels.

Displaying position-velocity plots is no problem, but processing is complicated by the arrangement of data in map sets. The production of a single spectrum at a single point, for example, might require 64 disk reads, or about three seconds. Obtaining data for 512 points, an entire image line, would likewise take 64 reads, but this amount of data cannot be stored in the core of the host computer.

The solution is to use four image memories to store the 32-bit real data. A fifth memory is used to display an 8-bit scaled version of the image.

Maps are read in horizontally, one line per channel map, and the data are read out vertically to produce spectra. Processing a whole line of spectra (equivalent to a slit spectrum in optical work) takes less than ten seconds.

RADIO DATA TECHNIQUES APPLIED TO PDS DATA

R. Wielebinski
Max-Planck-Institut für Radioastronomie, Auf dem Hügel 69, D-5300 Bonn 1

Mapping of an area of the sky with a single dish radio telescope is analogous to the scanning of an optical plate on a PDS machine. In radio astronomy the telescope executes a raster on the sky, recording the intensity data as a string of numbers arranged in subscans. The subscans are executed at regular intervals chosen so that no information about the true sky distribution is lost. From information theory a minimum of 2 points per beamwidth is required, but in practice, with a Gaussian beam shape, at least 2.6 points should be recorded for best results. From the subscans after correct filtering (to account for the beam shape) an array of numbers is derived which represents the true sky intensity distribution. The same procedure is followed in scanning an optical plate where beamwidth is analogous to slit-size. The end-product of scanning, the array, requires the same manipulations as the radio map, before a final two-dimensional picture is made, which gives information about the astronomical objects seen in the field.

Over many years a programming library designated NOD2 has been developed (Haslam, 1974, 1976; Haslam et al., 1979) to allow many manipulations of arrays. In addition, based on the NOD2 data format, numerous standard reduction and display techniques have been developed (Neidhöfer et al., 1978; Reich et al., 1978) for Calcomp and Versatec plotters. The NOD2 library is a collection of interdependent subroutines, which can be divided into a number of basic categories. Initially, the data must be arranged into a NOD2 format which gives the necessary information about the relevant data associated parameters such as date, time, position, type of observation in a header section, followed by the data set as a filled array. Book-keeping routines deal with labelling, checking and creation of new documents, including interfacing with document formats from other software

systems. Floating format input/output subroutines have been developed to remove some of the tedious restrictions of the Fortran column conventions. Mathematical routines allow interpolation, baseline fitting, etc., with special emphasis on two-dimensional processes. Document processing routines allow scaling, smoothing, retabulation of maps on new grids including a general spherical rotation allowing transfer of data between the various coordinate systems used in the observations. Finally, display routines make it possible to inspect the arrays in various ways (shadow plots, line density prints, contour plots, grey-scale plots, etc.). The NOD2 library is able to deal with polarisation data and has been used to produce coloured images. The programmes are operating in the Cyber 172 computer of the MPIfR, both in batch mode and interactively with Tektronix display terminals. The NOD2 system has been implemented on smaller computers like Modcomp 4, VAX and PDP 11/35.

A PDS photometer has been installed at the University of Bonn Astronomical Institutes (H.J. Becker, 1979). It has a PDP8 computer and a 7-track magnetic tape drive as accessories. The scans can be written in the NOD2 format and can thus be directly handled by all the NOD2 library routines. An example of the application of the NOD2 routines is shown in Figure 1, a scan of the Palomar Sky Survey print of M51 and its companion. An alternative method of presentation is in the isocontour form shown in Figure 3. Numerous similar scans either from POSS prints and more recently from ESO plates have been made.

An astronomical problem which requires both radio and optical "maps" is in the study of clusters of galaxies. Diffuse radio emission in the form of a halo is found in Coma (Jaffe et al., 1976). Diffuse radio emission resembling more a superposition of head-tail radio sources is found in some other clusters, e.g. A2256 (Bridle et al., 1979) or A754 (Haslam et al., 1979). It is of interest to note that all these clusters also have diffuse X-ray emission present. Plates of A754 were taken at ESO Schmidt telescope (Figure 2). The scanning was done in the PDS machine and the result in the form of a grey-scale/contour plot is shown in

Fig. 1: An image of M51/NGC 5195 from a Palomar Sky Survey print scanned on a PDS machine

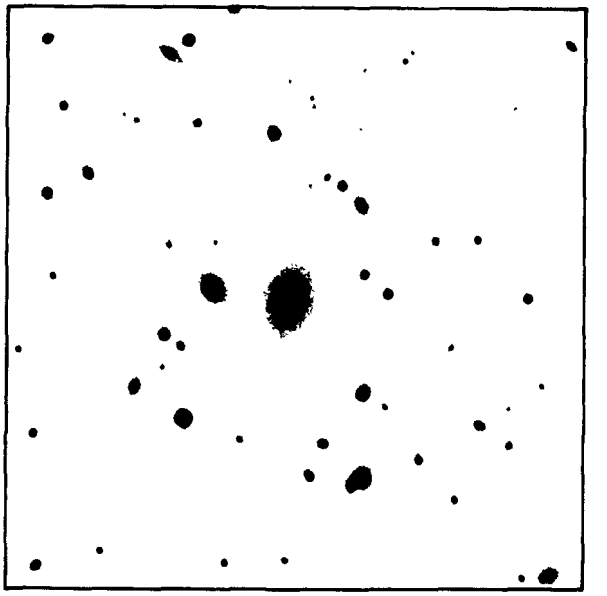

Fig. 2: A part of the cluster A754 showing the dominant cD galaxy. ESO Schmidt plate

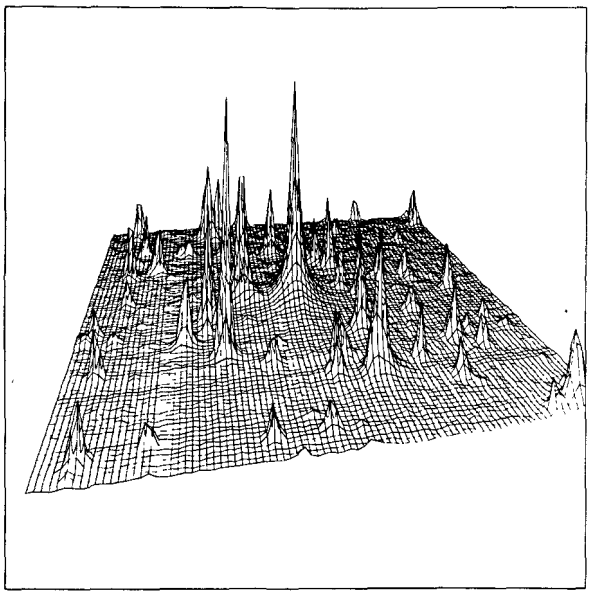

Fig. 3: An isocontour plot of A754

Figure 4. An area around the dominant cD galaxy in A754 is shown, obviously with a very large halo surrounding it. This halo is only marginally evident in the copy of the sky plate in Figure 2. Using one of the standard NOD2 routines the

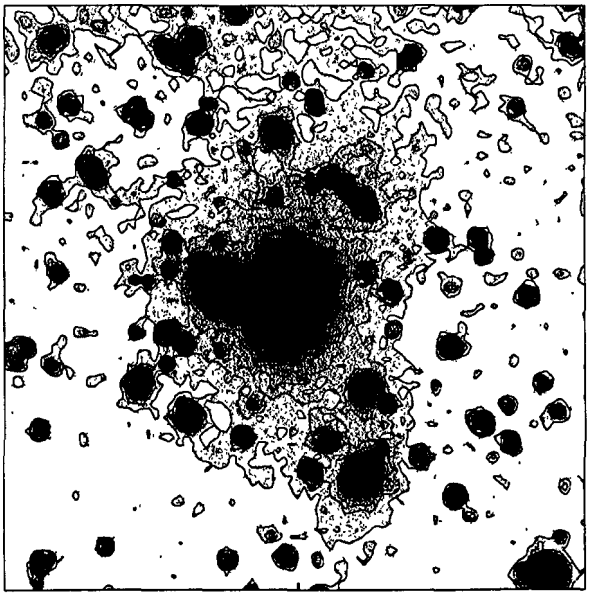

Fig. 4: A grey-scale/contour plot of A754

point sources in the scanned array were subtracted. This result is shown in Figure 5. This routine worked well except at the edges and for some of the strongest and weakest sources. The large halo around the cD galaxy is seen even more clearly.

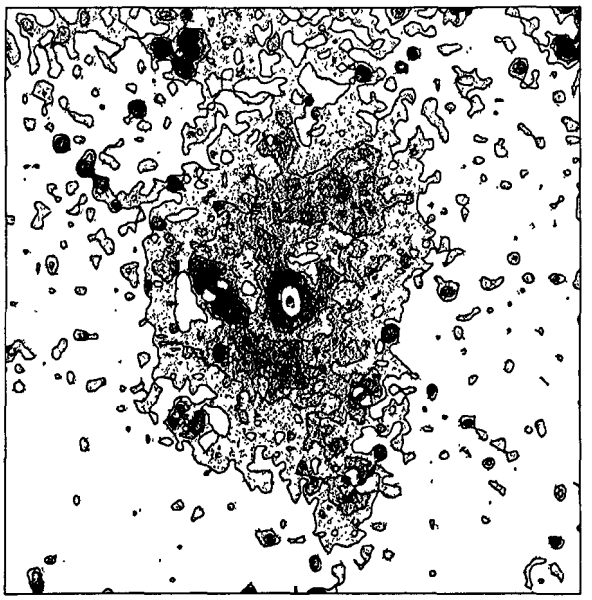

Fig. 5: A plot of A754 after source subtraction

The NOD2 procedures appear to be applicable to image processing of optical plates. The future development requires the use of array processors to speed up the two-dimensional array manipulation. Standardisation of software and data formats between workers in all fields of astronomy seems essential in the long run.

The ESO Schmidt plate of A754 was taken by Dr. H.E. Schuster. The PDS scans were made by Dr. W. Reich and Herr H.J. Becker of the Astronomical Institutes of Bonn University.

References

Becker, H.J.: 1979, Diplomarbeit, Bonn University

Bridle, A.H., Fomalont, E.B., Miley, G.K. and Valentijn, E.A.: 1979, Astron. Astrophys., in press

Haslam, C.G.T.: 1974, Astron. Astrophys. Suppl. 15, 333

Haslam, C.G.T.: 1976, Technischer Bericht No. 34, MPIfR Bonn

Haslam, C.G.T., Emerson, D.T. and Salter, C.J.: 1979, Technischer Bericht MPIfR Bonn (in preparation)

Jaffe, W.J., Perola, G.C. and Valentijn, E.A.: 1976, Astron. Astrophys. 49, 179

Neidhöfer, J., Wilson, W. and Haslam, C.G.T.: 1978, Kleinheubacher Berichte 21, 215

Reich, W., Kalberla, P. and Reif, K.: 1978, Kleinheubacher Berichte 21, 221

SECTION IV

Surface Photometry of Extended Objects — Recent Results and Future Projects

SURFACE PHOTOMETRY OF EXTENDED OBJECTS

Philippe Crane
European Southern Observatory

Abstract

This paper reviews the types of astrophysical problems which involve surface photometry. Strongest emphasis is put on observations in the optical wavelength region. Some of the more important technical problems of surface photometry are discussed as well as some of the relations between theory and observations especially for observations of galaxies.

I. Introduction

Surface photometry of extended objects covers many areas of astrophysical research and encompasses some of the most interesting and complex objects of our Universe. The advances in this branch of research have been rapid in the past few years and this can be traced to a few key developments. Much of the data available is already in digital format such as radio maps or could be put in digital format with scanning microdensitometers (see papers by Melnick and Swaans in this volume). Coupled with this was the arrival of a new range of computers capable of handling large volumes of data in a fast and affordable manner. These two major developments have opened the paths to answer a set of questions which were unapproachable ten years ago.

This paper will concentrate primarily on research in the optical region. However, it is important to realize that similar data are available from other regions of the spectrum. Table I summarizes and compares some relevant data on the current capabilities in the various wavelength ranges. The entries in this table are meant only to provide a general comparison and are not in any sense to be considered as rigid limitations. For example optical spatial resolution is limited by atmospheric

seeing whereas the radio resolution typically available is limited by array baselines. On the other hand VLBI radio observations do provide higher spatial resolutions, and Space Telescope will do the same for the optical range. It is also worth noting that developments in infra-red detectors are proceeding rapidly and one can anticipate that infra-red data similar to that presently available in the other wavelength ranges will be commonplace within a decade or so.

Table I : Comparison of Surface Photometry at Different Wavelengths

Wavelength Range	Spatial Resolution	Spectral Resolution	Polarization
Radio	1^{π}	1000	Yes
Infra-red	to be developed		
Optical	1^{π}	100	Yes
X-ray	1^{π}	10	Not Yet

Radio astronomers are some of the most prolific producers of surface photometry data results. It is interesting to compare the radio and optical data to see if there are any fundamental differences. Of course, the major advantage that radio astronomers have had is their data was already in a digital format and they were forced to use computer reduction techniques from the very beginning. The instrument profile of radio images is well known and, hence, questions of resolution and so forth were not a problem. Also perhaps of greater importance the radio sky does not produce the same kind of background as is seen in the optical. As discussed below the removal of sky background is a major job for the optical astronomer. There is one other point whose origin seems difficult to pin down precisely and this is that optical data seem not to be as amenable to generalized reduction procedures as radio data. This means that optical image processing requires more

astronomer intervention. Considering the above it is not surprising that radio astronomers have produced more surface photometry than optical astronomers. It is also clear that optical astronomers should take advantage of the advances already made in radio. (reduction techniques see also paper of R. Wielebinski).

The range of astronomical objects which are studied with the techniques of surface photometry covers very nearly the entire zoo of objects in the sky. Table II presents a summary. The second column of this table gives the names of individuals who have papers elsewhere in this volume dealing with the associated topics.

Table II : Summary of Astronomical Objects Studied by Surface Photometry

Topic		Names of authors with papers in this volume
Solar System Objects		
Planets		Degewij
Comets		
Planetary Nebulae and HII Regions		Feitzinger Wamsteker
Supernova Remnants		---
Star Clusters + Globular Clusters		Lindgren, Albrecht
Galaxies	Spirals	Grosbøl, van der Kruit Davoust, Worswick
	Ellipticals	Kormendy, Nieto, Valentijn, Frandsen
Clusters of Galaxies, including		
	Intergalactic gas	Schnur, Vignato
	X-rays	Travese

Figure 1 shows a montage of different exposures of the Crab nebula (see Davidson, Crane, and Chincarini, 1974). This picture illustrates a few specific applications of surface photometry and is typical of the kind of data and data processing which will proliferate in the next several years. The blue-shifted and red-shifted Hβ exposure tell the direction of motion of the filamets. Comparison between OIII and

Hβ line strengths at various positions gives an indication of relative excitation. Observations with adequate spatial resolution could give information on the relative positions of neutral and ionized species within the filaments. The range of information available in these kinds of data is enormous and the community is now beginning to learn how to take advantage of these data.

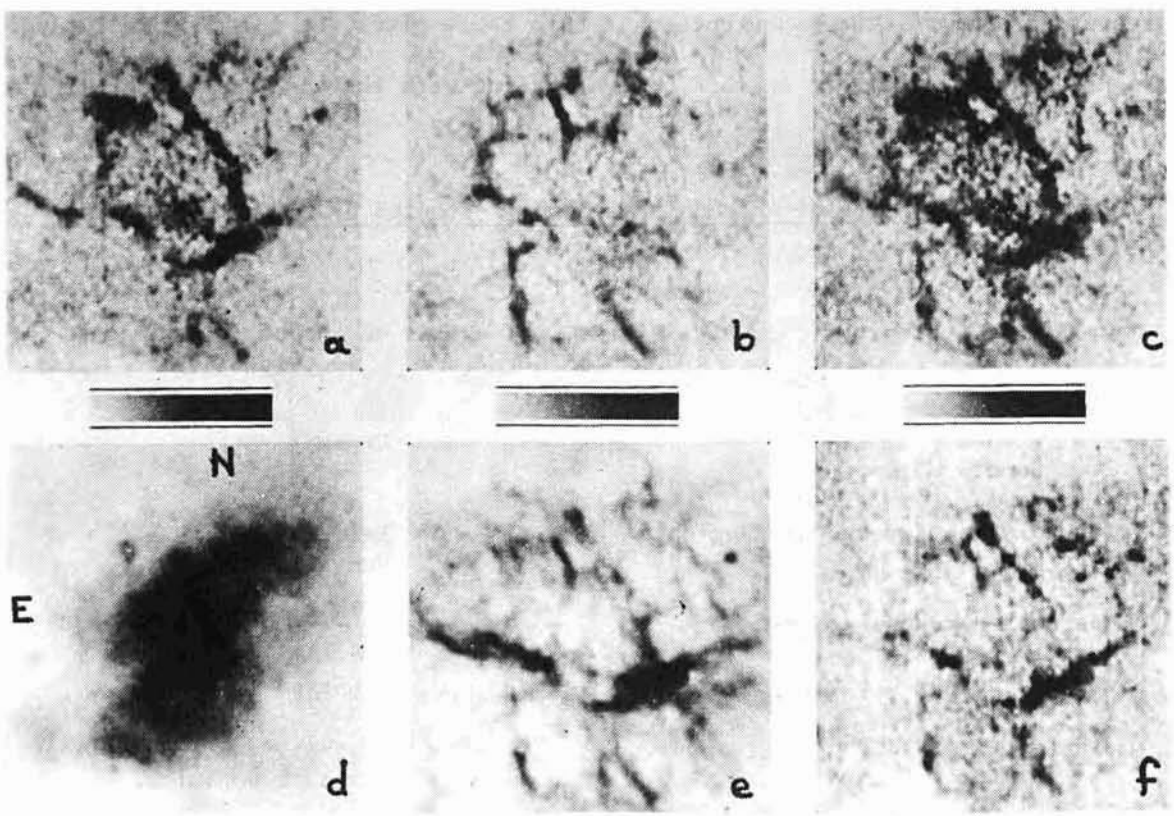

Figure 1 : Exposure of the Crab Nebula through different interference filters
a) Hβ blueward b) Hβ redward c) Hβ total (sum of a + b)
d) continuum at ∿ 5300 Å e) [OIII] λ4959 + λ5007
f) [OI] λ6300 + λ6363
The continuum and bright stars have been removed

II. Systematic Considerations in Optical Surface Photometry

Some of the major problems in doing surface photometry arise from the way in which the data are handled and not necessarily from the data themselves. This section discusses some of the major pitfalls that are encountered in practically all data sets. First, there is a discussion on sky subtraction techniques or background removal. Then some problems associated with lack of knowledge of the true image profile are presented, and finally, a short discussion is given of some of the problems that arise because the quantities derived from the data are not defined in a uniform way from one worker to the next.

In order to do surface photometry at a level which is a few percent of the sky background or less, it must be possible to measure the sky background itself to at least the desired precision of a few percent. Normally it is necessary to make the assumption that the real sky, S, is independent of position, $S \neq S(\alpha,\delta)$. This is generally not a radical assumption. The problem arises because the instruments that one uses generally have variations from place to place. This can be due to a variety of sources: vignetting of the optical path, variations in sensitivity, non-linearities in the instrument and time variation in the sky itself are major sources.

There are many techniques which have been used to attempt to measure the sky-background and to remove instrument induced effects.

The best way to treat instrument induced effect is, of course, to have a stable, reproducible instrument whose properties are well documented. This is decidedly not the case for photographic plates which is the detector that has been used most often for surface photometry. Electronic readout detectors such as ST Vidicons and Changed Coupled Devices offer the possibility to have a reproducible detector. The major drawback of these devices is their small format relative to the usual targets for surface photometry. This makes it difficult to measure the sky background.

Faced with incomplete knowledge of the detector, it has been necessary to

develop models of the instrument and sky background. The simplest technique has been to use the data around the periphery of the area of interest to construct smooth surfaces using polynomial functions (see Jones et al. 1967 for a well known algorithm). Using polynomials always runs the risk of introducing some non-physical effect and so the lower the order of the polynomial the better. Indeed it may be that polynomials of order greater than one may already be too great.

There are several other techniques for solving this problem. Among these are: solutions of the two dimensional Laplace equation ($\nabla^2 G = 0$), maximum entropy techniques; and spline fitting. The Laplace equation method looks attractive because it has some physical basis. Thus, given the value of G and its derivative on the boundary, the solution can be rigorously constructed over the entire area. This assumes, of course, that the instrument response function is smoothly varying. Nevertheless, there do exist some possible problems with this technique if, for example, the construction attempted to include a dipole source. Some subsidiary constraints on the boundary conditions would have to be introduced to avoid such problems.

Measuring the sky background and any small instrumental effects is crucial for working at very low surface brightness. Errors in the sky level will change the shape of the radial profile of a galaxy whereas errors in the slope of the sky will introduce changes in the ellipticity of the outer isophotes. An interesting discussion of some of the points is given by Carter (1978).

Problems of surface photometry associated with instrument resolution and knowledge of the point spread function have been discussed recently by Schweitzer (1979) in connection with the determination of core radii of elliptical galaxies. This paper points out that even when the derived core radii are apparently larger than the seeing resolution, nevertheless the effects due to seeing must be carefully analyzed before it is sure that the final result is not seeing dependent. A more technical discussion of certain aspects of extracting information from images is dealt with elsewhere in the volume (see the paper of Bijaoui).

The definition of the quantities measured in surface photometry appears to be continuing problem (see comment by King and Tinsley + Larson, 1977, pp 292). Metric magnitudes would seem to be a well defined quantity - the light contained within a diameter of fixed linear size at the source. However, a value for the Hubble constant and a cosmological model must be specified before the fixed linear size can be calculated at the source. For distant sources, a seeing correction should be applied since a larger fraction of light will spill out of the metric radius at larger distances (Hoffmann and Crane, 1976). Isophotal magnitudes face similar but different problems. K-corrections, galactic absorbtion, and seeing corrections must be applied before the isophotal level can itself be determined. Although these are all rather straightforward procedures they do not seem to have been applied with any uniformity by different workers. One active area of research is the study of various components of galaxies such as the bulge, the disk, the lens, the bar, and so forth. It would seem of critical importance in this work that a uniform working definition in mathematical terms be applied by various workers before any definitive conclusion are drawn by comparing their results.

III. Relation between observation and theory

There can be no doubt that the worst thing to happen to an observer after spending many hours of hard work on a project is to get technically correct results, that do not really matter. Surface photometry is already a difficult enough endeavor that it is important to set out to answer the appropriate questions from the beginning. Indeed, to arrive at the end of a major program with results that almost certainly contain important information is begging the question.

The problems of determining the radial profile of elliptical galaxies is an excellent illustration of the problems faced by both theoreticians and observers. A recent article (de Vaucouleurs and Cappacioli, 1979) mentions five radial profile laws which have all been used to describe ellipticals. Table III lists these laws.

All of these formulae except the King Law are purely empirical with no relation to any theoretical basis. The King Law, at least, has some basis in dynamics of many body systems. Nevertheless, most observers prefer the de Vaucouleur Law perhaps due to peer pressure, or perhaps because it has some convenient analytical properties. It would be extremely nice for observers to know what kind of data are needed to decide once and for all what the profiles of elliptical galaxies really look like. This may be too much to ask for since we do not yet have a deep understanding of the dynamics of ellipticals, but we need to start. We now have the observational tools.

Table III : Laws for the Radial Profiles of Elliptical Galaxies

Hubble Law	(1)	$I/I_o = (r + a)^{-2}$
Baum Law	(2)	$I/I_o = (2r\ (r + a))^{-1}$
Oemler Law	(3)	$I/I_o = (r + a)^{-2} \exp - (r/b)^2$
de Vaucouleurs Law	(4)	$I/I_o = \text{dex}\left[-3.33\ \left[(r/a)^{\frac{1}{4}} - 1\right]\right]$
King Law	(5)	$I/I_o = (1 + (r/r_c)^2)^{-\frac{1}{2}} - (1 + (r/r_t)^2)^{-\frac{1}{2}}$

Notes :

I_o is the central surface brightness

a,b are distance scaling parameters

r_c is the King core radius

r_t is the tidal radius

References:

(1) Hubble, E.P., 1930, Ap.J. 71,231

(2) Baum, W.A. 1955, P.A.S.P. 67,328

(3) Oemler, A. 1976, Ap.J. 209,693.

(4) de Vaucouleurs, G. 1948, Ann.Ap. 11,247

(5) King, I.R., 1962, A.J. 67,471

Along the same lines as the above discussion, observers are now in the position to answer a wider variety of questions than a few years ago. It should no longer be necessary to "assume" that the isophotes of elliptical galaxies are concentric ellipses with the same orientation. We should know definitively if they are ellipses, concentric, and with the same orientation. We should also know what these results imply. These are not easy questions but are well within reach observationally, and presumably within the reach of theoreticians.

There is an accumulating body of evidence suggesting that the disks of spiral galaxies are exponential with a fixed central surface brightness close to $(SB)_V$ = 21.S mag/(arcsec)^2. Freeman (1970) was the first to point out the apparent constancy of the central surface brightness. Subsequently Kormendy and Schweitzer have confirmed this, but there are still some lingering doubts. This result could have potentially far reaching implications if it were universally true. Nevertheless this is yet another example of observers leading the theoreticians to the data and demanding an explanation of a highly suggestive but not definitive observational results.

As the ability of observers to provide more quantitative and more reliable data increases, there should be an increasingly greater theoretical motivation for the majority of the research. This should not, however, preclude interesting programs where the theoretical motivation is minimal. Astronomy and, in particular, surface photometry is not yet such a mature science, but it is maturing.

IV Conclusions

Surface photometry of extended objects is moving away from being a descriptive art to being a quantitative science. Modern instruments and computers are mainly responsible for this growth, but there still remain many possible sources of errors. This paper has summarized some of the major sources of systematic error and emphasized some directions which future programs should attempt to follow.

References

Carter, D. 1978, MNRAS 182,797

Davidson, K., Crane, P., and Chincarini, G., 1974, A.J. 79,791

de Vaucouleurs, G. and Cappacioli, M., 1979, ApJ Suppl. 40,699

Freeman, K.C., 1970, Ap.J., 160,811

Hoffman, A.W. and Crane P. 1977, Ap.J. 215,379

Jones, W.B., Obitts, D.L., Gallet, R.M., and de Vaucouleurs, G.
Astronomical Surface Photometry by Numerical Mapping Techniques
Dept of Astronomy Publ. SerII Vol 1 No 8,1967

Schweitzer, F. 1979, Ap.J. 233,23

Tinsley, B.M. and Larson, R.B., The Evolution of Galaxies and Stellar Populations
New Haven: Yale University Observatory, 1977

PHOTOMETRIC STUDIES OF GALAXY DYNAMICS

John Kormendy
Kitt Peak National Observatory[1]

I. INTRODUCTION

The advent of efficient microphotometers and digital detectors has produced an explosion of data on galaxy brightness distributions. This has allowed us to progress beyond the descriptive stage of photometry to studies of the processes that shape galaxies. This review will discuss the use of photometry to investigate galaxy dynamics and evolution. A complementary historical review and a compilation of data sources have been published by de Vaucouleurs (1980) and Capaccioli (1979), respectively.

To keep the topic manageable, we will restrict ourselves to the most fundamental components, elliptical galaxies (§ II), bulges of disk galaxies (§ III), and disks (§ IV). Section V discusses the relation of mass and light distributions and the search for massive halos. We will scarcely be able to mention a number of other interesting features, including especially bars, lenses, and rings. Properties of these features have been reviewed by Kormendy (1979, 1980a).

II. ELLIPTICAL GALAXIES

We focus on three recent results of two-dimensional photometry. Studies of isophote twists and mean surface brightnesses have contributed to a growing belief that ellipticals are triaxial in shape and probably oblate. More detailed work on the form of their brightness profiles has demonstrated the surprising importance of tidal effects, even at low galaxy densities. Finally, relations between the characteristic parameters of ellipticals have provided basic structural data that constrain models of their formation.

---

[1]Operated by the Association of Universities for Research in Astronomy, Inc., under contract with the National Science Foundation.

a) Three-Dimensional Shape

A dramatic revision of our picture of elliptical-galaxy dynamics was precipitated by the demonstration, beginning with Bertola and Capaccioli (1977) and Illingworth (1977), that they rotate much less than predicted by models in which an oblate-spheroid shape is maintained by rotation. Binney (1976, 1978a) quickly recognized the important implication that initial velocity anisotropies had been preserved during the collapse phase of galaxy formation, producing a triaxial elliptical supported by (anisotropic) heat. These developments have been well reviewed by Binney (1978b); we concentrate here on how photometry has contributed to the revolution.

Photometric evidence for triaxial ellipticals includes observations of rotation in isophote position angles as a function of radius. Binney (1978b) points out that this would be a consequence of triaxial isodensity surfaces whose principal axes are all aligned, but whose axial ratios change with radius. The observed isophote twist is then a projection effect. Rotation of isophote position angles has now been observed by a number of workers. For example, of 16 ellipticals studied by King (1978), five appear to show twists, generally of 10°-20° and in one case (NGC 7626) of as much as 70°. Williams and Schwarzschild (1979a,b) find twists of $\sim 10^{\circ}$ in IC 1459 and NGC 584, and a smaller twist of $\sim 5^{\circ}$ in NGC 4697. Of the four ellipticals which they observed, only NGC 1052 fails to show a significant twist at the 5° level. Less accurate but more comprehensive surveys also show that twists are common, being detected in 40% of 15 galaxies studied by Carter (1978) and 47% of 75 ellipticals surveyed by di Tullio (1979). Thus the feeling has grown that photometry confirms the kinematic results, suggesting that most ellipticals are triaxial.

However, some caution is required in interpreting the above results. It is well known that twists can reflect tidal disturbances as well as intrinsic structure. Williams and Schwarzschild (1979b) recognize this possibility for NGC 584, which has a 2.8 mag fainter companion located 4′ away ($\approx D_{25}$ according to de Vaucouleurs, de Vaucouleurs, and Corwin 1976). Williams and Schwarzschild

estimate the tidal effect on NGC 584 to be negligible, and in any case, most of the twist occurs at small radii. However, there are indications that tidal effects are stronger than expected. We will see in § IIb that they can reach to surprisingly small radii. And, in fact, di Tullio (1979) has demonstrated a strong correlation between the occurrence of twists and the presence of companions. All of the 34 galaxies showing significant ($>10^{o}$) twists are in pairs, groups, or clusters. Thirty of the 34 have asymmetries in their isophotes. Examining previous work shows that 3/5 of the King (1978) galaxies and 2/3 of the Williams and Schwarzschild (1979a,b) ellipticals that have twists also have close companions (T3, according to the system of Kormendy 1977c; see § IId below). Companions are also common among the twisted galaxies found by Carter (1978), whose galaxies are located in the clusters Abell 2197 and 2199. We conclude that twists in a few isolated galaxies argue for triaxiality, but that the secure photometric evidence for frequent triaxiality is weak. Another complicating factor is the possible contamination of any sample by unrecognized S0s, especially ones with bars. Altogether, several kinds of further studies would be of obvious value. First, we need a thorough survey for twists in a large number of galaxies, with particular attention given to (a) the accuracy of the classification as elliptical, (b) the detection of small twists, especially in the inner parts, and (c) the lack of companions. A photographic survey would probably be most efficient. Second, the best candidates produced by the survey could be studied in detail by measuring rotation curves and detailed brightness distributions. This would provide basic information on possibly triaxial ellipticals, which dynamical models could then try to fit. Finally, given a better understanding of the frequency and degree of triaxiality in isolated ellipticals, a survey for twists in galaxies with companions should provide a useful probe of tidal effects, as suggested by the results of di Tullio (1979).

It remains to ask whether elliptical galaxies are predominantly prolate or oblate. This question has been addressed by Marchant and Olson (1979) and by Richstone (1979, 1980), who applied essentially similar arguments to two

different samples of galaxies. They note that both prolate and oblate objects should have mean surface brightnesses that correlate with apparent ellipticity, but in opposite senses. A prolate object appears brightest when it is seen to be round, i.e., end-on. In contrast, an oblate object is brightest when it appears flattest, i.e., as seen from its "equatorial" plane. Both investigations found that mean or characteristic surface brightness correlates with ellipticity such that the brightest objects are the flattest. This suggests that ellipticals are oblate. Tests of the significance of this result were applied by deriving various statistics for the galaxy sample and for Monte-Carlo simulations based on various models of intrinsic shape. Both Marchant and Olson (1979) and Richstone (1979,1980) concluded that prolate models are rejected by a wide margin.[2] The main question with this work is whether there exists an intrinsic surface brightness-ellipticity correlation which could affect the results.

In summary, the detection of isophote twists, especially in isolated ellipticals, supports the growing belief that ellipticals are triaxial. Since apparently flatter objects tend to have higher surface brightnesses, it is likely that these prolate shapes are largely oblate. Systematic problems which could affect these conclusions should be explored in more detail.

b) Digression on Profile Fitting Functions

In the next several sections we will discuss the size and brightness parameters which characterize elliptical galaxies and which provide probes of tidal and other effects on their structure. Such parameters are most conveniently derived by fitting simple analytic functions to the profiles. To understand how much these parameters can measure, and to establish the most useful functional form, requires a digression on fitting functions.

---

[2]Lake (1980) has applied similar arguments to the observed correlation of velocity dispersion with ellipticity. The results favor (rather weakly) the prolate models. Further measurements of velocity dispersions are required to provide a stronger test.

Further details can be found in the Appendix of Kormendy (1977c) and in a forthcoming paper (Kormendy 1980b).

The use of analytic approximations to observed profiles dates back to Reynolds (1913) and Hubble (1930), who found that ellipticals and the bulges of disk galaxies are well described by

$$\frac{I}{I_0} = \frac{1}{(r/a + 1)^2} \quad , \tag{1}$$

where I_0 and a are, respectively, brightness and length scales. Since then, a number of other functions have been used (see de Vaucouleurs 1959 and Kormendy 1977c for reviews). Prominent among these is the de Vaucouleurs (1948, 1953) fitting function

$$\log \left(\frac{I}{I_e}\right) = -3.33 \left[\left(\frac{r}{r_e}\right)^{1/4} - 1\right] \quad . \tag{2}$$

Here, r_e is the radius that contains half the light of the model profile, and I_e is the brightness at that radius. This defines the value of the multiplicative constant -3.3307127...; if another value is chosen, then r_e will contain some other fraction of the total light. These, and most other fitting functions, contain two free parameters. They therefore perform exactly the desired function — to measure the simplest size and brightness scales that characterize elliptical galaxies. However, a number of points need to be made about their applicability.

First, elliptical-galaxy profiles are very close to power laws (the asymptotic form of the Hubble law for $r \gg a$). Since a power law contains only one scale parameter (say, the brightness at fixed fiducial radius), how can we derive two from a complicated function which merely mimics a power law? The answer is that the profile is not a power law over the region of interest, i.e., the radius range over which a Hubble or de Vaucouleurs law fits the profile and the range interior to the tidal effects discussed below. That is, over this region r is comparable to a (i.e., $r/a \leq 8.4$). Where $r \gg a$, the Hubble law either no longer describes the profile (in isolated galaxies), or else is

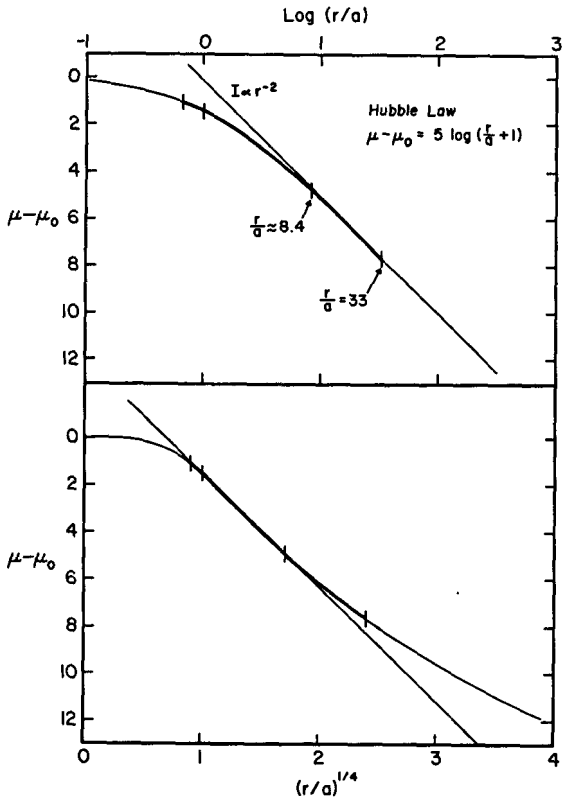

FIG. 1.— The basic Hubble law, plotted against log (r/a) and $(r/a)^{1/4}$. The heavy line marks the region that was found by Kormendy (1977c, see Fig. 6) to describe 17 elliptical galaxies measured by King (1978). The segment between the inner tick marks fitted isolated ellipticals, while the portion between the outer tick marks fitted galaxies with close companions. In the latter case, the rise of the profile above the extrapolation of the $r^{1/4}$ law shown (which excess, coincidentally, is close to a power law) is the tidal halo discussed in § IId. The straight lines shown are an r^{-2} power law (upper panel) and the best-fitting $r^{1/4}$ law (lower panel).

measuring the tidal halo (in galaxies with companions). This is evident in Figure 6 of Kormendy (1977c) and is illustrated in Figure 1 here. Thus the parameter a measures the slope of the profile interior to the radius at which it becomes a power law,[3] which is precisely the role of r_e (Kormendy 1977c). We conclude (1) that the profile is significantly different from a power law, so that a two-parameter fitting funtion is valid. However, we are, in a sense, measuring deviations from a power law, and these are not large. Thus (2) we must perform the fit over only that radius range in which the function very accurately matches the profile (i.e., to $\leq$0.1-0.2 mag arcsec^{-2}). If we do not demand a precise fit, we are not correctly exploiting the deviations from a power law, and so the parameters contain large errors that do not measure properties

---

[3]It is important to note (Kormendy 1977c) that a does not measure the isothermal core radius (King 1966). The Hubble law ceases to fit the observed profiles interior to r = a.

of the galaxies. This, for example, affects parameters derived by Strom and Strom (1978a,b,c), who made fits over given radius or brightness ranges without examining the quality of those fits.

We still need to know which fitting function is most useful. An examination of three-parameter functions (e.g., Oemler 1976) shows that their parameters are too strongly coupled to be very useful (Kormendy 1980b). We are restricted, for practical purposes, to functions which measure a characteristic brightness and radius scale. Kormendy (1977c) has examined a number of these and concluded the following: (1) Two-parameter fitting functions are largely equivalent in that they measure the same physical properties of galaxies. In particular, there are excellent correlations between a and r_e, and between I_0 and I_e, as derived from the Hubble and de Vaucouleurs laws, respectively. (2) The King (1966) dynamical model fits the profile less well than the Hubble or de Vaucouleurs relations (see also King 1978), so it is not recommended as an overall fitting function. However, it measures the dynamical core radius and central surface brightness, which are useful quantities (not entirely independent of r_e and I_e), again provided the fit is demanded to be precise. In view of conclusion (1), we adopt the most convenient fitting function, namely the $r^{1/4}$ law. Note that all the conclusions that follow could equally well have been derived by using a Hubble law (cf. Kormendy 1977c).

c) Characteristic Parameters

Systematic studies of elliptical-galaxy parameters have until recently suffered from a lack of data. With the publication of extensive photometry by Oemler (1976), King (1978), Strom and Strom (1978a,b,c, 1979), and others, this situation is now much improved. In fact, we have arrived at the unusual situation where measurements have gotten well ahead of interpretation: considerable further analysis is possible by using already-published data.

The pioneering study of elliptical-galaxy parameters was made by Fish (1964). For 29 galaxies with photometry available or measured in his paper, Fish found that total luminosity $L \propto r_e^2$. Values of I_e were not in general available,

but since $L \propto I_e r_e^2$ for an $r^{1/4}$ law, we infer that I_e = constant for all of the galaxies. By making a number of assumptions, chiefly that the mass-to-light ratio M/L is constant from galaxy to galaxy and within any galaxy, Fish derived the dynamically interesting consequence, namely that potential energy $\Omega \propto M^{3/2}$. He then used this result to explore the physical processes which went on during the collapse of protogalactic gas clouds into galaxies, concluding that the collapse was halted by the development of internal opacity. With 15 years of hindsight, and much better data available, many of the details of Fish's paper are now open to criticism. In particular, we will find below a different relation between L, r_e, and $B_e = -2.5 \log I_e$ + constant. However, none of this should obscure the important point which Fish realized, namely, that photometric parameters provide one of the few handles we have on the physical processes of galaxy formation.

Further progress became possible with the appearance of King's (1978) excellent photometry of 17 elliptical and near-elliptical galaxies. Kormendy (1977c) studied E-galaxy profiles and parameters using these data (kindly made available by King before publication) and photometry of eight other galaxies from Kormendy (1977a). These profiles provided considerably more accurate parameters. B_e was found not to be constant, independent of L. Instead, there is a tight correlation between B_e and r_e (Fig. 2), which takes the form

$$B_e = 3.28 \log r_e + 19.45 \text{ B mag arcsec}^{-2}. \qquad (3)$$

(Equation [3] differs slightly from equation [2] of Kormendy (1977c) because all of the ellipticals, not just the ones measured by King (1978), are included.) The parameter along the $B_e(\log r_e)$ relation is absolute magnitude M_B: lines of constant M_B have slope 5 in Figure 2. On the average, more luminous galaxies are more diffuse, i.e., have larger r_e and fainter B_e. This result is qualitatively confirmed by Strom and Strom (1978a,b,c). Since $M_B = B_e - 5 \log r_e$ + constant, the average way in which r_e and B_e vary with M_B is

$$M_B = -1.72 \log r_e + \text{constant} \quad ;$$
$$M_B = -0.53\, B_e + \text{constant} \quad . \qquad (4)$$

Note that the scatter about these relations is large, since lines of constant M_B are almost parallel to the $B_e(\log r_e)$ relation. Relations (3) and (4) replace Fish's (1964) law, $M_B = -5 \log r_e + \text{constant}$.

The implications of this result on the theory of galaxy formation are not yet explored. Recent discussions along the line of Fish's study have been made by Press and Schechter (1974), Saito (1979), Aizu (1979), and Norman and Silk (1980). The studies of Saito and Aizu still suffer from problems of poor data, being largely based on old measurements of questionable reliability. However, several quantities which Fish had to assume can now be calculated. In particular, the mass is now derived from the velocity dispersion instead of being inferred from M/L. Considerable further work remains to be done. Care must be taken to exclude tidal effects (§ IId). Perhaps the greatest problem is the assumption that r_e measures the size scale of the mass distribution; there is growing evidence (§ V) that M/L varies greatly with radius. Nevertheless, with

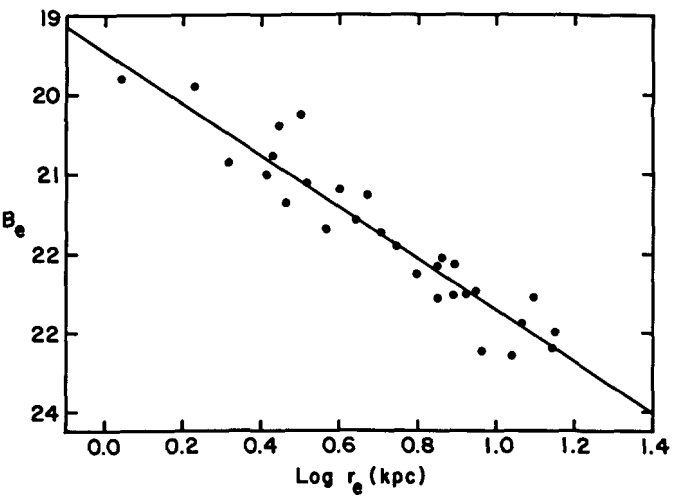

FIG. 2.— B_e versus log r_e for 29 "elliptical" galaxies in poor clusters, photometered by Kormendy (1977a), King (1978), and Williams and Schwarzschild (1979a,b). Included are three S0 galaxies whose disks are barely detected and assumed not to influence the bulge structure. These are NGC 524, 4382, and 4636. A least-squares straight line (eq. [3]) has been fit to the points. These and all other $r^{1/4}$-law parameters discussed in this paper refer to the mean profile, i.e., the profile along a line oriented at 45° to the major axis.

the large amounts of new data available, the time seems ripe for a new attack on this problem.

In the absence of an explanation of the parameter relations, they can still be used to compare galaxies of various kinds. In a major series of papers, Strom and Strom (1978a,b,c, 1979) have obtained U- and R-band brightness profiles of nearly 600 galaxies in eight clusters: spiral-poor — Coma, Perseus, A401, A2199, and A2670; spiral-rich — Hercules, A1228, and A1367. Their aim (Strom and Strom 1978a) was to explore problems of galaxy formation and subsequent (tidal) evolution by comparing galaxies in a wide variety of environments. Some of the results have been reviewed by Strom and Strom (1978d, 1980). Considerable evidence was found for tidal stripping (see the next section). Apart from this, the only difference detected was that ellipticals in spiral-poor clusters are on the average marginally smaller (by ~20%) than ellipticals in spiral-rich clusters. For example, there is no significant difference in the slope of the log $r_e(M_V)$ relations, either between central and outer parts of spiral-poor clusters or between spiral-rich and spiral-poor clusters (cf. Fig. 5). The Stroms found some differences between their parameter relations derived for galaxies in rich clusters and equations (3) and (4) valid in poor clusters, but these are probably caused by the different methods of measurement (see below and § IId). Thus the evidence argues for a great deal of similarity in the details of galaxy formation in a variety of environments. However, there are a number of reasons why the above comparisons are not very sensitive. (1) S0 galaxies were not, in general, rejected from the sample. They will appear too diffuse for their luminosity, both because disks have shallow brightness gradients and because bulges themselves are more diffuse than ellipticals (§ III). (2) The $r^{1/4}$-law fits were made between a fixed inner radius and a fixed outer brightness cutoff, without regard to the shape of the profile. The Stroms note that faint galaxies deviate below an $r^{1/4}$ law at large radii. Recall from § IIb that we must demand a precise fit of the fitting function. Finally, (3) tidal effects were neglected but have a major effect on the

parameter relations (§ IId). All of these effects contribute to increase the scatter in the parameter plots.

A new analysis of the data of Oemler and the Stroms is currently in progress (Kormendy 1980b) to investigate these effects in more detail. For example, we ask in Figure 3 whether the central parts of cD galaxies can be distinguished from giant ellipticals. Here we have added to Figure 2 the cD galaxies observed by Oemler (1976), together with other galaxies in A1314. The scatter in these points is slightly larger, because we have neglected tidal effects and because the photometry is less precise (fewer plates were used, and the clusters are more distant than King's 1978 ellipticals). Nevertheless, the cD galaxies clearly fall along the brightward extrapolation of the $B_e(\log r_e)$ relation for nearby galaxies. There is no evidence for any difference between the process of formation of these objects and of giant ellipticals, i.e., the central parts of cDs seem indistinguishable from normal giant ellipticals, except for their unusually high luminosity. Hoessel (1980) arrives at the same conclusion from an independent study of ~108 first-ranked cluster galaxies. In the same vein,

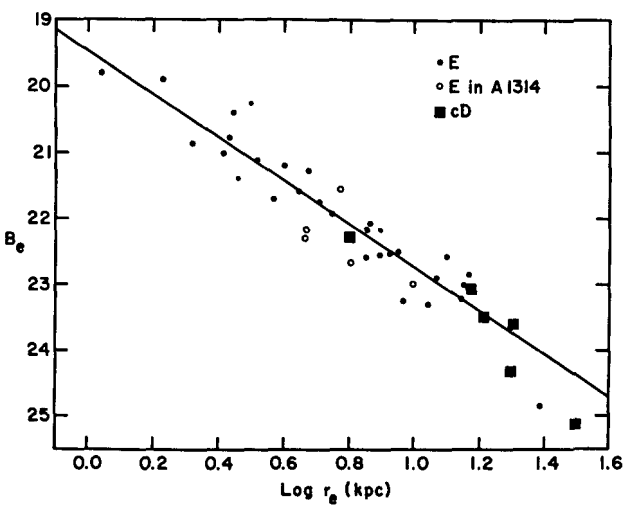

FIG. 3.— $B_e(\log r_e)$ relation for normal ellipticals and for cD galaxies measured by Oemler (1976). Lacking photoelectric photometry, we have transformed Oemler's V magnitudes to B by assuming an average B - V = 1.00. Distances to nearby ellipticals, mostly in the Virgo cluster, have been obtained by using a Hubble constant of 50 km s^{-1} Mpc^{-1}, in keeping with Fig. 2. However, the relative distances to A1314 and the cD galaxies have been calculated assuming a Hubble constant larger by a factor of 1.46, corresponding to $\Delta \log r_e = 0.165$ (Aaronson et al. 1980).

Oemler (1976, see Fig. 9) found that when the effect of the halo was subtracted, the remaining luminosity of cD galaxies displayed the same relationship to total cluster luminosity ($L_{galaxy} \propto L_{cluster}^{1.25}$) as did first-ranked ellipticals. Of course, the halo is enormous compared to the $r^{1/4}$ law fit (see also Oemler 1973, 1976). It can be formed by an entirely different process. But the basic $B_e(\log r_e)$ relation of the central parts seems unchanged from $M_B = -19$ to the brightest cDs at $M_B < -25$ ($H_0 = 50$ km s^{-1} Mpc^{-1}).

d) Tidal Effects

The possible importance of tidal effects on galaxy structure has been recognized for many years. King (1962) has discussed the process by which a smaller object is tidally truncated by a much larger one, developing an expression for the limiting radius, a preliminary fitting function for the profile, and later an approximate dynamical model (King 1966). Convincing demonstrations that globular clusters and dwarf galaxies are tidally limited by the Galaxy have been given, respectively, by King (1962, 1966) and by Hodge (see Hodge and Michie 1969 for a review). A few normal ellipticals also appear to be truncated, including M32 (King 1962), NGC 4486B (Rood 1965), and NGC 5846A (King and Kiser 1973). Faber (1973) has pointed out that these three objects have unusually high mean surface brightnesses (since they lack halos) and high metal abundances characteristic of more luminous galaxies; this further supports the tidal interpretation. These investigations have given rise to a folklore which says that the effect of tidal forces is to remove outer halos, thereby making galaxies smaller. Two main conclusions emerge from recent work in this subject. First, the above picture is oversimplified: tidal effects work to heat the outer halo, stripping it off only in cases of extremely high collision frequency or relatively small victim mass. Second, tidal effects are very strong, reaching to surprisingly small radii even in galaxies with few encounters, and significantly modifying most of the structure if an elliptical is located in the core of a rich cluster.

The fact that the classic picture is incomplete was suggested by Kormendy (1977c). His study of bright ellipticals measured by King (1978) and Kormendy (1977a) showed that the profiles do not all have the same shape.[4] Instead (Fig. 4), ellipticals with companions of comparable luminosity have bright envelopes above the extrapolation of an $r^{1/4}$-law fit to the inner parts. These envelopes are greatly reduced or absent in isolated galaxies. This effect was interpreted as a combination of reversible tidal stretching and irreversible dynamical heating produced by the encounter(s). The latter effect arises because the orbital periods of stars at large radii are comparable to the encounter timescale. These stars therefore see a gravitational potential that changes strongly but not periodically during one orbit, resulting in violent relaxation (Lynden-Bell 1967). Individual stars gain energy at the expense of the galactic

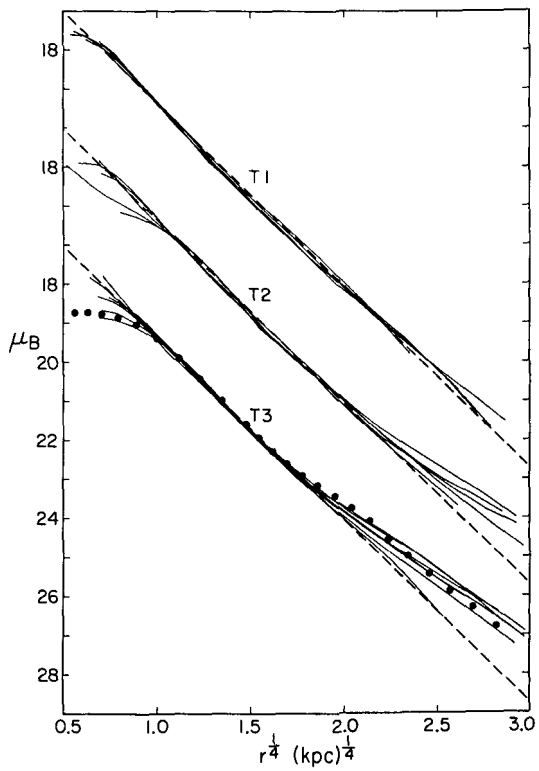

FIG. 4.— Brightness profiles of the King (1978) ellipticals, scaled to have a common de Vaucouleurs law (dashed lines), with r_e = 10 kpc and B_e = 23 B mag arcsec^{-2}. The galaxies have been divided into groups separated by 3 mag arcsec^{-2} intervals. T1 galaxies have no neighbors of significant luminosity. They should be dynamically isolated and are found to be well described by an $r^{1/4}$ law. T3 galaxies have at least one companion of comparable luminosity located within several diameters. With one exception (NGC 7626), they are not well described by a single $r^{1/4}$ law. T2 galaxies form an intermediate group where the degree of tidal influence is unclear (e.g., galaxies with several much fainter companions). Their behavior is intermediate. Tidal classes of the individual galaxies are given in Tables 1 and 2 of Kormendy (1977c). The dots represent the profile of NGC 3379, which is seen to behave exactly like the other T3 objects.

---

[4]King (1978) also noticed this effect. His Figure 11 contrasts two pairs of galaxies; in each case one is classified T1 and the other T3, according to the system described here in Figure 4.

orbit. Both halos expand, unless one galaxy is much less massive than the other, in which case its halo is stripped off (the classic picture). Tidal distension has now been seen in many numerical simulations (Gutowski and Larson 1976; van Albada and van Gorkom 1977; Wielen 1977; White 1978; Miller and Smith 1980). The dynamical friction on the orbit is of course well known and results in a rapid merging of the two systems once they begin to overlap significantly (Toomre 1977; White 1978; Miller and Smith 1980).

Another immediate consequence is illustrated in Figure 4. NGC 3379 is a bright elliptical with two companions, certainly classified T3 in the system of Figure 4 and Kormendy (1977c). It behaves exactly like the other T3 galaxies: the inner parts are relatively normal and follow an $r^{1/4}$ law well, while the outer profile seems tidally distended. The kink in the profile at $r \simeq 25''$, which marks the start of the tidal halo, has been observed by numerous workers (e.g., Burkhead and Kalinowski 1974; Okamura 1977; Burstein 1979b). Barbon, Benacchio, and Capaccioli (1976) note further that the region outside $r = 0.'8$ has a slightly different center than the inner part of the galaxy; NGC 3384 is similarly distorted. This might also be evidence for tidal effects. Thus, although NGC 3379 has been very popular as a galaxy to which dynamical models can be compared (e.g., King 1966; Prendergast and Tomer 1970; Larson 1974; Wilson 1975; but not Gott 1975), it is not very suitable for such comparisons.

Note in Figure 4 that the scaled value $r_e = 10$ kpc corresponds to $r^{1/4} = 1.78$. Thus the tidal halo begins at approximately $r = r_e$. It is easy to show that a typical stellar orbital period at this radius is much smaller than the encounter timescale. Therefore, tidal effects seem to reach to surprisingly small radii. This is not easy to understand on theoretical grounds.

In rich clusters tidal effects are even stronger. This has been demonstrated convincingly in the series of papers by Strom and Strom (1978a,b,c,d, 1979). Figure 5 shows log r_e plotted against absolute magnitude M_V for two spiral-poor clusters. In each case ellipticals are smaller at a given absolute magnitude if they are located in the central parts of the cluster.

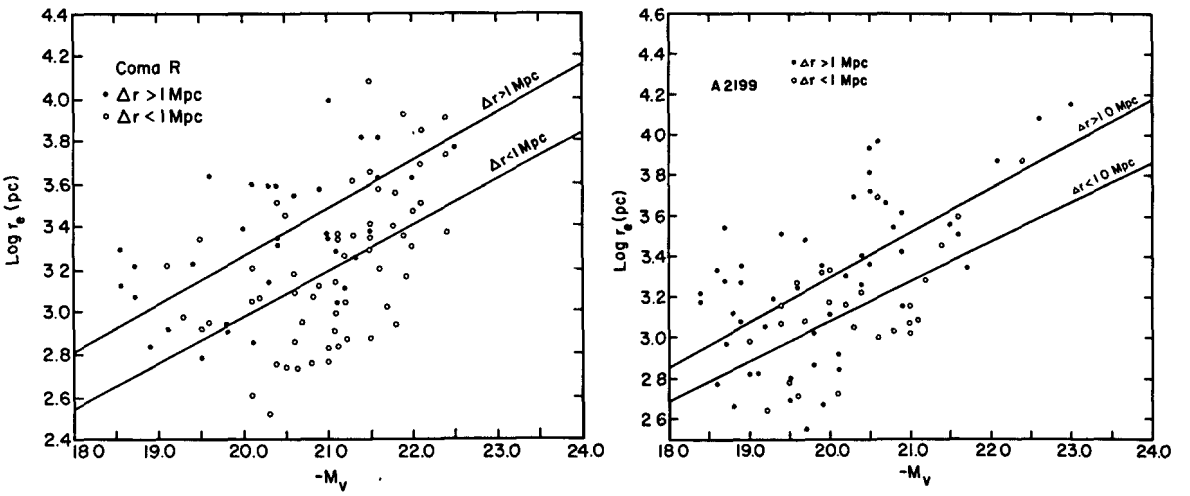

FIG. 5.— The log $r_e(M_V)$ relations for two spiral-poor clusters, from Strom and Strom (1978a,c). In each case least-squares straight lines have been fitted to the points for galaxies in the central and outer parts of the clusters.

A similar result holds for the other spiral-poor clusters studied, A401 and A2670. Even in the outer parts of these clusters, ellipticals are in general somewhat smaller than they are in spiral-poor clusters (e.g., Strom and Strom 1978d). Similar results were obtained when other parameters, such as isophotal radii, were used. The Stroms interpret this effect as being due to tidal stripping (but do not yet discard the possiblity that differences in galaxy formation are involved).

These results are confirmed by Kormendy's (1980b) reanalysis of the Oemler (1976) photometry. Three effects are present simultaneously. (1) The degree to which an $r^{1/4}$ law fits an undisturbed elliptical appears to depend on L. The brightest Coma ellipticals (excluding the cDs) have slightly more light at large radii than predicted by the de Vaucouleurs function, while the faintest galaxies have too little. The best fit occurs at intermediate magnitudes slightly fainter than first-ranked cluster galaxies. (2) Ellipticals in the outer parts of Coma are tidally distended if they have close companions (cf. Kormendy 1977c). In the central part of the cluster the collision rate is high, but the gravitational potential for tidal truncation is also high. Thus galaxy envelopes are still heated, but (3) they are heated so much that they are stripped off, in agreement

with results of the Stroms (1978a,b,c,d, 1979).

Figure 6 shows the effect on the characteristic parameters. The dispersion in the $V_e(\log r_e)$ relation is smaller for galaxies far from the cluster center; some experimentation shows that a good radius at which to divide the sample is 40′ (= 1.4 Mpc on the distance scale of Fig. 5). The $V_e(\log r_e)$ relation for r > 40′ is in reasonable agreement with that derived for nearby ellipticals (Fig. 2). The Stroms (1978a) came to a different conclusion, probably because they compared the $r_e(M_V)$ correlations, which have a great deal of scatter and which were calculated in very different ways by Strom and Strom (1978a) and by Kormendy (1977c). Most of the increased dispersion for galaxies at r < 40′ from the cluster center comes from faint galaxies made smaller by tidal truncation. However, the brightest galaxies show no sign of truncation. It is clear that faint galaxies are truncated more than bright ones. It is tempting to speculate that the brightest galaxies gain material rather than lose it, and that this process is instrumental in the formation of cD galaxies. This speculation is similar to previous suggestions that cDs are "junk piles" of material collected

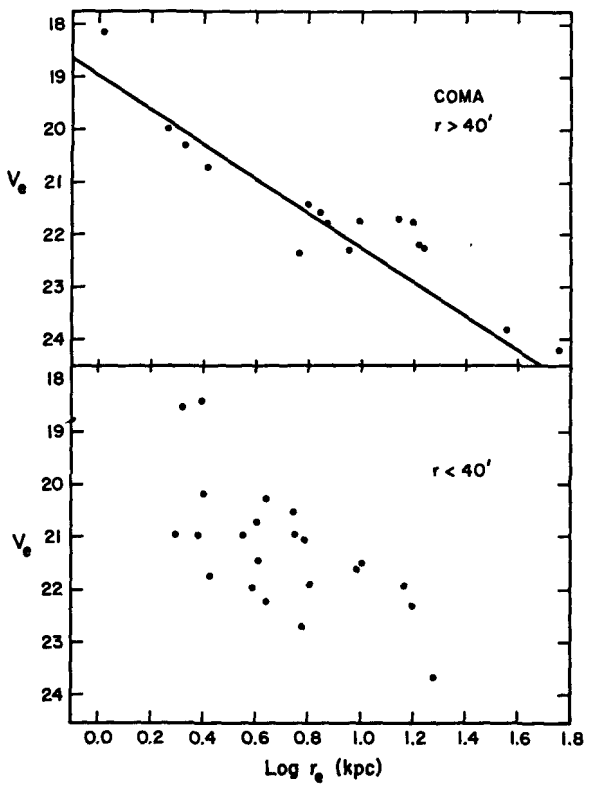

FIG. 6.— $V_e(\log r_e)$ relations for Coma cluster galaxies measured by Oemler (1976) and divided up according to their distances r from the cluster center. Equation 3 is illustrated in the upper panel, transformed to V assuming a B- V color of 1.0, and calculating distances as outlined in Fig. 3.

at the center of the cluster, perhaps by an unusually luminous galaxy that comes to reside there through mass segregation effects or mergers (see Oemler 1976 for a review), and the more recent picture that cDs form through successive mergers (Ostriker 1977). There is no reason why many galaxies above the cutoff luminosity cannot accrete material. And, indeed, Oemler (1976) found that NGC 4839, the third-brightest galaxy in the Coma cluster, has many of the characteristics of a cD. Clearly, one can test the hypothesis by estimating the amount of material lost as a function of luminosity by using profiles of galaxies at $r > 40'$ as templates. One of the main objectives of the Kormendy (1980b) work is to perform this test.

We can summarize this section by noting again that tidal effects are surprisingly strong. This is particularly true in rich clusters, where frequent encounters appear to have stripped off the halos of at least the fainter galaxies, producing an intergalactic sea of stars (Thuan and Kormendy 1977 and references therein) and contributing to cD halos. However, even in poor clusters like Virgo, tidal effects in pairs of galaxies can heat halos and have an effect at remarkably small radii. A great deal of observational work is required to investigate these phenomena in more detail. Comparisons to theoretical calculations of tidal and merger effects (e.g., Richstone 1975, 1976; Knobloch 1978; Hausman and Ostriker 1978 and references therein; Ostriker 1977; Roos and Norman 1979) have barely begun.

e) Other Questions

There are many other surface-photometry questions that we cannot discuss because of lack of space. (1) One of the most important is whether galaxy mergers leave any signature in the light distribution. Toomre (1977) has proposed that a significant fraction, perhaps even a majority, of ellipticals are formed by mergers of a small number of stellar systems. Promising candidates for imminent mergers or ones in progress have been listed by Toomre (1977). More advanced stages of probable mergers have been studied by Schweizer (1978b, 1980). Schweizer (1980) suggests that NGC 1316 (Fornax A) is a recent merger

product, but notes that the brightness profile is already close to an $r^{1/4}$ law. (2) The Stroms (1978a,b,c) have observed color gradients in about 20% of the galaxies they studied, usually extending over most of the visible galaxy. These gradients again contain information about galaxy formation and particularly about the question of whether dissipation was involved in the formation of ellipticals (see Strom and Strom 1978a for details). (3) Strom and Strom (1978c, 1979) have made the provocative suggestion that ellipticals in flattened clusters such as Perseus and A401 are flatter than normal and preferentially aligned with the cluster major axis. They conclude that the factors which influence cluster shape may also affect the structure of galaxies. (4) Finally, Young et al. (1978) have noted that the core of M87 differs from an isothermal distribution of particles of a single mass (e.g., King 1966) in that its profile does not level off at r = 0. Combining this with evidence that the velocity dispersion also continues to increase toward the center (Sargent et al. 1978) leads them to suggest that there is a massive object, perhaps a black hole, in the nucleus. A similar result is found for NGC 6251 (Young et al. 1979). Nonisothermal cores are not rare (King 1978). More photometry of galaxy cores, and further work on the dynamical processes which affect core profiles, would be very valuable. This subject will be reviewed in these proceedings by G. Illingworth. It is easy to see that we could spend the whole of this review discussing elliptical galaxies alone.

III. BULGES[5]

The conventional picture of a spiral or S0 galaxy is that it consists of an elliptical living in the middle of a disk. This view is based on the similarity seen in many basic properties of bulges and ellipticals (e.g., Freeman 1975a), including morphology (Sandage 1961), the shape of the brightness profile

---

[5]Throughout this review, we will refer to the ellipsoidal components of disk galaxies as bulges rather than spheroids, so as not to take an explicit stand on their three-dimensional shapes.

(de Vaucouleurs 1959), and stellar content (see Faber 1977 for a review). New data now allow us to examine these similarities in more detail. The resulting history of this subject has been to show that bulge components differ from elliptical galaxies (Kormendy and Bruzual 1978; Kormendy 1980b,c). In fact, the still-fragmentary data are beginning to suggest that there is a continuum of many properties from ellipticals through bulges to disks.

One early indication was the observation of "box-shaped" bulges in a number of edge-on spirals (Sandage 1961; de Vaucouleurs 1974). The most extreme example known is NGC 128, illustrated in Sandage (1961). Other examples from the above sources include NGC 4565, 5746, and 7332. Possible explanations include rapid rotation and/or the effect of the disk potential. In some cases we might also be seeing bars which are nearly end-on. Dynamical models that aim to interpret box-shaped bulges are being constructed by Freeman and his students (Freeman 1975a).

Another difference is found in the shape of the minor-axis profiles. We know that the major-axis profiles of bulges are well described by a de Vaucouleurs law (de Vaucouleurs 1958, 1959; Kormendy 1977a,b; Burstein 1979b,c). However, significant deviations from an $r^{1/4}$ law are sometimes seen in the minor axis. The best-studied example is NGC 4565 (Kormendy and Bruzual 1978); an up-to-date version of their Figure 1 is shown in Figure 7 below. As concluded by Kormendy and Bruzual, and confirmed by all the new photometry, the profile is qualitatively different from that of an elliptical. It consists of two distinct segments. Above 23.5 V mag arcsec^{-2} (hereafter μ), it is neither a power law nor an $r^{1/4}$ law. This inner segment is steep; very approximately, $I \propto r^{-3.7}$(KB). Below 23.5 Vμ, the profile is the power law $I \propto r^{-2.55 \pm 0.1}$, consistent with results of Kormendy and Bruzual (1978) and Spinrad et al. (1978). Thus the whole profile is steeper than that of a typical elliptical, in which $I \propto r^{-1.7}$ to $r^{-2.0}$ (Kormendy 1977c). The profile peculiarities correlate with isophote shape: the isophotes are most box-shaped at approximately the radius where the slope changes. Kormendy and Bruzual (1978) concluded that all of this was early evidence that bulges sometimes differ significantly from ellipticals.

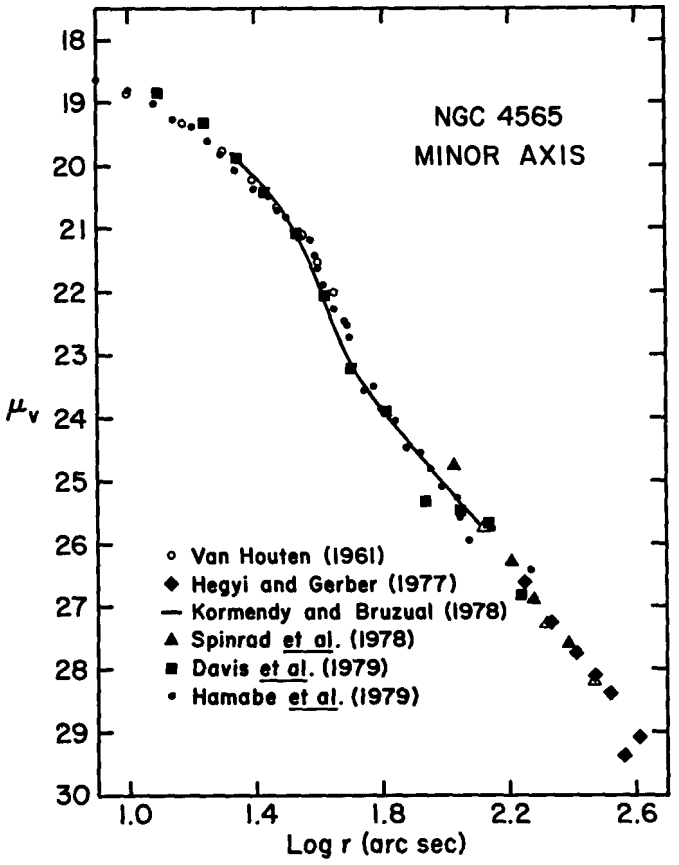

FIG. 7.— Composite brightness profile of the minor axis of NGC 4565. Surface brightness is in V mag arcsec^{-2} with the zero point of Hamabe et al. (1979b). Since zero-point errors are largely independent of errors in profile shape, the individual measurements have been shifted together in μ to minimize the scatter. Color differences have been neglected; these may contribute to the scatter, since bandpasses ranging from B to R were used. The data of van der Kruit (1979) and Jensen and Thuan (1980) are not shown; they deviate slightly from our average profile but still confirm the change in slope at r ~ 50". Below 23.5 V mag arcsec^{-2}, the profile is well described by the power law $I \propto r^{-2.55}$.

The data of Jensen and Thuan (1980) allow correction of the profile for the contribution of the thick disk (§ IVd). This correction is largest at ~50" and so increases the difference between the inner and outer segments.

Suggestions of similar deviations have been available for some time. Tsikoudi (1977) notes a small excess of light above an $r^{1/4}$ law, along the outer minor axes of several edge-on S0s, particularly NGC 3115. The deviation is much more subtle than in NGC 4565 (see also Strom et al. 1977). However, NGC 3115 is thoroughly bulge-dominated; Tsikoudi concludes that the bulge contributes 84% of the B and 95% of the V light. Hamabe et al. (1979a) have shown that the profile of NGC 5866, which is similarly bulge-dominated, is also normal, at least to ~25 Bμ. In contrast, Burkhead (1980a,b) finds that the minor-axis profile of M104 deviates seriously from an $r^{1/4}$ law below 24 Bμ. Such deviations can also be seen in some of Burstein's (1979b) profiles. We now need to know when and how often these "non-elliptical" profiles occur. For example, do they preferentially occur in galaxies (1) with box-shaped bulges, or (2) with small bulge-to-disk ratios, or (3) with relatively late morphological types?

A more quantitative comparison of bulge components and ellipticals can be made using profile parameters. We have already noted that $I(r) \propto r^{-2.55}$ along the minor axis of NGC 4565. Spinrad et al. (1978) found that bulge profiles in two other galaxies were similarly steep: $I \propto r^{-3.03 \pm 0.20}$ in NGC 253 and $I \propto r^{-2.56 \pm 0.15}$ in NGC 4594. (The latter slope is not confirmed by Burkhead 1980a, who finds $I \propto r^{-1.78}$ between 200" and 1200".) In NGC 5866, 3115, 4762, and 4111 Hamabe et al. (1980) find power-law indices n of -2.1, -2.1, -2.4, and -3.8, respectively. On the average, these are steeper than profiles of ellipticals, which have $-1.7 \geq n \geq -2$ (Kormendy 1977c). On the other hand, it is hardly fair to compare minor-axis profiles of edge-on bulges to mean profiles of a sample of randomly oriented ellipticals.

A better comparison is possible using the de Vaucouleurs parameters B_e and r_e. In Kormendy (1977c) several S0 bulges deviate below the $B_e(\log r_e)$ relation for elliptical galaxies. This is confirmed by Burstein (1979c) for a larger sample of galaxies. Figure 8 shows the $B_e(\log r_e)$ relation for photometry published to date. Only a few bulges satisfy the elliptical galaxy correlation. Generally these are objects in which the disk contributes so little light that it is barely detectable. On the other hand, galaxies such as M31 and M81 fall far below the ellipticals. Of the three objects which deviate most,

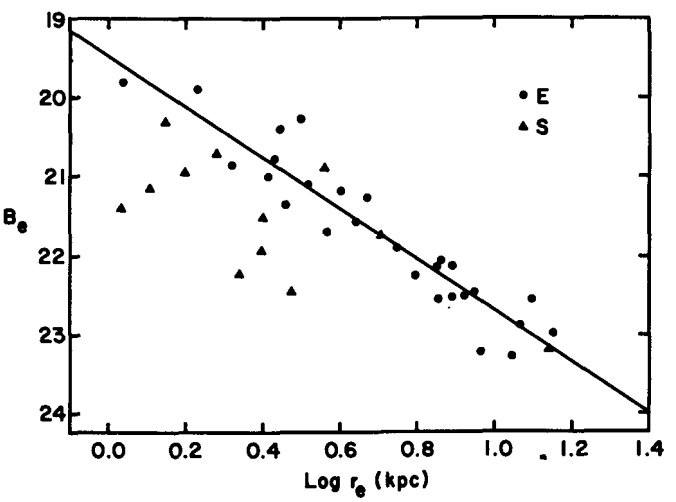

FIG. 8.— Comparison of the $B_e(\log r_e)$ relations for the mean profiles of bulges (triangles) and ellipticals (circles). The line shown is eq. (3). To provide a fair comparison to ellipticals, which are oriented randomly, edge-on galaxies have been discarded. Also discarded are galaxies in which the disk is likely to affect bulge parameters deduced from the observed profile. Sources of photometry: Barbon and Capaccioli (1975); Barbon, Capaccioli, and Tarenghi (1975); Brandt, Kalinowski, and Roosen (1972); Burstein (1979b); de Vaucouleurs (1958); Kormendy 1977a).

they are the ones with largest and smallest log r_e. Boroson (1980) reaches the same conclusion from a larger, nearly independent sample of objects (see also Pritchet 1979). We can express this result by stating that bulges are more diffuse than ellipticals of equal luminosity (Burstein 1979c; Kormendy 1980a). However, this may be misleading since we already know that the bulge of NGC 4565 is more compact than a typical elliptical. We conclude that, compared to ellipticals, bulges tend to have small r_e or faint B_e or both. Recalling from § IIc that the $B_e(\log r_e)$ relation contains information on galaxy formation, we argue that significant differences exist in the physical processes giving rise to ellipticals and bulges of spirals. Further work is required to establish the distribution of parameters in Figure 8, and especially to investigate whether deviations from the $B_e(\log r_e)$ relation correlate with bulge-to-disk ratio or rotation properties.

We turn next to intrinsic shapes. Several observations suggest that bulges are flatter than ellipticals, which typically have a shape ~E4 (Sandage, Freeman, and Stokes 1970). At the (faint) surface brightness involved, the observed ellipticity distributions in disk galaxies are dominated by the flat component. However, the bulge sometimes contributes most of the light, so when a two-component fit is made to the ellipticity distributions (de Vaucouleurs 1974) some information on bulges can be recovered. De Vaucouleurs concludes that bulges in the range Sa-Sc are slightly flatter than ellipticals (typically E4-E5, compared to E3.5). Note that these bulges are likely to be abnormally similar to ellipticals, precisely because they contribute so much of the light (cf. the above discussion). Secondly, Kormendy and Illingworth (1980) suggest that bulges are typically flatter than E4, based on the difficulty with which they found objects whose bulges extend far enough away from the disk for rotation-curve work. Finally, all five bulges for which Hamabe *et al.* (1980) have constructed three-dimensional models are found to be flatter than E4 even though several (NGC 3115, 5866, for example) contribute most of the light of the galaxy. With modern microphotometers, it should be a routine, if tedious, task to investigate

these hints by studying the distribution of disk-galaxy axial ratios at some suitably high surface brightness. Another approach is to construct detailed three-dimensional models (Hamabe et al. 1979a,b, 1980). With this in mind, Boroson (1980) is exploring three-dimensional profile decomposition of a sample of ~30 galaxies.

Two further observations bear on our comparison of bulges and ellipticals. Illingworth, Schechter, and Gunn (1980) and Kormendy and Illingworth (1980) have measured rotation rates in the bulges of five edge-on galaxies, far enough above the disk so that its contribution is negligible. In each case the rotation is higher than in typical ellipticals (Illingworth 1977) and is roughly consistent with rotating oblate-spheroid models (e.g., Binney 1978a). Furthermore, rotation velocities decrease smoothly from the disk into the bulge. This is a characteristic of gas-dynamic models of galaxy formation. The rotation observations have obvious implications on the interpretation of box-shaped structure, the higher degree of flattening of bulges, and the possibility that bulge structure is different along the equatorial and z-directions. Thus a number of differences between bulges and ellipticals are now established. Work on tying these differences together is under way.

IV. DISKS

In this section we will review the basic properties of disk brightness distributions. This includes work on the functional form of disk profiles, their characteristic parameters, and their three-dimensional shapes. It is well known that the brightness gradient in many disks is roughly exponential (de Vaucouleurs 1959; Freeman 1970a):

$$I(r) = I_0 \, e^{-\alpha r} \quad . \tag{5}$$

However, galaxy bulges often contribute significant light in the region of the disk. Thus a crucial step is the decomposition of observed profiles into bulge and disk components. This shows that some disks are rather far from being exponential. In fact, it is becoming clear that non-exponential disks are rather common; some examples will be illustrated below.

In the following discussion we should keep in mind the possibility that some disks are not self-gravitating systems; i.e., that they consist of test particles moving in the potential of an invisible halo (see § V). In what follows the emphasis will again be on uncovering the structural features that shed light on the disk formation process. However, since disks are a more complicated problem than ellipsoidal objects, our understanding of them is rather more primitive.

To keep the discussion manageable, we will omit problems of (a) spiral structure and recent star formation, and (b) bars, lenses, and associated phenomena. These problems will be mentioned briefly at the end.

a) Freeman's (1970a) Study of Disk Structure

The starting point for any observational discussion of disk structure is Freeman's (1970a) classic paper. In it he discussed photometry of the 36 disk galaxies which had been measured at that time, concluding the following. (1) The profiles were all exponential. (2) Sometimes the exponential had an inner cutoff, i.e., the profile leveled off before it reached the center ("Type II profile"). (3) The scale length was $2 \leq \alpha^{-1} \leq 10$ kpc in S0-Sbc galaxies, but always less than 5 kpc in Sc-Im galaxies ($H_0 = 50$ km s^{-1} Mpc^{-1}). (4) Surprisingly, the central disk brightness (corrected for inclination and Galactic absorption) was constant at $B(0)_c = 21.65 \pm 0.30$ (σ) $B\underset{\sim}{\mu}$ in 28 of the 36 galaxies. Except for one dwarf irregular, all the other disks were brighter. Finally, (5) the bulge-to-disk ratio correlated only weakly with morphological type. In particular, there existed S0s with both strong and weak bulges.

Freeman went on to explore the dynamical implications of these results. Assuming that the mass-to-light ratio M/L is constant with radius led, via result (4), to the conclusion that total mass and angular momentum are related by $M \propto h^{7/4}$. Furthermore, all disks then have the same form for their mass-angular momentum distributions. Following Mestel (1963), Freeman assumed further that each element of mass conserves angular momentum during the collapse phase of galaxy formation. Then either an efficient process was required to create the above properties, or they were properties of the protogalaxy. The origin of

exponential disks is completely unknown. For example, Freeman noted that the mass-angular momentum distribution of an exponential disk is nearly identical to that of a uniformly rotating uniform sphere, which is a plausible initial condition. However, such a sphere need not settle into an exponential during its collapse; there are other possible final forms. Altogether, the great uniformity in angular momentum properties establishes strict requirements for theories of how galaxies acquire angular momentum (see Thuan and Gott 1977; Efstathiou and Jones 1979; and Sharp, Lin, and White 1979 for recent discussions, and Freeman 1975b for a review).

Freeman (1980) points out that if disks are not self-gravitating then the observed exponential distribution is uniquely determined by the mass-angular momentum relation, and the requirements to produce exactly the correct angular momentum are even stricter.

There are a number of problems with Freeman's (1970a) study (Kormendy 1977b; Allen and Shu 1979 and references therein; Burstein 1979b,c), some of which will be discussed below. These problems weaken conclusions (1) and (4). However, the constraints set on galaxy formation theories are still severe. The paper is fundamental, because it begins work on so many of the basic questions of disk structure.

b) Decomposition of Observed Profiles into Bulge and Disk Components

Figure 1 of Kormendy (1977b) shows $r^{1/4}$-law and exponential fits to several S0 profiles. Only a modest extrapolation of the $r^{1/4}$ law is required to show that the bulge contributes significant light even where the profile looks exponential. Thus parameters derived by fitting the observed exponential (e.g., Freeman 1970a) can be seriously in error. Figure 3 of Hamabe et al. (1980) provides another illustration. This shows hypothetical face-on profiles and their component parts for five edge-on galaxies. Here the geometry allows a clear separation of component properties. Hamabe et al. (1980) conclude that disks in galaxies such as NGC 3115 or NGC 5866 contribute so little light that the composite profile is scarcely distinguishable from an $r^{1/4}$ law. This is

necessarily true if the galaxy is very bright. A typical Freeman (1970a) disk with $B(0)_c \sim 21.65$ B_{μ} and $2 \leq \alpha^{-1} \leq 4$ kpc has an absolute B magnitude of -18.6 to -20.3 ($H_0 = 50$ km s^{-1} Mpc^{-1}). Apparently, the only way to make a galaxy much brighter than this is to add more bulge light. Very bright S0s whose disks barely perturb an $r^{1/4}$ law include NGC 524 (Kormendy 1977a), NGC 4636 (Kormendy 1977c), and NGC 4382 (King 1978). In these cases especially, but also in most fainter galaxies, it is necessary to decompose the observed profile into its intrinsic components (Kormendy 1977b; Tsikoudi 1977; Burstein 1979c,d).

The need for profile decomposition has been recognized in a few papers for some time (de Vaucouleurs 1958, 1975; van Houten 1961). However, the first systematic study of this procedure was made by Kormendy (1977b). Two different one-dimensional algorithms and two bulge fitting functions (Hubble and de Vaucouleurs) were used. The uncertainties were explored in some detail. Two conclusions emerged which were independent of the form of the fitting function.

First, the near-universality of $B(0)_c = 21.65 \pm 0.3$ (σ) B_{μ} observed by Freeman (1970a) is largely due to the contribution of the bulge. The underlying disk can be much fainter. This result was based on exponential fits to model galaxies composed of $r^{1/4}$-law bulges and exponential disks, each with a wide range of parameters. If the model disk had bright $B(0)_c$ or large α^{-1}, it dominated the profile, and the composite yielded the correct value of $B(0)_c$. However, if the disk was faint or small, then $B(0)_c$ measured mostly the bulge. When the brightness limit of the photometry was ~25-26 B_{μ}, the bulge itself had $B(0)_c \simeq 21.7$ to 22.1 B_{μ}. These results are confirmed by Burstein (1979c) for a sample of 12 normal S0s, and by Hamabe et al. (1979a) for the edge-on galaxy NGC 5866. (Note that the bulge does not dominate the disk parameters if the disk is bright enough or large enough: Kormendy [1977b], Burstein [1979c], and Hamabe et al. [1979b] all illustrate such galaxies.) None of this conflicts with conclusions about selection effects reached by Allen and Shu (1979; see also Disney 1976). In both cases the conclusion is that disks much brighter than 21.65 B_{μ} must be rare, because they would not have been missed. However, if

disks much fainter than $B(0)_c$ = 21.65 B_{μ} exist, then they should turn up as careful photometry and profile decomposition disentangle them from other components (Kormendy 1977b), and as deeper surveys find objects previously overlooked (Allen and Shu 1979). In fact, Bosma and Freeman (see Freeman 1980) have searched the UKSTU IIIa-J survey and found a distribution of $B(0)_c$ values peaked near 21.65 B_{μ}, but with a tail extending much fainter and with a large overall dispersion. Also, Burstein (1979c) found $B(0)_c$ values uniformly distributed between 20.1 and 22.1 B_{μ}. Thus everyone seems to be converging on the view that there is a concentration of central disk brightnesses at 21.65 B_{μ}, but that the dispersion is much larger than Freeman (1970a) found. Considerable further work is required to establish how galaxies populate the low-surface-brightness tail of this distribution.

Kormendy's (1977b) second main conclusion is illustrated in Figure 9. I Zw 21 is an S0 galaxy with a fairly strong bulge and a larger-than-average ratio of disk-to-bulge scale lengths (Kormendy 1977a). If the disk is assumed to

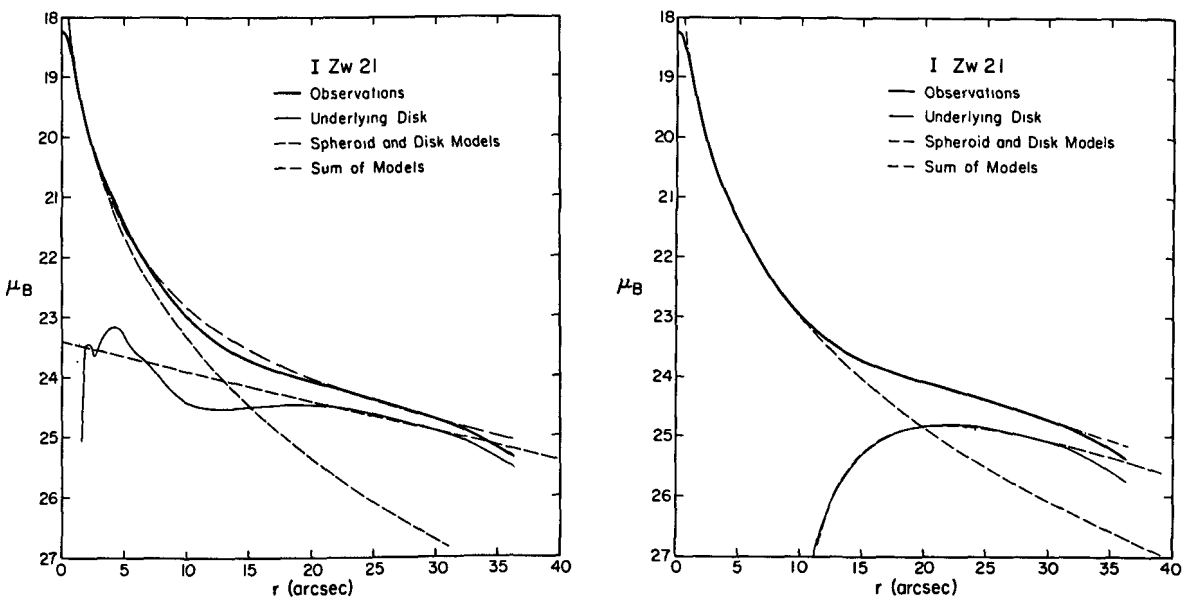

FIG. 9.— Decomposition of the profile of the S0 galaxy I Zw 21 from Kormendy (1977b). The bulge is assumed to satisfy an $r^{1/4}$ law. The disk is modeled at left by an exponential and at right by the cutoff exponential $I \propto \exp[-(\alpha r + \beta^3 r^{-3})]$. The light solid line is the underlying disk profile deduced by subtracting the bulge model from the observations. In both cases the fitting range excludes the transition region from bulge to disk (8".4 - 20" at left, 8".4 to 11".5 at right; see Kormendy 1977b for details of the fitting procedure). Both solutions imply that the disk has a central hole.

be exponential (left panel), then the best composite has too much light in the transition region between the components. We can subtract this excess light from either the bulge or the disk model. Dynamical and photometric arguments (Kormendy 1977b) suggest that the cutoff is in the disk. The right-hand panel then shows a decomposition made using a disk fitting function with an inner hole: $I(r) \propto \exp\ [-(\alpha r + \beta^3\ r^{-3})]$. It succeeds very well. The implication is that the disk has an inner cutoff, perhaps as much as a complete hole, perhaps only a turndown as in a Type II profile. Similar results were found for two other galaxies. In each case the underlying disks were broad plateaus with inner and outer cutoffs, i.e., above 25 B_μ they were nowhere exponential.

In an extensive study of normal S0 galaxies, Burstein (1979c) finds (1) that an exponential provides a good fit to the disk profile in each of 12 cases, and (2) that none of these profiles demands that the disk have a central cutoff. Kormendy (1977b) found a similar result in two galaxies with exponential disks. This suggests that only non-exponential disks have inner cutoffs; a possibility that needs to be tested with more data. Further results of Burstein's (1979c) study will be discussed in § IVe below.

A number of major studies are in progress to develop two-dimensional decomposition algorithms analogous to the above. The group of Hamabe, Kodaira, Okamura, and Takase are studying edge-on galaxies by applying empirical decompositions based both on fitting functions and on mass models. Their results on NGC 5866 (Hamabe et al. 1979a), NGC 4565 (Hamabe et al. 1979b), and a number of galaxies measured by other workers (Hamabe et al. 1980) have been discussed above and will be referred to further in § IVd. Boroson (1980) is applying two-dimensional decompositions to a sample of ~30 nearly face-on spirals ranging in type from S0/a to Sbc. He aims to derive bulge and disk parameters to compare to the S0 and E data discussed above. A further aim is to derive bulge ellipticities, again for comparison to ellipticals (cf. § III). Finally, bulge luminosities will allow a comparison of the metallicity-luminosity relation of bulges and ellipticals (see Faber 1977 for a review; Burstein 1979a).

This emphasis on profile decomposition is necessary if we are to make progress on composite systems. However, a few cautionary remarks should be made. (1) Since virtually no fitting function has a dynamical basis, and especially since we do not know what to expect when components interact, we should not interpret every deviation from a fitting function as evidence for a new component. For example, elliptical galaxies have taught us to expect that ellipsoidal components satisfy an $r^{1/4}$ law. But in a spiral galaxy the bulge must be affected by the disk potential (Freeman 1975a). Thus the failure of a bulge profile to fit an $r^{1/4}$ law is not necessarily evidence for a new component (Kormendy and Bruzual 1978), as interpreted by Tsikoudi (1977), Hegyi and Gerber (1977), and Hamabe et al. (1979b). Use of the terms "bulge" and "halo" for the segments of the NGC 4565 minor-axis profile is particularly unfortunate because of the extraneous connotations of the word "halo" (see Kormendy and Bruzual 1978 and § V). (2) There is a continuum of transition stars between any two components (Kormendy 1980a). This limits in principle the accuracy of any decomposition. (3) Whenever there are more than two components present, profile decomposition is extremely difficult. It is especially difficult when components are present which never occur in isolation (e.g., bars) and whose intrinsic profile shapes are therefore unknown. On the other hand, it is clear that components of significantly different structure exist and overlap (Kormendy 1980a). Thus some sort of decomposition is necessary. Two- and three-dimensional decomposition schemes offer considerable promise of further progress in separating out the properties of these features.

c) Oval and Non-Exponential Disks

I Zw 21 (Fig. 9) is an example of a galaxy whose disk is not exponential.[6] In this section we list a number of situations in which non-exponential disks are

---

[6]As Freeman (1978) points out, the disk may become exponential below the 25.5 B_μ limit of Kormendy's (1977a) photometry. However, this part of the profile is unlikely to contain a significant fraction of the total luminosity.

observed to occur, to emphasize the point that they are not rare (see also Kormendy 1977a; Burstein 1979b). In making this list we do not mean to imply that the types of galaxies listed are fundamentally different. A subset of the non-exponential disks turns out to be ovally distorted; photometric criteria for identifying ovals are also given.

1. Lenses are elliptical components occurring between the bulge and disk, which have very shallow brightness gradients interior to a sharp outer edge and then a steep outer gradient. Lens properties are discussed in Kormendy (1979). With a few exceptions, they are quite flattened, like disks (Kormendy 1977a, 1979; Freeman 1980). They are non-exponential by definition. However, they are components quite distinct from disks, whose properties are intimately connected with bars (Kormendy 1979) and therefore beyond the scope of this paper. We mention them because they are oval (Kormendy 1979) and because many kinds of non-exponential disks are superficially similar to lenses and should not be confused with them.

2. Early-type galaxies such as I Zw 21 often have disks with very shallow gradients and sharp outer edges. Other examples are given in Kormendy (1977b). Often these galaxies are barred and have lenses in addition to the non-exponential disks. Such disks were termed "outer lenses" in Kormendy (1979). Examples include NGC 936, 1302, 4596, and 5101.

3. Similarly, van der Kruit and Searle (1980) have shown that the disks of four late-type normal spirals have sharp outer edges in their light distributions at 3.5 to 5 scale lengths.

4. Certain global-pattern spirals with particularly strong spiral structure have prominently "Type II" profiles (Freeman 1970a). These include M51 (Schweizer 1976; Okamura, Kanazawa, and Kodaira 1976; Burkhead 1978) and M83 (Talbot, Jensen, and Dufour 1979). In the latter case Talbot, Jensen, and Dufour (1979) show that the Type II profile is produced by vigorous star formation in the inner disk; it is not known whether this explanation holds for other galaxies of this sort.

5. Filamentary-armed spirals (Kormendy 1979; Kormendy and Norman 1979) are often non-exponential. Examples from the Hubble Atlas are NGC 2775, the outer disk (not the ring) of NGC 4736 (Fig. 10), and especially NGC 7217 (Boroson 1980). These objects have profiles which to varying degrees resemble lenses (but are not lenses: NGC 2775 has a well-developed lens in addition to the filamentary-armed disk — see the Hubble Atlas).

NGC 4736 is particularly important because it is prototypical of an extremely interesting structure. Inside the nearly uniform disk, the brightness rises very steeply to one of the highest values observed in any galaxy (~15.0 V_μ at a seeing σ = 1".2, Mochnacki 1977). However, short-exposure plates show that the spiral structure extends to within a few arcseconds of the nucleus. This suggests that a hot component (bulge) does not dominate the light distribution at any radius. That is, the disk profile must turn steeply upward toward smaller radii. Once we admit the possibility that disks can rise toward smaller radii above an extrapolated exponential, how can we be sure that the features we see in S0 and Sa galaxies are always bulges? Clearly, we need more photometry to explore this problem.

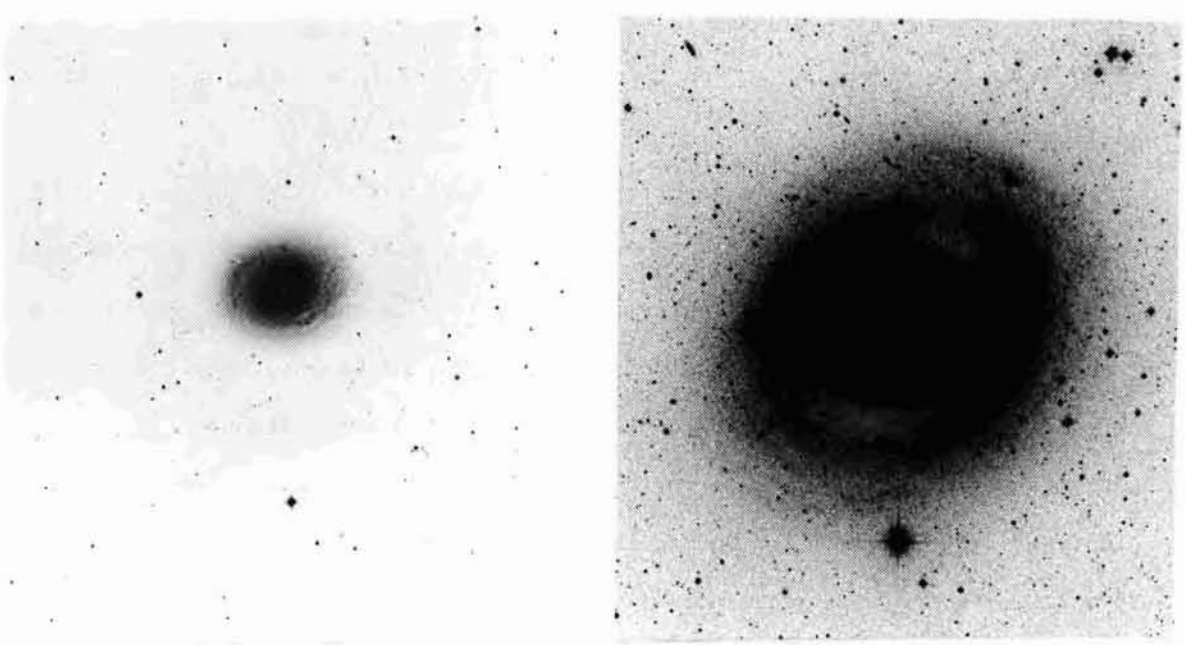

FIG. 10.— Short- and long-exposure photographs of the oval galaxy NGC 4736 taken with the Palomar Observatory 1.2 m Schmidt telescope. If the inner disk and outer ring are coplanar, they cannot both be round.

6. Oval disks form a subset of the non-exponential galaxies. An example is shown in Figure 10. Oval disks can be recognized by the following features (Kormendy 1979; Kormendy and Norman 1979). Like objects discussed above, their inner disks have a shallow brightness gradient and a sharp outer edge. Surrounding this is a fainter disk, or a faint ring, or a pair of spiral arms which almost close to form a pseudo-ring (i.e., the pitch angle of the arms becomes negative after $^1/_4$ revolution). Generally, the axial ratios and position angles of the inner disk and outer feature are different, implying that both features cannot be round. Kormendy (1979) showed that both inner and outer disks are usually oval. Photometry is not available for many oval disks, but examples illustrating the above features include NGC 4736 (Simkin 1967; Schommer 1977) and NGC 4258 (Capaccioli 1974; van der Kruit 1979).

Kinematic criteria for identifying oval disks are discussed by Bosma (1978; see also references in Kormendy and Norman 1979). The observed velocity field is symmetric about the nucleus, but the kinematic major axis changes position angle with radius. Generally, the optical and kinematic major axes are different. Finally, the kinematic major and minor axes are not perpendicular. Examples listed by Bosma include NGC 3198, 4236, 3359, 5383, 4258, 4151, 4736 (Fig. 10), and IC 342. The kinematic and photometric criteria for identifying ovals are in excellent agreement.

The origin of oval disks is not known. Binney (1978c) has suggested that oval distortions may result from the response of a disk to a triaxial dark halo (note that the disk can be self-gravitating as long as the triaxial perturbation of the halo is significant). Oval disks are important because they constitute (or else reflect) non-axisymmetric distortions in the gravitational potential. These distortions can produce a variety of effects analogous to those in barred galaxies (e.g., Kormendy and Norman 1979; Sanders and Tubbs 1979; see Kormendy 1980a for a review). Athanassoula (1979) has emphasized that other, less symmetric distortions can also have such effects; an example is M 101.

We conclude that while many disks are exponential a significant number show one or more non-exponential plateaus in their brightness profiles. We do not yet know how often this occurs or how to interpret its dynamical significance.

d) Thick Disks

We turn next to the structure of the disk perpendicular to its plane. Here an important recent result of studies of edge-on S0 galaxies is the recognition of a new component in the brightness distribution which Burstein (1979d) calls the "thick disk."

Preliminary evidence for thick disks is contained in Tsikoudi's (1977) photometry of the S0 galaxies NGC 3115, 4111, and 4762. Tsikoudi constructed plots at various distances from the center of surface brightness versus distance z from the plane. She reached the following conclusions. (1) All of the perpendicular profiles consisted of two segments, the outer one being shallower than the inner. (2) The outer segment was exponential to high accuracy and over a range of up to six scale lengths in z. In NGC 4762 it had a scale length of ~14" or ~1.5 kpc (H_0 = 50 km s^{-1} Mpc^{-1}). (3) It was possible to fit the inner segment with (the sum of the outer exponential and) one or two Gaussians. In NGC 4762 these had dispersions σ = 2".3 and 4".5 (0.25 kpc and 0.5 kpc), respectively. The Gaussian decomposition was made in analogy with population work in the Galaxy, in which the density distribution perpendicular to the plane is roughly Gaussian at small z and exponential higher up, with scale heights that depend on population (see Elvius 1965; Blaauw 1965 for reviews). It is not clear that "different" stellar populations are being separated by Tsikoudi's procedure, which may only be an operational way of describing the profile.

There are two main shortcomings to Tsikoudi's analysis. First, the contribution of the bulge was neglected. Second and more important, the effect of the disk being not quite edge-on was not estimated. Burstein (1979d) shows that only NGC 4762 of the galaxies studied is almost exactly edge-on. Thus we have quoted Tsikoudi's parameters only for NGC 4762. However, her important conclusions that the perpendicular profiles are composite and that the outer

segment is exponential are not affected by the above problems.

Burstein (1979d) has made a careful study of the z structure of five edge-on S0s measured in an earlier paper (Burstein 1979b). He made two-dimensional decompositions of the brightness distributions, using three-dimensional models of the structure (cf. § IVb). His conclusions can be summarized as follows. (1) In agreement with Tsikoudi (1977), the perpendicular profiles are rounded at small z, then become steep exponentials, and finally, are shallower exponentials at large z. This behavior is illustrated in Figure 11. (2) However, an infinitely thin exponential disk resembles the observed rounded exponential when seen nearly edge-on. Furthermore, the inner segment of the perpendicular profile ($\mu \leq$ 23.5 B_{μ}) is well fitted by a model consisting of a bulge and a highly inclined thin disk, whose parameters are taken from Burstein (1977c). (3) At large z, all of the perpendicular profiles deviate above the bulge-disk models. The shallower, outer exponential (Fig. 11) represents a new component with a scale height large enough so that the perpendicular profile measures its thickness.

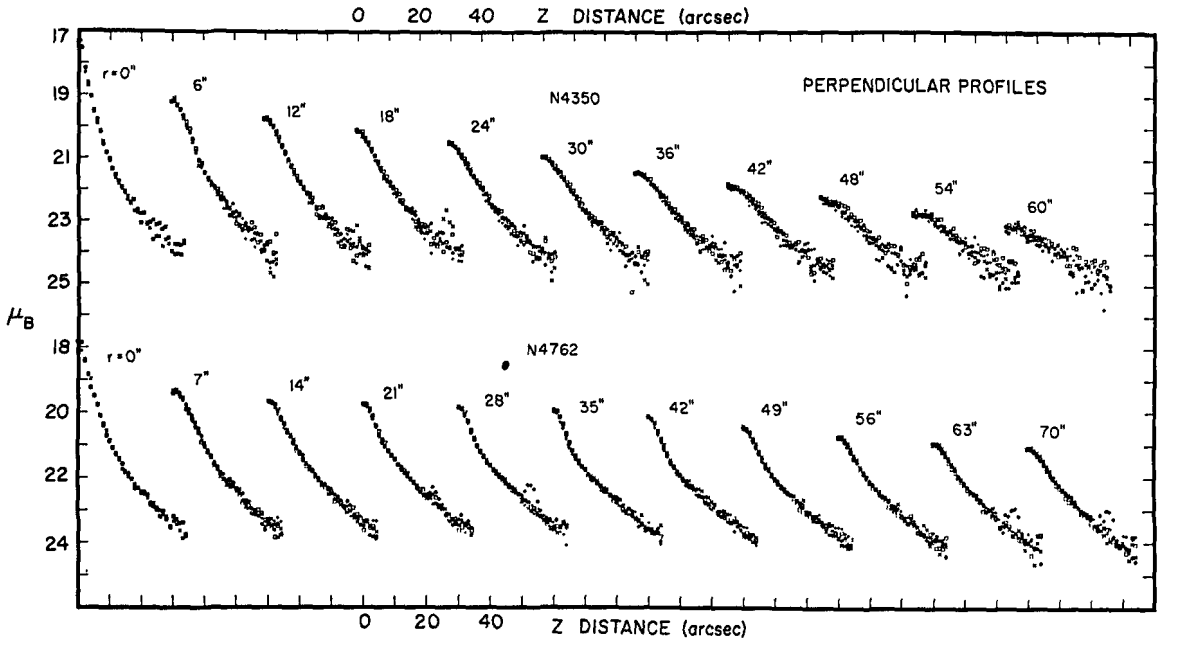

FIG. 11.— Brightness profiles in B mag arcsec^{-2} as a function of distance from the plane for two edge-on S0s from Burstein (1979d). Perpendicular profiles are shown at a number of distances r from the center, along the major axis. The shallow outer exponential represents the thick disk.

Burstein terms this the "thick disk." (4) Properties of thick disks include the following. They are intermediate in flattening between bulges and disks, i.e., E7-E8 compared with E9 or flatter for thin disks. Their brightness gradients parallel to the major axis are small, giving edge-on S0s a somewhat rectangular appearance on deep photographs (e.g., NGC 4762). (5) Burstein discusses evidence that thick disks are absent in spirals. He argues that this supports theories in which S0s form a transition stage between ellipticals and spirals, as opposed to "parallel sequence" theories in which many S0s are just spirals stripped of gas.

However, detailed studies of edge-on spirals show that thick disks are present in at least some spirals. Jensen and Thuan (1980) and van der Kruit and Searle (1980) both find that the Sb galaxy NGC 4565 has a thick disk, although one that is fainter than thick disks in S0s. Figure 12 shows how this thick disk dominates at moderately faint surface brightnesses. Similarly, van der Kruit and Searle (1980) detect a thick disk in the Sb galaxy NGC 891 which, like NGC 4565, has a significant bulge component. However, in two bulgeless Scs (NGC 4244 and 5907) they find no evidence for a thick disk.

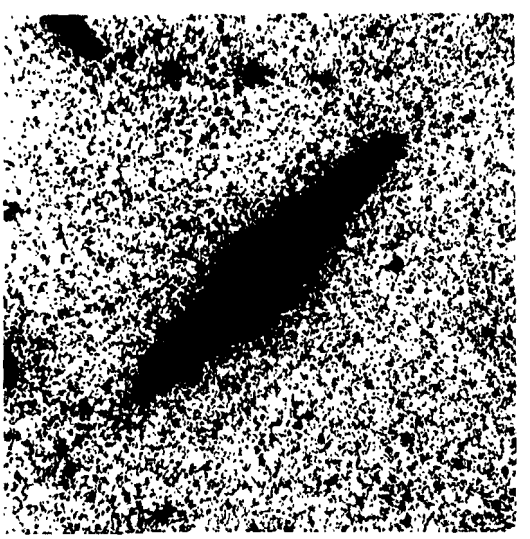

FIG. 12.— High-contrast, deep photograph of NGC 4565 from Jensen and Thuan (1980). The edge of the burned-out region is at ~24 $\frac{1}{2}$ $V\underline{\mu}$. At this surface brightness, the thick disk dominates so thoroughly that there is little sign of a bulge. However, at fainter brightness levels, the bulge has a shallow profile and is again visible. North is at right and east at the bottom. The scale is ~20" mm^{-1}.

As Burstein (1979d) points out, it is not clear whether thick disks are properly a part of the disk or of the bulge, or whether they are distinct components in the sense of Kormendy (1979, 1980a). However, at some level, the distinction is only semantic. To first order, thick disks seem to represent a distribution of stars intermediate in flattening between bulges and disks. As discussed in § III, Kormendy and Illingworth (1980) find that the rotation velocity in edge-on galaxies decreases smoothly with increasing z, with no sharp distinction between the components. That is, as z increases, there is a gradual decrease in rotational support in favor of the velocity dispersion. Thick disks may just represent the intermediate stages in this continuum of dynamical properties (see also van der Kruit and Searle 1980).

Despite this plausible picture, we still have too little data to know the role of thick disks in galaxy dynamics. We therefore need more photometry of edge-on galaxies, covering a larger range of Hubble types.

e) Bulge-to-Disk Ratios

The S0 morphological class was introduced by Hubble (Sandage 1961) as a transition stage between elliptical and spiral galaxies. A wide variety of S0 properties have since been found to bridge the gap in behavior between ellipticals and spirals; these include morphology (Sandage 1961, 1975), intrinsic shape (Sandge, Freeman, and Stokes 1970; de Vaucouleurs 1974), stellar and gaseous content (e.g., Faber and Gallagher 1976; Faber 1977; Burstein 1979a), mass-to-light ratios (Faber and Gallagher 1976, 1979), broad-band colors (Sandage and Visvanathan 1978), and brightness distributions (see earlier sections). Two alternative interpretations of S0 properties have been suggested (see Sandage and Visvanathan 1978 for a review). Parallel-sequence theories suggest that S0s are spirals that have been stripped of gas and dust by environmental processes; they now form a morphological sequence paralleling the classic Sa-Sb-Sc sequence (e.g., Gunn and Gott 1972; Biermann and Tinsley 1975; Gisler 1976; van den Bergh 1976; Gisler 1979 and references therein). Intrinsic-formation theories claim that the properties defining S0 galaxies were built in during galaxy formation

(e.g., Sandage, Freeman, and Stokes 1970). Sandage and Visvanathan (1978) point out two arguments that strongly favor the intrinsic-formation theories. First, there are many S0 galaxies outside of rich clusters, where environmental stripping processes are unlikely to operate. Second, bulge-to-disk ratios are generally higher in field S0s than in spirals. In particular, we do not know of any S0s with no bulge at all, corresponding to the spiral types Sc-Sm. The present section enlarges on this second point, which can now be made more quantitative through recent work by Burstein (1979c) and Dressler (1980a,b).

Burstein (1979c) has derived bulge-to-disk ratios B/D for 12 normal S0 galaxies by using a profile decomposition technique discussed in § IVb. Some ambiguity in B/D is introduced by the choice of fitting function, but few values are likely to be wrong by as much as a factor of 2, and most are much better than this. Only two galaxies are found to have B/D ratios differing from unity by more than a factor of 2. These are NGC 4459 ($B/D \sim 5$) and NGC 4762 ($B/D > 1/3$). That is, the bulge components in all of these S0s are far stronger than in Sc-Sm galaxies. This is true despite the fact that Burstein has chosen galaxies with a wide range of bulge strengths, and particularly favors small B/D values.

Burstein then makes a more specific comparison of S0 and spiral bulges, using a ratio of "bulge radius" to "disk radius," operationally defined from the brightness profile. This ratio can be defined in a consistent way for S0s and spirals, and includes corrections for effects of different stellar populations and internal extinction. The resulting approximate B/D ratios range from 0.2 to <0.07 for three Sc spirals. Nineteen S0 galaxies all have $B/D > 1/3$. If these S0s are typical, Burstein argues, then these results contradict predictions of the simplest parallel-sequence theories, at least in groups and loose clusters. Since S0 bulge-to-disk values can be arbitrarily large (see § IVb, Kormendy 1980a and references therein), they span the complete range between ellipticals and spirals. This is consistent with intrinsic-formation theories.

The above results leave open the plausible possibility that spiral stripping occurs only in rich clusters. To investigate these effects, Dressler (1980a,b)

has made a comprehensive study of 55 rich clusters, deriving positions, approximate total and "bulge" magnitudes, and morphological types for ~6000 galaxies. In particular, Dressler derives bulge magnitudes and indicative bulge-to-disk ratios for galaxies in 22 clusters. The results include the following (Dressler 1980b). (1) Bulge luminosities and B/D ratios are both higher in S0 galaxies than in spirals (cf. Burstein 1979c). This result might be consistent with parallel-sequence theories if there exists a selection effect such that small B/D spirals which are stripped fade below the magnitude limit of the survey. However, a 2 mag fading of the disk would be required, and then the luminosity functions of spirals and S0s would no longer be similar. This would then contradict observations. (2) The difference between S and S0 bulges is not a function of local galaxy density. At higher galaxy densities, the bulges of spirals and S0s are both brighter, but the difference between them is maintained. This argues against the view that disk sweeping takes place only in cluster cores. In particular, bulge-to-disk ratios increase with galaxy density, whereas sweeping would tend to produce small B/D systems in cluster cores where more late-type spirals are stripped. Altogether, the observations imply that ellipsoidal systems (E or bulge) are increasingly preferred over disk systems in the high-density environment of cluster cores. (3) Dressler therefore concludes that most S0s are not stripped spirals. To explain the prevalence of S0s in rich clusters, he suggests that disks take several billion years to form completely, presumably through infall. At higher galaxy densities, disk formation is halted sooner by collisions and by heating of the infalling gas. Thus he suggests that galaxies in rich clusters never acquired the interstellar medium and consequent star formation which we see in late-type spirals.

Although Dressler's arguments are persuasive, the conflict between intrinsic-formation and parallel-sequence theories is far from settled. The arguments on both sides range beyond the scope of this paper. Further arguments suggesting that S0 properties are intrinsic are given by Dressler (1980b). The alternative point of view is reviewed by Strom and Strom (1980), who note that

many of Dressler's observations may be explainable in parallel-sequence theories. For example, S0 galaxies may have larger B/D ratios than spirals because larger bulges produce more differential rotation, hence larger density-wave streaming, stronger shocks (as in Roberts, Roberts, and Shu 1975) and faster gas depletion. Thus Strom and Strom (1980) argue that spirals with larger bulges turn into S0s more rapidly. The difficulty is that the arguments on both sides are qualitative. Detailed theoretical development of these ideas is a formidable problem.

Probably both sets of theories are partly correct. It is difficult to maintain that all S0s are descendants of spirals when there exist isolated S0s like NGC 7457. It is equally difficult to believe that no S0s are stripped spirals when the evidence so strongly suggests that X-ray clusters contain abundant hot gas and an excess of S0s (Melnick and Sargent 1977; Dressler 1980b). There is no general agreement on how S0s between these extremes were formed. A clearly important next step is to make a concerted effort to find, particularly in rich clusters, S0 galaxies with virtually no bulge components but with luminosities comparable to those of field spirals.

f) Other Questions

As in § II, there are many important problems of disk photometry that we have had to omit. These include especially effects associated with spiral structure and star formation. For example, Schweizer (1976) has made a detailed study of disks in late-type galaxies, discussing the strength of spiral-arm star formation, showing that the arm amplitude increases with radius, and uncovering the density wave in the underlying disk. A further study of spiral-structure star formation has been made by Talbot, Jensen, and Dufour (1979). They show that the "Type II" profile of M83 is produced by young stars; the old disk is exponential. Both studies searched for population gradients across arms, which would suggest the passage of a density wave that triggers star formation. Such tests are difficult because the spiral structure is rather irregular even in these best cases. Another problem involves exploring the observational

implications of the stochastic-star-formation theory of spiral structure, and especially the question of distinguishing stochastic spirals from density waves (Gerola and Seiden 1978; Seiden, Schulman, and Gerola 1979; Seiden and Gerola 1979). Finally, there has been almost no work on filamentary-armed galaxies (Sandage 1961, 1975; Kormendy 1977d; Kormendy and Norman 1979). Since these lack density waves, they provide a much needed contrast to global-pattern spirals.

A second class of problems involves bars and other flat components associated with them (lenses, inner rings, and outer rings). All of these features are triaxial and therefore can interact and produce secular evolution in galaxy dynamics. These problems are discussed by Kormendy (1979, 1980a).

V. DARK HALOS

The evidence is now strong that at least the outer parts of galaxies are dominated by a hot, dark component which we call the halo (see Faber and Gallagher 1979 for a review). To what extent the halo affects the dynamics of the visible galaxy is unknown. One extreme point of view (White and Rees 1978) suggests that visible galaxies are formed entirely of residual gas falling into the previously formed potential well of the halo. Binney (1978c) has further explored a model in which this halo is so dominant that the disk is not self-gravitating. This model may explain warps and oval disks. However, other observations are difficult to understand if disks consist of test particles. For example, Freeman (1978) points out that exponential perpendicular profiles of disks (Tsikoudi 1977; Burstein 1979d) are naturally interpreted as isothermal sheets dominated by a disk potential. This explanation is untenable if the disk is massless. Second, the systematic behavior of the structure of barred galaxies is naturally explained by the effect of the bar on the disk and bulge; this includes the existence and properties of rings and triaxial bulges (see Kormendy 1979, 1980a for reviews). It is not easy to invoke the halo as the "engine" producing this structure: if the halo is formed without dissipation (White and Rees 1978), then it cannot have small-scale structure similar to the bar in these galaxies. Finally, if the disk is not self-gravitating, it becomes impossible to

interpret spiral structure as a self-sustained density wave. The considerable success of the current density-wave picture is uncomfortably accidental if it has really neglected the fact that the spiral structure is purely kinematic and forced by the halo. Thus the view that the disk is not self-gravitating may be too extreme.

On the other hand, it is equally clear that the halo is not negligible over the optical galaxy. It is easy to show (e.g., Spinrad et al. 1978) that a flat rotation curve in a spherical galaxy with profile $I \propto r^{-2}$ implies a mass-to-light ratio which grows linearly with radius. Constant rotation also implies an increasing M(r)/L(r) if the visible galaxy is an exponential disk (see Freeman 1970a). Since most galaxies have flat rotation curves (e.g., Bosma 1978; Rubin, Ford, and Thonnard 1978), mass-to-light ratios must generally be increasing with radius. There are now many detections of this increase. For example, Spinrad et al. (1978; see also Davis, Feigelson, and Latham 1979) show that the local M/L increases in NGC 4565 from $\sim 10^{0.5}$ near the center to $10^{2.5} - 10^{3}$ at 50 kpc radius. Schweizer (1978a) finds that the M/L within radius r increases in NGC 4594 by a factor of 4 between 2 and 15 kpc radius. Bosma and van der Kruit (1979) find that the local M/L increases by more than an order of magnitude over the disks for 12 of 13 spirals studied. In each case the mass-to-light ratio of the disk alone may (or may not) also be increasing. Finally, a detailed model of our Galaxy (Bahcall and Soneira 1980) also has a local M/L which increases with radius.

Naturally, there has been great interest in trying to detect this halo optically. For example, Hegyi and Gerber (1977) have developed a photoelectric photometer specifically designed for faint photometry. Their remarkably faint measurements of NGC 4565 are incorporated in Figure 7. Both Hegyi and Gerber (1977) and Davis, Feigelson, and Latham (1979) find weak evidence for redder colors at larger radii, which is consistent with the presence of late-type stars of large M/L. However, this does not establish that optical tracers of the dark halo have been detected. Kormendy and Bruzual (1978) have discussed the

interpretation of brightness profiles with respect to detection of halos as a new component (as in White and Rees 1978). Essentially, we look for departures from an "expected" profile and attribute these to tracers of the halo. However, we argued in § III that bulges are different from ellipticals, and so we do not *a priori* know what to expect of them. Kormendy and Bruzual (1978) concluded that the minor-axis profile of NGC 4565 refers only to the bulge; its peculiarities reflect the differences between bulges and ellipticals and not the halo. There may well be a population change at large radii, but halos seem to be important at all radii, including ones where (for example) bulges vary little in color. Altogether, with one possible exception, there is no evidence that we have ever seen stars belonging to the halo of any galaxy (Kormendy and Bruzual 1978; Spinrad *et al.* 1978).

The possible exception is NGC 253. This is a highly inclined Sc galaxy without an obvious bulge (see the Hubble Atlas). Spinrad *et al.* (1978) detect a faint envelope of light, rounder than the disk and visible out to r > 13 kpc on the minor axis (the major-axis 25 B_μ isophote is at 14.6 kpc radius [de Vaucouleurs, de Vaucouleurs, and Corwin 1976]). There is marginal evidence that the color becomes bluer at larger radii (opposite to the sense of any color gradient in NGC 4565). The interpretation of this observation is unclear. However, it emphasizes the obvious fact that optical searches for halos are favored in edge-on galaxies which do not have bulges. It would be very valuable to have more deep photometry of such objects.

A number of models have been made to explore or constrain the halo population (e.g., Dekel and Shaham 1979; Bahcall and Soneira 1980). All of these can produce large M/L values at large radii. The comparison of models to real galaxies suffers from a lack of good color data. The annular scanning photometer of Hegyi and Gerber (1977) and the grid-photometry technique of Davis, Feigelson, and Latham (1979) are both specifically designed for this difficult work. For example, a very sensitive color measurement would be possible using grid photometry and an emulsion sensitive to both bandpasses. Three alternating bands

could be used, one to monitor sensitivity variations and the others for the two colors. Accurate data on color gradients at faint light levels are urgently needed; with the techniques available, the measurements will hopefully be made soon.

Meanwhile, it is worth stressing that there is a more fundamental aim to this work than just finding high-M/L material. We are really trying to distinguish between two rather different theories of galaxy formation. (There are also intermediate points of view [e.g., Ostriker and Thuan 1975; Gunn 1977], but we will focus on the extremes for clarity.) A classical view might be that there is undetected dark material associated with the bulge and disk. This is certainly true in the vicinity of the Sun (Oort 1960; see Bahcall and Soneira 1980 for a recent discussion). There is considerable freedom to enrich the luminosity function at the faint end; Dekel and Shaham (1979) use this approach to suggest that the NGC 4565 halo is dominated by faint stars and nonluminous "Jupiters." That is, the luminosity function and mass-to-light ratio of the visible components may vary with radius. The current observations may be detecting this increase of M(r)/L(r), which helps to provide the mass required by dynamical observations. In contrast, the alternative picture of White and Rees (1978) views the halo as a distinct component, whose formation process is different from that of the visible galaxy. Such a halo is probably hot. Its mass distribution is not directly tied to the visible matter. If this view is correct, then there is no evidence that we have optically detected the halo (see above). Merely finding evidence for high-M/L stars at large radii does not prove that a new component is involved. What is needed is a clear test to distinguish between these theories of galaxy formation, or (more realistically) to find out where between these extremes the truth lies.

VI. CONCLUSION

The photometric studies of galaxy formation and structure which we have reviewed are basically of two kinds. One technique is basically phenomenological

in exploiting the regularities observed in brightness distributions. It looks for deviations from these regularities and then interprets them in terms of physical processes. Examples include the results on tidal effects in § IId, and on the differences between bulges and ellipticals in § III. This technique has been quite successful; it benefits from the fact that the regularities do not need to be explained. More fundamental are the investigations which establish the basic patterns (such as the rough constancy of $B(0)_c$, or the B_e-log r_e relation for ellipticals), and try to use them to deduce the physics of galaxy formation. Here we recall particularly the pioneering studies of Fish (1964) and Freeman (1970a). These uses of surface photometry are still at an early stage. For many years, the barrier to progress was a lack of data. Current technology allows us to very rapidly gather the data we need. The length of this paper reflects the considerable progress which has been made using such photometry. Hopefully, we will soon have still more data which can put meaningful constraints on theories of galaxy formation.

I am most grateful to the many people who have sent preprints, have allowed me to reproduce figures, or have agreed to let me discuss their work before publication. They are far too many to be named individually, but they can be identified from the references. I would also like to thank Drs. D. Burstein and S. E. Strom for valuable discussions.

REFERENCES

Aaronson, M., Mould, J., Huchra, J., Sullivan, W., Schommer, R., and Bothum, G. 1980, submitted to Ap. J.
Aizu, K. 1979, preprint.
Allen, R. J., and Shu, F. H. 1979, Ap. J., 227, 67.
Athanassoula, E. 1979, Ann. Phys. Fr., 4, 115.
Bahcall, J. N., and Soneira, R. M. 1970, Ap. J., in press.
Barbon, R., Benacchio, L., and Capaccioli, M. 1976, Astr. Ap., 51, 25.
Barbon, R., and Capaccioli, M. 1975, Astr. Ap., 42, 103.
Barbon, R., Capaccioli, M., and Tarenghi, M. 1975, Astr. Ap., 38, 315.
Bertola, F., and Capaccioli, M. 1977, Ap. J., 211, 697.
Biermann, P., and Tinsley, B. M. 1975, Astr. Ap., 41, 441.
Binney, J. 1976, M.N.R.A.S., 177, 19.
———. 1978a, M.N.R.A.S., 183, 501.
———. 1978b, Comments Ap., 8, 27.

———. 1978c, M.N.R.A.S., 183, 779.
Blaauw, A. 1965, in Galactic Structure, Stars and Stellar Systems, 5, ed. A. Blaauw and M. Schmidt (Chicago: University of Chicago Press), p. 435.
Boroson, T. A. 1980, in preparation.
Bosma, A. 1978, Ph.D. Thesis, Rijksuniversiteit te Groningen.
Bosma, A., and van der Kruit, P. C. 1979, Astr. Ap., 79, 281.
Brandt, J. C., Kalinowski, J. K., and Roosen, R. G. 1972, Ap. J. Suppl., 24, 421.
Burkhead, M. S. 1978, Ap. J. Suppl., 38, 147.
———. 1980a, in Proceedings of Conference on Photometry, Kinematics and Dynamics of Galaxies, ed. D. S. Evans, in press.
———. 1980b, in preparation.
Burkhead, M. S., and Kalinowski, J. K. 1974, A.J, 79, 835.
Burstein, D. 1979a, Ap. J., 232, 74.
———. 1979b, Ap. J., Suppl. 41, 435.
———. 1979c, Ap. J., in press.
———. 1979d, Ap. J., in press.
Capaccioli, M. 1974, Cont. Oss. Astr. Asiago, No. 301.
———. 1979, Trans. IAU. 17A, 27.
Carter, D. 1978, M.N.R.A.S., 182, 797.
Davis, M., Feigelson, E., and Latham, D. W. 1979, preprint.
Dekel, A., and Shaham, J. 1979, Astr. Ap., 74, 186.
de Vaucouleurs, G. 1948, Ann. d'Ap., 11, 247.
———. 1953, M.N.R.A.S., 113, 134.
———. 1958, Ap. J., 128, 465.
———. 1959, Handbuch der Physik, 53, 311.
———. 1974, in IAU Symposium No. 58, The Formation and Dynamics of Galaxies, ed. J. R. Shakeshaft (Boston: Reidel), p. 335.
———. 1980, in Proceedings of Conference on Photometry, Kinematics and Dynamics of Galaxies, ed. D. S. Evans, in press.
de Vaucouleurs, G., de Vaucouleurs, A., and Corwin, H. G. 1976, Second Reference Catalogue of Bright Galaxies (Austin: University of Texas Press).
Disney, M. J. 1976, Nature, 263, 573.
di Tullio, G. A. 1979, Astr. Ap. Suppl., 37, 591.
Dressler, A. 1980a, Ap. J. Suppl., in press.
———. 1980b, Ap. J., in press.
Efstathiou, G., and Jones, B. J. T. 1979, M.N.R.A.S., 186, 133.
Elvius, T. 1965, in Galactic Structure, Stars and Stellar Systems, 5, ed. A. Blaauw and M. Schmidt (Chicago: University of Chicago Press), p. 41.
Faber, S. M. 1973, Ap. J., 179, 423.
———. 1977, in The Evolution of Galaxies and Stellar Populations, ed. B. M. Tinsley and R. B. Larson (New Haven: Yale University Observatory), p. 157.
Faber, S. M., and Gallagher, J. S. 1976, Ap. J., 204, 365.
———. 1979, Ann. Rev. Astr. Ap., 17, 135.
Fish, R. A. 1964, Ap. J., 139, 284.
Freeman, K. C. 1970a, Ap. J., 160, 811.
———. 1975a, in IAU Symposium No. 69, Dynamics of Stellar Systems, ed. A. Hayli (Boston: Reidel), p. 367.
———. 1975b, in Galaxies and the Universe, Stars and Stellar Systems, 9, ed. A. Sandage, M. Sandage, and J. Kristian (Chicago: University of Chicago Press), p. 409.
———. 1978, in IAU Symposium No. 77, Structure and Properties of Nearby Galaxies, ed. E. M. Berkhuijsen and R. Wielebinski (Dordrecht: Reidel), p. 3.
———. 1980, in Proceedings of Conference on Photometry, Kinematics and Dynamics of Galaxies, ed. D. S. Evans, in press.
Gerola, H., and Seiden, P. E. 1978, Ap. J., 223, 129.
Gisler, G. R. 1976, Astr. Ap., 51, 137.
———. 1979, Ap. J., 228, 385.
Gott, J. R. 1975, Ap. J., 201, 296.
Gunn, J. E. 1977, Ap. J., 218, 592.

Gunn, J. E., and Gott, J. R. 1972, Ap. J., 176, 1.
Gutowski, W. J., and Larson, R. B. 1976, Pub. A.S.P., 88, 374.
Hamabe, M.,Kodaira, K., Okamura, and Takase, B. 1979a, Pub. A.S. Japan, 431 in press.
————. 1979b, Pub. A.S. Japan, in press.
————. 1980, in Proceedings of Conference on Photometry, Kinematics and Dynamics of Galaxies, ed. D. S. Evans, in press.
Hausman, M. A., and Ostriker, J. P. 1978, Ap. J., 224, 320.
Hegyi, D. J., and Gerber, G. L. 1977, Ap. J. (Letters), 218, L7.
Hodge, P. W., and Michie, R. W. 1969, A.J., 74, 587.
Hoessel, J. G. 1980, Ph.D. Thesis, California Institute of Technology.
Hubble, E. 1930, Ap. J., 71, 231.
Illingworth, G. 1977, Ap. J. (Letters), 218, L43.
Illingworth, G., Schechter, P. L., and Gunn, J. E. 1980, in preparation.
Jensen, E. B., and Thuan, T. X. 1980, in preparation.
King, I. 1962, A.J., 67, 471.
King, I. R. 1966, A.J., 71, 64.
————. 1978, Ap. J., 222, 1.
King, I. R., and Kiser, J. 1973, Ap. J., 181, 27.
Knobloch, E. 1978, Ap. J., 222, 779.
Kormendy, J. 1977a, Ap. J., 214, 359.
————. 1977b, Ap. J., 217, 406.
————. 1977c, Ap. J., 218, 333.
————. 1977d, in The Evolution of Galaxies and Stellar Populations, ed. B. M. Tinsley and R. B. Larson (New Haven: Yale University Observatory, p. 131.
————. 1979, Ap. J., 227, 714.
————. 1980a, in Proceedings of Conference on Photometry, Kinematics and Dynamics of Galaxies, ed. D. S. Evans, in press.
————. 1980b, to be published.
————. 1980c, in preparation.
Kormendy, J., and Bruzual A., G. 1978, Ap. J. (Letters), 223, L63.
Kormendy, J., and Illingworth, G. 1980, in preparation.
Kormendy, J., and Norman, C. A. 1979, Ap. J., 233, 539.
Lake, G. 1980, in Proceedings of Conference on Photometry, Kinematics and Dynamics of Galaxies, ed. D. S. Evans, in press.
Larson, R. B. 1974, M.N.R.A.S., 166, 585.
Lynden-Bell, D. 1967, M.N.R.A.S., 136, 101.
Marchant, A. B., and Olson, D. W. 1979, Ap. J., 230, L157.
Melnick, J., and Sargent, W. L. W. 1977, Ap. J., 215, 401.
Mestel, L. 1963, M.N.R.A.S., 126, 553.
Miller, R. H., and Smith, B. F. 1980, Ap. J., 235, in press.
Mochnacki, S. W. 1977, Ph.D. Thesis, University of British Columbia.
Norman, C. A., and Silk, J. 1980, in preparation.
Oemler, A. 1973, Ap. J., 180, 11.
————. 1976, Ap. J., 209, 693.
Okamura, S. 1977, Ann. Tokyo Astr. Obs., 16, 111.
Okamura, S., Kanazawa, T., and Kodaira, K. 1976, Pub. A.S. Japan, 28, 329.
Oort, J. H. 1960, Bull. Astr. Inst. Netherlands, 15, 45.
Ostriker, J. P. 1977, in The Evolution of Galaxies and Stellar Populations, ed. B. M. Tinsley and R. B. Larson (New Haven: Yale University Observatory), p. 369.
Ostriker, J. P., and Thuan, T. X. 1975, Ap. J., 202, 353.
Prendergast, K. H., and Tomer, E. 1970, A.J., 75, 674.
Press, W. H., and Schechter, P. 1974, Ap. J., 187, 425.
Pritchet, C. 1979, Ap. J., 231, 354.
Reynolds, J. H. 1913, M.N.R.A.S., 74, 132.
Richstone, D. O. 1975, Ap. J., 200, 535.
————. 1976, Ap. J., 204, 642.
————. 1979, Ap. J., 234, in press.

———. 1980, in Proceedings of Conference on Photometry, Kinematics and Dynamics of Galaxies, ed. D. S. Evans, in press.
Roberts, W. W., Jr., Roberts, M. S., and Shu, F. H. 1975, Ap. J., 196, 381.
Rood, H. J. 1965, A.J., 70, 689.
Roos, N., and Norman, C. A. 1979, Astr. Ap., 76, 75.
Rubin, V. C., Ford, W. K., and Thonnard, N. 1978, Ap. J. (Letters), 225, L107.
Saito, M. 1979, Pub. A.S. Japan, 31, 181.
Sandage, A. 1961, The Hubble Atlas of Galaxies (Washington, DC: Carnegie Institution of Washington.)
———. 1975, in Galaxies and the Universe, Stars and Stellar Systems, 9, ed. A. Sandage, M. Sandage, and J. Kristian (Chicago: University of Chicago Press), p. 1.
Sandage, A., Freeman, K. C., and Stokes, N. R. 1970, Ap. J., 160, 831.
Sandage, A., and Visvanathan, N. 1978, Ap. J., 225, 742.
Sanders, R. H., and Tubbs, A. D. 1979, preprint.
Sargent, W. L. W., Young, P. J., Boksenberg, A., Shortridge, K., Lynds, C. R., and Hartwick, F. D. A. 1978, Ap. J., 221, 731.
Schommer, R. A. 1977, Ph.D. Thesis, University of Washington.
Schweizer, F. 1976, Ap. J. Suppl., 31, 313.
———. 1978a, Ap. J., 220, 98.
———. 1978b, in IAU Symposium No. 77, Structure and Properties of Nearby Galaxies, ed. E. M. Berkhuijsen and R. Wielebinski (Dordrecht: Reidel), p. 279.
———. 1980, Ap. J., in press.
Seiden, P. E., and Gerola, H. 1979, Ap. J., 233, 56.
Seiden, P. E., Schulman, L. S., and Gerola, H. 1979, Ap. J., 232, 702.
Sharp, N. A., Lin, D. N. C., and White, S. D. M. 1979, M.N.R.A.S., 187, 287.
Simkin, S. M. 1967, A.J., 72, 1032.
Spinrad, H., Ostriker, J. P., Stone, R. P. S., Chiu, L.-T. G., and Bruzual, A., G. 1978, Ap. J., 225, 56.
Strom, K. M., and Strom, S. E. 1978a, A.J., 83, 73.
———. 1978b, A.J., 83, 1293.
———. 1980, in Proceedings of Conference on Photometry, Kinematics and Dynamics of Galaxies, ed. D. S. Evans, in press.
Strom, K. M., Strom, S. E., Jensen, E. B., Moller, J., Thompson, L. A., and Thuan, T. X. 1977, Ap. J., 212, 335.
Strom, S. E., and Strom, K. M. 1978c, A.J., 83, 732.
———. 1978d, Ap. J. (Letters), 225, L93.
———. 1979, A.J., 84, 1091.
Talbot, T. J., Jensen, E. B., and Dufour, R. J. 1979, Ap. J., 229, 91.
Thuan, T. X., and Gott, J. R. 1977, Ap. J., 216, 194.
Thuan, T. X., and Kormendy, J. 1977, Pub. A.S.P., 89, 466.
Toomre, A. 1977, in The Evolution of Galaxies and Stellar Populations, ed. B. M. Tinsley and R. B. Larson (New Haven: Yale University Observatory), p. 401.
Tsikoudi, V. 1977, Pub. Dept. Astr. Univ. Texas, No. 10.
van Albada, T. S., and van Gorkom, J. H. 1977, Astr. Ap., 54, 121.
van den Bergh, S. 1976, Ap. J., 206, 883.
van der Kruit, P. C. 1979, Astr. Ap. Suppl., 38, 15.
van der Kruit, P. C., and Searle, L. 1980, in Proceedings of ESO Workshop on Two-Dimensional Photometry, ed. P. O. Lindblad and P. Crane, in press.
van Houten, C. J. 1961, Bull. Astr. Inst. Netherlands, 16, 1.
White, S. D. M. 1978, M.N.R.A.S., 184, 185.
White, S. D. M., and Rees, M. J. 1978, M.N.R.A.S., 183, 341.
Wielen, R. 1977, in The Evolution of Galaxies and Stellar Populations, ed. B. M. Tinsley and R. B. Larson (New Haven: Yale University Observatory), p. 397.
Williams, T. B., and Schwarzschild, M. 1979a, Ap. J., 227, 56.
———. 1979b, Ap. J. Suppl., 41, 209.
Wilson, C. P. 1975, A.J., 80, 175.
Young, P. J., Sargent, W. L. W., Kristian, J., and Westphal, J. A. 1979, Ap. J., 234, 76.

Young, P. J., Westphal, J. A., Kristian, J., Wilson, C. P., and Landauer, F.P. 1978, Ap. J., 221, 721.

ARE ELLIPTICAL CLUSTER GALAXIES ASYMMETRIC AS A RESULT OF THEIR PECULIAR VELOCITIES?

J.B.G.M. Bloemen, Sterrewacht, Leiden
E.A. Valentijn, ESO, Geneva

Abstract

Astroscan microdensitometry tracings are reported for a sample of elliptical galaxies which are known to possess a radio tail. The direction of the radio tails is used to search for optical asymmetries in the same direction, under the hypothesis that the radio tails indicate the projected direction of motion of the galaxies. As a control test the direction perpendicular to the direction of motion has been investigated. Results are presented for a subsample of 13 galaxies, measured both on the red and the blue PSS glass copies. In eight out of the thirteen galaxies investigated in at least one colour, a significant (> 2.5 σ) asymmetry has been noted.

1. INTRODUCTION

Bertola and Perola (1973) have noticed an optical asymmetry in the outer regions of the two elliptical cluster galaxies NGC 1265 and NGC 7720. These authors observed an elongation of the optical images of these two galaxies, which pointed in the same direction as their associated head-tail radio sources 3C 83.1B and 3C 465. Since the direction of the radio tails is supposed to indicate the projected direction of motion of the parent galaxy, the observed asymmetries might also result from the peculiar velocities of these galaxies through their clusters.

However, individual cases are uncertain. Large-scale plate non-uniformities or superimposed stars could have caused the asymmetries observed. For that reason we have defined a statistical sample (Section 2), which we traced with the Leiden Observatory Astroscan microdensitometer on the PSS glass copies. Here we present the results of this 'pilot' survey (Section 6). A description of the measurements (Section 3) and the data reduction (Section 4) are given. Electrographic measurements of the E0 or S0 galaxy NGC 4881 by Ables and Ables (1972) were used for calibration (Section 5).

2. DEFINITION OF THE SAMPLE

The head-tail radio galaxies are unique in giving us information on the projected direction of motion of their parent galaxy. From a compilation of 44 head-tail radio galaxies (Valentijn, 1979) we have defined a subsample of 17 galaxies

with a $m_v \leq 15^m.0$. The original list is expected to be *optically* unbiased, and we refer to Valentijn (1979, Section 4), for a description of the selection effects present in this sample.

The galaxies of our sample are listed in Table 1. Four of these have been omitted in our analysis, since the galaxy images were too confused by superimposed stars (A 690/B2 0836 + 29, A 695/B2 0838 + 32A, A 1656/5C 4.81, and A 2151/NGC 6061).

3. THE MEASUREMENTS AND THE PLATE MATERIAL

The 17 galaxies were traced with the Astroscan microdensitometer of the Leiden Observatory, using both the red and the blue Palomar Sky Survey glass copies. The parameters of the measurements are listed in Table 2. The use of the PSS enabled us to deal with a set of homogeneous data, in red and blue, and has also some important particular advantages:

- low-density large-scale non-uniformities (generally density fluctuations smaller than 0.005 in a scanned area of 10 × 10 mm^2);
- almost equal photographic contrast for each plate, ($\gamma \simeq 1.8$, Minkowski and Abell, 1963) important for our calibration, Section 5;
- very small, saturated central galaxy regions (important for the determination of the centre positions of the galaxies).

Problems arising from the use of the PSS glass copies are:

- the plates are not extremely deep;
- there is the possibility of light-scattering during the plate copying process.

Table 2. Measuring parameters

Grid point distance	10 μ
Area scanned	5 × 5 or 10 × 10 mm^2
Repetition factor	8
Number of Reticon diodes used	100

4. DATA REDUCTION

The Astroscan measurements were transformed on-line to densities, using calibration measurements on neutral density filters. The resulting data arrays have been transformed to the WSRT data format in order to make use of the Westerbork Radiotelescope reduction packet. The following programs have been used:

- convolution program: to increase the signal-to-noise ratio, the data arrays were convolved with a Gaussian profile (FWHP = 6 arc sec), which results in a

gain of about one magnitude for a similar signal-to-noise ratio of extended low-surface brightness regions;

- program that makes contours and half-tone pictures to identify stars;
- data-print program to estimate background densities and to determine the centre position of the galaxies from an interpolation of the central densities (accuracy about 10 μ, or 0.67");
- program to translate the data from a rectangular to a circular grid, with the origin on the centre of the galaxy.

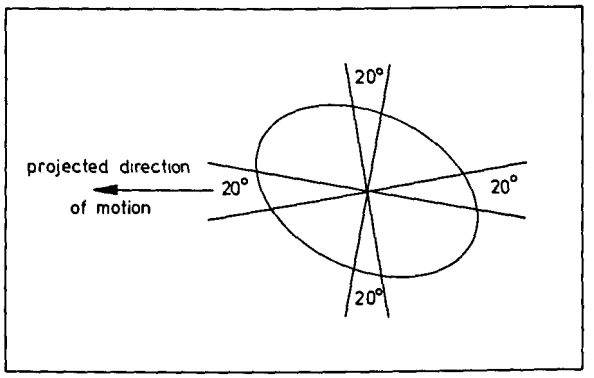

Fig. 1 Sketch of chosen cones in a galaxy image, as used in the APL program (Section 4).

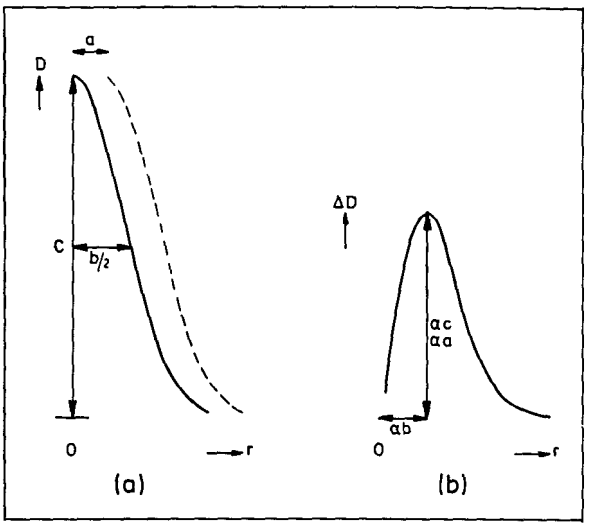

Fig. 2 a) Parameters of a Gaussian galaxy profile in central regions (density).
b) Residues caused by the position error of the centre.

An interactive APL program was written to search for asymmetries in the radial density distribution of each galaxy. In this program four cones, each of 20 degrees, were chosen: two opposite cones along the projected direction of motion and two perpendicular to this direction (see Fig. 1). Five radii were taken in each cone, and those data points influenced by foreground stars have been deleted. By means of the weighted addition of the five radii of a cone, a mean radial density distribution has been produced for each cone. Mean radial density distributions of two opposite cones were folded and subtracted. The residual density values were inspected for large-scale plate fluctuations, remnants of star profiles, and the effects of the error in the determination of the actual centre of the galaxy. Assuming a Gaussian galaxy density profile in the central galaxy region, the artificial residues caused by the position error of the centre can be predicted. The position of the largest density residue depends only on the FWHP of the Gaussian profile, and the value of this residue depends on the position error of the centre

and the central density of the galaxy above the background density (Fig. 2). Every residue found was checked to see whether it could have resulted from the position error in the centre which was found to be generally smaller than 1".

When the residues cannot be explained by the effects described above, we will call the galaxy image asymmetric and we will refer to the *additional* structure in the galaxy image which makes it asymmetric as an "asymmetry".

5. CALIBRATION

In order to have a feeling for the surface brightness levels we are dealing with, and for the B-V colour index of the asymmetries, we have made an indicative magnitude calibration.

For this calibration we have used the E0 or S0 galaxy NGC 4881. The reduction as described in Section 4 was also done for this galaxy. We have compared our radial density distribution, measured on the red and on the blue plate, with the radial surface brightness distribution obtained by Ables and Ables (1972) from combined photoelectric and electromagnetic measurements. Assuming V-R ≃ 0.4 (B-V = 1.05 for NGC 4881) for elliptical and lenticular galaxies (de Vaucouleurs, 1961), we can calibrate from density measurements in the R band to surface brightness values in V. The characteristic curve of our radial density distribution of NGC 4881 versus μ_B and μ_V is shown in Figs. 3 and 4. The lowest surface brightness part, above the background level of the two curves (μ_B > 27 mag arc sec^{-2} and μ_V > 26 mag arc sec^{-2}) is caused by the convolution of data points at μ_B = 27 and μ_V = 26 mag arc sec^{-2}, respectively, which is about the real limit in surface brightness of this survey.

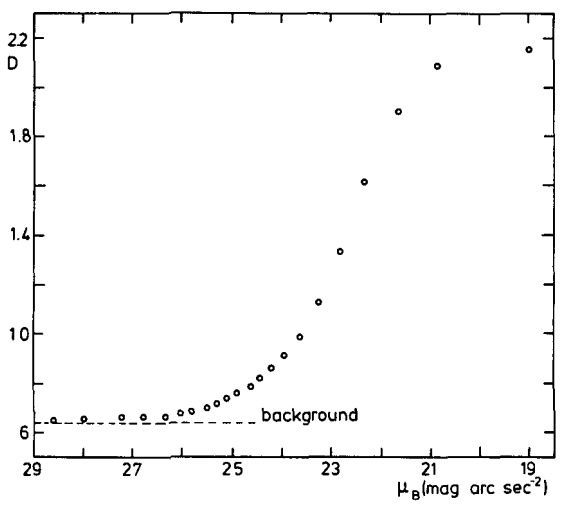

Fig. 3 Characteristic curve of density (convolved with a FWHP = 6 arc sec Gaussian function) versus surface brightness μ_B from NGC 4881 (Ables & Ables, 1972).

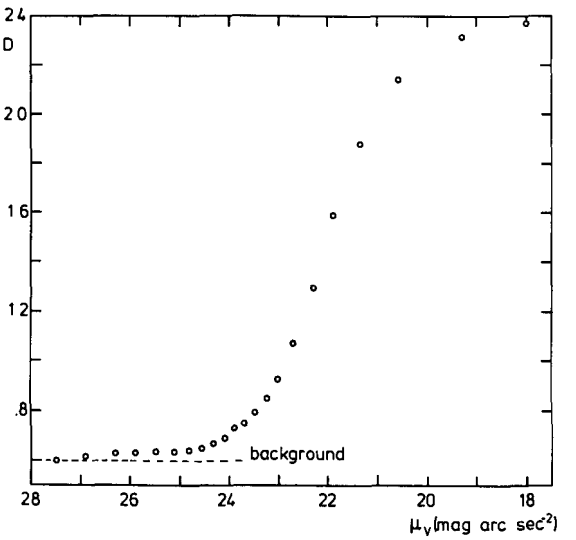

Fig. 4 Characteristic curve of density (convolved with a FWHP = 6 arc sec Gaussian function) versus surface brightness μ_V from NGC 4881 (Ables & Ables, 1972).

Table 1. Results of folding and subtracting cones for 13 elliptical cluster galaxies

(1)	(2)	(3)	Blue				Red				(12)	(13)
			(4)	(5)	(6)	(7)	(8)	(9)	(10)	(11)		
		(degrees)	(arc sec)	(D)	(D)	(σ)	(arc sec)	(D)	(D)	(σ)		
A 426	IC 310	40	80-180	0.004	0.014	< 1	80-180	0.005	0.010	< 1		Too marginal to determine colour
	0314 + 41W	220					20-40	0.014	0.010	2		
	NGC 1265	180	40-125	0.014	0.007	2	40-125	0.004	0.005	2.5	(0.0)	Red magnitude uncertain, so colour uncertain
A 1190	B2 1108 + 41	0	15-30	0.024	0.004	11						
A 1314	IC 708	100										Blue not measured
	IC 711	130	20-45	0.022	0.004	11					< 0.2	
A 1367	3C 264	210	55-195	0.011	0.006	7	30-240	0.020	0.004	20	1.6	Along major axis; enhancement to NW
A 2022	B2 1502 + 28	200					10-45	0.014	0.005	6		
A 2151	NGC 6034	90										
A 2199	3C 338	0/180	25-90	0.012	0.002	12	20-125	0.035	0.008	9	1.7	
A 2634	3C 465	40	40-180	0.025	0.012	10	40-180	0.032	0.006	20	1.0	
Zw.1615.8	4C 30.40	150										
Zw.2247.3	4C 11.71	50	120-275	0.010	0.007	7	120-260	0.012	0.008	7	1.0	
A 690	B2 0836 + 29											Too many stars superimposed on the galaxy
A 695	B2 0838 + 32A											
A 1656	5C 4.81											
A 2151	NGC 6061											

Assuming the slope γ of the characteristic curve to be nearly the same for each plate, the characteristic curves can be shifted for different density background levels. To test our calibrations, we compared the B-V for each galaxy, determined from our calibration curves, with the expected colour excess of about 1.0. In this way we were able to estimate the uncertainty of the calibration, which is about 0.3 mag arc sec^{-2}.

6. RESULTS

The results for the 13 galaxies are summarized in Table 1. With the exception of 3C 264, the data are from the two cones along the projected direction of motion. For 3C 264 the data from the cones along the major axis (angle of the major axis and the projected direction of motion is about 60°) are given. For the other twelve galaxies, the results from the cones perpendicular to the projected direction of motion are not included, since no asymmetries were found in that direction. The results in Table 1 are presented in the following format:

Columns 1 and 2 : The cluster and the radio source or galaxy names.

Column 3 : Position angle of the direction of motion. For 3C 264 the data listed are from cones along a line with p.a. = 150°.

Columns 4 and 8 : Limits of the region where an asymmetry has been found, measured from the centre of the galaxy in arc sec.

Columns 5 and 9 : The mean density of an asymmetry, i.e. the mean of the density residues in the region where an asymmetry was found.

Columns 6 and 10: Standard deviation σ of the background fluctuations in the particular area of the plate scanned with the Astroscan, which is the maximum of either the macro- or the micro-noise (density units).

Columns 7 and 11: Significance of the asymmetry in terms of signal-to-noise ratios, where the value of the noise was taken from columns 6 and 10 and taking into account the size (i.e. number of resolution elements) of the region in which the asymmetry was observed.

Column 12 : Indicative (B-V) colour excess of the asymmetries, uncertainty $\sim$ 0.4 magnitude.

Column 13 : Remarks.

The density residues are shown in Fig. 5. Positive residues are consistent with an excess of light on the "backside" of the galaxy. Remarks on the results of individual galaxies are given in the Appendix. The surface brightness

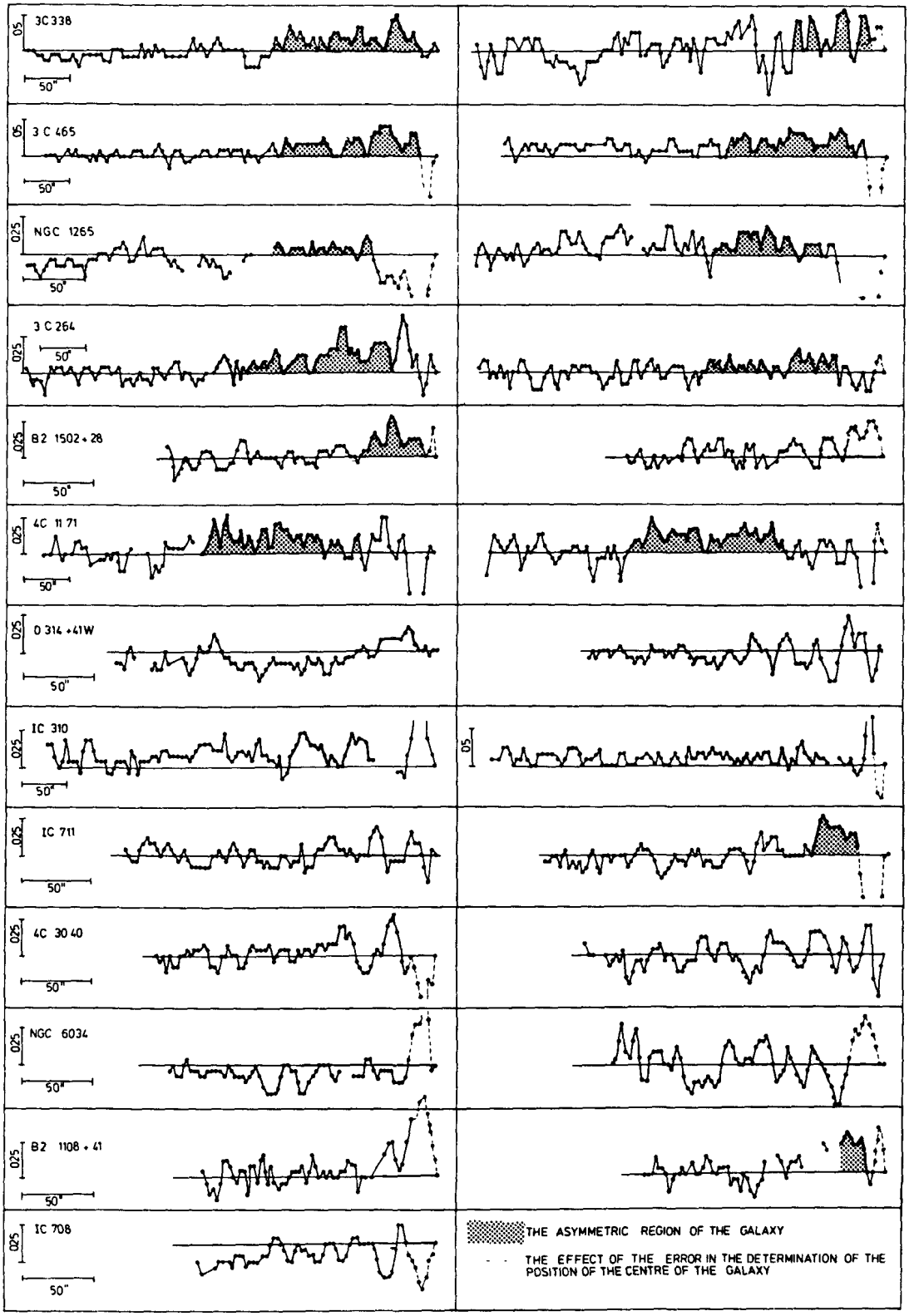

Fig. 5 Density residues in the Red (left) and the Blue (right). A positive residue means an excess of the optical light distribution opposite to the projected direction of motion. The centre of the galaxy is to the right. Suspected asymmetric regions ($S > 2\ \sigma$) are shaded.

of the asymmetries (i.e. the excess of light) varies between 26 and 28 mag arc sec^{-2} in the B-band and between 25 and 27 mag arc sec^{-2} in the visual. The asymmetries were superimposed on the galaxy halos with surface brightness levels typically ranging from μ_B = 24 mag arc sec^{-2} to μ_B = 26 mag arc sec^{-2} and from μ_V = = 23 mag arc sec^{-2} to μ_V = 25 mag arc sec^{-2}.

To summarize the results, we consider both the individual and the statistical significance of the asymmetries.

A subdivision of the individual significances is given in Table 3. In eight out of the thirteen galaxies an asymmetry (positive residue) has been found with a significance $\geq$ 2.5 σ in at least one colour.

Table 3. Significances (S) of the asymmetries found

Galaxy	Significance Red	Significance Blue
3C 338	$S \geq 2.5\ \sigma$	$S > 2.5\ \sigma$
3C 465		$S > 2.5\ \sigma$
NGC 1265		$0.5 < S < 2.5\ \sigma$
3C 264		$S > 2.5\ \sigma$
B2 1502 + 28		$S = 0$
4C 11.71		$S > 2.5\ \sigma$
0314 + 41W	$0.5 < S < 2.5\ \sigma$	$S = 0$
IC 310		$0.5 < S < 2.5\ \sigma$
IC 711	$S = 0$	$S > 2.5\ \sigma$
IC 708		Not measured
4C 30.40		$S = 0$
NGC 6034		$S = 0$
B2 1108 + 41		$S > 2.5\ \sigma$

From the addition of all the different foldings we have made, we can reach the following conclusions:

i) In the direction perpendicular to the projected direction of motion no asymmetries have been noted. There is one exception, 3C 264. Here the asymmetry has been found along the major axis of the galaxy image, which makes an angle of 60° with the projected direction of motion.

ii) For the 25 foldings along the direction of motion (13 red and 12 blue), we find:

- 12 cases (including 3C 264) with an asymmetry (positive residue) with a significance $\geq$ 2.5 σ;

- 4 cases with an asymmetry (positive residue) with a marginal significance between 0.5 σ and 2.5 σ;
- 9 cases without asymmetry;
- the number of positive residues (12 + 4) compared with the number of negative residues (three, NGC 1265 and IC 708; which were actually identified with remnants of stars) suggests that any random effect which might produce the asymmetries (background non-uniformities, low-brightness stars, centre choice) is very unlikely to have caused the observed asymmetries;

- In four cases the asymmetries were found to have a red colour; their B-V values range from 1.0 to 1.7. For IC 711 an upper limit of B-V < 0.2 has been found, and this galaxy is considered to be significantly exceptional in that it has a blue asymmetry.

The present work suggests a large-scale trend for elliptical galaxies to have an asymmetry correlated with their peculiar velocity. We note that Baggio et al. (1978) have shown that the velocity distribution of head-tail radio sources is not different from other cluster galaxies. Hence there is no *a priori* reason why the asymmetries should show up more clearly in a sample of head-tail galaxies than in any other sample of rich-cluster elliptical galaxies. In all probability most observers who studied the surface brightness distribution of elliptical galaxies either did not look for this kind of asymmetry or did not believe them. A further extensive study on this subject will be necessary.

Acknowledgements

The authors wish to thank R.S. Le Poole for many stimulating discussions, the complete Astroscan team for taking care of the smooth running of the device, and B. Jones for helpful comments on the manuscript.

REFERENCES

Ables, H.D., Ables, P.G.: 1972, Astron. J. 77, 642.

Baggio, R., Perola, G.C., Tarenghi, M.: 1978, Astron. Astroph. 70, 303.

Bertola, F., Perola, G.C.: 1973, Astrophys. J. 14, L7.

Minkowski, R.L., Abell, G.O.: 1963, Stars and Stellar Systems III, The National Geographic Society Palomar Observatory Sky Survey, 481.

Valentijn, E.A.: 1979, Astron. Astrophys. 78, 367.

de Vaucouleurs, G.: 1961, Astrophys. J. Suppl. 5, 233.

Appendix: REMARKS ON INDIVIDUAL GALAXIES

A426/IC310: star superimposed about 20″ from centre to the SW; large background fluctuations (0.014 D/10 × 10 mm^2); many confusing surrounding stars.

A426/NGC 1265: remnants of two star flanks in the region 20″-40″ from the centre to the S; many surrounding stars, especially in the region from 120″-350″ to the N.

A1190/B2 1108 + 41: in the blue residues diagram, star remnant at about 34″ from the centre to the S.

A1314/IC708: no residue measurements done in the B; star at about 36″ from the centre to the E; star at about 27″ from the centre to the W; background seems not to be uniform because of a nearby galaxy (about 2 arc min).

A1367/3C 264: along direction of motion (p.a. = 210°) no asymmetry found; enhancement to the NW along the major axis.

A2022/B2 1502 + 28: small remnant of a star flank in the blue, 20″ from the centre to the N.

A2151/NGC 6034: situation confused by stars, especially in the blue residues diagram; stars at 30″ and 55″ from the centre to the SW.

A2199/3C 338: wide-angle (opening angle = 160°) head-tail radio source; direction of motion not clear, either to the N or to the S; enhancement to the S; close double galaxy (distance < 13″) E-W; remnants of companion galaxy at 125″-140″ to the S.

A2634/3C 465: double galaxy, in blue background fluctuation of 0.12 D.

Zw. 1615.8/4C 30.40: stars superimposed on galaxy: difficult to subtract.

Zw. 2247.3/4C 11.71: enhancement in outer halo; galaxy seems to possess an optical tail (about 0.010 D above background level); star superimposed 25″ to the NE.

SURFACE PHOTOMETRY IN THE 30 DORADUS REGION

J.V. Feitzinger, Th. Schmidt-Kaler
Astronomical Institute
Ruhr-University
P.O. box 10 21 48
D-4630 Bochum 1
BRD

The 30 Doradus nebula in the Large Magellanic Cloud (LMC) is a supermassive, supergiant HII region. Assuming a distance of 56 kpc its optical diameter is 240 pc, with a bright central region of 25 pc radius. This inner part contains approximately $5 \cdot 10^5$ $M_\odot$ of ionized gas; the stellar mass is estimated at roughly $5 \cdot 10^6$ $M_\odot$.

30 Doradus is a unique, active object; we called it the activity center of the LMC (for a compilation of basic data compare Dufour, 1976 and Schmidt-Kaler and Feitzinger, 1976).

The areas of interest in this region are manifold and compiled in Tab. 1. Surface photometry is a cornerstone in understanding this and similar HII regions and gives a direct opportunity to answer some of the tabulated problems.

Tab. 1 Areas of interest

a) Exciting stars
   Star formation
   stellar associations and populations

b) Energy balance

c) Velocity fields
   Stellar winds

d) Dust properties
   Absorption features
   Scattering and polarization
   Magnetic fields

e) Emissionlines in different parts of the nebula

f) Radio, IR, EUV, X-Ray sources

g) Relation of the nebula to other main structural features of the LMC (spiral arm filaments)

Structure of the nebula

The structure of the nebula has been investigated by several authors (see Table 2). Despite the great diversity of observing methods there is at the moment no unified picture of the nebula deducable. Especially the results concerning the extinction law are contradictory. In the same way the velocity structure of the nebula is not at all clearly understood.

Fig. 1 shows the 30 Doradus region (Meaburn, 1979). The picture gives a section of a print of a 5h Hα+ NII photograph with the 1.2 m UK Schmidt camera that has been copied at high contrast through an unsharp mask. The many filaments of extremely faint nebulosity surrounding the 30 Doradus nebula are clearly seen. The whole complex has a diameter of approximately 2000 pc. Compared to the optical diameter of 240 pc this shows again the exceptional structure of this region. This is further illustrated by fig. 2, where the surface brightness in the light of Hß (Strauss et al. 1979) of the inner part of the nebula is given.

The nebula is the starting point of spiral filaments (Schmidt-Kaler 1975, Schmidt-Kaler and Isserstedt, 1976, Schmidt-Kaler, 1977) of the extremely young ($< 10^7$ years) populations of the LMC. These spiral arm filaments may be interpreted as the result of stochastic self-propagating star formation (Feitzinger et al. 1980; compare also Gerola and Seiden 1978, 1979). In fig. 3 the result of one of the model calculations is shown. The typical structure of the short, narrow and straight or abruptly curved spiral arm filaments found in the LMC is well reproduced. Surface photometry on larger scales with appropriate resolution ($\lesssim 1'$) will make it possible to check these models further.

Fig. 4 (Cantò et al. 1979) and fig. 5 (Feitzinger et al. 1979) reveal the inner part of the nebula (diameter 50 pc), with the central object R 136. Fig. 5 was obtained with the 3.9 m Anglo-Australian telescope (f/15) at λ 5007 Å ([OIII], $\Delta\lambda$ = 10 Å) and is a positive-masked print, where information at low frequences is filtered out (Malin 1977, 1978). Fig. 5 was obtained in the prime focus of the 3.6 m ESO telescope (f/11) at the wavelength 6563 Å (Hα, $\Delta\lambda$ = 220 Å) and was not further treated. The large scale features of the central region are clearly depicted, especially the relationship of ionized material to adjacent neutral absorbing globules and filaments. Many emission knots can be seen. The whole region is dominated by the central object R 136. It is surrounded by a shell-like structure with a radius of almost 40" (10 pc).

Tab. 2 A Selection of Studies of the 30 Doradus Region

(further references can be found in the literature cited)

Author	Method	Result
Doherty et al. 1956	objective prism photographs near H_α	intensity profiles
Faulkner 1967	red sensitive photographs	Balmer line isophotes; absorption
Davies et al. 1976	H_α photographs	over all structure of the nebula complex
Elliot et al. 1977	narrow band filter photographs; spectra	structure of the nebula core; comparison with the optical line splitting region;
Meaburn 1979	high contrast printing and mask techniques	detection of filaments of extremely faint nebulosity; cylindrical shells
Cantó et al. 1979	photographic unsharp mask techniques	structure of the nebula core
Strauss et al. 1979	photoelectric scanning techniques	Balmer line isophotes; strong absorption gradient across the nebula
Smith, Weedman 1972	Fabry-Perot interferograms	velocity structure
Borgman, Danks, 1977 Danks 1977	photoelectric spot photometry	extinction law
Koornneef 1978	area integrated EUV photometry	
Carruthers, Page 1977, 1978	EUV surface photography	surface brightness
Nandy et al. 1979 Nandy, Morgan 1978	EUV photometry IUE spectra	surface brightness, colour excess, extinction law
de Boer et al. 1979	IUE spectra	velocity structure
Werner et al. 1978 Hyland et al. 1978	IR photometry	surface brightness 2μ sources of inner region
Blades 1979	spectra	velocity structure
Mills et al. 1978	synthesis radio telescope observation	nebula structure; extinction

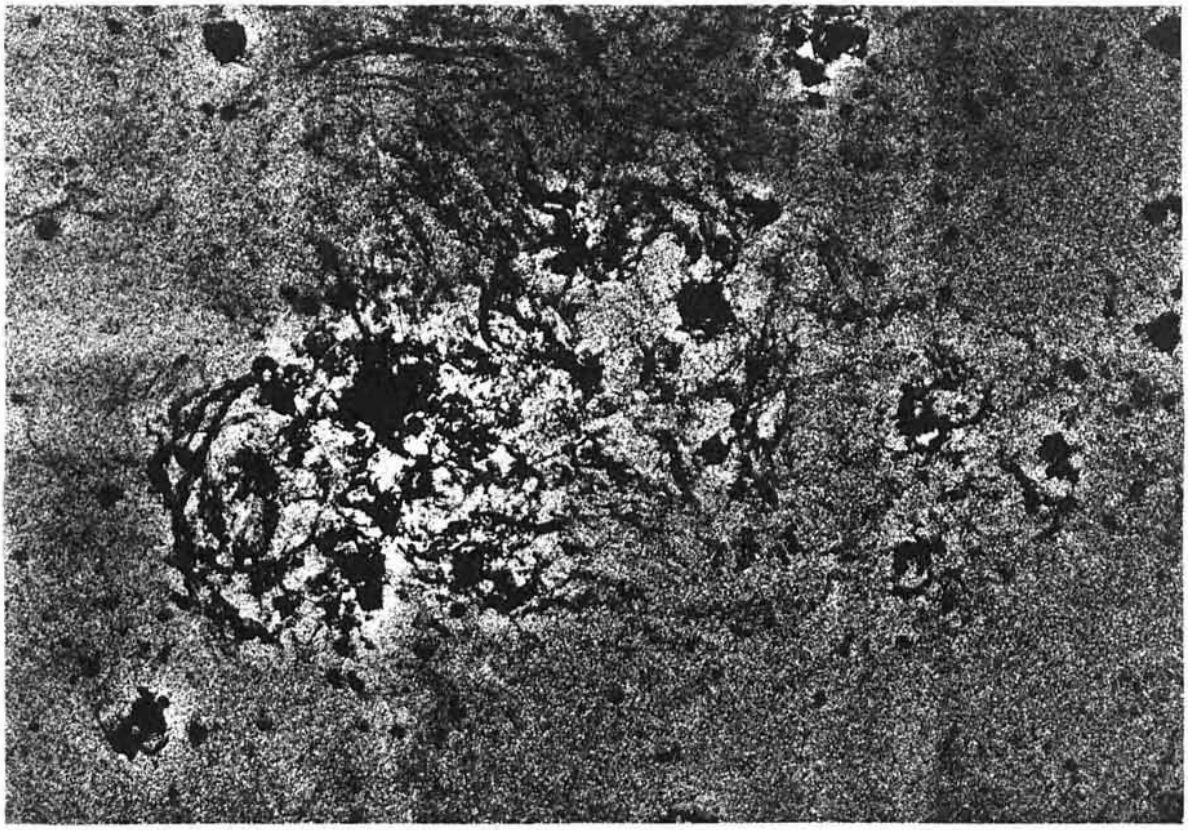

Fig 1 The 30 Doradus region in Hα . High contrast copy through an unsharp mask (Meaburn 1979)

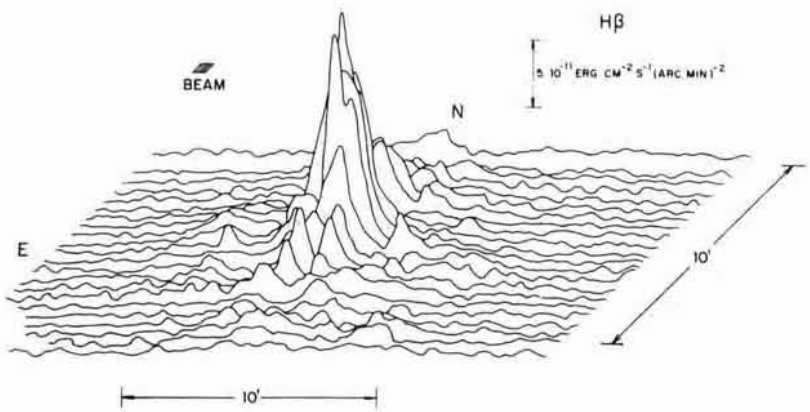

Fig. 2 The Hß photon count of 30 Doradus measured through a 30" x 30" square aperture (Strauss et al. 1979).

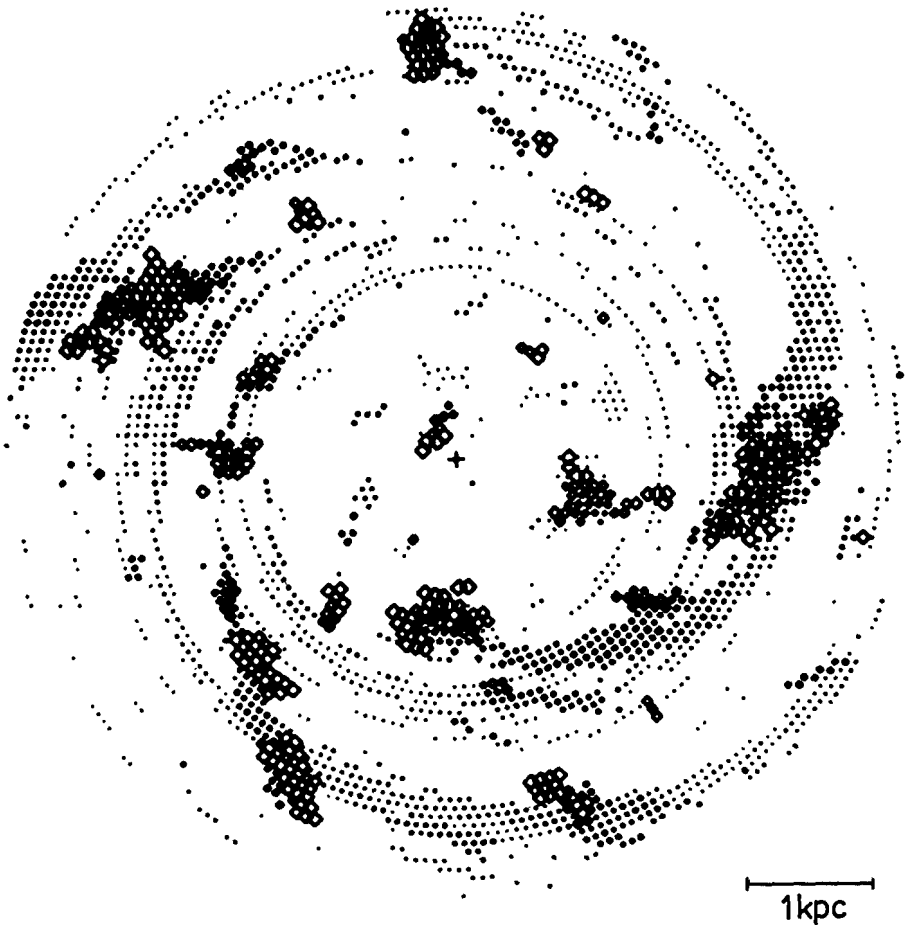

Fig. 3 Spiral arm filaments (B-band) according to an model of stochastic self-propagating star formation; LMC parameters are used (Feitzinger et al. 1980)

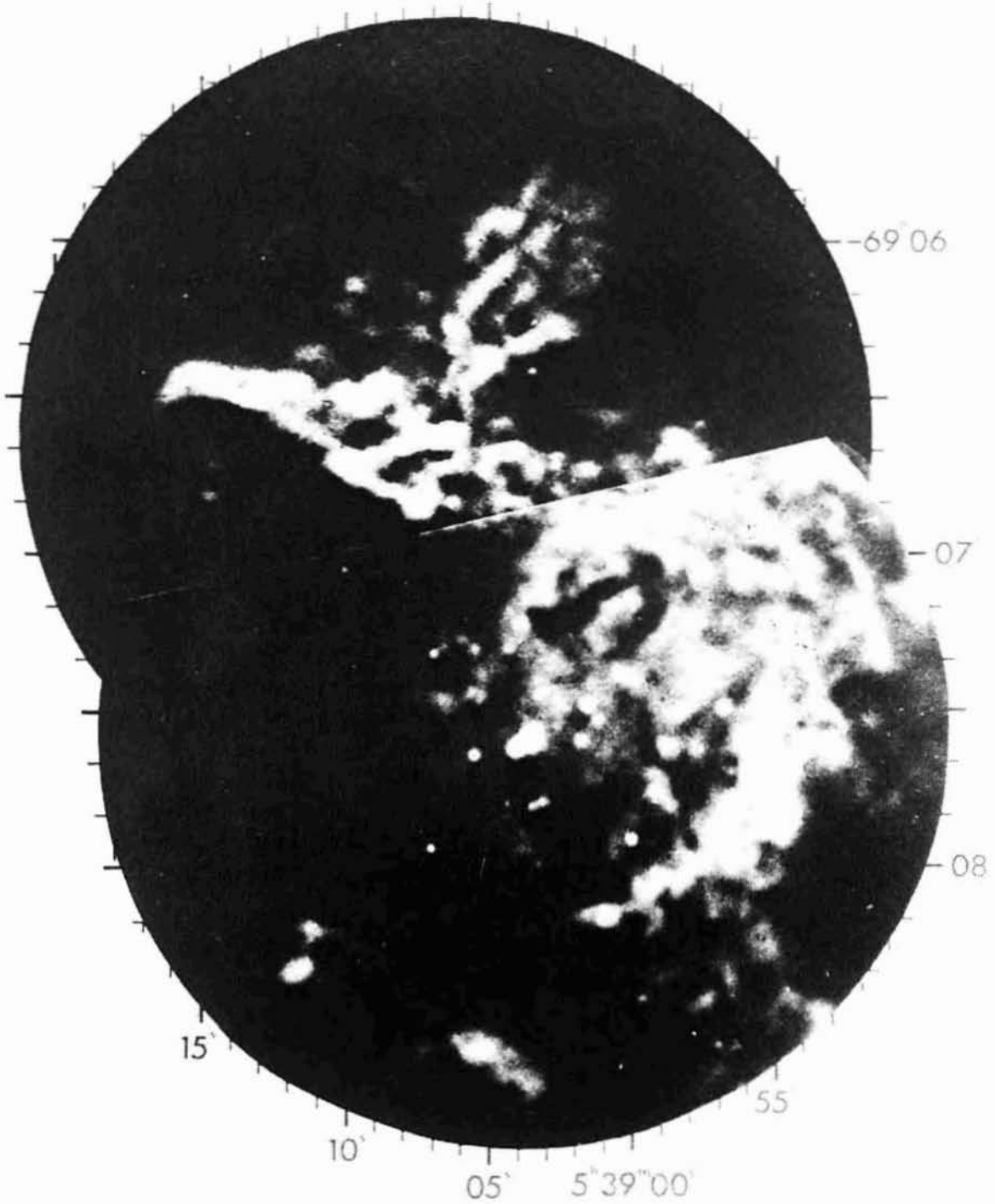

Fig. 4 Inner part of the 30 Doradus nebula obtained with 3.9 m Anglo-Austr. telescope. Positive masked print (5007 Å, [O III], Cantò et al. 1979)

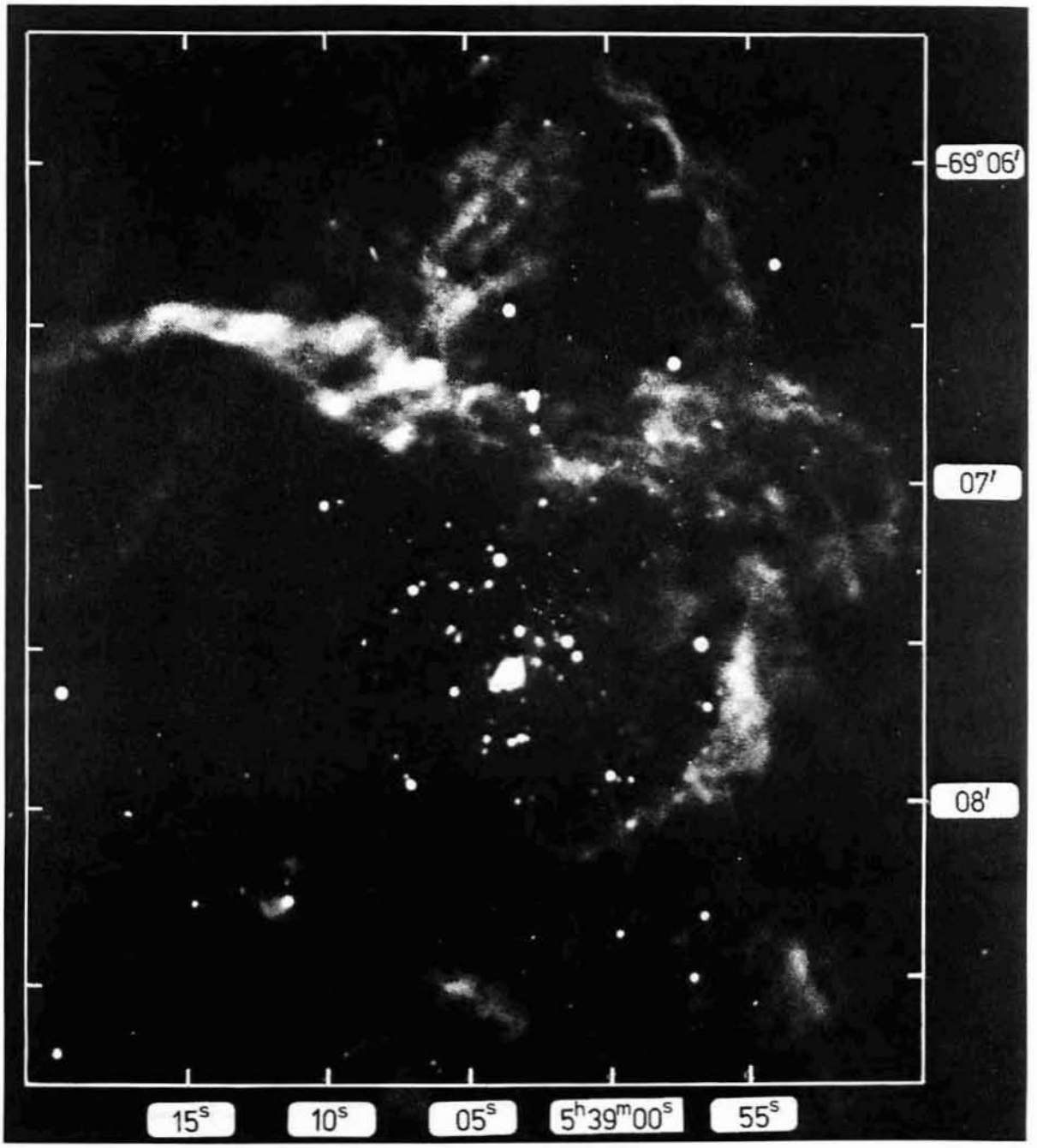

Fig. 5 Inner part of the 30 Doradus nebula. Untreated print of an H_α photograph obtained with the 3.6 m ESO telescope (Feitzinger et al. 1979).

The central object R 136

The structure of the central object can best be studied by image analysis methods (Feitzinger and Schlosser, 1978; Feitzinger et al. 1979), since often digitized pictures make a physical interpretation easier. In fig. 6 and fig. 7 the Hα-isophotes of R 136 in relative units are presented. The plate (shown in fig. 5) was scanned with the microphotometer of the Astronomical Institute (Ruhr-Universität Bochum); the aperture was 10μ x 10μ.R 136 shows a triple structure (a, b, c), dominated by R 136a. The main component covers an area of $(0.7\ pc)^2$. For the three components a colour gradient can be found; R 136a is much bluer than R 136c. The U isophotes (number of stars of 10th magnitude/square degree) are given in fig. 8. The infrared pictures (7100-8800 Å) are very diffuse and irregular, a consequence of the patchy dust distribution.

The absolute magnitude of R 136 is $M_V = -10.5$. The bolometric correction for WN5 or O5-8 stars lies between -4.7 and -2.8. Conservatively we have choosen BC = -3.5 and obtain: $M_{Bol} = -14.0$, $L/L_\odot = 3.1\ 10^7$, $50000 < T_{eff} < 55000$ and $250 < m/m_\odot < 1000$; the emission measure is 550 (pc/cm^2). Together with the other 15 WN and O stars of the inner region the central group determines the ionisation structure of the nebula. By far the major contribution originates from R 136.

The shell-like structure surrounding R 136 clearly visible in fig. 5 and fig. 4, can be interpreted as the result of a stellar wind. The age of the shell turns out to be $3.0\ 10^5$ years. This value is compar able with the typical age ($\sim 10^6$ years) of supermassive stars.

Further understanding of R 136 is expected from speckle interferometry and surface photometry in other wavelength bands, especially in spectral regions not including strong emission lines. Observations with the Einstein X-ray observatory will give us additional valuable information.

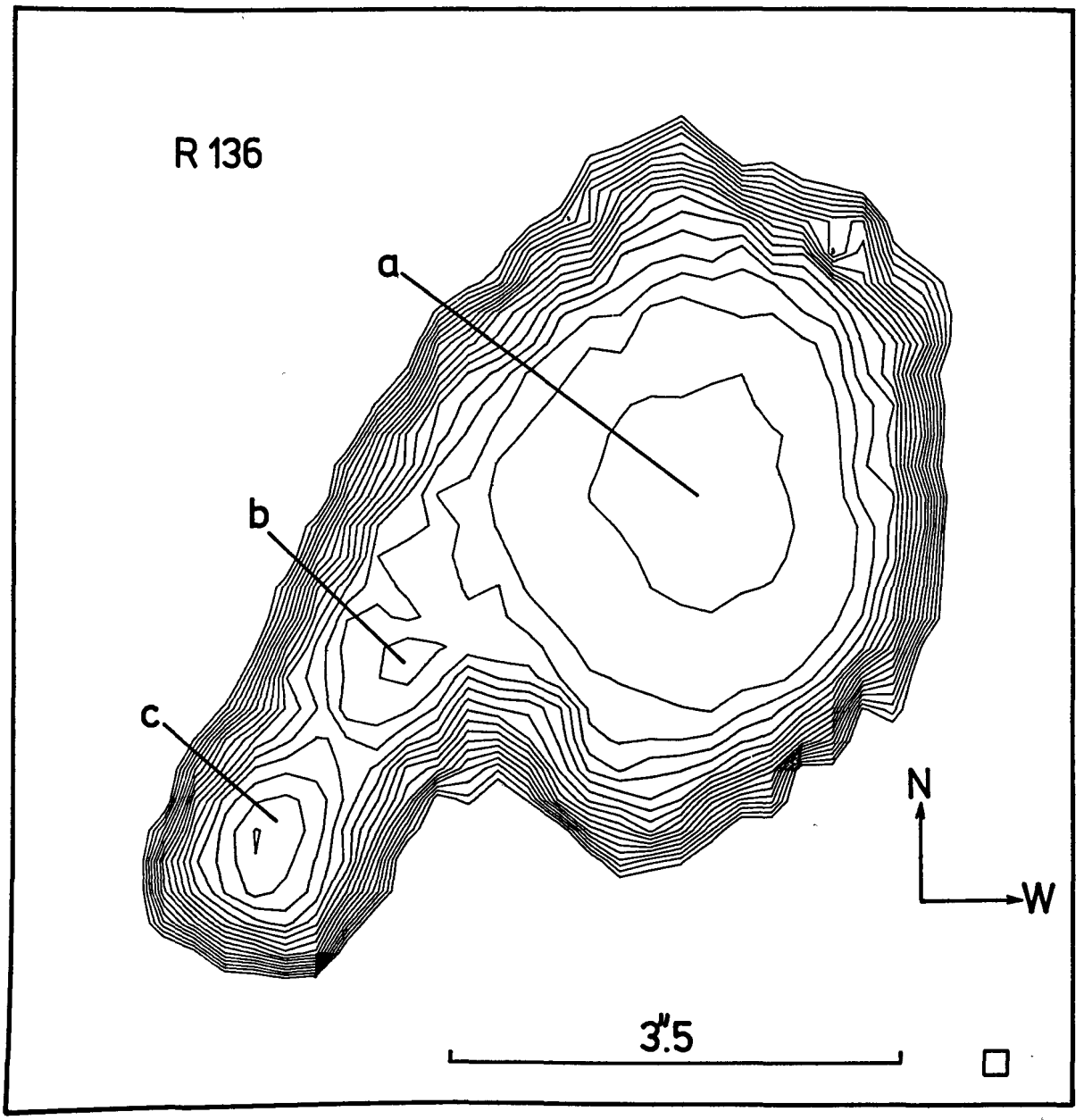

Fig. 6 Hα isophotes of R 136 and the three components a, b, c (Feitzinger et al. 1979)

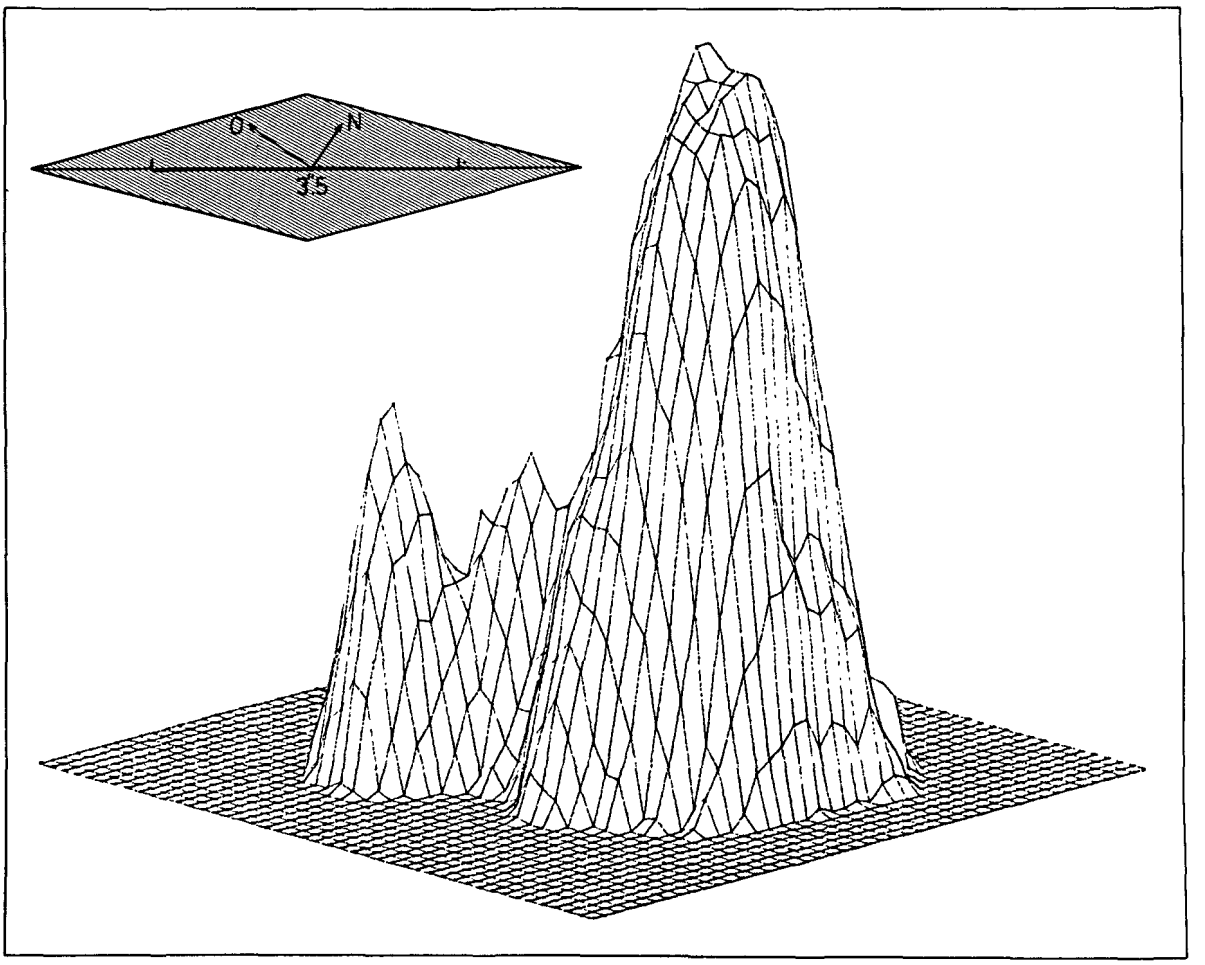

Fig. 7 Threedimensional presentation of the R 136 complex (Feitzinger et al. 1979)

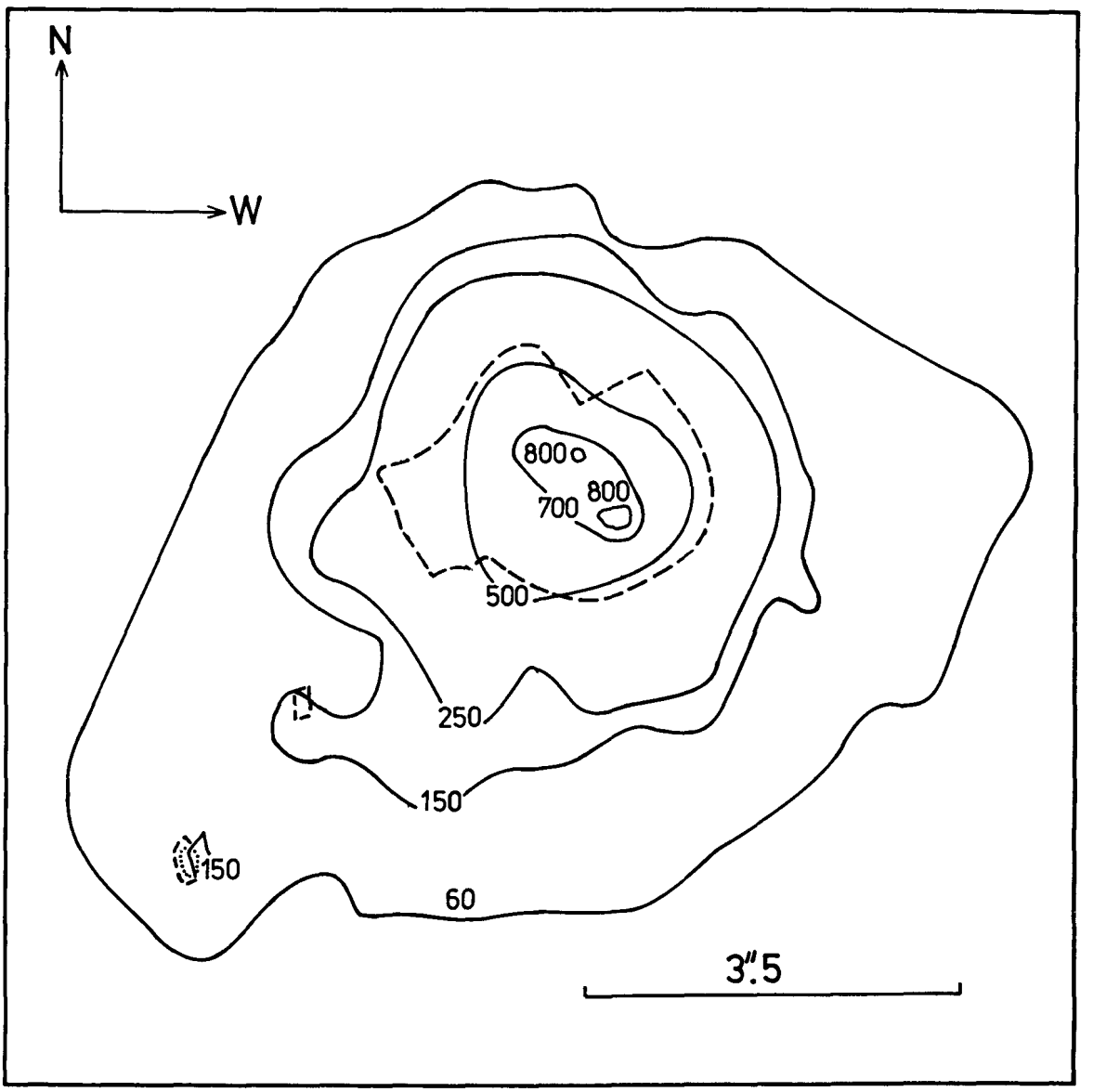

Fig. 8 The scaled U isophotes of R 136 (number of stars of 10th magnitude/square degree). The red isophote (6100 - 6700 Å) is also shown (Feitzinger et al. 1979)

References

Blades J.C., 1979, Anglo-Australian Obs. preprint
Boer de K.S., Koornneef J., Savage B.D., 1979, preprint
Borgman J., Danks A.C., 1977, Astr.Astrophys. 54, 41
Cantó J., Elliot K.H., Goudis C., Johnson P.G., Mason D., Meaburn J., 1979, Astron. Astrophys. in press
Carruthers G.R., Page T., 1977, Astrophys.J. 211, 728
Carruthers G.R., Page T., 1978, EUV Atlas of the LMC, NRL Report 8206
Danks A.C., 1977, Astron. Astrophys. Suppl. 30, 89
Davies R.D., Elliot K.H., Meaburn J., 1976, Mem.Roy.Astron.Soc. 81,89
Doherty L., Henize K.G., Aller L.H., 1956, Astrophys.J.Suppl. 2, 345
Dufour R.J., 1976, Earth and Terr. Sci. 2, 245
Elliot K.H., Goudis C., Meaburn J., Tebbutt N.J., 1977, Astron. Astrophys. 55, 187
Faulkner D.J., 1967, Mon.Not.Roy.Astron.Soc. 135, 401
Feitzinger J.V., Schlosser W., 1977, Astron. Astrophys. 56, 245
Feitzinger J.V., Schlosser W., Schmidt-Kaler Th., Winkler Chr., 1979, Astron. Astrophys. in press
Feitzinger J.V., Gerola H., Seiden P.E., 1980, in Vorbereitung
Gerola H., Seiden P.E., 1978, Astrophys. J. 223, 129
Hyland A.R., Thomas J.A., Robinson G., 1978, Astron. J. 83, 20
Koornneef J., 1978, Astron. Astrophys. 64, 179
Malin D.F., 1977, AAS Photo Bulletin No. 16, 10
Malin D.F., 1978, Nature, 276, 591
Meaburn J., 1979, Astron. Astrophys. 75, 127
Mills B.Y., Turtle A.J., Watkinson A., 1978, Mon.Not.Roy.Astr. Soc. 185, 263
Nandy K., Morgan D.H., Carnochan D.J., 1979, Mon.Not.Roy.Astr.Soc. 186, 421
Nandy K., Morgan D.H., 1978, Nature 276, 478
Schmidt-Kaler Th., 1975, in HII Regions and Related Topics, p. 484, T.L. Wilson, D. Downes Editors
Schmidt-Kaler Th., Feitzinger J.V., 1976, Astrophys. Space Sci.41,357
Schmidt-Kaler Th., Isserstedt J., 1976, Astrophys. Space Sci., 41,139
Schmidt-Kaler Th., 1977, Astron. Astrophys. 54, 771
Seiden P.E., Gerola H., 1979, Astrophys. J. 233, 56
Strauss F.M., Braz M.A., Ducati J.R., 1979, Astron. Astrophys.74,280
Werner M.W., Becklin E.E., Gatley I., Ellis M.J., Hyland A.R., Robinson G., Thomas J.A., 1978, Mon.Not.Roy.Astr.Soc. 184, 365

THE STRUCTURE OF THE BARRED GALAXY NGC 5921

P. J. Grosbøl[x]
European Southern Observatory, c/o CERN, Geneva

Introduction

The dynamic properties governing the formation and maintenance of bars in galaxies have been studied in a number of theoretical papers (see e.g. Contopoulos 1975, 1979; Contopoulos and Mertzanides 1977; James and Sellwood 1976; Sanders 1977). One interesting problem is the relationship between the extend of the bars and the main resonances in the galaxies as discussed by Contopoulos (1980). To confront the theoretical results with observations both accurate surface photometry and rotation curves of barred galaxies are needed. Concerning the latter none circular motions in the bar-region make the interpretation very difficult when the radial velocities are obtained from emission lines which represent the gas rather the stellar component. Some information about the motion of the spiral pattern and the bar relative to the material in the galaxy can be obtained from their color profiles assuming that the majority of stars are born in narrow regions along the dust lanes. A more detailed study of the color variations should however consider both the process of star formation and the motion of the young stars (see Yuan and Grosbøl 1980). The present paper gives the surface photometry and a rotation curve for the barred galaxy NGC 5921. In section 2 the data and the reduction procedure are described while the structure of the galaxy and the extend of its bar are discussed in the third section.

Data and reductions

The surface photometry was obtained using the 4-cm McMullan electronographic camera on the 1-m telescope at the Wise Observatory. The Johnson UBVR system was used so that the variation in the color index Q = (U-B) - 0.72 * (B-V) could be compared with the surface brightness distribution in the R-filter. There were taken

[x] Visiting astronomer, The Florence and George Wise Observatory, Tel Aviv University, Israel and European Southern Observatory, Chile.

several exposures with each filter to increase the signal to noise ratio by adding them and to find defects in the G5-emulsions used. The films were measured on the PDS-microdensitometer at Lund Observatory with an aperture corresponding to 0".8 x 0".8 while the seeing was 2" - 3". The G5 emulsion was assumed linear upto a density of 3 while pixels with higher densities were disregarded. The spatial sensitivity variation of the photocathode was mapped in all four filters by taking morning and evening flat field exposues of the sky in zenith. Each plate was corrected for the responce of the photocathode, while dust and failures in the emulsion were removed from the low gradient regions by a median filter which replaced a pixel by the median of the surrounding pixels if they differed more than 4 times the grain noise. The size of the median filter was approximately equal to that of the seeing disk. Thus it removes only failures with dimensions smaller than that given by the point spread function. For each color the plates were alined in the computer, compared to find remaining plate failures and added together giving the final surface brightness maps. To avoid major interference from foreground stars their central parts were replaced by the local background value.

The sky background was constant over the whole area of the V and R maps while there was a gradient from north to south of the order of 1 percent over the maps in U and B. This may be due to the variation in brightness over the night sky during the flat field axposures. Although the east-west asymmetry was removed by taking the mean of an equal number of morning and evening exposures there was not made

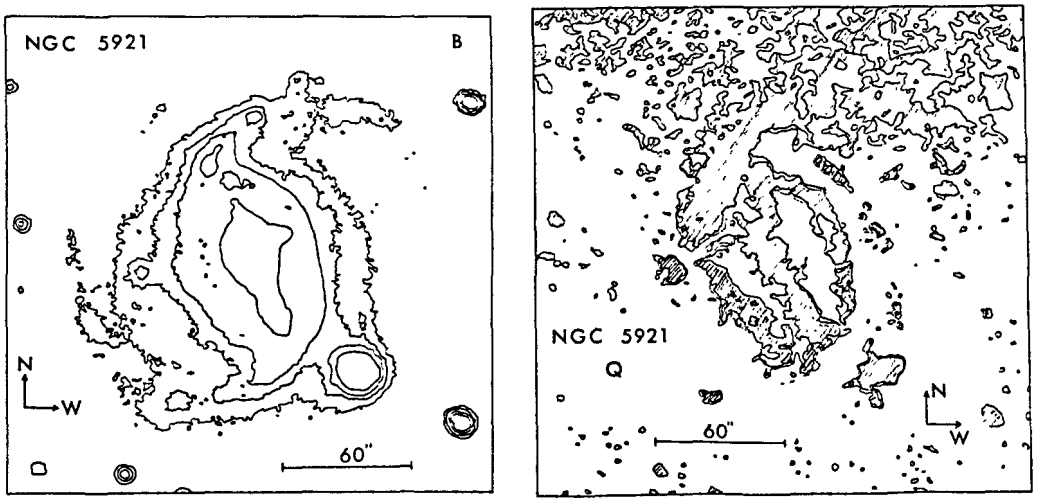

Figure 1 : Contour maps of NGC 5921 in B and Q. The hatched areas on the Q map indicate the bluer regions.

any correction for a gradient in the north-south direction. In all cases the mean sky background was subtracted from the intensities before the conversion to magnitudes was performed. The errors introduced in U and B are small in the inner part of the galaxy where the bar and the spiral structure are located. In figure 1 the maps of NGC 5921 are shown in B and Q.

Using the procedure described by Grosbøl (1980) the position angle and the tilt angle of the galaxy were estimated to $+28^{o}$ and 36^{o}, respectively. These values are in agreement with those obtained from the outermost isophotes. With these projection angles azimutial intensity profiles I_r along galacto-centric circles in the plane of galaxy were interpolated in the Q and R maps for a number of radii. Each profile was Fourier transformed in order to extract the information concerning the bar and the two-armed spiral pattern (i.e. the second harmonic). The errors in U and B due to the background subtraction will to the first order not effect the second harmonic but only the first. The amplitude and the phase of the second harmonic for both Q and R are given as functions of radius in figure 2. The uncertainty of the amplitudes is estimated from the power of the higher harmonics to of the order of 0.03 mag. The phases indicate the angle between the minor axis of the galaxy and the points where the most blue color for Q and the highst surface brightness in R are located.

The rotation curve was measured on a long slit spectrum using the H_{α} emission line. The spectrum was taken with a Carnegie image tube on the Boller and Chivens spectrograph at the ESO 1.5m telescope giving a dispersion of $5.9 * 10^{-6}$. The slit was alined along the major axis of the galaxy (i.e. almost along the bar) and had a width of 100 micron. A He-Ar comparison spectrum was used for making the wavelength calibration. Its shape was assumed not to vary in the direction perpendicular to the dispersion while the zero point was defined by the two OI night sky lines at 630.03nm and 636.38nm. The rotation curve relative to the center and corrected for the tilt of the galaxy is given in figure 3 as a function of radius. It was impossible to measure the rotation velocity in the bar itself due to the lack of H_{α} emission in this region. The dip in the rotation curve around 35" (i.e. at the end of the bar) is likely to be caused by none circular motions in the gas.

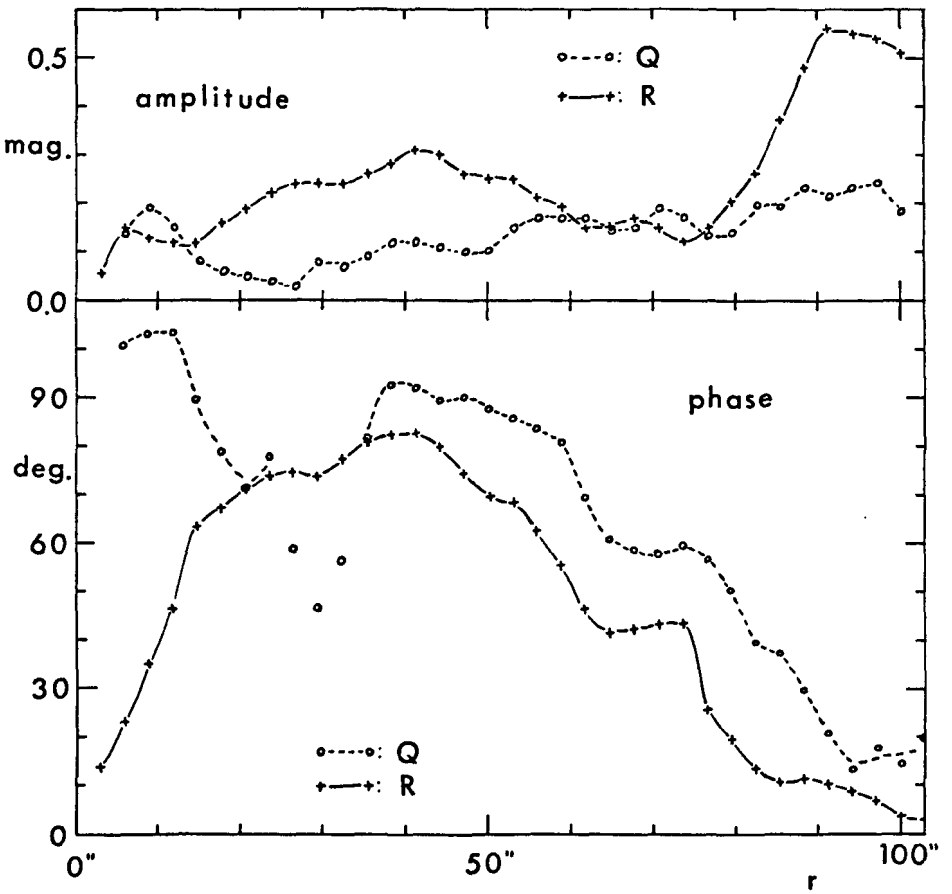

Figure 2 : Amplitudes and phases of the second harmonic (see text) in R and Q for NGC 5921 as functions of radius.

Results

The galaxy was classified by de Vaucouleurs (1970) to be of type SB(r)bc and can thus be divided into four radial zones, respectively dominated by bulge, bar, ring and spiral pattern. These regions can be identified in figure 2 on the phase diagram of the second harmonic for the R filter. A spherical bulge will have a phase equal to 0° due to projection effects. In the present galaxy the bar extends almost to the center causing a phase shift which depends on the bar to bulge ratio. At a radius of 15" the bar has become dominent and the phase remains nearly constant at 70° until the end of the bar around 30". Projected into the plane of the galaxy the ring is not circular as noted by de Vaucouleurs (1970). This fact makes a simple interpretation of the phase impossible in the interval from 30" to 35" where circles will intersect the ring. Outside this region the phase decreases corresponding to a logarithmic spiral with a pitch angle of approximately 25°. The hump at 70" is caused by an insufficient sub-

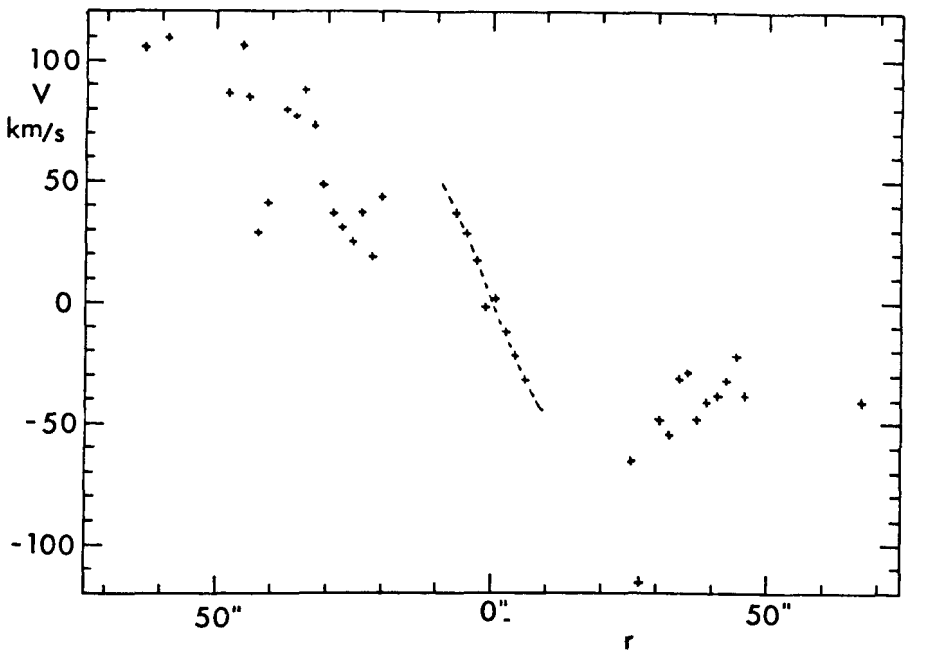

Figure 3 : The rotation curve of NGC 5921 relative to its center. The velocities have been corrected for the inclination of the galaxy.

traction of a very bright foreground star.

The phase of the second harmonic in the color index Q indicates the location of the most blue region. This is positioned at a larger angle than that found for the R-filter for all radii except in the ring region. If the blue region is caused by young stars formed in a shock close the potential minimum of a density wave it suggests that the corotation is located in the outer parts of the galaxy (assuming a trailing spiral). The phase difference between the second harmonics in Q and R is much smaller in the bar than in the spiral due to the elongation of stellar orbits in the bar. The amplitude of both the bar and the spiral is of the order of 20 percent in R.

Unfortunately, the rotation curve is not defined well enough for deriving the epicyclic frequence κ as a function of radius because this involves computing the derivative of the angular velocity Ω. However, qualitatively it shows that the galaxy has a slowly increasing rotational velocity in the center, and that the rotation curve becomes more flat outside the bar at a radius of 50". This could suggest that the function $\Omega - \kappa/2$ is close to zero at the center and has a maximum at a radius between 20" and 50". Thus, if the extend of the bar is associated to a resonance it will be the Inner Lindblad Resonance (ILR). It is plausible that the galaxy has

two ILR and that the bar, in this case, extends from the center to the inner ILR as suggested by Contopoulos (1979b). Only by using an accurate rotation curve based on absorption lines it will be possible to calculate the precise location of the resonances relative to the extend of the bar and thereby check the theory.

The Q map of the galaxy in figure 1 shows that both bar, ring and spiral are more blue than the disk. Due to saturation of the central parts of the galaxy in some exposures the color of the bulge is arbitrary. Both the color of the ring and the unusual fact that the spiral arms join the ring before the end of the bar could indicate that the ring feature rather is a very tightly wound spiral. This interpretation could also explain the sting of blue regions to the west of ring as young stars formed in a secondary shock in the gas.

Acknowledgement

I acknowlege the Wise Observatory of Tel Aviv University and the Smithsonian Research Fondation Grant SFC-0-3005 for the use of their facilities at Mitzpe Ramon, Israel.

References

Contopoulos,G.: 1975, Astrophys.J. 201, 566.

Contopoulos,G.: 1979, Astron.Astrophys. 71, 221.

Contopoulos,G.: 1980, Astron.Astrophys. (in press).

Contopoulos,G. and Mertzanides,C.: 1977, Astron.Astrophys. 61, 477.

Grosbøl,P.J.: 1980, Proc. of Photometry, Kinematics and Dynamics of Galaxies, Austin, Texas (in press).

James,R.A. and Sellwood,J.A.: 1978, Monthly Notices R.A.S. 182, 331.

Sanders,R.H.: 1977, Astrophys.J. 217, 916.

de Vaucouleurs,G.: 1970, IAU Sym. No.38, 18.

Yuan,C. and Grosbøl,P.J.: 1980, Astrophys.J. (submitted).

SURFACE PHOTOMETRY OF THE Sd SPIRAL NGC 7793

G. de Vaucouleurs and E. Davoust
Department of Astronomy and McDonald Observatory, The University of Texas

Abstract

Detailed surface photometry in blue light of the SA(s)d galaxy NGC 7793 is obtained from three photoelectrically calibrated photographs. The sky background density is subtracted by a numerical mapping technique. The luminosity distribution is dominated by an exponential disk of effective radius $a_e = 2'.11 = 1.92$ Kpc contributing 98.6% of the total luminosity $B_T = 9.51 \pm 0.06$. A decomposition of the disk into an underlying old pop. I component and a young arm component shows that 65.5% of the total luminosity comes from the old pop. I component which has a corrected central luminosity $\mu_c(o) = 21.06$. The spheroidal component subtracted from the disk and corrected for convolution effects by a gaussian point spread function is visible only in the vicinity of the nucleus. It can be represented by an $r^{1/4}$ law of effective radius $r_e^I = 6''.0 = 91$pc and total magnitude $B_T^I = 14.13$ or 1.4% of the total luminosity of the galaxy. A revised distance modulus $\mu_o = 27.48 \pm 0.25$ ($\Delta = 3.13 \pm 0.38$ Mpc) is derived from five distance indicators. The total absolute magnitude of the galaxy is $M_T^o = 18.35$.

NGC 7793 is a late ordinary spiral, the SA(s)d prototype and the fifth brightest member of the Sculptor group. The detailed photometric study reported here will contribute to extend the extragalactic distance scale beyond the local group in the southern hemisphere and will also provide useful constraints in the kinematical and dynamical study of this galaxy to be published elsewhere.

Three photographic plates in blue light, taken at the McDonald and Mount Stromlo observatories, were used. A photoelectric pulse count drift scan along the major axis of the galaxy was used to check the linearity of the photographic calibration.

The plates were scanned with the Skylab PDS microdensitometer of the University of Texas. The mapping of the sky density background follows the method of Jones et al. (1967):

- sample a large rectangular field around the galaxy
- fit a low (3rd degree) polynomial to the field and reject large residuals (stars and plate defects)
- iterate until distributions of positive and negative residuals

are similar

- fit a 6th degree polynomial to the remaining pixels. The significance of each coefficient is determined by a statistical test.

The density to intensity conversion was performed with the linearised characteristic (de Vaucouleurs 1968):

$$I = A\,\omega^{n}$$

where ω is the opacitance, n is determined by the photographic calibration with tube sensitometer spots and the coefficient A by photoelectric integrated magnitudes and colors in the U,B,V, system. The total apparent magnitude of the galaxy is $B_T = 9.51 \pm 0.06$. The photometric parameters are summarized in Table 1. The corresponding values for M33 and the LMC are listed for comparison. NGC 7793 is intermediate in luminosity between the two other galaxies, but it is 25% smaller and consequently its average blue surface brightness is about 0.5 mag brighter.

TABLE 1: Photometric parameters

Galaxy	M33	N7793	LMC
Type	SA(s)cd	SA(s)d	SB(s)m
Distance (Mpc)	0.72	3.13	0.046
Effective radius (kpc) a_e	2.53	1.92	2.50
Effective surface brightness $\mu_e(B)$	22.83	22.22	23.69
Corrected absolute magnitude M_T^o	-18.51	-18.35	-18.17
Corrected color indices $(U-B)_T^o$	-0.18	-0.15	-
$(B-V)_T^o$	0.44	0.46	0.43

An attempt has been made to decompose the galaxy into three distinct stellar populations: a spheroidal bulge, an old pop. I disk and a young arm component. The spheroidal component has been isolated after subtracting an exponential disk and with allowance for the point spread function, assuming the true profile to obey an $r^{1/4}$ law. The arm component has been subtracted from the disk by analyzing the brightness distribution in concentric rings (Schweizer, 1976). Table 2 summarizes the results. The corrected central surface brightness of the disk is slightly brighter than the average value $\mu_D(o) = 21.67 \pm 0.35$ (Freeman, 1970; Schweizer, 1976).

TABLE 2: Decomposition into spheroidal and disk components

	spheroid	old pop. I disk	arm comp.
Peak brightness $\mu_c(0)$	12.87	21.06	
Effective radius r_e	6".03	1'.76	
Absolute magnitude M_o	-13.73	-17.89	-17.15
Fractional luminosity	0.014	0.655	0.331

The new photometric data lead to an improved estimate of the distance of NGC 7793 from a variety of tertiary distance indicators. If the two extreme values are rejected, the mean weighted modulus is $\mu_o = 27.48 \pm 0.25$ corresponding to a distance of $\Delta = 3.13 \pm 0.38$ Mpc. The difference with the mean value $\mu_o = 27.0 \pm 0.2$ for the Sculptor group (de Vaucouleurs, 1978) is consistent with the depth in the line of sight that might be expected from the apparent diameter of the group ($20° = 0.9$ Mpc, de Vaucouleurs, 1959).

A more detailed report will be published in the Astrophysical Journal supplement series.

References

de Vaucouleurs, G. 1959, Ap. J. 130, 718

de Vaucouleurs, G. 1968, Applied Optics, 7, 1513

de Vaucouleurs, G. 1978, Ap. J. 224, 710

Freeman, K.C. 1970, Ap. J. 160, 811

Jones, W.B., Obitts, D.L., Gallet, R.M. and de Vaucouleurs, G. 1967, Pub. Dept. of Astronomy, University of Texas, ser. II, vol. I, n°8.

Schweizer, F. 1976, Ap. J. Suppl. 31, 313.

CCD OBSERVATIONS OF HII REGIONS AND GALAXIES

Willem Wamsteker
Anthony C. Danks
Patrice Bouchet

European Southern Observatory
La Silla
Casilla 16317, Correo 9
Santiago, Chile

Rudolf Albrecht*
Institute for Astronomy
University of Vienna
Türkenschauzstr. 17
A-1180 Vienna, Austria

Introduction:

Although the application of 2-dimensional solid state detectors holds great promise for future application in astronomical imaging and photometry, only a few detectors have been successfully applied to astronomical problems (e.g. Young, et.al., 1978 and Westphal, 1979). The main advantages of CCDs (= Charge Coupled Device) in comparison with other panoramic detectors are:

1. Geometric stability with no image distortion (as in most vidicons)

2. Linearity on a panoramic detector over a large dynamic range of $\sim 5 \times 10^3$ (as opposed to photographic emulsions)

3. High Quantum efficiency over a large wavelength interval extending into the infrared to $\lambda = 1\mu m$ (see Fig. 1)

One of the earlier CCD detectors operational for astronomical purposes was developed by Texas Instruments for NASA-JPL under NASA contract 7-100. This detector has been used at various observatories to test its performance. These tests are especially important in view of the future use of CCD detectors both in the Space Telescope and on the Galileo mission to Jupiter. We have used the JPL-CCD for a few nights at the ESO 100 cm telescope.

Due to the experimental nature of the chip, some of the results showed more of the limitations than of the capabilities; however, the experience gained has been extremely valuable for the treatment of the next generation CCDs. Improvements can already be seen between our results and those presented elsewhere in this workshop (see papers by Westphal and Illingworth) and are caused by a better understanding of the behavior, both mechanical and electronic, of such detectors. The experimental nature of the CCD used made us limit the observations to broad-band imaging and photometry.

* Guest investigator at the Cerro Tololo Interamerican Observatory, La Serena, Chile.

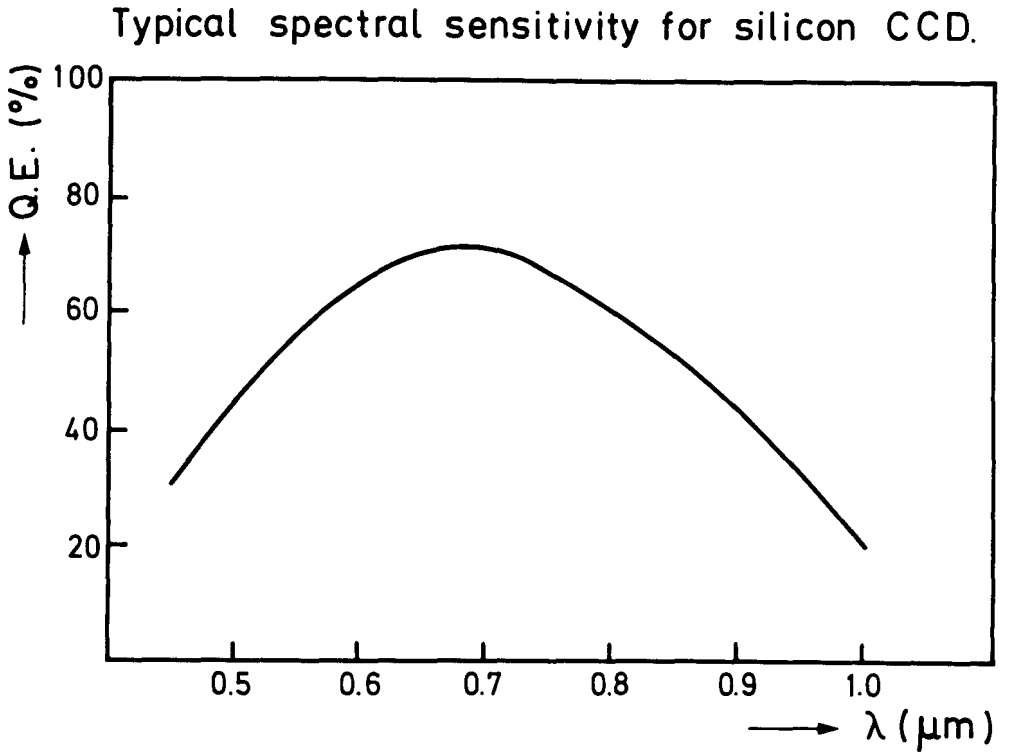

Fig.1
Quantum efficiency vs. wavelength for CCD detectors. The variations between different detectors are typically of the order of 10%. It can be seen that even at λ = 1μm such a detector still has a quantum efficiency which is considerably higher than e.g. an $S\text{-}_1$ photocathode (Q.E. at 1μm≈0.1 - 0.2%) The spectral response combined with an RG 1000 filter as used in the observations results in a band with an effective wavelength of $\lambda_{IR\ eff} \simeq 1.0\mu m$.

Detector:
The CCD detector itself consists of a MIS (Metal-Insulator-Semi-conductor) structure, with the silicon semiconductor side etched, in our case, to a thickness of 10μm. Detailed descriptions of the physical processes involved in the detector can be found in Steckl (1979), or also Marcus, et.al. (1979).

The detector was back-illuminated, i.e. light falls on the semiconductor side of the chip for better radiation transfer. The detector had 400 x 400 pixels and measured 9.14 x 9.14 mm, resulting in a pixel size of 0.34 arcsec at the ESO 1 m telescope.

The detector was contained in a simple evacuated cold box, with no transfer optics apart from the optical vacuum seal window. The dewar contained a remote controlled shutter. The detector itself was spring-loaded onto a layer of heat-sink compound at a cold finger. The cold finger was cooled internally by a forced evaporative flow of cold N_2 gas from a LN_2 dewar mounted separately on the telescope. A thermostat on the cold finger controlled a heating element in the LN_2, assuring a stable temperature. During the night the detector temperature was maintained at -80°C. This brought the dark current down to less than 1 e- pix^{-1} sec^{-1}. Therefore, nominally the dominant noise source for intermediate exposures was the read-out noise

of 30-50 e- pix^{-1} r.m.s.

The charge, accumulated on the detector during exposure was read-out through an 0.28 pF capacitance gated to the output FET, resulting in a sensitivity for the output stage of $0.5\mu V(e-)^{-1}$. Before A/D conversion this signal was amplified in 3 stages with a net gain of ~ 450. The stability of the -most critical- first amplification stage corresponded to about 4.5 e- r.m.s.

Since the detective elements are formed by potential wells generated in the semiconductor with metal electrodes, a CCD is not subject to the geometrical distortions one encounters in most video detectors, which rely on electron optics to direct the position of the electron read-out beam. However, the proper voltage levels for the charge shifting in the read-out process is very critical. Since the detector has only one single output gate the charge accumulated on a specific pixel has to be moved over the chip to the output gate as is normal for shift registers. The read-out process shifts the contents of each pixel one row at a time throughout the output gate. After one row has been read completely, the left-over rows are all shifted one up, so that the next row can be read-out.

This process is repeated until all pixels have been read. If the detector is adjusted properly the dynamic range of the detector itself is determined solely by the relation:

$$D.R. = \frac{\text{Full well signal}}{\text{Read-out noise}}$$

In our case, a full well signal corresponded to -7500 e-, giving a dynamic range of ~ 2000.

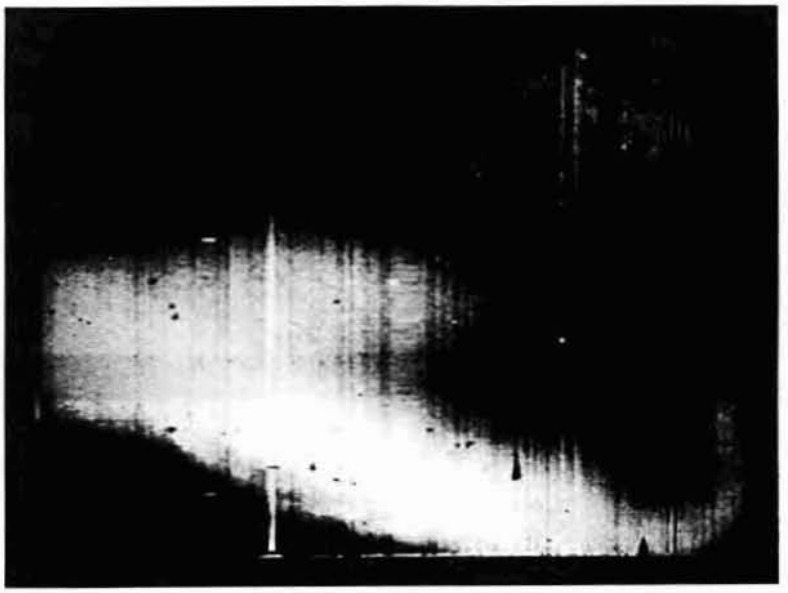

Fig.2
Flat field exposure on the diffusely illuminated inside of the dome. A large number of image defects have been removed already with a). the software mask shown in Fig.3, and b). interpolation between bad pixels. Note that although the pixel-to-pixel variation is not too bad, rather strong large scale sensitivity gradients are present.

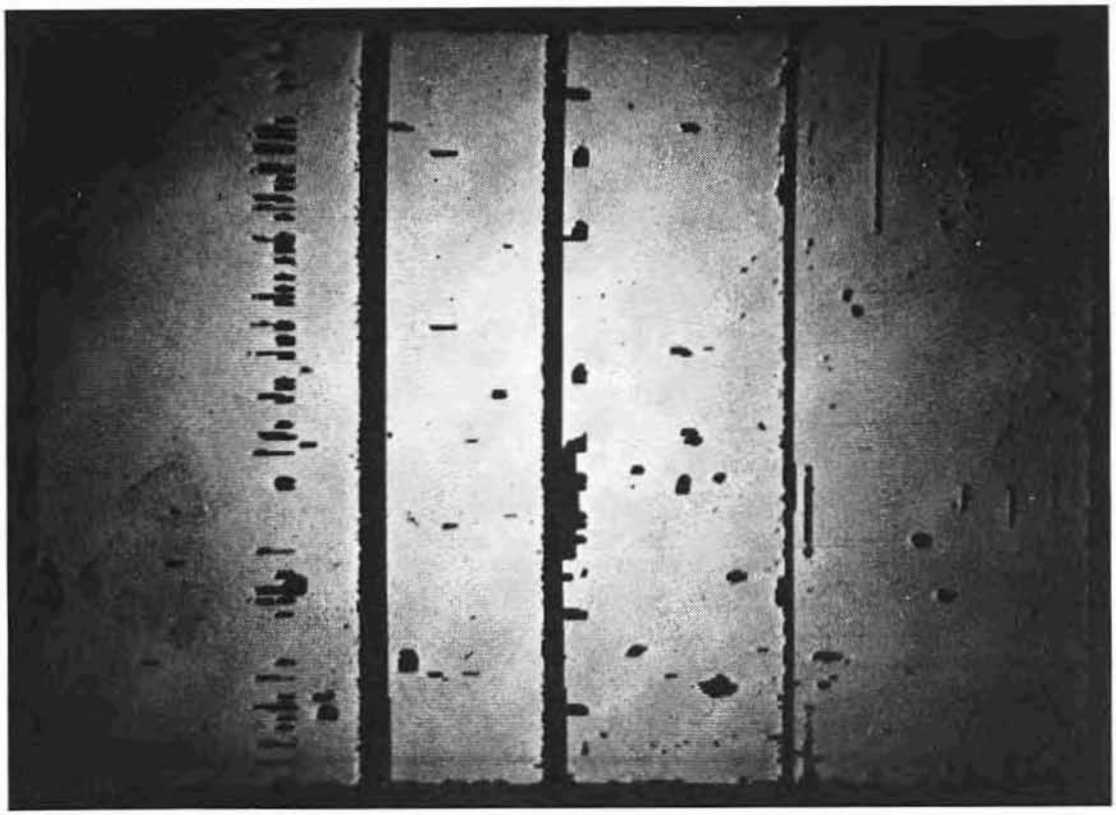

Fig.3
Software mask applied to the raw data to avoid confusion of hot pixels with real signals.

Support equipment and data reduction:

The support equipment consisted of 2 racks allowing full operation and limited monitoring of the results at the telescope: an image monitor, an oscilloscope, master control panel, a full frame memory, a tape recorder, a thermo-electric power supply, a heat exchange and the main power bay.

To obtain a single phtotmetric exposure, one has to make the following supportive exposures: bias exposure, dark current exposure, flat-field exposure (usually on diffusely illuminated dome). All this made that for a single exposure usually about 2 - 3 times the exposure time itself was needed. The stability of the temperature was good enough so that we could use for short exposures the appropriate fraction of one long dark current

exposure.

A filter slide with 4 locations for (Visual, Hα, λ10830 HeI, RG 1000) was mounted in front of the dewar. Focusing was done through optimisation of a single horizontal scan-line giving a stellar profile. For the longer exposures, guiding was done with a video off-set guider.

The observations were made from March 17 through March 20, 1978. All reductions were done at the computing center of the Cerro Tololo Interamerican Observatory in La Serena, Chile. The CTIO image processing system is described by Schaller, et al. (1977).

The data reduction procedures applied to the CCD generated data fell into two groups: removal and correction of instrumental effects, and display and scientific evaluation of the data. Given the performance of the detector, group one was the more difficult one.

The first step was the construction of a logical mask, which is an image of the size of the CCD frame with pixels containing the value of unity in areas without defects and pixels containing zeroes in the destroyed parts. A number of flat field exposures (Fig. 2) was used to construct this mask, which is shown in Fig. 3.

Multiplying the raw data frames with the mask resulted into unchanged values for good pixels and zeroes for the bad ones. Frames containing only low frequency information (flat and dark frames) were reconstructed by simple interpolation across the affected pixels. An energy conserving convolution filter (usually a 5 x 5 pixel cone) was used to smooth these frames.

A more elaborate technique is the conditional overlap of frames. It consists of at least two exposures, taken with an offset of 20 pixels in either direction, thus ensuring that in the area of overlap every point is represented by at least one good pixel. Suitable adding produced a satisfactory restauration of the intersecting area in most cases.

Some of the brighter objects had to be corrected for numerical overflows during read-out, caused by the fact that only 12 bits out of the 16 bit ADC range were recorded (see e.g. Fig. 4).

Bias (i.e. DC read-out level) and dark frame were subtracted from the data and the flat field correction was applied in the usual manner.

No particular effort was made to obtain or check for accurate absolute photometry; the reconstruction procedures applied to the frames would not have justified this. All the further evaluation was of a comparative and morphological nature.

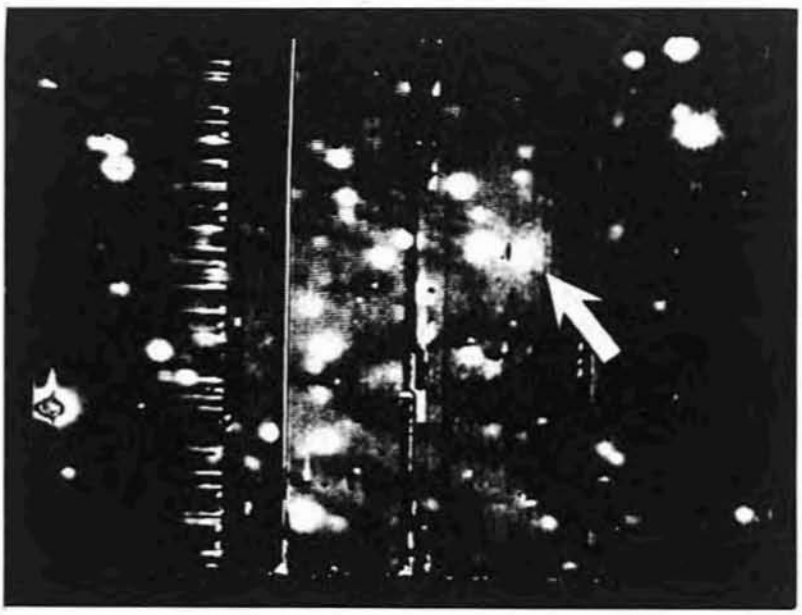

Fig. 4
Raw exposure (30 min, RG 1000) of the optical counterpart of the double radio source 13S6A (arrow). Comparing this with Fig. 2 illustrates the consequences of detector defects. The two brightest stars show dark centers caused by an easily removable digitization effect. North is at the top, East is to the left.

Results:
Observations were made of the HII regions G333.6-0.2, G 12.2-0.1, G 326.6-0.6, and the galaxies N 3783, N5253, and the highly obscured galaxy 13S6A. We will only give a short description of the results on N 3783 and G 333.6-0.2. A more extensive discussion of the photometry of this last HII region will be published elsewhere (Geballe et al., 1980).

To illustrate how the detector behaved, we show in Fig. 2 a typical flat field exposure of the diffusely illuminated inside of the dome. From this figure already a large number of image defects have been removed. Apart from bad pixels, which are illustrated in the software mask applied to the data (shown in Fig. 3), the pixel to pixel variations were generally less than 1%. The overall sensitivity variation over the full detector amounted to a factor of 2. The software mask shown in Fig. 3 was applied to the data to eliminate erratic pixels completely. Although usually only individual pixels were bad, problems -most likely associated with the charge transfer process- caused these to have tails extending in the x-direction over about 5 pixels adjacent to the bad one. The inclusion of these tails in the software mask makes it appear worse than was really the case. These problems appear to have been solved by proper detector adjustment (Janesick, 1980).

Fig. 4 shows a raw frame of 90 minutes exposure time on the optical counterpart of the double radio source 13S6A (Lausten et al., 1977). Comparing Fig. 4 with the results of Marcus et al. (1979) on a different CCD shows the improvement obtained over the last year in the performance of these detectors.

The homogenity of the flat field is considerably worse and the number of detector defects is larger in our data. A remarkable feature is that the JPL-CCD appears to be much less sensitive for "cosmic ray events" as was also found by Marcus et al. (1979). This is probably a consequence of the semiconductor layer of the TI detector being much thinner than that of the Fairchild CCD used by Marcus et al.

Stellar profiles:

During focusing at the telescope, no significant differences were found between the V and IR focus. However, reductions showed that stellar profiles were significantly different in these two bands. This makes the analysis of color differences over objects with nearly stellar nuclei, e.g. N 3783 difficult.

Stellar image profiles were determined on the horizontal scan lines through the peak of the stellar image. Individual profiles were determined for the left and right side of an image. For a typical star we found the following Gaussian profile for the core of a star (area containing 90% of the total stellar flux):

V:	left profile	: = 0".83 ± ".04
	right profile	: = 1".05 ± ".28
IR:	left profile	: = 1".19 ± ".25
	right profile	: 1".22 ± ".25

The fact that the visual and IR image profiles do not give the same standard deviation for the seeing disk is probably caused by interference effects in the semiconductor layer at the longer wavelengths. The left-right asymmetry in the visual image is of course disturbing; in all likelyhood, it is due to the earlier mentioned problems with the charge transfer over the chip. Since the last effect has a much steeper fall-off than the seeing disk in the IR, one does not notice it in the IR stellar profile, which is symmetric. It is, however, obvious that these effects make a direct comparison between the results obtained in the visual and IR for star-like sources e.g. the nuclei of galaxies, effectively impossible.

In Fig. 5, we show the radial brightness profile of the nearly face-on Seyfert I galaxy N 3783 (Osmer et al., 1974). These surface brightness vs. radius curves were generated by integrating the brightness over one-pixel wide rings centered on the galaxy nucleus. They extend to the region where the surface brightness did not decrease any more with increasing radius. Sky was subtracted from original data from another section of the same frame. The requirements imposed by retaining a relatively small number of bad pixels in the image is the main reason the profile does not extend fully beyond the ring at the end of the bar of this galaxy. Due to the algorithm used for the ring integration we stopped on the inside at a ring-size of 3 pixels (= 1"). Exposure times were V: 5 min; IR: 30 min.

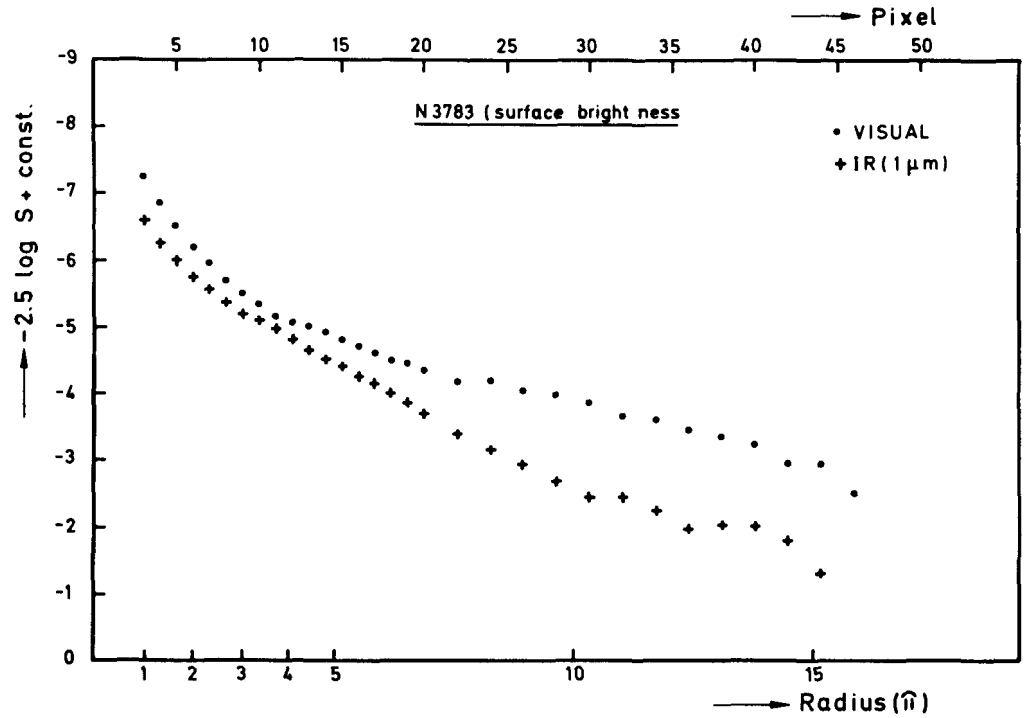

Fig. 5
Radial light distribution of the Seyfert galaxy N 3783 in V and IR (λ_o = 1μm). This was obtained by integration over 1 pixel-wide rings around the nucleus. The inner 3 pixels are excluded, since the algorithm used gives rise to large errors. In the visual, the bluer disk population is falling off much slower than the older stellar population which is predominant in the IR. The ring around 3783 appears much more pronounced in the IR than in the V.

The comparison of the two profiles shows the following characteristics:

1. Although the V seems to rise in the inside steeper than in the IR, this is probably due to the profile problems mentioned before.

2. Beyond 4" the drop-off in brightness is much slower in V than in the IR, illustrating the presence of young disk.

3. The ring structure around the galaxy between 10" and 15" radius appears much more pronounced in the IR than in the visual. In the IR also a clearly distinguishable double structure appears indicated.

In Fig. 6, we show some results on the extremely obscured ($A_V \simeq 20$ mag) HII region G333.6-0.2 at $\lambda \simeq 0.08\mu$m with the Radcliffe 1.88 m telescope (Churms et al., 1974). Fig. 6a shows a level plot of the CCD results (exp. time: 30 min) at $\lambda \simeq 1.0\mu$m. Apart from the brightest points in Fig. 6b one also sees the presence of an extended very low brightness halo around the source. An interesting feature of Fig. 6a is that one clearly notices at the very low brightness levels the column pattern in the noise; the larger portion of this noise has been suppressed by setting the lowest level just above the detector noise level. The stellar images in Fig. 6a confirm the results

mentioned before on the stellar profiles. On these, one does not see the left-right asymmetry which is quite obvious in the visual.

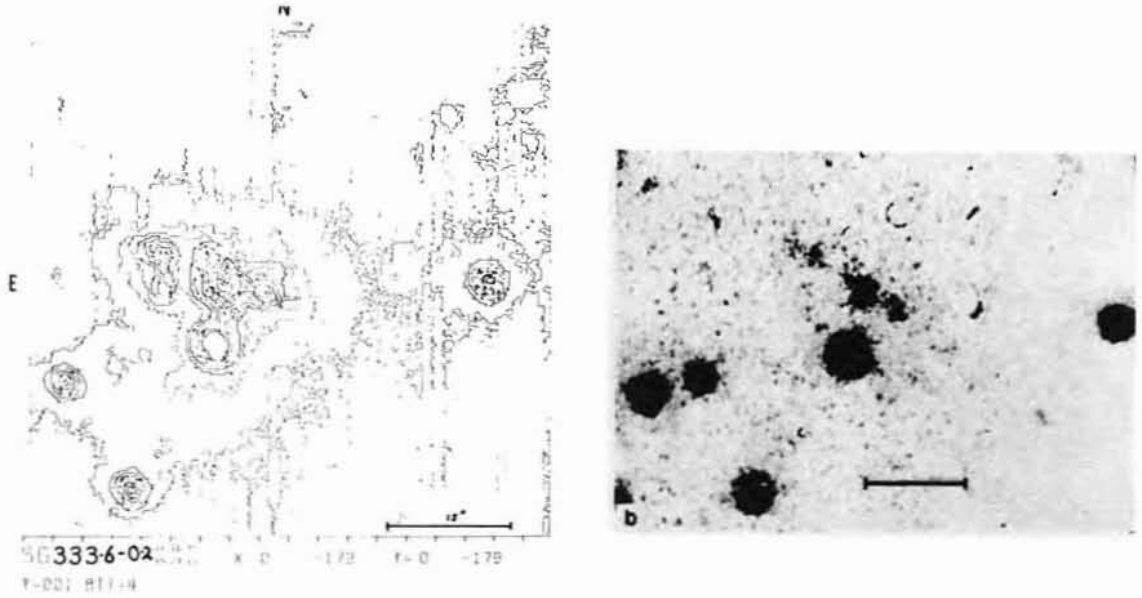

Fig. 6
6a) Level plot of the highly obscured HII region G 333.6-0.2;
6b) Direct photograph (Chrums et al. , 1974) (λ_o = 0.8μm) with the Radcliffe 1.88 m telescope. The low surface brightness halo is much better defined in the CCD plot than the photograph.

The brightness of the radio source 13S6A shown in Fig. 2 is estimated from the results of Goss et al. , (1978) to correspond at 1μm to a photon flux of 3 ± 2 photons pixel^{-1} sec^{-1}, on the detector. This indicates that the Q.E. of the detector at 1μm seems to be indeed of the order as indicated in Fig. 1.

Conclusions:

After the observations and reductions of some of the data obtained with the JPL-CCD at the ESO 1 m, we would like to summarize the following:

1. Since the detector we used was not the best available now, we were unable to test the full extent of the capabilities of such detectors as absolute photometric devices.

2. Apparently minor problems, such as bad pixels, make the reduction of the data difficult and at times impossible, depending on the astrophysical problem to which the detector is applied.

3. Although such problems as the wavelength dependence of the optical transfer function are in principle solvable in the reduction, it is

preferred to have these solved at the detector level.

4. Proper reduction of such data requires a complete image processing facility, generating problems for home reduction at small institutes.

In summary, we would like to express our feeling that the CCD detector does indeed have the great potential for astronomy as claimed; however, at present the detector still seems to be quite a way from the development level needed to operate it in a workhorse fashion.

Acknowledgements:

We would like to thank the following persons: Greg Cozza for his efficient and cheerful help with the detector and support instrumentation; Dr. Blanco for making the computing facilities at CTIO available; Dr. Woltjer for his support throughout this effort; Dr. Lasker for his assistance in making it possible for us to use the JPL-CCD; Dr. Schaller for his valuable help with the CTIO reduction system; M. Dennefeld for graciously making some of his observing time available. The operation of the camera system at the observatory was supported by JPL under NSF grant AST77-20893.

References:

Churms, J., Feast, M.W., Glass, I.S., Harding, G.A., Lloyd Evans, T., Martin, W.L., 1974, Mon. Not. R.A.S., 169, 39 P.

Geballe, T.R., Danks, A.C., Lacy, J., Wamsteker, W., 1980, in preparation.

Goss, W.M., Tritton, K.P., Longmore, A.J., 1978, Astron. Astrophys., 70, 423.

Janesick, J., 1980, Internal memo NASA-JPL.

Lausten, S., Schuster, H.E., West, R.M., 1977, Astron. Astrophys., 59, L3.

Marcus, S., Nelson, R., Lynds, R., 1979, SPIE Conference Instrumentation in Astronomy - III, Tuscon, Arizona.

Osmer, P.S., Smith, M.G., Weedman, D.W., 1974, Astrophys. J., 189, 187.

Schaller, S., Osmer, P.S., Albrecht, R., Lasker, B.M., 1977 in CTIO Facilities Manuel, ed. J.E. Hesser.

Steckl, A.J., 1979, The Infrared Handbook, eds. W.L. Wolfe and G.J. Zissisco, Office of Naval Research, Dept. of Navy, Washington, D.C.

ON THE DISTRIBUTION OF LIGHT AND COLOURS IN DISKS AND BULGES OF EDGE-ON SPIRAL GALAXIES

P.C. van der Kruit, Kapteyn Astronomical Institute, University of Groningen
L. Searle, Hale Observatories, Carnegie Institution of Washington

1. Introduction

There is currently much interest concerning the separation of the bulge and disk in the observed surface brightness distributions of spiral galaxies. It is customary to represent the light profile of the bulge by one of the standard functions, such as the "de Vaucouleurs $R^{\frac{1}{4}}$-law". Kormendy (1977a) has shown that the results depend only mildly on the actual functional representation chosen. An important justification for the use of analytical functions to represent the bulge is the fact that these very conveniently fit the light profiles of elliptical galaxies and bulges of relatively early-type galaxies (where the bulge often dominates the general light distribution). There is, of course, no a priori reason why these functions should also apply to bulges of later types in which the gravitational effects of the disk are likely to be much stronger. In fact, Kormendy (this meeting) has summarized some important differences between spiral bulges and elliptical galaxies. The disk is usually thought of as exponential with radius, although Kormendy (1977b) finds that often a different behavior remains when a bulge with an assumed analytical form is subtracted from the observations.

Burstein (1979) has also used this technique on slightly inclined S0 galaxies and has found that there is extra light at large distances from the plane that cannot be accounted for by summing a bulge and disk of the assumed form. He attributes this remnant light to a "thick disk" that he regards as a new component of galactic structure. More important is his contention that spiral galaxies do not possess a thick-disk component, which is - he argues - characteristic of S0 galaxies.

It is of interest for both these points and also for the general problem of component separation to investigate the light distribution of edge-on spirals. We use J-plates of the systems NGC 4244, 5907, and 4565 (published previously; van der Kruit 1979) and plates in three colours of NGC 891. The colour system is the one described by van der Kruit and Searle (1979) and consists of three colour bands U', J, and F that relate to standard UBV by

$$\begin{aligned} J &= B - 0.24\,(B-V) \\ (U'-J) &= 1.08\,(U-B) \\ (J-F) &= 1.25\,(B-V) \end{aligned}$$

2. Spirals with little or no bulge

We start out by trying to fit the light distributions in systems that are as pure disks as possible, in this case NGC 4244 and 5907. The isophote maps used are those published in van der Kruit (1979). Before attempting the fits the disturbing star images near the galaxies were removed by linearly interpolating the surface brightness across them. The model distributions used are the following, where L(R,z) is the space luminosity density:

$$L(R,z) = \begin{cases} L_0 \, e^{-R/h} \, \operatorname{sech}^2 \left(\frac{z}{z_0}\right) & R < R_{max} \\ 0 & R > R_{max} \end{cases}$$

This is a truncated exponential disk in the face-on projection, while the z-distribution is that of an isothermal sheet. For large z the latter is an exponential with scale height $z_0/2$. The edge-on aspect of this disk is:

$$\mu(R,z) = \mu(0,0) \, \frac{R}{h} \, K_1 \left(\frac{R}{h}\right) \operatorname{sech}^2 \left(\frac{z}{z_0}\right) \text{ for } R \leqslant R_{max},$$

where $\mu(0,0)$ corresponds to $2L_0h$. We fit this distribution to the z-profiles of the galaxies away from the central plane where the dust and young population is found. The fit to the R-distribution is done at $z \sim 1$ kpc. The result is that these models completely specify the observed surface brightness distributions. The galaxies must definitely have a rather sharp outer edge at about R_{max}, and they have no thick disk in Burstein's sense. The parameters are summarized in table 1 in section 5.

3. NGC 4565

This galaxy has a clear bulge for which Kormendy and Bruzual (1978) and van der Kruit (1979) presented a z-profile. We follow here the same procedure to fit the disk as above, except that we use only points more than 200" from the rotation axis. The parameters of the model disk are included in the table. Subtracting it from the observed surface brightness distribution leaves the bulge, for which we find the following features:

(i) For $\mu < 25$ J arcsec^{-2} the radial profile is very steep ($r \propto r^{-\alpha}$ with $\alpha > 3$), and the isophotes have consistent axis ratios of 0.78. Beyond this level of surface brightness the radial profile flattens (see also Kormendy and Bruzual), while the axis ratio starts to decrease rapidly to about 0.3 at $\mu_J = 27$ arcsec^{-2}. The second part of the bulge clearly is similar in all respects to Burstein's thick disks, including the quasi-exponential tails in z-profiles, except for the surface brightness, which is in this case a few magnitudes fainter.

(ii) The disk model cannot reproduce here the outer disk in the sense that the observed disk is not flat. A small warp in the same sense as the HI warp described by Sancisi (1976) is indicated. At this stage it is unclear whether thick disks resemble the old disk or halo population in colour, and we therefore now investigate the colour distribution in NGC 891.

4. NGC 891

Again the same procedure is followed for the three maps of NGC 891 (based on five plates). Here the magnitude scales have their zero-points derived from multi-aperture photometry in the literature.

It turns out that the disk model has the same parameters [except, of course, the magnitude scale fixed by $\mu(0,0)$] in the three colours. The remaining bulge now has the following features:

(i) At fainter levels the isophotes have in all colours axis ratios of about 0.4, compared to ~0.7 at brighter levels. However, the bulge seems to lack the concentrated central component that is so evident in NGC 4565.

(ii) The bulge has a systematic change in colour index towards the blue with distance from centre. The isochromes have similar axis ratios as the isophotes. Comparing the colour indices to integrated colours of galactic globular clusters of various metallicities, we find that the mean metallicity apparently changes from about -1.0 to around -1.7 to -2.0.

(iii) The general distribution is again in all respects except the surface brightness similar to Burstein's thick disks.

5. Concluding remarks

First we summarize some of the parameters of the fitted disks:

	NGC 4244	NGC 5907	NGC 4565	NGC 891
D(Mpc)	5.0	16.7	10.2	14.0
h(kpc)	2.64	8.66	5.47	7.26
z_0(kpc)	0.58	1.25	0.79	1.46
R_{max}(kpc)	13.7	29.3	24.9	33.7

The disks have apparent, central face-on surface brightnesses of 0.75 - 1.0 magn. fainter than the canonical 21.6 in B. This is not unreasonable if we consider the contribution of the younger populations (see e.g., Oort's (1958) listing of various components in the local disk of our Galaxy). The disk of NGC 891 has the colours of an old disk population like that of the Galactic disk in the solar neighborhood.

We summarize our results as follows:

(i) Disks have rather sharp outer edges in their light distributions at 3.5 to 5 scale lengths.

(ii) The z-distributions of the disks are well represented by isothermal sheets. Although this does not necessarily imply that they are self-gravitating, we suggest that this is a reasonable hypothesis.

(iii) Spirals with bulges have "thick disks," although these are fainter than those of Burstein's S0's. That these "thick disks" are population II systems is suggested by their colour. This and the change in axis ratio in the bulges with surface brightness leads us to propose that these misleadingly named "thick disks" are nothing other than the halo population responding to the gravitational field of the disk. The axis ratio changes because in the central regions the disk contribution to the potential is presumably small. The z-profiles of the thick disks indicate that the halo velocity distribution is isothermal, just like that of the disk, but with a larger velocity dispersion. This is in agreement with our hypothesis regarding the nature of these thick disks.

Acknowledgement

The plates of NGC 891 were taken as part of a research project supported by the NATO Scientific Affairs Division.

References

Burstein, D. 1979, Ap.J. (in press).
Kormendy, J. 1977a, Ap.J. 218, 333.
Kormendy, J. 1977b, Ap.J. 217, 406.
Kormendy, J., Bruzual, A.G. 1978, Ap.J. 223, L63.
Kruit, P.C. van der, Searle, L. 1979, In: Photometry, Kinematics and Dyanmics of Galaxies (Austin, Texas) (in press).
Kruit, P.C. van der 1979, Astron. Astrophys. Suppl. 38, 15.
Oort, J.H. 1958, Ric. Astr. Spec. Vat. 5, 415.
Sancisi, R. 1976, Astron. Astrophys. 53, 159.

MULTI-COLOUR SURFACE PHOTOMETRY OF M 51.

L.Swaans
Sterrewacht, Huygenslaboratorium
Wassenaarseweg 78, 2300 AX Leiden, The Netherlands

In this paper I will present some preliminary results obtained during the first stage of a project, which has as its final aim to find and fit models, which can describe evolution and structure in spiral galaxies on a basis of high resolution photometric data in several colours to be obtained by a two dimensional detector and detailed radio data from WSRT observations.
Theoretical work in this field has already been started by Yuan and Grosbøl (1979) and discussed by the latter during this workshop.
As galaxies to be investigated first M 51 (NGC 5194) and M 81 (NGC 3031) were chosen, because of the availability of WSRT observations, their distance which allows a spatial resolution of less than 100 pc, and their more or less face on orientation.
As the effects one is looking for can be small, one needs a photometric system with a highly discriminating capacity to these effects. The Strömgren system was chosen, extended with two narrow band filters centered on H_β and O III emission lines, being strong H II tracers, and with a broad band red filter (beyond H_α) to provide more information about the old disk stars and the dustlanes along spiral arms.
As a two dimensional detector the RGO electronographic camera (see McMullan, these proceedings) was used, which provides good quantum-efficiency, together with a linear response over a large dynamic range. Both properties are essential in order to meet the demands of the photometric system as well as the large dynamic input range of the objects under investigation. The camera was mounted to the 1 meter telescope of Wise Observatory (Mitzpeh Ramon, Israel). Due to the spatially non-uniform photocathode response flat field correction is necessary. However after applying such a flat field correction to the M 51 and M 81 plates deviations are still present (See Plate 1.). The main cause might be found in time dependent effects together with still not fully reliable procedures to obtain the sensitivity distribution of the photocathode at any arbitrary moment. Taking flat field exposures on the twilight sky, as we did, are only possible twice a day for very short periods. Besides the intensity of the twilight sky is very rapidly changing and thus the danger exists of


M 51
INTENSITY MAP
U


M 51
INTENSITY MAP
V


M 51
INTENSITY MAP
B


M 51
INTENSITY MAP
HBETA


M 51
INTENSITY MAP
Y

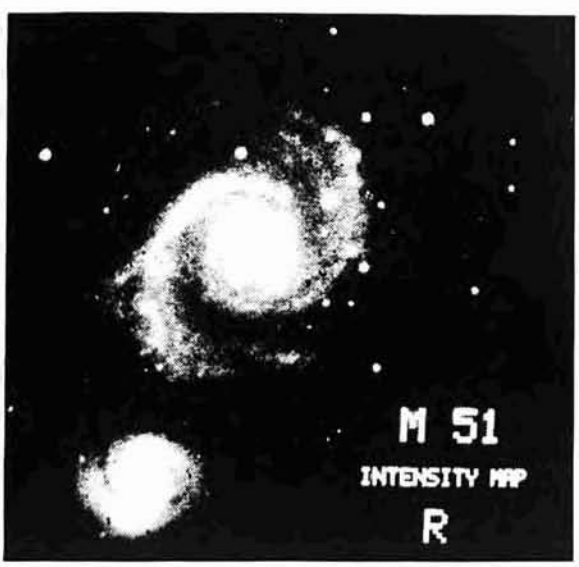
M 51
INTENSITY MAP
R

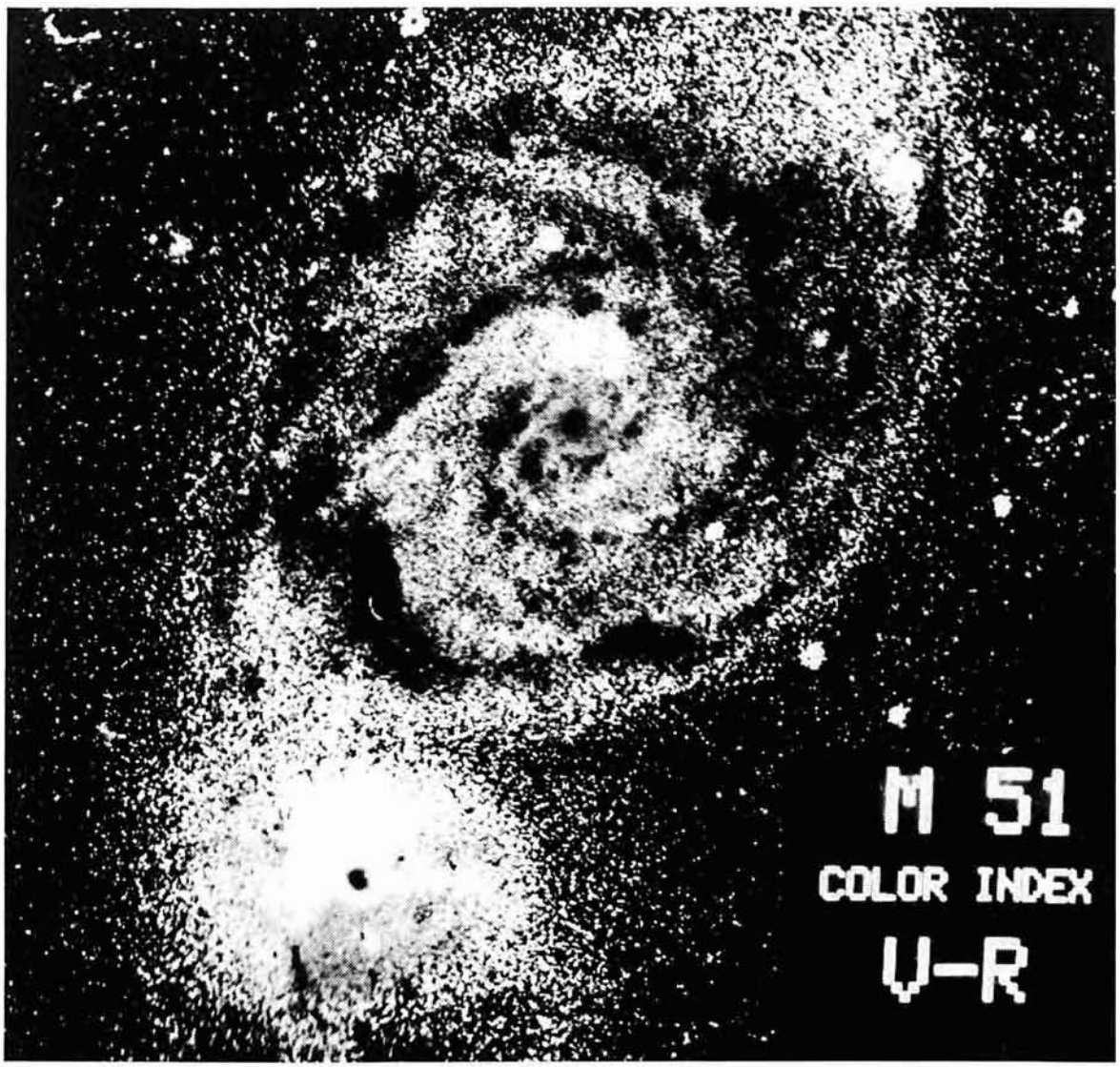

Plates 1-6 (left hand page, from left to right and top to bottom)
Exposures of M 51 made by A. Segalowitz at Wise Observatory, Israel (RGO electronographic camera, 1m telescope, F/7 Cassegrain focus) in six colours resp. the Strömgren u, v, b, narrow band H_β, the Strömgren y and a broad band r (beyond H_α). Plates are digitized by the ASTROSCAN, corrected for scattered light and crosstalk (see Swaans, these proceedings), for flat fielding and background. Prints are reproduced from a COMTAL image processing system and have thereby lost a major portion of their dynamic range, but they still show the broadening of the arms and their decreasing amplitude for longer wavelengths. Calibration errors are most pronounced in the u intensity map (Plate 1).
Plate 7 (above) Relative (v-r) colour-index of M 51.
Displayed intensity increases with colour-index, so the spiral arms form the dark pattern. Pixels for which no colour-index was calculated ("outside" the galaxy) are black. The blue cores of M 51 and its companion are caused by the limited range of the ASTROSCAN. The width of the plate represents a distance of about 28 Kpc. Spiral structure can be seen quite deep into the central region. At about 3 Kpc from the center there is a sudden change in this structure at points situated on an almost bottom-left to top-right line through the core. More inward the spirals are of other shape and less tightly wound.

overexposing the photocathode. In the worst case recovery of the photocathode requires a long time and might be position dependent. Furthermore absolute calibration, by taking exposures of stars with known magnitudes, did not yield consistent results, either caused by a very rapidly changing overall sensitivity of the photocathode or for other still unexplainable reasons.
Another problem I am facing is a very awkward geometric distorsion (quadrupole and higher order terms) produced by one of the cameras used. This prohibits at the moment the full use of especially the M 81 plates, which were partly taken by that camera, and therefore I will confine myself in the further discussion to the M 51 set of exposures.
What can be seen clearly in this set in a still qualitative way is the decreasing amplitude and the broadening of the arms as the passband wavelength increases (Plates 1-6). This of course is due to the fact that the mix of spectral types in a group of stars changes in time, as the younger stars rapidly evolve. Colours of clusters are strongly related to their stellar composition and by that also to their age. But in its turn the cluster age is, within some limits, related to its distance from its birthplace in a spiral arm and is in principle determined by the difference in cluster and pattern speed. So the bluer young stars exist only in the immediate vicinity of the arms, whereas the redder stars can be found at larger distances. Also the fractional contribution of the old disk stars increases with wavelength. Absolute calibration and quantitative interpretation can provide here powerful tools to discriminate between models describing the starformation (birthrate, IMF), cluster evolution and gaseous and stellar composition of a galaxy as function of time and position.
Another rather unexpected result was achieved by calculating the relative colour-index over the longest reliable baseline available (Plate 7).
Spiral structure is not only well recognized, but seen to go quite deep into the central region almost to the stellarlike core. Besides there is a sudden change in structure at about 3 Kpc from the center, which shows itself more evidently, as the spirals can be followed now further inward. In the intensity maps this structure is not visible because of the dominating intensity gradient towards the center. However due to the large dynamic range it is still present there, and will come out in a colour-index map, which flattens the radial gradient and by that can show amplitudes more easily for the colours involved. Within this 3 Kpc radius the arms are of other shape and less tightly wound. If this should indicate the corotation radius then stars and gas at larger radii will move from outer- to inneredge through a spiral arm if the arms are trailing. Again quantitative interpretation should provide here a decisive answer.

ACKNOWLEDGEMENT

Plates were obtained at the Wise Observatory of Tel Aviv University, in part supported by the Smithsonian Research Foundation Grant SFC-0-3005.

REFERENCES

Grosbøl P.: "These Proceedings"
McMullan D.: "These Proceedings"
Minn Y.K. and Greenberg J.M.: 1973 "Astronomy & Astrophysics" 24, p.393-404
Schweizer F.: 1976 "Astrophysical Journal Suppl." 31, p.313-332
Segalowitz A.: 1976 "Ph.D. Thesis"
Yuan C. and Grosbøl P.: 1979 (in preparation)

EMISSION LINE SURFACE PHOTOMETRY OF ACTIVE GALAXIES

K. Taylor
Royal Greenwich Observatory, Herstmonceux Castle, Hailsham, Sussex, England.

D. Axon
Astronomy Centre, University of Sussex, Falmer, Brighton, Sussex, England.

K. Gyldenkerne
Copenhagen University Observatory, Brorfelde, DK-4340, Tollose, Denmark.

S. Worswick
Royal Greenwich Observatory, Herstmonceux Castle, Hailsham, Sussex, England.

Introduction

The emission-line structure of active galaxies provides a powerful tool for assessing the physical conditions within such objects. The intensities of the forbidden lines are dependent not only on the temperature and density of the regions in which these lines are formed, but also on the abundances of their parent ions, while collisional excitation can lead to high fluxes in the forbidden lines of SII and OI. Therefore the determination of emission-line ratios provides abundance gradients as well as variations in both excitation conditions and excitation mechanisms.

Spectrophotometric observations of selected regions of a galaxy will yield this type of information but when the number of spatial elements of interest greatly exceeds the number of spectral elements required imaging becomes a more efficient approach. A linear detection process such as electronography simplifies the determination of relative emission-line fluxes. However, if these data are to be of significance in abundance studies they must be put on an absolute scale. This paper considers the accuracy which may be obtained by both internal and external calibration of electronographs, and our technique is illustrated by data obtained on the nucleus of the 'hot spot' galaxy NGC 1808.

Detection and Reduction System

The emission-line exposures were obtained using the RGO electronographic camera (McMullan et al 1976) and narrow band (20 to 50Å) interference filters. In addition, wider band (100Å) continuum exposures were taken to assess the continuum contribution to the line exposure. Ilford G5 emulsion was used since the fluxes involved were not high enough to use the slower L4. The densities in the exposures are usually less than 2D, and thus fall within the linear range of G5 emulsion.

To assess the sensitivity of the system at the different filter wavelengths standard stars of known spectral energy distribution were observed using the same filter and camera combination. A series of exposures were obtained for each filter and, together with the flat-field exposures taken of the twilight sky or dome interior, these were used to calibrate the system.

The exposures were digitised using the PDS microdensitometer at the Royal Greenwich Observatory. Deviations from linearity of this machine occur at both low ($D < 1$) and high ($D > 4$) densities. The densities at the low end of the range are below their true value, while those at the high end are too

large. Over the range of the present data (i.e. $0.5 < D < 2.5$) these non-linearities are $\sim$ 2% and are small in comparison with other sources of error within the system.

The PDS is controlled using a FORTH data acquisition and image processing system which provides facilities for operator interaction at the time of measurement. Using fiducial marks and field stars, both flat field and emission-line exposures may be spatially matched prior to scanning. The control computer calculates the translation and rotation required to align the two sets of fiducial features, the angle of the platten is adjusted by the operator, and the translation is automatically fed into the scan co-ordinates. An initial 'by eye' alignment to about 5 degrees is reduced in this manner to less than 0.1 degrees after a few iterations, which gives spatial alignment to better than 5 μm. The scan data may be stored as 'images' on either disk or magnetic tape and recalled for subsequent processing. Simple commands may be used to perform such tasks as the division of one array by another, the storing of the resultant array on disk, and a transfer to tape if desired. The estimates of volumes of stellar images required for calibration of the system in the different filter passbands are derived from either a direct numerical integration of the density values in the stellar image, or from a 2-dimensional elliptical gaussian fitting routine.

Production of Ratio Maps

Having obtained scans of spatially-matched emission-line exposures and flat fields the data were corrected for photo cathode non-uniformities. The flat-field data were sampled at the same spatial resolution as the galaxy, and then smoothed by passing a box car filter through them. The smoothing process reduced the emulsion grain noise of the flat field exposure while retaining the information on the large scale variations in system sensitivity. The night-sky level of the exposure was then subtracted, and the continuum emission from the galaxy in the emission-line filter passband assessed and likewise subtracted. This required knowledge of the slope of the continuum and the relative sensitivity of the system at the emission-line and continuum wavelengths. Commonly the galaxy continuum represented < 10% of the emission-line exposure.

Two emission-line exposures processed to this stage must then be compared to judge whether the seeing was significantly different for the two exposures. If so, the data must be convolved with the appropriate stellar profile to achieve the same spatial resolution in each data set.

The emission-line maps were then divided to yield ratio maps of relative line strengths. At this stage they were calibrated by using either spectrophotometric data for a few points in the map, or the electronographic exposures of the standard stars.

Accuracy of Internal and External Calibration of Ratio Maps

The accuracy of the uncalibrated map of relative emission line fluxes is governed by three factors.

(1) Noise arising from the granular structure of the emulsion

(2) Variation in emulsion sensitivity

(3) Accuracy of the assessment of the background and galaxy continuum contributions.

For small pixel areas the dominant source of inaccuracy is statistical fluctuations in the number of developed grains within the pixel. In the

linear range of G5 emulsion a grain noise of the order of 10% is obtained on a 100 sq micron pixel at unit density. Typical pixel sizes and exposure levels used for this work lead to emulsion grain noise of the order of 3% to 5%. The emulsion noise contribution from the flat field correction is negligible since the sample sizes used are considerably larger than those of the emission-line data.

Non-uniformity of emulsion response cannot be calibrated out using flat field techniques and accumulates with each additional exposure used in the calibration process. Small scale effects such as dust on the emulsion surface can be recognised and edited out before processing. Changes in the overall sensitivity of the emulsion have a scale length of a few centimetres (Walker, 1978) and are of the order of 5%. For observations in which the image sizes are only a few millimetres across, such non-uniformities are not a significant source of error.

The accurate removal of the galaxy continuum from the emission-line data required that the relative transmissions of the filters be well known. These data are obtained from electronographic exposures of standard stars. The volumes obtained by integrating the density under the stellar images are used as a measure of the system sensitivity at each wavelength. Given either a continuum filter close in wavelength to the emission lines, or a known slope of the galaxy continuum, the continuum exposure may be scaled with respect to the line exposure and subtracted. The stellar-image volume method yields relative filter sensitivities to better than 5%. Galaxy continuum is typically $\leq$ 10% of the emission line flux so that an error of 5% in the relative transmissions of the continuum and line filters has little effect on the final ratio data. Of more importance is the accuracy of the background level; in low flux regions small errors in zero level subtraction may severely distort line ratios. This requires that signal levels close to the noise on the background should be ignored, and that the detection limit should be set to a few standard deviations above the background.

For a ratio map calibrated using known line ratios from spectrophotometric data taken at specific points in the image, the predominant source of error is therefore emulsion noise associated with the finite number of grains in each pixel. In this case an overall accuracy of better than 10% is expected and typically accuracy is $\sim$ 5%.

If spectrophotometric data are not available the system must be calibrated by the standard star exposures. The transmissions of the two line filters must be compared, and further, it is necessary to know the bandpass shape and the position of the emission-line within it. These added complexities reduce the accuracy of the absolute calibration to about 10% when the emission-line is well centred in the passband. However if the line falls near the steep edge of the transmission profile accuracy is somewhat lower. The central wavelengths of the filters are selected to isolate the red-shifted emission-lines, but variations in temperature will shift the position of the passband and careful monitoring is required.

The best calibration is clearly achieved with spectrophotometric data for a small region of the map, and, whenever possible, this approach should be used.

The 'Hot-Spot' Galaxy NGC 1808

NGC 1808 is an example of the class of spiral and barred-spiral galaxies which contain multiple, peculiar, 'hot-spot' nuclei (Morgan 1958, Sersic and Pastoriza 1967, Sersic 1973). The central region of this galaxy consists of a number of compact emission-line objects apparently embedded in and connected

by a diffuse structure of low surface brightness filaments. The individual knots are a few tens of parsecs in diameter, and the whole nuclear complex is of the order of one kpc across, assuming a distance of 10 Mpc for the galaxy. Radial velocity measurements by Arp and Bertola (1970) revealed non-circular motions which have been interpreted as evidence of expansion of the hot-spot region.

To investigate the structure of the nucleus of NGC 1808 in further detail, the mapping techniques outlined in this paper were used to search for variations in physical conditions within the hot-spots. The observations were made with the ESO-Danish 1.5m telescope at La Silla using a 40mm RGO electronographic camera, with typical exposure times of one to two hours on G5 emulsion.

Figure 1a shows a Johnson V-band exposure of the galaxy and Figure 1b and 1c are the Hα and [NII] electronographs of the nucleus on an expanded scale. These latter exposures were made under conditions of excellent seeing (< 1") and the complex structure of the nucleus is readily apparent. Figure 2 shows this structure in some of the display modes available with the FORTH data-acquisition system of the PDS microdensitometer.

The [NII]/Hα ratio map (figure 2f) shows that there is one dominant hot-spot with an enhanced NII flux present in the nucleus, and that there is some evidence for a smaller increase of the [NII]/Hα ratio in an adjacent condensation. The remaining structure of the nucleus is no longer clearly defined, implying thst the other nuclear components possess a similar [NII]/Hα ratio. Figure 3 shows IDS (Image Dissector Scanner) spectra obtained on the ESO 3.6m telescope in November 1979. The knot designated 'A' is located at the NW end of the nucleus, while knot 'D' is the feature showing the enhanced [NII] emission. Preliminary measurements yielded an [NII]/Hα ratio for knot D of the order of 0.9, somewhat larger than the average value for HII regions in the spiral arms of galaxies ([NII]/Hα = 0.3), but within the range of values determined for HII regions in our own galaxy (.15 < NII/Hα < 1). Although there is a clear enhancement of the [NII] flux in knot D with respect to knot A ([NII]/Hα= 0.5) the change is much less than that seen in nuclear regions of some spiral galaxies ([NII]/Hα = 10; Burbidge et al 1963). Between knot D and knot A we obtained a relative [NII]/Hα ratio of 1.8 from the spectra and 1.7 from the electronographs. In the latter case the data are integrated over an area equivalent to the entrance aperture of the IDS.

Conclusion

It has been shown that relative emission line ratios of moderate accuracy may be obtained using electronographic techniques. When the number of spatial elements of interest exceed the number of spectral elements, the panoramic aspect of this linear process comes into its own.

Acknowledgements

The authors wish to thank the Director and staff at both La Silla and Copenhagen University Observatories for extending their facilities to us. The efforts of Jonathan McDowell in writing FORTH programs and Neil Trask in using them are acknowledged with much appreciation. D.J. Axon is supported by an SRC Research Fellowship.

References

Arp, H.C., & Bertola, F., 1970. Astrophys. Letters, 6, 65.

Burbidge, G.R., Gould, R.J. & Pottasch, S.R., 1963. Astrophys. J., 138, 945.

McMullan, D., Powell, J.R. & Curtis, N.A., 1976. Adv. in Electronics & Electron Phys., 40B, 627.

Morgan, W.W., 1958, Publ. astr. Soc. Pacific, 70, 364.

Sersic, J.L., & Pastoriza, M., 1967, Publ. astr. Soc. Pacific, 79, 152.

Sersic, J.L., 1973. Publ. astr. Soc. Pacific, 85, 103.

Walker, M.F. & Bell, M., 1978, Preprints of Papers presented at The Seventh Symposium a Photo-Electronic Image Devices Imperial College 4-8 September 1978, p. 245.

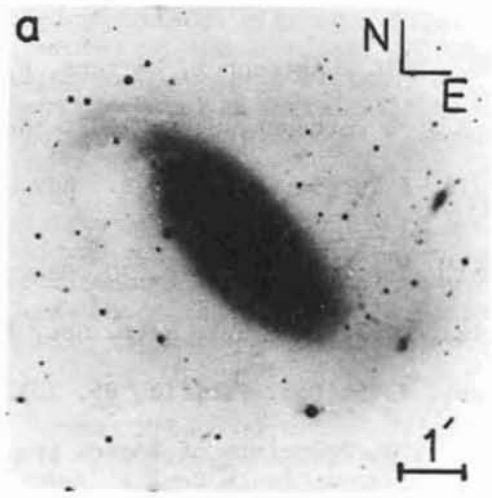

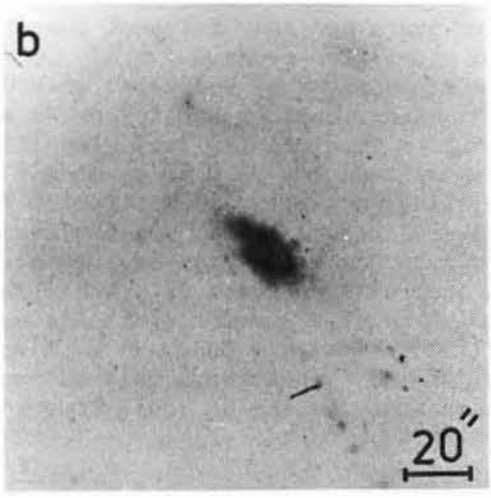

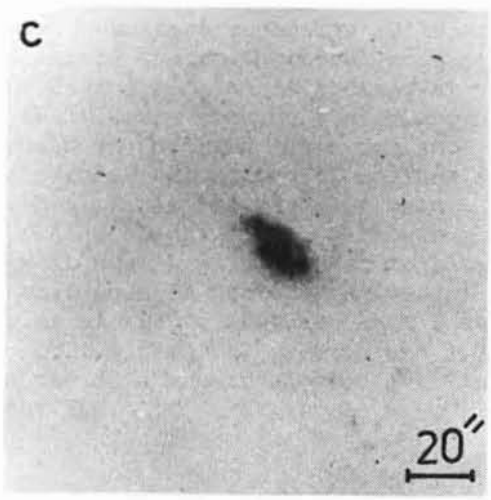

Figure 1

a) V-band electronograph of NGC 1808

b) Hα electronograph of nucleus

c) [NII] electronograph of nucleus.

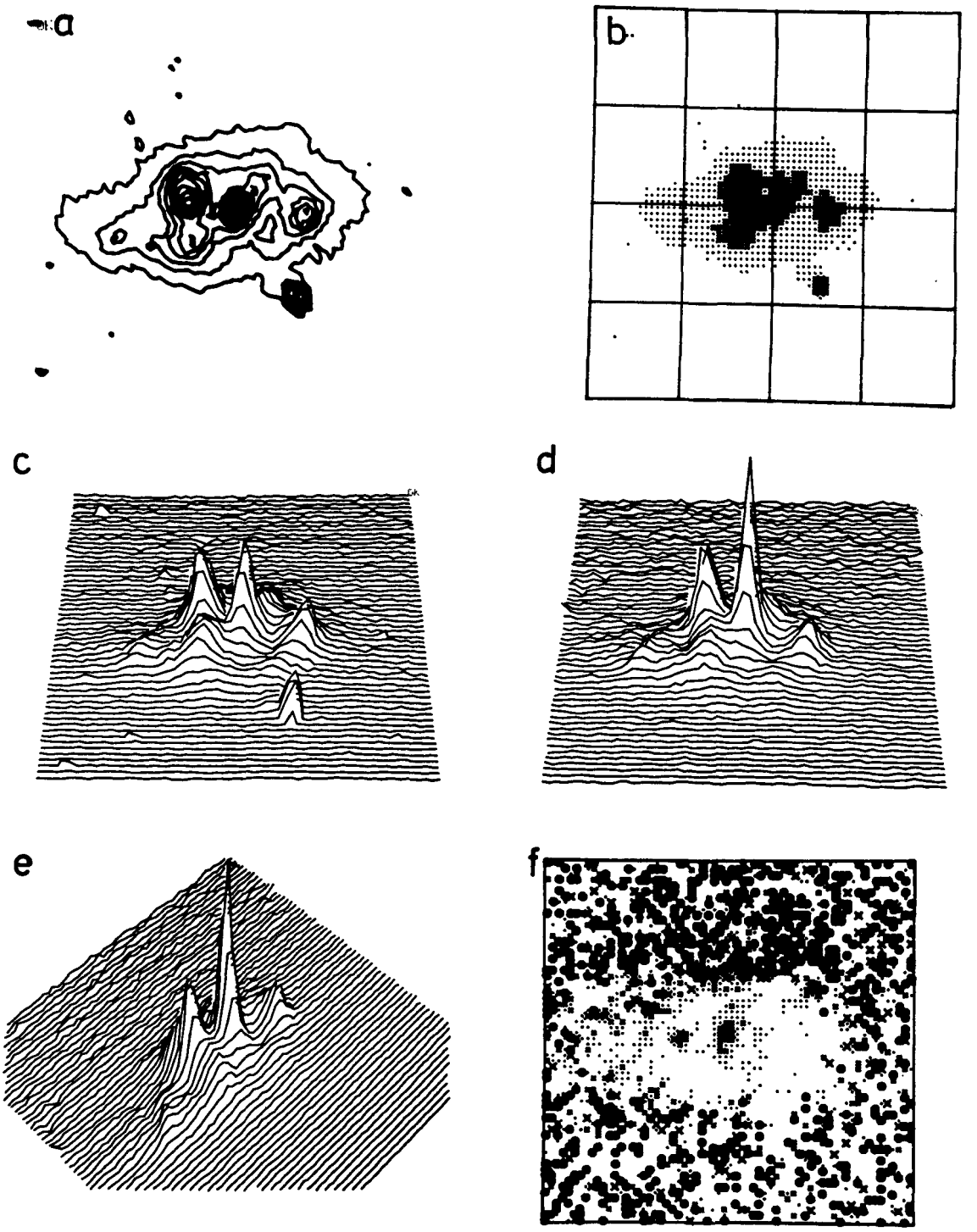

Figure 2

a) Contour map of Hα emission

b) Grey scale display of Hα

c) isometric plot of Hα

d) isometric plot of [NII]

e) Skew isometric plot of [NII]

f) [NII]/Hα ratio map.

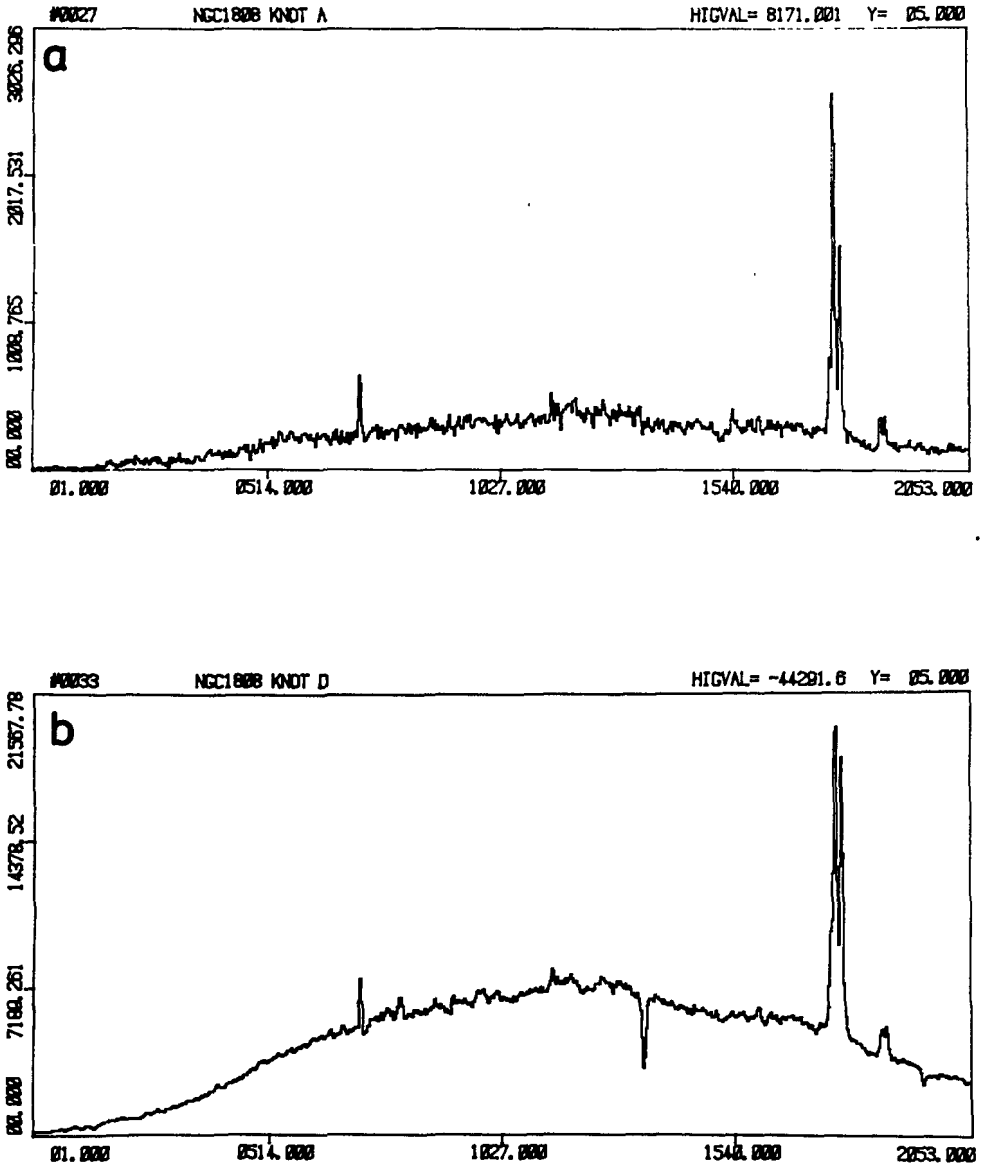

Figure 3

Image dissector scanner spectra of nucleus of NGC 1808

a) knot A at extreme NW end of nucleus

b) knot D, condensation showing enhanced NII emission.

CORE STRUCTURE IN EARLY-TYPE GALAXIES

Garth Illingworth
Kitt Peak National Observatory[1]

The core regions of early-type galaxies have not been investigated in much detail. Instrumental limitations have, to some extent, been the cause of this. For example, both photographic plates and vidicons (e.g., SITs) are subject to nonlinearities that are difficult to calibrate over the wide dynamic range required for this problem. The photographic study by King (1978) of the light distributions in a sample of E and S0 galaxies exemplifies the difficulties and the care required to ensure good results with nonlinear detectors such as these.

New detectors in the form of CCD imaging systems and photon-counting spectroscopic systems enable us to study these galaxies more extensively and reliably. An excellent example of the power of these detectors can be seen in a pair of papers published in 1978 by a group from the "West Coast Center for Fundamental Advances in Astronomy." These papers (Young *et al.* 1978 and Sargent *et al.* 1978, hereafter YSETC) gave surface brightness distributions and velocity dispersion profiles for two elliptical galaxies: the radio galaxy M87 and the "normal" elliptical galaxy NGC 3379. Their brightness distribution for M87 (Fig. 1) was derived from a CCD frame taken under very good seeing conditions. The signal-to-noise ratio in their data is clearly excellent. While there are some substantial disagreements with photographic surface photometry of this galaxy (Kormendy 1979), comparison with data from another linear detector, the digicon (the data were those used by Schmidt *et al.* [1978] in their study of the polarization of the jet in M87), shows good agreement for $r \geq 3''$. The seeing was worse (~2" FWHM) for the digicon data than for the CCD data (1".1 FWHM). This is reflected in the discrepancy between the two sets of data for $r \leq 3''$ where, as expected, the digicon data give a less pronounced light peak.

The data of YSECT not only provide examples of the excellent photometry that is now possible but, as we shall see, also provide an impetus for a study of a large sample of elliptical galaxies. From this work and studies by others, it appears that core structure is not well understood in normal ellipticals, let alone in radio galaxies such as M87.

M87 was, of course, the subject of all this attention because it is a radio galaxy with an optical jet and a small but active nucleus. Clearly, the hope in the studies by YSETC was that characteristics of M87's core structure could be

---

[1]Operated by the Association of Universities for Research in Astronomy, Inc., under contract with the National Science Foundation.

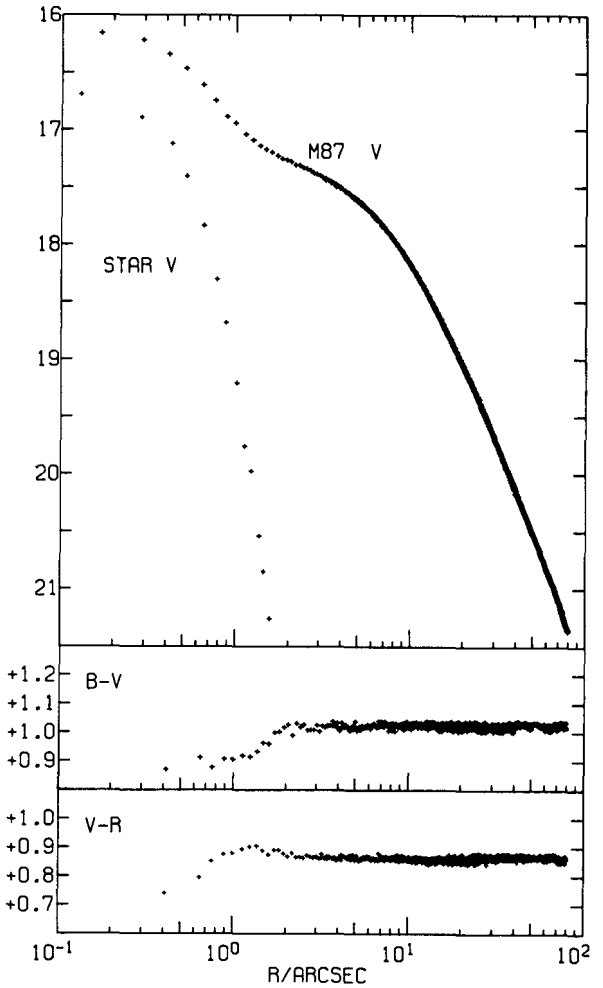

FIG. 1.—The V-band surface brightness distribution (V mag arcsec^{-2}) in M87 represented by mean values in concentric annuli. The data were derived from a CCD frame by Young et al. (1978). The instrumental and seeing point spread function used is denoted "star V" in the figure; it was derived from a star in the same frame. Colors are also shown.

found that would unravel some of the questions concerning the nature of the active nucleus. The discussion in these two papers centered on a comparison of the brightness distribution and velocity dispersion profiles of M87 and the normal elliptical NGC 3379. The authors' claim was that M87 had a light distribution in the core that differed substantially from that of NGC 3379, irrespective of any contribution from a central, unresolved nonthermal source in M87. NGC 3379 was noted as having an essentially isothermal core profile (a "King" model core; see King 1966). Unfortunately, their NGC 3379 data were not shown, so it was not possible to directly evaluate the extent to which NGC 3379 was consistent with this model. However, their conclusion is supported by Kormendy (1977, 1979), who found good agreement between a seeing-convolved isothermal core model and his photographic data for NGC 3379. On the other hand, de Vaucouleurs and Capaccioli (1979) recently claimed that the surface brightness distribution in NGC 3379 is more consistent with an $r^{1/4}$ law or, better still, an $r^{1/4}$ law plus a central Gaussian core, even though their data agree quite well with that of Kormendy (1979). This differing interpretation of similar data for NGC 3379

is the focus of some controversy. If one appeals to surface brightness data for other normal ellipticals (e.g., King 1978) to resolve this question and to establish the core structure that characterizes normal ellipticals, one finds examples that are well-fitted by isothermals (e.g., NGC 4472 in Kormendy 1977, 1979) and the ones that are well-fitted by seeing-convolved $r^{1/4}$ laws (e.g., NGC 4406 in Schweizer 1979).

The following questions then arise: (1) what really is the core profile in NGC 3379? and (2) is this core profile unusual? i.e., what is the surface brightness distribution like in a sample of apparently normal ellipticals? In particular, we would like to know if any apparently "normal" (i.e., nonactive) ellipticals display core light distributions like that of M87. Clearly, we need photometric data on a number of normal ellipticals. A program with this aim and using a CCD for a detector is now in progress.

The data of Sargent et al. (1978) raise a further question about the structure of the cores of NGC 3379 in particular, and possibly about normal ellipticals in general. They compared their velocity dispersion profile in NGC 3379 with that expected from a King isothermal core model and found satisfactory agreement. However, it turns out that when one plots their NGC 3379 velocity dispersion σ data in the same way as their M87 data (i.e., in log σ vs. log r), the trend in σ with radius appears to be very similar for both galaxies. This can be seen in Figure 2. Additional data from Davies (1979, 1980) for NGC 3379 confirm this trend. The logarithmic derivative of $\sigma^2(r)$ (important for the

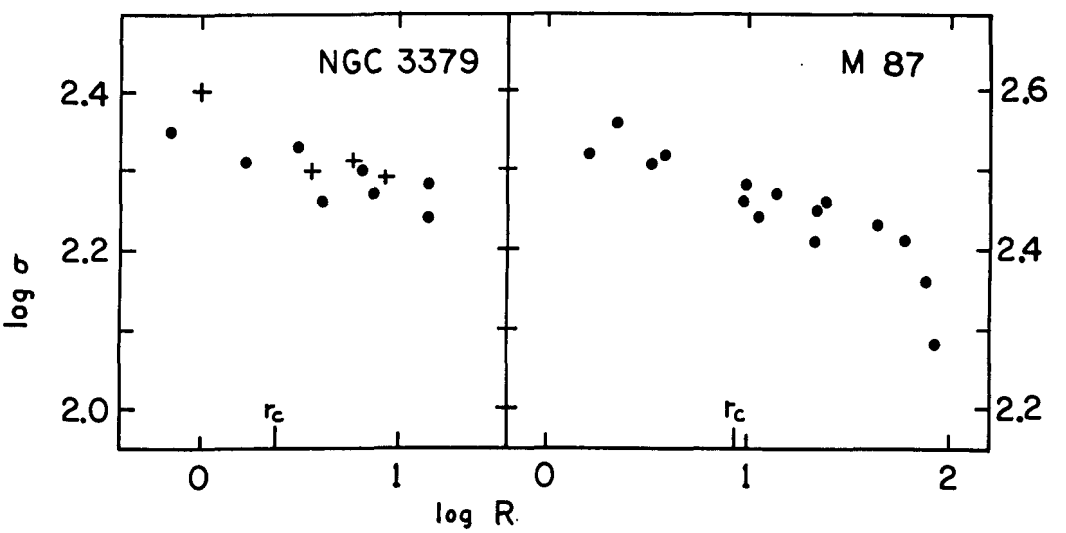

FIG. 2.—Velocity dispersion data σ for the elliptical galaxies NGC 3379 and M87 are shown plotted against radius in arcsecs on a log/log scale. The • symbols are data from Sargent et al. (1978), while the + symbols for NGC 3379 are Davies' (1979, 1980) data for $r \leq 4\ r_c$. The core radii r_c are taken from Young et al. (1978) for M87 and Kormendy (1977) for NGC 3379. The similarity in slope around r_c for the data from both galaxies is striking. Which one has the "black hole"?

discussion of the mass distribution in the core) is very similar for M87 and NGC 3379, i.e., d ln σ^2/d ln r $\approx$ 0.2 for both M87 and NGC 3379.

Does this suggest, as YSETC interpreted their M87 data, that NGC 3379 also has a large central mass (i.e., the ubiquitous "black hole"!)? Is NGC 3379 normal? If so, do all giant ellipticals have central black holes? Or should we be looking for another explanation for the light distributions and velocity dispersion profiles in these galaxies? The discussions by Young et al. and Sargent et al. are not as model-independent as they would have us believe (Binney 1979, 1980; Duncan and Wheeler 1980). There is further theoretical work required here as well as further observational data.

Clearly, investigation of a sample of elliptical galaxies at high spatial resolution and high S/N is required. A recent paper by Young et al. (1979), where the core light distributions of two Coma ellipticals are claimed to be consistent with an isothermal core profile (King model), is probably of little value for the problem discussed here. First, the galaxies are the brightest ellipticals in Coma, and hence might not be representative of typical ellipticals. Second, the derived profiles may well be strongly influenced by seeing, especially when the distance to Coma is considered. Recently, Schweizer (1979) has discussed the effect of seeing on the profiles of the cores of galaxies. He concluded that the uncertainties that seeing effects introduce enormously complicate the problem of establishing the core structure in ellipticals and other early-type galaxies. While the devastating effects of seeing, as he saw it, were partly the result of some basic premises which have been the subject of some disagreement among those active in this area, the attention that his paper has focused on the seeing problem will be of value.

Historically (e.g., King 1978; Kormendy 1977), the observed profiles of the cores of elliptical galaxies have been fitted with King (1966) models (essentially isothermal spheres) and described by a characteristic length scale, the core radius r_c. Common practice has been to establish r_c from fitting isothermal core profiles wherein r_c is defined to be the radius at which the surface brightness distribution drops by a factor of 2 from the central surface brightness.

In general, for ellipticals at the distance of the Virgo cluster, seeing has not been considered to be a major problem since r_c was found (King 1978) to be several times the standard deviation σ of the Gaussian core of a stellar image in the field, i.e., the galaxy core was considered "resolved." In only a few cases was $r_c \approx \sigma$, and hence the core was considered "unresolved." Thus seeing was considered to be more of a nuisance than a major problem.

Schweizer (1979) took a different approach. He noted, first, that in the two nearest galaxies, M32 and M31, r_c (for the elliptical-like bulge in the case

of M31) was extremely small — 0".5 for M31 and probably even less for M32 (Light, Danielson, and Schwarzschild 1974).[2] Even these galaxies required balloon observations to establish the core size; the core in like galaxies at Virgo distances would be unmeasurable. Second, the profiles of these two galaxies are well described by an $r^{1/4}$ law (see Schweizer 1979) to very small radii.

The following question then arose. If the two nearest galaxies display small cores and are well described by an $r^{1/4}$ law, is it not likely that the distant galaxies are like this also, and that they appear to us to have isothermal cores because of smearing by seeing? It turns out that, yes, this could be possible for a significant fraction of the galaxies for which data are available, but certainly not for all. A galaxy at Virgo distances and with an $r^{1/4}$-law profile extending to very small radii does, when convolved with a typical seeing profile, have a rather isothermal core-like profile. See Figure 3 which is taken from Schweizer (1979). Schweizer also demonstrated the effect of seeing on galaxies that have truly isothermal profiles, and how we can again be misled into thinking that we have determined r_c (see Fig. 4), although in this case if $r_c(\text{app})/\sigma(\text{seeing}) \geq 4$, then $r_c(\text{true})$ is very nearly $r_c(\text{app})$. However, there is no guarantee that the isothermal assumption is a priori true. All that one can say is that within the photometric errors such a profile is consistent with the data. A small core or nucleus may well be disguised by the smearing due to seeing.

A criticism that can be made here is that we are really comparing apples to oranges. It is not at all obvious that -21 to -23 mag giant ellipticals can rightly be expected to have the same density distributions as M32, a -15 mag elliptical, and as the -18 mag bulge component of M31. There may well be significant differences in the formation and/or evolution of these systems that result in differences in the core scale and structure. Schweizer's real contribution has been to emphasize (1) that the determination of the core parameters in galaxies is strongly dependent upon seeing effects, and (2) that the uncertainties associated with the core parameters are quite model-dependent.

In summary then, the best approach to this problem appears to be as follows. One's image data should have very high S/N and must have a stellar image in the same frame from which the instrumental point spread function (i.e., seeing) can be established to high accuracy. The light distribution of the galaxy within the image frame is then determined and tabulated along with the

---

[2]There is a continuing controversy as to the existence of a dynamically separate nucleus in M31. If the inner core is considered a dynamically separate subsystem, then r_c for the bulge should really be taken as $r_c \approx 19"$, not as $r_c \approx 0".5$. This undermines some of Schweizer's argument.

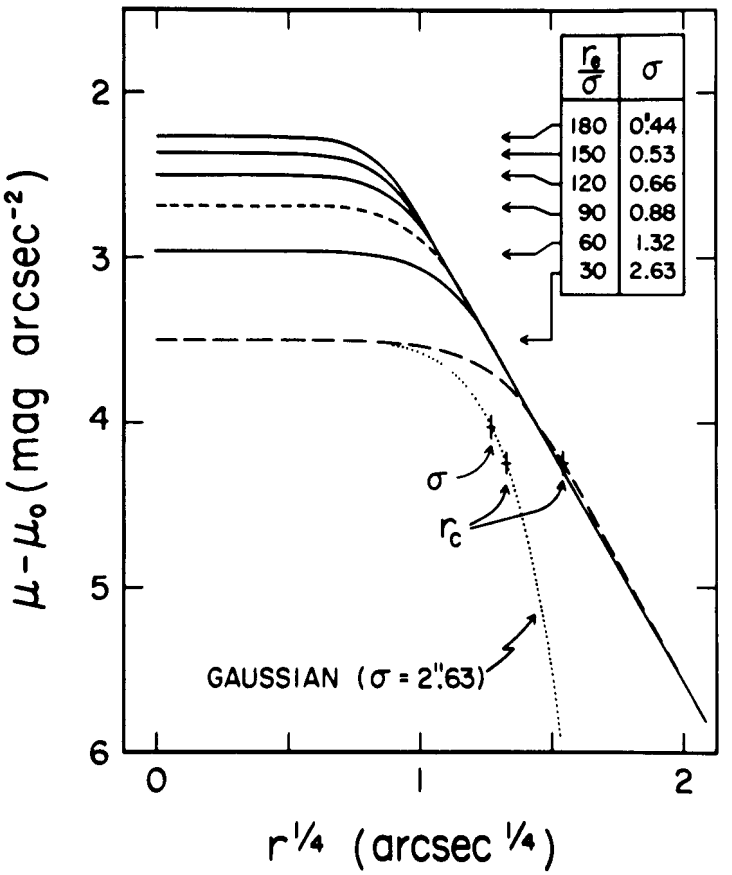

FIG. 3.—An $r^{1/4}$-law light distribution (V_e = 79") has been convolved with Gaussian (≡ seeing) profiles that have six different σ values (tabulated in the figure) in this figure from Schweizer (1979). The original $r^{1/4}$ law was a straight line in this plot with slope the same as that for $r^{1/4} \geq 1.5$ in the figure. The qualitative similarity to an isothermal and to typical elliptical profiles is apparent. The quantitative agreement is also excellent in some cases (e.g., NGC 4406), as Schweizer demonstrates. However, this is certainly not the case for all ellipticals, as is apparent from discussions by Schweizer (1979), King (1978), and Kormendy (1977, 1979). The dotted curve is the Gaussian of largest σ.

photometric errors. Models for the galaxy core surface brightness distribution are chosen and convolved with the point spread function and the goodness of fit to the data evaluated in a statistically well-defined way. The most appropriate model can then be selected, to some extent independent of the biases of those involved.

Work is in progress to obtain spectroscopic and CCD imaging data for a wide range of early-type galaxies at the highest possible spectral resolution. The aim is to establish the surface brightness distributions and velocity dispersion profiles in the cores of a sample of normal galaxies. While these data will clearly be valuable for discussions such as those of Young *et al.* (1978,1979) and Sargent *et al.* (1978), where comparison is required between these properties in

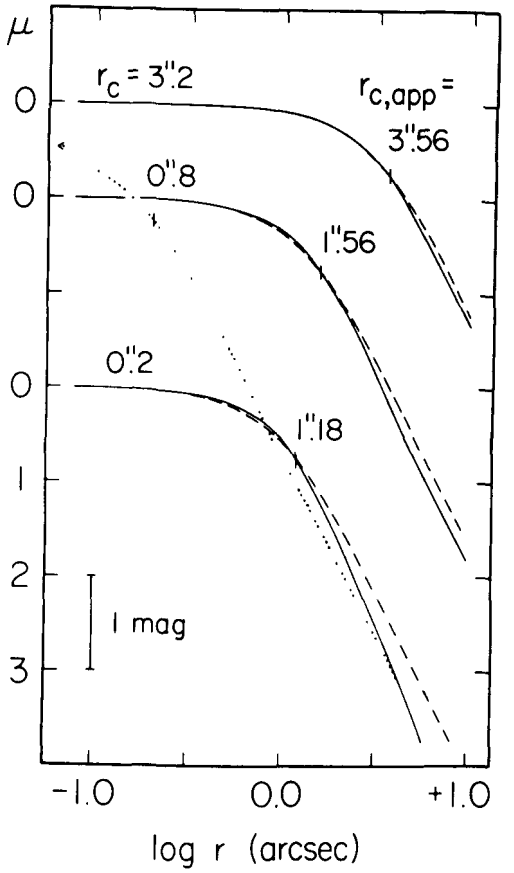

FIG. 4.—Several King models (≡ isothermal core) core profiles have been convolved with a Gaussian (with exponential wings) seeing profile that has σ = 0".75. Each of the seeing-convolved models (solid lines) is identified on the left by the original r_c (0".2; 0".8; 3".2), while the dashed lines and the r_c(app) values (1".18; 1".56; 3".56) represent the derived core scales if these convolved models are fitted with unconvolved models, i.e., if the effects of seeing are neglected. Clearly, one derives rather poor estimates of r_c(true) if r_c(true) ≤ 4 σ(seeing). The original (i.e., true) profile for the r_c = 0".2 case is shown by the dotted line. The figure is from Schweizer (1979).

active nuclei galaxies and normal galaxies, the data have much wider value in that they provide additional constraints on models of the formation and evolution of these systems, particularly when added to the extensive rotation, velocity dispersion, and surface brightness distribution data now available outside the core region in early-type systems (Schechter and Gunn (1979; Fried and Illingworth 1980; Kormendy and Illingworth 1980).

The first tentative results of such a program are available from CCD photometry of the M81 core. The data frame used is shown in Figure 5. This is a CCD frame (integration in the R band of 80 sec) from the KPNO Fairchild 244 x 190 chip. The star (R ~ 15 mag) used to define the point spread function can be seen in the picture, left of the center. The surface brightness results are shown in Figure 6 along with the stellar profile. The galaxy is clearly more extended. Fitting a King profile directly gives an apparent $r_c \approx 1".2$, although this result is very uncertain since M81 is not well fitted in the core by an isothermal profile. As we have discussed, fitting the profile directly to the observed data is an invalid procedure; it is necessary for us to convolve the King core profile with the seeing profile before fitting. By so doing (using a Gaussian seeing profile with $\sigma_{star} = 0".5$ determined from the star in Fig. 6), we find that, first, the isothermal core profile fits even more poorly than before,

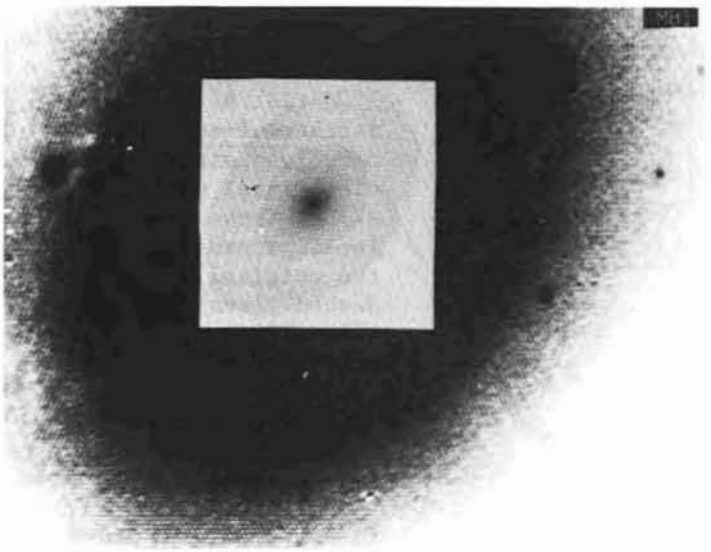

FIG. 5.—An R-band CCD frame of M81 from the 4 m prime focus. The exposure is 80 seconds. The field of the chip is approximately 80" x 100". This is a composite of two displays of the same data on the KPNO IPPS. Different contrast settings were used. The small, inner-square region is at the same scale and is used to show just the nucleus of M81. The dynamic range available in this frame is >4000.

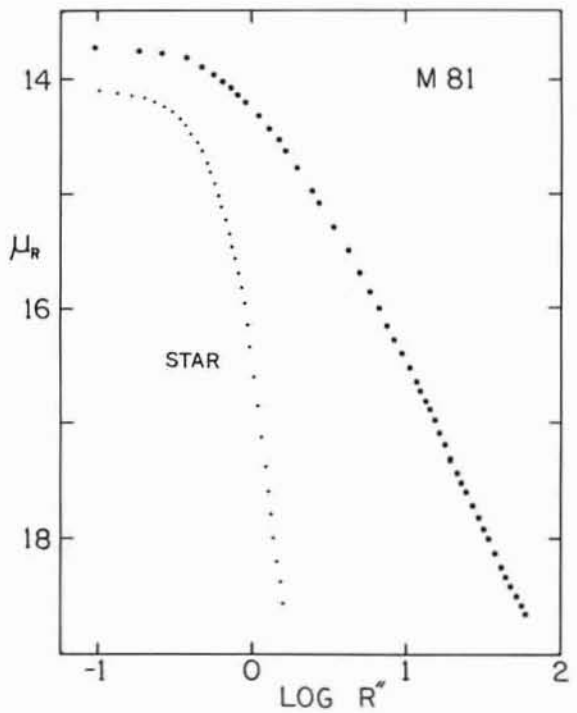

FIG. 6.—R-band surface brightness distribution μ_R from CCD data of the bulge of M81. The instrumental and seeing point spread function is given also for a star in the same CCD frame. The radius scale is in arcsecs. The star brightness distribution has been arbitrarily shifted in μ_R to allow easy comparison with the M81 data. The zero point for this R-band data is not established to better than 0.1 mag. The stellar profile has a σ of 0".5.

and second, $r_c \leq 1''$ with considerable uncertainty. Given the uncertainty in the profile shape and the poor resolution of the core implied by our best guess at r_c ($r_c \sim 2\ \sigma_{star}$ only), it is clearly more appropriate to note that M81 has a small, unresolved, rather nonisothermal core with an $r_c \leq 1''$ or $r_c \leq 15$ pc (distance taken from Aaronson, Mould, and Huchra 1980).

This is interesting. M81 is the next nearest Sb galaxy beyond M31, and it also displays a very small central core. Does this indicate, as has sometimes been thought from the single case of M31, that the cores of the bulges of disk systems are really quite small? While two examples are better than one, establishing a general case for this is somewhat of an extrapolation of the available data. Let us think of it as indicative!

I wish to thank John Kormendy for valuable discussions on the problems outlined here and Doug McElroy for his part in the M81 project.

REFERENCES

Aaronson, M., Mould, J., and Huchra, J. 1980, Ap. J., in press.
Binney, J. J. 1979, private communication.
———. 1980, M.N.R.A.S., in press.
Davies, R. D. 1979, Ph.D. thesis, Institute of Astronomy, Cambridge, England.
Davies, R. D. 1980, M.N.R.A.S., in press.
de Vaucouleurs, G., and Capaccioli, M. 1979, Ap. J. Suppl., 40, 699.
Duncan, M. J., and Wheeler, J. C. 1980, in press.
Fried, P. M., and Illingworth, G. 1980, in preparation.
King, I. R. 1966, A.J., 71, 64.
———. 1978, Ap. J., 222, 1.
Kormendy, J. 1977, Ap. J., 218, 333.
———. 1979, private communication.
Kormendy, J., and Illingworth, G. 1980, in preparation.
Light, E. S., Danielson, R. E., and Schwarzschild, M. 1974, Ap. J., 194, 257.
Sargent, W. L. W., Young, P. J., Boksenberg, A., Shortridge, K., Lynds, C. R., and Hartwick, F. D. A. 1978, Ap. J., 221, 731.
Schechter, P. L., and Gunn, J. E. 1979, Ap. J., 229, 472.
Schmidt, G. D., Peterson, B. M., and Beaver, E. A. 1978, Ap. J. (Letters), 220, L31.
Schweizer, F. 1979, Ap. J., 233, 23.
Young, P. J., Sargent, W. L. W., Kristian, J., and Westphal, J. A. 1979, Ap. J., 234, 76
Young, P. J., Westphal, J. A., Kristian, J., Wilson, C. P., and Landauer, F. P. 1978, Ap. J., 221, 721.

PHOTOMETRIC PROFILES IN CENTRAL REGIONS OF ELLIPTICAL GALAXIES

Jean-Luc NIETO
Observatoire du Pic du Midi - France

Abstract

The method leading to information on the photometric profiles in the central regions of elliptical galaxies by considering the effect of the instrumental function is presented.

The photometric profiles for three elliptical galaxies having different sub-types (giant - : M 87, normal -: NGC 3379, compact -: NGC 4486 B) are discussed and compared to different luminosity models.

I - Introduction

We know very little about the photometric profiles in central regions of galaxies. This is mainly due to the reduction procedure which must take into account the effects of the instrumental function (or point spread function, hereafter called PSF). As emphasized by de Vaucouleurs (1979) and by Cappacioli (1979) the best way to investigate the profile in regions affected by the PSF is to compare the observations with a photometric model convolved by the PSF, check the quality of the fit, and analyze the meaning of the departures. In the case of elliptical galaxies, the three models we consider are : King model (1962, 1966), de Vaucouleurs $r^{1/4}$ law (1948) and Young (1977) black hole model. This last model led Young et al. (1978) to suggest the existence of a supermassive object in the core of M 87, confirmed also by spectroscopic data (Sargent et al., 1978). The $r^{1/4}$ law fits very well with the luminosity profile of the main body of an elliptical galaxy; in that sense, the comparison of the observations with an $r^{1/4}$ law convolved by the PSF is a first step toward the relationship between the nucleus and the main body of elliptical galaxies. So far, results are available for three elliptical galaxies : the giant elliptical M 87 (Young et al., 1978; de Vaucouleurs and Nieto, 1979 a), its compact elliptical companion (de Vaucouleurs and Nieto, 1979 b) and the normal elliptical NGC 3379 (de Vaucouleurs and Capaccioli, 1979; Nieto and Vidal, 1980).

II - Elements of the reduction procedure

The PSF is represented by the combination of three gaussian curves, following Brown (1978) and de Vaucouleurs and Cappacioli (1979).

$$I \alpha G(r, \sigma_1^2) + a\, G(r, \sigma_1^2 + \sigma_2^2) + b\, G(r, \sigma_1^2 + \sigma_2^2 + \sigma_3^2) \quad (1)$$

with $G(r, \sigma^2) = \exp(-r^2/2\sigma^2)/\sigma^2$

$$a = b$$

$$\sigma_{i+1}/\sigma_i = \text{constant}.$$

The three parameters σ_1, a, σ_i + 1/ σ_i are adjusted to match the stellar profile. σ_1 as dispersion of the first gaussian is representative of the "seeing". The quality of the data for a galaxy having an effective radius r_e (radius within which half of the total flux of the galaxy is emitted) is given by the resolution factor r_e / σ_1.

The characteristics of the different models used are the following :

a) King model (1962,1966)

$$I \alpha \left\{ \frac{1}{\left[1 + \left(\frac{r}{r_c}\right)^2\right]^{1/2}} - \frac{1}{\left[1 + \left(\frac{r_t}{r_c}\right)^2\right]^{1/2}} \right\} \qquad (2)$$

In King's approach, r_c is the radius of the core of the galaxy and r_t is the limiting tidal radius. Technically r_c appears like a scale factor and r_t through the second term in formula (2) represents an adjusting parameter. De Vaucouleurs and Capaccioli(1979) have indicated that the core radius r_c is strongly dependant on the width of the PSF in NGC 3379. This was confirmed by Schweizer (1979) in the sample of the elliptical galaxies studied by King (1978) and by de Vaucouleurs and Nieto (1979) on NGC 4486 B. (The tidal radius r_t as well is a reflection of the observational detection threshold (de Vaucouleurs et Capaccioli, 1979)).

b) Young black hole model (1977)

Young has computed the projected density distribution of mass (and luminosity if M/L = const.) for isothermal spheres having a massive black hole in the center. This system is supposed to be thermally relaxed. The isothermal sphere is characterized by two parameters : a scale factor and an intensity factor. The third parameter of this model is the mass of the black hole.

c) De Vaucouleurs $r^{1/4}$ law (1948)

De Vaucouleurs has observed that the luminosity profile of the main body of an elliptical galaxy can be very well represented by an $r^{1/4}$ law.

$$\mu = \alpha\, r^{1/4} + \beta$$

At large distances from the center some departures exist, due to the "environment of the galaxy"(Kormendy, 1977 b and this meeting; de Vaucouleurs and Nieto, 1978).

III - The results

a) M 87

Using the black hole model set up by Young (1977), a photometric study by Young et al.(1978) has suggested the existence of a black hole of 5 x $10^9 M_\odot$ in the core of M 87. This suggestion was confirmed by the spectroscopic study of Sargent et al. (1978), assuming the isotropy of the velocity distribution. Duncan and Wheeler (1979) have shown that both density and velocity dispersion

profiles can be well matched by a collisionless stars distribution with an anisotropic velocity distribution.

The photometric profile obtained by Young et al. (1978) was confirmed by de Vaucouleurs and Nieto (1979) from a photometric analysis of three Mc Donald plates (figure 1). The comparison of the profiles obtained from our two high resolution plates (σ_1 = 0".61 and 0".65) and the profile obtained by the Hale team (σ_1= 0".46) to the black hole model set up by Young (1977) gives a black hole mass of $M = 1.7 \times 10^9 M_\odot$. A faint source of light must be added to the stars distribution; its B magnitude, B_S, is 16.75 for the Mc Donald plates (taken in I964) and 17.25 for Hale data (obtained in 75-77) suggesting a possible variability of this source. The comparison of the observations with a mean model ($M = 1.7 \times 10^9 M_\odot$, B_S = 16.95) convolved by the appropriate instrumental functions is presented in figure 2.

Figure 1.

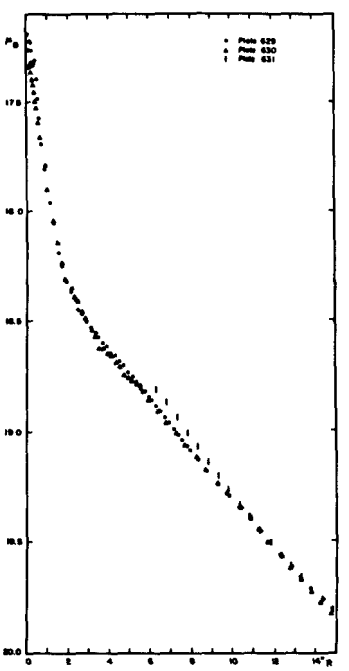

M 87 : Mean luminosity profile within 15" from the center for three Mc Donald plates

Figure 2.

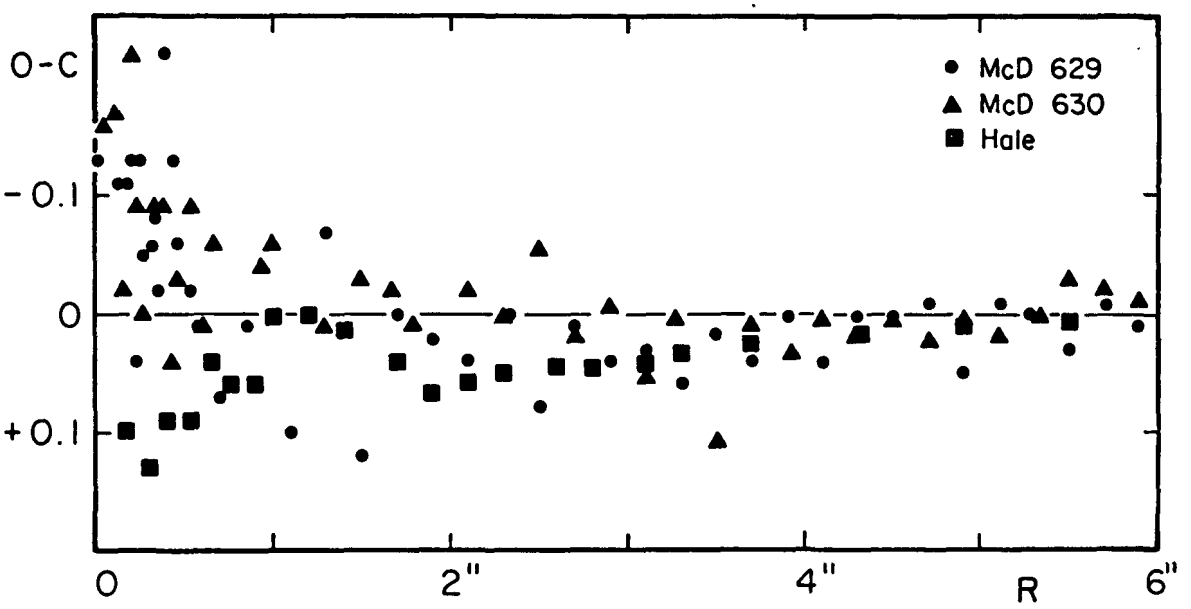

M 87 : Differences between Hale and Mc Donald data and the adopted mean black hole model convolved by the appropriate PSF

The comparison (figure 3) between the observations and the convolved $r^{1/4}$ law fitting the main body of the galaxy (de Vaucouleurs and Nieto, 1978) shows a departure from the $r^{1/4}$ law within 8 arc sec from the center where the observations are fainter than the model. This difference reaches a maximum at r = 1.5 arc sec within which appears a luminosity peak.

The same characteristics of the central luminosity profile was confirmed with a high resolution plate σ_1 = 0".55 taken at Pic-du-Midi Observatory (Nieto, 1979).

b) NGC 3379

This "normal" elliptical galaxy served as a standard galaxy in the spectroscopic study by Sargent et al. (1978) suggesting the existence of a black hole in M 87. The velocity dispersion profile was found to be rather flat by these authors, while recent measurements by Davies (1978) show it steep and similar to that of M 87. In an exhaustive photometric study, de Vaucouleurs and

Capaccioli (1979) showed that the photometric profile in the central region is well matched by a two-component-model, with an $r^{1/4}$ law $\mu_I = 3.0083\ r^{1/4} + 14.076$ on top of which in the central region there is a gaussian law $\mu_{II} = 0.03965\ r^2 + 18.565$. This result was obtained with one plate having a rather poor resolution ($\sigma_1 = 1''.27$) but confirmed by two plates taken at Mt Wilson by Kormendy (1977 b) with better resolutions ($\sigma_1 \sim 0''.90$). The reduction of three Pic-du-Midi-plates with much better resolutions ($\sigma_1 \sim 0''.60$) is under way (Nieto and Vidal, 1980)

Figure 3.

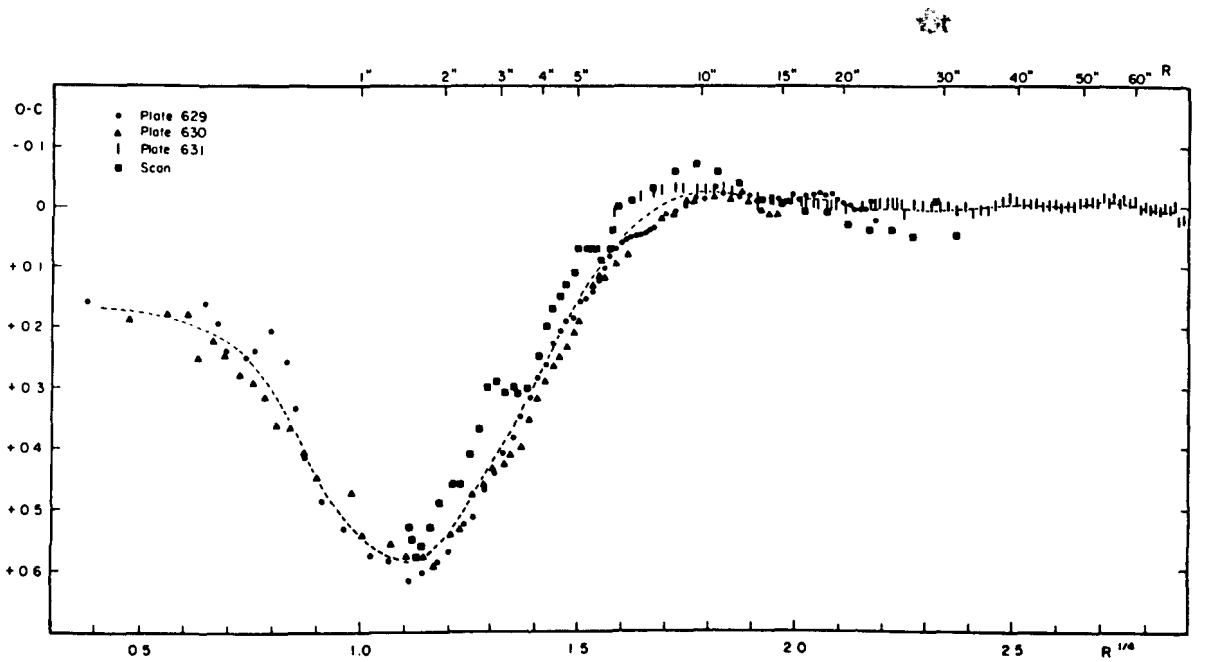

M 87 : Differences between Mc Donald photographic (and also photometric) data and the $r^{1/4}$ law convolved by the appropriate PSF.

c) NGC 4486 B

This galaxy isthe small compact elliptical companion of M 87 (r = 7 arc min) very similar in shape to M 32. As in M 32 it is supposed to present a tidal cut-off due to the gravitational field of M 87.

This galaxy is small in size : $r_e \simeq 5$ arc sec (de Vaucouleurs and Fraser, 1968). Therefore, on the three Mc Donald plates already used for the study of M 87, the resolution factor is $5/0.61 \sim 8$, very small with respect to

to that of M 87 (~ 150). It is then impossible to derive the photometric profile in the central region of this galaxy, but the problems raised to find the profile of the main body itself are very similar to that of the central regions of larger galaxies. The profiles obtained are presented in figure 4 for the three Mc Donald plates and one Pic-du-Midi plate (PM 8). We may suppose that the photometric profile of the galaxy follows an $r^{1/4}$ law down to a truncation radius r_m beyond which a departure from this model appears. If so, it turns out that the region where the galaxy follows an $r^{1/4}$ law is entirely affected by the instrumental function. After an iterative reduction procedure, within the accuracy of the data, a range of $r^{1/4}$ models is acceptable with a slope $\alpha \sim 5.5$. The differences between the observations and two $r^{1/4}$ laws sufficiently fitting the data and convolved by the appropriate PSF are presented in figure 5. If we consider an $r^{1/4}$ law throughout, r_e = 6".07 for α = 5.3 and 4".54 for α = 5.7. The departure from these $r^{1/4}$ laws appears respectively at a truncation radius r_m = 2.5 arc sec and at 4.5 arc sec. The fraction of remaining stars from the truncation is represented on figure 6 where our data were completed by data from Kormendy (1977 a) corrected to the B system.

Adapting r_t = 27" (Kormendy, 1977 a), we found that a King model having r_c = ".63 to fit the profile in the central region (the value r_c = 1".52 given by Kormendy (1977 a) did not consider the PSP effects), poorly fits our data (figure 7).

Discussion

We have presented the results obtained by different authors on the photometric profiles of three elliptical galaxies having a different sub-type (giant, normal and compact), and the differences between the observations and different models convolved by the appropriate PSF.

In order to understand better the possible relationship existing between the nucleus and the rest of the galaxy in these three galaxies, a first step is to compare the observations in the central region of the galaxy to the corresponding $r^{1/4}$ law matching the photometric profile in the main body of the galaxy : the normal elliptical NGC 3379 shows within the 10 central arc sec an excess of light at the center well represented by a gaussian curve; the giant elliptical M 87 presents a deficiency starting at 8 arc sec from the center on top of which a stellar spike exists within the central 3 arc sec. (Its model is rather better represented by Young's black hole model); for the compact elliptical NGC 4486 B, the resolution factor of our plate is too small to derive any result in the central region : a similar study of M 32 is necessary to know more about the galaxies of this sub-type.

Figure 4.

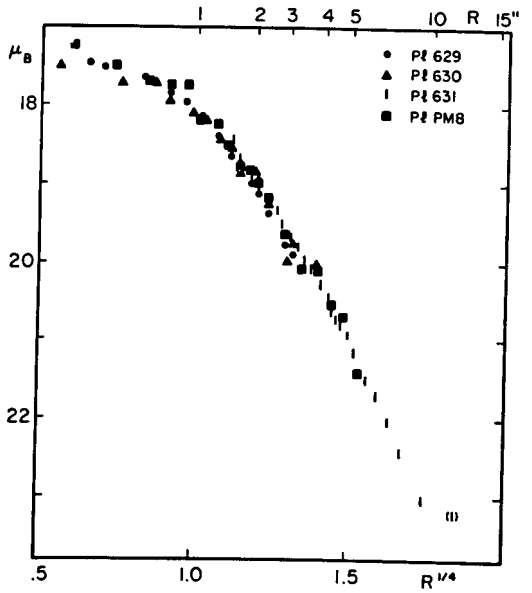

NGC 4486 B : Mean luminosity profile within 15" from the center for three Mc Donald plates and one Pic-du-Midi plate.

Figure 5.

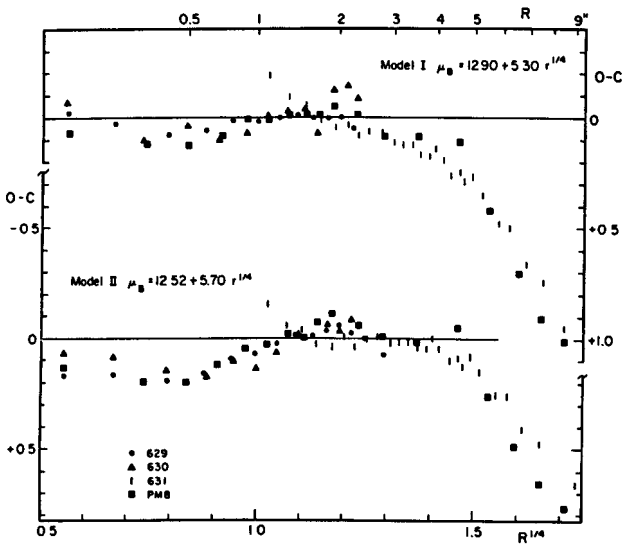

NGC 4486 B : Differences between Mc Donald and Pic-du-Midi data and two $r^{1/4}$models convolved by the appropriate PSF (see text)

Figure 6.

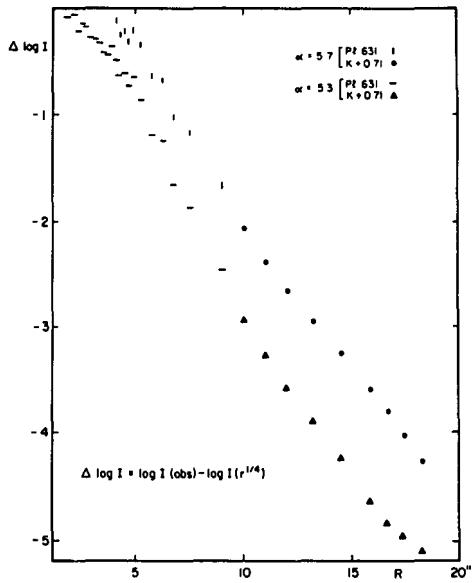

NGC 4486 B : Fraction of stars remaining from the truncation of an $r^{1/4}$ law luminosity profile for two $r^{1/4}$ models (see text)

Figure 7.

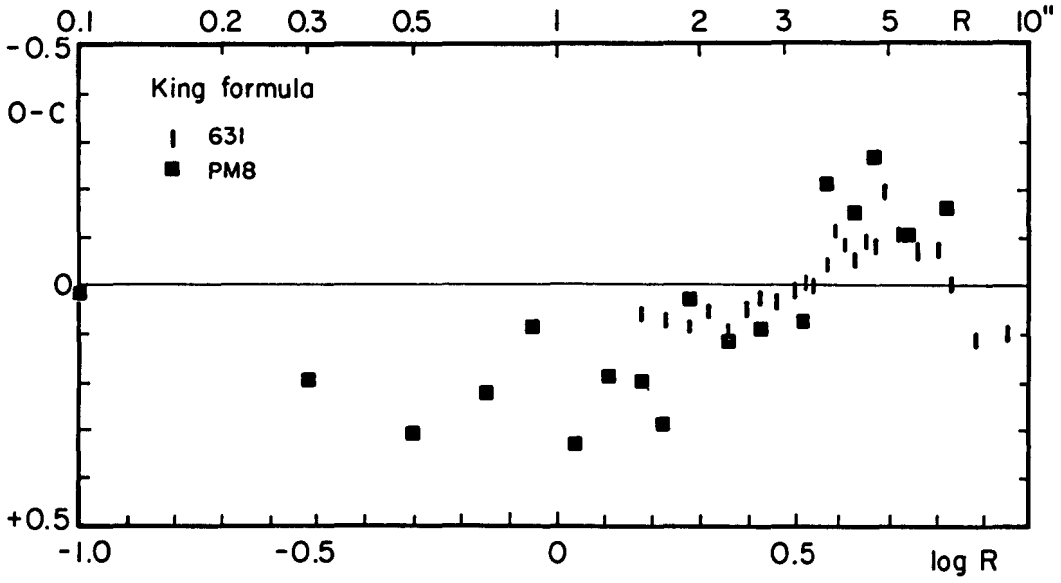

NGC 4486 B : Differences between Mc Donald and Pic-du-Midi data and a King luminosity model (see text).

References

Brown G.S., 1978, Publications in Astronomy n° 11, University of Texas

Capaccioli M., 1979, Conference on "Photometry, Kinematics and Dynamics of galaxies", D. Evans Ed.

Davies,R.L., 1978, Ph.D. Thesis, Cambridge University.

de Vaucouleurs, G., 1948, Ann. Astrophys, 11, 247

de Vaucouleurs, G., 1979, Conference on "Photometry, Kinematics and Dynamics of galaxies", D. Evans Ed.

de Vaucouleurs, G., Capaccioli, M., 1979, Astrophys. J. Supplts. series 40, 699

de Vaucouleurs, G., Fraser, C.W., 1968, unpublished

de Vaucouleurs, G., Nieto,J-L., 1978, Astrophys. J., 220, 449

de Vaucouleurs, G., Nieto,J-L., 1979 a, Astrophys. J., 230, 697

de Vaucouleurs, G., Nieto,J-L., 1979 b, in preparation

Duncan,M.J., Wheeler,J.C., 1979, preprint

King, I.R., 1962, Astron. J., 67, 471

King, I.R., 1966, Astron. J., 71, 64

King, I.R., 1978, Astrophys. J., 222, 1

Kormendy, J., 1977 a, Astrophys.J., 214, 359

Kormendy, J., 1977 b, Astrophys.J., 218, 333

Nieto, J-L., 1979, unpublished

Nieto, J-L., Vidal, J-L., 1980 in preparation

Sargent, W.L.W., et al., 1978, Astrophys.J., 221,731

Schweizer, F., 1979, Astrophys.J., 233, 23

Young, P.J., 1977,"Massive Black holes in galactic nuclei" paper presented, NATO conference "Energy sources and Emission mechanisms in QSO's, Cambridge

Young, P.J., et al., 1978, Astrophys. J., 221, 721

DETERMINATION OF FUNDAMENTAL PARAMETERS FOR ELLIPTICAL GALAXIES USING TWO DIMENSIONAL FOURIER-TRANSFORM TECHNIQUES

S. Frandsen[*] and B. Thomsen[*]
Institute of Astronomy, University of Aarhus
DK-8000 Aarhus C, Denmark

It is convenient if an object can be described by a small number of welldefined parameters. The smooth and featureless appearance of an elliptical galaxy indicate, what many investigations over the years have shown, that this is indeed possible for elliptical galaxies, at least to a first approximation. However for a distant elliptical galaxy such parameters are not easily found due to the effect of the atmospheric seeing. We shall discuss mainly one parameter: The angular size of an elliptical galaxy.

We shall assume, that the radial light distribution of all elliptical galaxies can be fitted by one function $\phi(r)$. Then the surface brightness (SB) of two galaxies will be related by

$$\phi_1(r) = A \cdot \phi_2(r/\alpha). \qquad (1)$$

The scale parameter α defines the relative size of the two distributions, and if it is normalized by some convention, it becomes an absolute angular size.

There are two aspects of the determination of the scale α: The choice of a standard profile for the galaxies and the compensation for image degradation primarily due to seeing.

Standard Profile

There exists a number of analytical expressions, which approximates the SB-distribution of elliptical galaxies. What becomes important for the technique described later is, that the standard profile should be easy to compute both in the image and the Fourier domain. We have studied 3 alternatives:

a. The standard galaxy image profile and the corresponding Fourier transform profile are obtained as an average of a small number of scaled observed profiles in either domains.
b. Use of a function series expansion, which transforms analytically. The coefficients are obtained as average values of least square fits to observed profiles.
c. The de Vaucouleurs' formula with the transform numerically evaluated and tabulated.

In an earlier paper (Frandsen and Thomsen, 1979) we have applied the first choice. The resulting profile is not a very general one, due to the limitations by the available data. There is no complete coverage of the whole radial interval, which means that an extrapolation from the data might be necessary. The second choice is also non-general. The derived standard profile depends on the available data. On the other hand it has the advantage, that as soon as the coefficients are determined and fixed, the profiles are easy to compute in <u>either</u> domains. The number of possible series expansions are very limited, if we demand that the series shall have an analytical two-dimensional Fourier transform. We have used the following:

[*] Based on observations collected at the European Southern Observatory, La Silla, Chile.

Fourier domain:

$$F(\omega) = \left(\sum_{i=o}^{n} a_i \cdot \omega^i \right) e^{-\alpha\omega} \qquad (2)$$

Image domain:

$$f(r) = 2\pi \sum_{i=1}^{n+1} a_{i-1}\, y^{i+1}\, \Gamma(i+1)\, P_i(\alpha y) \qquad (3)$$

where

$y = (\alpha^2 + (2\pi r)^2)^{-\frac{1}{2}}$ and P_i are Legendre polynomia and Γ the gamma function. A normalization to $\alpha = 1$ and $a_o = 1$ is possible giving the new coefficients

$$a_i' = \alpha^{-i} \frac{a_i}{a_o} \qquad i = 1, 2, \ldots, n \qquad (4)$$

F and f are a Hankel transform pair. The Hankel transform is equivalent to a two dimensional Fourier transform of a rotationally symmetric function. In figure 1 the first functions in the expansion for f(r) are shown normalized at r = 0.

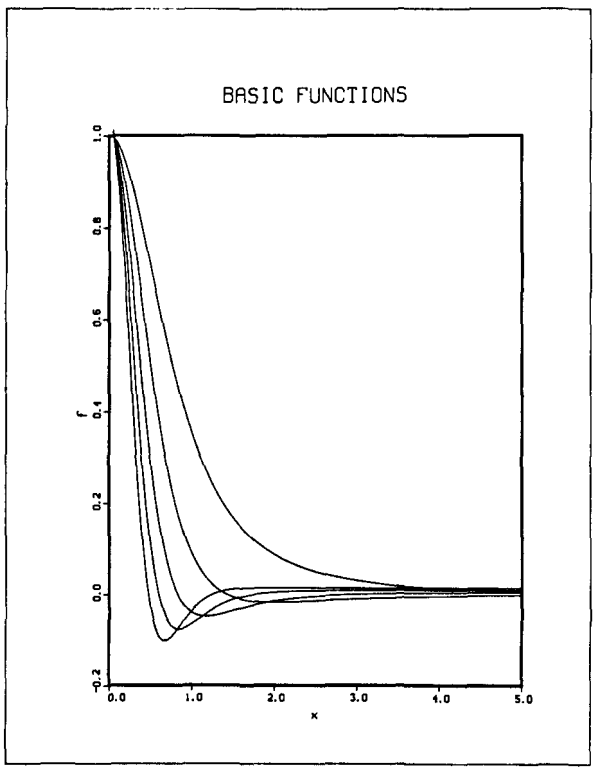

Fig. 1

Using data from King (1978), Kormendy (1977), Strom and Strom (1978) and Bertola and Cappacioli (1975), we have determined some trial standard profiles according to (2) and (3). We have also found an approximation to de Vaucouleurs' law using these functions. We have not corrected for any influence of the seeing on the data. Some results using such profiles are shown in the next figures. Figure 2 is a comparison of effective radii in arc seconds determined by Strom and Strom (1978) with the scale parameter found using an approximation to de Vaucouleurs' law. The agreement is very good for all galaxies, where this law

is a good approximation. The crosses are galaxies which are not fitted well by this law.

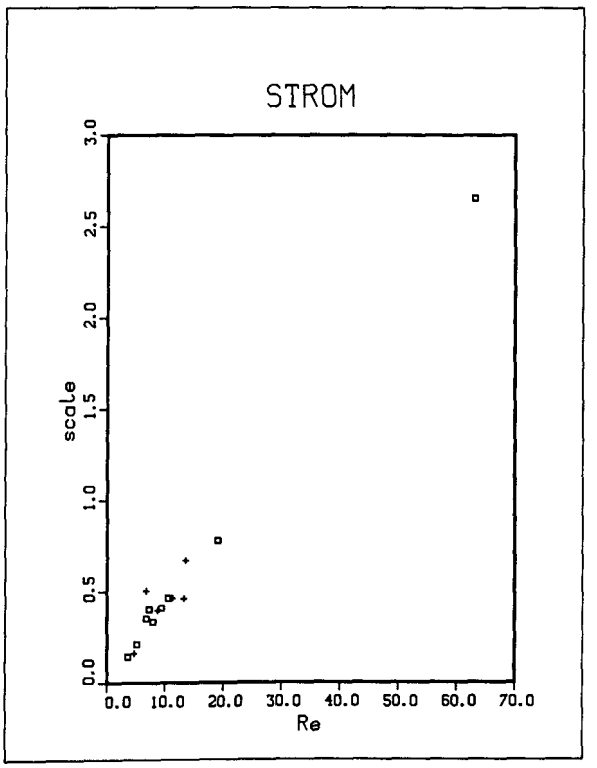

Fig. 2

Figure 3 compares results obtained using a second order expansion and a fourth order expansion respectively. This figure also gives an impression of the accuracy to be expected from such scale determinations. Crosses are again examples of bad fits.

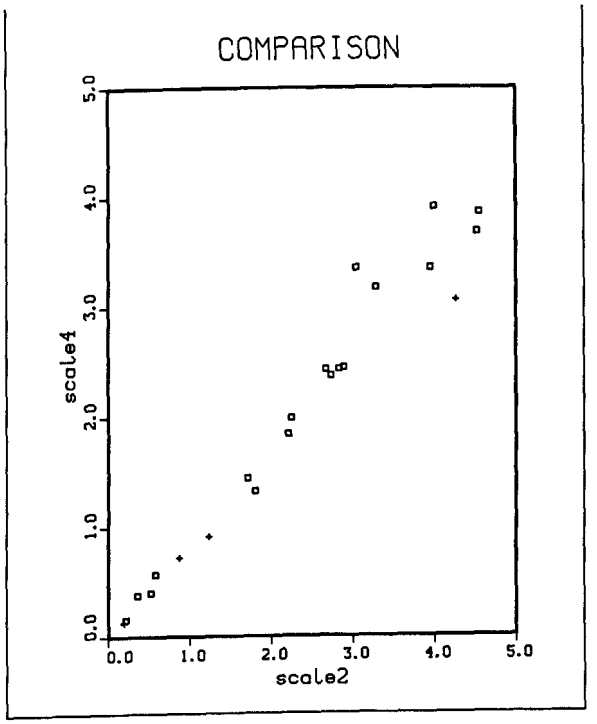

Fig. 3

A less satisfactory relation is shown on figure 4, where our measure of the size of a galaxy is compared to the effective aperture in arc seconds taken from SRCBG (1976). There seem to be some disagreement between the two size measures.

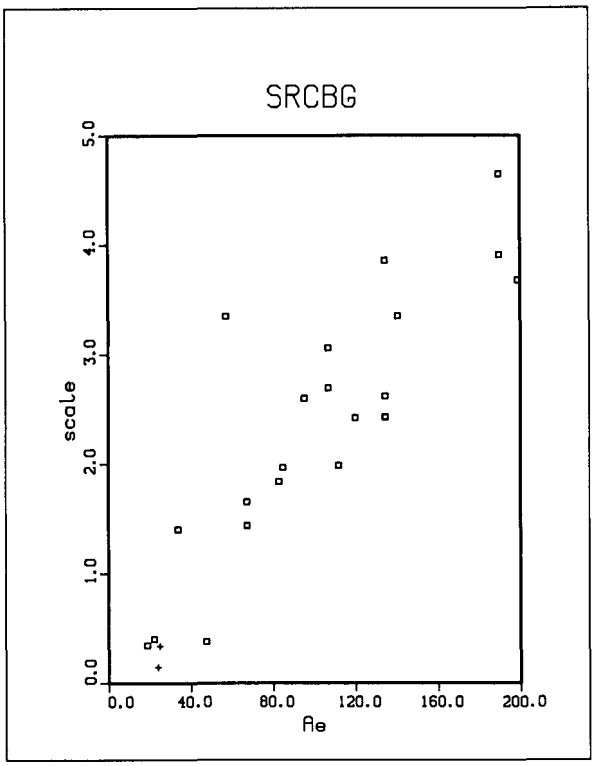

Fig. 4

Although the series expansion does give some reasonable fits to the data taken from the sources already mentioned, we find that the fitted profiles are not quite smooth, and also have some difficulties in representing the very high SB-values in the central part of the galaxies. Their main force is the ease with which the Hankel transform is obtained. In spite of this we finally decided to work with de Vaucouleurs' formula as our standard profile. A table of the transform was calculated numerically for the relevant points in the frequency domain. As the formula has a very sharp peak, this demands some care, and is quite time consuming, but it only has to be done once. Later we use quadratic interpolation in the calculated table.

Seeing compensation

For large nearby galaxies we can fit our standard profile directly to the observed radial SB-profile. But in many other cases a substantial part of the profile is influenced by the seeing. To take this disturbing effect into account, it is practical to work in the Fourier domain, using Fast Fourier Techniques to evaluate the discrete transform of the data. In the Fourier domain the convolution of the original image with the point spread function (PSF), corresponding to the seeing, is a simple multiplication.

The necessary data are two dimensional grids of points (frames) giving the observed SB of a galaxy and one or more frames of stars representing the PSF. The data come from scans of the same plate or from direct simulaneous observations using modern detectors. The reductions are very much facilitated, if the PSF is nearly rotationally symmetric and invariant to translation on the plate. Although we previously have worked with the numerical functions, our general philosophy is to use an analytical approximation if possible. We have already

discussed this in case of the galaxy.

For the PSF we have found, that a good representation of the transform - the transfer function - is given by

$$H(\omega,\theta) = \exp(-(\omega/\omega_o(\theta))^n) \tag{5}$$

where (ω,θ) are polar coordinates in the frequency domain and $\omega_o(\theta)$ is an ellipse centered on the origin

$$\omega_o^{-2}(\theta) = \gamma^{-2}(1+a_2\cos 2\theta + b_2\sin 2\theta), \tag{6}$$

which allows the PSF to have an elliptical shape. The PSF is then fixed by the numbers n, γ, a_2 and b_2. The PSF is found by performing the inverse transformation. By comparing this transformation with the image of the star, suitably normalized, a rejection of points that are clearly in error can take place. This procedure can be performed repeatedly. Normally the procedure is repeated only once. This approximation to a star profile has proven useful also for doing photometry of isolated stars.

Next let us in detail describe the reduction technique for the galaxies. We shall do it in a rather formal way. A continuous function f(x,y) is discretized into a two dimensional array by taking N samples Δx units apart along the x-axis and M samples Δy units apart along the y-axis. It is convenient to use (x,y) as either discrete or continuous variables, depending on the context of the discussion. This is done by defining the discrete function:

$$\tilde{f}(x,y) = f(x_o+x\cdot\Delta x,\ y_o+y\cdot\Delta y), \tag{7}$$

where x assumes the discrete values 0, 1, ...N-1 and y the discrete values 0, 1, ..., M-1. The discrete Fourier transform pair is given by the equations (Brigham, 1974, Gonzalez and Wintz, 1977).

$$\tilde{F}(u,v) = \sum_{x=0}^{N-1}\sum_{y=0}^{M-1} \tilde{f}(x,y)\ \exp\left(-j\cdot 2\pi\ \left(\frac{ux}{N}+\frac{vy}{M}\right)\right) \tag{8}$$

for u = 0, 1, ... N-1, v = 0, 1,...M-1 and

$$\tilde{f}(x,y) = \frac{1}{NM}\sum_{u=0}^{N-1}\sum_{v=0}^{M-1}\tilde{F}(u,v)\ \exp\left(j\cdot 2\pi\left(\frac{ux}{N}+\frac{vy}{M}\right)\right) \tag{9}$$

for x = 0, 1, ...N-1 and y = 0, 1, ...M-1.

The discrete Fourier transform $\tilde{F}(u,v)$ corresponds to samples of the continuous function

$$F(u\Delta u,\ v\Delta v) = \Delta x\ \Delta y\ \tilde{F}(u,v) \tag{10}$$

The sampling increments in the spatial and frequency domains are related by

$$\Delta u = 1/(N\Delta x), \quad \Delta v = 1/(M\Delta y). \tag{11}$$

We have in our case that N = M and $\Delta x = \Delta y$. We shall omit the ($\sim$) in the following. The dicrete transform is obtained using the FFT. The discrete Fourier transform and its inverse are periodic with period N. The Fourier transform exhibits conjugate symmetry because f(x,y) is real

$$F(u,v) = F^*(-u,\ -v) \tag{12}$$

The importance of doing the analysis in the frequency domain is due to the convolution theorem: A convolution in the spatial domain is equivalent to a multiplication in the frequency domain. But let us also point out the importance of Parseval's theorem:

$$\sum_{x=0}^{N-1}\sum_{y=0}^{M-1}|f(x,y)|^2 = \frac{1}{MN}\sum_{u=0}^{N-1}\sum_{v=0}^{M-1}|F(u,v)|^2. \tag{13}$$

This equation shows that a least squares fit in the spatial domain is equivalent to a least squares fit in the frequency domain as long as all the samples have equal weights and are uncorrelated.

Our objective is to fit the observed brightness distribution of an elliptical galaxy with a suitably scaled standard distribution convolved with a realistic PSF. In order to keep the number of free parameters small we shall assume, that the isophotes of the standard galaxy are concentric ellipses with a constant ellipticity and a constant direction of the major axis. It can be shown that the isophotes of the norm of the Fourier transform of such a distribution again are concentric ellipses with the same ellipticity as the one in the image plane, and with the major axis parallel to the direction of the minor axis in the image plane. The two dimensional brightness distribution (and its Fourier transform) is then defined by the ellipticity, the position angle of the major axis and a radial function (profile) of one variable. We shall further assume that the radial profile is completely determined by two parameters: One representing the angular size, the other one the surface brightness of the galaxy.

As described previously we decided to use a normalized de Vaucouleurs' law as the standard profile in the image plane:

$$\phi(r) = \frac{\beta^8}{\pi 8!}\, e^{-\beta r^{1/4}} \tag{14}$$

Half of the luminosity is radiated inside r = 1 if we choose $\beta = 7.67$. In the Fourier domain we get the Hankel transform

$$\Phi(\omega) = 2\pi \int_0^\infty \phi(r)\, J_o(2\pi\omega\, r) r dr \tag{15}$$

where $\omega^2 = u^2 + v^2$. Note that $\Phi(0) = 1$.

An elliptical isophot is given by

$$r^{-2}(\theta) = r_m^{-2}(1 - C_2 \cos 2\theta) \tag{16}$$

The more commonly used effective radius is given by

$$r_e^2 = (1 - C_2{}^2)^{-\frac{1}{2}}\, r_m{}^2 \tag{17}$$

The brightness distribution of an elliptical galaxy is assumed to have the form

$$f(r,\theta) = a\phi\left(\frac{r}{r_m}(1 - C_2 \cos 2\theta)^{\frac{1}{2}}\right) \tag{18}$$

where a and r_m are scale parameters.

The same distribution in rectangular coordinates is:

$$f(x,y) = a\phi\left(r_m^{-1}\,(r^2 - C_2(x^2 - y^2)^{\frac{1}{2}}\right) \tag{19}$$

or

$$f(x,y) = a\phi\left(\left[\left(\frac{1-C_2}{1+C_2}\right)^{\frac{1}{2}}\left(\frac{x}{r_e}\right)^2 + \left(\frac{1+C_2}{1-C_2}\right)^{\frac{1}{2}}\left(\frac{y}{r_e}\right)^2\right]^{\frac{1}{2}}\right) \quad (20)$$

The scaling theorem then gives (Gonzalez and Wintz, 1977)

$$F(u,v) = a\, r_e^2\, \Phi\left(\left[\left(\frac{1+C_2}{1-C_2}\right)^{\frac{1}{2}} r_e^2\, u^2 + \left(\frac{1-C_2}{1+C_2}\right)^{\frac{1}{2}} r_e^2\, v^2\right]^{\frac{1}{2}}\right) \quad (21)$$

or

$$F(u,v) = a\, r_e^2 \Phi\left(\Gamma^{-1}(\omega^2 - C_2(v^2 - u^2)^{\frac{1}{2}})\right) \quad (22)$$

where

$$r_e = \Gamma^{-1}(1 - C_2{}^2)^{1/4} \quad (23)$$

The total luminosity, L, is

$$L = a\, r_e^2$$

The Fourier transform of the brightness distribution of a galaxy of arbitrary orientation is given by:

$$F(u,v) = L \cdot \Phi\left(\Gamma^{-1}(\omega^2 + a_2(u^2 - v^2) + 2b_2\, u\, v)^{\frac{1}{2}}\right) \quad (24)$$

Above we have assumed that the centre of the galaxy is placed at the origin of the coordinate system. However, this will generally not be the case. Let instead the galaxy be placed at (x_c, y_c). The Fourier transform of $f(x-x_c, y-y_c)$ is $F(u,v)\exp(-j2\pi(x_c u + y_c v))$. Finally we have to multiply our transformed model galaxy with the transfer function $H(u,v)$. This means, we have to deal with a non-linear least squares problem with the added complication of a convolution for each iteration. This is exactly why it is such an advantage to do the fit in the frequency domain. The final function, which is fitted to the discrete Fourier transform of the data, is

$$G(u,v) = L\Phi\left(\Gamma^{-1}(\omega^2 + a_2(u^2 - v^2) + 2b_2 uv)^{\frac{1}{2}}\right) \exp(-j2\pi(x_c u + y_c v) \cdot H(u,v) \quad (25)$$

The frequency domain is not well suited for noise rejection, except in the case of periodic noise. The removal of bad pixels is best done in the image domain. The next step is therefore to make an inverse transform, $g(x,y)$, of the fitted function, $G(u,v)$. Scratches, dead spots and faint stars or galaxies are then removed in the following way: A data value which deviates more than 3σ from the transformed value is replaced by the latter value. Finally the frequency domain analysis is repeated.

Results of the use of the technique

We have used the procedure described above on two electronographic plates of the cluster STR 0431-616 (Duus and Newell, 1977). The plates were obtained at the Danish 1.5 m telescope at La Silla using the large field RGO camera (Gyldenkerne et al., 1979). The plates are a 2 hour V-exposure and a 2½ hour B-exposure. Using the PDS-microphotometer at the Lowell Observatory a number of stars and galaxies have been digitized. In the following table the parameters for some of the galaxies are given. The seeing is a little below 2 arc seconds (full width half maximum) and the exponent in the transfer function was found to be $n \sim 1.5$.

The PSF therefore is different from a Gaussian (n=2). The redshift of the cluster has not yet been measured.

Table 1

Galaxy	type	r_e(V)	r_e(B)	$\frac{b}{a}$(V)	$\frac{b}{a}$(B)
4	E	14".4		0.99	
5	E	6.1	6".4	0.79	0.79
6	E	5.1	6.0	0.84	0.81
10	SO	3.4	3.2	0.71	0.74
11	SO?	2.0	2.2	0.68	0.71
15	E?	5.6	-	0.76	-
16	E	2.0	1.8	0.79	0.78

$\Delta x = 20\mu = 0".379$

The two dimensional technique has some limitations. We have worked with a grid size of 64 x 64 and 128 x 128 for the stars and the galaxies, respectively. The pixel size is fixed by the typical width of the PSF, and as a result we can not work on galaxies with effective radii larger than $\sim$ 10 times the seeing, without increasing the dimensions of the galaxy grid. An alternative is to work only with the radial part of the transforms as we have done earlier (Frandsen and Thomsen, 1979). The accuracy is limited by the quality of the fit whereas statistical noise is not very serious. Our experience is, that the effective radius derived in this way is a measure of size within an accuracy of $\pm$ 10%. As galaxies are very often disturbed by neighbouring galaxies or stars, slight distortions of the profiles are unavoidable. This is the case for galaxy 6 in Table 1, where a blue star at the edge of the grid was not removed adequately.

We still need to verify, that we get consistent results with different plates having different PSF's. If this test is positive, the technique could be used for faint galaxies in very distant clusters to a redshift around z = 0.5. Of course the more distant clusters should only be observed under very good conditions - seeing of 1". We hope that one can obtain valuable information about the galaxies at an early epoch in this way.

Acknowledgement. The observations were part of a collaboration on 4 cm and 9 cm McMullan electronography at the Danish 1.5 m telescope described by Gyldenkerne, Nielsen and McMullan (1979).

References

Bertola, F. and Cappacioli, M., 1975, Astrophys. J. 200, 439
Brigham, E.D., 1974, The Fast Fourier Transform, Prentice Hall
Duus, A. and Newell, B., 1977, Astrophys. J. Suppl. 35, 209
Frandsen, S. and Thomsen, B., 1979, Astron Astrophys. 72, 111
Gonzalez, R.C. and Wintz, P., 1977, Digital Imaging Processing, Addison-Wesley Publishing Company
Gyldenkerne, K., Nielsen, F. and McMullan, D., 1979, The Messenger, ESO No. 17, p. 36
King, I.R., 1978, Astrophys. J. 222, 1
Kormendy, J., 1977, Astrophys. J. 214, 359
Strom, K.M. and Strom, S.E., 1978, Astron. J. 83, 73
de Vaucouleurs, G., de Vaucouleurs, A., Corwin Jr., H.G., 1976, Second Reference Catalogue of Bright Galaxies, University of Texas Press.

B PHOTOMETRY OF THE COMA CLUSTER

D. Nanni, G. Pittella, D. Trevese and A. Vignato

Osservatorio Astronomico di Roma
Via del Parco Mellini 84
00136 Roma (Italy)

ABSTRACT

A method to calibrate a photographic plate is described.
It requires the knowledge of the opacitance profiles of some stars in the field and their magnitudes, together with the hypothesis of identity in the shape of the corresponding intensity distribution.
The resulting calibration curve applied to a set of galaxies gives magnitudes which differ from the photoelectric data by less than 0.1 mag (r.m.s.).
We further on apply the same calibration to the Tifft sample of Coma galaxies to deduce the nuclear B magnitudes in order to test the red-shift-magnitude band pattern claimed by Tifft.

1. INTRODUCTION

Among the various calibration techniques for the photographic photometry of galaxies, the most common is based on the deduction of the characteristic curve of the plate by means of photometric spots.
The application of such a procedure is affected by two main sources of error (de Vaucouleurs,1968): the first is the non simultaneous exposure of the plate to sky and to calibration spots; the second is the necessary transfer of the characteristic curve from the calibrated part of the plate to the region to be measured.
As a good accuracy that is obtainable in this way we quote the 0.03 mag. error attained by the Stroms (1978).
Another method was proposed by Kormendy (1973) who uses brightness profiles of field stars as standard light sources. The sources of error of this method are the differences in the star profiles due to the use of different telescope, filter, emulsion and seeing conditions. The photometric error may range from 0.5 mag., for very different experimental conditions, to 0.1 mag. obtained by Kormendy in optimal conditions.
In this paper we describe a new calibration method which requires the knowledge of the transparency (and not brightness) profiles of some stars in the field together with their magnitudes. From the transparency profiles we obtain the magnitude versus isophotal radius relation for the stars, and from this relation we deduce just the brightness profile of the stars and a calibration curve of the plate.
This method avoids, at least in principle, some sources of errors of the most common techniques and is suitable for application to a large

number of photographic plates which have not sensitometric spots. An application of our technique to a sample of Coma cluster galaxies shows a r.m.s. photometric error of 0.06 mag. respect to photoelectric determinations.
As a preliminary result on the B photometry of the Coma cluster, the determination of the magnitudes of the Tifft's (1973) sample of galaxies enabled us to confirm the existence of the redshift-magnitude band phenomenon claimed by Tifft.

2. THE CALIBRATION METHOD

Suppose we know the magnitudes m_i ,i=1,N of a sufficient number N of stars in the field.
The basic assumption of the method is that all these stars have the same intensity distribution respect to the distance r from the center of the image i.e.:

$$I_i\ (r) = I_{0i}\ f(r) \tag{1}$$

where I_{0i} is the amplitude, depending on the star, and f(r) is the shape independent of the star; so that we have:

$$m_i = 2.5\log\left[2\pi\int_0^\infty I_i\ (r)rdr\right] = -2.5\log I_{0i} - 2.5\log 2\pi S$$

where: $$S = \int_0^\infty f(r)rdr. \tag{2}$$

By a microdensitometric scanning of the images we obtain the transparency profiles T(r), and from these we compute the opacitance profiles:

$$\omega = (Tb/T)-1 \tag{3}$$

to take into account the local variation of the background transparency, Tb, on the plate (de Vaucouleurs 1968).
From the opacitance profiles, which are different in shape, we can deduce for each value ω_j an isoopacitance radius r_{ij} for each star (the first index refers to the i-th star and the second to the j-th opacitance value) as shown in fig. 1.

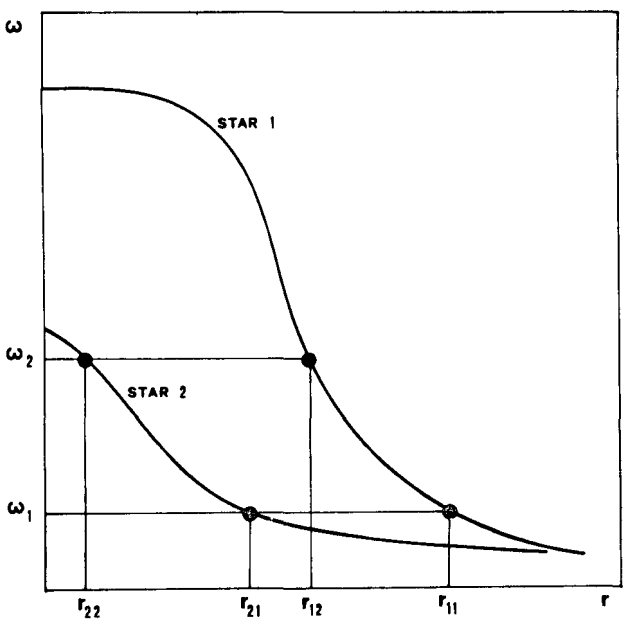

Fig.1 - Schematic plot, in arbitrary units, of the opacitance profiles ω (r) of a bright star, STAR 1, and of a fainter star, STAR 2 ($m_1 < m_2$). Iso-opacitance radii for two opacitance values $\omega_2 > \omega_1$ are also indicated.

Assuming a correspondence between the opacitance and the intensity and using eqs. (1) and (2) we have :

$$m_i = 2.5\log\left[f(r_{ij})\right] - 2.5\log I_j - 2.5\log(2\pi S) \quad ; \; I_j \equiv I(\omega_j). \tag{4}$$

Eq.(4) shows that by the r_{ij} values we can construct, in a m-r plane, a set of curves :

$$m = m(r) + C_j \quad ; \quad C_j = -2.5\log I_j - 2.5\log(2\pi S) \tag{5}$$

one for each opacitance value ω_j, which are identical in shape and are shifted each other by a constant dependent on ω_j only, all representing in log scale the shape of the brightness profile f(r) (see fig.2).

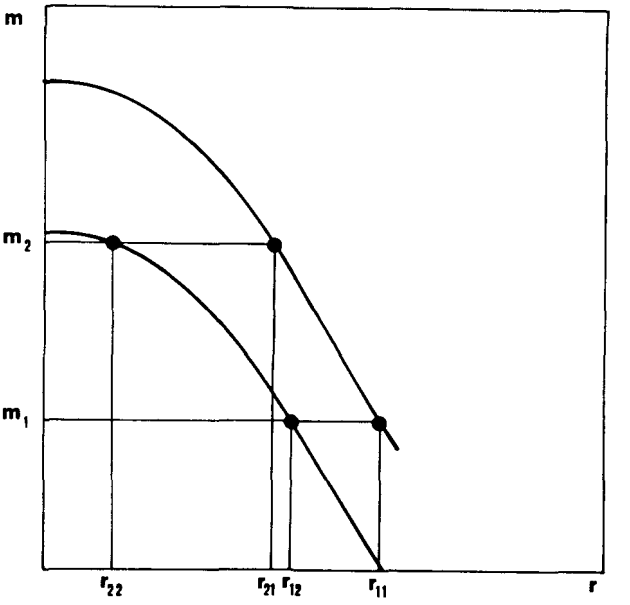

Fig. 2. - Schematic plot in arbitrary units, of two m(r) curves constructed for two opacitance values, $\omega_2 > \omega_1$ by the iso-opacitance radii deduced from the opacitance profiles (fig.1).

By a best fit procedure we can deduce from these curves both the shape f(r) of the brightness profile and the value of C_j .
Once C_j is known, we have from (5):

$$\log I(\omega_j) \equiv \log I_j = \log(2\pi S) - C_j/2.5 \equiv F(\omega_j) \tag{6}$$

namely the calibration curve.

The photometry is based on a blue noncalibrated plate (IIa0+GG13 filter)taken with the 150 cm telescope of the Bologna University. The center of the plate is approximately at $\alpha = 12^h\ 57^m\ 40^s$, $\delta = 28°13'$ near NGC 4874, the second brightest galaxy in the Coma cluster. The size of the plate is 20 x 20 cm which corresponds, at the scale of the telescope (17"/mm), to a field of about $1°$. Details about data acquisition are described in (Agnelli et al., 1979).
We had not a set of standard stars in our field (plate A), but we possessed a blue plate (plate B), taken with the 48" Schmidt telescope of the Palomar Observatory, partially overlapping plate A and containing 13 photoelectrically measured stars (Abell , 1977) from which we deduced by the usual iris-photometer technique, a set of 19 secondary standard stars belonging to the overlapping region, with a r.m.s. error of 0.08 mag.
The fitting procedure was performed assuming, as suggested by Moffat (1969), the profile:

$$f(r) = [1+(r/R)^2]^{-\beta} \tag{7}$$

so that:

$$m_i = -2.5\beta \log[1+(r_{ij}/R)^2] + C_j \tag{8}$$

Of course the result was that the parameters β and R were not strictly independent of ω_j, so we chose the best β, R values by a maximum likelihood method, described in (Agnelli et al. 1979), and we obtained $\bar{R}=57\mu$, $\bar{\beta}$ = 2.25. Then we fitted again the m(r) curves with R=R and $\beta=\bar{\beta}$ and varying only C_j, obtaining in this way the calibration curve

$$\log I_j = C_j/2.5 + \text{const.} \tag{8}$$

The constant was determined applying the calibration curve to the standard stars and obtaining a bias $b=0.5\pm0.06$ mag.
It is worthwhile to note that the shape of the calibration curve is not dramatically affected by the assumed f(r) (the 'true' f(r) would give const.=0), although a precise knowledge of the 'spread function' f(r) could be useful for deconvolving the brightness profiles of the galaxies.

3. PHOTOMETRY OF GALAXIES AND THE REDSHIFT-MAGNITUDE BANDS

To test the photometric accuracy we applied the calibration curve obtained with the method described above to some galaxies for which accurate photoelectric photometry with various diaphragms was known (Sandage, 1972).
The results are shown in tab.1 and fig.3.

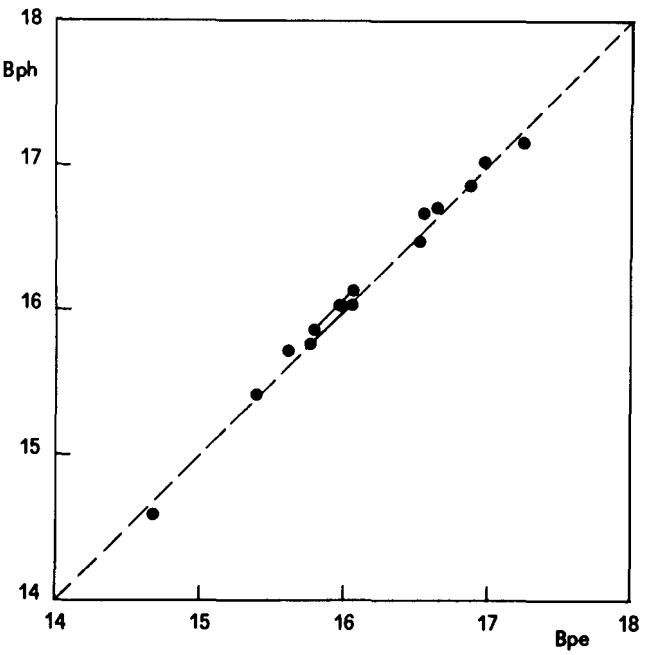

Fig.3 -Photographic versus photoelectrical blue magnitudes for the galaxies of table 1. Points linked by a thin line represent the same galaxy measured with two different diaphragms.

TAB 1.

Name	A(sec)	B_{pe}	B_{ph}	D
RB 42	12.19	17.24	17.17	+0.07
RB 46	12.19	16.97	17.01	−0.04
IC 3998	7.62	16.86	16.85	+0.01
RB 45	12.19	16.64	16.72	−0.08
IC 4011	12.19	16.55	16.69	−0.09
NGC 4873	7.62	16.53	16.48	+0.05
NGC 4883	12.19	16.06	16.14	−0.08
	18.80	15.79	15.87	−0.08
NGC 4906	12.19	16.05	16.04	+0.01
	18.80	15.76	15.76	0.00
IC 4042	12.19	15.97	16.02	−0.05
NGC 4886	12.19	15.94	16.02	−0.08
	18.80	15.60	15.72	−0.12
NGC 4874	12.19	15.38	15.41	−0.03
NGC 4889	12.19	14.69	14.58	+0.11
Mean				−0.03
Standard deviation				0.06

The r.m.s. standard deviation σ = 0.06 shows that the accuracy is of the same order as the one obtained by spot sensitometry. The zero point is known with an accuracy less than σ .
The work to obtain a sample of blue brightness profiles of the Coma galaxies is now in progress.
As a preliminary result we obtained the magnitudes ,B(4.8"), within a circular diaphragm of 4.8" for 103 galaxies of the Tifft's (1972, 1973) sample, which are in our field.
We show a plot, fig.4, of our B(4.8") magnitudes in a redshift magnitude diagram, to be compared with the analogous diagram obtained by Tifft using the V(4.8") magnitudes computed by the major -and minor-axis intensity profiles given by Rood and Baum (1968).

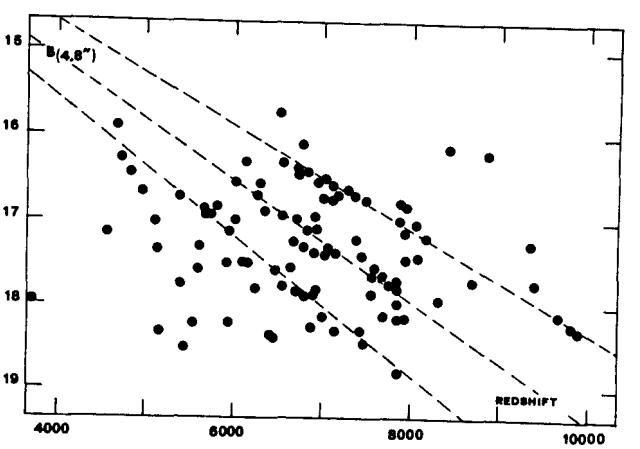

Fig.4 -B(4.8") magnitude vs. redshift, in km/sec, for the Coma cluster. Lines indicate the bands.

At present neither the physical interpretation nor even the statistical significance of the bands seems to be definitively established (Tifft 1979 and ref. therein, Simkin 1977). However, as a qualitative evidence of the band fig.5 shows the distribution of the redshift-magnitude points respect to the 'angular' variable

$$x = p \arctan [1000(m-m_o)/(v-v_o)] + q$$

where (m_o, v_o) is a fixed point in the redshift-magnitude plane and p and q are chosen such as x ranges from 0 to 1.

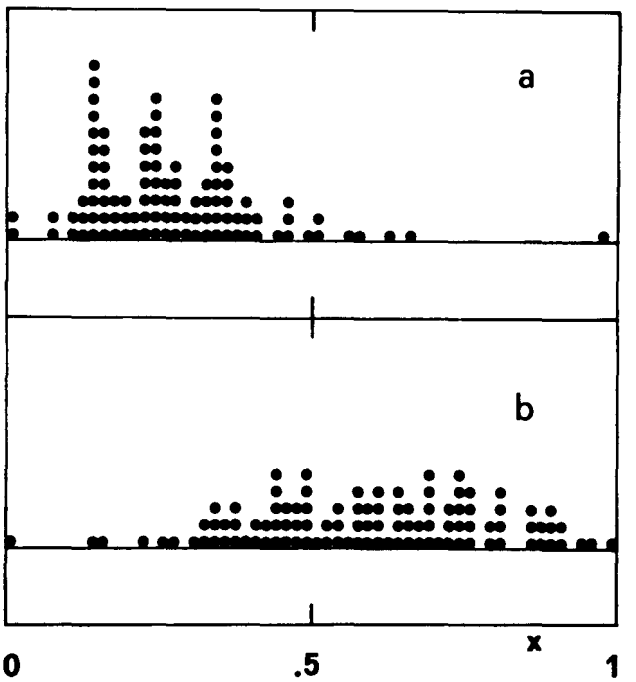

Fig.5 -Histograms of the distribution of the x variable computed using the projection points m_o =12.24, v_o = 0 (a) and m_o = 18.50, v_o = 0 (b)

In fig.5a is shown a histogram of our data with m_o = 12.25, v_o = 0 defines the point of convergence of the bands.
In fig.5b is shown an analogous histogram with m_o =18.5, v_o =0 defines a direction nearly orthogonal to the previous one.
Grouping of points in three main clumps is evident in fig.5a whereas fig.5b does not show any significant clumping. This different behaviour with respect to the projection direction is not to be expected for a random distribution of points.

4. CONCLUDING REMARKS

Our calibration method gives results comparable with spot sensitometry. Due to the presence of various sources of errors, the main of which being a r.m.s. error of 0.08 in the magnitude of the standard stars, we think that the accuracy of the method can be improved. The importance of this technique is also that it can be applied to a large number of photographic plates which have not sensitometric spots.
The qualitative evidence of the red-shift magnitude bands, obtained in a different color band and by direct measure of the intensity profiles suggest further study of the problem with new data and independent statistical analysis.

REFERENCES

Abell G.O.:1977 Ap.J. 213,327
Agnelli G.,Nanni D.,Pittella G.,Trevese D.,Vignato A:1979 A&A 77,45
Kormendy J.:1973 Astron.J. 78,225
Moffat A.F.J.:1969 A&A 3,445
Rood H.J.,Baum W.A.:1968 Astron.J. 73,442
Sandage A.:1972 Ap.J. 176,21
Simkin S.M.:1977 A&A 55,369
Tifft W.G.:1972 Ap.J. 175,613
Tifft W.G.:1973 Ap.J. 179,29
Tifft W.G.:1979 Ap.J. 233,799
de Vaucouleurs G.:1968 Appl.Opt. 7,1513

SECTION V

Detection, Classification and Measurements of Objects Near the Detection Limit

NUMBER MAGNITUDE COUNTS OF FAINT OBJECTS

Richard S. Ellis
Durham University, England

1. INTRODUCTION

I wish to discuss both technical and interpretational difficulties encountered in faint object surveys. I hope to show that the accuracy of the data is not the main limitation in this field, rather it is the insufficient knowledge of basic astronomical quantities needed to model and thereby interpret the data.

Automatic detection, photometry and classification of images seen using panoramic detectors is becoming increasingly important (and popular) as a means of monitoring the statistical properties of large numbers of faint objects. There have been surveys compiled by visual searches (Rudnicki et al 1972; Karachentsev and Kopylov 1977) but they are probably affected by undeterminable selection effects related to image size and surface brightness. Such effects also limit automated surveys but the impartiality and digit al aspects of the data makes them more amenable to inspection and control.

In this review I shall refer to three published faint object surveys; those of Kron (1978,1980), Tyson and Jarvis (1979, hereafter TJ) and Peterson, Ellis and Kibblewhite (1979, hereafter AAT for data was taking using the Anglo-Australian telescope). Kron (1979) has already discussed these results. Here I shall first describe in greater detail than is available in the literature the current photometric techniques and their limitations. I shall then comment on the comparison between the 3 surveys in the light of Kron's remarks. Finally I shall attempt to interpret the counts of faint galaxies with respect to possible evolutionary effects.

2. METHODS OF FAINT PHOTOEMETRY

2.1 Scanning and Data Reduction

The AAT counts were derived from PDS microdensitometer scans at a resolution of 25 μm ($\sim$ 0.3 arc sec) over an area of 0.2 deg^2 on a 60 minute AAT J plate (Kodak IIIaJ plus Schott GG395). The raw data was processed using software developed by Kibblewhite for his Automated Plate Measuring (APM) facility at Cambridge (Kibblewhite 1979). By early 1980 this image processing package will be hardwired into the scanning/control system. The complete scanning and simultaneous data reduction of such an area will only take an hour.

The sky background is determined from the mode of a local intensity distribution covering 64 x 64 pixels. A theshold of 2.5% above the background is imposed. This corresponds to 26.5 J mag arcsec^{-2}. All pixels lying above this isophote are counted. Single pixel events are expected to be noise features and are used to monitor the constancy of the isophote. Events with more than 10 contiguous pixels are determined to be "images". For these the software analyses the intensity distribution and determines a centroid position, an isophotal area, an isophotal magnitude (hereafter J_o), a mean areal profile and position-weighted intensity moments (for formulae see Kibblewhite 1979).

Counting noise events is an important part of the analysis. Experimentally we found a good correlation between the mean surface density of single pixel images and the isophote level. The spatial variation in the surface density at any adopted isophote then defines the accuracy to which that isophote is constant. In the case of the AAT data we determined the limiting isophote to be 2.5 $\pm$ 0.5% of the background.

2.2 Errors

The above tolerance is important in understanding the size of the errors in our faint photometry. Before embarking upon a discussion of the errors it is worth remarking that the interpretation of faint counts relies most on the slope of the differential number-magnitude relation i.e. d log N(m)/dm, hereafter α. In the case of the galaxy counts, α is usually compared to the value expected in the absence of luminosity evolution (Tyson and Jarvis 1979; Ellis 1979b). The deviation might then be interpreted in terms of various evolutionary models. In the case of star counts, α is used to determine the density fall-off away from the Galactic plane (Shanks et al 1980) as well as the likelihood of QSO contamination (Peterson, Ellis and Kibblewhite 1979). It is more important, therefore, to understand the effects that errors have on the slope than, for example, to consider the effect of small uncertainties in the photometric zero point which do not change the slope at all.

Random photometric errors can be caused by fluctuations in the isophote, random digitisation errors in the measuring machine and noise inherent in the photographic plate. A typical $J_o \approx 24$ galaxy occupies 35 pixels above the 26.5 mag arcsec^{-2} isophote and the 0.5% variation in this isophote leads to a random error of $\pm$ 0^m.2 at this magnitude. This is the largest contribution to the random error and can affect the slope α, via a phenomenon referred to as Malmquist bias. Since the counts increase faintward, a larger number of faint objects are errored into a given bin than vice versa. To demonstrate the size of this artificial steepening of the count slope, let N(i) di be the true number of objects with intensity in the range i, i + di. Also assume that over a limited range of i,

$$N(i) = K\, i^{-\gamma} \tag{1}$$

whence $\alpha = 0.4\gamma$. For a square-wave error distribution (which is somewhat unrealistic but is worse than a Gaussian of the same characteristic width and more convenient to treat algebraically), the observed counts become

$$N_{obs}(i) = \int_o^\infty A(i-j)N(j)dj \qquad A(x) = \begin{cases} 1 & |x| \leqslant \Delta \\ 0 & |x| > \Delta \end{cases} \tag{2}$$

For $i > \Delta$ (small errors, which may not always be in the case see §3), the observed slope is:

$$-\gamma' = (1-\gamma)\left[\frac{(1+\varepsilon)^{-\gamma} - (1-\varepsilon)^{-\gamma}}{(1+\varepsilon)^{1-\gamma}\ (1-\varepsilon)^{1-\gamma}}\right] \quad \text{where } \varepsilon = \Delta/i \tag{3}$$

At $J_o = 24$ $\varepsilon = 0.2$ and $(\gamma'/\gamma - 1)$ is only 0.029, i.e. a 3% steepening which is satisfactorily small.

In photography systematic photometric errors are normally dominated by inaccuracies in relative calibration. One advantage of studying faint objects is the small dynamic range involved; a surface brightness 5 magnitudes above the threshold is only a magnitude above the background. (Because of this, there is no real advantage is using linear detectors which have poor panoramic

coverage). The major systematic error here is due to a possible bias in the mode of the background determination because of non-random image/noise contamination. The effect is minimised by taking a large area for background sampling. The assymetry of the resulting distribution around the selected mode gives some indication of the error. We determine the total systematic shift to be $\lesssim$ 0.003 D which, at J_o = 24, amounts to a scale error of less than $0^m.05$ per magnitude - a value also quoted by Kron.

Adding random and systematic errors the total slope error in the AAT data is < 8% at J_o = 24, 4% at J_o = 23 and 2½% at J_o = 22. As we shall see later, this measurement error is considerably smaller than the uncertainties introduced in the interpretation. In other words the accuracy of the data is not hampering the analysis.

2.3 Classification

Stars and galaxies can be separated by a variety of methods and each group fiercely argues its own is the best! The problem is more acute on Schmidt data where the surface density of stars generally exceeds that for galaxies (the numbers are equal at high Galactic latitudes for J $\lesssim$ 22). The separating criterion is usually related to the image intensity profile (Kron 1978; Peterson, Ellis and Kibblewhite 1979), the mean opacitance - magnitude relation (Oemler 1974) or the central surface brightness - isophotal area relation (MacGillivray 1975; Shanks et al 1979). The criteria are all manifestations of the fact that galaxies are extended sources.

Using the large plate scale of the AAT (65 μm/arcsec; 15.3 arcsec/mm) images could be classified to a 5% accuracy to J_o = 23 using the mean exponential slope of the intensity profile (Peterson et al Fig. 1). Fainter classification becomes impossible to check and involves a quasi-theoretical extrapolation of the trends found at brighter magnitudes. As fas as galaxy counts are concerned however, star/galaxy separation fainter than J_o = 22.5 is not really necessary because galaxies outnumber stars by a wide margin - an important and fortunate discovery noted independently by all analyses of deep surveys. To illustrate this, on the AAT data an error of only 1% in the galaxy count slope is caused by extremes in the classifying algorithm over $21.5 < J_o < 24.5$.

It is only for analyses of star/QSO counts that the separation becomes crucial. Future progress both in classifying stars and galaxies and in sub-classifying both groups probably lies with the distribution of images in the colour - colour plane (Kron, this meeting) or in the colour - profile plane (Shanks et al 1980).

2.4 Completeness limit for galaxies

The faint objects have been limited in area in the initial data acquisition to exclude large numbers of noise images. This is of course a plate limit that is related to isophotal magnitude in a complex form. To determine at which magnitude the galaxy sample is unaffected by size and related selection effects, the magnitude and redshift distributions must be modelled (for a fuller discussion see Ellis, Fong and Phillipps 1977; Ellis 1979a). Galaxies are modelled with a variety of parameters such as their luminosity functions, space densities, K-corrections and surface brightness profiles as determined by morphological studies of nearby catalogues (de Vaucouleurs et al 1976; Kirschner et al 1978). In the models the apparent profile of a distant galaxy is the convolution of its true (but cosmologically corrected) light distribution and a Gaussian point-spread function. The intersection of the apparent profile and the isophote of interest determines

the image area and its isophotal magnitude.

The predicted magnitude distribution for galaxies on typical Schmidt and AAT plates is shown in Fig. 1. The solid line shows the relation expected if there were no seeing or surface brightness effects. The point at which the dashed curves fall away from the solid curve defines a completeness limit. Brighter than this the slope is not expected to be affected by these selection processes, although it is important to realise that predictions must still be made in the isophotal framework. In fact the counts fainter than the AAT completeness limit $J_o = 24.5$ do not fall off as steeply as the model predicts. This is due partly to the fact that the model makes no allowance for the large errors which affect the faint distribution. Successful modelling of the turnover would also require a precise form for the point-spread function, the empirical estimate of which is sample limited. Finally, the 0.5% threshold fluctuations have enormous effects at $J_o = 25 - 26$ and will introduce a very significant noise contribution. The important point is that for $J_o < 24.5$ the data is expected to be well-behaved in terms of photometry, slope and completeness. The corresponding limit for the best Schmidt samples is $J_o \lesssim 22.5$.

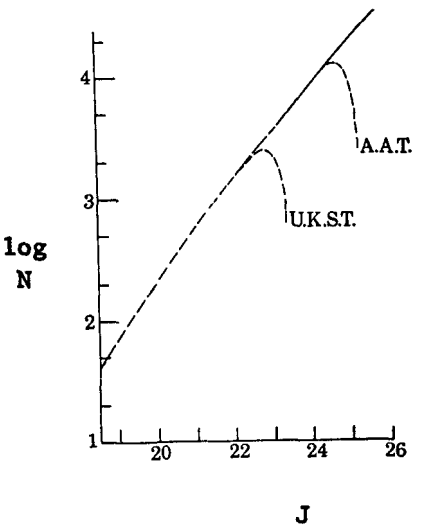

Fig. 1: Differential number magnitude counts per sq. deg. in 0.5 mag bins expected for typical UK Schmidt and AAT galaxy samples. The isophote is 26.5 J mag/arcsec 2, the seeing FWHM is 0.8 arcsec and the limiting diameters are 4.3 arcsec (UKST) and 1.4 arcsec (AAT). All curves assume no luminosity evolution.

3. COMPARISONS

Fig. 2 shows a comparison between the faint galaxy counts of various observers. All counts have been colour corrected to the J band defined earlier. Tyson and Jarvis (1979) have a measurement scheme almost identical to that described above. Their data agrees quite well with that from the AAT. Taking into account the AAT error, at $J_o = 23 \pm 1.5$, $\alpha_{AAT} = 0.455 \pm 0.018$ whereas $\alpha_{TJ} = 0.41$. At brighter magnitudes I include counts derived from UK Schmidt plates scanned with the COSMOS machine (Pratt 1977). The counts are complete to $J_o = 21.5$ (Shanks et al 1979). This is brighter than the limits discussed in §2.4 because the COSMOS spot acts as a substantial contribution to the overall seeing.

There are zero point uncertainties in the southern data (UKST/AAT) because of the shortage of reliable faint absolute photometry. A shift brightward of $0^m.2$ would improve the agreement between UKST and TJ. However, at very bright magnitudes ($J \simeq 17$) the TJ counts (not shown) remain considerably flatter and lie above the UKST counts, those of Kirschner et al (1978) and those obtained

recently from unpublished work of Peterson and Zou. At the faint end, however, it is gratifying to see good agreement between TJ and AAT.

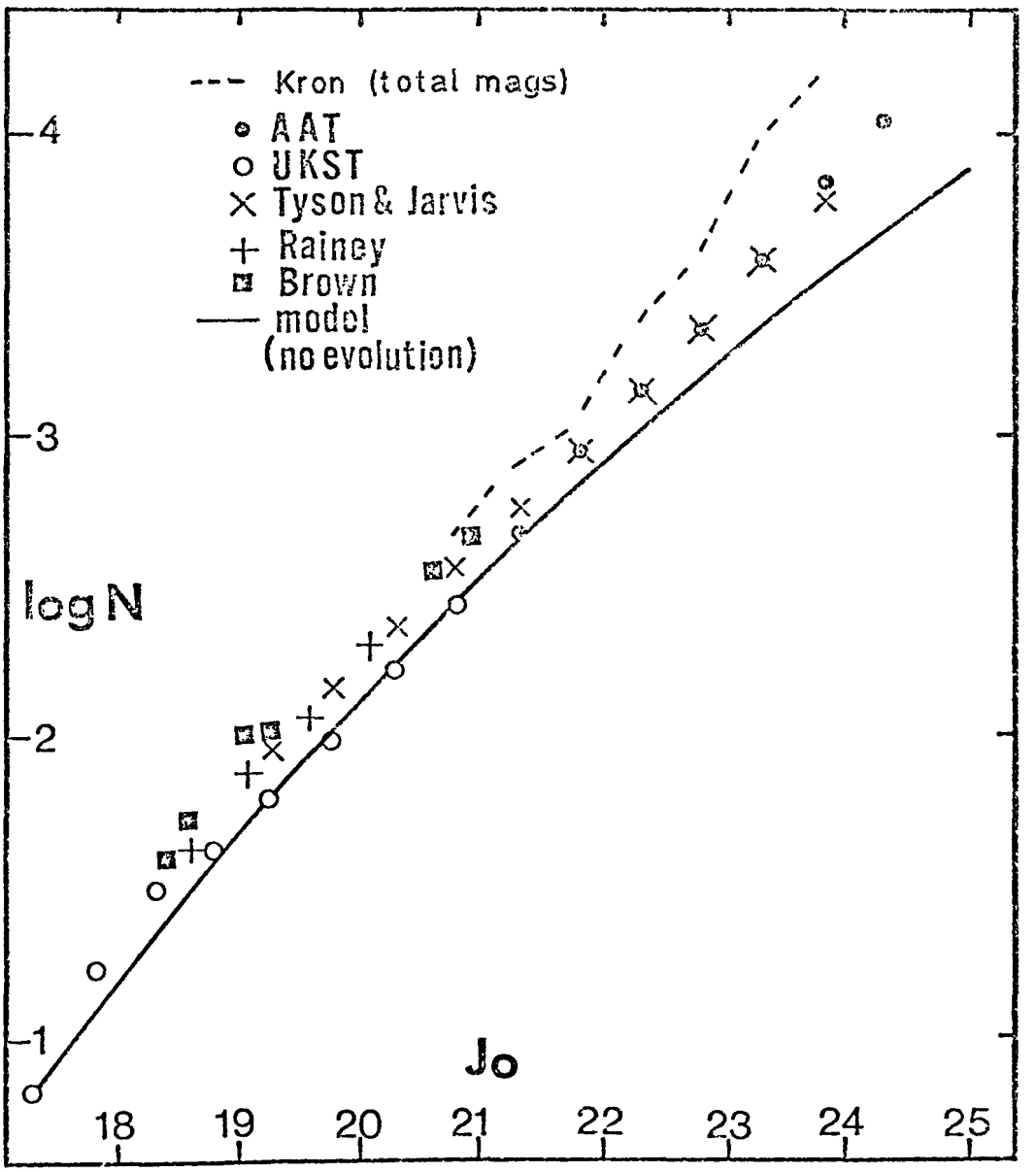

Figure 2 : Differential galaxy counts deg^{-2} per 0.5 mag interval in the J band. The counts of Kron refer to total magnitudes.

Figure 2 also shows counts presented by Kron (1978, 1980) which are considerably steeper and noisier for J $\gtrsim$ 22. A direct comparison is however misleading as Kron has a different photometric procedure (see Kron 1979 for a justification of his methods). Magnitudes here are estimated by summing the light distribution to a limiting radius chosen to be where the logarithmic derivative of the light growth curve (the integral profile) is smaller than some value. Kron claims that this method guarantees approximately the same fraction ($\approx$ 90%) of light is measured at all magnitudes independently of the seeing. I shall refer to this method as the "total" scheme.

Kron discussed three principles on which the measurement of faint images should be based. The first principle is that the method should extract the maximum information from the image. A drawback of the isophotal scheme is that a smaller fraction of the galaxy luminosity is detected for fainter images. The point is, of course, that the isophote is adopted because, below this level it is considered that the information is seriously contaminated by noise. Were there a consistent and reliable way of extracting information closer to the background the isophote could be lowered. In an individual 24th magnitude galaxy it is impossible to measure a reliable surface profile (c.f. Kron (1979)'s Figure 4); statistically it may be possible to gain insight into signals at lower sky-subtracted light levels but only at the expense of considerably increased errors, some of which may be systematic. The difference between Kron's counts and those of the AAT is only partially because of the greater fraction sampled in his scheme; at J_o = 23 where the total counts have already deviated significantly from the isophotal ones, the fraction sampled by the isophotal scheme is above 80%.

The second principle referred to precision; the technique should be optimised so that random and systematic errors produce the smallest possible effects. Kron has re-measured samples of his data using the isophotal method; he then obtains counts in good agreement with those of TJ and AAT. The steeper slope in the total scheme is caused mostly by Malmquist bias as the result of considerably larger photometric errors. We saw in §2.2 that the slope steepening in the isophotal system amounts to $\approx$ 4% at J_o = 23 whereas the steepening apparent in the total scheme is $\approx$ 22% ($\alpha_{Kron}{}^{o}$ = 0.53). To understand the larger errors Kron is fortunate in having duplicate plates for each emulsion and field. Photometric errors can thus be studied via cross-comparisons. For his best plates the rms error at J = 24 is $2^m.0$, some 8 times larger than in the isophotal scheme. Thus although the total scheme is self-optimised to produce the minimum error, it is considerably more imprecise (at least in photometric quantities).

The final principle concerns the interpretation. Accurate quantities are of course meaningless if they cannot be usefully modelled. By using a scheme which measures most of the galaxy light, Kron's counts are less affected by first order problems such as seeing and profiles as well as second order problems such as colour gradients. The isophotal model of Fig. 2 has to make assumptions about these problems. But even in the total scheme the profile is not unaffected by these factors. For large images the fraction of light detected is dependent upon the galaxy type, perhaps as much as in the isophotal scheme. For small images the fraction is seeing dependent. Any attempt to collate data from more than one plate must at least consider these effects and therefore model them also.

To summarise, the isophotal scheme slices the data at a fixed signal to noise, the magnitude of <u>each</u> galaxy has an error which is understood. The total scheme operates statistically, it has considerably larger photometric errors at the faint end but these can be empirically modelled via plate-to-plate comparisons. The total magnitude system may be aesthetically more pleasing in that the photometry is less sensitive to the point spread function. Its main

disadvantage is that it distorts precisely what we want to measure, the slope of the galaxy counts. The distortion is so astonishly large that the error functions necessary to interpret the total magnitude counts must be extremely accurately understood.

Despite these remarks I think it is extremely important that this young subject has not adopted a single "best" method for faint photometry; each method has its disadvantages and it is only by collaborative projects, such as those now underway amongst the three groups involved, that we can determine how best to proceed. It is also encouraging that preliminary work strongly suggests that the three sets of deep counts are consistent after the necessary photometric adjustments have been made.

4. INTERPRETATION

The discussion above might seem academic considering that regardless of how galaxies are photometered the slope of the no-evolution model (Fig. 2) is uncertain to $\approx \pm$ 15% because of our poor knowledge of the intrinsic properties of galaxies en masse. I have already described this pessimistic (and personal) viewpoint in some detail (Ellis 1979a, 1979b). Here I briefly highlight two of the most serious problems and how we might try to resolve them.

4.1 K-corrections

Despite much interest in ultraviolet astronomy recently, extragalactic research in the optical waveband has been plagued by a shortage of reliable uv fluxes for normal galaxies. Early results (Code et al 1972; Carnochan et al 1975) were in considerable disagreement for spiral galaxies. It is now clear that although comparisons are affected by aperture and calibration effects, there are definite variations in the uv flux even amongst galaxies with similar optical colours (Code and Welch 1976). The model in Fig. 2 reveals that galaxies are being lost from the sample typically over redshifts $0.3 < z < 0.8$ which, for the J band, necessitates an understanding of the flux at $\approx$ 2500 Å. The ANS and OAO-2 passbands are really too few in number to define a meaningful flux curve. On the other hand the low dispersion IUE spectrograph has the ideal resolution (7 Å) but has a very small aperture (10 x 20 arcsec). We are currently measuring the uv fluxes for both disk and nuclear regions of bright spirals (Ellis and Gondhalekar 1980). Together with ANS and OAO-2 data the measurements will delineate the integrated K-corrections sufficiently well to estimate the variation from type to type and also the scatter within each type. At present the data on spiral galaxies is simply too meagre to even begin estimating the scatter.

Historically cosmologists have paid more attention to elliptical galaxies since these form a homogeneous sample, can be very luminous and might have evolved significanlty over redshifts of less than 1. We have some idea of the effect on the number magnitude counts of the scatter in the uv fluxes of ellipticals. The uncertainty introduced by comparing some K-corrections derived from satellite measures of 3 ellipticals (Fig. 3) is not too large. This scatter is the absolute minimum we can expect for the combined population since later types are far more likely to have a variable content of moderately hot stars.

4.2 Galaxy mix

Despite the interest in ellipticals that followed the magnitude-redshift test, it turns out that the vast majority of galaxies on deep surveys are late-type spirals. The galaxy mix derived in Kirschner et al (1978) is based upon a study of $\approx$ 160 galaxies of which $\approx$ 25 - 30 are classified as late-types (Scd to Sm and Irr). From our approximate knowledge of the uv spectra of these types (see Pence 1976 and confirmed in our new IUE results), these galaxies

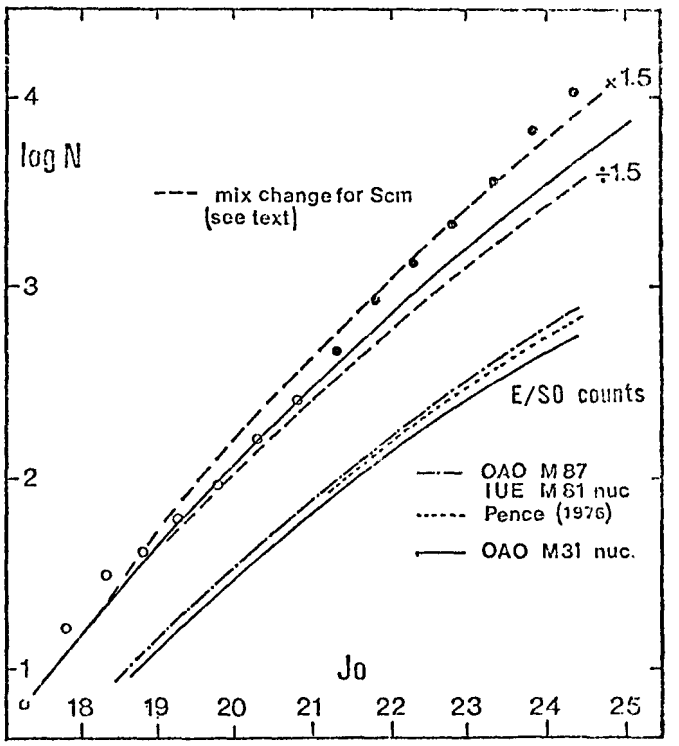

Figure 3 : The effect of various uncertainties on the predicted number magnitude counts for the J band. The lower curves represent predictions for E/S0 galaxies only.

have a very flat flux curve below 3000 Å and so have much smaller K-corrections at moderate redshifts than the earlier types. Provided there is no strong luminosity evolution in one type of galaxy, the apparent mix (Fig. 4) becomes dominated by these late-types at faint magnitudes. If we perturb the true proportion of these galaxies by ± 50% (∿ 2σ for the Kirschner et al sample) we change the predicted count slope in Fig. 3 by 20%. This is sufficient at one extreme to explain the AAT data without any luminosity evolution at all.

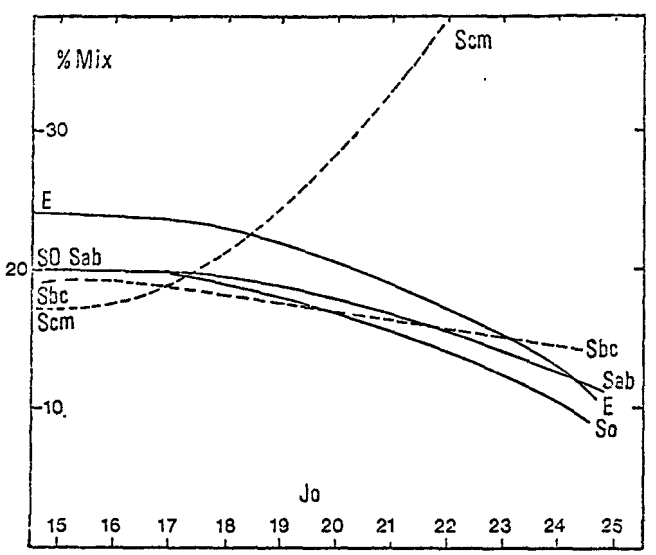

Fig. 4 : Apparent galaxy proportions at various limiting J magnitudes.

These remarks are intended to stimulate action at less glamorous depths. I do not suggest that the Kirschner et al mix is so uncertain as to make analysis of the deep counts impossible. Some attempts were made at interpreting the AAT counts in Ellis (1979a). It does seem, however, ridiculous to get excited about the prospect of studying 28th magnitude galaxies with the Space Telescope when we hardly understand what is happening on our own doorstep.

5. FUTURE PROGRESS

Much of the dilemma interpreting the counts of galaxies will be eased with colour information (Kron, this meeting). Nevertheless we still require accurate K-corrections and luminosity functions for the various galaxy types. There are several long-term projects (Kirschner and colleagues, Durham/AAT group) involving photometric and redshift studies of complete samples of galaxies limited at $J_{16.0} - 16.5$. The aim is to classify the luminosity function via observables such as colours and profile widths (rather than morphological patterns) so that the deep samples can be similarly sub-classified and interpreted independently of one another. These projects are demanding in telescope time, not very glamorous (and have a very low publication/telescope time ratio!). They are essential however if we wish to reap the benefits of optical cosmology with the Space Telescope.

6. ACKNOWLEDGEMENTS

I acknowledge many stimulating discussions with Richard Kron. I also thank Tom Shanks, Dick Fong, Bruce Peterson and Ed Kibblewhite for their invaluable help and advice.

References

Carnochan, D., Navach, I. and Wilson, R. 1975, M.N.R.A.S., 172, 27P.
Code, A.S., Welch, G.A. and Page, T.L. 1972, NASA SP 310, p559.
Ellis, R.S. 1979a, Proc. Roy. Sci., in press.
Ellis, R.S. 1979b, I.A.U. Symposium 92, in press.
Ellis, R.S., Fong, R. and Phillipps, S. 1977, M.N.R.A.S., 176, 265
Ellis, R.S. and Gondhalekar, P. 1980, in preparation.
Karachentsev, I.D. and Kopylov, A.I. 1977, Soc. Astr. Lett., 3, 130
Kibblewhite, E.J. 1979, SRC Automated Plate Measuring Machine Facilities Manual, Institute of Astronomy, Cambridge.
Kirschner, R.P., Oemler, A. and Schechter, P.L. 1978, Astr. J., 83, 1549.
Kron, R.G. 1978, Ph.D. Thesis, University of California at Berkeley.
Kron, R.G. 1979, Physica Scripta, in press.
Kron, R.G. 1980, Astrophys. J. Suppl., in press
Macgillivray, H.T. 1975, M.N.R.A.S. 176, 265
Oemler, A. 1974, Astrophys. J. 194, 1.
Peterson, B.A., Ellis, R.S., Kibblewhite, E.J., Bridgeland, M.T., Hooley, T. and Horne, D. 1979, Astrophys. J., 233, L109.
Pence, W.D. 1979, Astrophys. J. 203, 39.
Pratt, N.M. 1977, Vistas Astr. 21, 1.
Rudnicki, K., Dworak, T.Z., Flin, P., Baranowski, B. and Sendrakowski, A. 1972, Acta Cosmologica 1, 1.
Shanks, T., Fong, R., Ellis, R.S. and MacGillivray, H.T. 1979, M.N.R.A.S. in press.
Shanks, T., Fong, R. and Phillipps, S. 1980, in preparation.
Tyson, J.A. and Jarvis, J.F. 1979, Astrophys. J. 230, L153
de Vaucouleurs, G., de Vaucouleurs, A. and Corwin, H.G. 1976. Second Reference Catalogue of Bright Galaxies, Texas Press.

COLORS AS A CLASSIFICATION DISCRIMINANT

Richard G. Kron
Yerkes Observatory

Automatic surface photometry of large numbers of faint objects is a new and rapidly growing industry, due to the recent wide availability of fast scanning microphotometers, emulsions with high storage capacity, and large, fast telescopes with wide fields. This type of photometry allows a wealth of information to be gathered efficiently about the statistics of faint objects: some examples of this work are studies of galaxy cluster luminosity functions (Oemler 1973, Dressler 1978, Carter and Godwin 1979), stellar luminosity functions in globular clusters and in the Magellanic Clouds (Newell and O'Neil 1974, Herzog and Illingworth 1977, Butcher 1977), and the distribution of faint field galaxies (Tyson and Jarvis 1979, Peterson et al. 1979, Kron 1978). (Not all of these studies feature fully automatic photometry, but the distinction is not particularly important for this discussion.) The galaxy-count efforts have also produced as a byproduct star counts in several different directions, which have obvious importance for constraining models for the Galactic halo and disk and the stellar luminosity function.

Most of the data derived so far from two dimensional photometry of faint objects have been analysed for magnitude, position, and type of image (i.e., stellar or resolved). This short contribution will, among other things, take the opportunity to stress the measurement of integrated color to be used as an additional discriminator between different populations of objects.

The procedures for automatically classifying an object as either a star or as a galaxy have been addressed by several of the observational papers mentioned above; Jarvis and Tyson (1979) should be consulted for a more detailed discussion of their techniques. See also Sebok (1979) and the contribution of Malagnini and Sicuranza (1980) to this Workshop. Another level of discrimination involves separating Galactic stars from extragalactic objects of stellar appearance. Before reviewing some ways in which this can be done, I present in Figure 1 some theoretical expectations for galaxy counts, star counts, and QSO counts down to a magnitude limit achievable with current ground-based technology (the models of Figure 1 do not include distortion in the counts due to random observational error). The galaxy count prediction comes from Bruzual and Kron (1980); it employs evolving energy distributions for eight distinct histories of star formation, added together in such a way as to match the distribution of present-day broadband colors of galaxies. The connection between look-back time and redshift is fixed by our assumption $H_0 = 60$ km sec^{-1} Mpc^{-1}, $q_0 = 0$, and an age of all galaxies at $z = 0$ of 16 Gyr. (This model was actually calculated for a band blueward of V, and has been plotted here transformed to V by the mean color at $V \sim 21$. Since fainter galaxies are in the mean bluer (Bruzual and Kron 1980), the true V counts would be less steep.) The star count model is due to K. Brooks (in preparation) and applies to the Galactic poles. The luminosity functions adopted for both Pop I and Pop II were based on published data, but were perturbed to better represent the

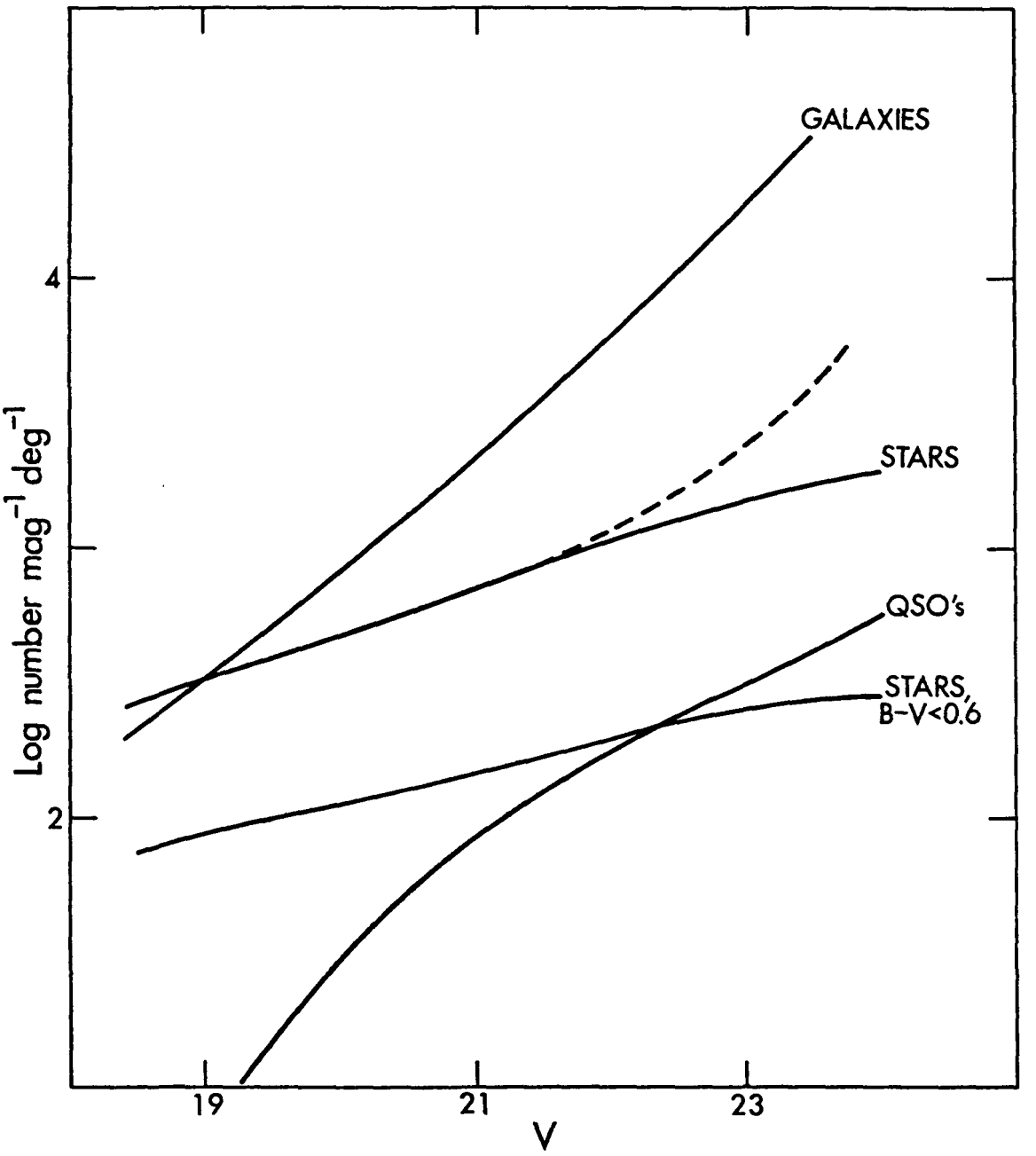

Figure 1. Expected differential counts per square degree at the Galactic pole for all stars, blue stars, QSO's, and galaxies, from models as described in the text. The dashed line represents star counts with increasing contamination by galaxies.

unpublished star counts of I. King and L. Hinrichs; the same can be said for the treatment of the density law in the disk and in the halo. Disk stars are predicted to outnumber halo stars at V = 18.5 by a factor of 1.4, whereas at V = 24.5 halo stars should outnumber disk stars by about the same amount. The model is slightly steeper than that of Bahcall and Soniera (1979), but the actual numbers of stars expected to be seen at V = 22 agree very well. The expected counts of QSO's brighter than V = 22 are due to a model by Mathez (1978) which successfully describes the observed QSO magnitude and redshift distributions with an assumed form for exponential luminosity evolution, without density evolution. This model also assumes H_0 = 60 km sec^{-1} and q_0 = 0, but the most important parameters involve the specifics of the luminosity function (in particular, the value for the lower limit in luminosity). Using Mathez' adopted parameters, I have extended the model to fainter magnitudes, but this extension should not be dignified by calling it a "prediction". Since the nature of QSO evolution is not understood physically, any such effort to discuss QSO statistics in an unexplored realm really amounts to extrapolation. The extension of the QSO counts is presented here only in order to provide some basis for further discussion, and no further qualification of its reliability will be made.

Figure 1 indicates that galaxies are expected to outnumber stars by a factor of 20 at V = 23, and that stars probably outnumber QSO's. The bluest faint stars (B-V < 0.6) are predominantly subdwarf F and G stars, but Brooks' model in the present form suggests that ∿30% of the faintest blue stars could be disk white dwarfs; note that Chiu (1978) found that the scale height for white dwarfs is large, 400 to 500 pc. At any rate, Figure 1 would indicate that QSO's overtake blue Galactic stars fainter than V ∿ 22.5.

The observational limits for V > 20.5 on the numbers of QSO's, and the relative numbers of QSO's and stars, are at present indirect. An example of a recent result (Kron 1978) is the color-magnitude diagram for stellar objects (Figure 2) on a photographic J, F system: J is similar to B, and (J+F)/2 is similar to V. Note the presence of a bimodality in the color distribution, the existence of which was beautifully predicted by Brooks' models. The "blue sequence" corresponds to halo subdwarfs, and the "red sequence" corresponds to disk M dwarfs. There is not much room here for a substantial contribution from unresolved extragalactic objects, which would not be expected to have this particular color distribution. (The bimodality in Figure 2 is washed out at faint magnitudes because the random photometric error in color becomes large, and because there is contamination from galaxies misclassified as stars—more about this below).

On the other hand, both Tyson and Jarvis (1979) and Peterson *et al.* (1979) remark on an upturn in the faintest bins in their star counts, which might conceivably be due to an extragalactic population, since it is not clear how a nonpathological stellar luminosity function could produce such a feature [Bahcall and Soniera (1979) have suggested that the upturn could be due to a just-visible population of halo stars with a very extended spatial distribution]. Since we expect very many more faint galaxies than faint stars at J = 24, it could also be that random misclassification of very faint galaxies as stars produces the upturn in the

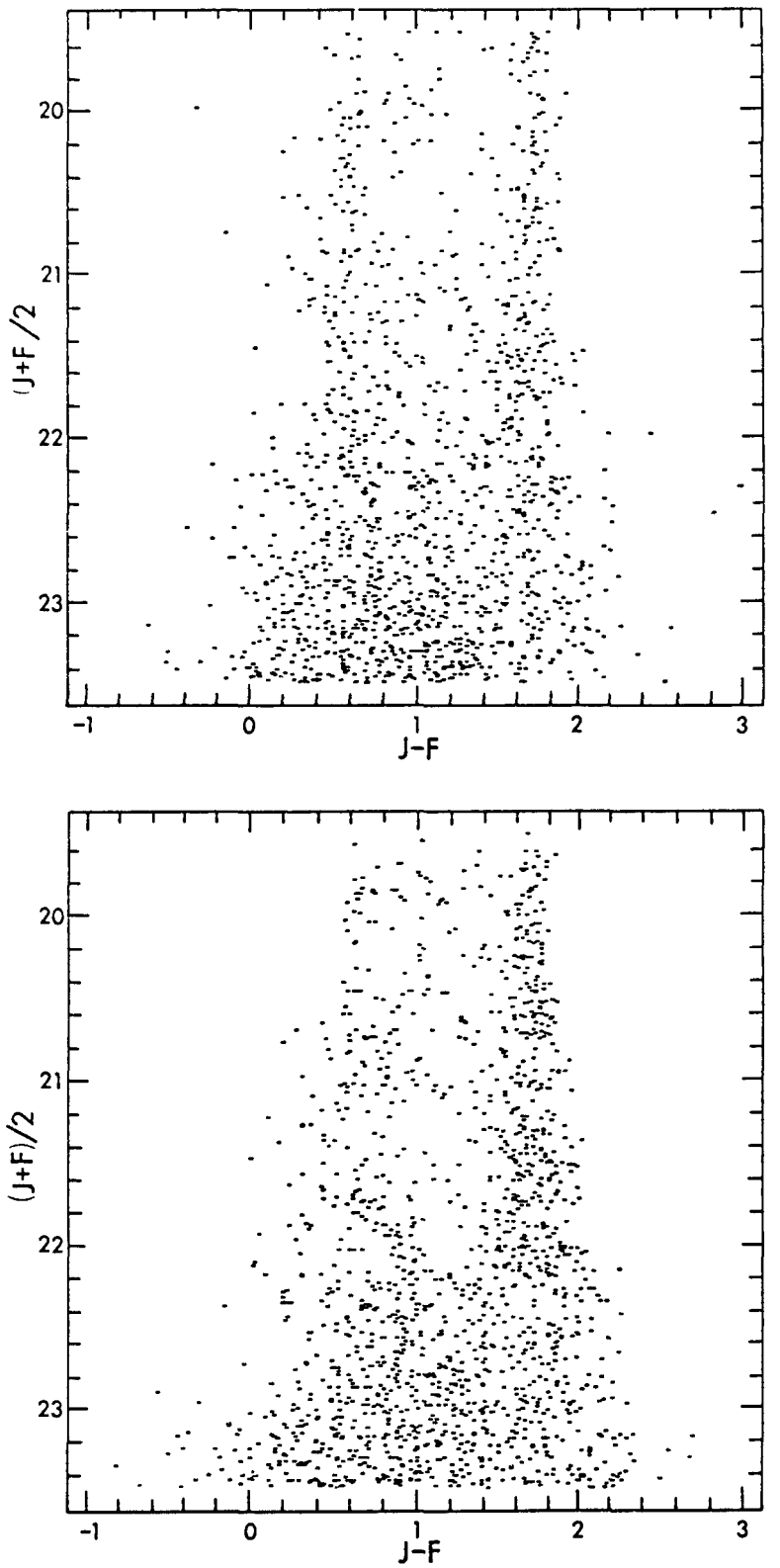

Figure 2. Color-magnitude diagrams for field stars. Top: Selected Area 57, b = +86°; bottom: Selected Area 68, b = -46°.

counts, as suggested by Tyson and Jarvis (1979). This circumstance can be easily modeled from the curves displayed in Figure 1; the heavy broken line gives the predicted "star" counts when an increasing percentage of all objects have been misclassified, up to 8% at V = 23.5. Tyson and Jarvis have performed an important test by obtaining CCD photometry of parts of their fields, and comparing their photographic classifications with the higher signal-to-noise ratio CCD classifications. The results of this direct test were encouraging in the sense that no systematic effect was apparent, but then an 8% bias could be hard to detect unless a large sample were available.

In order to make further progress in the determination of the QSO/star ratio at faint limits, we clearly need more information about each object. Some limits from color measurements have already been mentioned. Recently D. Koo and I have made further progress in this direction, thanks to additional plates obtained in late August of Selected Area 68 (b = -46°) in a photographic U band (IIIaJ+UG5) and in a photographic I band (called here "N" after the IV-N emulsion, +RG 695). These data allow individual objects to be plotted in color-color diagrams, the distributions to be compared with the expected distributions for stars, galaxies, and QSO's. So far we have reduced an area of only 130 arc min^2 in order to study the systematics of the various calibrations before the photometry of the whole field is attempted. Preliminary results are presented here in the interests of illustrating what can be done with very faint multi-band photometry, but the detailed calibration is not yet complete. In particular, the new U and N photometry has been done using the object list already generated from the J and F plates (Kron 1978); we have not yet attempted to photometer objects as <u>found</u> on the U and N plates.

Figure 3 shows the U-J, J-F diagram for objects called stars by a simple algorithm discussed by Kron (1978); the magnitude limits are U = 23, J = 23.5, and F = 22.5. The solid line indicates the expected main sequence Pop I stellar locus as derived from our assumed sensitivity functions for the three bandpasses, and the compilation of stellar spectrophotometry by Straizys and Sviderskiene (1972). The diagram is quite similar to the familiar U-B, B-V diagram, so that the deviant points with U-J excess establish an upper limit to the number of blue QSO's. A random error in the J magnitude would tend to move points along a line of slope -1, i.e., perpendicular to the main sequence, and since some of the points with J-F $\sim$ +0.2, U-J $\sim$ +0.3 may only be explainable this way, it seems reasonable that some points deviant in the opposite sense, in the QSO domain, may also be due to such errors. This does not explain why there are more points on one side of the locus than on the other, nor why there are no deviant points for red colors, but then the error in magnitude as a function of magnitude may not be comparable for the three bands, and the error surfaces could be quite complex. Finally, we have to consider the contamination due to galaxies (Savage and Bolton 1979, Steppe <u>et al.</u> 1979) by looking at the galaxy distribution in the same color-color diagram (to be considered shortly). Having said all this, let us suppose that, say, 6 to 9 out of the 59 objects in Figure 3 are actually QSO's: such statistics are consistent with the curves in Figure 1, especially considering that the star counts for SA 68 should be $\sim$1.65 times larger than that predicted for the Galactic pole, and considering that an object near the

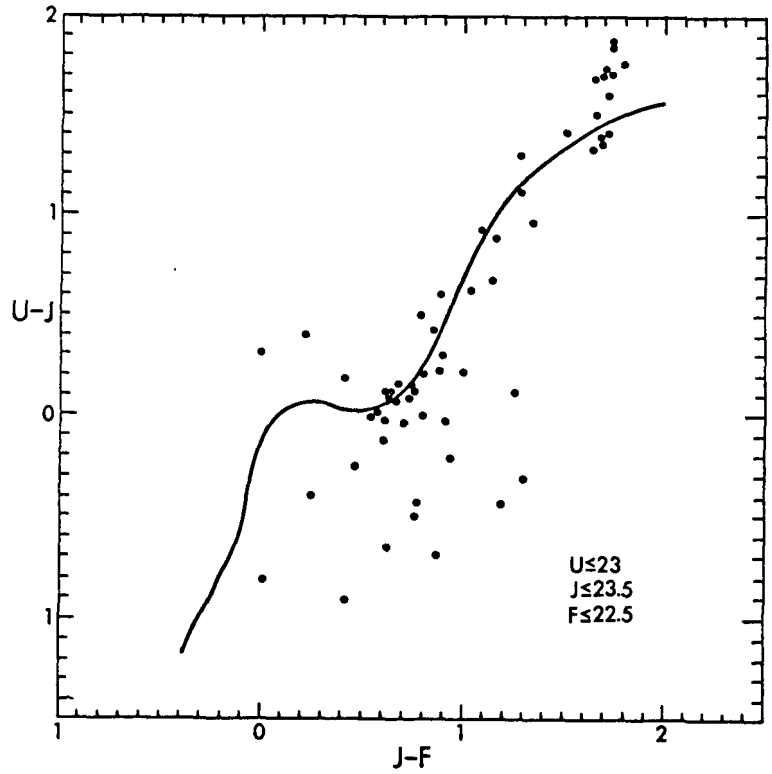

Figure 3. U-J, J-F diagram for stellar objects in SA 68. The solid line is the expected locus for main sequence Population I.

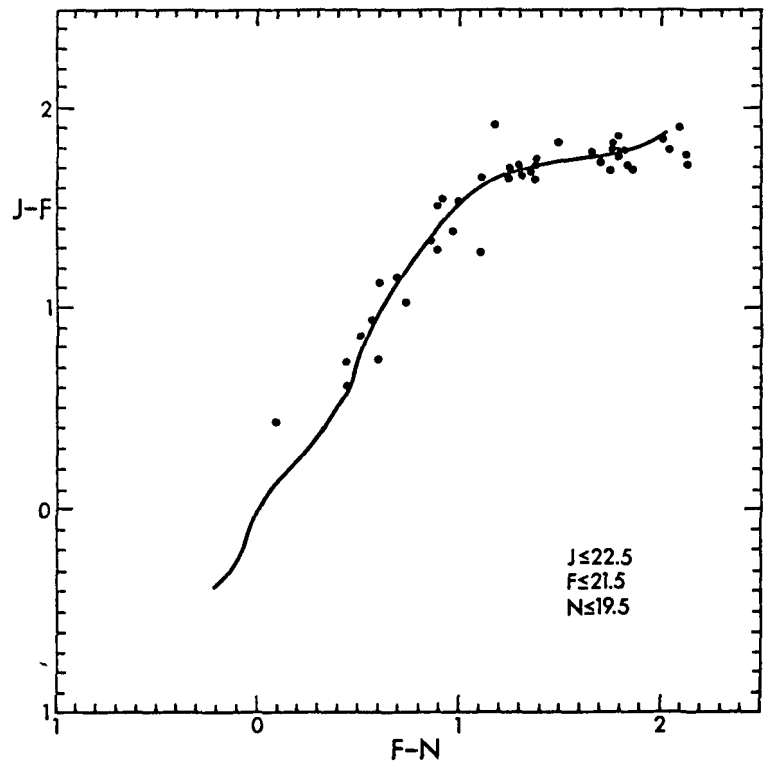

Figure 4. J-F, F-N diagram for stellar objects in SA 68.

limit U = 23 cannot be bluer than U-J = -0.5 if it is to be plotted. It seems then that the QSO counts really do turn over at faint magnitudes, thus avoiding the "X-ray catastrophe" discussed by Setti and Woltjer (1979).

In Figure 4 the equivalent data are plotted in a J-F vs. F-N diagram; here the magnitude limits are J = 22.5, F = 21.5, and N = 19.5. There are few deviant points, partly because the magnitude limits are brighter, and partly because without the U band the differences between QSO's and common stars are less pronounced. Plots of the data in a U-J, F-N diagram should help to separate QSO's from white dwarfs (Braccesi 1967). A salient feature of Figure 4 is the separation in F-N of the stars clumped at J-F = 1.7. F-N is similar in behavior to R-I, and is thus an excellent luminosity indicator for dwarf M stars. A photometric modulus for each red star can then be established with some precision, enabling the density and luminosity function for such stars to be derived readily, unlike the case in which the only color available for each star is B-V, or equivalently J-F.

Another powerful way to distinguish stars from QSO's is by proper motion measurement, as exemplified by Luyten's surveys of faint blue stars. A recent development which should allow such studies to be pursued even fainter is Chiu's (1976) demonstration of the practicality of using plates from different large reflectors: this should allow, for instance, first epoch plates from the Mt. Wilson 100-inch telescope to be followed by second epoch plates from, say, the Kitt Peak 4-m telescope. Another important finding, by van Altena and by Chiu, is that the precision with which the center of a star image can be determined is much higher for the IIIa emulsions than for the 103a emulsions—the unit-weight standard error for star positions on KPNO 4-m IIIaJ and IIIaF plates is 0.4 microns (Chiu 1978) at a scale of 18.7 arc sec mm^{-1}. The telescope was dedicated in the summer of 1973, so by now we have a 6 1/2 year baseline over which such fine-grained plates exist. A star at a distance of 20 kpc traveling with a transverse velocity of 200 km s^{-1} would show a displacement of 0.73μ in 6.5 years, which should be detectable if a number of plate pairs enter the solution for the motion. The detection of such a motion could discriminate between a blue halo star and a QSO; much easier would be distinguishing between a nearer white dwarf and a QSO, despite the smaller expected transverse velocity. Chiu's (1978) practical magnitude limit for reasonably precise positions was V ∿ 20 (J ∿ 20.5), but this was limited by the first-epoch, coarse-grained plates. It may not be too optimistic to hope for J = 22 as a limiting magnitude for proper motions good enough to distinguish QSO's from stars if IIIaJ plates exist for both epochs and if the baseline is greater than about ten years.

Chiu surveyed three fields, one of which was Selected Area 57 at the North Galactic Pole. Figure 5 presents a comparison of the B-V color distribution of objects in this field which had detected motions ($\mu \geq 3\ \sigma$ in both coordinates) and the color distribution of those that did not. The area surveyed was 0.1 deg^2, and the magnitude limits chosen were $18.9 \leq V < 20.9$, with the brighter magnitude interval shaded. The distributions are qualitatively similar in the sense that the color bimodality is evident in each, but the motionless objects have proportionately more blue objects. The baseline over which these stars were observed ranges between

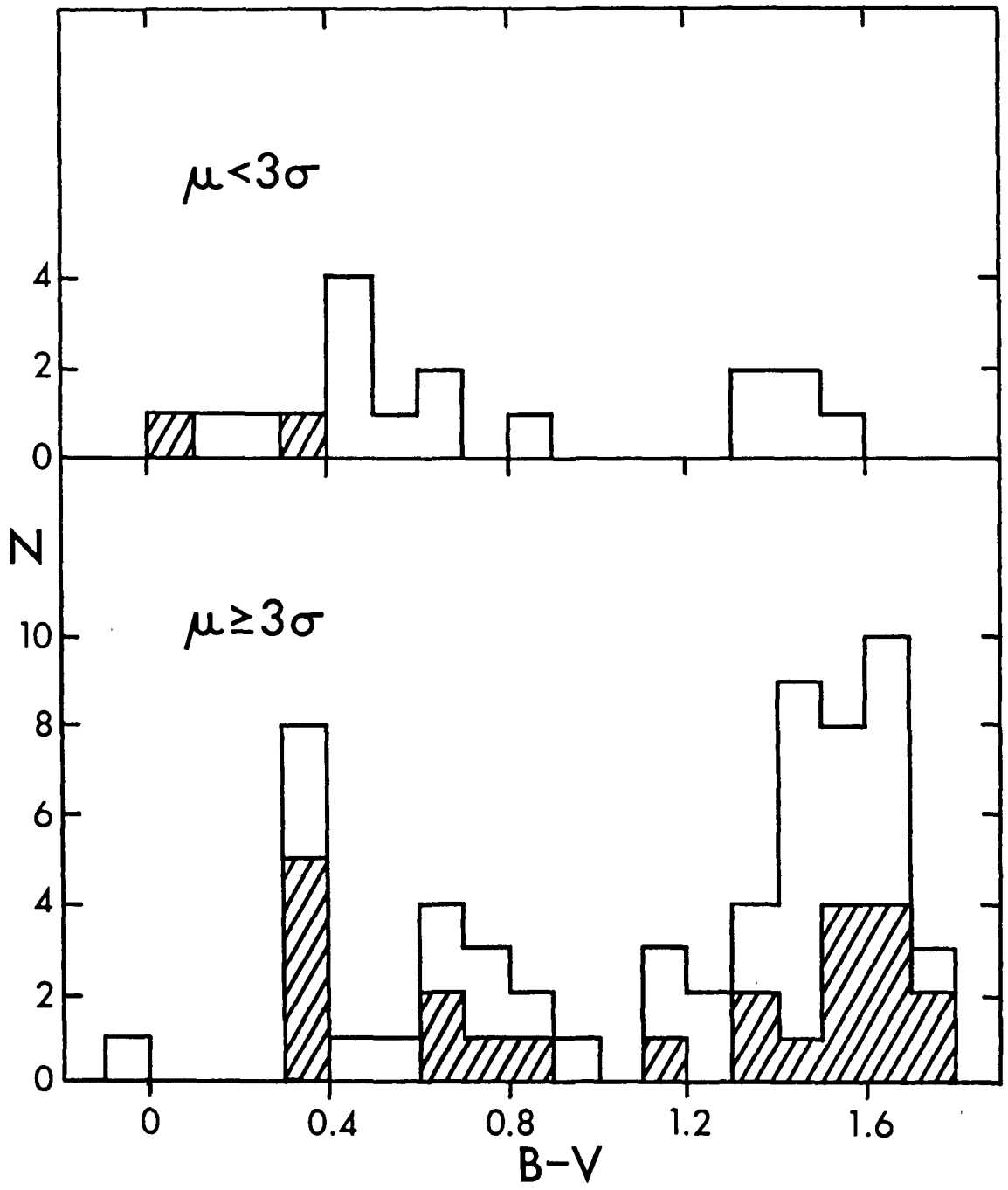

Figure 5. Color distributions for stars in SA 57. Fig. 5a (bottom) stars with detected proper motion; Fig. 5b (top) stars without detected motion. The magnitude range is $18.9 \leq V < 20.9$, with the brighter magnitude interval shaded.

9 and 25 years, depending on brightness and how far each star is from the center of the field. If an additional criterion for a motionless object were T > 15 years, then most of the redder objects in Figure 5b would be excluded. Some contamination of the motionless objects by Galactic stars seems very likely—while there do exist red QSO's, it would be a remarkable coincidence if they were to clump at the same B-V as disk dwarf M stars. If, for the sake of the argument, we assume that there are no true motionless red objects in this sample, then the ratio of objects redder than B-V = 1.3 between Figure 5a and Figure 5b gives the contamination factor, and we would then conclude that there are about 100 objects per square degree brighter than V = 20.9 which are QSO candidates on the basis of showing no motion, which, within the obvious uncertainties, is consistent with the summary of QSO number densities given by Steppe et al. (1979). The importance of Chiu's result is that it is sensitive to all varieties of compact extragalactic objects, regardless of UV excess, emission line strengths, variability, or radio emission. The color distribution was used only in the relatively unimportant role of estimating the contamination factor from Galactic stars; this selection can clearly be dispensed with if spectroscopic calibration of the contamination factor is available. Proper motions of faint stars may be the most efficient way of discovering red QSO's without strong lines.

A corollary to be derived from Figure 5a is that there are many Galactic stars with B-V's overlapping those of QSO's, so that any QSO survey must use some criterion other than, or as well as, B-V, especially if the survey is away from the Galactic poles. A case in point are the faint blue stars discussed by Luyten (1978). Figure 1 indicates that the QSO numbers could exceed blue stars at fainter magnitudes, but this needs spectroscopic confirmation.

[The bluest object in Figure 5b was suggested to be a QSO by Sandage on the basis of UBV photometry—it is one of the Sandage-Becker SA 57 faint blue objects (Sandage and Luyten 1969). Chiu (1978) defined its motion to be zero, and showed that the frame of reference defined by the positions of galaxies was consistent.]

The final topic for discussion is the use of colors in the analysis of faint galaxy statistics. On the technical side, colors can be used as a star/galaxy discriminator because the two types of object generally occupy different regions of color-color diagrams. On the scientific side, the colors of galaxies depend on their redshifts and on their intrinsic colors, enabling a variety of evolutionary and cosmological tests to be imagined, if not performed (Bruzual and Kron 1980). The main new result again involves the U and N data in SA 68 obtained with the collaboration of D. Koo. Below I will display some color-color diagrams analogous to Figures 3 and 4, and the same cautionary remarks apply—more so, since the photometry of faint galaxies is more difficult than that for faint stars.

Figure 6a gives the predicted redshift loci for galaxies in the U-J, J-F diagram, and Figure 6b is the same for J-F vs. F-N. The predictions are derived from synthetic evolving model energy distributions due to G. Bruzual (1980). To fix the scale between time and redshift, these diagrams assume $q_0 = 0$, $H_0 = 50$ km sec^{-1} Mpc^{-1}. The lines are loci of constant redshift, as indicated. Along each of these loci, the variable quantity is the integrated history of the star formation rate, i.e., the type of galaxy—giant elliptical

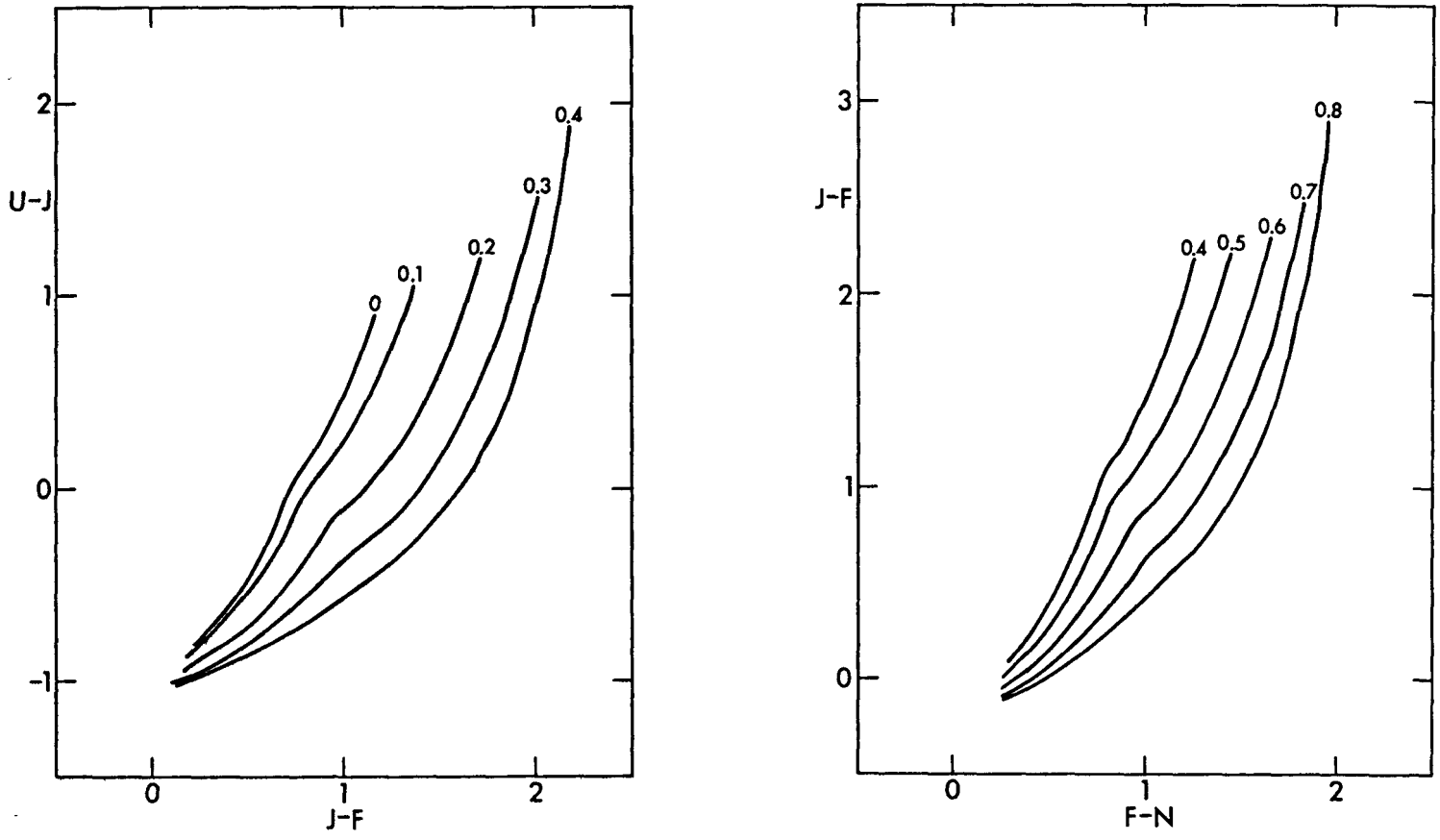

Figure 6ab. Expected redshift loci for galaxies in two color-color diagrams. Each line spans the expected range of apparent colors of field galaxies at constant redshift.

galaxies are at the red limit, and extreme Sdm's are at the blue limit. For fixed apparent magnitude, the distribution of observed points along any such locus reflects the distribution of intrinsic colors, at that redshift, at fixed absolute magnitude. Evolutionary effects can be sought by examining these distributions as a function of apparent magnitude and redshift. Cosmological effects are directly revealed via the volume element, which can be tested if galaxies are conserved. Note that an error in the evolutionary models will affect the predicted distribution of galaxies along each constant-redshift locus, but will not affect either the general position of the locus (which depends only on the general nature of galaxy energy distributions), nor will it affect the total number of objects counted down to a characteristic magnitude (which is determinable from the observed luminosity function).

That broadband colors can determine redshifts with precision adequate for these tests is a fortunate circumstance of nature, due mainly to a change in slope of the galaxy spectra near $\lambda 4000$. Figure 6a shows that U-J, J-F separates out redshifts well for $z \lesssim 0.4$, whereas Figure 6b shows that J-F, F-N performs a complementary function for $0.4 \lesssim z \lesssim 0.8$.

Selected Area 68 is one of the fields in which E. Turner has been measuring redshifts for random galaxies down to about B = 20. Fifteen preliminary redshifts are so far available, and when more data are reduced (both photometry and spectroscopy), the number of faint galaxies with redshifts, and photometry in at least three bands, will be more than three dozen. This sample allows an excellent check on the models and interpretation sketched above. Figure 7 shows the redshift residuals from the photometry of the 15 galaxies. (These galaxies were distributed over the whole field of our plates, and so in general did not fall in the small 130 arc min^2 area previously discussed. The photometry was therefore carried out by Koo specially for this sample of galaxies with an interactive photometry program.)

Figure 8 shows the automatic photometry results for galaxies in the 130 arc min^2 area in SA 68. The magnitude limits for Figure 8a are U = 22.5, J = 23, F = 22, and for Figure 8b are J = 23, F = 22, N = 20. Some points fall to the left, in a "forbidden" region of the diagram. By their colors, these objects could be stars, but upon visual inspection their images rule this possibility out. At this point in the analysis, it seems most likely that they are objects with large random errors—this conclusion is based on the fact that the proportional severity of the effect increases as the magnitude limit for the plotted points is increased. Currently, some spectroscopic attention is being paid by H. Spinrad and myself to galaxies which, by their colors in the J-F, F-N diagram, may well be at very large redshift.

In summary, this discussion has reemphasized a number of classical ideas, such as finding white dwarfs and QSO's by their ultraviolet excess, and using proper motions to distinguish between them. The application of these techniques to very faint samples has been demonstrated. Preliminary work on multi-band photometry of galaxies at cosmologically interesting distances has been presented here by way of illustration of what may be learned about galaxy evolution. Automatic two-dimensional photometry over large areas of sky allows these studies to be pursued with high efficiency.

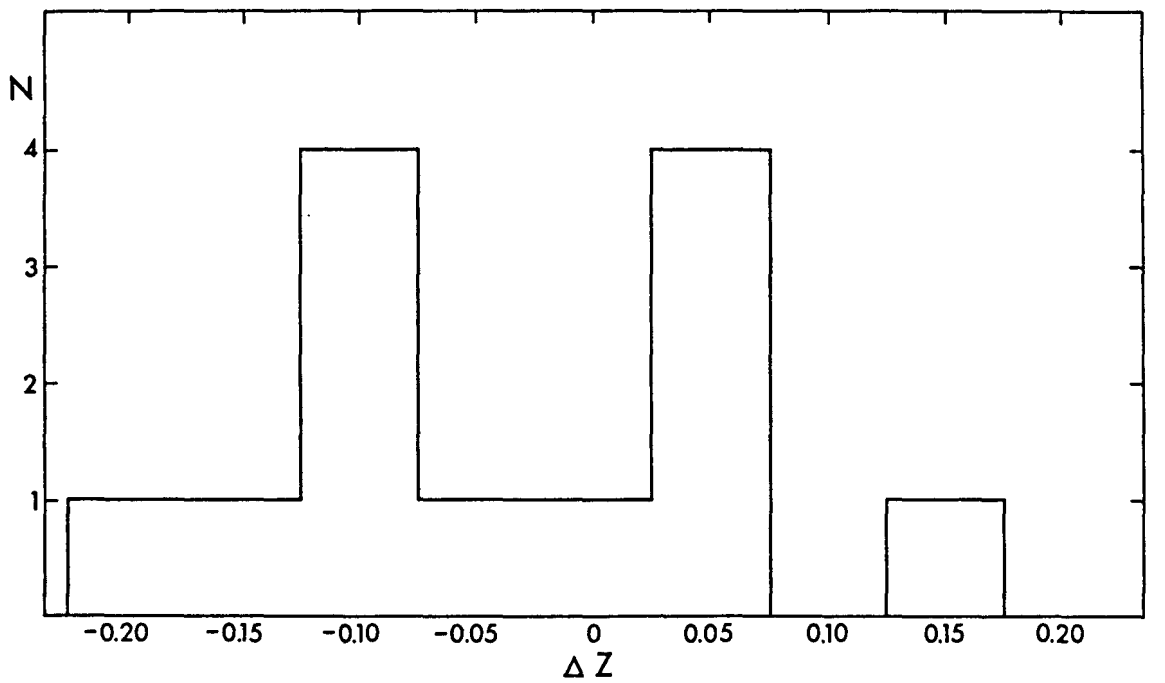

Figure 7. Redshift residuals in the sense of photometrically estimated redshift minus redshift from Turner's spectroscopy, for 13 galaxies in SA 68. Two galaxies measured by Turner are omitted because their photometry places them in the negative-redshift region of the U-J, J-F diagram.

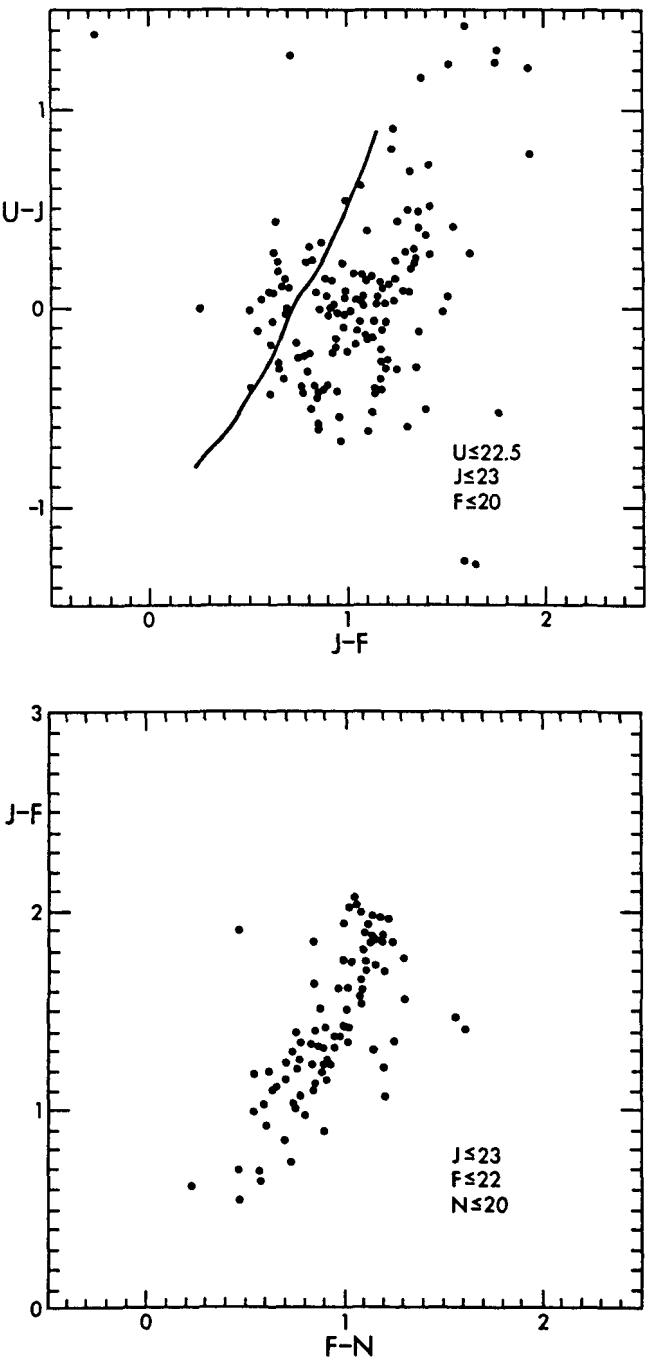

Figure 8ab. Galaxy colors in SA 68. The zero-redshift locus in the U-J, J-F diagram has been replotted from Figure 6a to illustrate the existence of galaxies in a "forbidden" region.

Very little of this could have been written without the assistance of Kate Brooks, Gustavo Bruzual, George Chiu, Dave Koo, and Ed Turner, all of whom have kindly allowed me to present some aspects of their work in advance of publication.

References

Bahcall, J. N., and Soniera, R. M. 1979, preprint.

Braccesi, A. 1967, Nuoro Cimento X, 49, 148.

Bruzual-A., G. 1980, Ph.D. thesis, University of California, Berkeley (in preparation).

Bruzual-A., G., and Kron, R. G. 1980, preprint.

Butcher, H. 1977, Ap. J., 216, 372.

Carter, D., and Godwin, J. G. 1979, M.N.R.A.S., 187, 711.

Chiu, L.-T. G. 1976, Pub. A.S.P., 88, 803.

_____. 1978, Ph.D. thesis, University of California, Berkeley.

Dressler, A. 1978, Ap. J., 223, 765.

Herzog, A. D., and Illingworth, G. 1977, Ap. J. Suppl., 33, 55.

Jarvis, J. F., and Tyson, J. A. 1979, Proc. SPIE, Instrumentation in Astronomy III, 172, 422.

Kron, R. G. 1978, Ph.D. thesis, University of California, Berkeley.

Luyten, W. J. 1978, Proc. Natl. Acad. Sci. USA, 75, No. 10, 4640.

Malagnini, M. L., and Sicuranza, G. L. 1980, in "ESO Workshop on Two-Dimensional Photometry".

Mathez, G. 1978, Astron. Astrophys., 68, 17.

Newell, E. G., and O'Neil, E. J. 1974, in Electrography and Astronomical Applications, eds. G. L. Chincarini, P. J. Griboval and H. J. Smith, (University of Texas: Austin) p. 153.

Oemler, A. 1973, Ap. J., 180, 11.

Peterson, B. A., Ellis, R. S., Kibblewhite, E. J., Bridgeland, M. T., Hooley, T., and Horne, D. 1979, Ap. J. (Letters), 233, L109.

Sandage, A., and Luyten, W. J. 1969, Ap. J., 155, 913.

Savage, A., and Bolton, J. G. 1979, M.N.R.A.S., 188, 599.

Sebok, W. L. 1979, A. J., 84, 1526.

Setti, G., and Woltjer, L. 1979, Astron. Astrophys., 76, L1.

Steppe, H., Veron, P., and Veron, M. P. 1979, Astron. Astrophys., 78, 125.

Straizys, V., and Sviderskiene, Z. 1972, Bull. Vilnius Astr. Obs., 35, 1.

Tyson, J. A., and Jarvis, J. F. 1979, Ap. J. (Letters), 230, L153.

PHOTOELECTRIC SURFACE PHOTOMETRY OF EXTENDED SOURCES

Gerhard f.o. Schnur
European Southern Observatory
La Silla

1. Abstract:

For the measurement of extended faint diffuse light we have devised a new observing method using two telescopes. It allows to compensate accurately for rapid airglow variations. Provisional results on the background light in the cluster of galaxies A0754 and for the extragalactic background light, observed in Lynds L134 are reported.

2. Introduction

The problem of measuring faint diffuse light (FDL) over small areas will be easily solved in the future with the availability of good CCD or CID detectors. The problem will however remain when the areas to be measured extend from half a degree to several degrees. Such problems are incorporated in investigations of the background light in clusters of galaxies (BLCG), see for instance the Coma Cluster studies (T.X. Thuan, J. Kormendy, 1977), or in the studies of extragalactic background light (EBL), as discussed recently by R.R. Dube et al. (1979).

Several observing methods for the measurements of the FDL have already been applied. We will discuss a new photoelectric method of observing FDL.

Finally we report shortly on some of our results.

3. The Light of the Night Sky (LONS)

F.E. Roach and J.L. Gordon (1973) in their monograph - The Light of the Night Sky - discuss in detail the individual components of the LONS. Fig. 1, taken from their monograph, shows the typical contributions of the different components of the night sky.

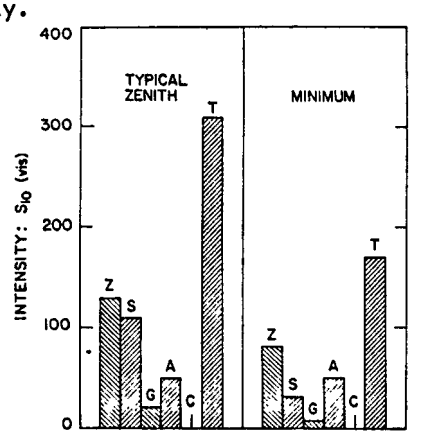

Fig. 1 Components of the light of the night sky. Minimum values for zodiacal light, starlight, and the airglow occur at the ecliptic pole, the galactic pole, and the zenith, respectively. Z = zodiacal light; S = integrated starlight; G = diffuse galactic light; A = airglow; C = cosmic light; T = total.

It is obvious that one has to minimize the contributions from all of the brightest components of the LONS in order to be able to determine with reasonable accuracy any FDL, shown in their figure to be close to the zero level. The strong variation of the airglow with time and its patchy structure aggravates the problem of observing the FDL.

4. Photoelectric Methods of Observing the FDL

A. Airglow problem: In principle photoelectric surface photometry should be as accurate as normal stellar p.e. photometry - 0.2 to a few percent - if the problem of the varying LONS contributions - airglow mainly - can be taken accurately enough into account. Light from individual stars or galaxies can be avoided in most cases by selecting the measuring areas carefully; zodiacal light is a rather constant component of the LONS and can be easily taken care off.

Fig. 2 shows the variation of the night sky brightness during one night at three different celestial positions.

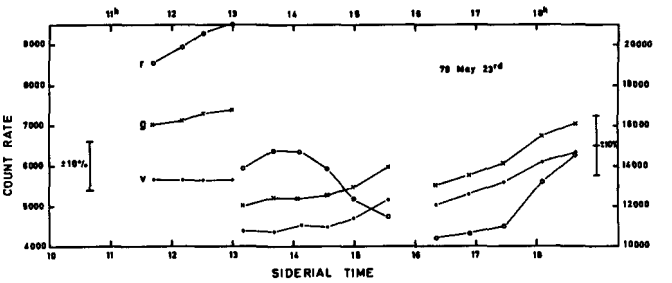

Fig. 2 : Variation of night sky brightness in the v g r colour bands (Thuan, Gunn, 1976). The three Abell clusters A0754, A1517 and A2224 were observed in this order during the night of 79 May 23rd.

The large scale structure of the airglow can be realised from the strong change in intensity when the telescope was moved from one cluster of galaxies to the next. The airglow variation with time is clearly visible (see also Fig. 3).

B. Differential Method: The principle of the p.e. observations of the FDL is that one measures differentially to detect the faint signal against the great confusing component. Differential in this sense means that areas on the sky are selected in which one expects the sought for signal and compares them with adjacent areas where no signal is expected to exist (on-off source principle). Due to the rapid variation of the airglow one has to make sure that its variations are well-known all the time, when one switches between on-and off-sources! From Fig. 3a, b it is clear that one should monitor the airglow on a time scale not much longer than a minute, if one wants to detect a FDL signal that is of the order of a few percent of the total airglow.

How can we monitor the airglow variations while measuring the FDL?

C. Observations of the FDL with One Telescope: To measure the FDL accurately and the airglow simultaneously with only one telescope is very difficult! Either too much time is spent measuring the signal, or too much time for the airglow monitoring. Any compromise leads to reduced accuracy compared to the one that would be obtained if both components were to be measured simultaneously but separately.

D. Observations of the FDL with Two Telescopes: One telescope - the monitor telescope -, monitors the LONS brightness at a suitable spot: the reference point. The second telescope will be used for the actual measurements. In order to establish a relation between the two photometric systems of the telescopes the measuring telescope observes several times per night the reference point also. This will then allow to derive the relation, that will serve later to transform the monitoring data on the variation of the airglow into those of the measuring system for airglow compensation.

For the observations of the "on and off" sources we can operate the measuring telescope in two different modes:

For a reasonable strong extended source of FDL for which one likes to obtain its distribution the telescope scans the interesting area. This method has been used by Melnick et al. (1977) for BLCG-studies of the Coma Cluster.

For very faint diffuse light however, where the detection of the FDL, and not its distribution is of importance, we think that the differential measuring technique provides the optimum solution.

Only a few selected areas, "on" and "off" source areas, are selected for measurements. They are selected in such a way that they do not contain stars or galaxies that are visible on the POSS. Because the monitor telescope follows the airglow variations closely, it is then possible to spend long integration time at these areas. This allows to measure with different filters in a rapid interlaced sequence for a long time, leading to accurate colour determinations.

5. Observations and Reductions

We used our new observing technique - the two telescope differential method- during May and June of this year for the study of BLCG in the Abell Clusters A0754, A1517 and A2224 and for a study of the EBL in the Lynds cloud L 134.

Instrumentation:

Both the ESO 1-m and the ESO 50-cm telescopes were available. For the two photometers we selected photomultipliers and filter-sets to be as similar in characteristics as possible. In the monitor telescope - the ESO 50-cm - we cleaned the light path from all possible obstructions and obtained in this way an effective diaphragm diameter of about 7'. The diaphragm used in the measuring telescope - the ESO 1-m - had the largest possible diameter of 88".

Both photometers are of similar mechanical design and operate under the same software control. This is an important detail, because it allowed us to run them in nearly synchronous operation: when the observing telescope was measuring through filter X, the monitor telescope measured as well

through its filter X; this was the same for all filters. It means that the monitor telescope was always observing the LONS through the same filter as the measuring telescope, even when that was observing "on" or "off" sources.

Observational Details and Reduction

The monitor telescope was pointing all night at one measuring area: the reference point. To establish the relation between the two photometers, we pointed the measuring telescope to this same area several times during the night. Otherwise the measuring telescope observed the "on" and "off" areas.

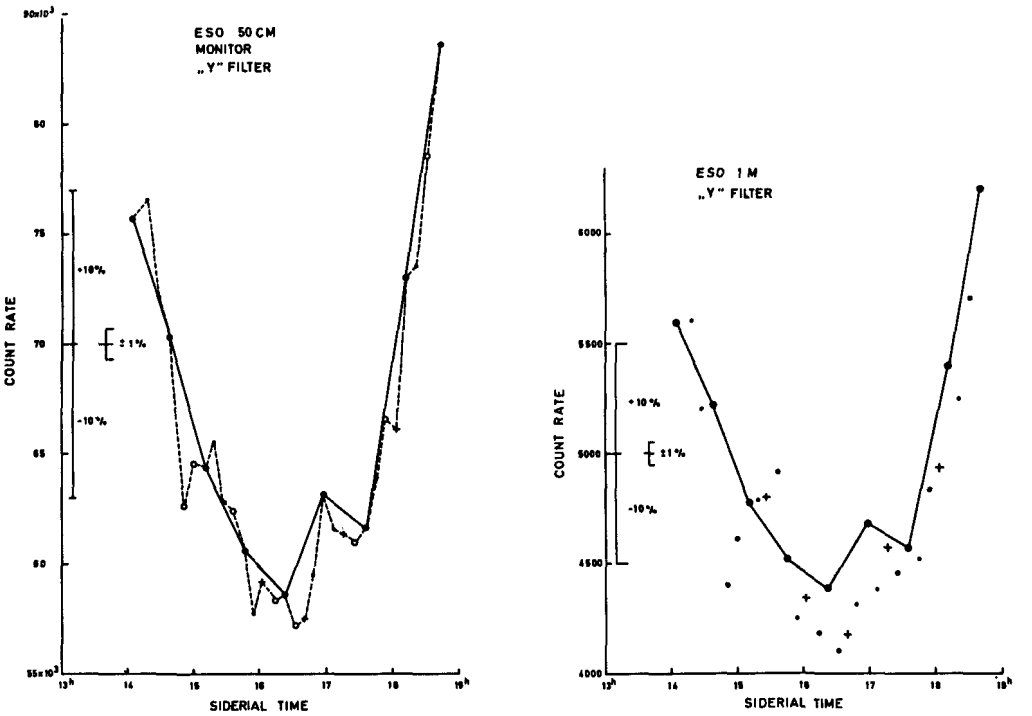

Fig. 3 a,b: Observed count-rates in the Strömgren Y-Band.
a) Monitor telescope - ESO 50-cm
b) Measuring telescope - ESO 1-m
● Simultaneous measurements with both telescopes observing the reference point.
+, o, · "off" and "on" source measurements.

In Fig. 3 a, - ESO 50-cm data - we show the variation of the brightness of the reference point. The different symbols refer only to the corresponding "on" or "off" positions that were measured at the same times with the 1-m telescope.

In Fig. 3 b the "on" and "off" source count data from the measuring telescope are displayed.

The simultaneous observations of the reference points (● in Fig. 3) allowed us to establish the relation between the two photometric systems:

$$\Delta \text{ count rate} = \text{count rate (ESO 50-cm)} - K_j \times \text{count rate (ESO 1-m)}$$

$$K_j = \frac{\Sigma \text{ count rate (ESO 50-cm)}}{\Sigma \text{ count rate (ESO 1-m)}}$$

K_j = const for each night and filter

Fig. 4 displays the result for the four filters used in the investigation of the EBL. For the narrow filter ($\Delta\lambda \simeq 15$ nm) we are able to convert the data from the monitor telescope system into those of the observing telescope system with an accuracy of $\pm$ 4 counts, corresponding to about 0,2 percent of the total counts. For the Strömgren filters we obtain a somewhat lower accuracy of $\pm$ 30 counts, corresponding to about $\pm$ 0.6 percent of total counts.

Similar relations were derived for the u v g r observations of the BLCG in the Abell clusters (See below)

Thus accurate compensation of the airglow became possible.

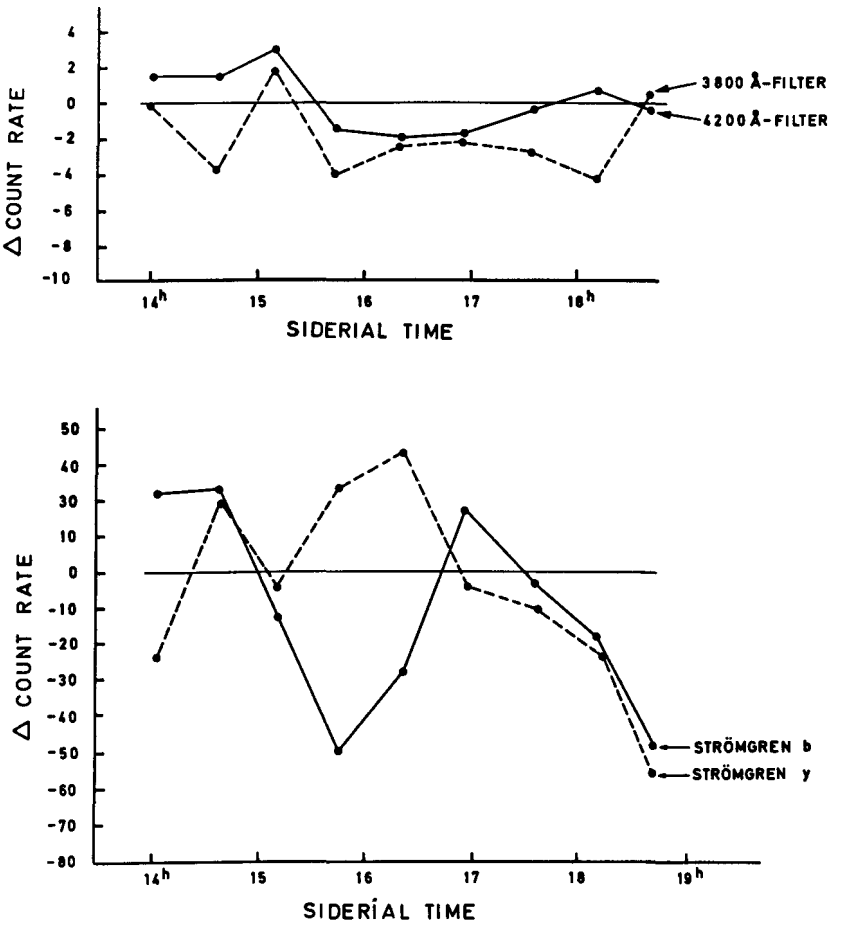

Fig. 4: Relation between the photometric systems of the ESO 1-m and ESO 50-cm telescope for the different colours.

$$\text{count-rate} = \text{observed count-rate}\,[\text{ESO 50-cm}] - K_j \times \text{observed count-rate}\,[\text{ESO 1-m}]$$

6. Provisional Results:

A. Background Light in the Clusters of Galaxies A0754, A1517 and A2224

Clusters of galaxies are a well-known class of X-ray objects. (McHardy, 1978). Recently a number of clusters of galaxies have also been detected to show extended emission at 11.1. cm. (Haslam **et al.** 1978). Together with R. Wielebinski (MPI für Radioastronomie Bonn) we selected the three Abell clusters A0754, A1517 and A2224 to search for possible optical FDL. Based on the observations during only two nights no significant signal could be detected for A1517 and A2224. (Wielebinski et al. 1979).

In A0754 however, we detected a significant signal at two positions, shown in Fig. 5. Both detections are close to giant elliptical galaxies. At 4 other positions situated in between Pos 1 and 2 no signal could be detected. So the possibility exists that the observed detections might just be extended halos of the two galaxies and that we have not yet detected extended optical emission inside the cluster.

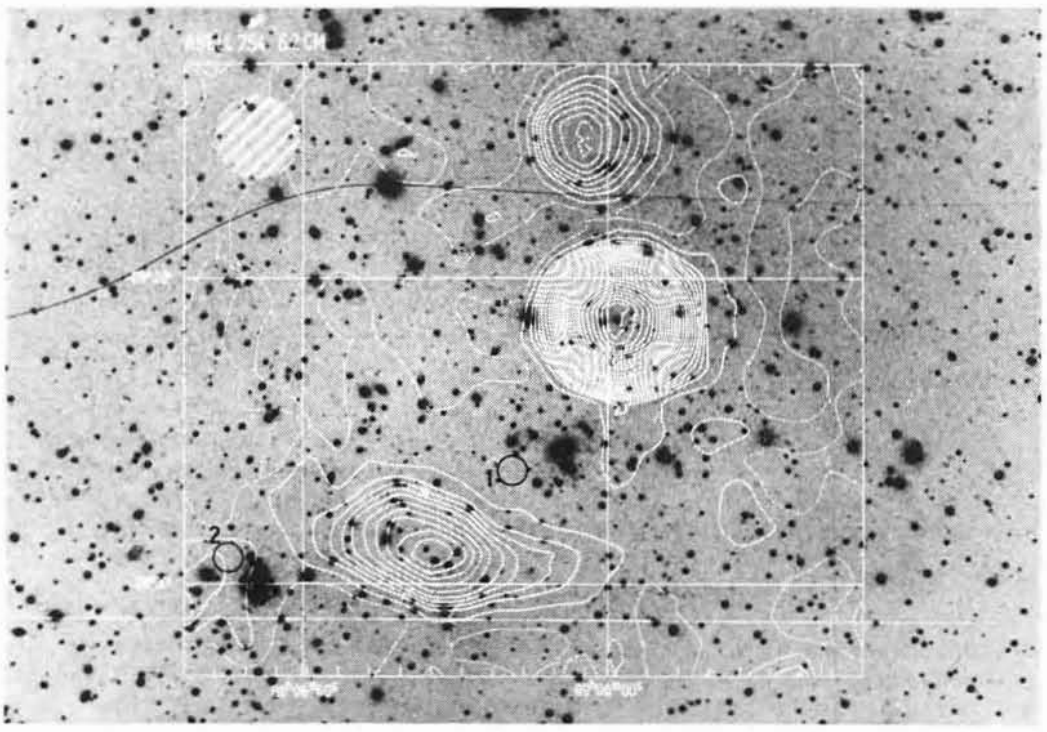

Fig. 5: Cluster of Galaxies A0754. Contours are radio contours. (Waldthausen, 1979). The two positions, where a significant signal was detected, are indicated. Pos. 2 is in the error box of the X ray source: 2A0906-095.

The colours in the Thuan and Gunn (1976) colour system at these positions are:

Position	u-v	v-g	g-r	
1	$-0^m.0$	$0^m.3$	$0^m.1$	with probable errors of $\pm 0^m.3$
2	-0.2	0.2	0.3	

B. Extragalactic Background Light Observations in the Dark Cloud Lynd L134

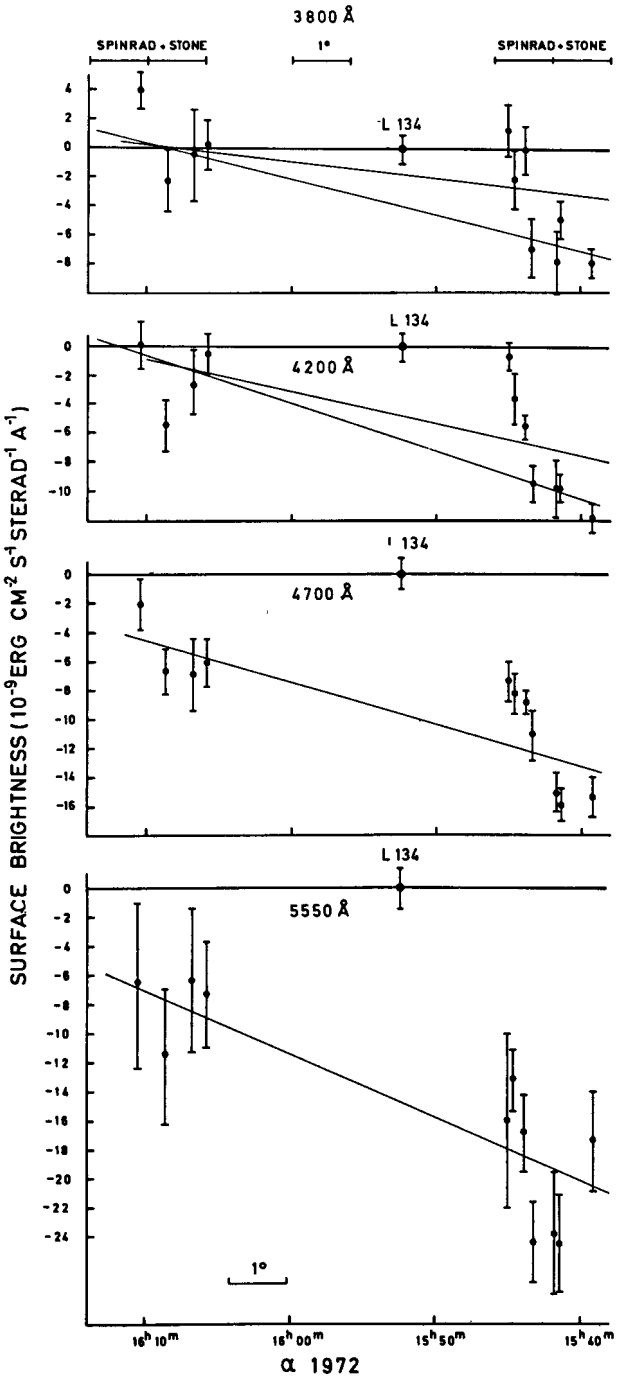

The problem of determining the level of the EBL has most recently been discussed by R. Dube et al. (1979). Mattila (1976) and Spinrad and Stone (1978) using very similar observing techniques determined very discrepant levels for the EBL. This was our (Mattila's, Schnur's) reason for repeating these observations, using our new observing technique. For any details on the EBL observations and their reduction we refer to Mattila (1976). In Fig. 6 we display the individual measurements of the surface brightness of L134 and its surroundings; and in Fig. 7 we compare Mattila's old (1976), Spinrad & Stone's (1978) and our results. L134 turns out to be brighter than the surrounding areas, confirming Mattila's result, but not Spinrad & Stone's. Judging from our new data and Mattila's (1976) Fig. 8 we arrive at the conclusion that the EBL is probably lower than Mattila's old value of 10_{S10}, but an exact value will have to await further observations.

Fig. 6: Surface brightness in L134 and the surrounding areas in the four filter pass bands.
L134: mean from six areas in the L134 cloud.
Otherwise the individual "off" source values are shown.

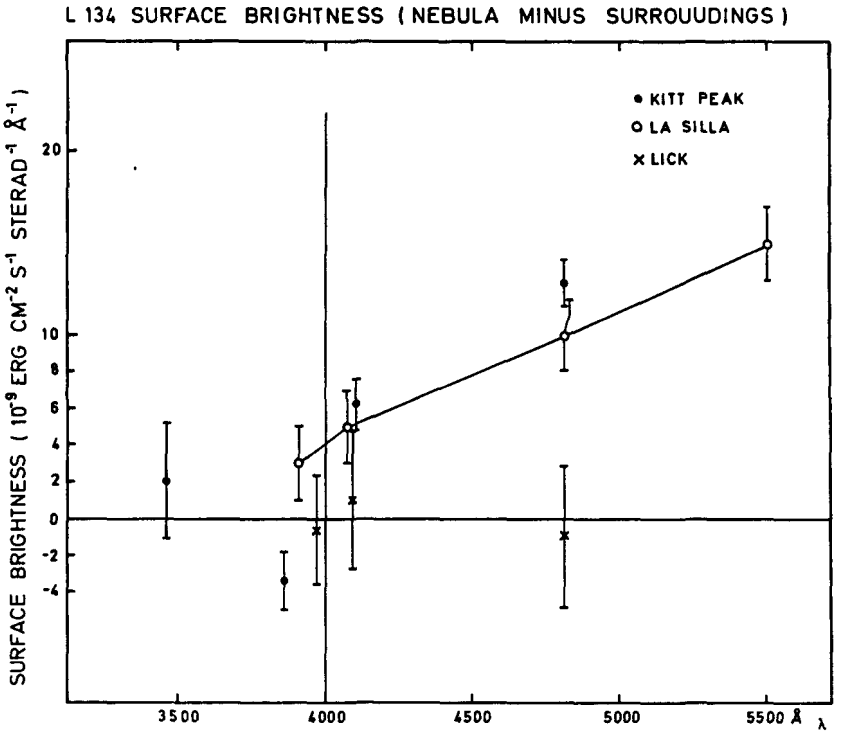

Fig. 7: Comparison of the observed spectral energy distribution of the excess surface brightness of L134.

- • Kitt Peak: Mattila (1976)
- × Lick : Spinrad & Stone (1978)
- o La Silla : new results (Mattila, Schnur 1979)

7. Appendix

Night-Sky Lines and Colour System for Surface Photometry at La Silla

One important point we would like to stress is the selection of suitable wavelength regions for surface photometry. Thuan and Gunn (1976) have proposed a new uvgr colour system for surface photometry that avoids most of the artificial and natural night sky lines.

As Fig. 8 shows the strongest lines in night sky of La Silla are the OI 557.7 nm, NaD 589.3 nm, OI 630.0 nm and OI 636.4 nm lines. Thuan and Gunn's filter system does include only the OI 630.0 and 636.4 nm lines, which could be excluded by a slightly modified red filter. More unfortunate is that most "visual" band passes include the OI 5577 line, which can undergo quite rapid and strong variation during one night. It seems the best to exclude the wavelength region 550 nm to 650 nm for any kind of surface photometry.

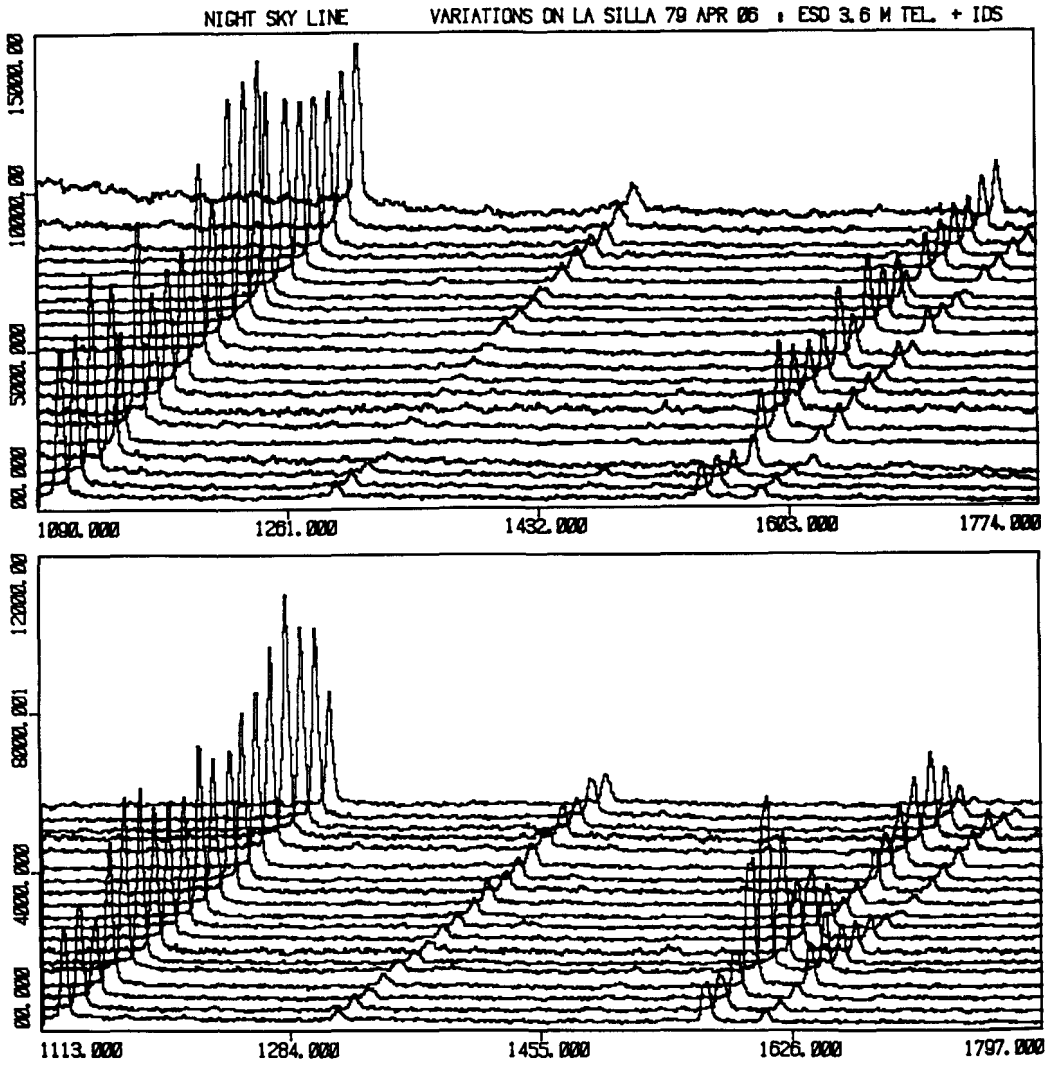

Fig. 8: Night sky line variation during autumn time on La Silla. Observed with the Image Dissector Scanner at the ESO 3.6-m telescope at an dispersion of 171 Å/mm. Only the wavelength region 550 nm to 650 nm is shown.

References:

1. Dube, R.R., Wickes, W.C., Wilkinson, D.T. 1979, Astrophys. J. 232,333
2. Haslam, C.G.T., Kronberg, P.P., Waldthausen, H., Wielebinski, R., Schallwich, D. 1978, Astron. & Astrophys. Suppl. 31, 99
3. Mattila, K. 1976, Astron. & Astrophys. 47, 77
4. Mattila, K., Schnur, G.F.O. 1979, in preparation
5. Mc Hardy, I. 1978, Mon. Not. R. Astr. Soc. 184, 783
6. Melnick, J., White, S.D.M., Hoessel, J. 1977, Mon. Not. R. Astr. Soc. 180, 207
7. Roach, F.E., Gordon, J.L. 1973, Geophysics and Astrophysics Monographs Vol. 4: The Light of the Night Sky, D. Reidel Publishing Comp., Dordrecht/Boston
8. Spinrad, H., Stone, R.P.S. 1978, Astrophys.J. 226, 609
9. Thuan, T.X., Gunn, J.E. 1976, Pub. Astr. Soc. Pac. 88, 543
10. Thuan, T.X., Kormendy, J. 1977, Pub. Astr. Soc. Pac. 89, 466
11. Waldthausen, H. 1979, in preparation
12. Wielebinski, R., Schnur, G.F.O., Mattila, K. 1979, in preparation

PHOTOMETRY OF A VERY DISTANT CLUSTER OF GALAXIES

D. Nanni, G. Pittella, D. Trevese and A. Vignato

Osservatorio Astronomico di Roma
Via del Parco Mellini 84
00136 Roma (Italy)

ABSTRACT

The calibration procedure described in the paper of Nanni et al. (this volume), was applied to the extremely distant cluster of galaxies Zw 1305.4 + 2941.
This cluster is particularly suitable for the application of our calibration method due to the adiacency of the Kapteyn selected area 57 in which many photometric stars are present.
Preliminary results concerning the B and V photometry of some galaxies in this cluster are presented.

1. INTRODUCTION

There are many features of distant cluster of galaxies that deserve more photometric work. Of these characteristics it is worthwhile to mention:
a) the stationarity of the brightest galaxy both in colour and in magnitude down to z=0.4 so that it is possible to search for the deceleration parameter of the universe from the measure of their redshift and magnitude once one takes carefully into account observational selection effects.
b) the presence of a large population of blue galaxies near the center of two rich centrally concentrated clusters at high redshift, in contrast with the characteristics of morphologically similar nearby clusters (Butcher and Oemler, 1978)
c) the steadiness of the cluster mass density distribution found by Zwicky, 1957 in near spherically simmetric clusters, in contrast with some other characteristics like, for example, the secondary maximum in density profiles (Oemler, 1974).
It seems realistic to presume to find in the near future the corresponding characteristics of distant clusters with deep plates or by other means(ISIT systems).
The calibration procedure described by Agnelli et al. (1979) (see also this volume, Nanni et al.) is applicable to cluster galaxies in regions where it is possible to have stars with precise values of the magnitudes.
For these reasons we choose for our work the Zwicky cluster 1305.4 +2941 which is classified compact (i.e. with a single outstanding concentration among the bright member galaxies), 'extremely distant' (i.e. with an extimated redshift greather than 0.2).
The cluster has the number 35 in the field #160 of the Zwicky and Herzog catalogue (1963): in fig. 1, there is a reproduction of this field.
The Zwicky and Herzog counts give a population of 99 galaxies in a

region with a 1.1 cm diameter : this dimension corresponds to 2 Mpc at redshift 0.2 at the scale of the 48" Schmidt telescope (H=100 km /sec/Mpc).

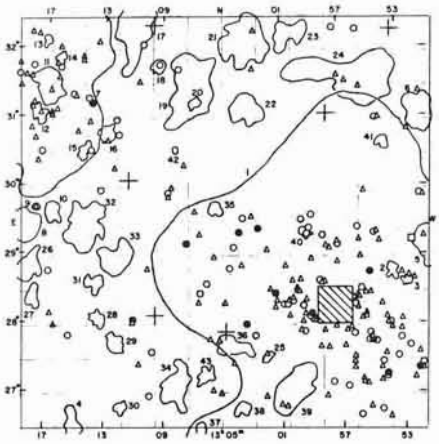

Fig. 1

Fig. 2

This cluster is near the Kapteyn selected area 57 which includes about 90 stars with magnitudes ranging from 6.6 to 23 in B band.
The photometry is based on a 12 minutes 103aO+GG13 (B) plate and on a 25 minutes 103aD+WR12 (V) plate taken by A. Braccesi on the Palomar 48 inch telescope with a transmission grating. Fig. 2 is the reproduction of a pert of the V plate.

2. REDUCTION PROCEDURE AND MEASUREMENTS.

A 10x10 μm aperture was used to scan a 4x4 cm square region of the plates around the cluster 1305.4 + 2941 using the PDS microdensitometer at the Observatory of Neaples : we obtained therefore an array of 4000x4000 transmission measures. The reduction of these data was carried out on the PDP 11/70 system at the Observatory of Rome.

2.1 Segmentation process

Due to the large number of objects involved in our problem ($5 \cdot 10^5$), any interactive procedure is impracticable, so an effort was made to completely automatize the object-extraction procedure.
The main feature of the automatic process is the segmentation procedure to be performed on the original image: that is, we divide our region in connected domains containing the objects of our interest.
The process require a threshold level in order to detect the objects: the choice for this is made looking at the histograms of the transmission values in regions of the plate sufficiently large respect to the mean dimension of the objects, so that these histograms can be considered, in a good approximation, as representing the background statistics.
We choose then, for the value of the threshold tranmission the one which leaves the 90% of the pixels below it (T90).
The value 90 was selected because the random association of pixels

with values of transmission less than T90 can give rise, in a random distribution, to objects having a maximum area less than about 20 pixels. After this the segmentation program detects all the connected areas rejecting the ones with a number of pixels less than 20. Fig. 3 is an example of the results of the segmentation procedure.

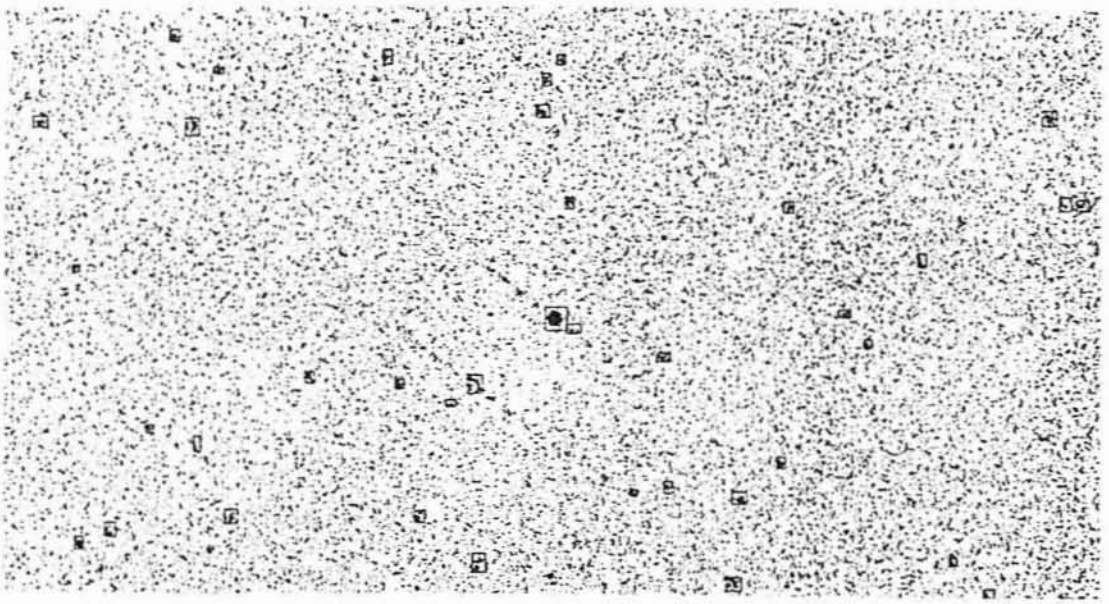

Fig. 3

A scan of the entire image-file is performed reading from mass storage one line at a time. Each line is scanned searching for pixels overcoming the threshold value. Pixels above threshold that dist from each other no more than $\sqrt{2}$ times the pixel size, are attributed to the same object. The information about size and position of each object are stored in a memory-resident one-way list structure, where they are mantained and updated only during the time between the appearing and the disappearing of the object during the scan; that is, whenever an object has no more pixels in the current scan, the corresponding descriptor is written on the output file and the space in the list is made available for insertion of a new element: so we can handle a large number of objects, providing memory only for those which have pixels in the current line.
The program takes about 50 minutes to detect 2000 objects with n>20.
Details on this procedure can be found in Pittella and Vignato, (1979).

2.2 Smoothing procedure

A smoothing procedure was then applied to the image of each object: the procedure has the aim to achieve a nearly constant signal to noise ratio for the different values of the opacitance.
This was made by convolution of the image with a mask in which the weights of the pixels are variable according to the transmission value of the cantral part. Let us assume for the weights the following-form:

$$w \propto \exp(-\alpha r^{2}) \qquad (1)$$

where r is the distance from the central pixel.
Using the approximation in which the number of grains developed by

the source are a linear function of the opacitance, i.e.:

$$ng \propto W = (Tb/T) - 1 \qquad (2)$$

We may obtain the same ng and, therefore, the same S/N ratio for all the pixels with transmission greather than or equal to a reference value Tr, if we give to α the following expression:

$$\alpha = (Tb - T)Tr/(Tb - Tr)T \qquad (3)$$

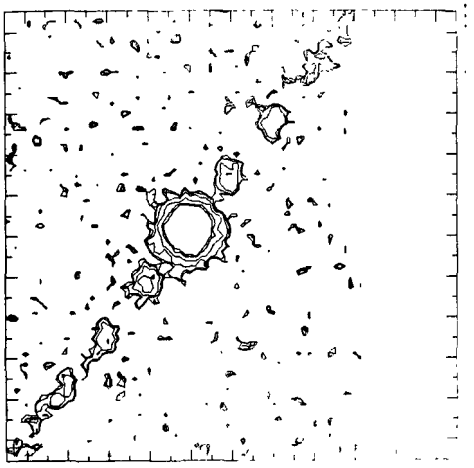

Fig. 4-Isophotal map of unfiltered image of a star.

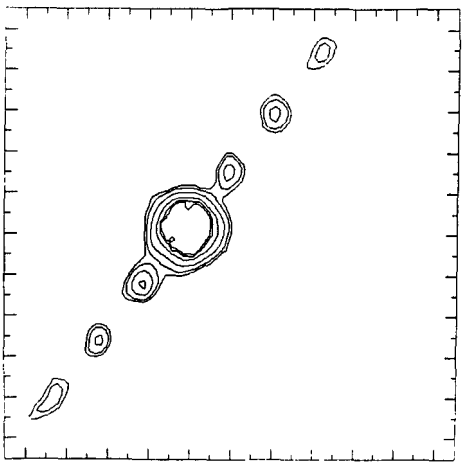

Fig. 5-Isophotes of the corresponding smoothed image.

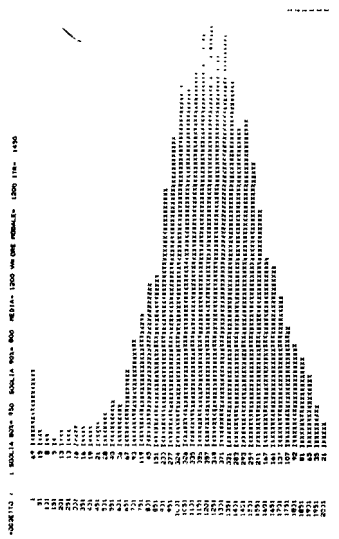

Fig. 6-Histogram of unfiltered image.

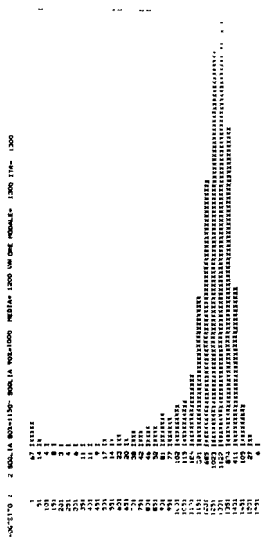

Fig. 7-Histogram of the smoothed image.

A fast algorithm has been developed for this computation in which the weights are determined by a look-up table.
Figures 4 to 7 illustrate the results of the smoothing process.

3. CALIBRATION AND PHOTOMETRY

The calibration procedure, described in Agnelli et al. (1979) and in Nanni et al. (this volume), was applied to the smoothed data.
An intermediate step in the procedure are represented graphically in figure 8 where three m(r) set of points corresponding to different ω values are plotted.

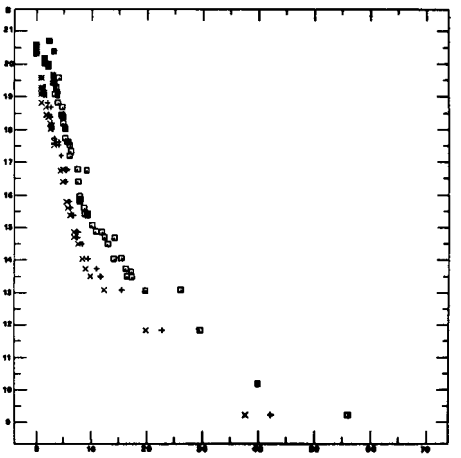

Fig. 8

The β and R values in the Moffat star profile i.e.:

$$I(r)=I_0\,[1+(r/R)^2\,]^{-\beta} \qquad (4)$$

were found independent on the ω value, as theoretically expected, avoiding the problems which arose in our previous work (see Fig. 8).
This seems reside mainly on the fact that:
1) A greater number of reference stars was available;
2) An improved method for finding the isophotal radii on the smoothed data of the stars was adopted, which is independent on the precise knowledge of their centers.

The β and R values were:

$\beta = 1.72$, $R = 21.4$ for the B band
$\beta = 1.71$, $R = 22.6$ for the V band.

If we apply the corresponding calibration curves to the opacitance values of non saturated photoelectric stars we are able to evaluate the bias:

$$b=1/N \sum_1^N (m_i - m_i^*) \qquad (5)$$

where m_i are the photoelectric values and m_i^* are the computed magnitudes.
The values found are:

b= 0.02 ±0.06 in the B
b= 0.50 ±0.04 in the V

able 1 contains preliminary photometric data which result by the ap-
ication of the above calibration curves to some objects in our field
ome of these (the one marked by a *) are galaxies which probably
elong to the cluster. Fig. 9 shows the identification of the objects.
he only possible check on our magnitude scale is made comparing our
value (15.66) and the photographic magnitude (15.7) of the Zwicky
alaxy 1306.6 + 2918.
e compute for the above mentioned objects the isophotal B and V ma-
nitudes within the 25 mag/ □" isophote; we compute also V 24.5, 24.5
ag/ □" beeing the isophote which corresponds approximately to the 25.
ag/ □" B isophote due to the differential k-correction (Pence, 1976)
n the z range 0.2-0.4.

TABLE 1

N	B 25	V 25	V 24.5	Δ25	Δ24.5
1	17.21	15 94	15.98	1.27	1.23
2	18.19	17.34	17.37	0.85	0.82
3	19.02	17.51	17.61	1.51	1.41
4	19.08	18.18	18.25	0.90	0.83
5	17.27	16.70	16.73	0.57	0.54
6	18.01	16.18	16.26	1.83	1.75
7	20.38	18.55	18.70	1.83	1.68
8*	19.44	16.94	17.20	2.50	2.24
9*	19.19	17.28	17.30	1.91	1.89
10*	19.72	18.50	18.75	1.22	0.97
11	19.00	17.14	17.21	1.86	1.79
12*	19.21	17.36	17.40	1.85	1.81
13	18.63	17.34	17.40	1.29	1.23
14	18.76	17.39	17.46	1.37	1.30
15	19.63	17.94	18.03	1.69	1.60
16	18.91	17.22	17.30	1.69	1.61

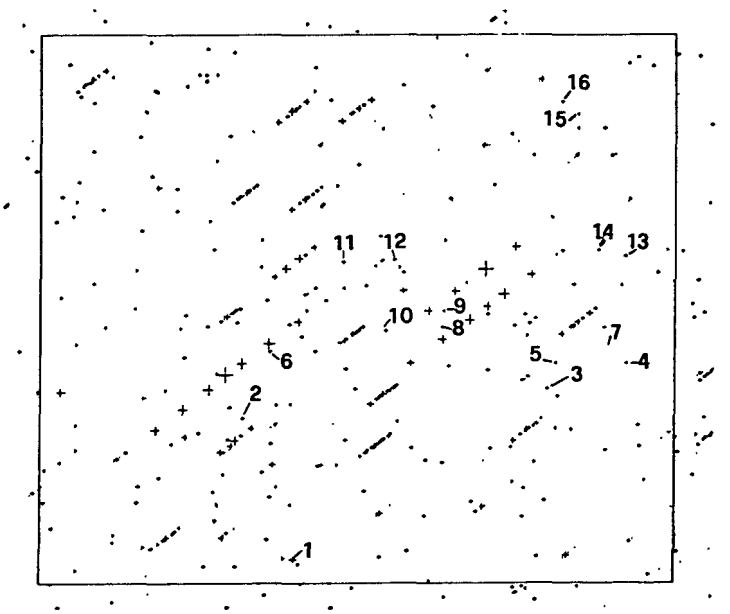

Fig. 9

Note the large color dispersion; the B-V value of the central galaxy (#8 in the list) is greater than the mean value (1.5) of ellipticals in the above z range, while the color of the galaxy #10 corresponds to the color of a redshifted spiral galaxy.
Finally if the mean luminosity of the most prominent members of the cluster is related to the z value throught the classical magnitude-redshift relation for the brightest galaxy (Sandage, 1972) we extimated a value of the redshift for the cluster of about 0.2.

REFERENCES

Agnelli G., Nanni D., Pittella G., Trevese D. and Vignato A.: 1979 A&A 77, 45
Butcher H. and Oemler A.: 1978, Ap. J. 219, 18
Sandage A.: 1972, Ap. J. 178, 1
Moffat A. F. J.: 1969, A&A 3, 455
Pence W.: 1976, Ap. J., 203, 39
Pittella G. and Vignato A.: 1979, Mem. Soc. Astr. Italiana, 50, 537
Oemler A.: 1974, Ap. J. 194, 1
Zwicky F.: 1957, Morphological Astronomy, Springer Verlag
Zwicky F. and Herzog E.: 1963, Catalogue of Galaxies and Clusters of Galaxies Vol. II

SECOND-ORDER STATISTICS FOR IMAGE CLASSIFICATION

M.L. Malagnini
Osservatorio Astronomico di Trieste
Via G.B. Tiepolo 11 , 34131 Trieste, Italy

G.L. Sicuranza
Istituto di Elettrotecnica e di Elettronica
Università di Trieste
P.le Europa 1 , 34100 Trieste, Italy

ABSTRACT

A procedure is proposed for classifying different categories of objects by means of objective criteria.

The procedure can be automated and can be applied to the discrimination of cluster-like objects from stars.

The classification parameters are derived from the analysis of the joint probability density distributions of the gray levels present in the images.

1. INTRODUCTION

The problem of the discrimination and classification of different categories of astronomical objects has been analyzed from various points of view. In most cases the authors refer to a set of astronomical parameters which are immediately comprehensible such as surface brightness and/or the moments of the density of the images (see for instance : MacGillivray et al., 1976; Herzog and Illingworth 1977; Jarvis and Tyson, 1979).

We will present here an approach to the problem of image discrimination and classification which differs from other methods in two main respects:

- first of all, because it is based on statistical properties derived from a subset of objects selected as prototypes of the different categories;
- second, because statistics do not refer directly to the gray levels of the images, but to the distributions of the gray differences in the images.

2. METHOD

The procedure has been derived and adapted to the specific astronomical problem from the gray-tone spatial-dependence method already successfully applied to different kinds of imagery (Haralick et al., 1973; Haralick, 1979, and references therein).

The basic idea is that the texture information on an image can be described by the spatial relationships between the different gray levels present in the image. These relationships are expressed by a matrix, named the co-occurrence matrix, of the relative frequencies of the image tonal variations.

Formally, each (i,j)-th entry in the co-occurrence matrix is the number of times P_{ij} with which two neighboring resolution cells sep

arated by a distance ϱ occur in the image, one with gray level i and the other with gray level j.

Let's consider an image I given in digital form, as an array of N_y by N_x pixels, and quantized in N_g gray levels.

For simplicity's sake, Figure 1 shows how the co-occurrence matrix can be constructed for resolution cells at distance one between them in a given direction α.

1	2	2	3
2	3	4	4
1	2	3	4

i \ j	1	2	3	4
1	0	2	0	0
2	2	2	3	0
3	0	3	0	2
4	0	0	2	2

Fig. 1. On the left, an image I(3x4) quantized in $N_g = 4$ gray levels; on the right, the corresponding co-occurrence matrix P_{ij} evaluated for i,j = 1,2,3,4, $\varrho = 1$, and $\alpha = 0°$ (horizontal direction).

From matrices of this kind, for any given distance between the resolution cells and a given direction, we can derive textural features which contain information about the textural characteristics of the images. It is worth emphasizing that it is no easy matter to connect these textural features strictly with the characteristics of the images resulting from visual inspection.

From among a variety of textural features derived from the co-occurrence matrices, we can choose a set of parameters which characterize different kinds of objects.

We give below some details of the procedure and preliminary results for the specific problem we are interested in, that is the selection of cluster-like objects in the field "0" of M31.

First of all, the objects to be analyzed have a spatial roughly circular symmetry, so we are concerned with properties without regard to any specific direction. Second, preliminary tests suggested suitably weighting the distance between the resolution cells in the derivation of the co-occurrence matrix. As weighting functions, rotated versions of one-dimensional B-spline functions have been used (Mottola and Sicuranza, 1979).Figure 2 is a pictorial representation of the relative weights evaluated by spline functions $B_h(\varrho,d)$ for h = 0,1 and d = 2. On the left, we have the one-dimensional mask of the B-spline function of order h = 0. Starting from each pixel of the image, we evaluate with the same weight the contributions to the co-occurrence matrix from all the neighboring pixels with a distance of up to two. On the right side, we see that the first-order spline function acts so that all surrounding pixels at a distance of from one to four contribute to the co-occurrence matrix with weights pro

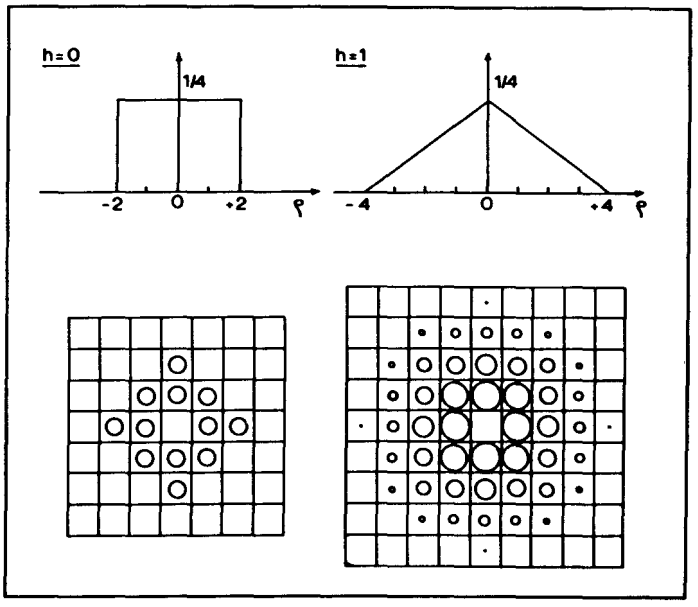

Fig. 2. In the upper portion of the figure, one-dimensional masks of $B_h(\varrho,d)$-spline functions for d = 2 and h = 0,1; in the lower half , the corresponding relative weights (proportional to the diameters of the circles).

portional to the diameters of the circles. The co-occurrence matrix derived taking into account the weighted contributions from all the pixels surrounding any given resolution cell in two dimensions has been referred to as the "modified" co-occurrence matrix (Malagnini and Sicuranza, 1979, a,b).

As to the procedure, it can be described in a schematic way by the following steps:

a. Pre-selection of the candidates

To save computer time and test the method, about a thousand objects have been pre-selected by visual inspection.

b. Measurements

Each object has been measured with the PDS microdensitometer of the Naples and Trieste Observatories. For each object we chose a standard format of 32x32 pixels, with a resolution of 20x20 microns, centered on the image, in density mode. The dynamic range has been reduced to N_g = 16 gray levels, in order to have significant classes for the statistics.

c. Statistics

For each array the following statistics have been derived:

(1) histogram of the gray levels
(2) marginal distributions
(3) modified co-occurrence matrix with h = 1, d = 2.

d. Classification parameters

The choice of the parameters is problem-dependent and has to be

made after analysis of the peculiarities of the co-occurrence matrix for a training set of objects. The objects we have to separate in the central field of M31 are mainly globular clusters and stars; so we chose as a training set one group of well-known globular clusters and, on the other hand, one of Arp's stellar sequences. To discriminate these objects from other images and classify them as stars or clusters, we found it convenient to use the following parameters:

ENTROPY :

$$E(RL) = -\frac{1}{\alpha_{RL}} \cdot \frac{1}{N_g} \cdot \sum_{RL}^{N_g} \sum_{1}^{N_g} P_{ij} \cdot \mathrm{Log}\, P_{ij} \qquad (1)$$

CONTRAST :

$$B2(RL) = \frac{1}{\alpha_{RL}} \cdot \sum_{RL}^{N_g} \sum_{1}^{N_g} P_{ij} \cdot BWH \qquad (2)$$

SMOOTHNESS :

$$A2(RL) = \frac{1}{\alpha_{RL}} \cdot \sum_{RL}^{N_g} \sum_{1}^{N_g} P_{ij} \cdot BWL \qquad (3)$$

where:

N_g = number of gray levels

RL ="rejection level" = 1, 2, ..., N_g

α_{RL} = normalization constant, depending on the number of pixels having $i \geq RL$

P_{ij} = (i,j)-th entry of the modified co-occurrence matrix

BWH, BWL = second-order Butterworth-type filters

The general formula for a second-order Butterworth-type filter is:

$$BW = \frac{1}{1 + \left(\dfrac{|i - j| - \dfrac{N_1 + N_2}{2}}{\dfrac{N_2 - N_1}{2}} \right)^4} \qquad (4)$$

where $|i - j|$ is the absolute value of the difference between the gray levels i and j corresponding to the (i,j)-th entry of the modified co-occurrence matrix, and N_1, N_2 are the limits corresponding to the conventional cut-off frequencies of the filters.

Figure 3 shows the masks of the two particular filters used in (2) and (3). The first filter, BWH, enhances the high-value differences, while the second, BWL, enhances the low-value differences,so we used the terms "contrast" and "smoothness" respectively for B2(RL) and A2(RL).

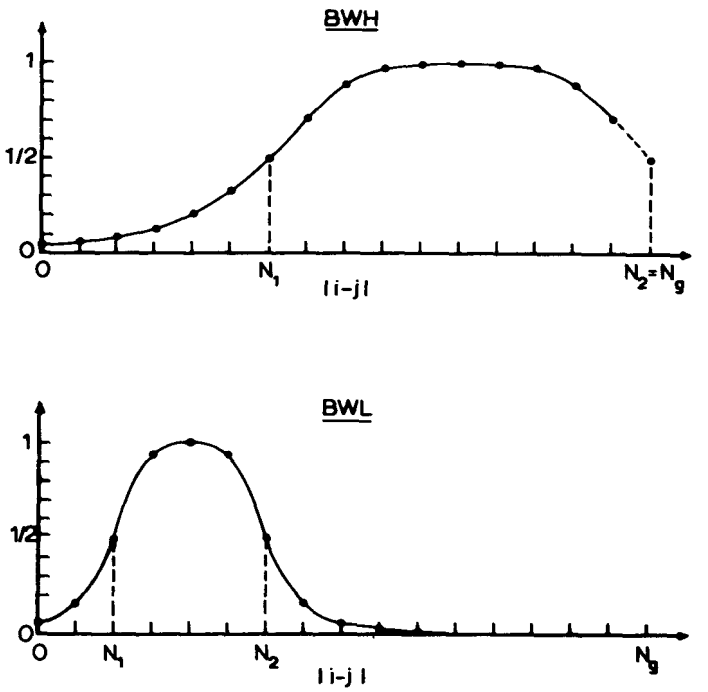

Fig. 3. Masks of the second-order Butterworth-type filters used in (2) (upper part), and (3) (lower part) as functions of the absolute values of the difference i-j of the gray levels.

For RL = 1, we have the values of the parameters evaluated for all the pairs (i,j). For RL = 2, the parameters are evaluated only for $i \geq 2$, and any j, and so on.

3. RESULTS

The first parameter, E(1), say the entropy of the second-order distribution of the gray levels of the 32x32 array, is used to separate well-shaped, regular images from irregular ones, plate defects, and images merged in too noisy a background. This preliminary selection is accomplished by rejecting all images having entropy above the values corresponding to the 95 % confidence level derived from the distribution of the entropy for the objects of the training set.

For the other two parameters, we chose the maximum value in a suitable interval of RL, an interval which is representative of the gray level distribution in the object rather than in the whole 32x32 array. Figure 4 is a two-dimensional plot of the classification parameters (B2,A2) for all the objects : we note a rather large dispersion mainly in the contrast parameter. Figure 5 shows the same kind of plot, but only for those objects which pass the test on entropy : we see that the dispersion is smaller than in Fig. 4 and that the points begin to cluster.

The classification in the two main categories of clusters and stars is then accomplished by means of a linear classifier, assuming normal distributions for the training sets.

A membership probability of 95% and of 90% is assigned on the basis of the two corresponding confidence levels.

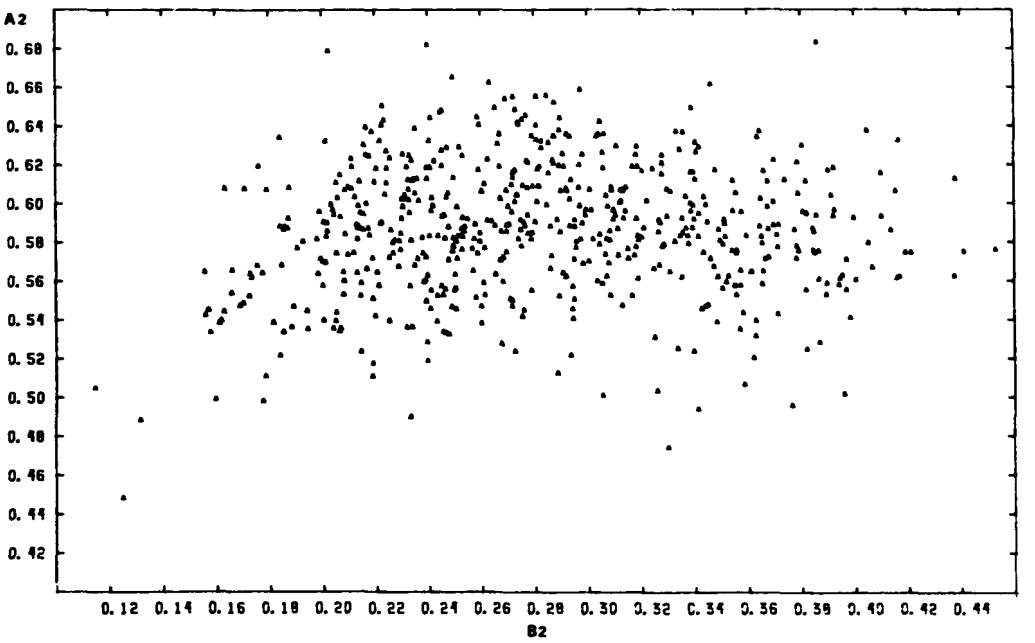

Fig. 4. Plot of smoothness versus contrast for all the objects to be classified.

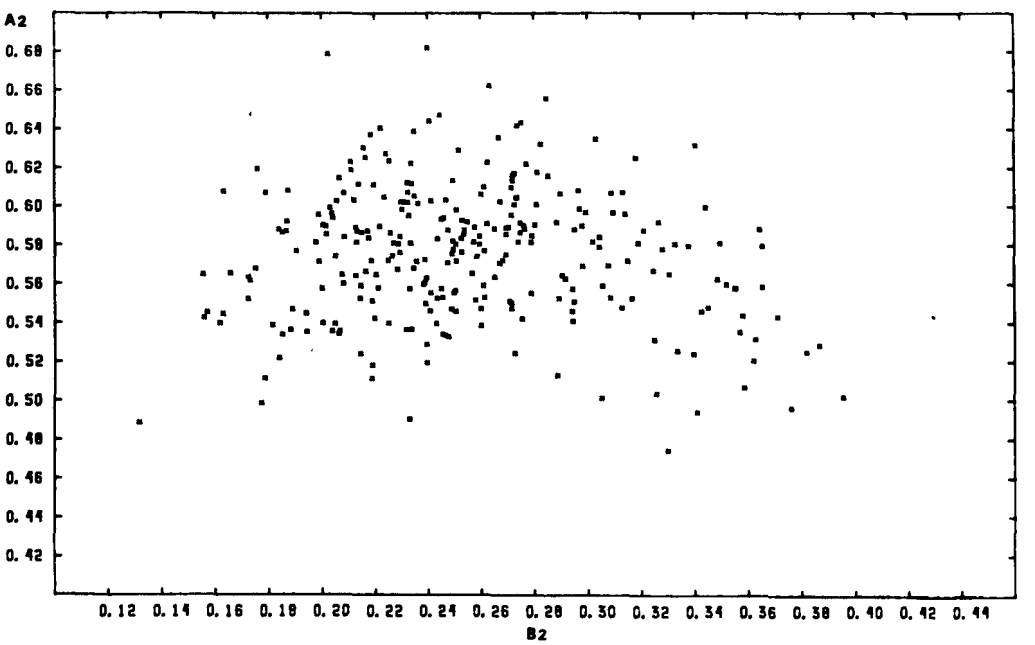

Fig. 5. The same as in Fig. 4, but for the objects which pass the test on entropy.

We used two different linear classifiers, referred to by Nagy (1968) respectively as "distance from means" and "correlation" methods. The discrimination line derived by the first method is plotted in Fig. 6, where we have the separation between stars (lower right) and clusters (upper left). Small symbols correspond to membership probability at the 90 % confidence level, while the large ones refer to the 95% confidence level.

It is easy to see that the two classes are separated at least at the 2σ level.

The separation line due to the second classifier has a slighty different slope than the previous one, while the results are the same at the 95% and 90% confidence levels. The difference between the two linear classifiers is due to the fact that the second takes into account only the amplitude of the weighting vector separating the two classes, while the first depends also on the orientation.

At present, we do not have the complete astronomical results, because they are being checked by Battistini, Bonoli, Braccesi, Fusi-Pecci, and Marano (Astronomical Observatory of Bologna, Italy), who are responsible for the plate, the visual selection and the PDS measurements of the objects.

Preliminary tests look promising, and we hope to extend the method to different categories of objects and problems in the near future.

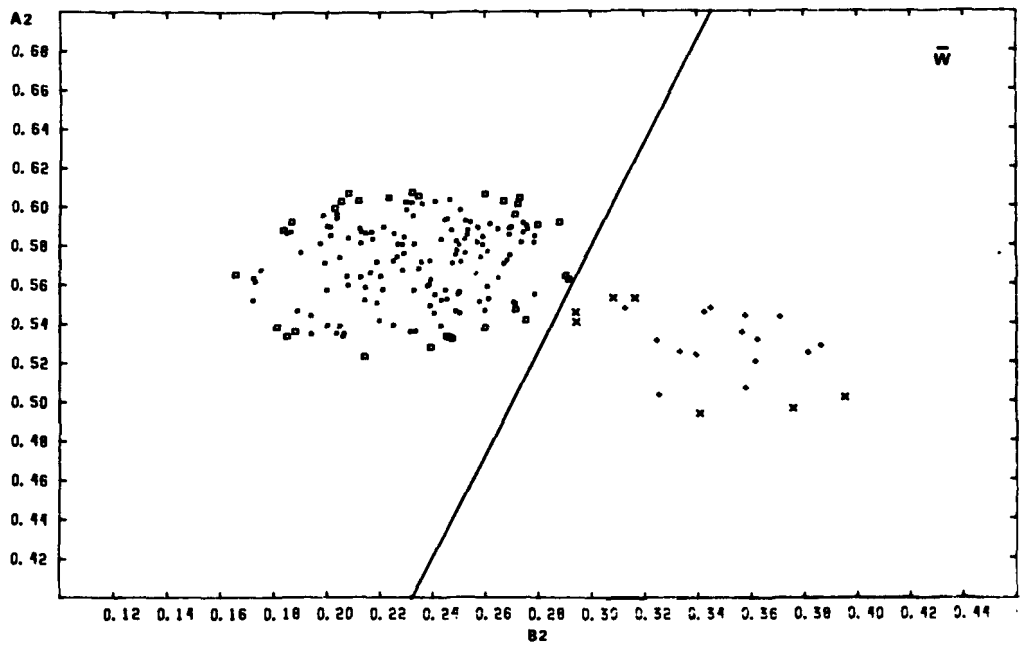

Fig. 6. Final plot for cluster-like objects (upper left) and stars (lower right), separated by the "distance from means" linear classifier. Small symbols refer to the 90% confidence level, large ones to the 95% confidence level.

REFERENCES

Haralick, R.M., Shanmugam, K., and Its'Hak Dinstein : 1973, IEEE Trans. SMC-3, 610.

Haralick, R.M. : Proc. IEEE, Vol. 67, No. 5, 786.

Herzog, A.D., and Illingworth, G. : 1977, Ap. J. Suppl. Vol. 33, 55.

Jarvis, J.F., and Tyson, J.A. : 1979, Proc. SPIE Vol. 172, 422.

MacGillivray, H.T., Martin, R., Pratt, N.M., Reddish, V.C., Seddon, H., Alexander, L.W.G., Walker, G.S., and Williams, P.R. : 1976, M.N.R.A.S. Vol. 176, 265.

Malagnini, M.L., and Sicuranza, G.L. : 1979a, Mem. S.A.It. Vol. 50, No. 3, 497.

Malagnini, M.L., and Sicuranza, G.L. : 1979b, International Workshop on Image Processing in Astronomy, Trieste ICTP (in press).

Mottola, R., and Sicuranza, G.L. : 1979, Alta Frequenza Vol. 10.

Nagy, G. : 1968, Proc. IEEE Vol. 56, No. 5, 836.

THE DETECTION AND PROPERTIES OF DISTANT CLUSTERS OF GALAXIES FROM COSMOS MACHINE MEASURES ON A FIELD IN SCULPTOR

R. J. Dodd and H. T. MacGillivray
Royal Observatory Edinburgh

Abstract

The COSMOS machine, its modes of operation and a method for separating star from galaxy images are described.

The distribution of galaxies in a field in Sculptor is analysed using different techniques and the apparent luminosity function of the galaxies given.

Introduction

There are many problems in astrophysics which benefit from the analysis of large samples of data; examples are: distribution of stars of different spectral type in our galaxy, the hierarchical clustering of galaxies in the universe, and the intensity distribution of light in HII regions.

These problems remained intractable on the large scale without the aid of fast automatic measuring machines of which COSMOS is an example.

Outlined below is a description of the COSMOS machine, its modes of operation and a method for separating the images of galaxies from those of stars. In conclusion, a discussion of the results of three different analyses of the same machine data on a field in Sculptor is given along with the apparent luminosity function derived for the galaxies in the sample.

COSMOS

The COSMOS machine (Pratt 1977) is a high speed automatic scanning microdensitometer. The plate to be examined is placed in a holder which is located at three points on the (X , Y) carriage and scanned by the image of a microspot CRT with a photomultiplier measuring the transmitted light. A raster scan is generated by drifting the machine in the Y-direction whilst the CRT traces parallel to the X-direction. At the end of each drift the start point of the X-scan is incremented one scan width and the Y-value reset to build a complete picture of the plate. The length of the CRT trace always represents 128 pixels which may be of 8 μm, 16 μm or 32 μm diameter. The corresponding time to

measure an entire 35 cm square Schmidt plate are then 18 hours, 5 hours and 1½ hours.

There are currently three modes of operation (Stobie et al 1979):
1) Mapping Mode: In this mode the machine digitizes a complete area and stores the transmission value of every pixel. The main astronomical use of this mode is the detailed investigation of structure in gaseous nebulae and in nearby galaxies. At 8 μm resolution a 625 mm^2 area is measured in 8 minutes and fills a 750 m magnetic tape with some 10 million pixels. Obviously this mode is not suitable for measuring entire large plates (e.g. a 35 cm square plate would need nearly 200 magnetic tapes!).
2) Thresholded Mapping Mode: The measurement proceeds as in the Mapping Mode except that only those pixels with transmission values less than a certain pre-assigned percentage (usually 7-10%) below the measured plate background are stored. The local background transmission is found via a digital filtering technique (Martin and Lutz 1979). In addition to the transmission value of each pixel its coordinates must also be retained. A data compression factor of greater than 10 is commonly achieved over the Mapping Mode output.
3) Astronomical Image Analysis Mode: Currently this mode is carried out off-line using the data from either modes 1) or 2) though shortly it will be transferred on-line using a fast dedicated microprocessor. In this mode the thresholded mapping data are passed through a software pattern analyser (Lutz 1979) which connects up pixels belonging to the same image.

Star-Galaxy image separation

In problems involving stellar or galaxian statistics there is a need when sampling large numbers of celestial objects to find a quick and convenient automatic way of distinguishing between images of stars and galaxies.

In measuring star plates with the COSMOS machine first and second order intensity weighted moments are calculated. The intensities are usually obtained from a step wedge or sensitometric spot calibration of the photographic emulsion. Each intensity value has had the local sky background subtracted from it so that the sky subtracted intensity of each pixel should be proportional to the number of photons reaching that pixel from the object in space. It is true that calculating image parameters from the moments of the intensity distribution will not be as accurate as applying more complicated off-line fitting procedures, nevertheless they are particularly valuable in real time analysis.

A plot of the maximum intensity (≡ minimum transmission) in the image, corrected for the sky background, against its area can be used to separate single

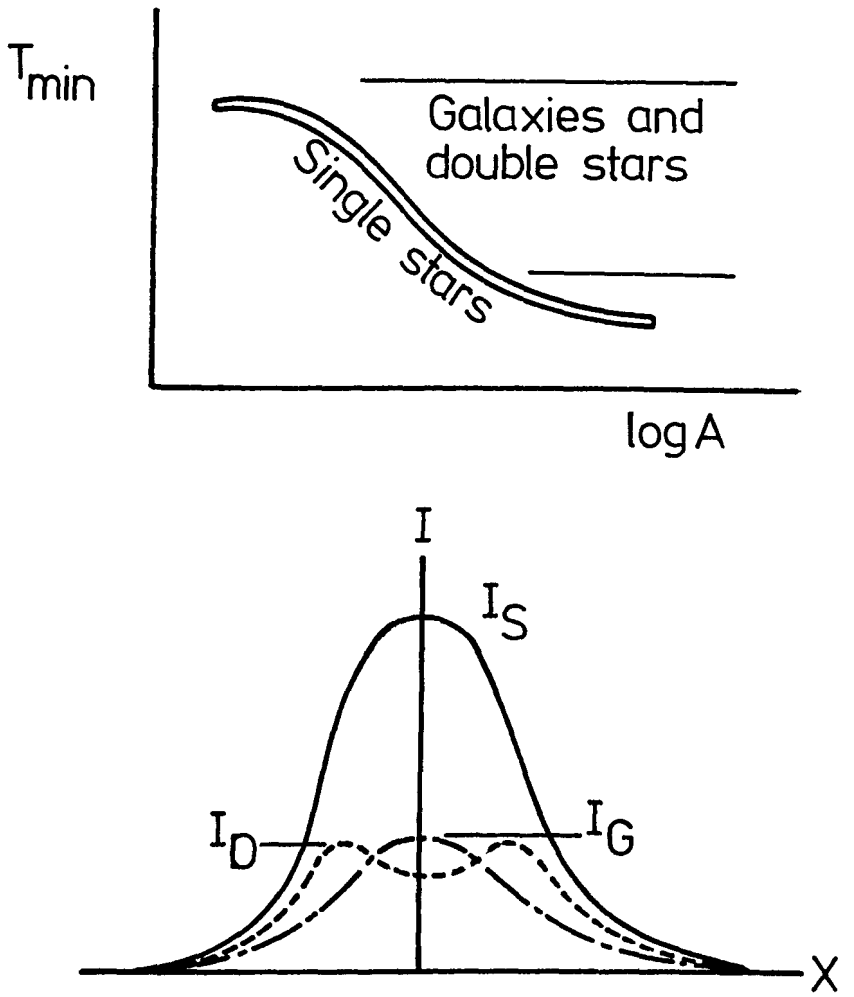

Figure 1.

Separation of star images, both double and single, from galaxy images using a T_{min} - log A plot and the second order intensity weighted moments of the image.

star images from those of double stars and galaxies (MacGillivray et al 1976). The examination of the second moments of the images can differentiate between double stars and galaxies.

Consider three images: a single star, a double star and a galaxy all with the same area as measured on the plate. Their intensity profile along an arbitrary X-axis through the major axis of the galaxy and the line of centres of the binary would appear as shown in figure 1.

The single star may be separated from the galaxy because, though their images have the same area

$$I_S > I_G$$

The galaxy may be separated from the double star because, for the same image area and maximum intensity ($I_D = I_G$)

$$\left(\frac{\Sigma x^2 I}{\Sigma I}\right)_D > \left(\frac{\Sigma x^2 I}{\Sigma I}\right)_G$$

Using this method the probability of an image being correctly identified has been shown to be greater than 90% by comparing COSMOS output with original plate material. For the observational material cited below the limiting magnitude to which successful separation between different types of image could be carried out was $m_J \sim 22$.

Observational Data

The photographic plate used (J2697) was obtained with the 1.2 m U.K. Schmidt Telescope in Siding Spring N.S.W. It was a 55 minute exposure through a GG395 filter on to a IIIaJ emulsion centred on $\alpha(1950) = 01^h32^m$, $\delta(1950) = -30^o00'$ ($\ell = 231^o$, $b = -80^o$).

Measurements were made with COSMOS on the unvignetted central 20 cm ($\simeq 3^o.8$) square of the plate. Output for this investigation were image centroids (to $\pm$ 1.5 μm (Stobie et al 1979)) and magnitudes (to $\pm 0^m.15$ (Dodd et al 1979)) for 28872 galaxies to $m_J = 22$.

Image magnitude was obtained by converting the pixel transmission to intensity by means of the step wedge exposure on the plate, and summing the intensities above the isophotal threshold level ($m_J = 25.25$ mag arcsec^{-2} isophote for these data) after subtraction of the sky component. Zero point calibration for the magnitudes was provided by the recalibrated night sky photometer reading which was recorded whilst the plate was being exposed.

Figure 2.

Covariance function for 28,872 galaxies in the 15 square degrees centred on $\ell = 231^{o}$, $b = -80^{o}$ to $m_J = 22$.

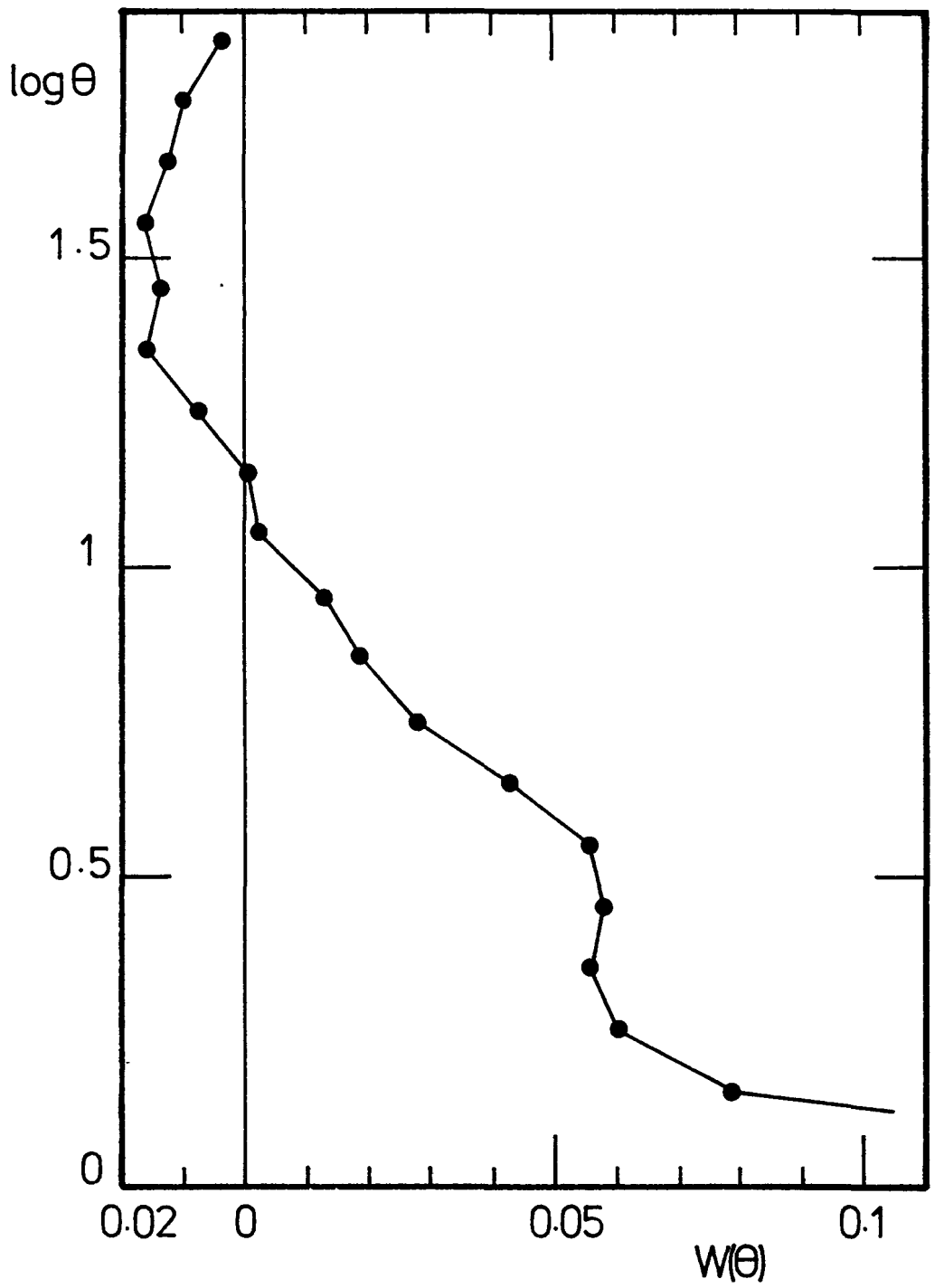

Distribution of Galaxy Images

The distribution of the galaxy images was examined in three different ways: using firstly the method of Fesenko and Pit'ev (1975) and Fesenko and Fesenko (1978), secondly the covariance technique of Peebles (1973) as modified by Dodd et al (1976) and thirdly by comparing the observational data with computer generated stochastic models (Dodd (1977), MacGillivray et al (1979)).

Using the first technique the measured region was divided into 2304 (48 x 48) cells of side 4.27 mm ($0^{\circ}.08$ in each of which counts of galaxy images to a limiting magnitude $m_J = 22$ were made (see MacGillivray and Dodd (1980)). Several rich clusters are visible (Braid and MacGillivray (1978)) but the scale of the density fluctuations they introduce is smaller than that of the field.

If the number of galaxies in any cell is n with n' in an adjacent cell then the following expression gives a value $< s >$ for the mean number of galaxies per cluster

$$< s > = \frac{< n^2 > - < nn' >}{< n >}$$

This value is dependent on the cell size chosen and was recomputed for different cell sizes from $0^{\circ}.08$ to $0^{\circ}.64$ side. For cell sizes larger than $0^{\circ}.16$ side $< s >$ increases linearly with $< n >$. A straight line fitted through these points was used to find the value of $< s >$ which corresponds to $< n > = 0$. This value is 3.6 galaxies per cluster.

To examine the angular distribution of the galaxies the covariance function described by Peebles (1973), Dodd et al (1976) and Phillipps et al (1978) was used. For deep small angle surveys the covariance function may be expressed in the form

$$1 + w(\theta) = n(\theta)/(N_c N \delta\Omega)$$

where $n(\theta)$ is the number of pairs of images with separation θ, N_c is the number of galaxies taken as centres, N is the number of galaxies per steradian and $\delta\Omega$ is the solid angle of the ring of width $\delta\theta$ at distance θ. In practice counts are performed in semi-annuli to avoid counting galaxies in the same pair twice. For the random, no clustering, case $w(\theta) = 0$, and if the galaxies are clustered then $w(\theta) > 0$.

A plot of $w(\theta)$ against $\log\theta$ for the galaxies measured is shown in figure 2. If we take $q_0 = +1$ and $z^* = 0.44$ (for ellipticals at B = 22 with $M^* = -21$ and K-corrections from Pence (1976) assuming no absorption near the galactic poles) then for this region the characteristic linear size for clustering, R_c^*, works out at $6\,h^{-1}$ Mpc which may be compared with the $9\,h^{-1}$ of Groth and Peebles (1977) for the counts of the Lick catalogue to a limiting magnitude of B = 19 and the $3\,h^{-1}$ of Shanks et al (1980) for an adjacent region to a limiting magnitude of $m_J \sim 21.5$.

The third method used to examine the distribution of the galaxies in the field was to compare the observations with a series of stochastically generated models and look for a best fit.

In the model (MacGillivray et al 1979) a volume of space is populated whose dimensions are specified by the actual angular extent of the photographic plate measured and an arbitrarily chosen distance range ($100 \leq r \leq 3000$ Mpc). The galaxies may be solitary objects or members of a cluster which in turn may be a member of a supercluster. The apparent magnitude of a galaxy was determined (Dodd 1977) by pseudo-random number pair selection biased by the absolute luminosity function of Arakelyan and Kalloglyan (1970), distance dimmed and corrected for both cosmological (Mattig 1958, Sandage 1961) and K (Pence 1976) effects. No correction was made for the effect of galactic absorption which was assumed to be minimal at the high galactic latitude of the observed field. If the determined apparent magnitude were greater than the known actual limiting magnitude of the real plate then the model galaxy was rejected.

Parameters which were varied were the value of q_0, the number of clusters in a supercluster, the number of galaxies in a cluster, the sizes of both clusters and superclusters, and the percentage of galaxies appearing as isolated field objects.

As with the observations, the field being modelled was divided, in projection, into an array of cells 2 mm square. The number of galaxies in each cell was determined and thence the number of cells with a given number of galaxies per cell. The modelled distribution was compared with the observed distribution using the χ^2 statistic.

In all cases for a given set of parameters the inclusion of superclustering made the χ^2 fit less good. The best fit was obtained for a model with 60% field galaxies and the rest in small clusters of 2 or 3 members of diameter 2 Mpc.

This result agrees well with that using the method of Fesenko and Pit'ev remembering that the value for mean clustering membership in that case makes no allowance for field galaxies which in consequence are presumed to be members of a cluster. Fesenko and Fesenko (1978) also estimate that 60% of galaxies in the Lick data are isolated, with the majority of the remainder in small groups.

Galaxian Apparent Luminosity Function

The number-magnitude count for galaxies from the COSMOS data in this field is shown as the filled circles in figure 3. Error bars represent the statistical $\sqrt{N}$ errors of the points. Also shown are the counts at the North Galactic Pole

Figure 3.

Number-magnitude count for galaxies in the field of side 3.8^{o} centred on $\ell = 231^{o}$, $b = -80^{o}$ to $m_J = 22$.

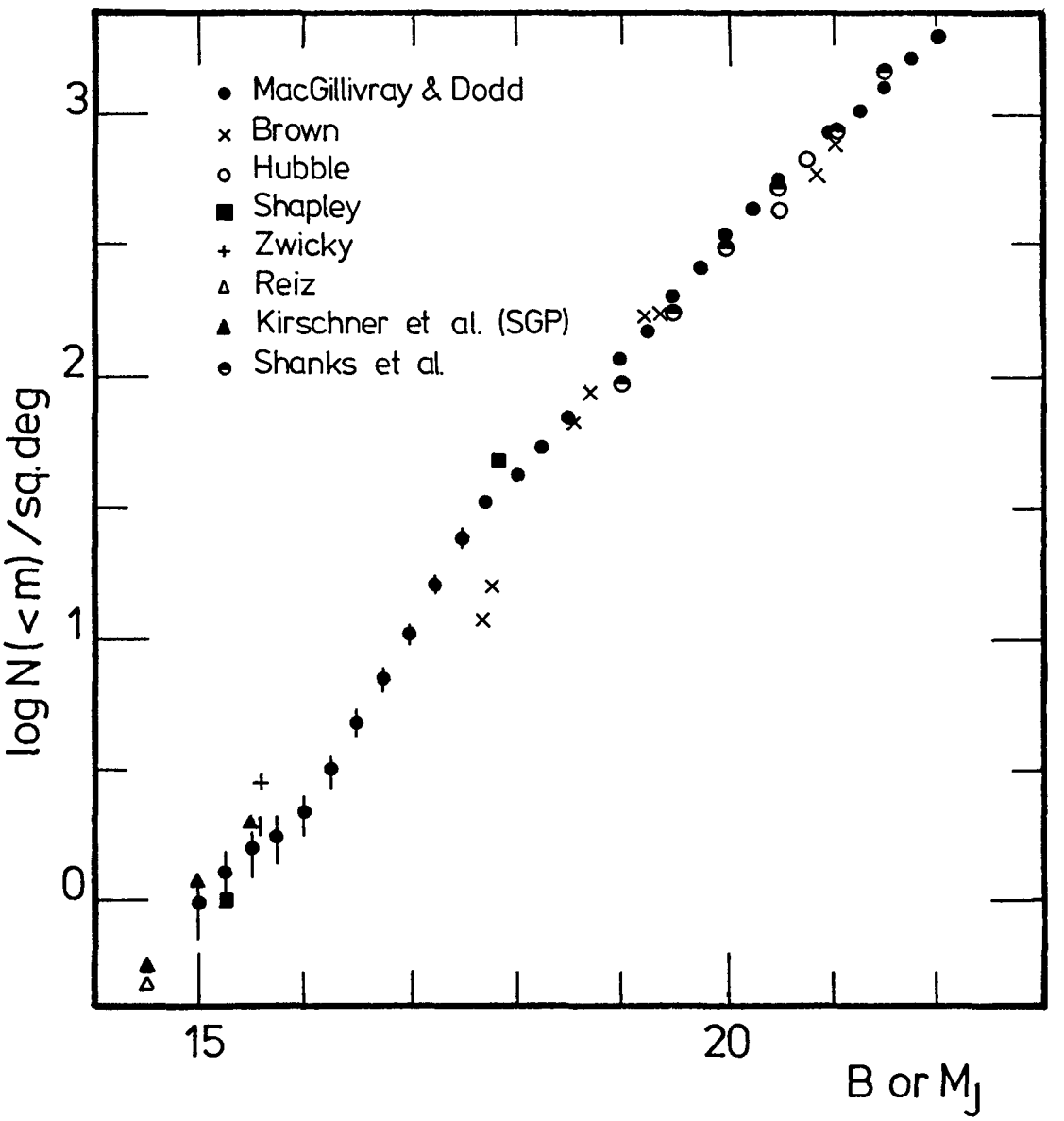

by other investigators and counts at the South Galactic Pole by Kirschner et al (1978) and Shanks et al (1979). The abscissa may be plotted as either B or m_J since very little difference was found in comparing the magnitudes of galaxies in the B and m_J systems (Dodd et al 1979). The uncertainty in the zero point may cause the m_J magnitudes to be too bright or too faint by a few tenths of a magnitude. This zero point error serves to slide the points along the abscissa only.

Comparing the distribution of faint galaxies between the North and South Galactic Pole regions suggests that no large scale anisotropy is present. However there is a deficiency in the counts of galaxies at $m_J \sim 16.0$ which is similar to that at $B \sim 17.5$ in the northern sky. Brown (1974) and de Vaucouleurs (1977) interpret this deficiency as indicating the 'edge' of the local supercluster, beyond which there is a lower than average galaxy density until the next large scale structure is detected. The fact that the deficiency occurs at a brighter apparent magnitude in the southern sky might be taken to suggest that in the direction of the SGP we are closer to the edge of the Local Supercluster than at the NGP.

Conclusions

Described above are two of the uses to which COSMOS data may be put in the study of the spatial and luminosity distribution of galaxies. Other parameters which have also been studied, with particular reference to clusters of galaxies, are orientations, ellipticities and colours.

References

Arakelyan, M. A. and Kalloglyan, A. T., 1970. Sov. Phys. Astr., 13, 953.

Braid, M. K. and MacGillivray, H. T., 1978. Mon. Not. R. astr. Soc., 182, 241.

Brown, G. S., 1974. Ph.D. Thesis, University of Texas at Austin.

de Vaucouleurs, G., 1977. Occ. Rep. R. Obs. Edinburgh, No. 2.

Dodd, R. J., 1977. Astrophys. Sp. Sc., 46, 499.

Dodd, R. J., MacGillivray, H. T., Ellis, R. S., Fong, R. and Phillipps, S., 1976. Mon. Not. R. astr. Soc., 176, 33P.

Dodd, R. J., MacGillivray, H. T., Smith, G. M. and Ellery, L. A., 1979. International Workshop on Image Processing in Astronomy, Trieste, Italy.

Fesenko, B. I. and Pit'ev, N. P., 1975. Sov. Astron., 18, 436.

Fesenko, B. I. and Fesenko, L. M., 1978. Sov. Astron., 22, 155.

Groth, E. J. and Peebles, P. J. E., 1977. Astrophys. J., 217, 385.

Kirschner, R. P., Oemler, A. and Schechter, P. L., 1978. Astron. J., 83, 1549.

Lutz, R. K., 1979. International Workshop on Image Processing in Astronomy, Trieste, Italy.

MacGillivray, H. T., Martin, R., Pratt, N. M., Reddish, V. C., Seddon, H, Alexander, L. W. G., Walker, G. S. and Williams, P. R., 1976. Mon. Not. R. astr. Soc., 176, 265.

MacGillivray, H. T., Dodd, R. J. and McNally, B. V., 1979. Astrophys. Sp. Sc., In press.

MacGillivray, H. T. and Dodd, R. J., 1980. Mon. Not. R. astr. Soc., Submitted.

Martin, R. and Lutz, R. K., 1979. International Workshop on Image Processing in Astronomy, Trieste, Italy.

Mattig. W., 1958. Astron. Nachr., 284, 109.

Peebles, P. J. E., 1973. Astrophys. J., 185, 413.

Pence, W., 1976. Astrophys. J., 203, 39.

Phillips, S., Fong, R., Ellis, R. S., Fall, S. M. and MacGillivray, H. T., 1978. Mon. Not. R. astr. Soc., 182, 673.

Pratt, N. M., 1977. Vistas Astr., 21, 1.

Sandage, A., 1961. Astrophys. J., 133, 355.

Shanks, T., Fong, R., Ellis, R. S. and MacGillivray, H. T., 1980. Mon. Not. R. astr. Soc., In press.

Stobie, R. S., Smith, G. M., Lutz, R. K. and Martin, R., 1979. International Workshop on Image Processing in Astronomy, Trieste, Italy.

DEEP IMAGERY OF QUASAR FIELDS: TECHNIQUES

P. A. WEHINGER* AND T. GEHREN
Max Planck Institut für Astronomie, Heidelberg, FRG

AND

S. WYCKOFF*
Arizona State University, Tempe, AZ, USA

ABSTRACT:

Deep large-scale photographic plates of 16 quasar fields have been obtained to search for faint underlying structure (≲10 arc sec) to surface brightness levels of approximately ~1 percent of the red night sky (~26 mag/sq. arc sec). The imagery data are presented in the form of logarithmic intensity contour maps and logarithmic intensity profiles. PDS scanning techniques and reduction procedures are described, including details about intensity calibration, evaluation of the sky background, improvement in the signal-to-noise ratio by circular averaging of the quasar intensity profiles, and desaturation of stellar and quasar images.

INTRODUCTION:

This paper deals with the techniques used to detect subtle extended structures associated with photographic images of quasars. Sandage (1971) proposed that quasars are the luminous nuclei of giant elliptical galaxies; while Kristian (1973) suggested that quasars are events in the nuclei of active galaxies. Extended underlying structures have been detected around the quasars PKS 0837-12 (Wehinger and Wyckoff 1978, Wyckoff *et al.* 1980a) at z = 0.200 and Markarian 205 (Stockton *et al.* 1979) at z = 0.070.

In general, if these structures are galaxies at the cosmologi-

* Visiting Observers, European Southern Observatory, 1979.

cal redshifts of the associated quasars, then their surface brightness can be expected to be less than 10 to 15 percent of the night sky (~22 to 24 mag/sq arc sec). Thus an extremely careful procedure is required to recover reliable information from photographic plates about such faint extended objects. Similar image processing of galaxy photographs has been done recently by Burstein (1979). However, his work relates to disk profiles of SO galaxies, which are extended on a scale appreciably larger (~10's of arc sec) than our quasar profiles (≲5-10 arc sec).

For this purpose, the morphological structure of the quasar images may be divided into two categories: (a) QSO's which show asymmetric extensions like jets or tails, and (b) QSO's that exhibit symmetric image profiles which are broader than the stellar point-spread-function (PSF). Large-scale asymmetric structure, if not clearly visible on the plate itself, can be recovered quantitatively from careful processing of the isophote maps. The extension to the north of PKS 0812+020 (Fig. 1) is one such example. Further information on extended structure may be concealed in the image profile, only slightly larger than the seeing disk, and of very low surface brightness. Here we consider a quasar image to be "extended" if its surface brightness at a certain distance from the image center is well in excess of the PSF determined from scans of appropriate comparison stars. Then, instead of applying time consuming two-dimensional noise-filtering techniques, the assumption of radial symmetry of the profiles allows us to increase the signal-to-noise ratio by circular averaging. After having removed all obviously asymmetric features from the averaging procedure, the resulting one-dimensional profile of the quasar is compared with that of a star of the same magnitude.

Section II describes the observations, scanning the plates

with a PDS microdensitometer, and the calibration. In section III we explain how the sky background is evaluated, how the contour maps are produced, and the raw intensity profiles are obtained for quasars and comparison stars. An analysis of the PSF is given for stars of different color. Section IV deals with extension of the dynamic range of the stellar PSF, the desaturation of image profiles of bright objects, and finally the resulting decomposition of the quasar into a true point source and an extended underlying structure.

A detailed description of these observations as well as the astronomical results of this investigation are presented elsewhere (Wyckoff et al. 1980b).

II. OBSERVATIONS, CALIBRATION, AND SCANNING:

Observations of a sample of 16 low redshift quasars were obtained at the prime focus of the ESO 3.6-m telescope in March and September 1979, using the single-element Gascoigne corrector, recorded on Kodak IIIa-F plates, baked in forming gas, through a Schott OG 570 (3 mm) or OG 550 (10 mm) filter. The resulting bandpass was 5700-6900 Å with a plate scale of 18.9 arc sec/mm.

The quantitative investigation of nearly point-like objects recorded on photographic plates is severly hampered by the low detective quantum efficiency (DQE $\lesssim$ 1-0.1 percent) yielding a rather poor signal-to-noise ratio, especially in the 5700-6900 Å spectral region. The situation becomes even more restrictive when trying to obtain spatial information on a scale not much larger than the average size of the developed grains (of the order of 10-15 μ on IIIa-F plates). Thus the digital presentation of the photographic data is governed by the aperture used with the scanning device, in our case the PDS microdensitometer at MPIA in Heidelberg. Our

final choice of a 25μ x 25μ aperture was dictated by the necessity of measuring more than a single grain through the aperture in order to minimize the scatter in the data. The sampling step was set at 10μ in x and y. Difficulties with the slow response of the log amplifier in the PDS were overcome by using one of the slowest scanning rates (2 PDS scan units or ~150μ /sec).

Intensity calibration was provided by means of the ESO spot sensitometer (Wood, 1975). The onset of saturation was approximately at a density of 3.5, giving a reliable, though non-linear calibration up to a density of 4.0. Above that level any direct information on image intensity is lost completely by saturation. However, under certain assumptions the intensity can be recovered by the desaturation method described in Section IV. For each plate the images of the quasar and at least two comparison stars were scanned, converted to intensities, and stored in two-dimensional arrays of 150 x 150 pixels, thus extending out to 15 arc sec from the image center.

III. BASIC IMAGE PROCESSING AND INTENSITY PROFILES:

The evaluation of the night sky level, depending on (x,y) position, presents a problem very similar to the determination of the continuum as a function of wavelength from one-dimensional spectrograms. To our knowledge no straightforward solution exists. In the one-dimensional case, more information on continuum position may be recovered by spectral synthesis. What can be done, by analogy to spectroscopy, is to search for background "windows" within which all samples are fitted to a least-square surface of a specified order. This approach has been successfully used in our analysis. The night sky windows, lying as far as possible from the image center, were chosen to be free from non-uniform features. The samples

were fitted to a first-order intensity surface (to account for large-scale gradients), and the isophotal map served as a final test. This method is equivalent to the one described by Burstein (1979). In fact, using a density distribution method yields the same results to within 0.5 percent.

The average night sky was subtracted from the intensity array and the remaining intensity values imaged onto an isophotal map. In order to present the full range of image intensities, the isophotes were spaced logarithmically, starting with the first contour between 2 and 6 percent of the night sky surface brightness. The contour plot included optional averaging up to 5 x 5 pixels in order to smooth the plate-grain noise.

A photographic print and isophotal map of the quasar PKS 0812+020 (z_e = 0.402) are shown in Figs. 1 and 2, respectively, reproduced from an ESO 3.6-m prime-focus plate. Isophotal maps of two comparison stars are presented in Figs. 3a and 3b, derived from the same plate. The numbers to the left of each isophotal map denote the contour intensity values in percent of the red night sky surface brightness. The scale on the right is in arc seconds.

The position and area of the background windows for PKS 0812+020 are shown in Fig. 2a (as dashed circles); where the single isophote respresents the intensity average over the total array. Thus position and extension of all features standing out from the background are clearly visible. Figs. 2b, 3a, and 3b show the final contour maps for the QSO and for the two comparison stars. The brightest isophotes (shown in Fig. 3) are slightly irregular in shape, thus indicating slight guiding errors. The asymmetric extension 3-6 arc sec north of the QSO, as well as some possible faint cluster galaxies (F = ~20-22 mag) are easily detected.

To recover possible extended structure of the QSO, intensity

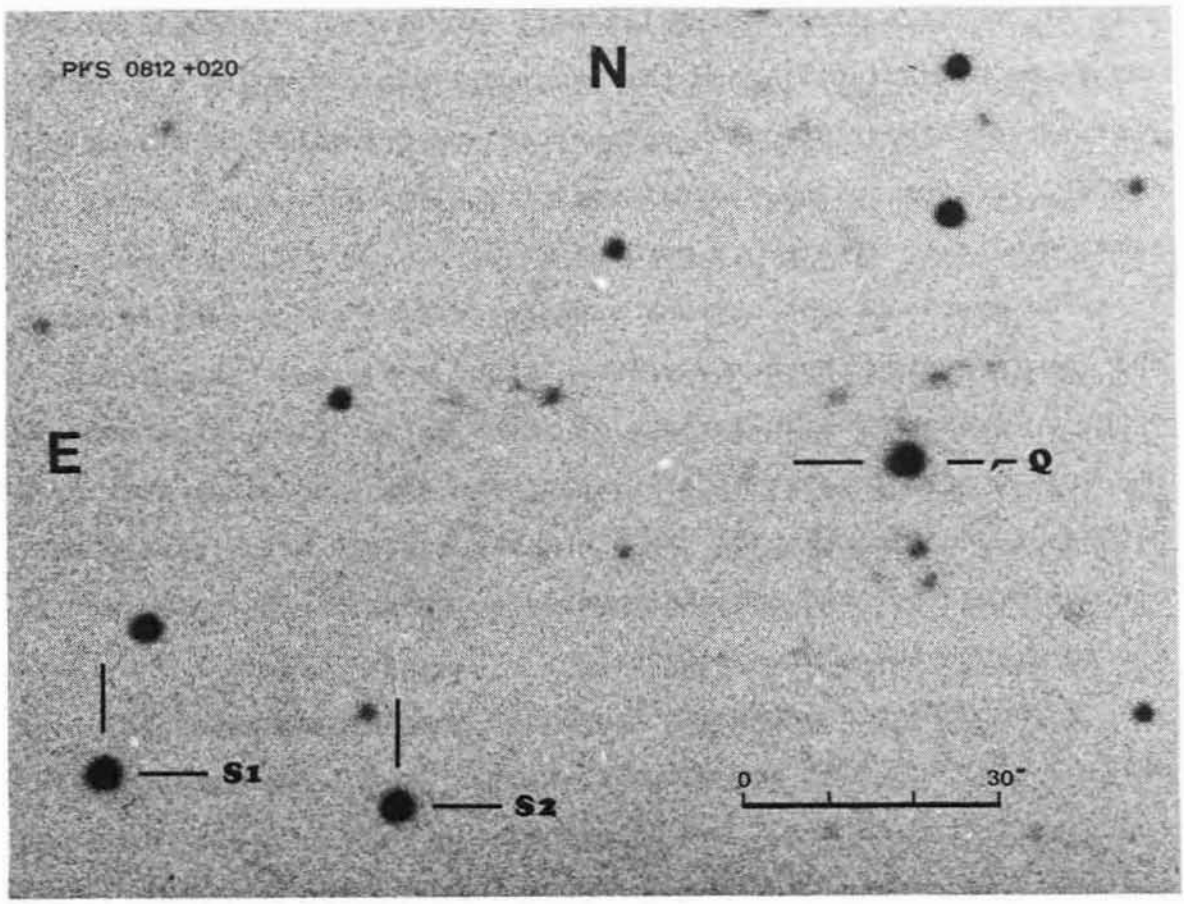

Figure 1. Photographic print of the quasar PKS 0812+020, ESO 3.6-m IIIa-F plate + OG 550 filter, 60-min exposure. Quasar and comparison stars are labeled (Q, S1, and S2).

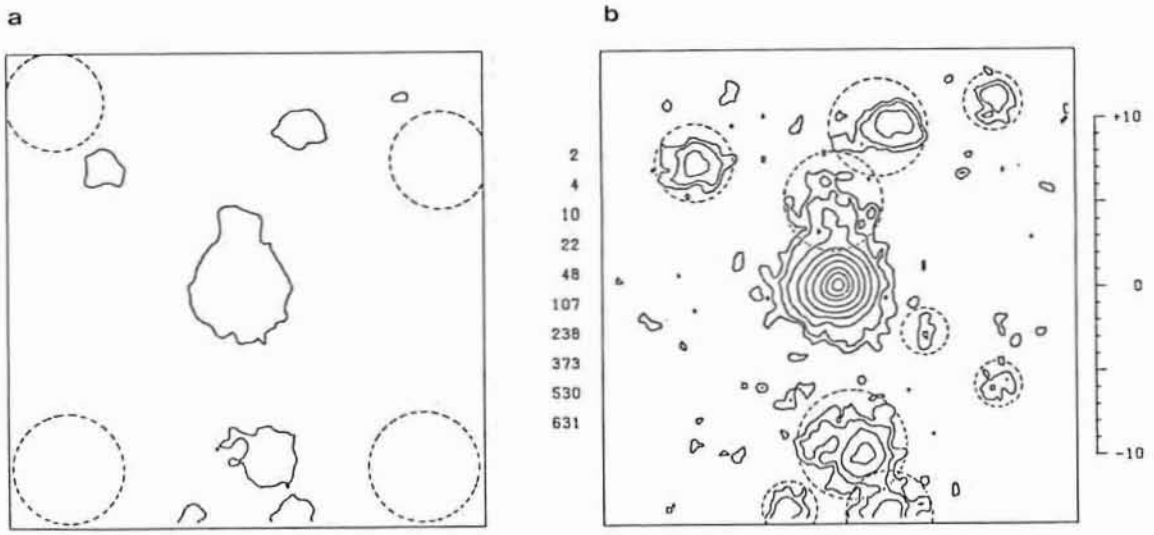

Figure 2a. Partial isophotal map used to determine the average sky background (see text). Figure 2b. Logarithmic intensity contour map of the quasar PKS 0812+020. Scale is given at right in arc sec. Quasar is at center.

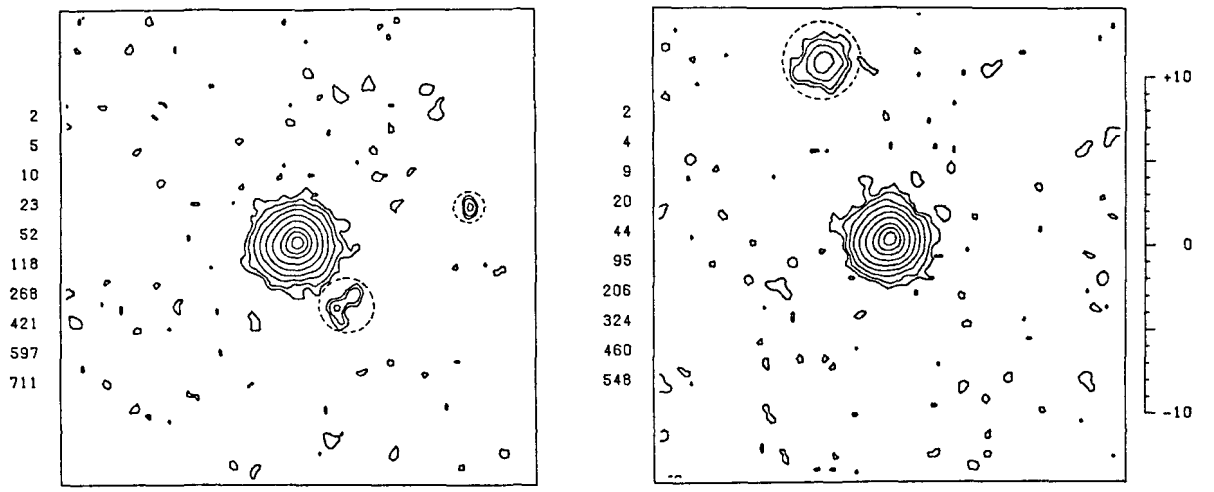

Figure 3a and 3b. Logarithmic intensity contour maps of two comparison stars (S1 and S2, from Fig. 1). Surface brightness is given at left of each map in percent of the red night sky.

profiles of the quasar and the comparison stars have been constructed assuming radial symmetry of the objects. The profile sampling area was chosen around each object so that: (a) the outer limit (~15 arc sec) merged with the local background, and (b) all samples were excluded that obviously deviated from radial symmetry (indicated by the dashed circles in Figs. 2b, 3a, and 3b). The remaining samples have been grouped according to their distance from the object center. Thus the nth subset included all samples with $r_{n-1} \leq r < r_n$, where $r_o = 0$ and $r_n - r_{n-1} = 10\mu$ (corresponding to 0.189 arc sec). Finally, within each group, angular distances (r) and intensities were averaged. Admittedly, the assumption of radial symmetry, necessary for this method, is only a rough approximation to the true intensity distribution, especially if, for example, the underlying structure is a galaxy seen edge-on. However, this method provides for a reasonable measure of extended structure and gives a reliable estimate of the object's average surface brightness and integrated magnitude (cf. Section IV).

The circular averages of the object profile have been normalized to the intensity of the object centers and are shown in Fig. 4

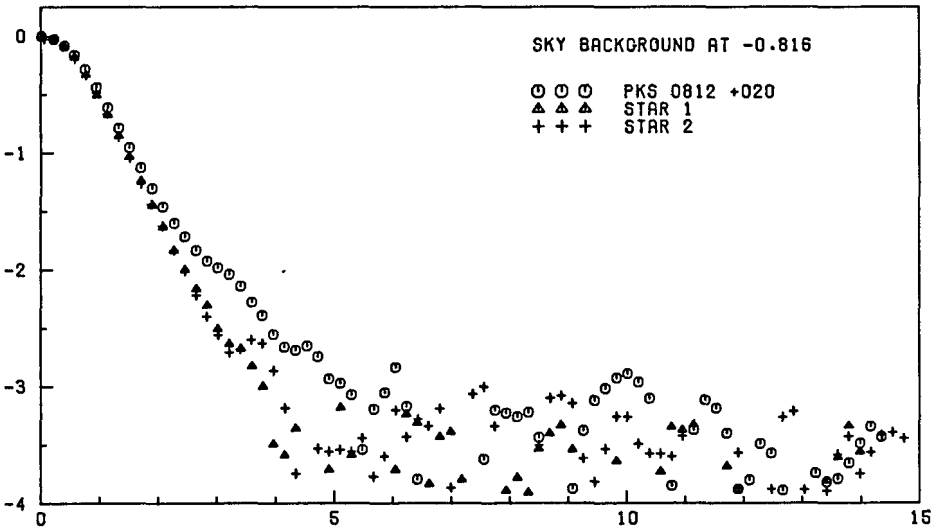

Figure 4. Image profiles for the quasar PKS 0812+020 and two comparison stars. Logarithmic intensity versus radial distance in arc sec. Central intensity has been normalized to QSO. The extended image profile of the quasar (circles) is most prominent 2-5 arc sec from the QSO image center at 10-1 percent of red night sky surface brightness.

on a logarithmic intensity scale. Profiles for the QSO and the two comparison stars are given in Fig. 4 , where the excess intensity of the quasar profile is immediately evident outside $\sim$ 2.5 arc sec. At 5-6 arc sec the QSO profile merges with the noise inherent in the PSF.

In order to use the stellar intensity profiles as the seeing disk of a point source (PSF), its independence upon color has to be verified, since the QSO's are blue objects whereas our comparison stars are normally red. For one plate such a comparison of the profiles of blue and red stars, selected according to their appearance on the Palomar Sky Survey plates is shown in Fig. 5. All stars are $\sim$ 18-19 mag and were normalized to their central intensity, which is 2-3 mag/arc sec sq. above the night sky. No systematic differences between the blue and red PSF's can be seen; hence it seems justified to refer to a stellar seeing disk as "the" point spread function, irrespective of color within the observed band-

pass (5700-6900 Å).

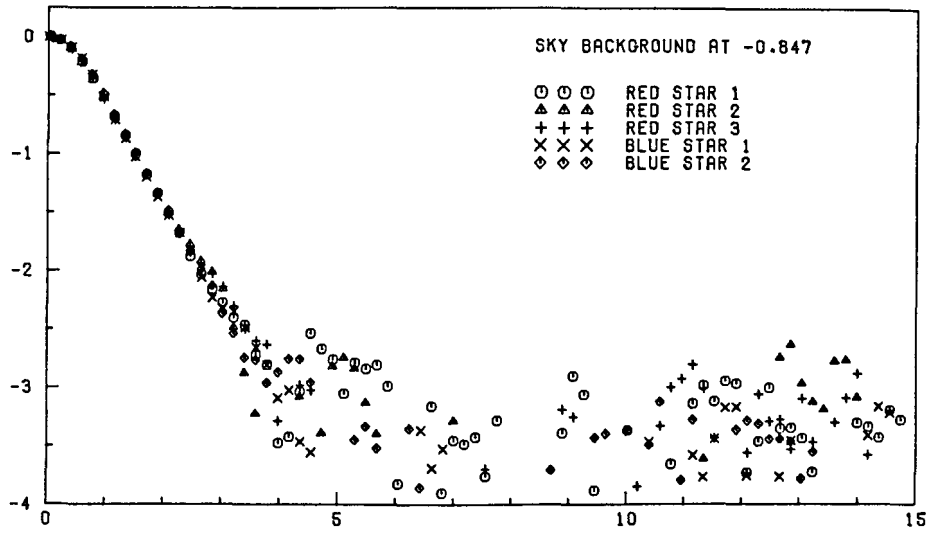

Figure 5. Comparison of image profiles of three red stars and two blue stars. Logarithmic intensity versus radial distance in arc sec. Profiles derived from PDS scans from one plate in the 5700-6900 Å bandpass.

IV. DESATURATION AND DECOMPOSITION:

Since the extended structures associated with the quasars are very faint, exposure times had to be adjusted to recover a sufficient signal-to-noise ratio near the sky background. As a result some of the quasar centers were saturated, forming a plateau out to r_s = 1 arc sec. In these case a desaturation method was used to recover an approximate brightness scale and to properly adjust the QSO profile and the PSF. The comparison stars were selected so that one of them was strongly saturated at the center, whereas the second was comparatively faint and unsaturated. After having determined a distance $r_o > r_s$, where the bright comparison star was clearly unsaturated, the profiles of both comparison stars were renormalized at r_o. The final PSF was taken to be the profile of the faint star for $r \leqslant r_o$ and from the bright star for $r > r_o$. This procedure is simply based on image growth and it implies that at

$r = r_o$ both comparison star profiles have the same intensity gradient. It has the additional advantage that the near background parts of the composite PSF show an improved signal-to-noise ratio. This procedure has been applied to the comparision stars in general, even if none of these objects were saturated. Thus, the outer parts of the PSF are always taken from the brighter of the two comparison stars.

The desaturation of the quasar profile is based on the same principle: a radius $r_q > r_s$ was determined, at which the intensity profile gradients of the QSO and the composite PSF were the same. The desaturated quasar profile then was taken to be the composite PSF for $r \leq r_q$ and the original quasar profile, renormalized to the PSF at r_q, for $r > r_q$. The desaturation method described here has been checked independently by comparing surface brightness scales derived from the integrated magnitude of some well saturated quasar images with the level of the sky brightness computed relative to the QSO center and consistent results were found.

The final image profiles of PKS 0812+020 and the composite PSF of the comparison stars are presented in Fig. 6, where the surface brightness is given in mag/sq arc sec (for the 5700-6900 Å region, i.e. the 'F' bandpass) on the left and in terms of the surface brightness of the red night sky on the right. Here we have assumed that the integrated apparent magnitude in V and F bandpasses are approximately equal. While the zero point of the night sky level is determined from the PDS scans, the object surface brightness (in mag/sq arc sec) scale depends on the measured photoelectric magnitude of the quasar (for PKS 0812+020, V = 18.50, as given in Burbidge et al. 1977).

We now assume that the quasar profile is composed of a central point source (the quasar itself) and an extended underlying

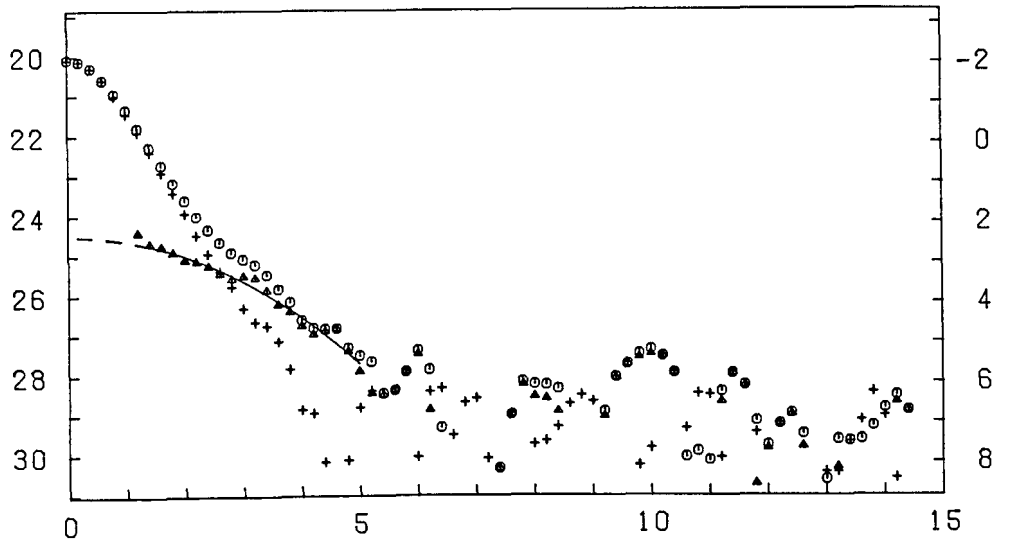

Figure 6. Calibrated surface brightness (mag/sq arc sec in 5700-6900 Å bandpass) (on left) versus radial distance in arc sec for the quasar PKS 0812+020. Symbols: QSO (o), stellar PSF (+), difference between QSO and PSF (△). Averaged best-fit profile (solid line) underlying extended structure. Surface brightness relative to red night sky in mag/sq arc sec (on right).

structure. Then, the average profile of the underlying structure is represented by the difference between the quasar profile and the PSF, which is also shown in Fig.6 . The integrated apparent magnitude of the underlying structure is F = 21.0 mag, i.e. of the same order as the surrounding extended objects, which are probably cluster galaxies.

We wish to thank David Burstein, John Kormendy, Harry van der Laan, and Jim Westphal for suggestions and helpful comments. We are grateful to the ESO Observing Program Committee for telescope time and to ESO for partial support of this research.

REFERENCES

Burbidge, G.R., Crowne, A.H., and Smith, H.E. 1977, Ap. J. Suppl. 33, 113.

Burstein, D. 1979, Ap. J. Suppl. 41, No. 3 (in press).

Kristian, J. 1973, Ap. J. Letters 179, L61.

Sandage, A. 1971, in Pont. Acad. Sci. Scripta Varia, 35, Nuclei of Galaxies, ed. by O'Connell, D.J.K., p. 271.

Stockton, A., Wyckoff, S., and Wehinger, P.A. 1979, Ap. J. 231, 673.

Wehinger, P.A., and Wyckoff, S. 1978, M.N.R.A.S. 184, 335.

Wood, H.J. 1975, ESO Bulletin, No. 11, p.21.

Wyckoff, S., Wehinger, P.A., Spinrad, H., and Boksenberg, A. 1980a, Ap.J. (in press).

Wyckoff, S., Wehinger, P.A., and Gehren, T., 1980b, preprint.